

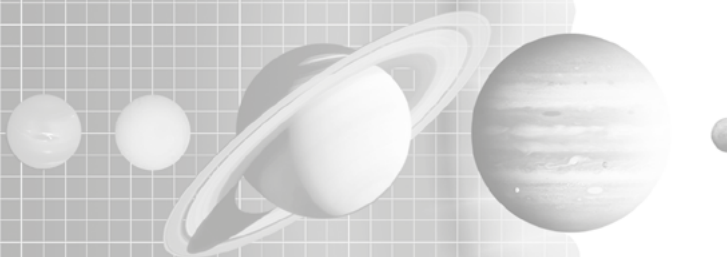
ДЕВЯТЫЙ
МОСКОВСКИЙ
СИМПОЗИУМ
ПО СОЛНЕЧНОЙ СИСТЕМЕ

THE NINTH
MOSCOW
SOLAR SYSTEM
SYMPOSIUM



8-12 ОКТЯБРЯ 2018
ИНСТИТУТ
КОСМИЧЕСКИХ ИССЛЕДОВАНИЙ РАН
МОСКВА

8-12 OCTOBER 2018
SPACE RESEARCH INSTITUTE
MOSCOW



SPONSORED BY:

- Russian Foundation for Basic Research (RFBR)
- Grant of the Government of the Russian Federation
- Space Research Institute RAS

WITH PARTICIPATION:

- Vernadsky Institute of Geochemistry and Analytical Chemistry RAS
- Brown University, USA
- Earth Physics Institute RAS
- Keldysh Institute of Applied Mathematics RAS
- Radio Electronics Institute RAS
- Sternberg Astronomical Institute, Moscow State University

TABLE OF CONTENT

INTRODUCTION

PROGRAM COMMITTEE

PROGRAM

overview PROGRAM

scientific PROGRAM

ABSTRACTS

INFORMATION

ADDRESS

METRO MAP

REGISTRATION AND INFORMATION DESK

SCIENTIFIC SESSIONS

POSTER SESSIONS

SOCIAL PROGRAM

INTERNET ACCESS AND WiFi

LUNCH POINTS

THE NINTH MOSCOW SOLAR SYSTEM SYMPOSIUM 9M-S³

**SPACE RESEARCH INSTITUTE
MOSCOW, RUSSIA
October 8-12, 2018**

Starting from 2010, the Space Research Institute holds annual international symposia on Solar system exploration. Main topics of these symposia include wide range of problems related to formation and evolution of Solar system, planetary systems of other stars; exploration of Solar system planets, their moons, small bodies; interplanetary environment, astrobiology problems. Experimental planetary studies, science instruments and preparation for space missions are also considered at these symposia.

The Ninth Moscow international Solar System Symposium (9M-S³) will be held from October 8 till 12, 2018.

Subject matter of this symposium will cover many problems of the Solar system science with the central topic "Moon, Mars and Venus research". This topic relates to scientific problems of several missions: «Mars Express», «Venus Express», the missions under development in Russia: "Luna-Glob", "Luna-Resource", "ExoMars 2016" and "ExoMars 2020" (Roscosmos-ESA).

THE FOLLOWING SESSIONS WILL BE HELD DURING THE SYMPOSIUM:

- OPENING SESSION
- session: MARS
- session: VENUS
- Session: EXOPLANETS
- Session: SOLAR WIND INTERACTIONS
WITH PLANETS AND SMALL BODIES
- Session: SMALL BODIES
- Session: GIANT PLANETS
- Session: DUST AND DUSTY PLASMA IN SPACE
- Session: MOON SCIENCE AND EXPLORATION

Space Research Institute holds this symposium with participation of the following organizations:

- RUSSIAN FOUNDATION FOR BASIC RESEARCH, RUSSIA
- VERNADSKY INSTITUTE OF GEOCHEMISTRY AND ANALYTICAL CHEMISTRY, RUSSIA
- BROWN UNIVERSITY, USA
- EARTH PHYSICS INSTITUTE, RUSSIA
- KELDYSH INSTITUTE OF APPLIED MATHEMATICS, RUSSIA
- RADIO ELECTRONICS INSTITUTE, RUSSIA
- STERNBERG ASTRONOMICAL INSTITUTE, MOSCOW STATE UNIVERSITY, RUSSIA

Symposium website: <https://ms2018.cosmos.ru>
Contact email address: ms2018@cosmos.ru

*Мероприятие проводится при финансовой поддержке
Российской академии наук,
Российского фонда фундаментальных исследований, проект
№ 18-02-20132,
Правительства РФ, грант №14.W03.31.0017 от 16 февраля 2017г.*

PROGRAM COMMITTEE

chair:

acad. **ZELNYI L.M.** IKI RAS

members:

BAZILEVSKIY A.T. GEOHI RAS

BIBRING J.-P. IAS,CNRS, France

BOLTON S.J. Southwest Research Institute, USA

BOROVIN G.K. Keldysh AMI RAS

CHICARRO A. ESTEC, ESA

DUXBURY T. George Mason University, USA

HEAD III J. Brown University, USA

KORABLEV O.I. IKI RAS

KOSTITSYN Y.A. GEOHI RAS

MAROV M.Ya. GEOHI RAS

MITROFANOV I.G. IKI RAS

RODIN A.V. IKI RAS

SHEVCHENKO V.V. GAISH MSU

SMIRNOV V.M. IRE RAS

SVEDHEM H. ESTEC, ESA

VAISBERG O.L. IKI RAS

VOROBYOVA E.A. MSU

WITASSE O. ESTEC, ESA

WU Ji National Space Science Center, China

ZHARKOV V.N. IFZ RAS

ZAKHAROV A.V. IKI RAS

ZASOVA L.V. IKI RAS

secretary:

ROSTE O. IKI RAS, ms3@iki.rssi.ru

overview 9M-S³ program

THE NINTH MOSCOW SOLAR SYSTEM SYMPOSIUM (9M-S³)

IKI RAS, 8-12 october 2018

	8 october	9 october	10 october	11 october	12 october
10.00	OPENING SESSION	session 2. VENUS	session 5. SMALL BODIES	session 6. GIANT PLANETS	session 8. MOON SCIENCE AND EXPLORATION
	session 1. MARS	session 3. EXOPLANETS	session 5. SMALL BODIES	session 6. GIANT PLANETS	session 8. MOON SCIENCE AND EXPLORATION
11.40	coffee	coffee	coffee	coffee	coffee
12.00					
	session 1. MARS	session 3. EXOPLANETS	session 5. SMALL BODIES	session 6. GIANT PLANETS	session 8. MOON SCIENCE AND EXPLORATION
13.00	lunch	lunch	lunch	lunch	lunch
14.00		session 4. SOLAR WIND	session 5. SMALL BODIES	session 7. DUST	session 8. MOON SCIENCE AND EXPLORATION
	session 1. MARS	session 4. SOLAR WIND	session 5. SMALL BODIES	session 7. DUST	session 8. MOON SCIENCE AND EXPLORATION
16.00	coffee	coffee	coffee	coffee	coffee
16.20					
	session 1. MARS	session 4. SOLAR WIND	session 5. SMALL BODIES	CONCERT	session 8. MOON SCIENCE AND EXPLORATION
17.40					
18.00	POSTER SESSION	SOCIAL EVENTS IN MOSCOW	POSTER SESSION	RECEPTION	SOCIAL EVENTS IN MOSCOW
19.00	WELCOME PARTY	SOCIAL EVENTS IN MOSCOW	SOCIAL EVENTS IN MOSCOW	RECEPTION	SOCIAL EVENTS IN MOSCOW
20.00					

9M-S³ SCIENTIFIC PROGRAM

monday, 8 october 2018

Lev ZELENYI	opening remarks	10.00-10.10
Lori GLAZE	Overview of the NASA planetary science	10.10-10.30

session 1. MARS 10.30-17.45
convener: **Oleg KORABLEV**

9MS3-MS-01	Anna FEDOROVA et al	The Atmospheric Chemistry Suite (ACS) Experiment on Board the ExoMars Trace Gas Orbiter: the Results of First Six Months of Operations	10.30-10.45
9MS3-MS-02	Alexey MALAKHOV et al	Fine Resolution Epithermal Neutron detector onboard ExoMars Trace Gas Orbiter: Mars neutron mapping first results and new areas of interest	10.45-11.00
9MS3-MS-03	Jordanka SEMKOVA et al	Recent results for the space radiation environment in Mars orbit provided by FRIEND Liulin-MO dosimeter aboard ExoMars TGO	11.00-11.15
9MS3-MS-04	Dmitrij TITOV et al	Mars Express: 15 years of hard work and discoveries	11.15-11.30
9MS3-MS-05	Denis LISOV et al	Low-Fe regions along the Curiosity path in the Gale crater based on DAN active neutron probing data	11.30-11.45

coffee-break 11.45-12.15

9MS3-MS-06	Majd MAYYASI et al	Echelle Observations of Lyman-alpha emissions of H, D, and Interplanetary Hydrogen at Mars	12.15-12.30
9MS3-MS-07	James HEAD and Robin WORDSWORTH	Deciphering Noachian geological and climate history of Mars: major geologic processes and their climatic consequences	12.30-12.45
9MS3-MS-08	James HEAD et al	Two Oceans on Mars?: History, Problems and Prospects	12.45-13.00

lunch 13.00-14.00

9MS3-MS-09	Sohan JHEETA	ASTrobiology - a new kid on the block	14.00-14.30
9MS3-MS-10	Ashley PALUMBO and James HEAD	Oceans on Mars: The possibility of a Noachian groundwater-fed ocean in a sub-freezing martian climate	14.30-14.45
9MS3-MS-11	Benjamin BOATWRIGHT and James HEAD	An Integrated Model of Precipitation, Infiltration, and Groundwater Flow on Mars	14.45-15.00

9MS3-MS-12	Jessica FLAHAUT et al	Fumarolic alteration on Mars: lessons learned from terrestrial analog fieldwork	15.00-15.15
9MS3-MS-13	Vladimir A. KRASNOPOLSKY	Photochemistry of Water in the Martian Thermosphere and Its Effect of Hydrogen Escape	15.15-15.30
9MS3-MS-14	Anatoliy PAVLOV et al	High rate of atmospheric methane losses in reactions with cosmic rays produced ions as possible source of seasonal methane variations on Mars	15.30-15.45
coffee-break			15.45-16.15
9MS3-MS-15	Vladimir OGIBALOV	Non-equilibrium radiative transfer in the ro-vibrational CO ₂ bands in the Martian atmosphere taking account of radiation extinction by aerosols	16.15-16.30
9MS3-MS-16	Salvador JIMÉNEZ et al	Retrieval of an induced magnetic field in Mars ionosphere from MARSIS data. Effects of crustal and noncrustal fields	16.30-16.45
9MS3-MS-17	Oleg VAISBERG et al	Dayside magnetosphere of Mars in MSE coordinate system	16.45-17.00
9MS3-MS-18	Jürgen OBERST et al	Benefit for Mars polar science from a mission to very-low (< 150 km) orbit	17.00-17.15
9MS3-MS-19	Rustam LUKMANOV et al	Biosignatures detection from 1.88 Ga Gunflint chert with LMS suite	17.15-17.30
9MS3-MS-20	Haiming WANG et al	Bibliometric Evaluation of the Development Trend of Mars Exploration Research	17.30-17.45
POSTER SESSION (all sessions)			18.00-19.00

tuesday, 9 october 2018

session **2. VENUS**
convener: Ludmila ZASOVA

10.00-13.00

9MS3-VN-01	Daria EVDOKIMOVA et al	Variations of the lower cloud layer and H ₂ O in the deep atmosphere of Venus from the night windows observations by SPICAV-IR/VEX	10.00-10.15
9MS3-VN-02	Vladimir KRASNOPOLSKY	Venus Nighttime Photochemical Model: Nightglow of O ₂ , NO, OH and Abundances of O ₃ and ClO	10.15-10.30
9MS3-VN-03	Kandi JESSUP et al	Venus' cloud top response to the excitation of planetary scale GWs at Aphrodite	10.30-10.45
9MS3-VN-04	Ludmila ZASOVA et al	Traces of surface topography in Venus mesosphere on Venera 15 and Venus Express data	10.45-11.00
9MS3-VN-05	Mikhail LUGININ et al	Study of aerosol properties in upper haze from SPICAV-UV and -IR data	11.00-11.15
9MS3-VN-06	Sanjay LIMAYE et al	Venus as an Astrobiology Target	11.15-11.30
9MS3-VN-07	Valeriy SNYTIKOV and Leonid KSANFOMALITY	About the possible nature of living forms on Venus	11.30-11.45
coffee-break			11.45-12.00
9MS3-VN-08	Irina KOVALENKO and Natan EISMONT	Trajectory and orbit design for the Venera-D mission	12.00-12.15
9MS3-VN-09	Mikhail IVANOV et al	Venera-D Landing Site Constraints	12.15-12.30
9MS3-VN-10	Oleg VAISBERG et al	Dynamic processes in the solar wind as the cause of Venus magnetosphere and ionosphere disturbances and loss of mass	12.30-12.45
9MS3-VN-11	Sergey KOLOMIETS et al	A new criterion of the geometrical optics applicability as a foundation of a novel approach to radio occultation data interpretation	12.45-13.00

Lunch

13.00-14.00

session **3. EXOPLANETS**

14:00-16:00

convener: Alexander TAVROV

9MS3-EP-01	Shingo KAMEDA et al	Ultraviolet Spectrograph for Exoplanets (UVSPEX) onboard World Space Observatory Ultraviolet (WSO-UV)	14.00-14.20
9MS3-EP-02	Valery SHEMATOVICH et al	Atmospheric mass loss of close-in exoplanets irradiated by stellar superflares	14.20-14.40
9MS3-EP-03	Masahiro IKOMA et al	Theoretical Spectra of Highly-Irradiated Atmospheres of Transiting Exoplanets	14.40-15.00
9MS3-EP-04	Takanori KODAMA et al	The threshold of the runaway greenhouse effect for Earth-like planets	15.00-15.20
9MS3-EP-05	Jean-Loup BERTAUX et al	A new numerical inversion scheme of $m \sin i$ exoplanet mass distribution: the Neptune-Saturn desert remains after inversion	15.20-15.40
9MS3-EP-06	Vladislava ANANYEVA et al	Exoplanet mass distribution considering the observation selection factors	15.40-16.00

coffee-break

16.00-16.20

session **4. SOLAR WIND INTERACTIONS WITH PLANETS AND SMALL BODIES**

16.20-18.05

convener: Oleg VAISBERG

9MS3-SW-01	Eduard DUBININ et al	Different faces of the Martian magnetosphere	16.20-16.35
9MS3-SW-02	Eiena GRIGORENKO et al	A multiscale structure of the cross-tail Current Sheet and its relation to the ion composition according to MAVEN observations in the Martian magnetotail	16.35-16.50
9MS3-SW-03	Vladimir ERMAKOV et al	Analysis of Martian magnetic barrier	16.50-17.05
9MS3-SW-04	Sergey SHUVALOV et al	Dynamics of Hot Flow Anomalies at Mars	17.05-17.20
9MS3-SW-05	Valery SHEMATOVICH et al	Aurorae at Mars: modeling and comparison with observations	17.20-17.35
9MS3-SW-06	Peter WURZ et al	Surface release processes to populate Mercury's exosphere	17.35-17.50
9MS3-SW-07	Christoph LHOTKA et al	Motion of dust subject to solar wind and interplanetary magnetic fields	17.50-18.05

wednesday, 10 october 2018

session **5. SMALL BODIES**

10.00-17.40

conveners: Alexander BASILEVSKY,
Sergey VOROPAEV

9MS3-SB-01	Mikhail MAROV et al	Numerical simulation of thermal evolution of the comet 67 P/Churyumov-Gerasimenko nucleus	10.00-10.20
9MS3-SB-02	Jean-Loup BERTAUX and Rosine LALLEMENT	D/H ratio in water ice and in solid organics of comet 67P : Implications for the formation of the Solar system	10.20-10.40
9MS3-SB-03	Yuri SKOROV et al	Gas production rate: myths and analysis	10.40-11.00
9MS3-SB-04	Anton KOCHERGIN et al	Slow-ejected dust particles forming a crust on a cometary nucleus	11.00-11.20
9MS3-SB-05	Leonid KANFOMALITY	Some dynamic characteristics of the Hale-Bopp comet nucleus (by 1997 observations)	11.20-11.40
coffee-break			11.40-12.00
9MS3-SB-06	Alexander BASILEVSKY et al	Lineaments on the surface of consolidated material of the comet 67P nucleus	12.00-12.20
9MS3-SB-07	Sergey EFIMOV and Vladislav SIDORENKO	Semi-analytical study of mean motion resonances with application to dynamics of Kuiper belt objects	12.20-12.40
9MS3-SB-08	Vladimir BUSAREV et al	Confirmations of ice sublimation process near perihelion on primitive main-belt asteroids 779 Nina, 704 Interamnia and 145 Adeona: A search for common reasons	12.40-13.00
lunch			13.00-14.00
9MS3-SB-09	Atila PORO et al	Light Curve analyze of 50 asteroids based on the ALCDEF database	14:00 – 14:20
9MS3-SB-10	Vacheslav EMEL'YANENKO	Dynamical evolution and origin of meteorites with short cosmic-ray exposure ages	14:20 – 14:40
9MS3-SB-11	Sergei IPATOV	Migration of bodies to the Earth and the Moon from different distances from the Sun	14:40 – 15:00
9MS3-SB-12	Richard HOOVER and Alexey ROZANOV	Microfossils, biomolecules and bioelements in the Orgueil meteorite	15:00 – 15:20

9MS3-SB-13	Evgenij ZUBKO et al	Significant spatial heterogeneity of regolith on asteroid (3200) Phaethon	15:20 – 15:40
9MS3-SB-14	Sergey VOROPAEV	Asteroid disruption by planets at near flyby	15:40 – 16:00
coffee-break			16.00-16.20
9MS3-SB-15	Evgeny SLYUTA and Sergey VOROPAEV	Gravitational deformation of small Solar system bodies	16:20 – 16:40
9MS3-SB-16	Jing SUN et al	Preliminary work on promoting asteroids radio astronomical study in China	16:40 – 17:00
9MS3-SB-17	Thomas DUXBURY et al	The international Phobos/Deimos surface characterization and site selection working group: 2018 status	17:00 – 17:20
9MS3-SB-18	Evgeny SLYUTA et al	Proposals to Russian program for research of small bodies of the Solar system	17:20 – 17:40
POSTER SESSION (all sessions)			18.00-19.00

thursday, 11 october 2018

session **6. GIANT PLANETS**
convener: **Scott BOLTON**

10.00-15.20

9MS3-GB-01	Scott BOLTON and Jack CONNERNEY	Juno's Surprising Results at Jupiter	10.00-10.20
9MS3-GB-02	Michel BLANC et al	A short introduction to magnetosphere-ionosphere-thermosphere studies at Jupiter with Juno	10.20-10.40
9MS3-GB-03	Jack CONNERNEY et al	Juno Magnetometer Observations of Jupiter's Magnetic Field and Magnetosphere	10.40-11.00
9MS3-GB-04	Alessandro MURA and A. ADRIANI	The auroral footprints of Galilean moons at Jupiter	11.00-11.20
9MS3-GB-05	Masafumi IMAI et al	Multi-instrument investigation for Jupiter lightning-induced whistler and sferic events using Juno	11.20-11.40

coffee-break

11.40-12.00

9MS3-GB-06	Sadie ELLIOTT et al	Electron acceleration to high energies via whistler-mode wave-particle interactions in the Jovian polar regions	12.00-12.20
9MS3-GB-07	Paolo RACIOPPA et al	Jupiter's gravity field determination from Doppler tracking of the Juno spacecraft	12.20-12.40
9MS3-GB-08	Paolo RACIOPPA et al	Saturn's gravity field determination from Doppler tracking of the Cassini spacecraft	12.40-13.00

lunch

13.00-14.00

9MS3-GB-09	Vladimir KRASNOPOLSKY	On the carbon isotope ratio in Titan's atmosphere and interior	14:00 – 14:20
9MS3-GB-10	Vladislav SIDORENKO	The multi-shell models of celestial bodies with an intermediate layer of fluid: dynamics in the case of the large values of the Ekman number	14:20 – 14:40
9MS3-GB-11	Michel BLANC et al	Planetary exploration, Horizon 2061: from key questions to representative space missions and enabling technologies	14:40 – 15:00
9MS3-GB-12	Theodore CLARKE	Juno and the New Renaissance	15:00 – 15:20

coffee-break

15.20-15.40

session **7. DUST AND DUSTY PLASMA
IN SPACE** 15.40-17.00

Convener: Alexander ZAKHAROV

9MS3-DP-01	Sergei IPATOV	Migration of interplanetary dust particles to the Earth and the Moon	15:20 – 15:40
9MS3-DP-02	Sergey POPEL et al	Formation of two dusty plasma clouds as a result of a meteoroid impact onto the Moon	15:40 – 16:00
9MS3-DP-03	Ekaterina CHORNAYA et al	The 10- μ M silicate feature in sub-millimeter compact olivine particles	16:00 – 16:20
9MS3-DP-04	Marina FRONTASYEVA et al	Cosmic dust studied by the moss analysis	16:20 – 16:40
9MS3-DP-05	Tatiana SALNIKOVA and Sergey STEPANOV	On the dust charged particles as a part of Kordylewski clouds	16:40 – 17:00
	CONCERT		17.00-18.00
	RECEPTION		18.00-20.00

friday, 12 october 2018

session **8. MOON SCIENCE
AND EXPLORATION**

10.00-18.00

conveners: Igor MITROFANOV, Maxim LITVAK

9MS3-MN-01	Carle PIETERS et al	Transformative Lunar science	10.00-10.20
9MS3-MN-02	Jessica FLAHAUT et al	Lunar polar regions of interest for future exploration	10.20-10.40
9MS3-MN-03	Ariel DEUTSCH et al	Analysis of subsurface impact and volcanic structures on the Moon with gravity recovery and interior laboratory (GRAIL)	10.40-11.00
9MS3-MN-04	Mariia SUNDEEVA et al	The distribution of the concentrations (anomalies) of the water equivalent of hydrogen as a function of the relief at the polar regions of the Moon regarding the LRO data	11.00-11.20
9MS3-MN-05	Igor MITROFANOV	So many discoveries of water on the Moon	11.20-11.40
coffee-break			11.40-12.00
9MS3-MN-06	James HEAD and Lionel WILSON	Lunar basaltic volcanic eruptions: gas release patterns and variations in lava vesicularity: fissures, mare flows, and ring moat dome structure (RMDS) morphology	12.00-12.20
9MS3-MN-07	Mikhail IVANOV et al	Geology of the northern portion of the SPA basin on the Moon: evidence for compositional stratification of the ancient lunar crust	12.20-12.40
9MS3-MN-08	Valeriy TENISHEV	Kinetic modeling of sodium population in the lunar exosphere	12.40-13.00
lunch			13.00-14.00
9MS3-MN-09	Jinsong PING et al	Some pre-studies about the candidate landing area for CHANG'E-4 project	14.00-14.20
9MS3-MN-10	Maya DJACHKOVA et al	Landing site selection process for future Moon polar missions	14.20-14.40
9MS3-MN-11	Rico FAUSCH et al	Neutral gas mass spectrometer for the Luna-Resurs mission: status, performance and scientific implications	14.40-15.00
9MS3-MN-12	Mingyuan WANG et al	Lunar ionosphere and planetary radio emissions detection based on radio experiments of Chinese space mission	15.00-15.20

9MS3-MN-13	Bernard FOING et al	EuroMoonMars pilot programme for research, technology, training and field simulations	15.20-15.40
9MS3-MN-14	Weiwei FAN et al	Bibliometric analysis of solar system exploration missions	15.40-16.00
	coffee-break		16.00-16.20
9MS3-MN-15	Maxim LITVAK et al	Lunar round-trip mission: objectives	16.20-16.40
9MS3-MN-16	Neeraj PRADHANN	The modular mobile lunar base concept the most redundant approach for habitat architecture [HAB-ROB]	16.40-17.00
9MS3-MN-17	Alexander GUSEV et al	On eve of the glorious jubilee: 60 years of the Moon's exploration by spacecrafts	17.00-17.20
	PANEL DISCUSSION	Integration of manned and robotic missions on the Moon	17.20-18.00

POSTER SESSION

8 october 18.00-19.00

10 october 18.00-19.00

MARS

- | | | |
|------------|---|---|
| 9MS3-PS-01 | Adeene DENTON and James HEAD | Closed depressions in Arabia Terra, Mars: Implications for subsurface mass removal |
| 9MS3-PS-02 | Ashley PALUMBO and James HEAD | Early Mars climate history: Characterizing a «warm and wet» martian climate with a 3D global climate model and testing geological predictions |
| 9MS3-PS-03 | Mikhail LUGININ et al | Retrieval of aerosol properties from TIRVIM solar occultations onboard ExoMars/TGO |
| 9MS3-PS-04 | Alexey BATOV et al | On the location of potential marsquakes' sources |
| 9MS3-PS-05 | Tamara GUDKOVA et al | Model estimates of stress state in Mars for three-level loading |
| 9MS3-PS-06 | Eugene BRUSNIKIN and A. DUBOVITSKAIA | The study of influence of Mars climate on Slope streaks formation process |
| 9MS3-PS-07 | Mikhail MALENKOV et al | ExoMars - 2020 program: on the concept of the marsokhod locomotion system |
| 9MS3-PS-08 | Diego RODRÍGUEZ DÍAZ et al | AMR instrument for ExoMars' 2020 Surface Platform. Development status, calibration and qualification |
| 9MS3-PS-09 | Maxim ZAITSEV et al | The use of the EO gas sterilization process for the planetary protection requirements fulfillment on the «ExoMars-2020» mission |
| 9MS3-PS-10 | Gennady DOLNIKOV et al | Investigation of Martian Dust with Dust Complex onboard the ExoMars-2020 landing platform |
| 9MS3-PS-11 | Imant VINOGRADOV et al | M-DLS experiment for the ExoMars-2020 stationery landing platform |
| 9MS3-PS-12 | Mikhail GERASIMOV et al | The Martian Gas Analytical Package (ExoMars mission, 2020) |
| 9MS3-PS-13 | Maxim KULIKOV and Alexander SKALSKY | Mars: Electromagnetic survey at the landing platform |
| 9MS3-PS-14 | Alexander KOSOV et al | LaRa (Lander Radioscience) on the ExoMars 2020 Surface Platform – Rotation of Mars and Positioning of the Surface Platform |
| 9MS3-PS-15 | Ekaterina GRISHAKINA et al | Martian soil simulant for large-scale field experimental research |
| 9MS3-PS-16 | Mikhail IVANOV et al | ExoMars landing sites in Oxia Palus and Mawrth Vallis: geological characterization |
| 9MS3-PS-17 | Mikhail IVANOV et al | ExoMars landing sites in Oxia Palus and Mawrth Vallis: small craters and boulders |
| 9MS3-PS-18 | Manuel Maria DOMINGUEZ-PUMAR et al | A miniaturized 3D wind sensor for planetary exploration |

9MS3-PS-19	Simone DELL'AGNELLO et al	Next-Gen Laser Retroreflectors for Mars (ExoMars 2016-2020, Mars 2020, InSight 2018)
9MS3-PS-20	Jose Luis VAZQUEZ-POLETTI et al	Serverless On-Demand MARSIS Ionogram Processing on a Public Cloud Computing Infrastructure
9MS3-PS-21	Maria Pilar VELASCO et al	Fractional Models to Simulate the Martian Atmospheric Dust Dynamics
9MS3-PS-22	Gennady KOCHEMASOV	The new wave planetology shown in the martian satellites: shrinking Phobos and swelling Deimos
9MS3-PS-23	Alexandra BERMEJO et al	Potential of nanoparticle self-assembled layer for optical instruments
9MS3-PS-24	Vladimir CHEPTSOV et al	Viability of desert soil microbial community after irradiation with accelerated electrons under simulated extraterrestrial conditions
9MS3-PS-25	Andrey BELOV et al	Halotolerance of bacteria from extreme ecosystems: implications for astrobiology
9MS3-PS-26	Margarita KRIUCHKOVA et al	The influence of high energy electrons (HEE) on fungal community from desert soil
9MS3-PS-27	Sergey BULAT	Subglacial Antarctic Lake Vostok vs. subglacial South Pole Martian lake and hypersaline Canadian Arctic lakes – prospects for life

VENUS

9MS3-PS-28	Ludmila ZASOVA et al	Venera-D: from science objectives to mission architecture
9MS3-PS-29	Dmitry GORINOV et al	Circulation of Venesian atmosphere at 90-110 km based on apparent motions of the O ₂ 1.27 μm nightglow from VIRTIS-M (Venus Express) data
9MS3-PS-30	Michael BONDARENKO and Anatoly GAVRIK	Gravity wave activity as possible cause of ionospheric layers registered at 90-115km on Venus
9MS3-PS-31	Anatoly GAVRIK	Wave-like structures in the Venus ionosphere during radio occultation
9MS3-PS-32	Evgeniya GUSEVA	Main global extensional regimes on Venus
9MS3-PS-33	Vladimir ZHARKOV and Tamara GUDKOVA	On the estimate of precession constant for Venus
9MS3-PS-34	Daria EVDOKIMOVA et al	Improved retrieval of gaseous concentration profiles in Venus mesosphere using SPICAV-UV/VEX stellar occultation data
9MS3-PS-35	Vladimir GROMOV and Alexander KOSOV	An accuracy of the retrieving of Venesian atmospheric data from the radiometer instrument in the Venera- D mission

EXOPLANETS

9MS3-PS-36	Elena POPOVA	Nonlinear theory of stability of nanocraft equipped with a sail accelerated by an intense laser beam
------------	---------------------	--

9MS3-PS-37	Artem BEREZUTSKY et al	Numerical study of the planetary atmosphere of Gliese 436B
9MS3-PS-38	Sergey BULAT et al	Marinilactobacillus SP and two more bacteria in the subglacial Antarctic Lake Vostok
9MS3-PS-39	Yuhiko AOYAMA et al	Theoretical Model of Hydrogen Line Emission from Accreting Gas Giants
9MS3-PS-40	Valery KOTOV	Superfast exoplanets and 9600 seconds
9MS3-PS-41	Andrey YUDAEV et al	Interference coronagraph with rotational shear for ground-based and space telescopes

SOLAR WIND INTERACTIONS WITH PLANETS AND SMALL BODIES

9MS3-PS-42	Oleg KHAVROSHKIN and A.B. KHRUSTALEV	Chandler's precece, sun processes: spectral analysis
9MS3-PS-43	Oleg KHAVROSHKIN and Vladislav TSYPLAKOV	Sun and temperature fields of the Earth

SMALL BODIES

9MS3-PS-44	Veniamin FEDULOV et al	Stepwise degassing of the original gray matter of the meteorite Chelyabinsk (LL5)
9MS3-PS-45	Pauli LAINE	Accessing icy moon's ocean with thermonuclear reactor
9MS3-PS-46	Elena PETROVA and V.P. TISHKOVETS	Retrieval of surface properties using polarization and intensity of light reflected by atmosphereless celestial bodies
9MS3-PS-47	Larissa GOLUBEVA and Dmitry SHESTOPALOV	Asteroids: spectral properties of polarization degree
9MS3-PS-48	Vladimir BUSAREV and Sergei IPATOV	Observational evidences and possible dynamical reasons of sublimation activity of primitive asteroids in the main-belt
9MS3-PS-49	Dorsa ASGARIAN	Comparative Study of Orbital Parameters and Magnitude of Short and Long Period Comets

GIANT PLANETS

9MS3-PS-50	Ivan PENSIONEROV et al	Models of the Jovian magnetodisc vs. Juno magnetometer data
9MS3-PS-51	Petr LYSSENKO et al	The ammonia absorption in the Jovian Great Red Spot
9MS3-PS-52	Yaroslav ILYUSHIN and Paul HARTOGH	Submillimeter wave radiometry of the Jovian icy moons' crust: numerical simulations
9MS3-PS-53	Anna DUNAEVA et al	Hydrated phases in the Titan's core
9MS3-PS-54	Victor KRONROD et al	Dependence of the planetesimals mass captured in giant planets accretion disks from ablation processes

9MS3-PS-55 **Gennady KOCHEMASOV** Terrestrial catastrophic atmospheric phenomena of the wave nature (El-Nino, cyclon, tornado) and comparison of cyclones on Earth and Jupiter

DUST AND DUSTY PLASMA IN SPACE

9MS3-PS-56 **Alexey DEMYANOV and Vasiliy VYSOCHKIN** Detector of cosmic dust "METEOR-L"

9MS3-PS-57 **Yulia IZVEKOVA et al** Lower-hybrid turbulence in dusty plasmas over the Moon

9MS3-PS-58 **Yulia IZVEKOVA and Sergey POPEL** Dusty plasmas and vortex motions in the atmosphere of Mars

9MS3-PS-59 **Vladimir CHEPTSOV et al** Survivability of bacteria in an impact-type plasma torch

9MS3-PS-60 **Alexander ZAKHAROV et al** Investigation of lunar dusty exosphere with future Russian lunar missions: Development of the Instrument & Simulation Control

9MS3-PS-61 **Andrew LYASH et al** Development of the Experimental Set-up for Lunar Dust Particles Investigation and Instruments calibrations

9MS3-PS-62 **Vladimir GUBENKO et al** Coupling between the internal atmospheric waves and tilted sporadic E-layers in the Earth's ionosphere

MOON SCIENCE AND EXPLORATION

9MS3-PS-63 **John CLARKE et al** A High Resolution UV Spectrograph to Study Lunar and Planetary Atmospheres and the Interplanetary Medium

9MS3-PS-64 **Mikhail GERASIMOV et al** The Gas Analytical Complex for study of the Lunar subpolar regolith volatiles

9MS3-PS-65 **Ilya KUZNETSOV et al** Numerical modelling of the lunar exosphere and lunar lander interactions with SPIS-DUST

9MS3-PS-66 **Svetlana PUGACHEVA et al** Impact of asteroids and meteorites on the lunar surface

9MS3-PS-67 **Egor SOROKIN et al** Experimental simulating of a micrometeorite impact on the Moon

9MS3-PS-68 **Ekaterina KRONROD et al** Coupled geophysical-geochemical modeling of the Moon

9MS3-PS-69 **Andrei DMITROVSKY and Evgeny SLYUTA** Geomorphological map of the Mons Rümker province

9MS3-PS-70 **Anastasia ZHARKOVA et al** Mercury relief: analysis and morphological classification

9MS3-PS-71 **Sergey KRASILNIKOV and Mikhail IVANOV** Geological mapping of the South Pole of Moon

9MS3-PS-72	Alexander STARK et al	Lunar rotation from high-resolution laser altimeter DTMs at the lunar poles
9MS3-PS-73	Wenxiao LI et al	Lunar Radio Ranging and the Prospect of Martian Radio Ranging
9MS3-PS-74	Yangxiaoyi LU and Vladislav SHEVCHENKO	Lunar physical exploration system of Chang'e-4 landing area
9MS3-PS-75	Olga TRETYUKHINA et al	The choice of the landing site and the route of the lunokhod for research and exploration of volatile components in the lunar soil
9MS3-PS-76	Boris IVANOV	Seismic shaking role in small lunar crater degradation
9MS3-PS-77	Sergei IPATOV et al	Variation of near-Earth object population based on analysis of diameters of lunar craters
9MS3-PS-78	Ekaterina FEOKTISTOVA et al	Lunar craters formed by encounters of satellite systems of near-Earth objects with the Moon
9MS3-PS-79	Ekaterina FEOKTISTOVA et al	Doublet craters on the Moon and Mercury
9MS3-PS-80	Maria KOLENKINA et al	Morphometry of lunar craters having 1-10 km in diameter
9MS3-PS-81	Natalia BULATOVA	The study of the Moon's movements with spatio-temporal technology
9MS3-PS-82	Boris EPISHIN and Mikhail SHPEKIN	Analysis of occultations of stars by the Earth on the lunar sky
9MS3-PS-83	Anna SITNIKOVA et al	Moon gallery ArtMoonMars programme for public engagement, outreach, international cooperation, space exploration through art
9MS3-PS-84	Žhanna RODIONOVA and Renato DICATI	The History of Researches of the Moon by Space Vehicles Depicted on the Postage Stamps of the World
9MS3-PS-85	Azariy BARENBAUM and Mikhail SHPEKIN	Cumulative formation of mares and mascons on Moon by galactic comets
9MS3-PS-86	Azariy BARENBAUM	Galaxy Cycles in Solar System

THE ATMOSPHERIC CHEMISTRY SUITE (ACS) EXPERIMENT ON BOARD THE EXOMARS TRACE GAS ORBITER: THE RESULTS OF FIRST SIX MONTHS OF OPERATIONS

**A. Fedorova¹, O. Korablev¹, F. Montmessin², A. Trokhimovskiy¹,
N. Ignatiev¹, A. Grigoriev¹, A. Shakun¹, M. Luginin¹, D. Belyaev¹,
A. Patrakeev¹, N. Kokonkov¹, K. Olsen², L. Baggio², J.L. Bertaux^{2,1},
J.A. Parejo³, C.F. Wilson³, and the ACS Team**

¹*Space Research Institute RAS, Moscow, Russia,*

²*LATMOS Laboratoire Atmosphères, Milieux, Observations Spatiales,
Paris Cedex 05, France;*

³*Physics Department, Oxford University, Oxford, UK*

The Atmospheric Chemistry Suite (ACS), one of four science experiments on board ESA-Roscosmos ExoMars 2016 Trace Gas Orbiter (TGO) mission has started science operations in April 2018. ACS consists of three infrared spectrometers targeting sensitive detection of trace gases of potential geophysical or biological interest. ACS channels feature very high accuracy (ppt level), very high resolving power (>10,000) and broad spectral coverage (0.7 to 17 μm). The near-infrared (NIR) channel covers the 0.7-1.6 μm spectral range with a resolving power of $\geq 20,000$. This channel is operated in solar occultation and nadir. In nadir NIR is mostly measuring water vapor and dayside oxygen emission. In solar occultation NIR demonstrates profiling of CO₂, H₂O with high accuracy and in a broad altitude range, and also the molecular oxygen O₂, the first ever profiling in the lower atmosphere. NIR observes occultations together with the two other ACS channels MIR and TIRVIM, either together with TIRVIM, and another spectrometer aboard TGO, NOMAD. The mid-infrared (MIR) channel is a high spectral resolution (resolving power of $\sim 50,000$) instrument dedicated to solar occultation measurements in the 2.2-4.4 μm range. MIR is conceived to accomplish the most sensitive measurements of the trace gases in the Martian atmosphere, allowing also parallel profiling of the abundant components such as CO₂, H₂O and their isotopologues. The thermal-infrared channel (TIRVIM) is a Fourier-transform spectrometer with cryogenically-cooled detector encompassing the spectral range of 1.7-17 μm . Observing the CO₂ 15- μm band in nadir TIRVIM returns temperature profiles from the surface up to 50-60 km, together with the dust and water ice optical depth. Also the surface temperature is measured. In solar occultation TIRVIM delivers profiles of CO₂, CO, H₂O and aerosols, as well allowing to distinguish between mineral and condensate aerosols. ACS has monitored the state of the Martian atmosphere before and during the dust event 2018A. Key findings available by the time of the conference will be reported.

FINE RESOLUTION EPITHERMAL NEUTRON DETECTOR ONBOARD EXOMARS TRACE GAS ORBITER: MARS NEUTRON MAPPING FIRST RESULTS AND NEW AREAS OF INTEREST

A.V. Malakhov, I.G. Mitrofanov, D. V. Golovin, A. B. Sanin, M. L. Litvak
Space Research Institute, Profsoyuznaya 84/32, 117997, Moscow, Russia, malakhov@np.cosmos.ru.

Keywords:

Mars, water, hydrogen, neutron, mapping

ExoMars is a two-launch mission undertaken by Roscosmos and European Space Agency. Trace Gas Orbiter, a satellite part of the 2016 launch carries the Fine Resolution Epithermal Neutron Detector (FREND) instrument [1] as part of its payload. The instrument aims at mapping hydrogen content in the upper meter of Martian soil with high spatial resolution up to 60 km diameter spot. The instrument's neutron collimator, the first of its kind to map Mars, explains this capability.

Martian neutron flux measurement from orbit is a good sign of hydrogen presence in the regolith up to 1 m in depth. Similar measurement technique is used by another Russian instrument, HEND, onboard Mars Odyssey [2]. It provided maps of hydrogen distribution for 16 years of mapping [3]. Major difference between FREND and HEND is FREND's spatial resolution: without the collimator, HEND sees from horizon to horizon, resulting in a 600 km surface pixel, which is not enough for characterization of particular geological features on Mars.

First measurements of FREND during the scientific mapping phase already provided enough mapping data to begin characterization of local features on the surface, and comparison with the map of HEND allows identifying areas of particular interest, where hydrogen or water presence was not previously observed, due to larger spatial resolution of HEND.

We will present initial mapping results of FREND as well as particular findings in the places of interest.

References:

Use the brief numbered style common in many abstracts, e.g., [1], [2], etc. References should then appear in numerical order in the reference list, and should use the following abbreviated style:

- [1] Mitrofanov, I. et al. Fine Resolution Epithermal Neutron Detector (FREND) Onboard the ExoMars Trace Gas Orbiter // *Space Science Reviews*. 2018. V. 214. P. 86.
- [2] Mitrofanov, I. et al. Maps of Subsurface Hydrogen from the High Energy Neutron Detector, Mars Odyssey // 2002. *Science*. V. 297. P. 78-81.
- [3] Mitrofanov I.G. et al., Soil Water Content on Mars as Estimated from Neutron Measurements by the HEND Instrument Onboard the 2001 Mars Odyssey Spacecraft // 2004. *Solar System Research*. V. 38. P. 253-257.

RECENT RESULTS FOR THE SPACE RADIATION ENVIRONMENT IN MARS ORBIT PROVIDED BY FRENDO LIULIN-MO DOSIMETER ABOARD EXOMARS TGO

J. Semkova¹, R. Koleva¹, K. Krastev¹, V. Benghin³, S. Drobyshev³, Yu. Matviichuk¹, B. Tomov¹, N. Bankov¹, T. Dachev¹, St. Maltchev¹, P. Dimitrov¹, I. Mitrofanov², A. Malakhov², D. Golovin², M. Mokrousov², A. Sanin², M. Litvak², A. Kozyrev², V. Tretyakov², S. Nikiforov², A. Vostrukhin², N. Grebennikova², V. Shurshakov³

¹Space Research and Technology Institute, Bulgarian Academy of Sciences, Sofia, Bulgaria, jsemkova@stil.bas.bg;

²Space Research Institute, Russian Academy of Sciences, Moscow, Russia, mitrofanov@np.cosmos.ru;

³State Scientific Center of Russian Federation, Institute of Biomedical Problems, Russian Academy of Sciences, Moscow, Russia, v_benghin@mail.ru

Keywords:

Mars, galactic cosmic rays, radiation risk, ExoMars, TGO, FRENDO dosimeter, manned space missions.

We present recent results from measurements of the charged particle fluxes, dose rates, linear energy transfer spectra and estimation of dose equivalent rates in ExoMars TGO science orbit and comparison with the data obtained during the cruise and in high elliptic Mars's orbit, provided by Liulin-MO dosimeter of FRENDO [1] instrument aboard TGO.

The results are important for future manned mission to Mars radiation risk estimations.

Introduction:

The estimation of the radiation effects for a long-duration manned space mission requires: i) Knowledge and modeling of the particle radiation environment; ii) Calculation of primary and secondary particle transport through shielding materials; and iii) Assessment of the biological effect of the dose.

The FRENDO's dosimetry module Liulin-MO aboard the ExoMars TGO provided information about the radiation environment during the cruise stage and now-on Mars' orbit.

The main goal of the Liulin-MO dosimetric experiment is investigation of the radiation conditions in the heliosphere at distances from 1 to 1.5 AU from the Sun. The main scientific objectives of the Liulin-MO investigation are: a) To measure the dose and determine the dose equivalent rates for human explorers during the interplanetary cruise and in Mars orbit; b) Measurement of the fluxes of galactic cosmic rays (GCR), solar energetic particles and secondary charged particles during the cruise and in Mars orbit; c) Together with other detectors of the FRENDO instrument to provide data for verification and benchmarking of the radiation environment models and assessment of the radiation risk to the crewmembers of future exploratory flights.

An additional goal of Liulin-MO measurements is to increase the accuracy of the neutron measurements by providing information about radiation fluctuations from charged particles that can have an impact on the signals from the neutron detectors of the FRENDO.

Methodology and measured parameters of Liulin-MO:

Liulin-MO contains two dosimetric telescopes - A&B, and C&D arranged at two perpendicular directions. Each pair of the dosimetric telescopes consists of two 300 μm thick, 20x10 mm area rectangular Si PIN photodiodes. The parameters, provided by Liulin-MO simultaneously for two perpendicular directions have the following ranges: absorbed dose rate from 10^{-7} Gy h^{-1} to 0.1 Gy h^{-1} ; particle flux in the range 0 - 10^4 $\text{cm}^{-2} \text{s}^{-1}$; energy deposition spectrum and coincidence energy deposition spectrum in the range 0.08 - 190 MeV.

Liulin-MO recent data:

The average flux from GCR during the transit to Mars for the period April 22 - September 15, 2016 is $3.12 \text{ cm}^{-2} \text{ s}^{-1}$ and $3.29 \text{ cm}^{-2} \text{ s}^{-1}$ in two perpendicular directions. For November 01, 2016 - January 17, 2017 in Mars capture orbit 1 (MCO1) it is 3.26 and $3.42 \text{ cm}^{-2} \text{ s}^{-1}$ in two perpendicular directions. In the pericenter the average decrease of the particle flux is $0.77 \text{ cm}^{-2} \text{ s}^{-1}$. The flux for February 24, 2017 - March 07, 2017 in MCO2 is slightly higher [2].

The average flux from GCR for April 16-July24, 2018 in Mars science orbit is 2.99 and $3.1 \text{ cm}^{-2} \text{ s}^{-1}$ in two perpendicular directions.

Table 1 summarizes the dose rate in silicon, the quality factors and dose equivalent rates obtained during the different phases of TGO flight.

Table 1. Dose rate in silicon D (Si), quality factors Q and dose equivalent rates H during different TGO phases

Time frame/ TGO phase	D (Si) (AB)/ D (Si) (DC) $\mu\text{Gy d}^{-1}$	Q (AB)/ Q (DC)	H (AB)/ H (DC) mSv d^{-1}
April 22 - Sep- tember 15, 2016/ Cruise	$372 \pm 37/390 \pm 39$	$4.08 \pm 0.3/4.02 \pm 0.3$	$1.97 \pm 0.4/2.04 \pm 0.4$
November 01, 2016 - Janu- ary 17, 2017/ MCO1	$405.6 \pm 41/422 \pm 42$	$4.23 \pm 0.33/4.12 \pm 0.3$	$2.23 \pm 0.5/2.26 \pm 0.5$
February 24 -March 07, 2017/ MCO2	$410 \pm 41/425 \pm 42.5$	$4.31 \pm 0.33/4.17 \pm 0.3$	2.3 ± 0.55
April 16 -July 24, 2018/ TGO Mars Science Orbit	$342 \pm 34/359 \pm 36$	3.5 ± 0.26	$1.56 \pm 0.31 /1.63 \pm 0.32$

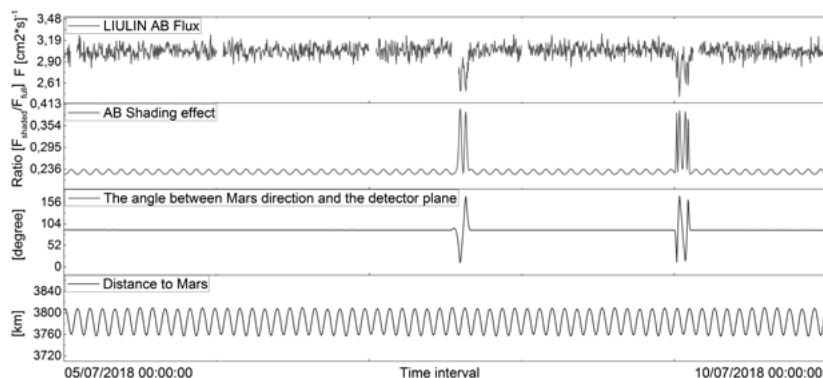


Fig. 1. Plots from top to bottom: 1. Liulin-MO flux; 2. Part of FOV shadowed by Mars – on average 22%; 3. Angle between Liulin-MO axis and nadir; 4. Distance of TGO from Mars.

The dosimetric measurements in Mars' orbit demonstrate strong dependence of the charged particle fluxes of Liulin-MO field of view shadowed by Mars.

Figure 1 presents an example of the Mars shadow effect on the measured flux. In the period July 05-10, 2018 sharp decreases of Liulin-MO fluxes are observed. These decreases are due to the increase of Mars shadow effect on the Liulin-MO FOV. The change of Mars shadow is due to the change of the angles between Liulin-MO axes and the nadir axis from their usual value about 90° up to about $90^\circ \pm 90^\circ$.

Summary and Conclusions:

The increase of the charged particles dose rate and flux measured from April 22, 2016 to March 07, 2017 corresponds to the increase of GCR intensity during the declining phase of the solar activity.

The obtained data show that during the cruise to Mars and back (6 months in each direction), taken during the declining of solar activity, the crewmembers of future manned flights to Mars will accumulate at least 60% of the total dose limit for the cosmonauts/ astronauts career in case their shielding conditions are close to the average shielding of Liulin-MO detectors - about 10 g cm^{-2} .

In April-July 2018 in TGO Mars science orbit the flux is $\sim 90\%$, dose rate is $\sim 84\%$, dose equivalent rate is $\sim 70\%$ of that in February-March 2017 in MCO2.

In TGO Mars science orbit a strong dependence of the measured fluxes on the part of the FOV shadowed by Mars is observed. The decreases of the fluxes due to FOV shadowing do not affect significantly the corresponding dose rates.

A similar module, called Liulin-ML for investigation of the radiation environment on Mars' surface as a part of the active detector of neutrons and gamma rays ADRON-EM on the Surface Platform is under preparation for ExoMars 2020 mission.

References:

- [1] Mitrofanov I., et al: Fine Resolution Epithermal Neutron Detector (FRIEND) Onboard the ExoMars Trace Gas Orbiter // Space Sci. Rev. 2018 214:86. <https://doi.org/10.1007/s11214-018-0522-5>.
- [2] Semkova, J., et al: Charged particles radiation measurements with Liulin-MO dosimeter of FRIEND instrument aboard ExoMars Trace Gas Orbiter during the transit and in high elliptic Mars orbit // Icarus 303. 2018. P. 53–66. <https://doi.org/10.1016/j.icarus.2017.12.034>.

MARS EXPRESS: 15 YEARS OF HARD WORK AND DISCOVERIES

D. Titov¹, J.-P. Bibring², A. Cardesin³, T. Duxbery⁴, F. Forget⁵, M. Giuranna⁶, F. González-Galindo⁷, M. Holmström⁸, R. Jaumann⁹, A. Määttä¹⁰, P. Martin³, F. Montmessin¹⁰, R. Orosei¹¹, M. Pätzold¹², J. Plaut¹³, and MEX SGS Team³

¹ESA-ESTEC, Noordwijk, The Netherlands, dmitri.titov@esa.int;

²IAS-CNRS, Orsay, France;

³ESA-ESAC, Madrid, Spain;

⁴George Mason University, Fairfax, VA, USA;

⁵LMD, Paris, France;

⁶IAPS-INAF, Rome, Italy;

⁷IAA, Granada, Spain;

⁸IRF, Kiruna, Sweden;

⁹IPF-DLR, Berlin, Germany;

¹⁰LATMOS/IPSL, CNRS, Guyancourt, France;

¹¹IRA-INAF, Bologna, Italy;

¹²RIU-Uni Cologne, Cologne, Germany;

¹³JPL, Pasadena, CA, USA

Keywords:

Mars, surface, geology, evolution, atmosphere, climate, aeronomy, escape.

Introduction:

After almost 15 years in orbit Mars Express remains one of ESA's most scientifically productive Solar System missions whose publication record now exceeds 1120 papers. Geological maps of Tharsis volcanoes have just been released. Characterization of the geological processes on a local-to-regional scale by HRSC, OMEGA and partner experiments on NASA spacecraft has allowed constraining land-forming processes in space and time. Recent results suggest episodic geological activity as well as the presence of large bodies of liquid water in several provinces (e.g. Eridania Planum, Terra Chimeria) in the early and middle Amazonian epoch and formation of vast sedimentary plains north of the Hellas basin. New analysis of the subsurface dielectric properties by MARSIS radar sounder revealed that the deposits in Meridiani Planum, previously interpreted as ice-rich, may contain little or no ice at all. Mars Express observations and experimental teams provided essential contribution to the selection of the Mars-2020 landing sites.

More than a decade-long record of the atmospheric parameters such as temperature, dust loading, water vapor and ozone abundance, water ice and CO₂ clouds distribution, collected by SPICAM, PFS and OMEGA spectrometers as well as subsequent modeling have provided key contributions to our understanding of the martian climate. Recent spectroscopic monitoring of the dust storms revealed dust properties and their spatial and temporal variations during the dust storm events.

More than 10,000 crossings of the bow shock by Mars Express allowed ASPERA-3 to characterize complex behavior of the magnetic boundary topology as function of the solar EUV flux. ASPERA-3 observations of the ion escape during complete solar cycle revealed important dependencies of the atmospheric erosion rate on parameters of the solar wind and EUV flux and established global energy balance between the solar wind and escaping ion flow. This led to important conclusion that the ion escape at Mars is production rather than energy limited. Comparison to the similar observation record by Venus Express would allow quantification of the role of planet gravity in the escape processes.

The structure of the ionosphere sounded by the MARSIS radar and the MaRS radio science experiment was found to be significantly affected by the solar activity, the crustal magnetic field, as well as by the influx of meteorite and cometary dust. MARSIS and ASPERA-3 observations suggest that the sunlit ionosphere over the regions with strong crustal fields is denser and extends

to higher altitudes as compared to the regions with no crustal anomalies. Reconnection of solar magnetic field lines carried by the solar wind with field lines of crustal origin opens channels through which the ionospheric plasma escapes to space, producing strong and narrow cavities in the density. The situation is very different on the night side where the ionosphere has patchy structure. Such patchy ionizations are observed in the regions where field lines have a dominant vertical component. Through these patches the ionospheric plasma from the dayside penetrates and supplies the nightside ionosphere. Several models of the upper atmosphere and plasma environment are being developed based on and in support of the collected experimental data. The models aim at creating user-friendly data base of plasma parameters similar to the Mars Climate Database that would be of great service to the planetary community.

A significant recent achievement was the flawless transition to the “gyroless” attitude control and operations mode on the spacecraft, that would allow mitigating the onboard gyros aging and extending the mission lifetime. The mission extension till the end of 2020 is approved pending technical evaluation in 2018. The extension plan includes both augmenting the coverage and extending long-time series, as well as new elements and potentially new opportunities for discoveries. It will be boosted by collaboration and synergies with NASA’s MAVEN, ESA-Roscosmos Trace Gas Orbiter (TGO) and other missions. In 2018 the major challenge would be to pass the bi-annual extension review and elaborate a convincing science case for new extension till the end of 2022. The talk will give the Mars Express status, review the recent science highlights, and outline future plans focusing on synergistic science with TGO.

LOW-FE REGIONS ALONG THE CURIOSITY PATH IN THE GALE CRATER BASED ON DAN ACTIVE NEUTRON PROBING DATA

D.I. Lisov¹, I.M. Mitrofanov¹, A.B. Sanin¹, M.L. Litvak¹

¹*Space Research Institute of the Russian Academy of Sciences;*

Keywords:

Mars, nuclear planetology, neutrons, neutron absorption, Fe abundance

Introduction:

Dynamic Albedo of Neutrons is an experiment on the NASA Curiosity rover in which the Martian surface is irradiated with high-energy neutron pulses [1]. The DAN active mode data provides information on the abundances of neutron moderators (hydrogen) and absorbers (chlorine and iron) [2].

The standard soil model used in DAN data processing contains a single layer with variable water and chlorine content, while the other soil components are added in fixed proportions derived from the average APXS data. This model accounts for 75% of the over 750 DAN active measurements to date [3].

For a subset of the DAN active measurements (over 4% of the total number) in a few regions over the Curiosity traverse an alternative model is required that allows for lower total neutron absorption by having lower FeO content than the APXS-derived value of 16.7%. We have estimated the best-fit FeO content from these active measurements and found that it can be as low as 10%.

References:

- [1] Mitrofanov I.G., Litvak M.L., Varenikov A.B. et al. Dynamic Albedo of Neutrons (DAN) Experiment Onboard NASA's Mars Science Laboratory // *Space Science Reviews*. 2012. V. 170 Issue 1-4 P. 559-582
- [2] Sanin A.B., Mitrofanov I.G., Litvak M.L. et al. Data processing of the active neutron experiment DAN for a Martian regolith investigation // *Nuclear Instr. and Methods in Physics Research A*. 2015. V. 789 P. 114-127
- [3] Lisov D.I., Litvak M.L., Kozyrev A.S. et al. Data Processing Results for the Active Neutron Measurements by the DAN Instrument on the Curiosity Mars Rover // *Astronomy Letters*. 2018. V. 44 Issue 7 P. 482-489

ECHELLE OBSERVATIONS OF LYMAN-ALPHA EMISSIONS OF H, D, AND INTERPLANETARY HYDROGEN AT MARS

M. Mayyasi¹, J. Clarke¹, E. Quémerais², O. Katushkina³, MAVEN-IUVS-EUV-NGIMS and SOHO-SWAN teams

¹Center for Space Physics, Boston University, 725 Commonwealth Ave., Room 506, Boston, MA 02215, USA, majdm@bu.edu;

²Laboratoire Atmosphère Milieux Observations Spatiales, 11 Boulevard d'Alembert, 78280, Guyancourt, France;

³Space Research Institute of Russian Academy of Science, Leninsky Ave 14, Moscow, Russia 119991

Keywords:

Ultraviolet Spectrograph, Interplanetary Hydrogen, Mars, Echelle, Lyman-alpha, D/H ratio.

Introduction:

The Mars Atmosphere and Volatile Evolution Mission (MAVEN) is a mission designed to study atmospheric loss at Mars [1] and is equipped with an Ultraviolet Imaging Spectrograph (IUVS) instrument. The IUVS design includes a high-resolution echelle channel that is capable of resolving Lyman-alpha emissions of H and D at 1215.67 and 1215.35 Angstroms, respectively [2]. During the MAVEN spacecraft cruise to Mars in 2014, the echelle instrument was calibrated at the Lyman-alpha wavelength using observations of Interplanetary Hydrogen (IPH) diffuse emission, observations from the Solar Wind Anisotropy (SWAN)

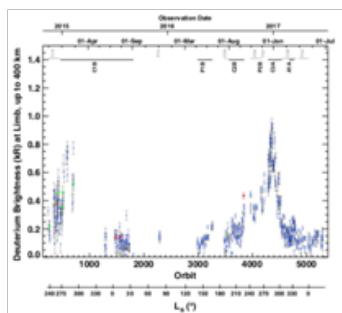
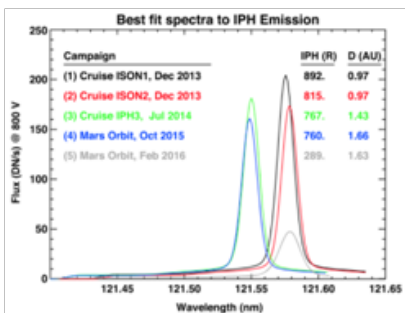


Fig. 1. IPH observations made during MAVEN cruise and early science orbits, used to calibrate the echelle instrument at H-Lyman-alpha. From Fig. 3 of [3].

Fig. 2. The variability of D Lyman-alpha brightness emissions observed at the sun-lit limb of Mars. From Fig. 1 of [4].

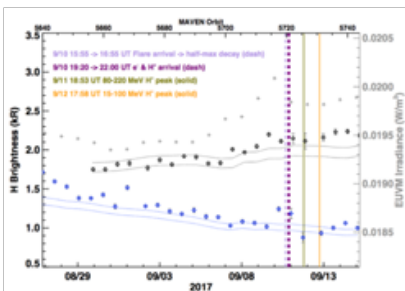


Fig. 3. The response of H Lyman-alpha emission brightness to solar weather event in Sept 2017. Short scale brightness enhancements in H were found to be due to storm-related increased atmospheric temperature. From Fig.1 of [8].

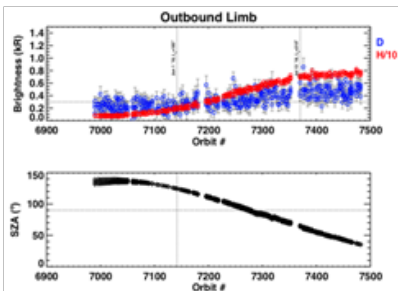


Fig. 4. Top: The most recent response of D and H Lyman-alpha emission brightness response to seasonal variations, and possibly, to the planet encircling dust storm commencing in June 2018. Bottom: The solar zenith angle of the tangent point along the line of sight.

instrument, and models of the IPH [3]. During science orbit at Mars, the echelle channel has been observing diffuse emissions of D and H Lyman-alpha as well as emissions from other species such as O triplet and forbidden double lines at 1304 and 1356 Angstroms, respectively [4]. Special campaigns to observe IPH emissions have been conducted during times of optimal doppler shifts between the interplanetary flow and IUVS line of sight. These observations are used to monitor the instrument performance and calibration.

The brightness of Lyman-alpha emissions from D and H, mapped throughout the MAVEN mission timeline, are presented. These emissions are seen to vary on multiple timescales and due to different physical drivers. These D and H emissions are produced by solar-resonant scattering and therefore show a direct variability with varying solar irradiance on multiple timescales. Diurnal variations due to changing solar zenith angle along the line of sight, near-monthly variations due to solar rotation, and seasonal variations due to Mars' proximity to the Sun are evident in the variation of the emission properties observed by echelle [4]. The optically thin D emission and optically thick H emission values have been analyzed to show repeatable seasonal patterns that peak near Mars' southern summer solstice. This variability is consistent with the onset of seasonal dust turbulence at lower altitudes and is useful for determining the effects of upwelling of D and H into higher altitudes at which these species can escape [5, 6].

The current baseline of MAVEN science observations spans over 2 Mars years (September 2014 through present). During this time, Mars experienced a strong solar weather event (in Sept 2017) [7] as well as a planet encircling dust event (in Jun 2018). The properties obtained from analyzing the echelle observations of D and H emissions during these times have revealed insights into the variability and dependencies of the escape rate of water from Mars at times of extreme external (solar weather) events [8] as well as internal (dust storm).

References:

- [1] Jakosky, B. et al., *Science*, 2015, 350(6261), 643, doi:10.1126/science.aad3443
- [2] McClintock, W. et al., *Sp. Sci. Rev.*, 2015, 195(1-4), 75-124, doi:10.1007/s11214-014-0098-7.
- [3] Mayyasi, M. et al., *J. Geophys. Res. // Space Physics*, 2017a, 122, doi:10.1002/2016JA023466.
- [4] Mayyasi, M. et al., *J. Geophys. Res. // Space Physics*, 2017b, 122, doi:10.1002/2017JA024666.
- [5] Clarke, J., *Nature*, 2018, doi:10.1038/s41550-018-0383-6
- [6] Kass, D., *Eighth International Conference on Mars*, No. 1791, 1169, 2014, 14018 July.
- [7] Lee, C. et al., *Geophys. Res. Lett.*, 2018, doi:10.1029/2018GL079162.
- [8] Mayyasi, M. et al., *Geophys. Res. Lett.*, 2018, 45, doi:10.1029/2018GL077727.

DECIPHERING NOACHIAN GEOLOGICAL AND CLIMATE HISTORY OF MARS: MAJOR GEOLOGIC PROCESSES AND THEIR CLIMATIC CONSEQUENCES

J. Head¹, R. Wordsworth², F. Forget³, M. Turbet³

¹*Brown University, Providence, RI 02912 USA, james_head@brown.edu;*

²*Harvard University, Cambridge MA 02138 USA;*

³*Lab. de Météorolog Dynamique du CNRS, Université Paris 6, Paris, France*

Keywords:

Noachian, impact, mineralogy, climate optimum, volcanism.

Introduction:

We apply a stratigraphic approach to the major Noachian geological processes and observation, knowns and unknowns [1-3] to provide insight into potential changes as a function of time, and to assess their climatic consequences.

Early Noachian:

This is the era of large impact basins, with Hellas Basin defining the base of the Noachian, followed by formation of Isidis and Argyre. Impacts are known to have size-dependent effects in terms of ejecta and influence on the atmosphere, ranging from blowing off a significant part of the atmosphere, through global distribution of silicate vapor that results in precipitation of silicate vapor cloud condensate, and significant but short-lived very hot rainfall [4-6]. Recent research has underlined the size-dependent effects, finding that large basins could form global effects while those below ~50 km would have only local effects [7]. Could the global effects form a global stratigraphic marker horizon for the major Noachian basin analogous to the Imbrium basin on the Moon?

The Noachian Mineralogical Alteration Paradox:

Ever since OMEGA [8] documented the dominance of phyllosilicates (clays) in the Noachian, a solution has been sought to provide the three necessary ingredients to account for their formation: 1) abundant liquid water, 2) temperatures >273K, and 3) prolonged exposure [9], while at the same time accounting for other observed minerals (e.g., olivine) that are unstable under these conditions. A "warm and wet" climate has often been cited as the solution [10], but the phyllosilicates do not clearly coincide in time or space with the Late Noachian VN/CBL/OBL assemblage [3], leading many to consider that at least some of the phyllosilicates formed deeper in the crust under hydrothermal conditions [11]. A solution to this paradox might be found in the formation of impact basins earlier in the Noachian: In an update [6] of the global effects of impact basin formation [4-5], the immediate aftermath of the vapor cloud condensation is shown to be characterized by the global precipitation of sustained hot rains (considerably above 273K), and lasting for several centuries. This mechanism (Fig. 1) [6] provides widespread, extremely hot water interacting with the surface and near-surface substrate for centuries, a duration sufficient to provide leaching of decameters of substrate. Support for this hypothesis [6] comes from extensive the association of many of the phyllosilicates with the Noachian basins Hellas, Isidis and Argyre [9, 12-13] and other extensive deposits dated to this period [14]. These deposits may provide stratigraphic time-markers for the specific impact basins [6, 15].

Middle-Late Noachian:

This is the post-Argyre basin period; impact cratering at the sub-large basin scale continues with declining flux. In the "warm and wet/arid" climate scenario [10], the dominant process of crater degradation (loss of small craters; erosion of larger crater rim/ejecta, infilling of crater interior) is rainfall-related diffusional processes that are intermittent and at sufficiently low rates that water infiltration dominates over surface runoff and VN systems do not form. In this scenario, although the climate is arid, MAT is required to be >273 K [10], implying a vertically integrated hydrologic system in the equa-

torial/mid latitudes. This ambient “warm and arid” climate is envisioned to persist for several hundred million years [10] (Fig. 1). The Late Noachian dominance of the VN-CBL-OBL geomorphic assemblage is envisioned as representing a “climatic optimum” [16], producing “warm and wet” conditions characterized by sufficient rainfall precipitation to overcome infiltration, and cause widespread fluvial and lacustrine activity. Here we separate out the “crater loss/degradation” component of the “warm and arid/wet geomorphic assemblage” and treat separately the remaining “pluvial/fluvial/lacustrine” VN/CBL/OBL component.

“Crater Loss/Degradation” Component:

Are there alternatives to the “warm and arid crater loss/degradation” [10] scenario? Could the formation of the earlier Noachian impact basins have played a role? Following [4-5], [6] have proposed that global deluge-scale rainfall phases that immediately follow basin formation could obliterate small craters and cause extensive planation and infilling of pre-existing distal craters. Furthermore, [7] have shown that smaller basins and large craters may also produce regional erosion and degradation effects. Detailed stratigraphic analyses are required to assess this option further [6]. A second alternative, involving the “cold and icy” climate scenario [17-19]; [20] explores the effects of a regional ice sheet predicted by this model in masking the sub-ice surface from smaller impacts, and facilitating the observed rim degradation and infilling of Noachian craters. Neither of these two options requires MAT in the >273 K range. We conclude that the “crater loss/degradation” component of the “warm and arid/wet geomorphic assemblage” may also be consistent with other climate scenarios.

Volcanism and Volcanic Resurfacing:

The beginning of the LN-EH volcanism phase; resurfacing of Arabia Terra and other Noachian plains formation, potential explosive volcanism, and peak eruptive phases could potentially cause decades to centuries of warming [22].

Late Noachian “Climate Optimum”:

This is the known period of dominance of the VN-CBL-OBL geomorphic assemblage envisioned as representing a “climatic optimum” [16] (Fig. 1), transitioning from “warm and arid” to produce “warm and wet” conditions characterized by sufficient rainfall precipitation to overcome infiltration, and cause widespread fluvial and lacustrine activity. Because of the alternative explanations for the “crater loss/degradation” component [6, 20], not involving MAT in the 273 K range, here we focus only on the “pluvial/fluvial/lacustrine” component (VN/CBL/OBL) of the “warm and arid/wet geomorphic assemblage” and assess the climate implications (Fig. 1). Key questions are: Nature of ambient climate [10, 18], source of water [21], volume of water [21], continuous or discontinuous conditions [21], intermittency [23], total duration [23], and presence of oceans [24]?

The Late Noachian Climate Paradox (LNCP):

The Late Noachian climate paradox [1] can be stated as follows: 1) Robust LN Mars climate and general circulation models [17-18] predict MAT ~ 225 K, and an altitude-dependent stability of snow and ice, such that the surface water inventory is deposited preferentially above an ELA of $\sim +1$ km (southern uplands and south circumpolar regions), the “icy highlands” model [18-19]. In this ambient atmosphere, no combination of spin-axis/orbital parameters can produce significant melting of this snow and ice anywhere on the planet [25]. 2) The well-documented, “pluvial/fluvial/lacustrine (VN/CBL/OBL)” component of the “warm and wet geomorphic assemblage” [10, 16], in contrast, shows unequivocally that liquid water flowed extensively across the surface, ponded, and overflowed, creating fluvial networks systems as long as 1000 km [3]. Clearly, these two aspects are incompatible and represent a paradox. On the one hand, climate modelers find great difficulty in achieving MAT >273 K (no combination of sustained greenhouse gas sources have been able to achieve MAT >273 K for the duration of M-L Noachian), and geologists have not found an alternate explanation to widespread flowing liquid water for the VN/CBL/OBL fluvial assemblage.

A Candidate Solution to the Late Noachian Climate Paradox:

We propose that a solution to the LNCP lies in a “cold and icy” ambient background climate (MAT ~ 225 K) [17-19] that undergoes multiple episodic/periodic

regional to global warming perturbations, that either individually or collectively are sufficient to account for the observed “warm and wet geomorphic fluvial assemblage”. Among the candidates for such perturbations are: 1) periods of abbreviated greenhouse gas release sufficient to raise MAT 10-15 K so that peak seasonal (PST) seasonal or peak daytime melting (PDT) can melt snow-pack to form the observed VN/CBL/OBL [19, 25]; 2) Effusive/explosive volcanic eruptions at high enough fluxes that SO_2 release causes equatorial/mid-latitude atmospheric heating for decades to centuries to form the VN before global cooling [22]; 3) Post-Argyre large crater/small basin formation sufficient to perturb the atmosphere regionally to form the VN [7].

Conclusions:

A stratigraphic approach to understanding the climate of Noachian Mars [1-3] indicates that: 1) The Early Noachian is dominated by the formation of Hellas, Isidis and Argyre basins; associated with each basin is the collapse of a global vapor plume, condensation of silicate vapor and a hundreds of year long phase of torrential hot rains, potentially accounting for significant alteration of surface materials to phyllosilicates [15]. The formation of each basin emplaced a global meters-thick isochronous silicate condensate time marker accompanied by significant associated alteration to phyllosilicates [15]. The Early Noachian ambient background climate was profoundly perturbed by each impact event, with exact recovery pathways and times uncertain [7]. On the basis of the difficulty of sustaining a “warm and wet/arid” climate [10] for several hundred million years (Fig. 1), we adopt the “cold and icy” post-basin period (MN-LN) climate to be the ambient background climate. The LN “climatic optimum”, during which the VN/CBL/OBL systems formed, is interpreted to be due to one or more climatic perturbations operating to perturb MAT, PST, and/or PDT on the “icy highlands” climate model. These ideas can be tested with further analyses of the critical stages as described above. The transition from the Late Noachian to Early Hesperian sulfate formation is interpreted to be related to EH basaltic flood volcanism resurfacing at least 30% of the planet [26]; the subsequent waning global volcanic flux [21], together with losses to space [27], transitioned the global atmosphere toward decreased atmospheric pressure [28], an end to the “icy highlands”, the reduction of south polar cap (DAF) area/volume [29], the beginning of a bi-polar Mars, and reduction to even lower weathering/erosion rates.

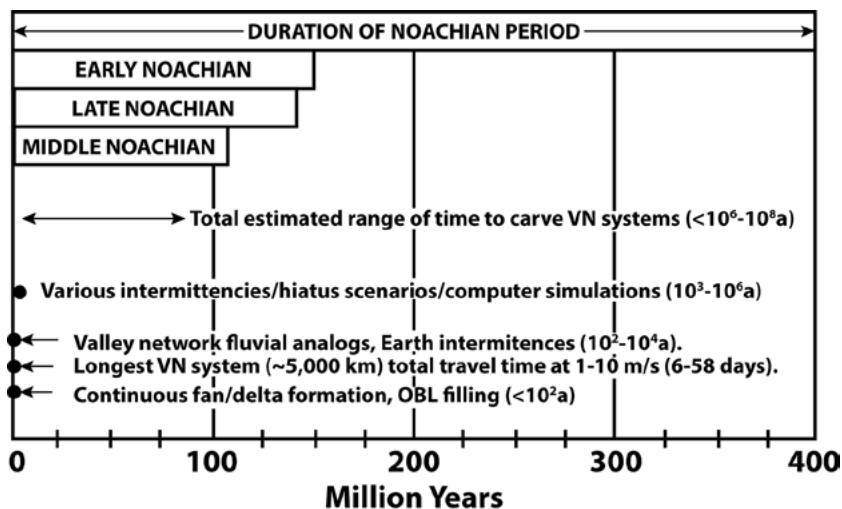


Fig. 1. Estimates for VN formation duration (from [23]).

References:

- [1] Head et al., 4th EMC, 2017;
- [2] Head et al., LPSC 46, #2176, 2015;
- [3] Fassett & Head, Icarus 211, 2011, 1204;
- [4] Segura et al., JGR, 2008, 113, E11;
- [5] Toon et al., AREPS 38, 2010, 303;

- [6] Palumbo et al., 6th MAMO, 2017;
- [7] Turbet et al., 6th MAMO, 2017;
- [8] Bibring et al., Science 312, 2006, 400;
- [9] Bishop et al., LPSC 48 1804, 2017;
- [10] Craddock & Howard, JGR 107, 2002, 5111;
- [11] Ehlmann et al., HNature 479. 2011, 53;
- [12] Murchie et al., JGR 114, 2009;
- [13] Mustard et al., JGR 112, 2006;
- [14] Bishop & Rampe, EPSL 448, 2016, 42;
- [15] Palumbo & Head, 8th Moscow S3, 2017;
- [16] Irwin et al., JGR 110, 2005, E12515;
- [17] Forget et al., Icarus 222, 2013, 5111;
- [18] Wordsworth et al., Icarus 222, 2013, 1;
- [19] Head & Marchant, Ant. Sci. 26, 2014, 774;
- [20] Weiss and Head, Planet. Space Sci. 117, 2015, 401;
- [21] Carr & Head, GRL 42, 2015, 1;
- [22] Halevy & Head, Nat. Geosci.1-4, 2014;
- [23] Buhler et al., Icarus 241, 2014, 130;
- [24] Clifford & Parker, Icarus 154, 2001, 40;
- [25] Palumbo et al, LPSC 48 2107, 2017;
- [26] Head et al., JGR 107, 2002, E1;
- [27] Jakosky et al., LPSC 45 1114, 2017;
- [28] Halevy & Head, LPSC 48 2519, 2017;
- [29] Scanlon et al., LPSC 47 1315, 2016.

TWO OCEANS ON MARS?: HISTORY, PROBLEMS AND PROSPECTS

J. Head¹, F. Forget², R. Wordsworth³, M. Turbet², J. Cassanelli¹, A. Palumbo¹

¹Brown University, Providence, RI 02912 USA, james_head@brown.edu;

²Lab. de Météorologie Dynamique du CNRS, Université Paris 6, Paris, France;

³Harvard University, Cambridge, MA 02138 USA

Keywords:

Oceans, shorelines, water volumes, outflow channels, Noachian, Hesperian, cryosphere.

Introduction and History:

Geological data have been cited to support the presence of two separate oceans in the past history of Mars, one during the Late Noachian and a later one during the Late Hesperian [1]. The presence of oceans remains a critical question, as evidenced by one of the driving questions of the 2017 4th Early Mars Conference: “*Did early Mars have oceans, lakes, and seas? If so, how did they form? How long did they last? And what was their fate?*” We briefly review the history of these concepts and then use a series of questions to address the current state of understanding of the hypothesis of the two oceans, working backward in time.

Late Hesperian Ocean:

Mariner 9 data first revealed evidence for extensive outflow channels (OC) emptying into the northern lowlands (NL) and the Hellas basin (see summary in [2]). After an early debate about the processes that carved them [3], water was quickly settled on as the medium, and the search for the fate of the water began. Early studies emphasized the possible presence of lakes at NL OC termini, but the complex geology of the NL precluded consensus on their size, fate of the water and sediment, and climatic effects of each event, particularly in the context of the current hyperarid, hypothermal Mars climate. At one end of the spectrum, many favored local NL lakes and little climate influence from the OC events [2], while at the other end, some favored an extensive ocean whose presence induced a warm climate [4] and was marked by several shorelines [5]. After extensive debate [2-3], a landmark paper [6] (Clifford, A Model for the Hydrologic and Climatic Behavior of Water on Mars) integrated a variety of data and perspectives and proposed that OCs formed in the circum-Tharsis region by cracking of a thick cryosphere, catastrophic release of groundwater under hydrostatic pressure, to flood the NL; recharge of the global aquifer was by basal melting of the south polar ice cap. Variations on this basic hypothesis [6] represent the current understanding and context for critical outstanding questions about the presence of an Hesperian ocean. 1. Where did the water come from? Virtually all hypotheses call on cracking of a globally continuous cryosphere and derivation of water from the groundwater (GW) system, but details differ about the exact cryosphere-cracking mechanism [7]. 2. What was the climate at the time? For the cracked cryosphere/pressurized groundwater release mechanism to work, there must have been a globally continuous cryosphere much like today [8]; supporting evidence comes from glacial-like features at Mangala Valles [9]. 3. How much water was there in each outflow event? This is still highly debated [10]; early estimates [3,4] assumed bankfull flow and later analyses revealed serious difficulties in sustaining very high flux estimates due to porosity, permeability, and overpressure factors [7]. These early very high estimates are likely to represent peak fluxes and thus lower overall total water volumes [11], with recent total OC volume estimated at 40 m GEL [10]. 4. Does the OC event change the climate to warm and wet? What happens to the OC/NL water during and between the OC events? Recent climate models show that if the global MAT was similar to today, as required by the cryosphere-breach model, each outflow event would produce a severe regional weather disturbance, local snow precipitation, but no

rainfall or any lasting effect on the global climate system [12]. If, for some reason, water did accumulate, a NL lake or ocean would rapidly freeze, sublime and go to cold traps [13]. There is no known mechanism to sustain an ocean in the intervening periods between OC events. 5. What was the period of time between outflow events? There are numerous outflow channels ranging in age from Hesperian to late Amazonian [14], and the average recurrence is likely to be tens to hundreds of millions of years. There is no known plausible mechanism to preserve an ocean over the time period between OC events; even water in a debris-rich ice-covered salty ocean would rapidly sublime and migrate to cold traps [13]. 6. In the OC breached-cryosphere hypothesis, how does the groundwater (GW) aquifer get recharged between OC events? MOLA data [15] showed that the Tharsis region cannot be recharged by the traditional south polar cap basal melting hypothesis [6]. Others have shown that top-down ice accumulation and basal melting are not plausible mechanisms for significant groundwater recharge [16] except at volcanic edifice heat pipes, which are volumetrically insufficient. A plausible mechanism for aquifer recharge is not currently available. 7. If the OC/GW breached-cryosphere hypothesis is correct, is there subsurface groundwater at other times in the Amazonian? The 236 km Lyot crater is an early/mid Amazonian-aged drillhole into the GW system below the cryosphere in the northern lowlands. It does not appear to sample groundwater [17, 18]. This raises the question of the time at which the global ice-cemented cryosphere stabilized, and when the groundwater system might have been depleted due to a growing cryosphere [19]. 8. Is there evidence for the evaporative loss of ocean water in the northern lowlands? It has been suggested that the Vastitas Borealis Formation (~100 m thick) which overlies km-thick Early Hesperian ridged plains in the NL [20], might be the sublimation residue of OC effluent [13,21]. 9. There is no ocean today: Is there evidence for northern lowlands ocean residual ice buried beneath later deposits? It has been proposed that significant buried residual ice from an Hesperian ocean lies buried beneath the NL surface [22], but the suggested thicknesses are not consistent with the documented stratigraphy [23] and cannot be readily distinguished from later obliquity-induced mid-high latitude phases of glaciation [e.g., 24]. 10. Are there alternative scenarios for OC/GW formation for OCs? No comprehensive model comparable to [6] has yet been proposed, but volcano-ice contact and deferred melting may provide potential meltwater generation and aquifer recharge mechanisms [25,26]. **Remaining Unexplained:** Several investigators have proposed that unusual features near the dichotomy boundary represent tsunami deposits from impacts into a northern lowland ocean [27-29]. Alternative explanations have not been proposed. Several previously proposed shorelines [5,8] have been shown to vary significantly from predictions for an equipotential surface [30], but not all (e.g., Utopia) have been explained by alternate mechanisms. **Synthesis:** Clearly, the OCs provided water to the NL periodically, but the total volumes, residence times and cumulative effects all still remain unclear. The issues and questions discussed above must be resolved before the presence of an Hesperian ocean can be confidently confirmed.

Late Noachian Ocean:

Evidence exists for a “warm and wet” Mars (valley networks, enhanced weathering rates and crater degradation) [31] in the Noachian before the cryosphere had become globally continuous. These features suggest the presence of rainfall and overland flow. 1. Where did the oceanic water come from? The “warm and wet” interpretation [8] implies global MAT >273K and a vertically integrated hydrologic system; these surface conditions further imply direct connections between the surface and the groundwater system and the presence of a NL ocean [8]. A “cold and icy” climate might permit breaching of the cryosphere in the lowest regions with MAT elevated 30-40 K [37]. 2. How much water was there? Noachian shorelines suggest at least a 10% greater area covered than the Late Hesperian Contact 2 (estimated at 100 m GEL) [29], but these contacts are not well defined [30] and alternative estimates for the inventory at this time are much lower [10]. 3. Do the proposed Noachian shorelines define an equipotential surface expected of an ocean? Proposed

Noachian shorelines [8] (e.g., Contact 1) are not well defined and deviate significantly from an equipotential surface [30]. 4. Was the Noachian ocean episodic (as in the OC input to the Hesperian ocean)? The Noachian ocean is predicted to persist as long as MAT exceeded 273K and the hydrologic system was vertically integrated. Eventual transition to a global cryosphere would have caused freezing of an ocean and growth of polar ice caps. 5. What climate and MAT are needed to sustain a Noachian northern lowland liquid ocean? To maintain a vertically integrated hydrologic cycle and a groundwater-fed ocean, MAT must exceed 273K. An MAT >273 climate [32-33] predicts some rainfall, but not in places consistent with the distribution of valley networks [32], and requires a robust and continuous warming mechanism of undetermined character [37]. 6. Where did Noachian oceanic water go? As the climate transitioned to the nominal Hesperian-Amazonian climate, the ocean froze, sublimated and migrated to cold traps, the ice-cemented cryosphere became globally continuous and sealed off the groundwater system from the surface [8]. 7. What are the implications of the loss of the Noachian ocean for the surface/near-surface water budget? The estimated volume of the Noachian global ocean (> 100 m GEL) is added to the polar/surface/near surface ice budget. There is a discrepancy between the surface-near surface water budget and these values [10], which is not readily accounted for solely by the freezing of GW to form the cryosphere [22]. 8. Is there evidence for Noachian northern lowlands ocean residual ice buried beneath later deposits? Any such deposits [22] would lie beneath ~1-2 km of Early Hesperian volcanic ridged plains [23]; at this lava thickness, buried ice would undergo either top down heating and melting during emplacement, and/or deferred melting and loss to the groundwater system [25-26]. 9. Are there alternative scenarios to the presence of a Noachian ocean to explain the observations? Recent Late Noachian climate models [34-35] predict global MAT ~225K, a globally continuous cryosphere and no rainfall or surface melting under a wide range of conditions. Punctuated heating events [36], however, are required to cause top-down melting of snow and ice to form the observed fluvial features. Synthesis: Multiple subsequent events in the NL have obscured direct evidence for a Noachian ocean; its presence requires sustained global MAT >273K, in conflict with recent climate models. Establishing the presence of a Noachian ocean requires reconciliation of these issues.

References:

- [1] Carr & Head, 2010, EPSL 294, 185;
- [2] Carr, 1996, *Water on Mars*, Oxford;
- [3] Baker et al., 1992, in *Mars*, 493, U of A.;
- [4] Baker et al., 1991, *Nature* 352, 589;
- [5] Parker et al., 1989 *Icarus* 82, 111;
- [6] Clifford, 1993, *JGR*, 98, 10973;
- [7] Andrews-Hanna & Phillips, 2007, *JGR* 112, E08001;
- [8] Clifford & Parker, 2001, *Icarus* 154, 40;
- [9] Head et al., 2004, *GRL* 31, L10701.;
- [10] Carr & Head 2015, *GRL* 42, 1;
- [11] Wilson et al., 2004, *JGR* 109, E09003;
- [12] Turbet et al., 2017, *Icarus* 288, 10;
- [13] Kreslavsky & Head, 2002, *JGR* 107, 5121;
- [14] Tanaka et al, 2014, USGS SIM 3292;
- [15] Carr, 2002, *JGR* 107, 5131.
- [16] Cassanelli et al., 2015, *PSS* 108, 54;
- [17] Russell & Head, 2002, *GRL* 29, 1827;
- [18] Weiss et al., 2017, *GRL* 44, 5336.
- [19] Weiss & Head, 2017, *Icarus* 288, 120;
- [20] Head et al., 2002, *JGR* 107 (E1);
- [21] Carr & Head, 2003, *JGR* 108, 5042;
- [22] Clifford & McCubbin, 2-16, *PLPSC* 47, 2388;
- [23] Kreslavsky & Head, 2002, *JGR* 107, 5121;
- [24] Head et al., 2003, *Nature* 426, 797;
- [25] Cassanelli & Head, 2016, *Icarus* 271, 237;
- [26] Cassanelli & Head, 2018, DOI: 10.1016/j.icarus. 2018.01.001;
- [27] Rodriguez et al., 2016, *Nat. Sci. Rpt.* 6, 25106;
- [28] Costard et al., 2017, *JGRP* 122, 633;
- [29] Clifford & Costard, 2017, 4th Early Mars, 3083;

- [30] Head et al., 1999, *Science* 286, 2134.
- [31] Craddock & Howard, 2002, *JGR* 107, 1;
- [32] Wordsworth et al., 2015, *JGR* 120, 1201;
- [33] Palumbo et al., 2018, *LPSC* 49;
- [34] Forget et al., 2013, *Icarus* 222, 81;
- [35] Wordsworth et al., 2013, *Icarus* 222, 1;
- [36] Head et al., 2017, 4th Early Mars, 3046/3047.
- [37] Palumbo et al. 9th MS3.

ASTROBIOLOGY – A NEW KID ON THE BLOCK

S. Jheeta,

NoR HGT & LUCA, 1 Scott Hall Crescent, Leeds LS7 3RB, UK;

Keywords:

Astrobiology, origin of life, Earth, Mars, Universe,

Introduction:

Since time immemorial it has been our persistent desire to discover where we come from and, every time we look up at the sky, we've asked ourselves, is there life elsewhere in the Universe. There is no simple answer to either of these questions, but in recent times our desire to find the answers has taken on a new dimension in the form of astrobiology. Astrobiology is a hot bed of research as more and more universities worldwide begin to incorporate this field into mainstream subjects such as biology, chemistry, geology and even medicine; all working to answer the questions posed above. More importantly, astrobiology has brought into focus the nature and origin of life in settings other than Earth. Our knowledge of the diversity of life on Earth has increased significantly since the time of the Viking missions to Mars in the mid-1970s (Soffen, 1977) and as a result we now have a better understanding of the extreme conditions under which life could possibly have originated and then evolved. This oral presentation seeks to review the current understanding of the of life and life elsewhere in the Universe

References:

- [1] Soffen, G.A., The Viking Project // J. Geophysics Research. 1977. V. 82(28) P. 3959–3970
- [2] Jheeta, S., Final frontiers: the hunt for life elsewhere in the universe // Astrophysics and Space Science. 2013. V. 348. P. 1-10.

OCEANS ON MARS: THE POSSIBILITY OF A NOACHIAN GROUNDWATER-FED OCEAN IN A SUB-FREEZING MARTIAN CLIMATE

A.M. Palumbo¹, J.W. Head¹

¹*Department of Earth, Environmental and Planetary Sciences, Brown University, Providence RI 02912, USA, Ashley_Palumbo@Brown.edu*

Keywords:

Mars, oceans, groundwater, climate, fluvial activity, cold and icy, Noachian.

Introduction and Background:

Numerous factors imply that one or more oceans persisted in the martian northern lowlands (NL) earlier in history, including putative shorelines [1–5], possible tsunami deposits [6,7], outflow channels that released catastrophic amounts of groundwater to the surface [8], the distribution of deltas [9], the Vestitas Borealis Formation [1], and the possibility of a once warmer and wetter climate, characterized by abundant pluvial activity and ponding of water at the surface [10–12]. Age variations in these factors imply the existence of two oceans, one in the Noachian and one in the Late Hesperian [13].

It is hypothesized that over-pressurization of the groundwater system led to cracking of the cryosphere and release of groundwater onto the surface [13], which ponded in the NL and formed the Hesperian ocean. Groundwater release was likely to have been important in the Noachian as well [2,13], albeit through a different release mechanism: if global MAT was >273 K, the balance between geothermal heating and heat conduction from the surface into the subsurface would not allow for a stable global cryosphere. Assuming a large enough groundwater reservoir, the groundwater system would be in contact with the surface at locations where the thickness of the cryosphere is zero, and groundwater would be released through the crust and pond at the surface, with release continuing until the system reaches hydrostatic balance [2]. Thus, the critical factors for hydrostatic stabilization of the groundwater system through groundwater release in the Noachian is a region with MAT >273 K, which is guaranteed if the climate was “warm and wet”, and sufficient volumes of groundwater such that groundwater system was in contact with the surface, which is likely to have existed in the Noachian due to the evidence for large volumes of groundwater release in the Late Hesperian [2].

However, whether the climate was “warm and wet”, as canonically considered with respect to a Noachian ocean, or “cold and icy”, as predicted by climate models, is a topic of ongoing research. Although the proposed “cold and icy” climate is characterized by global MAT $<<273$ K, there is significant regional and temporal temperature variation [e.g. 16]; lower elevation regions, such as the Hellas basin and Utopia Planitia, can have local MAT much higher than global MAT, which has important implications for the formation of a groundwater-fed ocean in a globally sub-freezing climate.

Therefore, in this analysis, we reconsider whether a Noachian ocean would preclude a “cold and icy” climate, or whether regional and temporal temperature variations could be sufficient to permit the formation of an ocean in a globally sub-freezing climate. To accomplish this, we address these questions:

- 1) What is the coldest possible global MAT at which groundwater release could occur somewhere on Mars?
- 2) In what locations would groundwater release occur?
- 3) At locations where local MAT is slightly below 273 K, are seasonal temperature variations sufficient to melt through the cryosphere and permit groundwater release?
- 4) What is the required near-surface water inventory for groundwater release?
- 5) If a given set of climatic conditions (which permit groundwater release) persisted because of punctuated heating in an ambient “cold and icy” climate, global MAT ~ 225 K, how long must the warmer climate persist to melt through the cryosphere and permit groundwater release?

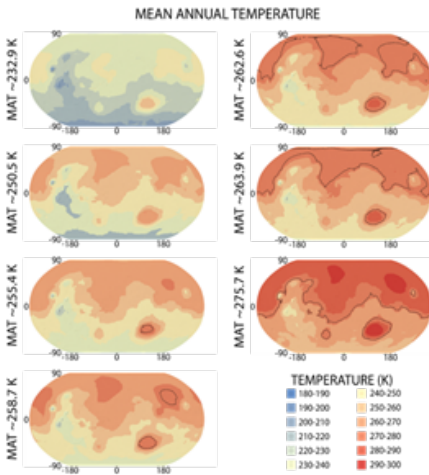


Fig. 1. Results of 25° obliquity simulation showing variations in regional MAT. Black line is 273 K contour.

Methods:

We utilize two methods to explore the possibility of a groundwater-fed Noachian ocean in a globally sub-freezing climate. (1) We implement the 3D LMD GCM and simulate the early climate for spin-axis/orbital and atmospheric pressure conditions representative of the Noachian [17,18]. To produce simulations of a range of global MATs spanning 225 K to 273 K, we introduce artificial greenhouse warming into the atmosphere through the use of a gray gas, which absorbs evenly across the IR spectrum at a defined absorption coefficient to imitate greenhouse warming. (2) We develop a basic heat conduction thermal model, following the methods of [13,19] and using reasonable estimates for porosity (following [19]), geothermal heat flux [19–22],

and pore closure depth (~10 km) [13]. Results and Conclusions:

We found that groundwater release and the formation of an ocean is possible in a globally sub-freezing climate. Our results and conclusions based on our findings from addressing the five research questions follow:

Previous hypotheses suggested that the existence of a groundwater-fed Noachian ocean requires a “warm and wet” climate [13]. This is because $\text{MAT} \geq 273 \text{ K}$ is required for there to be no cryosphere, permitting the groundwater to be in contact with the surface and allowing for groundwater to release onto the surface. However, regional MAT can deviate significantly from global MAT [16,23]. By exploring regional variations in MAT, we find that local $\text{MAT} \geq 273 \text{ K}$ exists somewhere on the planet for global $\text{MAT} > \sim 255 \text{ K}$ (Fig. 1, 2); groundwater release is possible at those locations.

Because of the adiabatic cooling effect [15,24], the locations with the highest local MAT are also the lowest elevations. Consequently, local $\text{MAT} \geq 273 \text{ K}$ occurs at the floor of the Hellas basin for global $\text{MAT} > \sim 255 \text{ K}$, but higher global MAT is required for groundwater release elsewhere on the planet (Fig. 1, 2). The second-lowest elevation location on Mars is the floor of Utopia Planitia; global $\text{MAT} > \sim 258 \text{ K}$ is required for local $\text{MAT} \geq 273 \text{ K}$. If the volume of water released at Utopia Planitia was large enough, this mechanism could lead to the formation of an ocean in the NL in a globally sub-freezing climate. Our results predict that a groundwater-fed ocean in the NL would not be possible without a corresponding groundwater-fed body of water in Hellas.

- 1) In regions where MAT is $< 273 \text{ K}$, we used a basic thermal model to estimate the response of the cryosphere to seasonal temperature variations in order to test the hypothesis that hot summer temperatures could be responsible for effectively removing the cryosphere and permitting groundwater release. We find that this effect only occurs in locations where MAT is $\sim 272 \text{ K}$, very close to the melting point of water.
- 2) We estimated the volume of water that is required to be in the subsurface in order for the groundwater system to be in contact with the lowest elevation points in Hellas basin and Utopia Planitia, which is required for groundwater release. The required volume of water changes as a function of global MAT because colder climates imply a larger cryosphere, which requires more water to be trapped as ice cement in the cryosphere before the crustal pore space can be filled with groundwater. We also estimated the absolute minimum volume of water that would be required to be in the subsurface. In this climate scenario, surface temperatures are $> 273 \text{ K}$ everywhere on the planet, implying that there is no cryosphere anywhere on the planet and all subsurface water is in the groundwater system. We find that the absolute minimum required volume of subsurface water for groundwater release at Hellas is $\sim 63 \text{ m GEL}$ and at Utopia is $\sim 170 \text{ m GEL}$.

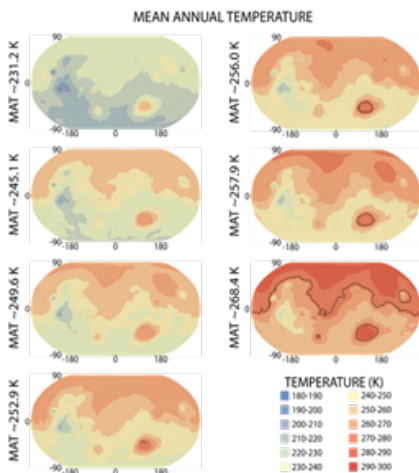


Fig. 2. Same as fig. 1, but with 45° obliquity.

consecutive years for groundwater release to be possible at Utopia. A punctuated heating event of this duration could be caused by either (1) impact cratering-induced heating in the early- to mid-Noachian following basin-scale impacts which would increase temperatures $\gg 273$ K for tens to hundreds of years, or (2) a transient reducing greenhouse atmosphere which could increase global MAT to ~ 273 K for up to $\sim 10^5$ years.

In conclusion, the formation of a groundwater-fed ocean is possible in a globally sub-freezing climate. If global MAT was ever ~ 255 K in the Noachian and the subsurface contained ~ 63 m GEL water, the groundwater would release onto the surface at Hellas and pond within the basin. If global MAT was ever ~ 258 K and the subsurface contained ~ 170 m GEL water, an additional groundwater-fed body of water would form at Utopia, possibly leading to flooding of the NL and the formation of an ocean. An ocean sourced at Utopia in a globally sub-freezing climate would have been preceded by and concomitant with a sea in Hellas and the ocean would remain ice-free for a geologically short period of time, possibly only a few hundred days.

Acknowledgements:

This work was supported by NASA Headquarters under the NASA Earth and Space Science Fellowship Program for AMP (Grant 90NSSC17K0487) and by NASA for participation in the Mars HRSC Team (JPL 1488322) for JWH.

References:

- [1] Carr and Head, *JGR*, 2003, 108, DOI 10.1029/2002JE001963.
- [2] Clifford and Parker, *Icarus*, 2001, 154, 40–79.
- [3] Head et al., *Science*, 1999, 286, 2134–2137.
- [4] Parker et al., *JGR*, 1993, 98, 11061–11078.
- [5] Parker et al., *Icarus*, 1989, 82, 111–145.
- [6] Costard, F. et al., *JGR Planets*, 2017, 122, 2016JE005230.
- [7] Rodriguez et al., *Sci. Rep.*, 2016, 6, 25106.
- [8] Baker et al., *Nature*, 1991, 352, 589.
- [9] Achille and Hynes, *Nat. Geosci.*, 2010, 3, 459.
- [10] Craddock and Howard, *JGR Planets*, 2002, 107, 5111.
- [11] Ramirez, *Icarus*, 2017, 297, 71–82.
- [12] Ramirez and Craddock, *Nat. Geosci. Perspect.*, 2018, 11, 230–237.
- [13] Clifford, *JGR Planets*, 1993, 98, 10973–11016.
- [14] Head and Marchant, *Antarct. Sci.*, 2014, 26, 774–800.
- [15] Wordsworth et al., *Icarus*, 2013, 222, 1–19.
- [16] Palumbo et al., *Icarus*, 2018, 300, 261–286.
- [17] Laskar et al., *Icarus*, 2004, 170, 343–364.
- [18] Jakosky et al., *Science*, 2017, 355, 1408–1410.
- [19] Clifford et al., *JGR*, 2010, 115, E07001.
- [20] McGovern et al., *JGR Planets*, 2004, 109, DOI 10.1029/2004JE002258.
- [21] Solomon et al., *Science*, 2005, 307, 1214–1220.
- [22] Zuber, *Nature*, 2001, 412, 220–227.
- [23] Richardson and Mischna, *JGR*, 2005, 110, E03003.
- [24] Forget et al., *Icarus*, 2013, 222, 81–99.

AN INTEGRATED MODEL OF PRECIPITATION, INFILTRATION, AND GROUNDWATER FLOW ON MARS

B.D. Boatwright, J.W. Head

Brown University, Providence, RI USA, benjamin_boatwright@brown.edu

Keywords:

Mars, hydrology, landform evolution, geomorphology, climate

Introduction:

The evolution of landscapes is often understood through analogies with fluid mechanics, and models of sediment transport are typically based on some form of the advection-diffusion equation. Disentangling the relative contributions of advective and diffusive processes on the surface of Mars remains challenging, as both processes are likely to have had some effect on the landscape we observe today. Much work has been carried out over the past few decades with the MARSSIM landform evolution model, otherwise known as DELIM or MSLM [1], which has used the advection-diffusion relation to successfully recreate the gross morphology observed in ancient martian terrains [2-9]. Despite its extensive use and reuse, relatively little has changed about the fundamental equations that underlie it since its original formulation some three decades ago. This is a testament to its robustness and wide applicability, but also highlights the fact that a critical assessment of the model has not been made in quite some time. We first describe the theory that governs the MARSSIM model. We then suggest modifications that could improve the existing model to even better represent the hydrologic cycle of Mars, with particular emphasis on an integrated system of precipitation, infiltration, and groundwater flow.

Theory:

The MARSSIM model is written in the Fortran programming language, and operates by running several scripts that each simulate a separate geomorphic process. These scripts modify a digital elevation model (DEM) of the surface according to an input parameter file. The model can simulate erosion through fluvial channels, mass wasting, groundwater seepage, eolian transport, and impact cratering. The model uses a finite difference approximation to calculate the sediment flux into and out of each cell in the DEM, which redistributes the sediment into a modified surface topography after each iteration.

Fluvial channels.

Erosion in fluvial channels can be divided into weathering-limited and transport-limited regimes. Erosion is weathering-limited when the total sediment flux is less than the capacity load, such that the availability of sediment in the stream is the limiting factor; erosion is transport-limited when the total sediment flux meets or exceeds the capacity load of the stream, such that the discharge is the limiting factor. Both weathering-limited and transport-limited erosion are functions of the shear stress imparted by the fluid flow on the sediment. In addition, transport-limited erosion is controlled by the grain size, specific weight, and porosity of the bedload sediment. The erosion rate due to transport in fluvial channels can be written as a power law function of the topographic slope S and contributing area A . The constants K_z , e , and b are functions of the channel geometry, and τ_c is a critical shear stress for transport [2,4-7]:

$$\frac{\partial z_f}{\partial t} = -K_t (K_z S^{0.7} A^{0.6e(1-b)} - \tau_c) \quad (1)$$

Mass wasting.

Mass wasting is used collectively to refer to the downslope movement of material under the influence of gravity through such processes as creep, landsliding, or rainsplash. These are modeled in a single equation that takes

into account the combined influences of slope and near-failure components with a characteristic diffusivity K_s or K_p , respectively. Erosion due to mass wasting varies nonlinearly with topographic slope as the slope approaches some threshold value S_c , analogous to an angle of repose for the given material beyond which slope failure is expected to occur [2,4-7,10]:

$$\frac{\partial z_m}{\partial t} = K_s S + K_f \left(\frac{1}{1 - (S/S_c)^a} - 1 \right) \quad (2)$$

Groundwater flow.

The infiltration and distribution of groundwater into the subsurface is modeled by Darcy's law with the DuPuit–Forchheimer assumption of an unconfined, steady-state aquifer. It is dependent on the transmissivity of the subsurface $K_0 h_e$, which decays exponentially with depth, and the hydraulic gradient S_{gw} in the x and y directions. The groundwater flow rate is offset by a constant recharge rate I_{xy} [6]. Discharge from groundwater seepage when the water table intersects the surface is added to the preexisting discharge from runoff:

$$-K_0 h_e S_{gw} + I_{xy} = 0 \quad (3)$$

Eolian transport.

Erosion due to deflation and scour by the wind is given as a non-mass conserving average of the minimum and maximum eolian erosion rates E_{min} and E_{max} , scaled by an exposure index I_{ek} that quantifies the topographic prominence of any given point. The exposure index will preferentially erode isolated peaks and ridges and deposit wind-blown sediment in depressions and valleys [4,6]:

$$\partial z_\varepsilon / \partial t = (E_{min} + E_{max})/2 + (E_{min} - E_{max})/2 \left[\frac{K_\varepsilon}{(1 + K_\varepsilon^2)^{1/2}} \right] \quad (4)$$

$$K_\varepsilon = \frac{1}{\sqrt{2}} \left(\frac{2I_{ek}}{E_{90} - E_{10}} - 1 \right)$$

Impact cratering.

The emplacement of impact craters is modeled as a static process according to a global model of fresh crater geometry for Mars [10]. Impacts are generated based on a -2 power law size-frequency distribution [11] at a defined time interval between events. An inheritance parameter I_i governs how much of the preexisting topography remains after the impact, and the crater profile is given as a deviation ΔH from the average pre-impact elevation z_{avg} . The constant G is also a function of the inheritance parameter [5]:

$$\Delta z_i = \left\{ \begin{array}{l} \Delta H(r_i) + (1 - I_i) \left(\frac{2r_i}{D} \right)^2 (z_{avg} - z_i) \quad r \leq D \\ \Delta H(r_i) + G(z_{avg} - z_i) \quad r > D \end{array} \right. \quad (5)$$

An integrated hydrologic model:

The above description provides an overview of the way in which various sediment transport processes are represented in the model. Discharge Q due to surface runoff is given as a power law function of the contributing area A multiplied by a factor known as the runoff yield P [2,4-7]:

$$Q = PA^e \quad (6)$$

The runoff yield can be defined implicitly by subtracting infiltration from precipitation, such that the runoff yield is equal to the amount of precipitation that remains on the surface as runoff after some fraction has infiltrated into the subsurface as groundwater. The infiltration rate is defined separately in the groundwater flow equation as a recharge rate I_{xy} (Equation 3) and is thus not functionally related to the precipitation rate, which we will call P' , or the runoff yield P at the surface.

We propose a relatively straightforward modification such that the runoff yield and recharge rate are connected via precipitation and infiltration. This requires determining the appropriate infiltration rate to substitute for

the groundwater recharge rate I_{xy} . We make the following assumptions: the instantaneous depth of precipitation is negligible (no water ponded at the surface), the pore space immediately below the surface is unsaturated, infiltration occurs only in the vertical direction, and groundwater recharge comes only from infiltration (no hydrothermal component). Infiltration through unsaturated pore space can be modeled by a simplified version of Equation 3, solved at zero depth in the z direction, where the transmissivity is equal to the hydraulic conductivity at the surface:

$$I_{xy} = K_0 S_{gw} \quad (7)$$

$$S_{gw} = \frac{\partial}{\partial z} (H_g + H_p)$$

The hydraulic gradient S_{gw} measures the change in hydraulic head with distance. The hydraulic head is equal to the sum of the gravitational head H_g and pressure head H_p . For flows with negligible depth, the pressure head is zero since no pressure is imparted onto the flow by overlying water. Since the flow is in the vertical direction, the distance ∂z is equivalent to the gravitational head, so the hydraulic gradient is unity. This means the groundwater recharge rate I_{xy} is equal to the surface hydraulic conductivity K_0 , assuming K_0 does not decrease appreciably with depth. The runoff yield P can now be written as a function of the precipitation rate P' and recharge rate I_{xy} . The definition of discharge (Equation 6) can also be written as a function of the same variables:

$$P = P' - I_{xy} = P' - K_0 \quad (8)$$

$$Q = (P' - K_0) A^c$$

This allows the model to reflect the intuitive relationship between runoff and infiltration as two components of precipitation. The MARSSIM literature has not treated runoff and infiltration as connected processes, but rather assumed either complete runoff or complete infiltration [4-7]. The interactions between the two processes are particularly important to consider in the context of early Mars climate, when infiltration with limited runoff under arid conditions might have resulted in the particular pattern of degradation observed in highland craters during the Middle and Late Noachian [3-4,13-15]. Future studies should focus on the influence of infiltration in crater degradation and how it might be manifested in the hydrology and morphology of the surface.

References:

- [1] Howard A.D. 2009, MARSSIM Landscape Evolution Model, <http://erode.evsc.virginia.edu>;
- [2] Howard A.D., Water Resources Res., 1994, 30;
- [3] Craddock R.A. et al., JGR, 1997, 102;
- [4] Forsberg-Taylor N.K. et al., JGR, 2004, 109;
- [5] Howard A.D., Geomorph, 2007, 91;
- [6] Luo W., Howard A.D., JGR, 2008, 113;
- [7] Barnhart C.J. et al., JGR, 2009, 114;
- [8] Matsubara Y. et al., JGR, 1987, 116;
- [9] Matsubara Y. et al., JGR, 2013, 118;
- [10] Roering J.J. et al., Water Resources Res., 1999, 35;
- [11] Garvin J.B. et al., 6th Intl. Conf. on Mars, 2003, #3277;
- [12] Werner S.C., Tanaka K.L., Icarus 215, 2011;
- [13] Craddock R.A., Maxwell T.A., JGR 98, 1993;
- [14] Hynek B.M., Phillips R.J., Geol. 29, 2001;
- [15] Irwin R.P. et al., JGR 116, 2011.

FUMAROLIC ALTERATION ON MARS: LESSONS LEARNED FROM TERRESTRIAL ANALOG FIELDWORK

J. Flahaut¹, J.L. Bishop², F. Viveiros³, C. Silva^{3,4}, I. Daniel⁵, S. Silvestro⁶,
D. Tedesco⁷, J.V. Cruz³, L. Moreno^{3,4}, P. Freire³

¹CRPG, CNRS/Université de Lorraine, 15 rue Notre Dame des Pauvres,
54500 Vandœuvre-lès-Nancy, France, flahaut@crpg.cnrs-nancy.fr;

²SETI Institute/NASA-ARC, Mountain View, CA, 94043;

³IVAR, Universidade dos Açores, Ponta Delgada, Portugal;

⁴CIVISA, Universidade dos Açores, Ponta Delgada, Portugal;

⁵LGL-TPE, CNRS/Université de Lyon, 69622 Villeurbanne Cedex, France;

⁶INAF- Osservatorio Astronomico di Napoli, Italy;

⁷Campania University - Luigi Vanvitelli, Caserta, Italy

Keywords:

Mars, Hydrothermalism, alteration pattern, fumaroles, hot springs, mineralogy, Earth analogs, spectroscopy.

Introduction:

Since their discovery in the 1970's, deep sea hydrothermal vents are considered a likely cradle for the origin of Life on Earth (e.g., [1]). As this hypothesis does not respect the chemistry conservation principle, a proposed alternative is that Life might have rather appeared in continental hydrothermal systems [2]. In both cases, vents could provide the necessary energy and a source of catalysts (e.g., metals, sulfides....) and appear to be prime targets for the search of ancient Life elsewhere in the Universe.

On Earth, plate tectonic processes destroyed most surface rocks formed within the first ~1 billion years, limiting our ability to provide limits on planetary habitability at the time Life is thought to have developed, and to test the previous hypotheses. In contrast, Mars has been much less tectonically active, and large outcrops of ancient rocks, including hydrothermal vents, are preserved and accessible on the surface [3]. The first definitive evidence for continental vents on Mars is the in situ detection of amorphous silica-rich outcrops (>90% wt opal-A) by the Mars Exploration Rover Spirit, which have been tentatively interpreted as either acid sulfate leaching in fumarolic environments or direct precipitation from hot springs [4,5]. Multiple detections of hydrated minerals made from orbit, such as amorphous silica in Valles Marineris [6,7] or within the Nili Patera caldera [8] have also been interpreted as the products of volcanic hydrothermal alteration, although their definitive identification is more difficult with remote sensing instruments. This year, putative ancient deep-sea vents have been reported in the Eridania region of Mars, but this interpretation is still hotly debated [9,10].

The identification and interpretation of hydrated mineral assemblages, within ancient aqueous environments on Mars, are key to the evolution of the Martian surface and its past habitability. In order to help the identification of fumarole and hot spring deposits on Mars, we surveyed their characteristics (especially mineralogic assemblages, but we also investigate biological potential/diversity) at a few terrestrial analog sites. Several techniques of mineral identification (VNIR spectroscopy, Raman spectroscopy, XRD) will be used and compared. Results obtained from field observations and laboratory sample analyses at the Solfatara Volcano (Campania, Italy), Pico Alto Volcano and Furnas Volcano (Azores archipelago, Portugal) are presented hereafter.

Geological context:

The Solfatara volcano is the most active site of the Phlegrean fields caldera in Italy. This 4000 year old volcanic crater is located in the Campanian extensional back-arc, only a few kilometers west of the city of Naples. Current volcanic activity is expressed at the surface through fumarole emissions, thermal pools, and seismic activity [e.g., 11] (Fig 1a). Several vents emitting fluids at 90°C were observed along the crater fractured walls. The maximum temperature of 160°C was found in the SE sector of the crater, at the Bocca Grande vent, and is responsible

for the formation of very distinct deposits [12]. Fumarole gas emissions include mostly H_2O (80-90%), while the dry gases show more than 99% of CO_2 and H_2S . Previous geochemical analyses showed that this H_2S is the precursor of sulfate minerals via oxidation to H_2SO_4 , acidic interaction with rocks and crystallization of salts [13].

The Pico Alto and Furnas volcanoes are, respectively, located on the Terceira and São Miguel Azorean Islands. Located in the Atlantic Ocean at the triple junction of the Eurasian, North American and Nubian tectonic plates, the Azores are thought to originate from the combination of the mid-oceanic ridge activity and a hotspot [14]. The two polygenetic volcanoes display hydrothermal fumaroles with temperatures ranging between 97-100 °C [15] (Fig 1b,c). Gas compositions were roughly similar not only between the various vents within the same volcano but also on the different islands. Gas emissions include H_2O and CO_2 as major components with H_2S , H_2 , CH_4 , CO , Ar, O_2 and N_2 as minor species [16]. In addition to the fumaroles, the Furnas volcano also has several hot springs discharges.

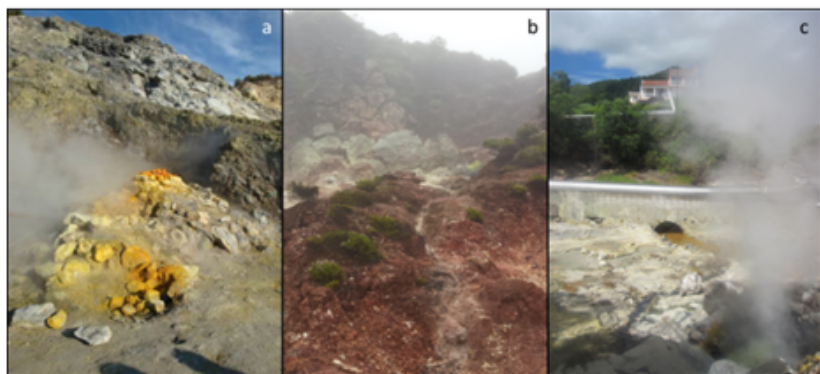


Fig. 1. Alteration around the fumaroles and hot springs at the Solfatara (a), Pico Alto (b) and Furnas (c) volcanoes.

Alteration at these sites was studied with portable instruments (VNIR and Raman spectrometers) during field campaigns carried out at the fall 2015 and 2017. Samples were collected for further characterization by XRD and whole rock + water chemical analyses [12, 17].

Observed alteration patterns:

Table 1. Main characteristics of the 3 study sites.

	Solfatara		Pico Alto	Furnas
alteration minerals detected	Amorphous silica Alunite / Jarosite Alunogen Alum-K Coquimbite Goldichite	Amorphous silica Realgar Cinnabar Orpiment Other As bearing species	Amorphous silica Alunite Kaolinite Montmorillonite Jarosite Hematite	Amorphous silica Alunite Alum-K Alunogen Copiapite Goldichite
Fluid T (°C)	95	160	98	98
Fluid composition	H_2O , CO_2 , H_2S , N_2 , H_2 , CH_4 , He, Ar		H_2O , CO_2 , H_2S , H_2 , N_2 , CH_4 , He, Ar	H_2O , CO_2 , H_2S , H_2 , N_2 , CH_4 , He, Ar
Bedrock composition	Mineralogy: Trachyte, K-feldspars (mostly sanidine). Chemistry: high Si (>80wt%), high Ti (>0.7wt%), high S (>0.4 wt%) --> leached.		Mineralogy: Comendite, Feldspars, quartz, riebeckite. Chemistry: 64 wt% Si, 11 wt% Al, 9wt% Fe.	Mineralogy: Trachyte, Feldspars, quartz, phlogopite. Chemistry: 61 wt%Si, 17 wt% Al, 4wt% Fe.
Bedrock texture	pumice, porous bedrock		lava flow	pumice

Characterization of the collected rock samples revealed a variety of mineralogical assemblages and alteration patterns at the three sites (Table 1). All three volcanoes are of trachytic affinity, but show subtle differences in their bedrock composition (see [12,17] for more details).

Discussion and perspectives:

An obvious observation is the influence of temperature on the resulting assemblages found at the Solfatara crater various vents. Nevertheless at the other sites (Furnas and Pico Alto), various mineralogical assemblages are observed despite roughly similar temperatures, fluid and bedrock compositions. Whereas Pico Alto shows the presence of Al-rich clays and hematite, Furnas Volcano is, like the Italian Solfatara 90°C vents, dominated by amorphous silica and Al/Fe hydroxyl-sulfates. Different assemblages may be produced based on a number of factors that control hydrothermal alteration such as the rock type, but also temperature, pressure, permeability, fluid composition and event duration [18]. In our case, subtle differences in bedrock texture and porosity (lava versus pumice), the (unknown) alteration duration or the surface proximity of the water table could all explain the differences in the resulting alteration patterns. In fact, at Furnas and Solfatara volcanoes the presence of shallower hydrothermal systems is confirmed by the existence of hot springs.

The mineralogy of the alteration and depositions minerals was surveyed with various techniques : VNIR spectroscopy, Raman spectroscopy and XRD analyses. All the instruments we used had somehow the capacity to detect the iron and hydrated minerals previously described and should therefore be able to identify and map them on Mars. We found that VNIR spectroscopy was more sensitive to the presence of coatings, and Raman spectroscopy was more limited towards the characterization of amorphous material, but their results are in accordance with XRD analyses. The XRD techniques were the only one to provide access to the full mineralogical assemblage in case of complex mixtures, whereas with VNIR and Raman measurements, we could often only identify a few phases. However, XRD is challenging for remote, field observations as it requires a dry, finely powered and sieved sample. Therefore a combination of these techniques, is probably the best way to derive the most comprehensive information on the sample suite. That is fortunately what will be carried on the next generation of Mars rovers, such as Mars 2020 and ExoMars 2020, which might have the opportunity to encounter past hydrothermal environments in Gusev Crater [4] or Mawrth Vallis [19, 20].

Acknowledgments:

Support from the NWO, CNES (APR ExoMars and Luna attributed to J. Flahaut), IVAR/Univ of Azores, ASDinc, NAI the Solfatara staff is much appreciated.

References:

- [1] Nisbet, E.G., & Sleep, N.H. (2001) *Nature*, 409(6823), 1083-1091.
- [2] Da Silva, L. et al. (2015) *J. Mol. Evol.*, 2015, 80, 86.
- [3] Carr, M.H. & Head III, J.W. (2010) *EPSL*, 294(3-4), 185-203.
- [4] Ruff S.W. et al. (2011) *JGR*, 116, E00F23.
- [5] Squyres S.W. et al. (2008) *Science*, 320, 1063-1067.
- [6] Thollot P. et al. (2012) *JGR*, 117, E11.
- [7] Milliken, R.E. et al. (2008) *Geology*, 36(11), 847-850.
- [8] Skok, J.R. et al. (2010) *Nature Geoscience*, 3(12), 838.
- [9] Michalski, J.R. et al. (2017), *Nature communications*, 8, 15978.
- [10] Osterloo, M.M. et al. (2008), *Science*, 319(5870), 1651-1654.
- [11] Chiodini G. et al. (2017), *Sci. Reports*, 7, 4472.
- [12] Flahaut, J. et al. (2017) *LPSC*, #2071.
- [13] Valentino, G.M. et al. (1999) *JVGR*, 91.
- [14] Yang, T. et al. (2006), *Earth Planet. Sci. Lett.*, 250, 11–26.
- [15] Ferreira, T. et al. (2005) *An. of Geophysics*, 48(4-5).
- [16] Caliro, S. et al. (2015) *GCA*, 168.
- [17] Flahaut, J. et al. (2018) *EPSC*, #2018-804. [
- [18] Browne, P.R.L. (1978) *An. Rev. of Earth and Plan. Sci.*, 6, 229-250.
- [19] Farrand, W.H. et al. (2009) *Icarus*, 204(2), 478-488.
- [20] Farrand, W.H. et al. (2014), *Icarus*, 241(C), 346–357.

PHOTOCHEMISTRY OF WATER IN THE MARTIAN THERMOSPHERE AND ITS EFFECT ON HYDROGEN ESCAPE

V.A. Krasnopolsky

Moscow Institute of Physics and Technology, Moscow, Russia,
vlad.krasn@verizon.net

Keywords:

Mars, atmosphere, photochemistry, ionosphere, hydrogen escape.

Introduction:

The martian hydrogen corona is described by two parameters: density of H at 250 km and temperature. However, the altitude extent in the orbiter observations may be insignificant for measurement of T, and the Mariner 6 and 7 flybys and HST imaging could provide more reliable data (Fig. 1).

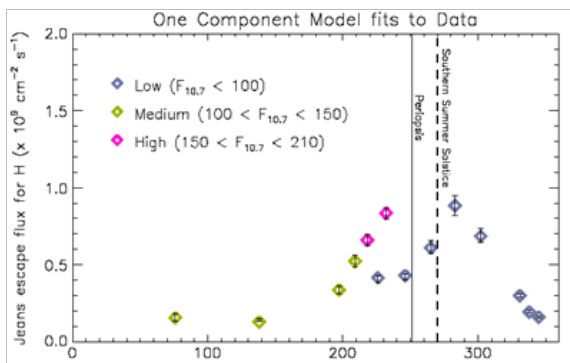


Fig. 1. HST observations of hydrogen escape from Mars in 2007-2017 [1].

These observations confirm the MEX data [2] that the escape rate at the perihelion season ($L_s = 200-330^\circ$) may be very large and exceed the diffusion limit of $4 \times 10^8 \text{ cm}^{-2} \text{ s}^{-1}$ for $\text{H}_2 = 17 \text{ ppm}$ [3, 4]. The observations correlate with the recent detections of high H_2O abundances up to $\approx 80 \text{ km}$ in the perihelion season using the SPICAM IR solar occultations [5, 6]. If H_2O can reach the thermosphere, it may significantly affect its chemistry and increase hydrogen escape. However, the MAVEN/NGIMS measurements of the ion composition [7, 8] do not support significant abundances of water in the thermosphere. Here we will create a photochemical model to account for all aspects of the problem.

Model

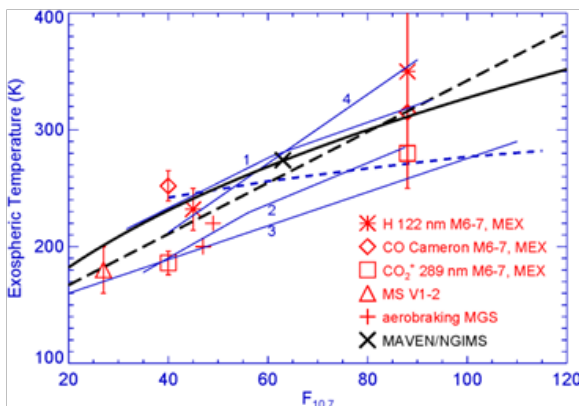


Fig. 2. Observed exospheric temperatures and their linear fit (long dashes). Blue lines are the MGTM versions of 2000, 2008, 2009, and 2015 at fall equinox. Solid line is a fit to the MAVEN point by thermal balance equation.

Our one-dimensional self-consistent model of neutral and ion composition in the martian atmosphere at 80-300 km is based on the model [3] with non-thermal escape of light species (H, H₂, D, HD, and He) from [4]. The model accounts for vertical transport of species by eddy, molecular, and ambipolar diffusion. Temperature profiles are adopted by the least-square linear fit to observed exospheric temperatures (Fig. 2) that results in

$$T_{\infty} = 123 + 2.19 F_{10.7}.$$

Temperature at 80 km is either 128 K with no water or that for the saturation conditions of water. Temperatures from 80 and 300 km are interpolated using an analytic expression. 30 reactions, which account for the basic photochemistry of H₂O, H₂O⁺, H₃O⁺, O₂, and their products, are added to the model.

Results

Photolysis of H₂O increases significantly the productions of H and H₂ and their escape. The following sequence of the ion reactions is also important in the balance of H₂O and its products:

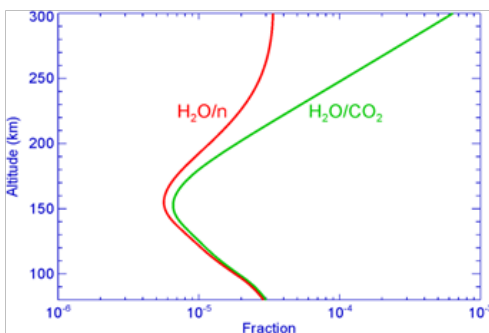
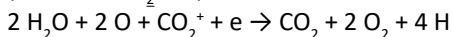
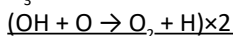
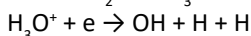
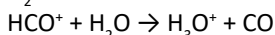
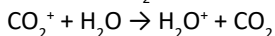


Fig. 3. Profile of the H₂O mixing ratio in the model at $F_{10.7} = 70$ and $f_{\text{H}_2\text{O}} = 30$ ppm at 80 km.

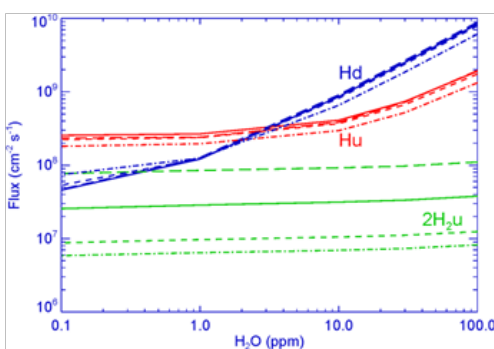


Fig. 4. Upward (u, escape) and downward (d, at 80 km) fluxes of H and H₂ for various H₂O abundances at 80 km and solar activity: $F_{10.7} = 40, 70,$ and 100 (short dashes, solids, and long dashes, respectively).

Both photolysis and ion chemistry strongly deplete the H₂O mixing ratio (Fig. 3) with a minimum at 160 km and further increase by the diffusive enrichment of light species.

Our models do not confirm the conclusion in [8] that significant H₂O abundances strongly deplete HCO⁺ densities and are therefore incompatible with the MAVEN/NGIMS measurements. Loss of HCO⁺ in our models is weaker

in the reaction with H_2O than that in recombination, while the production is greater in the reaction $\text{CO}_2^+ + \text{H}$ because of the greater H for large H_2O . Variations of the H and H_2 escape and densities at 250 km with H_2O at 80 km and solar activity are shown in Fig. 4 and 5. The escape flux of H may be approximated by

$$\Phi_{\text{H}\uparrow} (\text{cm}^{-2} \text{s}^{-1}) = 1.6 \times 10^8 + 1.7 \times 10^7 f_{\text{H}_2\text{O}} (\text{ppm}).$$

The results agree with those in Fig. 1 if H_2O reached 40 and 15 ppm at 80 km in the martian falls of 2014 and 2016, respectively.

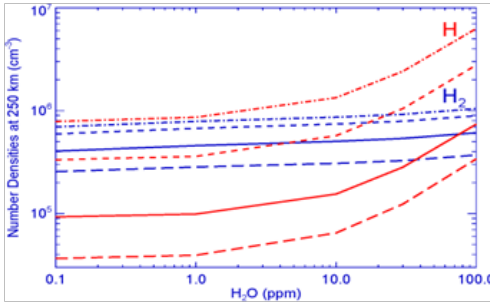


Fig. 5. Densities of H and H_2 at 250 km for various H_2O at 80 km and $F_{10.7} = 25, 40, 70$, and 100 (dash-dots, short dashes, solid, and long dashes).

Acknowledgement.

This work is supported by a grant of Russian Science Foundation to MIPT and V.A. Krasnopolsky.

References

- [1] Bhattacharyya D. et al. JGR 122A, 11754, 2017.
- [2] Chaufray J.Y. et al. Icarus 245, 282, 2015
- [3] Krasnopolsky V.A. JGR 107E, E12, 5128, 2002
- [4] Krasnopolsky V.A. Icarus 207, 638, 2010
- [5] Maltagliati L. et al. Icarus 223, 942, 2013
- [6] Fedorova A. et al. Icarus 300, 440, 2018
- [7] Benna M. et al. GRL 42, 8958, 2015
- [8] Fox J.L. et al. GRL 42, 8977, 2015

HIGH RATE OF ATMOSPHERIC METHANE LOSSES IN REACTIONS WITH COSMIC RAYS PRODUCED IONS AS POSSIBLE SOURCE OF SEASONAL METHANE VARIATIONS ON MARS

A.K. Pavlov, D. A. Tsurkov, A.A. Pavlov, G.I. Vasilyev

*Ioffe Physical Technical Institute Russian Academy of Sciences,
anatoli.pavlov@mail.ioffe.ru*

Origin of methane in Martian atmosphere is intensive discussed more ten years because methane is a potential “biosignature” of hypothetical martian biosphere. Atmospheric abundance of methane is very low (around ppb level) and demonstrate high variations (0.1-10 ppb) in depend on Martian seasons and regions. Particularly, measurements of MSL mission within several years show strong seasonal variations of background levels of methane in air (Webster et al., 2018). Methane has a photochemical lifetime of 350 years. But global mixing time of martian atmosphere is 1-2 years. To explain seasonal methane variations, we need a process of rapid destruction of methane. We propose reactions methane molecules with ions O_2^+ , $O_2O_2^+$ in atmosphere as such process. Main ions in martian atmosphere at mean concentration of water vapor is H_3O^+ which is not able to react with methane. Therefore, we modeled reactions of methane with cosmic rays produced ions in polar region lower atmosphere during winter season. Extremely low temperatures within this period lead to very low concentration of water vapor in atmosphere and enrichment of non-condensable gases including methane up to 4-5 times. Both factors sharply increase the rate of methane destruction. Methane lifetime decrease down to 1-3 years and depend on variations of galactic and solar cosmic ray fluxes. As result, this process can be considered as possible way to explain methane variations in Martian atmosphere.

NON-EQUILIBRIUM RADIATIVE TRANSFER IN THE RO-VIBRATIONAL CO₂ BANDS IN THE MARTIAN ATMOSPHERE TAKING ACCOUNT OF RADIATION EXTINCTION BY AEROSOLS

V.P. Ogibalov

*Department of Atmospheric Physics, St.Petersburg State University,
Ulyanvskaya st. 1, St.Petersburg-Petrodvorets, 198504 Russia,
v.ogibalov@spbu.ru*

Keywords:

Radiative transfer, infrared molecular bands, vibrational non-LTE, carbon dioxide, Martian atmosphere, aerosol extinction

Introduction:

The Martian atmosphere has a relatively low density. Therefore, the rarity of molecular collisions, on the one hand, and the high rate of excitation of the vibrational states of the CO₂ and CO molecules due to the absorption of solar radiation in the near-infrared (NIR) spectral range of $\sim 1.05\div 5\ \mu\text{m}$, on the other hand, result in the breakdown of the Boltzmann distribution in values of the concentrations (populations) of the vibrational states of these molecules. So, the breakdown of the local thermodynamic equilibrium (LTE) over the vibrational degrees of freedom of these molecules (vibrational non-LTE) takes place. The altitude of the level in the Martian atmosphere, lower which one needs to take into account for the vibrational non-LTE effects when assessing the populations of vibrational states of the CO₂ and CO molecules, varies depending on the wavelengths of the fundamental band in which the excitation of these states by absorption of the solar NIR radiation from the molecular ground state takes place.

Aerosols are always present in the Martian atmosphere up to the heights of $50\div 70\ \text{km}$, and their optical thickness, τ_a , in the visible and NIR spectrum can achieve significant values². Thus, for periods when the Martian atmosphere is calm, the typical values are of order $\tau_a=0.1\div 0.3$. While during global dust storms, there can be observed the values of order $\tau_a=3\div 5$. At the same time, the optical thickness of the entire Martian atmosphere for a variety of ro-vibrational (R-V) radiative transitions, which are necessary to be included into the model of non-equilibrium emission in the NIR bands of the CO₂ and CO molecules, varies in a very wide range. Thus, for the main isotopologue ¹²C¹⁶O₂, the values of the optical thickness in the center of the strongest line, τ_{mol}^r of the fundamental transitions belonging to the bands at wavelengths 4.3, 2.7, 2.0, 1.6, 1.4, 1.25, 1.2 and 1.05 μm are approximately 2.3×10^8 , 2.5×10^6 , 4.4×10^4 , 4.9×10^2 , 1.5×10^3 , 87.7, 34.5, 1.75, respectively. As regarding to the R-V transitions belonging to the secondary CO₂ isotopologues as well as the subordinate R-V transitions of the molecule ¹²C¹⁶O₂, which also create a significant contribution to the emissions in these bands, the values of τ_{mol}^r in the center of the most intensive lines of such radiative transitions are much less than unity. By another words, such values of τ_{mol}^r are comparable to the optical thickness τ_a of aerosols which constantly present in the Martian atmosphere.

The problem of radiative transfer in the ro-vibrational molecular bands under condition of the LTE breakdown in a planetary atmosphere is generalized for the case taking into account the extinction (i.e. scattering and absorption) of the continuum radiation produced by aerosols. The method for calculating the non-equilibrium populations of vibrational states of gas molecules in the planetary atmospheres is developed. Formation of the values of the non-equilibrium populations of the excited vibrational states of the CO₂ molecules (in the application to the atmosphere of Mars) within the framework of the model of radiative transfer in the NIR bands of this molecule taking into account the extinction of radiation in the continuum produced by aerosol particles has been investigated for the first time.

The model of the carbon dioxide molecule which was previously developed [1] for studies of non-equilibrium CO₂ emissions in the nighttime Martian

atmosphere has been taken as the basis for the present study. To study the radiative transfer in the CO_2 and CO bands in the NIR spectral range in the daytime Martian atmosphere, the optical model has been significantly expanded. It takes into account for the 206 vibrational states of 7 isotopologues of CO_2 molecule (the highest excited state included into the model is the 20031 vibrational state of the molecule $^{12}\text{C}^{16}\text{O}_2$ with the energy of the order of 9500 cm^{-1}) and the 8 vibrational states of 2 isotopologues of CO molecule (the highest state is the one excited four times in the fundamental stretch mode). In total the 555 vibrational transitions numbering about 64200 R-V lines within the spectral range of $1.05\div 15 \mu\text{m}$ are considered. The spectroscopic parameters of the R-V lines of the CO_2 and CO molecules (the frequency, intensity, and Lorentz half-width) are taken from the HITRAN2012 database.

To explore qualitatively the effects on the values of the non-equilibrium populations of the CO_2 and CO molecules when accounting for the aerosol scattering of radiation, the simple model of aerosols in the Martian atmosphere from the study [2] has been supplemented

The method of calculating the value of the non-equilibrium populations of the molecular vibrational states with the detailed accounting of the overlap in frequency of the spectral lines as well as accounting for the reflection of radiation by the surface of the planet has been described in the study

For the first time, for the daytime atmosphere of Mars, the calculations of non-equilibrium populations n_l of excited vibrational states (labeled by index l) of the CO_2 and CO molecules were carried out taking account for the aerosol extinction of radiation in the bands of these molecules at wavelengths of the NIR spectral range. A number of aerosol models with parameters in the ranges of values that are likely for the atmosphere of Mars were used to estimate qualitatively the impact of the process of aerosol extinction of radiation on the values n_l .

The analysis of the results, obtained taking into account aerosol scattering of radiation in the transport approximation, shows the following. (1) The inclusion of the aerosol extinction of radiation at the wavelengths of the NIR bands of the CO_2 and CO molecules (1 to $5 \mu\text{m}$) leads to a decrease of the values n_l of excited vibrational states of these molecules in the surface layer of the atmosphere. Other words, in this layer there is a tendency to becoming the values of the vibrational state populations to the equilibrium values. (2) The influence of aerosol scattering on the vertical profile of the values n_l is the stronger the higher the excitation energy of vibrational states and the lower the abundance of isotopologues of the CO_2 and CO molecules. (3) The larger the values of the concentration of aerosol particles in the Martian atmosphere (i.e., their optical thickness τ_a), the greater the changes in the non-equilibrium populations of excited vibrational states in comparison to their values n_l for the case of aerosol absence.

On the basis of obtained results we can conclude that accounting for the process of aerosol extinction of radiation in the NIR bands of the CO_2 and CO molecules is the one of the important processes in modeling the transfer of radiation in the bands of these molecules. Including the aerosol extinction of radiation into the non-LTE models of the emissions within the NIR spectral range of the CO_2 and CO bands in the Martian atmosphere would allow to obtain a more reliable assessment of the values n_l of non-equilibrium populations of excited vibrational states of these molecules.

Developed approaches and techniques may be useful for studying the layer over the clouds in the Venusian atmosphere and for studying the atmosphere of Titan, which also contains a significant amount of aerosol particles.

References:

- [1] Ogibalov V. P., Shved, G. M. An improved optical model for the non-LTE problem for the CO_2 molecule in the atmosphere of Mars: Nighttime populations of vibrational states and the rate of radiative cooling of the atmosphere // Solar Syst. Res. 2003. V. 37. No. 1. P. 23–33.
- [2] Ogibalov, V. P. Radiative Transfer in the near-infrared CO_2 bands taking account of continuum absorption by aerosol particles in the Martian atmosphere // Vestnik of St. Peterburg Univ. (Series 4). 2008. No. 3. P. 27–36.

RETRIEVAL OF AN INDUCED MAGNETIC FIELD IN MARS IONOSPHERE FROM MARSIS DATA. EFFECTS OF CRUSTAL AND NONCRUSTAL FIELDS

S. Jiménez¹, M. Ramírez-Nicolás², D. Usero², P.J. Pascual³, M.P. Velasco¹, L. Vázquez²

¹Universidad Politécnica de Madrid, Spain;

²Universidad Complutense de Madrid, Spain;

³Universidad Autónoma de Madrid Spain;

s.jimenez@upm.es

Keywords:

Mars, Magnetic Field, Ionosphere, Solar Radiation, Crustal Magnetic Field, Solar wind, MARSIS.

Introduction:

Evidence of an induced magnetic field in the ionosphere of Mars was measured indirectly through its effects on the electron density behaviour [1], based on the observations by the Mars Advanced Radar for Subsurface and Ionospheric Sounding (MARSIS) onboard Mars Express [2].

We have extended systematically the procedure used in [1], analysing the data for all orbits as measured by MARSIS during its ongoing mission.

The measures are in the form of ionograms representing the time delay of the echo of the signal as a function of the emitted frequency. From the ionospheric echos [3] and the cyclotronic frequencies the inferred periodic electron trajectories, it is possible to deduce the modulus of the magnetic field at the spacecraft height. That magnetic field can be due to fossil magnetic fields on the planet and to the induced effect of the charged particles of the solar wind.

A procedure can be applied to try and determine each component of the field, by comparison with a standard model [4]. This can be used, in turn, to discriminate the effects of crustal magnetic fields and that of the Solar irradiation, especially during episodes of strong Solar wind. The results are checked against previous observations [5].

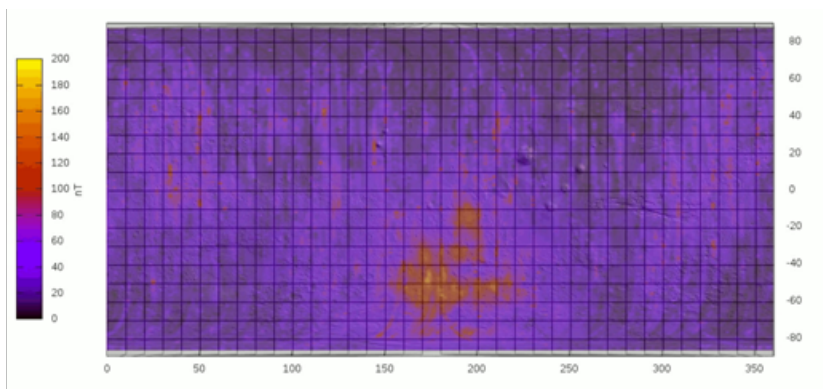


Fig. 1.

Acknowledgements:

The authors are grateful for partial support by the Spanish Ministry (MINECO) under grant: ESP2016-79135-R.

References:

- [1] M. Ramírez-Nicolás, B. Sánchez-Cano, O. Witasse, P.-L. Blelly, L. Vázquez. The effect of the induced magnetic field on the electron density vertical profile of the Mars' ionosphere // A Mars Express MARSIS radar data analysis and interpretation, a case study", Planetary and Space Science 126 (2016) 49–62.
- [2] R. Orosei, R.L. Jordan, D.D. Morgan, M. Cartacci, A. Cicchetti, F. Duru, D.A. Gurnett, E. Heggy, D.L. Kirchner, R. Noschese, W. Kofman, A. Masdea, J.J. Plaut, R. Seu, T.R. Watters, G. Picardi. Mars Advanced Radar for Subsurface and Ionospheric

Sounding (MARSIS) after nine years of operation: A summary // *Planetary and Space Science* 112 (2015), 9--114.

- [3] Sánchez-Cano, B., Witasse, O., Herraiz, M., Radicella, S.M., Bauer, J., Bliely, P.-L., Rodríguez-Caderot, G. Retrieval of ionospheric profiles from the Mars Express MARSIS experiment data and comparison with radio occultation data // *Geoscientific Instrumentation, Methods and Data System* 1, 1, 77-84, 2012.
- [4] Akalin, F., Morgan, D.D., Gurnett, D.A., Kirchner, D.L., Brain, D.A., Modolo, R., Acuña, M.H., Espley, J.R. Dayside induced magnetic field in the ionosphere of Mars // *Icarus* 206, 104-111, 2010.
- [5] E. Dubinin, M. Fraenz, T. L. Zhang, J. Woch, and Y. Wei, Magnetic fields in the Mars ionosphere of a noncrustal origin: Magnetization features // *Geophysical Research Letters*, 41, 6329–6334, doi:10.1002/2014GL061453, 2014.

DAYSIDE MAGNETOSPHERE OF MARS IN MSE COORDINATE SYSTEM

O.L. Vaisberg¹, V.N. Ermakov¹, S.D. Shuvalov¹, L.M. Zelenyi¹, E. Dubinin²

¹Space research institute RAS

²Max-Planck-Institute for Solar System Research

Keywords:

Mars, solar wind interaction, magnetosphere, structure of magnetosphere
MAVEN spacecraft with its comprehensive scientific payload and high temporal resolution measurements provided possibility to study dayside magnetosphere's structure and processes. Dayside magnetosphere of Mars is a thin layer of magnetized planetary plasma between shocked solar wind flow and ionosphere. It is formed of solar magnetic flux tubes loaded by the heavy planetary ions during its convection from the subsolar region to the terminator. Asymmetric structure of the dayside magnetosphere was found from analysis of MAVEN measurements at the Solar Zenith Angle $\sim 70^\circ$. Magnetic field and motional electric field asymmetries lead to asymmetric ion pick-up and loaded magnetic field tubes convection that result in asymmetric characteristics of dayside magnetosphere. Both magnetosphere's magnetic field and magnetospheric plasma have different characteristics depending on location in MSE coordinate system.

We extend this analysis to all dayside hemisphere of Mars at various solar-zenith angles from the subsolar region to the terminator. Only measurements performed in the North of Mars are used in the analysis in order to avoid the influence of the magnetic anomalies concentrating in the Southern regions of the planet. Analysis is performed in the MSE coordinate system determined from upstream the shock direction of the interplanetary magnetic field component transverse to the solar wind velocity. Another set of data for cases when spacecraft was not cross the shock was analyzed with use of magnetosheath magnetic field direction. Performed analysis shows asymmetry of dayside magnetosphere in MSE coordinate system and the change of magnetospheric structure from subsolar region to the terminator.

BENEFIT FOR MARS POLAR SCIENCE FROM A MISSION TO VERY-LOW (< 150 KM) ORBIT

J. Oberst^{1,2}, K. Wickhusen¹, F. Damme², A. Stark¹, S. Annibaldi¹,
F. Lüdicke¹, H. Hussmann¹

¹*DLR Institute of Planetary Research; Rutherfordstrasse 2, 12489 Berlin, Germany Juergen.Oberst@dlr.de;*

²*TU Berlin; Institute of Geodesy and Geoinformation Science; Strasse des 17. Juni 135; 10623 Berlin*

Keywords:

Mars, Orbit, Electric Propulsion, Remote Sensing

Introduction:

We investigate possible missions in Low Mars Orbit (LMO), where atmosphere drag forces acting upon the spacecraft are compensated by an electric propulsion system. We show that a one-year mission is possible in a circular Mars orbit at altitudes as low as 150 km. Such a mission opens opportunities for novel remote sensing approaches and new science cases. While any Mars remote sensing may benefit from such a mission, we focus on polar areas.

Mission:

Given standard atmospheric models and assuming a medium-size spacecraft in a circular orbit, the drag force within the Mars atmosphere acting upon the craft is approximately 100 mN at a height of 150 km, with a resulting orbit lifetime of less than two weeks. However, given typical system parameters of an electric propulsion system, a spacecraft like Dawn would be capable to compensate this atmospheric drag by operating its ion thrusters.

Science Cases:

Remote sensing can benefit very much from operation in Low Mars Orbit. We anticipate new opportunities for spacecraft instrumentation including high-resolution imaging (not requiring excessive telescope equipment), as well as radar sounding and next-generation Laser altimetry (not requiring excessive power). We focus on polar areas:

- Study seasonal and regional variations in snow-deposits in polar areas to improve models of the CO₂ cycle. Study the interior structure and layering of polar deposits.
- Carry out detailed mapping of polar scarps to study dynamics of ice sheets: identify rock falls and avalanche events.
- Map intricate rotation function of the planet, in particular variations in length-of-day for interpretations in terms of moment of inertia and comparisons with observed seasonal mass-redistributions.
- Carry out magnetic field measurements at high spatial resolution to map patterns and determine origins of polar magnetic anomalies.
- Map density structure of the low Martian atmosphere, expected to be varying regionally and over time.

We foresee new opportunities to improve our knowledge on the characteristics and dynamics of planet Mars, in particular its polar areas.

BIOSIGNATURES DETECTION FROM 1.88 Ga GUNFLINT CHERT WITH LMS SUITE

R.A. Lukmanov¹, M. Tulej¹, R. Wiesendanger¹, A. Riedo², P. Wurz¹

¹*Space Research and Planetology Division (WP), Physics Institute, University of Bern, Bern, Sidlerstrasse 5, Switzerland, Rustam.lukmanov@space.unibe.ch;*

²*Sackler Laboratory for Astrophysics Leiden Observatory, University of Leiden, Leiden, Netherlands.*

Keywords:

Biosignatures, Microfossils, Mass spectrometry (MS), Microscopy.

Introduction:

Chemical analysis of planetary solids is of primary importance in understanding origin and evolution of planetary bodies. In-situ laser mass-spectrometry can be a valuable and important method, delivering sensitive context chemical information. The mineralogical deciphering of rock units requires accurate identification of mineral phases on spatial scales at the micrometer level. A single-grain analysis could provide an insight into sample formation and evolution [3], determine winding pathways of matter permineralization and help to reconstruct past environments in which these rocks are formed.

Here we present LA-TOF-MS (Laser Ablation - Time of Flight - Mass Spectrometry) based data from a 1.88 Ga Gunflint chert sample, collected in-situ on individual and dense microfossil colony spots, at the micrometer scale, which are compared with data collected on host areas. Measurements are performed with the laboratory-based prototype of highly miniaturized mass-spectrometer (LMS) coupled with femtosecond laser ablation ion source. Precise probing of the sample material on the areas of interest is achieved by using a vacuum compatible microscopy system. We will present a scoring approach to test the credibility of the biogenic origin of the sample as well as all supportive information describing a number of detected with LMS biosignatures.

The LMS Instrument suite:

LMS is a miniature reflectron-type time-of-flight mass spectrometer designed for in-situ measurements of solids on surfaces of planetary bodies. In the current state, mass analyzer is downsized to 160 mm in length and 60 mm in diameter and fulfills strict requirements for scientific instrumentation on rover or lander missions on planetary surfaces. The suite is complemented with UHV compatible microscopy system with micrometer resolution and translational stage, which allow precise sample positioning and probing material from various areas of interest. The laboratory-based version of LMS coupled with ultrashort-pulsed IR (775nm), UV (SHG - 387nm, THG - 258 nm) laser ablation ion sources with optical beam guiding system. Detailed information about instrument could be found in our previous publications [1], [2], [3], [4].

Gunflint chert:

Gunflint chert sample from Schreiber beach, Ontario, Canada, is considered in our study as Martian analog sample. Investigated Gunflint chert contain mainly microquartz [6] as the primary host mineral. Minor mineral phases on microfossil spots and host areas identified as iron oxides and different carbonate minerals (calcite, dolomite, magnesite, and aragonite). Studied microscopic images reveal diverse morphologically preserved microfossils of different shapes. Dense microfossil spots show high C, Mg, S, Fe, Mn content with trace amounts of V, Cr, and Cu. Measurements on host area contain almost negligible or noticeably lower concentrations of these elements. Altogether, with this contribution, we will demonstrate that the LMS instrument suite is capable of accurate and sensitive elemental and isotopic studies with high lateral and depth resolution and able to perform an investigation of natural samples such as Si-rich cherts and collect mutually supportive pieces of evidence supporting biological origin of some of the structures inside the host matrix.

References:

- [1] Riedo, A., et al., Performance evaluation of a miniature laser ablation time-of-flight mass spectrometer designed for in situ investigations in planetary space research. *J Mass Spectrom*, 2013. 48(1): P. 1-15.
- [2] Riedo, A., et al., Coupling of LMS with a fs-laser ablation ion source: elemental and isotope composition measurements. *Journal of Analytical Atomic Spectrometry*, 2013. 28(8): P. 1256-1269.
- [3] Tulej, M., et al., Chemical Composition of Micrometer-Sized Filaments in an Aragonite Host by a Miniature Laser Ablation/Ionization Mass Spectrometer. *Astrobiology*, 2015. 15(8): p 669-682.
- [4] Tulej, M., et al., CAMAM: A Miniature Laser Ablation Ionization Mass Spectrometer and Microscope-Camera System for In Situ Investigation of the Composition and Morphology of Extraterrestrial Materials. *Geostandards and Geoanalytical Research*, 2014. 38(4): P. 441-466.
- [5] Vago, J.L., et al., Habitability on Early Mars and the Search for Biosignatures with the ExoMars Rover. *Astrobiology*, 2017. 17(6-7): P. 471-510.
- [6] Wiesendanger, R., et al., Chemical and optical identification of micrometer sized 1.9 billion-year-old fossils with a miniature LIMS system combined with an optical microscope. *Astrobiology*, 2018.

BIBLIOMETRIC EVALUATION OF THE DEVELOPMENT TREND OF MARS EXPLORATION RESEARCH

H. Wang¹, F. Yang¹, L. Han¹, W. Fan¹

¹*Institutes of Science and Development, Chinese Academy of Sciences, 33 Beisihuan Xilu, Zhongguancun, Beijing, P. R. China, 100190, wanghaiming@casisd.cn*

Keywords:

Mars exploration, bibliometric analysis, research output, research cooperations

The study analyses the research performances of the countries from 1963 to 2015 in the field of Mars exploration based on bibliometrics statistics and visualization analysis method (bibliographic data of Mars Exploration missions are derived from the Web of Science database). The work assesses the publication scale, academic influence, dominant disciplines, and research hotspots of major countries in Mars exploration research, hope to contribute to a comprehensive understanding of national research strength, discipline and development potential for future Mars explorations. It is found that all Mars exploration researches produced a total of 5625 papers. The number of the published papers increase steadily with an overall annual growth rate of 12.8%. The United States contribute most of the research papers and ESI highly cited papers, and thus show predominant position. France, Germany, Russia, the UK, and Italy are major contributors in Mars exploration researches. Almost all of the core papers are led or participated by the US institutions, and the TOP 10 institutions are almost swept by the USA. NASA, as the major funding agency of several Mars exploration missions, undoubtedly produces most core papers. CALTECH, Univ California System, Univ Arizona, Arizona State Univ, and US Geol Survey also perform outstandingly. Russian Acad Sci and the MAX PLANCK SOCIETY are the only two non-US institutions on the list of TOP 10 institutions. Moreover, the work also discusses the characteristics and evolution trends of research cooperations between major countries. Among the top 10 countries, France, Germany, Spain, and Sweden mainly carried out independent research, while USA mainly carried out cooperative research.



Fig. 1.

References:

- [1] NRC. Vision and Voyages for Planetary Science in the Decade 2013-2022 // <http://www.nap.edu/catalog/13117/vision-and-voyages-for-planetary-science-in-the-decade-2013-2022>
- [2] ISECG. ISECG Global Exploration Roadmap (3rd edition). https://www.globalspace-exploration.org/wordpress/wp-content/isecg/GER_2018_small_mobile.pdf
- [3] NSSDCA. Mars Exploration Missions. <https://nssdc.gsfc.nasa.gov/planetary/planets/marspage.html>

VARIATIONS OF THE LOWER CLOUD LAYER AND H₂O IN THE DEEP ATMOSPHERE OF VENUS FROM THE NIGHT WINDOWS OBSERVATIONS BY SPICAV-IR/VEX

D.G. Evdokimova¹, A.A. Fedorova¹, D.A. Belyaev¹, O.I. Korablev¹, E. Marcq², J.-L. Bertaux^{2,1}

¹Space Research Institute of the RAS (IKI), 84/32 Profsoyuznaya Str., Moscow 117997, Russia. evd.dar@yandex.ru

²LATMOS, CNRS/UVSQ/IPSL, 11 Boulevard d'Alembert, Guyancourt 78280, France.

Keywords:

Venus, clouds, H₂O, transparency windows, SPICAV IR

Introduction:

Venus cloud layer is one of the reasons of the strong greenhouse effect forming the current planet's climate. It locates within the altitude range of 46-70 km and its opacity obstructs the remote investigation of the lower atmosphere. The main component of their aerosols is a solution of the H₂SO₄. Four modes of aerosol particles can be distinguished prevailing in different layers of the clouds [1]. The mode 1 and 2 having radiuses of < 0.4 and 1 μm [2] are contained in the upper layer (50-70 km) and haze (>70 km). The mode 2' and the biggest mode 3 particles prevailed in the middle and lower clouds (46-50 km) and the lower haze. The mode 3 radius is 3-4 μm and these particles determine the opacity and bulk of the Venus cloud layer [1].

The only IR emission of the lower atmosphere is obtainable within narrow transparency windows where the CO₂ absorption is weak. Intensity of the windows is defined by the scattering within the cloud layer. There are also a water vapor absorption band spreads in the interval of 1.10-1.20 μm which provides an information about water abundance in deep atmosphere. Its volume mixing ratio was declared varying near the value of 30-35 ppm by the VIRTIS and SPICAV-IR observations [3, 4] and the recent ground-based measurements [5].

Night thermal emission observed by the SPICAV IR:

The IR channel of the SPICAV instrument was able to measure the night emission in spectral range of 1.0-1.31 μm that covered five of the windows at 1.0, 1.10, 1.18, 1.28, 1.31 μm. The database was accumulated for the annual period from 2006 to 2014 years what allowed to cover almost the whole Venus globe with a good spatial resolution.

The registering emission variations depend on several factors. The main of them is scattering in the middle and lower clouds desk. The water absorption is presented in 1.1- and 1.18-μm and the emission is also affected by surface emissivity changes. The 1.28-μm window is contaminated by an oxygen emission at 1.27 μm produced at 95 km [6]. The 1.31-μm intensity is much lower than others.

Modeling of the night windows emission:

The emission of the night windows is modeling implementing the multiple scattering radiative transfer model calculated by the SHDOMPP program. The program realizes the spherical harmonic discrete ordinate method [8] for plane parallel geometry that was adopted for the Venus night-side observations in [4, 7]. The a priori parameters are a temperature-pressure profile and a composition of the aerosol particles assumed being spherical. The VIRA database was used for the temperature and pressure distributions. The H₂O lines are taken the BT2 linelist [9]. The aerosol composition is the 75% solution of the H₂SO₄. An optical depth, a single scattering albedo and an asymmetry parameter are calculated according to the Mie theory for the aerosol profiles of different modes presented by Haus et al. (2016) [10].

Retrieval of lower cloud layer parameters and water vapor abundance:

Previously, the data of SPICAV-IR showed that the maximum intensity of the 1.28-μm window varied from 0.05 to 0.1 W/m²/μm/ster and it had

slightly higher values in the north hemisphere than in the south one [11]. These variations are determined by opacity changes in lower clouds. For the further study a fitting of the experimental data by model spectra is performing. A synthetic spectrum is calculated based on the cloud model and the windows features described above. A scaling factor implementing to the concentration distributions of the 2nd and 3rd modes, water vapor volume mixing ratio and a surface emissivity are taken as free parameters of the model. This work is analyzing the whole dataset of SPICAV observations.

Acknowledgements:

D. G. Evdokimova, A. A. Fedorova, D. A. Belyaev and O. I. Korablev acknowledge the support from the RFFI #16-52-16011. J.-L. Bertaux and D. G. Evdokimova also acknowledge a partial support from the Ministry of Science of Russian Federation grant #14.W03.31.0017.

References:

- [1] Esposito L.W. et al. Chemistry of lower atmosphere and clouds. Venus II, The University of Arizona Press. 1997. P. 415–458.
- [2] Luginin M. et al. Aerosol properties in the upper haze of Venus from SPICAV IR data. // *Icarus*, 2016. V. 277. P. 154-170.
- [3] Haus R. et al. Lower atmosphere minor gas abundances as retrieved from Venus Express VIRTIS-M-IR data at 2.3 μm // *Planetary and Space Science*, 2015. V. 105. P. 159-174
- [4] Bezarad B. et al. The 1.10- and 1.18- μm nightside windows of Venus observed by SPICAV-IR aboard Venus Express. // *Icarus*, 2011. V. 216. P. 173-183.
- [5] Arney G. et al. Spatially resolved measurements of H₂O, HCl, CO, OCS, SO₂, cloud opacity, and acid concentration in the Venus near-infrared spectral windows. // *J. Geophys. Res.* V. 119. Pp. 1860-1891.
- [6] Crisp, D. et al. Ground-based near-infrared observations of the Venus nightside: 1.27- μm O₂ ($\text{a}\Delta\text{g}$) airglow from the upper atmosphere. // *J. Geophys. Res.* 1996. V. 101, E2. P. 4577-4594.
- [7] Fedorova A. et al. The CO₂ continuum absorption in the 1.10- and 1.18- μm windows on Venus from Maxwell Montes transits by SPICAV IR onboard Venus Express. *Planet. Space Sci.*, 2014. V.113-114. P. 66-77.
- [8] Evans, K. F. The spherical harmonic discrete ordinate method for three-dimensional atmospheric radiative transfer. *J. Atmos. Sci.* 1998. V. 55. P. 429-446.
- [9] Barber R. J., et al. A high-accuracy computed water line list. *Mon. Not. R. Astron. Soc.* 2006. V. 368. P. 1087–1094.
- [10] Haus R. et al. Radiative energy balance of Venus based on improved models of the middle and lower atmosphere. *Icarus*. 2016. V. 272. P. 178–205.
- [11] Evdokimova D. et al. Venus cloud parameters modulating the 1.28- μm night-side window emission observed by SPICAV IR. The 8th Moscow Solar System Symposium 2017, Moscow, Russia. 8MS3-PS-02.

VENUS NIGHTTIME PHOTOCHEMICAL MODEL: NIGHTGLOW OF O_2 , NO, OH AND ABUNDANCES OF O_3 AND CLO

V.A. Krasnopolsky

Moscow Institute of Physics and Technology (PhysTech), Moscow,
Russia, vlad.krasn@verizon.net

Keywords:

Venus, atmosphere, photochemistry, atmospheric composition, nightglow.

Introduction:

Detections and first studies of Venus' O_2 and NO nightglow were made four decades ago using the Venera 9 and 10, Pioneer Venus, and ground-based observations. Long-term Venus Express observations revealed the OH rovibrational bands and the NO band at 1.224 μm in Venus' nightglow and made detailed studies of morphology of all types of the nightglow on Venus. The nighttime stellar occultations resulted in detections of ozone layers near 95 km. Recently ClO was detected on the Venus night side using the ground-based high-resolution submillimeter spectroscopy (Sandor and Clancy 2018). Photolysis lifetimes of O_3 and ClO are 60 and 80 s on the day side. Therefore the global-mean and dayside-mean models are inapplicable for comparison with the observed abundances. Here we will update our photochemical model for the nighttime atmosphere and nightglow at 80-130 km (Krasnopolsky 2013, hereafter Paper I) to account for the detected ClO.

Model

The nighttime chemistry is induced by transport of atomic species O, N, H, and Cl from the day side. Their fluxes are the model parameters in Paper I. However, fluxes of H and Cl were poorly constrained, because (1) a significant part of H is converted to Cl in the reactions of H and OH with HCl and (2) vibrational states v'' of the products in quenching of $OH(v')$ are unknown, and the difference between two limiting assumptions, $v'' = 0$ (sudden death) and $v'' = v' - 1$ (collisional cascading), is too large. Therefore the detection of the second chlorine species, ClO, provides the important constraint to the Cl flux in our model (Fig. 1).

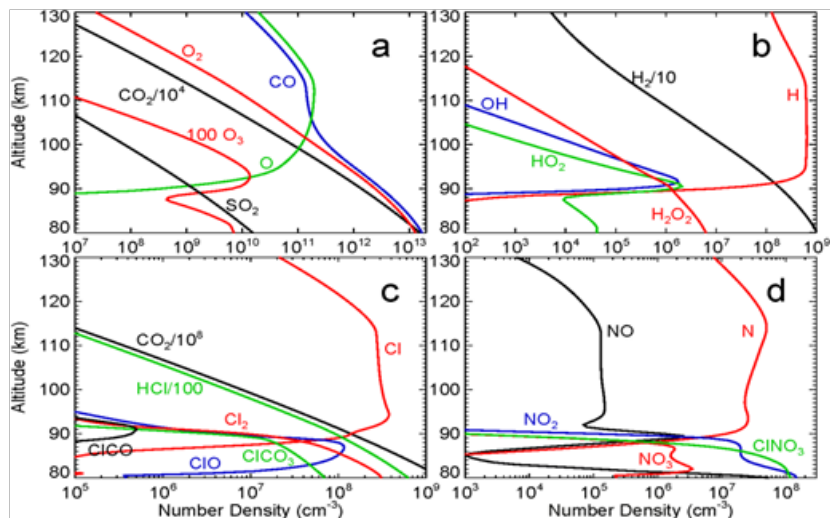


Fig.1. Chemical composition of the mean nighttime atmosphere at 80-130 km: (a) CO_2 products and SO_2 , (b) hydrogen species, (c) chlorine species, and (d) nitrogen species.

To fit the nightside-mean nightglow intensities and the measured abundances of O_3 and ClO, the fluxes of O, N, H, and Cl are equal to 3×10^{12} , 1.2×10^9 , 9×10^9 , and $3 \times 10^9 \text{ cm}^{-2} \text{ s}^{-1}$, respectively. We adopt flux of CO at $2 \times 10^{12} \text{ cm}^{-2} \text{ s}^{-1}$ to sim-

ulate the nighttime CO bulge. Photochemistry predicts comparable abundances of Cl and HCl at 100-150 km on the day side. Therefore fluxes of these species should be comparable as well, and we adopted equal fluxes of Cl and HCl in the basic model. This model agrees with all observational constraints. The calculated mixing ratios of chlorine species are shown in Figure 2.

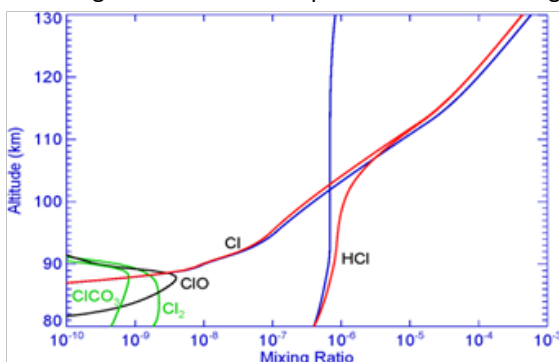


Fig. 2. Mixing ratios of chlorine species in the mean nighttime atmosphere. Those of HCl and Cl in the model with $\Phi_{\text{Cl}} = 4 \times 10^9 \text{ cm}^{-2} \text{ s}^{-1}$ and $\Phi_{\text{HCl}} = 0$ are shown as well (blue lines).

The submillimeter observations of HCl by Sandor and Clancy (2017) agree at 70-80 km with the ground-based observations by Young (1972) and Krasnopolsky (2010) and give ≈ 400 ppb on both day and night sides. However, the observed HCl mixing ratios reduce to zero at 85-100 km on the both sides that disagrees with the photochemical models.

The VEX SOIR solar occultations (Mahieux et al. 2015) revealed the HCl abundances increasing from ≈ 60 ppb at 65 km to ≈ 1000 ppb at 110 km. The data at 65 km disagree with the ground-based observations, while the data at 110 km observed at sunset and sunrise agree with our nighttime model. The large vertical gradients of the HCl mixing ratio in both VEX and JCMT observations require significant sources and sinks of HCl that are not supported by the current photochemical models.

Variations of the nighttime composition and nightglow

To simulate these variations, the incoming fluxes of O, H, Cl, and HCl are adopted smaller and greater than those in the basic model by factors of 2. The results are presented in Table.

#	Φ_{O}	Φ_{H}	Φ_{Cl}	Φ_{HCl}	O_2 1.27 μm	OH ($\delta v = 1$)	O_3 limb	f_{ClO} (90 km)
1	3+12	9+9	3+9	3+9	483 kR	6.14 kR	8 . 1 + 1 5 cm-2	2 . 1 1 ppb
2	1.5+12	9+9	3+9	3+9	204	2.08	3.6+15	1.31
3	6+12	9+9	3+9	3+9	1114	17.6	1.8+16	3.30
4	3+12	4+9	3+9	3+9	508	4.26	1.2+16	10.8
5	3+12	18+9	3+9	3+9	452	6.48	4.0+15	0.10
6	3+12	4+9	3+9	3+9	482	6.97	9.4+15	0.36
7	3+12	9+9	1.5+9	3+9	487	4.55	6.2+15	13.4
8	3+12	9+9	3+9	1.5+9	482	6.23	8.4+15	1.27
9	3+12	9+9	3+9	6+9	485	5.96	8.0+15	4.23

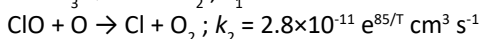
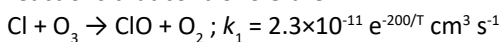
Fluxes are downward at 130 km in $\text{cm}^{-2} \text{ s}^{-1}$, 3+12 = 3×10^{12} , and the OH nightglow intensities refer to the $\delta v = 1$ sequence at 2.7-3.1 μm .

Oxygen is a part in all observable species that are therefore sensitive to variations of Φ_{O} . Variations of Φ_{O} by a factor of 4 induce variations of the OH nightglow by a factor of 8, the O_2 nightglow and ozone by factors of 5, and ClO by a factor of 2.5. Variations of Φ_{H} by a factor of 4.5 weakly affect the O_2 and OH (by a factor of 1.5) nightglow. The ozone and ClO abundances anti-

correlate with Φ_{H} by factors of 3 and 100, respectively. The OH nightglow and O_3 anticorrelate with Φ_{Cl} by factors of 1.5 if the latter varies by a factor of 4, while ClO correlates and varies by a factor of 35. Variations of Φ_{HCl} by a factor of 4 affect only ClO that varies by a factor of 3.3.

The nighttime ozone layer peaks at 93 ± 1 km in our models. The ClO abundance refers to a 10-km layer that peaks at 90 ± 1 km (Figure 2). The abundances calculated for $h > 85$ km are smaller by $\approx 4\%$, similar to those in Sandor and Clancy (2018).

ClO is very sensitive to small variations of the fluxes of H and Cl, and the expected variations of ClO may exceed two orders of magnitude, greater than those of the other observable species on the night side. Major reactions that control ClO are



(Burkholder et al. 2015). If transport is neglected, then

$$[\text{ClO}] \approx 0.8 e^{-285/T} [\text{Cl}] [\text{O}_3]/[\text{O}].$$

All species involved are highly variable near 90 km (Figures 1 and 2) where ClO forms, and $[\text{O}_3]/[\text{O}]$ is sensitive to the fluxes of H and Cl.

Acknowledgments

This work is supported by Grant 16-12-10559 of the Russian Science Foundation to Moscow Institute of Physics and Technology (PhysTech) and V.A. Krasnopolsky.

References

- [1] Burkholder, J.B., et al., 2015. Chemical Kinetics and Photochemical Data for Use in Atmospheric Studies. Evaluation Number 18. JPL Publication 15-10.
- [2] Krasnopolsky, V.A., 2010. Spatially-resolved high-resolution spectroscopy of Venus. 1. Variations of CO_2 , CO, HF, and HCl at the cloud tops. *Icarus* 208, 539-547.
- [3] Krasnopolsky, V.A., 2013. Nighttime photochemical model and night airglow on Venus. *Planet. Space Sci.* 85, 78-88.
- [5] Mahieux, A., et al., 2015. Hydrogen halides measurements in the Venus mesosphere retrieved from SOIR on board Venus Express. *Planet. Space Sci.* 113-114, 264-274.
- [6] Sandor, B.J., Clancy, R.T., 2017. Diurnal observations of HCl altitude variation in the 70-100 km mesosphere of Venus. *Icarus* 290, 156-161.
- [7] Sandor, B.J., Clancy, R.T., 2018. First measurements of ClO in the Venus atmosphere – Altitude dependence and temporal variation. *Icarus* 313, 15-24.
- [8] Young, L.D.G., 1972. High-resolution spectra of Venus. *Icarus* 17, 632-658.

VENUS' CLOUD TOP RESPONSE TO THE EXCITATION OF PLANETARY SCALE GWS AT APHRODITE

K.L. Jessup¹, E. Marcq², J.L. Bertaux², F. Mills³, S. Limaye⁴, A. Roman⁵

¹Southwest Research Institute, Boulder, CO 80302, USA,

jessup@boulder.swri.edu;

²LATMOS/IPSL, UVSQ Université Paris-Saclay, Sorbonne Université, CNRS, Guyancourt, France

³Australian National University, Canberra, Australia

⁴Space Science and Engineering Center, University of Wisconsin, 1225 W. Dayton St, Madison, WI 53706, USA;

⁵Space Science Telescope Institute, Baltimore, MD USA

Keywords:

Venus albedo, clouds, ultraviolet spectroscopy, atmospheric chemistry, atmospheric dynamics

Introduction:

Venus is permanently covered with ubiquitous $\text{H}_2\text{SO}_4 \cdot \text{H}_2\text{O}$ cloud and haze layers of temporally and vertically variant abundance and opacity [1-5]. Recent analysis of cloud top imaging data obtained during the Akatsuki and Venus Express (VEx) missions are now showcasing the interdependence of the cloud top properties on both Venus local solar time and topography [6-10]. Most notably, brightness temperature perturbations captured in 10 ± 2 micron Akatsuki cloud top images reveal planetary scale gravity waves are excited above Aphrodite Terra (and other elevated regions) at Venus local solar times (LSTs) subsequent to 9 hr, that remain active until ~ 19 hr [7]. Though the amplitude of the brightness temperature perturbations varies with local solar times, the center longitudes of the excited GW fronts are stable and are located between ~ 85 and 120 E longitude as depicted in Figure 1; and as the figure shows the bow shaped features can extend as far westward as 50 E longitude.

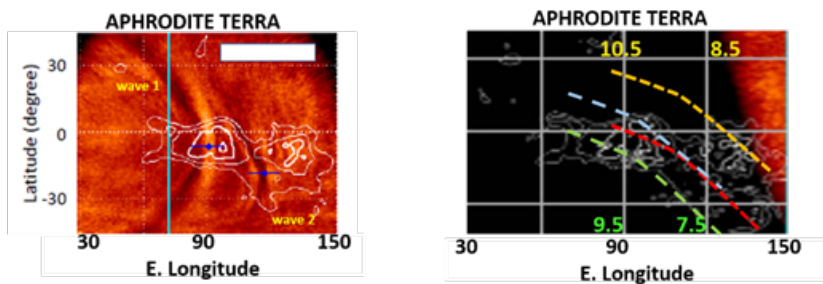


Fig. 1. (left) $10 \mu\text{m}$ images of the waves induced by Aphrodite's mountain topography from [7]. The central longitude of the dominant wave features labeled as wave 1 and wave 2 is indicated by a diamond and square, respectively. (right) dashed colored lines show HST slit positions in the month of January 2011. The local solar time at 90 E and 120 E longitude on the two dates of observations are depicted at the bottom (date 1, long dashed lines) and the top (date 2=date 1+5 Earth days, short dashed lines). The topographical relief of the Aphrodite Terra mountains is provided in each frame as a reference.

Hubble Space Telescope Imaging Spectrograph (HST/STIS) observations were obtained in 2010/2011 that recorded the cloud top properties above the Aphrodite Terra mountains between 70 and 140 E longitude at UV and visible wavelengths; and also above a low elevation region downwind of Aphrodite [11]. In each case, the spectra recorded the cloud top properties through LSTs extending from 7 to 11 hr (Fig. 1). As Figure 1 shows, the spectral data obtained above the mountains directly intersected regions

where GW features are known to manifest. The HST/STIS mountain observations were obtained on two dates segregated by five Earth days in January 2011. Serendipitously, on the first date (long dashed lines) the observations correlate to when the 70-100E region first intersects LSTs of 9 to 11 hr, thus the cloud top response at the onset of the GW excitation in the 70-100E region is observed; while the observations obtained 5 days later show the impact of the GW within overlapping longitude regions that had rotated ~ 1 hr westward in local solar time. Our analysis of these data shows distinct latitude trends in Venus' cloud top properties (such as the albedo levels at 245 nm, 365 nm, and the overall cloud top SO₂ gas abundance) as function of terrain type (mountain/plains) and as a function of the number of Earth days transpired between the onset of the planetary scale gravity wave excitation at the cloud tops above the western (70-100 E. longitude) portion of Aphrodite [11]. By comparing our observations to the statistical average behaviors inferred from Venus Express SPICAV [12] and Venus Monitoring Camera observations [7] we obtain new insights regarding the sensitivity of the vertical and horizontal transport processes to the underlying surface topography—and how this impacts the relative roles of chemistry and dynamics in maintaining the cloud top properties. These results may be used to validate and inform radiative transfer, microphysics and dynamics models designed to investigate Venus' general circulation behavior and climate evolution [13-14].

References

- [1] Hansen, J.E. and J.W. Hovenier, Interpretation of the polarization of Venus // *Journal of Atmospheric Sciences*, 1974. 31: p. 1137-1160.
- [2] McGouldrick, K. and C. C. C. Tsang, Discovery of a 150 day period in the Venus condensational clouds // *Icarus*, 2017. 286: p.118–133.
- [3] Gao, P. et al. Bimodal distribution of sulfuric acid aerosols in the upper haze of Venus // *Icarus*, 2014. 231: p. 83-98.
- [4] Wilquet, V. Drummond, R. & Mahieux, A., Robert, S., Vandaele, A. C., Bertaux, J-L. Optical extinction due to aerosols in the upper haze of Venus // *Four years of SOIR/VEX observations from 2006 to 2008. Icarus*, 2012. 217(2): p. 875-881.
- [5] Luginin, M., et al. Scale heights and detached haze layers in the mesosphere of Venus from SPICAV IR data // *Icarus*, 2018. 311: p. 87-104.6. Peralta, J. et al. Stationary waves and slow cloud features challenge Venus's night side superrotation. *Nature Astronomy*, 2017. 1, id. 0187.
- [7] Kouyama, T., et al. Topographical and local time dependence of large stationary gravity waves observed at the cloud top of Venus // *Geophysical Research Letters*, 2017. 44: p. 12,098–12,105.
- [8] Horinouchi, T. et al. Mean winds at the cloud top of Venus obtained from two-wavelength UV imaging by Akatsuki // *Earth, Planets and Space*, 2018. 70: #10, 19
- [9] Fukuhara, T. et al. Large stationary gravity wave in the atmosphere of Venus *Nature Geoscience* 2017. 10: p. 85–88.
- [10] Bertaux, J-L., et al., Influence of Venus Topography on the zonal wind and UV albedo at the cloud top level // *The role of stationary gravity waves. J. Geophys. Res.* 2016. 121: p. 1087–1101.
- [11] K.-L. Jessup, et al., On Venus' Cloud Top Chemistry, Convective Activity and Topography: A Perspective from HST // *Icarus*, 2018. Submitted.
- [12] Marcq., et al. Climatology of SO₂ and UV absorber at Venus' cloud top from SPICAV-UV nadir dataset, in preparation
- [13] Gierasch, P.J., et al. The general circulation of the Venus atmosphere // *An assessment. In Venus II — Geology, Geophysics, Atmosphere, and Solar Wind Environment. J.W. Bucher, D.M. Hunten, and R.J. Phillips, Eds. University of Arizona Press, 1997, pp. 459-500*
- [14] Titov, D. V., Bullock, M. A. & Crisp, D., Renno, N. O., Taylor, F. W., Zasova, L. V. Radiation in the atmosphere of Venus. *Exploring Venus as a Terrestrial Planet, Geophysical Monograph Series // American Geophysical Union, Washington, DC, 2007. 176: p. 121-138.*

TRACES OF SURFACE TOPOGRAPHY IN VENUS MESOSPHERE ON VENERA 15 AND VENUS EXPRESS DATA

L. Zasova, I. Khatuntsev, M. Patsaeva, D. Gorinov
Space Research Institute, RAS, Russia

Keywords:

Surface topography, atmosphere, temperature, clouds

We study the traces of influence of the Venus' topographic features on the Venus atmosphere. From Fourier Spectrometry on Venera-15 (FS V-15), the 3-D temperature and clouds fields in mesosphere were obtained (temperature and aerosol profiles were retrieved in self consistent way from each single spectrum [1]). Geometry (orbits trough North pole) and spectral range ($40\text{-}1650\text{ cm}^{-1}$) allow to study Venus atmosphere in the Northern hemisphere on the day and night sides practically simultaneously (within 1-2 h) through 12 h local time from N-pole to 20N and altitudes from 55- 60 km to 90-100 km. Earlier it was found that distribution of temperature at different levels vs. local time is described by the Fourier decomposition with 1, 1/2, 1/3, and 1/4 and upper boundary of clouds with 1, 1/2 days harmonics in Solar-fixed coordinates. The amplitudes of diurnal and semi-diurnal harmonics reach 10 K. We found that in the Solar- fixed coordinates both maxima and minima are shifted from noon and from midnight to westwards by of 2 - 3h [1]. To study how the surface influences on the atmosphere we compare the isotherms at different levels in the mesosphere and position of the upper boundaries of clouds with Magellan topography maps [2]. Of course, in retrieval of temperature and aerosol procedure we don't use any information about surface topography. For low boundary condition we take the temperature and pressure at 50 km altitude from VIRA: it is 5 points for latitudes $<30^\circ$, 45° , 60° , 70° and 85° . Isotherms and clouds isolines repeat the most pronounced details of relief but the "images" shifted by $\sim 30^\circ$ (of 2 hours) in the direction of superrotation relative to topography map. Thus "image" of relief in the atmosphere and extrema of thermal tides are strongly linked.

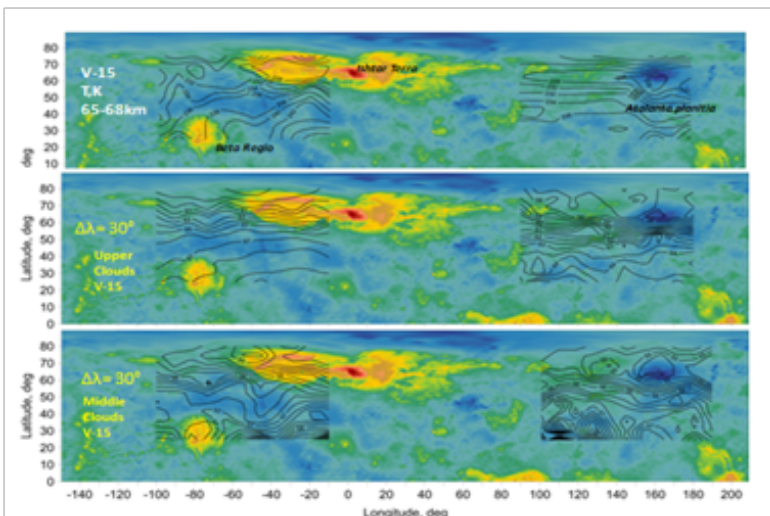


Fig. 1. Examples of isotherms (V-15, Northern hemisphere) at upper boundary of clouds (upper), altitude of position of upper boundary of clouds (altitude of opacity equal to 1 in thermal IR) (middle) and middle clouds (bottom) plotted above the Magellan topography map. One may see that the isotherms and the isolines of the clouds boundary altitudes reproduce the most pronounced surface features Ishkar, Atalanta Planitia and Beta Regio. Temperature at the upper boundary of clouds decreases along with the increase of surface altitude. Correlation with the surface details reaches 80-90 %.

It was found by [3] that surface topography influence the wind speed in UV (VMC VEX) above Aphrodite Terra through stationary gravity waves, generated in the lower atmosphere. Problem is how gravity wave overcome nonstable region in the middle clouds? After more detailed study UV VMC data [4] absolute minimum of wind speed above Aphrodite Terra was identified exactly at noon. It looks like atmosphere becomes more stable, may be as a result of Solar heating. For thermal IR it is known even from ground based observations of 1960th (also OR Pioneer Venus, FS V-15 etc.) that extrema of thermal tides are shifted from noon and midnight (by 2-3 hours), which was explained by input from superrotation. As well a bow shaped feature, observed by Akatsuki above Aphrodite Terra is found also at 2 - 4 h afternoon [5]. For observation in UV the altitudes of 70 -72 km are available. The difference in altitude of effective levels between thermal IR (65-68 km) and UV may exceed 5 km. Different local time behavior relative to noon between UV and IR may be explained by changing the phase with depth in the clouds [1]. We found strong link between solar tides and extreme surface topography which may indicate as in the case of Mars, that we deal with non-migrating solar tides.

References

- [1] Zasova, L.V., Ignatiev N.I., Khatuntsev I.V. et al. Structure of the Venus atmosphere // Planet. Space Sci. 55, 1712-1728, 2007.
- [2] Saunders, R. S. et al. The Magellan Venus radar mapping mission // JGR 95, 8339–8355, 1990.
- [3] Bertaux, J.-L., Khatuntsev, I. V., Hauchecorne, A. et al. Influence of Venus topography on the zonal wind and UV albedo at cloud top level: The role of stationary gravity waves, JGR // Planets, 121, 1087–1101, 2016.
- [4] Patsaeva M.V., Khatuntsev, I.V., Zasova, L.V., et al. Solar related variations of the cloud top circulation above Aphrodite Terra from VMC/Venus Express wind fields, submitted to JGR // Planets, 2018.
- [5] Fukuhara, T., Futaguchi, M., Hashimoto, et al. Large stationary gravity wave in the atmosphere of Venus, Nat // Geosci., doi:10.1038/ngeo2873, 2017

STUDY OF AEROSOL PROPERTIES IN UPPER HAZE FROM SPICAV-UV AND -IR DATA

M. Luginin¹, D. Belyaev¹, A. Fedorova¹, F. Montmessin², O. Korablev¹, J.-L. Bertaux^{2,1}

¹Space Research Institute (IKI), Moscow, Russia,
mikhail.luginin@phystech.edu;

²LATMOS/IPSL, Guyancourt, France

Keywords:

Infrared observations; atmosphere of Venus; solar occultation; upper haze; detached layers.

Venus is totally enshrouded by a thick layer of clouds extending from 40 to 70 km with thin upper haze layer lying above. Cloud top particles are spherical and consist of droplets of sulfuric acid [1]. Clouds are stratified into three layers, the upper cloud region is composed of mode 1 ($\sim 0.2 \mu\text{m}$) and mode 2 ($\sim 1 \mu\text{m}$) particles. Before Venus Express, the upper haze was believed to be populated by only mode 1 particles [1].

Early independent study of three channels of SPICAV/SOIR instrument with data set from three selected orbits showed presence of bimodality in size distribution [2]. Analysis of aerosol properties from single SPICAV-IR spectrometer for the whole data set obtained from May 2006 till November 2014 has proved it [3]. In this work, we report retrieval of upper haze aerosol properties from SPICAV-UV and -IR solar occultation observations for the whole data set.

Firstly, aerosol extinction are calculated. Inversion procedure for SPICAV-UV is identical to the one used for SO_2 abundance retrievals [4]. Aerosol extinction retrieval from SPICAV-IR data is the same as used in [3]. Secondly, particle size distribution is retrieved by fitting spectral dependence of experimental normalized aerosol extinctions to their corresponding theoretical values. The aerosol extinction is modeled according to Mie theory with adoption of 75% H_2SO_4 sulfuric acid refractive indices. In our retrieval procedure, unimodal and bimodal lognormal size distributions are considered independently. Finally, aerosol number density are calculated as a ratio of experimental extinction coefficient to modeled extinction cross section.

We have processed 71 simultaneous solar occultation observations from SPICAV-UV and -IR instruments from orbit #339 (February 2008) to #2464 (April 2011). Aerosol properties are determined using 6 wavelengths in 200–300 nm range from SPICAV-UV and 10 wavelengths in 650–1550 nm range for SPICAV-IR.

In Fig. 1, examples of the fitted normalized extinction at altitudes 89 and 92 km of orbit #444 are shown. At 89 km, bimodality provides the best fit with effective radius (r_{eff}) $0.13 \pm 0.02 \mu\text{m}$ and $0.81 \pm 0.1 \mu\text{m}$ and number density (n) $13 \pm 3 \text{ cm}^{-3}$ and $(5.4 \pm 0.5) \cdot 10^{-3} \text{ cm}^{-3}$ for mode 1 and mode 2 respectively. At 92 km, unimodal distribution is chosen with $r_{\text{eff}} = 0.15 \pm 0.1 \mu\text{m}$ and $n = 4 \pm 2 \text{ cm}^{-3}$.

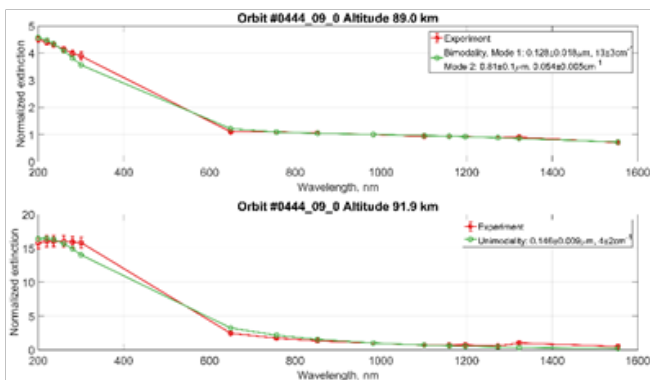


Fig. 1. Examples of fitted spectral dependence of aerosol extinction at altitudes 89 and 92 km of orbit #444.

Overall, aerosol size distributions have been retrieved at 127 altitudes from 71 solar occultation sessions mostly in the altitude range 86–96 km; bimodality has been observed 68 times most frequently in the altitude range 86–92 km, unimodality has been observed 59 times (Fig. 2c).

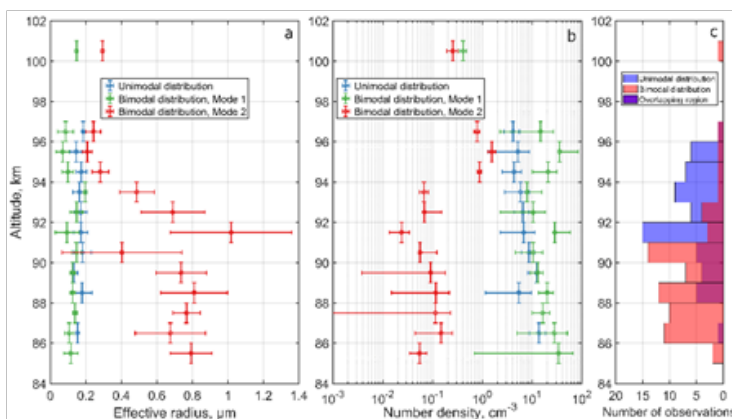


Fig. 2. Profiles of r_{eff} (a) and n (b) for unimodal and bimodal cases. (c) Altitude distribution of all observations.

All values of r_{eff} and n are averaged in 1 km altitude bins and plotted as vertical profiles in Fig. 2a and b. In addition, we have calculated mean values of r_{eff} and n for unimodal case in the whole altitude range ($0.17 \pm 0.03 \mu\text{m}$ and $6 \pm 3 \text{ cm}^{-3}$) and for bimodal case in the 86–92 km altitude range ($0.12 \pm 0.03 \mu\text{m}$ and $19 \pm 12 \text{ cm}^{-3}$ for mode 1 and $0.7 \pm 0.2 \mu\text{m}$ and $0.09 \pm 0.05 \text{ cm}^{-3}$ for mode 2).

Acknowledgments.

Russian authors acknowledge support from RFFI grant № 16-52-16011. J.-L.B. acknowledges support from Ministry of Science and Higher Education of the Russian Federation, grant №14.W03.31.0017.

References:

- [1] Esposito et al. Venus. Univ. of Arizona, 1983. Ch. 16. The clouds and hazes on Venus. Pp 484–564.
- [2]. Wilquet et al. Preliminary characterization of the upper haze by SPICAV/SOIR solar occultation in UV to mid-IR onboard Venus Ex-press // JGR. 2009. No 114, E00B42.
- [3]. Luginin et al. Aerosol properties in the upper haze of Venus from SPICAV IR data // Icarus. 2016. No 277, 154–170.
- [4] Belyaev et al. Night side distribution of SO₂ content in Venus' upper mesosphere // Icarus. 2017. No 294, pp. 58–71.

VENUS AS AN ASTROBIOLOGY TARGET

S.S. Limaye¹, R. Mogul², K.L. Jessup³, T. Gregg⁴, R. Pertzborn¹, A. Ocampo⁵, Y.J. Lee⁶, M. Bullock⁷, D. Grinspoon⁸

¹Space Science and Engineering Center, University of Wisconsin, 1225 W. Dayton St, Madison, WI 53706, USA, sslimaye@wisc.edu;

²Chemistry and Biochemistry Department, California State Polytechnic University, Pomona, CA 91768, USA, rmogul@cpp.edu;

³Southwest Research Institute, Boulder, CO 80302, USA, kandilea@boulder.swri.edu;

⁴Department of Geology, University of Buffalo, Buffalo, NY 14260, USA, tgregg@buffalo.edu;

⁵NASA HQ, Washington, DC 20546, USA;

⁶Department of Complexity Science and Engineering, University of Tokyo, Kashiwa, Japan, leeyj@edu.k.u-tokyo.ac.jp;

⁷Science and Technology Corp., Hampton, VA 23666, USA, mbullock75@gmail.com;

⁸Planetary and Space Science Institute, Tucson, AZ 85719, USA, grinspoon@psi.edu

Keywords:

Venus, microorganism, habitable, clouds, particles, aerosols, spectroscopy, albedo
Venus' clouds are responsible for nearly half of the energy absorbed from the sun by the planet at wavelengths < 600 nm [1]. The global cloud layer has been sampled by the Venera [2, 3] and Pioneer Venus entry probes [4], and two VeGa balloons [5] and landers [6]. Venus has also been investigated using ground-based [7] and spacecraft observations [8-12]. Venus' cloud layer extends from ~47 km in altitude to the cloud tops at ~ 72 km at low latitudes, and to ~ 67 km in the polar latitudes [13]. The clouds consist of droplets of aqueous sulfuric acid with concentrations ranging between 75-85%. Sulfuric acid however, does not contribute to absorption at the ultraviolet and visible wavelengths. Hence, the presence of other chemical species is required [14] to explain the albedo and observed cloud contrasts of Venus [15]. While more than a dozen possible absorbers have been proposed, no individual candidate satisfactorily explains the contrasts and temporal evolution of the cloud features.

Recently, the potential for bioorganic contributions to Venus' contrasts was explored (Figure 1) by Limaye et al. [16]. The possibility of life was explored earlier by Morowitz and Sagan [17] and investigated further by Cockell [18] and discussed by Grinspoon [19], Grinspoon and Bullock [20] and others [21-23]. Figure 1 summarizes the hypothesis proposed by Limaye et al. [17]. Life could have evolved on Venus independently when it had liquid water on its surface with the same life sustaining biochemistry present in Earth's early atmosphere [24, 25].

In the lower cloud layer (47.5-50.5 km), the estimated pH of the aerosols is ~0, the atmospheric pressure is ~ 1 atm, and temperature is ~60 °C, which together are compatible with many forms of terrestrial microbial life. The aerosols in the lower clouds also account for ~70% of the total columnar mass, with particles of 2-8 μm in diameter (mode 2' and 3) comprising ~94% of the mass within the lower clouds. For these particles, the physiochemical comparisons show similarities between the (i) size regime for the Venus aerosols and the aerosols from Earth containing cultivable bacteria, (ii) estimates of theoretical Venus biomass and cell densities with measured values from Earth, and (iii) estimates of Venus mass extinction coefficients with those obtained from ground-based spectroscopic studies.

Together, these similarities suggest that Venus' aerosols contain sufficient mass to harbor microorganisms, water, and bulk solutes, and sufficient optical extinction coefficients to be amenable to spectral studies for habitability or life. Further, when considering Venus' atmospheric constituents and terrestrial microbial analogs (for life in low pH, high temperature, and sulfur-rich environments), a plausible geochemical cycle, inclusive of the phototrophic reduction of CO₂ and a coupled Fe/S metabolism can be constructed.

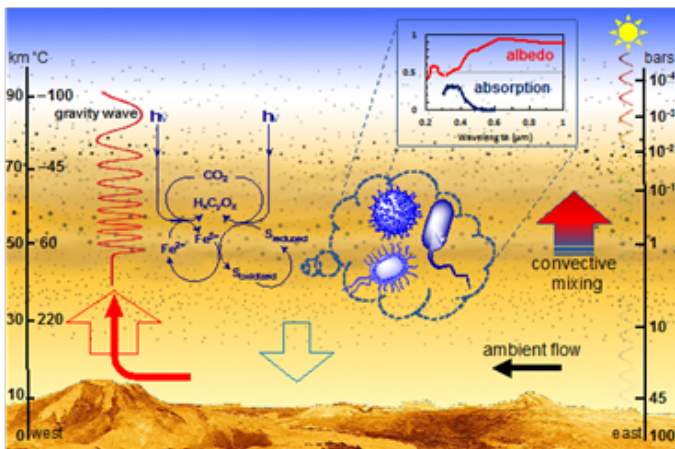


Fig. 1. Schematic representation of the habitable zone in the cloud layer of Venus from Limaye et al. [18].

One hypothesis for the origin of life on Earth, is that it may have evolved at mid-ocean ridges, where the thermal energy from the magma stored < 5 km beneath the ocean floor may have contributed to chemical and biochemical evolution. As hot seawater flowed through the solidified basalts, abundant chemical nutrients (largely in the form of sulfur compounds) were likely extracted, and clays may have reorganized to provide macromolecular scaffoldings or templates for organic catalysis [26].

There is ample evidence that Venus once had an ocean of liquid water [27]. Volcanism has been a dominant geologic process on Venus, and recent observations by Venus Express suggest that Venus may still be volcanically active [28]. As Venus lost its surface water over time, it is possible that thermophilic and sulfur-metabolizing bacteria may have been transported into the atmosphere, ultimately finding a habitable niche in the clouds. Hence, Venus' cloud contrasts may currently include contributions from sulfur compounds, other chemicals, and microorganisms. The spectral similarity between Venus' cloud contrasts and terrestrial biomolecules [18] support this premise. Further, the persistent nature of the contrasts suggest the presence of solar cycles, and contributions from gravity waves and convection, and possibly explain at least some of the observed long-term variations of Venus' UV albedo [29] which may be due to the effects of EUV radiation on the microorganisms at the cloud tops.

Previous studies on Venus' clouds could not distinguish between abiotic and biological aerosols. We need laboratory measurements of the physical, chemical, spectral, and biological properties of terrestrial candidate microorganisms capable of thriving in Venus' clouds. The biological explanation of absorption and cloud contrasts can be tested by examining the nature and identity of the absorbers from aerial platform missions with Raman and UV-Visible spectrometers, imaging microscopes, and other life detection instruments [30, 31]. Acidity level (pH) measurements in the cloud layer will be crucial because microorganisms can modify the environmental pH [32].

Venera-D, a collaborative proposed mission between Roscosmos and NASA, is capable of including such a platform and deserves serious consideration for development. The search for life in our solar system and the exploration of the possibility of life on terrestrial exoplanets is drawing the interest of international space agencies. Venus is rapidly attainable and presents an easily accessible habitable zone that poses significantly less engineering hurdles, such as those associated with exploration of the icy moons or the Martian subsurface.

References

- [1] Crisp, D., Radiative forcing of the Venus mesosphere. I - Solar fluxes and heating rates. *Icarus*, 1986. **67**: p. 484-514.

- [2] Avduesvskii, V.S., et al., Parameters of Venus' atmosphere at Venera 11 and 12 landing sites - An analysis of the results of measurements made by these automatic interplanetary stations. *Cosmic Research*, 1980. **17**: p. 655-660.
- [3] Avduesvskii, V.S., et al., Preliminary results of an investigation of the lighting conditions in the atmosphere and on the surface of Venus. *Cosmic Research*, 1977. **14**: p. 735-742.
- [4] Tomasko, M.G., et al., Measurements of the flux of sunlight in the atmosphere of Venus. *Journal of Geophysical Research*, 1980. **85**: p. 8167-8186.
- [5] Zhulanov, Y.V., L.M. Mukhin, and D.F. Nenarokov, Aerosol counts in Venus clouds - Preliminary VEGA 1, 2 density profiles, H = 63-47 KM. *Pisma v Astronomicheskii Zhurnal*, 1986. **12**: p. 123-130.
- [6] Bertaux, J.-L., et al., VEGA 1 and VEGA 2 entry probes: An investigation of local UV absorption (220-400 nm) in the atmosphere of Venus. *J. Geo. Res.*, 1996. **101**: p. 12709-12746.
- [7] Hansen, J.E. and J.W. Hovenier, Interpretation of the polarization of Venus. *Journal of Atmospheric Sciences*, 1974. **31**: p. 1137-1160.
- [8] Kawabata, K., et al., Cloud and haze properties from Pioneer Venus polarimetry. *J Geophys Res*, 1980. **85**.
- [9] Markiewicz, W.J., et al., Glory on Venus cloud tops and the unknown UV absorber. *Icarus*, 2014. **234**: p. 200-203.
- [10] Petrova, E.V., Glory on Venus and selection among the unknown UV absorbers. *Icarus*, 2018. **306**: p. 163-170.
- [11] Ksanfomaliti, L.V. and E.V. Petrova, Photometry at 3500 A from Venera 9 and Venera 10. *Kosmicheskie Issledovaniia*, 1978. **16**: p. 886-894.
- [12] K.-L. Jessup, et al., On Venus' Cloud Top Chemistry, Convective Activity and Topography: A Perspective from HST. *Icarus*, 2018. **Submitted**.
- [13] Knollenberg, R., et al., The clouds of Venus - A synthesis report. *Journal of Geophysical Research*, 1980. **85**: p. 8059-8081.
- [14] Pollack, J.B., et al., Distribution and source of the UV absorption in Venus' atmosphere. *Journal of Geophysical Research*, 1980. **85**: p. 8141-8150.
- [15] Travis, L.D., On the origin of ultraviolet constrasts on Venus. *Journal of Atmospheric Sciences*, 1975. **32**: p. 1190-1200.
- [16] Limaye, S.S., et al., Venus' Spectral Signatures and the Potential for Life in the Clouds. *Astrobiology*, 2018. **10(10)**: p. null.
- [17] Morowitz, H. and C. Sagan, Life in the Clouds of Venus? *Nature*, 1967. **215**: p. 1259.
- [18] Cockell, C.S., Life on venus. *Planetary and Space Science*, 1999. **47(12)**: p. 1487-1501.
- [19] Grinspoon, D.H., Venus revealed : a new look below the clouds of our mysterious twin planet. Reading, MA: Addison-Wesley, 1997 xix, 355 p.20. Grinspoon, D.H. and M.A. Bullock, *Astrobiology and Venus Exploration, in Exploring Venus as a Terrestrial Planet*. 2007, Amer. Grophys. Union. p. 191-206.
- [20] Schulze-Makuch, D., et al., A Sulfur-Based Survival Strategy for Putative Phototrophic Life in the Venusian Atmosphere. *Astrobiology*, 2004. **4**: p. 11-18.
- [21] Shimizu, M., Ultraviolet absorbers in the Venus clouds. *Astrophysics and Space Science*, 1977. **51**: p. 497-499.
- [22] Way, M.J., et al., Was Venus the first habitable world of our solar system? *Geophysical Research Letters*, 2016. **43**: p. 8376-8383.
- [23] Kumar, M. and J.S. Francisco, Elemental sulfur aerosol-forming mechanism. *Proceedings of the National Academy of Sciences*, 2017.
- [24] Czaja, A., N. Beukes, and J. T. Osterhout, Sulfur-oxidizing bacteria prior to the Great Oxidation Event from the 2.52 Ga Gamohaana Formation of South Africa. *Vol.* 44. 2016. 983.
- [25] McCollom, T.M., G. Ritter, and B.R. Simoneit, Lipid synthesis under hydrothermal conditions by Fischer-Tropsch-type reactions. *Orig Life Evol Biosph*, 1999. **29(2)**: p. 153-66.
- [26] Donahue, T.M., et al., Venus was wet - A measurement of the ratio of deuterium to hydrogen. *Science*, 1982. **216**: p. 630-633.
- [27] Shalygin, E.V., et al., *Active volcanism on Venus in the Ganiki Chasma rift zone*. *Geophysical Research Letters*, 2015. **42**: p. 4762-4769.
- [28] Lee, Y.J. *Venus, Seen From the UV Imager Onboard Akatsuki*. in *Proceedings of the Venera-D Modeling Workshop 2017*. Moscow, Russia.
- [29] Yamagishi, A., et al., *LDM (Life Detection Microscope): In situ Imaging of Living Cells on Surface of Mars*. *Trans. Japan Soc. for Aeronautical and Space Sciences, Aerospace Technology, Japan*, 2016. **14(ists30)**: p. Pk_117-Pk_124.
- [30] Jessup, K.-L., et al., *Current Problems and Future Solutions for Identifying Venus' Unknown Absorber*, in *Lunar and Planetary Science Conference*. 2018.
- [31] Ratzke, C. and J. Gore, *Modifying and reacting to the environmental pH can drive bacterial interactions*. *PLOS Biology*, 2018. **16(3)**: p. e2004248.

ABOUT THE POSSIBLE NATURE OF LIVING FORMS ON VENUS

V.N. Snytnikov¹, L.V. Ksanfomality²

¹*Boreskov Institute of Catalysis SB RAS, Novosibirsk, Russia, snyt@catalysis.ru*

²*Space Research Institute RAS, Moscow, Russia, leksanf@gmail.com*

Keywords:

Venus, biosphere, biocenosis, heterogeneous catalytic cycle, living forms

The problems of origin and evolution of the biosphere were studied mainly for the surface of the Earth for "normal" conditions. These studies formed our basic views about terrestrial biocenoses biocenoses. The missions to Venus discovered that on its surface the pressure of the carbon dioxide atmosphere is 93 times higher than the earth's pressure, and the temperature is 735 K, which is fundamentally different from the conditions on the Earth. The Venusian pressure and temperature conditions are reproduced on Earth in a number of high-pressure reactors used in chemical technologies to produce products and for research purposes in the study of chemical catalytic processes. The report discusses the chemical foundations of hypothetical biocenoses on the surface of Venus. The discussion is based on previously published data on the results of missions to Venus and literature data on catalysis in terrestrial reactors. In particular, the following issues are considered. 1. What heterogeneous catalytic cycle can underlie hypothetical biocenoses on the surface of Venus? 2. What chemical compounds can hypothetical living objects on the surface of Venus consist of? 3. What chemical compound can act as a functional water replacement in biocenoses on Venus? 4. What is the nearest terrestrial analogue of the Venusian biocenosis? 5. What data from the surface of Venus about the chemical processes will be critical for the hypothesis of the existence of biocenoses on the surface of Venus?

TRAJECTORY AND ORBIT DESIGN FOR THE VENERA-D MISSION

I.D. Kovalenko, N.A. Eismont

¹Space Research Institute, Russian Academy of Sciences, Russia

Keywords:

Venus; orbiter; mission trajectory; L1 lagrangian point

Venera-D mission is a project of space probe to Venus [1], planned to be launched in 2026. The project is led by Roscosmos and Russian Academy of Sciences in cooperation with NASA. The baseline mission includes an entry capsule and an orbiter system. The capsule contains one principal and some smaller long-lived landers, aimed at surface studies by measurements from different regions of Venus surface, and aerial balloons to sample the cloud layer. The orbiter part is a system of two satellites, operating in a same orbit, for atmospheric studies and communication between the Earth and the landers and balloons. The possibilities to include an aerial platform, an inflatable aircraft and a L1 lagrangian point orbiter are also discussed.

In this work we consider main aspects of the Venera probe trajectory design. The main goal of our analysis is the optimization of total delta-V cost of the mission to increase the possible mass of the scientific payload. The prior trajectory and orbit design task is to insure the deployment of the lander, insertion of the orbiter into desired orbit, collection of data from the principal lander to the orbiter for transmission to the Earth. The secondary task requires the data relay from the small long-lived landers, balloons and the aerial platform through the orbiter to the Earth. These potential elements may provide a crucial enhancement to the Venera-D science goals for super-rotation [2] and looking for evidence of biosignatures [3].

The following launch scenario is analyzed. All mission elements are launched on Angara rocket into a near-circular low Earth orbit with an altitude about 200 km and inserted into a transfer orbit toward Venus. At a distance about one million from the Venus, an impulse is applied onto the main orbiter with the subsatellite, directing them onto an orbit about the planet. The operational orbit of the satellites is planned to be a near polar orbit with one day period. For this target orbit an additional inclination changing manoeuvre may be required. For the entry module, containing the principal lander, small long-lived landers and balloons, no deceleration impulses are planned. Namely, it is supposed to enter the atmosphere directly from the transfer orbit. The aerial platform/aircraft, if included into the mission, needs an additional manoeuvre, reducing its speed to avoid its direct enter to the atmosphere. It is supposed that, firstly, the aircraft is inserted into an orbit about Venus, and then it deploys into the atmosphere and begins its autonomous flight.

For the data relay tasks, the orbit design for the satellite (and subsatellite) needs to consider the surface locations of the main lander and the long-lived stations, but also to ensure collection of data from balloons and the aerial platform.

References:

- [1] Vorontsov, V. A., et al. "Prospective spacecraft for venus research // Venera-D design." *Solar System Research* 45.7,2011.: 710-714.
- [2] Bougher, S. W., Hunten, D. M., & Phillips, R. J. (Eds.). (1997) // *Venus II--geology, Geophysics, Atmosphere, and Solar Wind Environment* (Vol. 1). University of Arizona Press.
- [3] Venus Exploration Analysis Group // <https://www.lpi.usra.edu/vexag/>

VENERA-D LANDING SITE CONSTRAINTS

M.A. Ivanov¹, L. Zasova², T.K.P. Gregg³ and the Venera-D Joint Science Definition Team

¹Vernadsky Inst., RAS, Russia, Mikhail_ivanov@brown.edu

²AffiliationSpace Research Institute (IKI), Dept. of Planets, Physics and Solar Systems Small Bodies, Moscow, Russia

³University at Buffalo, Dept. of Geology, Buffalo NY, USA

Keywords:

Landing site, Venera-D, volcanic plains, regional plains

Introduction:

The Venera-D (in which the “D” stands for долгоживущий, or “long-lasting”) is a mission concept being explored by a joint NASA-IKI/Roscosmos Science Definition Team (VDJSDT) [1, 2]. Using the highly successful Soviet-era Venera and VEGA missions as a strong foundation, the VDJSDT has been charged with defining the science-driven architecture of a mission consisting of an orbiter, lander, and a long-lived in-situ solar system explorer (LLISSE) [3] that may survive for 2 months on the Venusian surface.

Landing Site Selection:

The criteria used for landing site selection include: 1) lander safety; 2) ability for orbiter and lander to communicate reliably during the lander lifetime (~2 – 3 hours); and 3) scientific value. Based on the Venera landers, we assume a landing ellipse of 300 km, so these criteria must be met within that continuous distance. Topographic data for Venus has, at best, a 5km/pixel horizontal resolution [4], so we must rely on morphologic interpretations of Magellan radar data [5] to select landing sites that meet these criteria.

Lander safety requires that we land on smooth, flat-lying plains that provide a horizontal to sub-horizontal platform for the lander within the region of the landing ellipse. The smoothest plains are those that have a uniformly low radar backscatter [6], and are not deformed by obvious faults or folds over a 300-km footprint.

The lander’s ability to communicate with the orbiter depends on the precise orbit selected, but a lander located near the north pole (poleward of 70° lat) would provide the optimal amount of communication time between the orbiter and the lander.

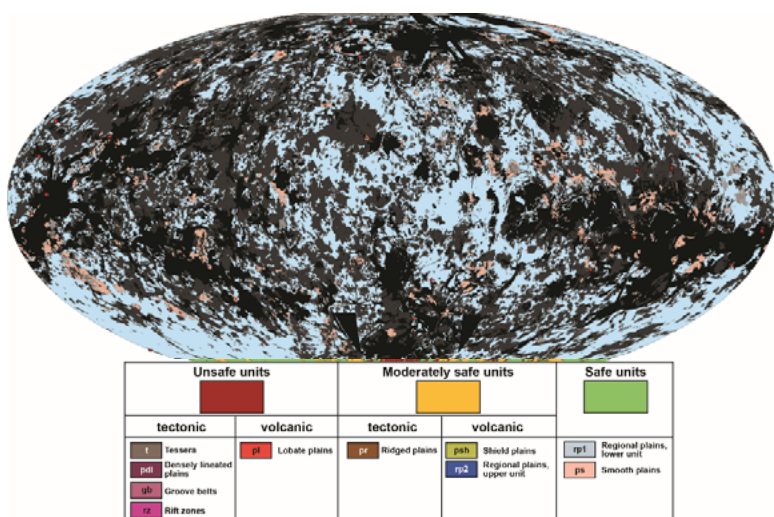


Fig. 1. Distribution (in blue) of “Regional plains 1” that cover >30% of the Venusian surface. In terms of both lander safety and the potential scientific return, any 300-km-wide region within these blue plains would be acceptable. Units mapped as black or dark gray are unacceptable, primarily because of safety issues. (After Ivanov and Head, 2011.)

For us to be able to best interpret any results from Venus surface sample analyses, the landing site should consist of geologic materials that cover a significant percentage of the Venus surface (the analyzed samples should not be exotic or unique) and are likely to therefore be representative of Venus. For example, analysis of Venus' surface within the Venera 8 landing ellipse revealed materials with anomalously high K_2O , U and Th compared to results from the other Venera landing sites [7]. Unlike the other Venera landing sites, the Venera 8 landing ellipse contains exotic volcanic morphologies such as steep-sided domes and a possible collapse calderas. The unique chemistry may be related to the unique morphology—or it may simply be a coincidence. The range of volcanic morphologies within the landing ellipse makes the results difficult to interpret and we would like to avoid this scenario with Venera-D by selecting a morphologically uniform landing site.

On Venus, the landing site that best fulfills these criteria would be located on what has been mapped as “regional plains 1” as defined by Ivanov and Head [8]. This geologic unit consists of gently deformed volcanic plains that are mostly horizontal to sub-horizontal, cover 30% of the planet's surface (see Figure 1), and are essentially homogenous at the scale of Magellan radar data (~100 m / pixel). They are interpreted to be flat-lying lava flows, emplaced in a single, long-lived volcanic episode. Furthermore, these volcanic plains may provide straight-forward geochemical insight into the evolution of Venus' upper mantle.

Given the abundance of these flat-lying volcanic plains (Figure 1), we anticipate being able to select a safe and representative landing site for any appropriate launch readiness date for the Venera-D mission.

References:

- [1] Senske, D., L. Zasova, A. Burdanov, T. Economou, N. Eismont, M. Gerasimov, D. Gorinov, J. Hall, N. Ignatiev, M. Ivanov, K.L. Jessup, I. Khatuntsev, O. Korablev, T. Kremic, S. Limaye, I. Lomakin, M. Martynov, A. Ocampo, S. Teselkin, O. Vaisberg and V. Voronstov, 2018, Development of the Venera-D mission concept, from science objectives to mission architecture, 49th Lun // Planet Sci. Conf., Abstract #1243.
- [2] Venera-D Joint Science Definition Team, 2017, Venera-D: Expanding our Horizon of Terrestrial Planet Climate and Geology through the Comprehensive Exploration of Venus, <https://www.lpi.usra.edu/vexag/reports/Venera-D-STDT013117.pdf>.
- [3] Kremic, T., G. Hunter and J. Rock, 2018, LLISSE: a long duration Venus surface probe 15th Venus Exploration Analysis Group, Abstract #8035.
- [4] Ford, P.G., 1991, Global Altimetry and Radiometry Data Records, MIT-MGN-GxDR SIS Version 2.3, 40 p., Magellan CD-ROMS, https://astrogeology.usgs.gov/search/map/Venus/Magellan/RadarProperties/Venus_Magellan_Topography_Global_4641m_v02.
- [5] Saunders, R.S., G.H. Pettengill, R.E. Arvidson, W.L. Sjogren, W.T.K. Johnson and L. Pieri, 1990, The Magellan Venus radar mapping mission, *J. Geophys. Res.* 95(B6):8339-8355.
- [6] Wall, S.D., S.L. McConnell, C.E. Leff, R.S. Austin, K.K. Beratan and M.J. Rokey, 1995, User guide to the Magellan synthetic aperture radar images, NASA Reference Publication 1356, NASA/JPL, Pasadena, CA, https://pds-imaging.jpl.nasa.gov/software/MGN_SAR_UserGuide.pdf.
- [7] Basilevsky, A.T., OIV. Nikolaeva and C.M. Weitz, 1992, Geology of the Venera 8 landing site region from Magellan data // Morphological and geochemical considerations, *J. Geophys. Res.* 97(E10):16,315-16,335.
- [8] Ivanov, M.A. and J.W. Head, 2011, Global geological map of Venus // *Planetary Space Sci.* 59(13):1559-1600.

DYNAMIC PROCESSES IN THE SOLAR WIND AS THE CAUSE OF VENUS MAGNETOSPHERE AND IONOSPHERE DISTURBANCES AND LOSS OF MASS

O.L. Vaisberg¹, A.Yu. Shestakov¹, S.D. Shuvalov¹

¹*Space Research Institute RAS, 117997, Moscow, Russia, 84/32 Profsoyuznaya str.*

Keywords:

Venus, solar wind interaction, magnetosphere, ionosphere, mass losses

Introduction:

Upper atmosphere and ionosphere of Venus are not shielded from the solar wind flow due to absence of the planetary magnetic field. Mass-loading of the solar wind flow past Venus by exospheric photo-ions leads to loss of atmospheric constituents and to formation of induced or accreted magnetosphere. Other important ionospheric effects caused by the solar wind include intermittent magnetization of ionosphere and strong ionospheric convection from the dayside to the night-side whose magnitude reaches supersonic velocity at the terminator.

The tail of induced magnetosphere is filled with escaping planetary ions making solar wind-induced mass loss an important fraction of total mass losses. Due to existence of dense atmosphere these losses are of not very important factor of atmospheric evolution at Venus. However, predominate loss of lighter atmospheric constituents and lighter isotopes may be important for change of atmospheric composition during the lifetime of the solar system.

Usually solar wind-induced losses are calculated from the set of measurements obtained along the spacecraft trajectories in the tail with some assumptions about distribution across the cross-section of the tail. In calculating average loss rate it is assumed usually that these losses are relatively stable in time. However, observations of cometary plasma tail suggest that non-stationary interplanetary phenomena like coronal mass ejections may cause dramatic one-time loss of cometary ionized material. Some cometary "tail disconnection" events suggest that that sporadic interplanetary phenomena can cause very large cometary plasma losses. These events exemplify similar phenomena at Venus and Mars, and require estimation of transients to total mass loss. Another cause of transient induced mass losses at Venus (and Mars) may be Hot Flow Anomalies that form as a result of interplanetary current sheets. These phenomena were studied at the Earth, and were also observed at Venus and Mars. These HFAs lead to very strong disturbances of flow within magnetosheath / ionosheath of Venus with dramatic variations of dynamic pressure on planetary scale. Like CME-associated disturbances, HFA-associated variations of plasma flow should very strongly influence ionosphere of Venus and may lead to additional mass loss of its atmosphere. We show examples of magnetosheath variations associated with HFAs and emphasize the importance of investigations of similar phenomena at Venus as possible source of atmospheric losses.

A NEW CRITERION OF THE GEOMETRICAL OPTICS APPLICABILITY AS A FOUNDATION OF A NOVEL APPROACH TO RADIO OCCULTATION DATA INTERPRETATION

S.F. Kolomiets¹, A.L. Gavrik¹, Y.A. Gavrik¹, T.F. Kopnina¹, Ya.A. Ilyshin²

¹*Kotel'nikov Institute of Radio Engineering and Electronics, Fryazino branch, V.A. Vvedensky sq. 1, Fryazino, Moscow region, Russia;*

²*Moscow State University, Leninskie Gory, Moscow, Russia.*

Keywords:

occultation, radio wave, geometrical optics, diffraction, data processing.

Introduction:

It would seem that structural characteristics of the ionosphere and atmosphere of Venus have been thoroughly investigated by means of the occultation technique. Indeed, although a great deal has been learned about the Venusian ionosphere and extensively described in the literature, our understanding still remains rather shallow in most aspects. The reason for that is quite obvious. During the whole history of occultation experiments there was only one experimental scheme utilized predominantly (i.e. down-link occultation) as well as there was only one predominant approach to signal processing and interpretation.

It is a well-known fact now that, in order to gain new findings by means of the classical scheme of occultation experiments, it is necessary either to wait for an occasional detection of new effects or decrease instrumental noise and frequency of radio lines. The former is risky; the latter poses a lot of technical difficulties and contradicts with requirements of high information capacity of radio-channels. As far as we can say, an efficient solution may also present itself in the realm of up-link occultation and new data processing techniques.

An Adiabatic Criterion of the Geometrical Optics Applicability:

It can be deduced by the mathematically rigid way for the signals refracted on media with spherical symmetry that changes of energy flux density are directly proportional to the value of the gradient of a wave vector deviation angle until the geometrical optics is valid [1]. It implies that power fluctuations of signals detected in atmospheric and ionospheric occultation experiments must be directly correlated to the speed of frequency changes because these media can be seen as spherically symmetrical due to the impact of the gravity field. On the one hand, the idea of proportionality is logically contained in the basic relations describing occultation experiments in terms of geometrical optics, and so might be called an adiabatic invariant of refraction on spherically symmetrical media [2-4]. But on the other hand, it has never been used in data interpretation procedures and so it may be seen as a new reliable criterion of diffraction distortion of signals.

Applying it to numerical solutions of parabolic equation one can find an interval of trajectory heights above the planetary surface or distances between the spacecraft and planetary limb where the diffraction distortion is negligible and so the geometrical optics can be used as a foundation of signal interpretation. With a specially adjusted fit of vertical profiles of electron concentration utilizing sums of smooth functions with smooth derivatives, one can find that such an interval of distances between the spacecraft and planetary limb extends from 2000 km to 12000 km. It is important to note that using non-smooth functions (or if their derivatives are non-smooth) may result in calculation artefacts that are sometimes very similar to elements of a diffraction fringe. Such evaluations are very useful. For even weak but sustainable deviation of a certain signal parameter from the noise level (more precise – from the level of instrumental errors of the measurements) can be seen as an effect of refraction without having to resort to speculation about diffraction. This result allows us taking finer features of signals into interpretation.

A Novel Radio Science Data Processing:

Signals may receive a new representation from the point of view of adiabatic invariant. It consists of splitting signals into correlated (effective) and uncorrelated (pure noisy) parts. And this approach paves the way to a novel data processing technique and interpretation which is expected to allow us to gain deeper insight into the ionosphere and investigate the processes of interaction between the atmosphere and ionosphere more reliably (including propagation of density fluctuations from the atmosphere to the lower ionosphere).

The data interpretation discussed requires not only the absence of diffraction but absence of scattering and absorption as well. *Ceteris paribus* the level of instrument noise must be as low as possible. That is why the data of the Venera-15 and 16 missions where the deep-space probes operated with higher transmitted power and at lower frequencies than in other missions were used for the feasibility study and proof of concept of a novel interpretation technique. The most intriguing result obtained with this data is that the investigation of fine structures of the Venusian ionosphere at extremely low altitudes of about 80-120 km above the planetary surface level where the concentration of electrons is still extremely low becomes possible.

Typical stratified periodical variations of signal power are presented in Fig. 1. They depend on the local refractive index and a part of them are supposedly the result of wave-like interactions between the atmosphere and ionosphere of Venus.

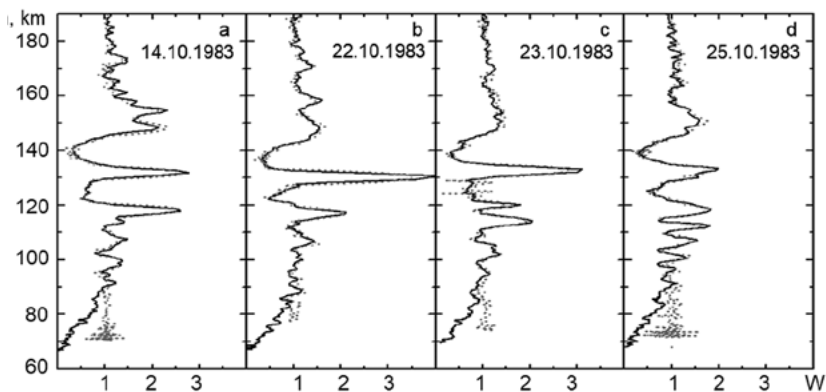


Fig. 1. Comparison of profiles of $W_0(h)$ – experimentally observed variations of signal power at 32 cm wavelength due to the refraction in the atmosphere and ionosphere at h – altitude above the surface level (solid line, arbitrary units) with $W_1(h)$ – a ‘prediction’ of signal power calculated on the basis of signal frequency.

The idea of the novel technique comes from a comparison of two diagrams with values of signal power (X-axis) along altitudes (Y-axis), while one of them stands for experimentally observed variations and fluctuations of signal power (W_0) in the atmosphere and ionosphere and the other stands for a ‘prediction’ of the same parameter (W_1) calculated on the basis of the adiabatic invariant. It must be emphasized that this kind of prediction applies to the ionosphere only, and so the difference allows us to investigate the upper atmosphere more precisely.

One can see a good match between diagrams within a range of altitudes from 90 km to 180 km. But fluctuations above 180 km bear a pure stochastic nature, which indicates that this interval of altitudes does not contain detectable layers with steady deviations of the refractive index.

As it follows from Fig. 1 the refractive attenuation of radio waves in the atmosphere rapidly increases below 80 km and there is no detectable ionized layer. It indicates that lower layers constantly exist not only in the Earth’s ionosphere, but also in the dayside ionosphere of Venus. A deeper investigation of the nature of such perturbations will be possible with higher potential of radio-lines. Apart from the decrease of frequency, the latter could be achieved by means of experiments with up-link occultation scheme.

Conclusions:

The approach proposed can be seen as one of the possible ways of the occultation technique development. In case of using an up-link scheme of an occultation experiment, it will allow us to study a fine structure of the interaction between the atmosphere and ionosphere using variations in the power and frequency of two coherent radio waves. As a result, new findings of the propagation of density perturbations from the atmosphere into the ionosphere could be revealed very likely, including the propagation of wave-type atmospheric perturbations.

The work is partially supported by the RAS Presidium Program № 28.

References:

- [1] A.L. Gavrik, Yu.A. Gavrik, T.F. Kopnina, E.A. Kuleshov. Oscillations Detected near the Lower Boundary of the Venus Ionosphere from the Radio Occultation Measurements of the Venera-15 and Venera-16 Satellites // *Journal of Communications Technology and Electronics*. 2013. V. 58. No. 10. P. 985–995.
- [2] G. Fjeldbo, A.J. Kliore, R. Eshleman. The Neutral Atmosphere of Venus as Studied with the Mariner V Radio Occultation Experiments // *Astronomical journal*. 1971. V. 76. No. 2. P. 123-140.
- [3] N.A. Armand, et al. Results of solar wind and planetary ionosphere research using radiophysical methods // *Physics-Uspekhi*. 2010. V. 53. № 5. P. 517-523.
- [4] J.-C. Gérard et. al. Aeronomy of the Venus Upper Atmosphere // *Space Sci. Rev*. 2017. V. 212: P. 1617–1683.

ULTRAVIOLET SPECTROGRAPH FOR EXOPLANETS (UVSPEX) ONBOARD WORLD SPACE OBSERVATORY ULTRAVIOLET (WSO-UV)

S. Kameda¹, A. Tavrov², N. Osada¹, G. Murakami³, K. Enya³,
T. Kodama⁴, N. Narita⁴, M. Ikoma⁴, O. Korablev², M. Sachkov⁵

¹Rikkyo University, Japan, kameda@rikkyo.ac.jp;

²Space Research Institute of RAS, Russia;

³ISAS/JAXA, Japan;

⁴The University of Tokyo, Japan;

⁵INASAN, Russia

Keywords:

exoplanet, exosphere, oxygen, ultraviolet, space telescope

Introduction:

Many Earth-sized planets have been discovered and some appear to lie in the habitable zone. Moreover, several Earth-sized planets were recently detected around low temperature stars near the solar system. However, it is difficult to characterize them as Earth-like or Venus-like. Transit spectroscopy for exoplanetary atmosphere has been performed to characterize larger exoplanets but it requires very high accuracy because of their small size. Hydrogen exosphere has been detected around Neptune-sized exoplanet [1], but an Earth-sized exoplanetary exosphere has not been detected. Recently, Earth's hydrogen exosphere was re-investigated and it was revealed that the Earth's exosphere is extended to ~ 38 Earth radii [2]. On the other hand, Venus' and Mars' hydrogen exosphere is not so much extended because of its low temperature of upper atmosphere. This is caused by the difference of mixing ratio of CO_2 in the upper atmosphere. Venus and Mars have CO_2 -rich atmospheres with a lower exospheric temperature. On Earth, CO_2 was removed from its atmosphere by a carbon cycle with its ocean and tectonics [3]. Translating these arguments to exoplanets in a habitable zone presents a possible marker to distinguish an Earth-like planet from a Mars-like or Venus-like planet. The expanded exospheres can be observed in UV, during the exoplanet transit event in a primary eclipse. It reduces the stellar flux, when an exoplanet orbiting in front of the host star.

Instrumentation:

High sensitivity (photon counting) is required for M-type star faint in UV. Spectral resolution of 0.5 nm is enough for separating major emission lines of exospheric atoms. The spectral resolution will be achievable by spectrometers in the main WUVS block, however, it is difficult to measure the weak flux from M-type stars without a photon-counting detector. To realize exoplanet transit observations in oxygen spectral lines with the desired accuracy, we equip the WSO-UV telescope with the UVSPEX spectrograph. The main engineering requirements for the UVSPEX are following. The spectral resolution is better 0.5 nm to separate O I line from other spectral lines. The spectral range is to exceed the wavelengths from 115 nm to 135 nm to detect at least H Lyman alpha 121.6 nm to O I 130 nm. The throughput is better 0.3% accounting more than four terrestrial exoplanets distanced at 5 pc. To achieve these requirements, a simple spectrograph design is proposed, containing the slit, the concave (toroidal) grating as a disperse element and the imaging photo-detector. This optical concept is conventional and used in the other space missions for UV spectroscopy.

Spectrometer slit is aligned at primary focus of the telescope from off-axial sub-FoV. Slit width is 0.2 mm, corresponding to 5 arc-sec. The concave grating is laminar type with groove density of 2400 grooves per mm. It has a toroidal shape with the curvature radii of 266.4 mm in horizontal direction and of 253.0 mm in vertical direction. The effective area has nearly \varnothing 25 mm and the focal length is ~ 250 mm. The surface is coated by Al + MgF2 to increase the reflectance, and diffraction efficiency of $\sim 29\%$ can be achieved.

References:

- [1] Ehrenreich, D. et al., A giant comet-like cloud of hydrogen escaping the warm Neptune-mass exoplanet GJ436b // *Nature* 522, 459-461, 2015.
- [2] Kameda, S. et al., Ecliptic North-South Symmetry of Hydrogen Geocorona // *Geophysical Research Letters* 44, 11,706-11,712, 2017.
- [3] Abbot, D. S., Cowan, N. B. & Ciesla, F. J., Indication of insensitivity of planetary weathering behavior and habitable zone to surface land fraction, *Ap. J.* 756:178(13pp), 2012

ATMOSPHERIC MASS LOSS OF CLOSE-IN EXOPLANETS IRRADIATED BY STELLAR SUPERFLARES

V.I. Shematovich¹, D.V. Bisikalo¹, A.A. Cherenkov¹, L. Fossati², C. Möstl²

¹*Institute of Astronomy of the Russian Academy of Sciences, Moscow, Russia, shematov@inasan.ru*

²*Space Research Institute, Austrian Academy of Sciences, Graz, Austria*

Keywords:

Hot Jupiters and Neptunes, sporadic stellar activity, atmospheric mass loss, aeronomic model.

Introduction:

Hot-Jupiters and -Neptunes are exoplanets with masses and radii close to the parameters of Jupiter and Neptune in the Solar System, but with much higher thermospheric temperatures, up to 10^4 K. High thermospheric temperature is caused by absorption of the high-energy stellar flux, which is very strong for close-in planets [1].

An important area of exoplanets research is the study of the influence of extreme stellar activity (flares, coronal mass ejections) on the evolution of the atmospheres of hot-Jupiters, -Neptunes, super- and exo-Earths, in particular, evaluating the mass loss from their atmospheres due to sporadic stellar phenomena. Analyses conducted on the basis of Kepler observations allowed to detect of 187 superflares on 23 solar-type stars whose bolometric energy ranges between 10^{32} and 10^{36} ergs [2]. It is evident that in the case of a stellar superflare, the exoplanet atmosphere reacts on the extra absorption of extreme-UV radiation and the consequent heating of atmospheric gas causes a change of the dynamic state of the atmosphere. Recently developed one-dimensional aeronomic model of the upper atmosphere of hot-Jupiters and -Neptunes [3] allows us to take into account these impacts of stellar flares on the state of the atmosphere. This model is self-consistent and takes into account both heating of the atmospheric gas due to absorption of stellar radiation in the soft X-ray and extreme ultraviolet bands by the hydrogen-dominated upper atmosphere and reactions involving suprathermal photoelectrons. The model allows to compute the hydrodynamic distribution of density, velocity, and temperature in giant planets atmospheres.

Results of calculations of the dynamic response of the atmosphere of the planet HD 209458b to the impact of the host star superflare are presented in this report. It is shown that the absorption of the additional energy of the stellar flare in the extreme ultraviolet leads to a substantial local heating of the atmosphere. One of the consequences of this is the formation of two shock waves, propagating in the atmosphere of the planet [4]. The possible observational manifestations of the shock waves and feasibility of their detection both in the luminosity of the atmosphere of the exoplanet in the Ly- α line profile and in the total energy fluxes in this line from the atmosphere of the exoplanet and of the host star are discussed. An additional loss of matter from the atmosphere due to its dynamic response to the stellar flare is estimated.

Acknowledgements:

This work is supported by the Russian Science Foundation (project No. 18-12-0447).

References:

- [1] Yelle, R. // *Icarus*. 2004. V.170. P. 167-179.
- [2] Maehara H., et al. // *Earth, Planets & Space*. 2015. V. 67. P. id.59 (10 pp.).
- [3] Ionov, D.E., et al. // *Astron. Reports*. 2017. V. 61. P. 387-392.
- [4] Bisikalo D.V., et al. // *Astron. Reports*. 2018. V. 62 (in press).

THEORETICAL SPECTRA OF HIGHLY-IRRADIATED ATMOSPHERES OF TRANSITING EXOPLANETS

M. Ikoma¹, Y. Ito^{1,2}, Y. Kawashima^{1,3}, N. Osada⁴, S. Kameda⁴

¹The University of Tokyo, Bunkyo-ku, Tokyo, 113-0033, Japan, ikoma@eps.s.u-tokyo.ac.jp;

²Hokkaido University, Sapporo, Hokkaido, 060-0808, Japan;

³Tokyo Institute of Technology, Meguro-ku, Tokyo, 152-8550, Japan;

⁴Rikkyo University, Toshima-ku Tokyo, 171-8501, Japan

Keywords:

exoplanet, atmosphere, UV

Introduction:

Diversity in measured mean density of transiting exoplanets indicates that close-in exoplanets have atmospheres of different compositions. Transiting planets, which are orbiting close to their host stars, are highly irradiated with stellar UV and visible light. Thus, they could have different properties from those of the planets in the solar system. Among highly irradiated planets, of special interest are volatile-free, molten rocky super-Earths (i.e., magma-ocean planets), volatile-rich super-Earths, and Earth-like water-ocean planets. Here we aim to evaluate the detectability of such exoplanet atmospheres with near-future space-based telescopes.

Methods:

We have developed 1D atmospheric models that include detailed photochemistry, radiative transfer and hydrodynamics for magma-ocean super-Earths and cloud/haze-particle microphysics for volatile-rich super-Earths. From the calculated atmospheric properties, we have generated theoretical spectra that would be observed when the planet passes in front of (primary transit) or behind (secondary eclipse) its host star.

Results and conclusion:

The magma-ocean planet has an atmosphere composed mainly of Na and SiO. Both absorb incident stellar UV and visible light efficiently, which brings about thermal inversion in the atmosphere. Such an atmosphere shows distinct emission features in the infra-red during secondary eclipse [1]. Since volatile-rich super-Earths usually have reducing atmospheres, high UV irradiation leads to photochemical production of organic haze in their atmospheres. Depending on irradiation level, such atmospheres contain haze layers with different particle sizes and densities at different altitudes. This suggests that diverse transmission spectra are observed for volatile-rich super-Earths during primary transit [2]. High UV irradiation also results in hot upper atmospheres, which causes the atmosphere to expand and eventually escape. Hydrogen and oxygen in such expanded atmospheres of Earth-like ocean planets absorb substantial fractions of stellar UV during primary transit [3]. Those absorption and emission features are detectable via near-future space-based observation with JWST, WSO-UV and ARIEL.

References:

- [1] Ito, Y., Ikoma, M., Kawahara, H., et al. Theoretical emission spectra of atmospheres of hot rocky super-Earths // *ApJ* 2015, 801, 144.
- [2] Kawashima, Y., Ikoma, M. Theoretical transmission spectra of exoplanet atmospheres with hydrocarbon haze: Effect of creation, growth, and settling of haze particles. I. Model description and first results // *ApJ* 2018, 853, 7.
- [3] Alexander T., Kameda, S., Yudaev, A. et al. Stellar imaging coronagraph and exoplanet coronal spectrometer - two additional instruments for exoplanet exploration onboard the WSO-UV 1.7 meter orbital telescope // *JATIS*, submitted

THE THRESHOLD OF THE RUNAWAY GREENHOUSE EFFECT FOR EARTH-LIKE PLANETS

T. Kodama¹, H. Genda², R. O'ishi¹, A. Abe-Ouchi¹, Y. Abe^{3,4}

¹*Center for Earth Surface System Dynamics, Atmosphere and Ocean Research Institute, University of Tokyo koda@aori.u-tokyo.ac.jp;*

²*Earth-Life Science Institute, Tokyo Institute of Technology;*

³*Department of Earth and Planetary Science, University of Tokyo;*

⁴*Deceased*

Keywords:

Habitable planets, Exoplanets, Climate, Habitable zone, Runaway greenhouse effect.

The habitability of extrasolar planets has been actively discussed. Liquid water is thought to be necessary for the emergence and evolution of life on the planetary surface. It is typical to assume that habitable planets, like the Earth, have liquid water on the planetary surface. The habitable zone has been defined as the region around the central star where liquid water is stable on the planetary surface [1, 2]. Planets with liquid water on their surface are classified into two modes: the aqua planet mode and the land planet mode. An aqua planet is a planet covered with ocean globally. On a land planet, the distribution of surface water is controlled by the atmospheric circulation, thus, water accumulates in the cool region of the planet [3]. Liquid water vaporizes entirely when planets receive insolation above a certain critical value, which called the runaway greenhouse state [4, 5]. This threshold forms the inner most limit of the habitable zone. Because of the difference in the water distribution, a land planet can maintain liquid water at much larger insolation than an aqua planet.

We focus on the distribution of surface water on the planetary surface and investigate the inner edge of the habitable zone using three-dimensional climate model (the general circulation model: GCM). As a result, we recognized two climate regimes: the aqua planet regime and the land planet regime. We showed that each regime is controlled by the atmospheric circulation, especially the Hadley circulation. We found that the inner edge of the habitable zone varies continuously with the water distribution on the planetary surface from 130% (an aqua planet) to 180% (the extreme case of a land planet) of the insolation of the present Earth's orbit. Our results indicate that the inner edge of the habitable zone is not a single sharp boundary, but a border whose location varies depending on the surface water distribution.

References:

- [1] Kasting J.F., Whitmire D.P., and Reynolds R.T., Habitable zones around main sequence stars // *Icarus*, 1993, 101, 108-128.
- [2] Kopparapu R. K., Ramirez R., Kasting J. F., Eymet V., Robinson T. D., Mahadevan, S., et al., Habitable zones around main-sequence stars // *New estimates. The Astrophysical Journal*, 2013, 765, 2.
- [3] Abe Y., Abe-Ouchi A., Sleep N. H., and Zahnle K. J.. Habitable zone limits for dry planets // *Astrobiology*, 2011, 11(5), 443-460.
- [4] Nakajima S., Hayashi Y.-Y., and Abe Y.. A study on the runaway greenhouse effect with one-dimensional radiative-convective equilibrium model // *Journal of the Atmospheric Sciences*, 1992, 49(23), 2256-2266.
- [5] Leconte J., Francois F., Charnay B., Wordsworth R., and Pottier A., Increased insolation threshold for runaway greenhouse processes on Earth-like planets // *Nature*, 2013, 504, 268-271.

A NEW NUMERICAL INVERSION SCHEME OF $m \sin i$ EXOPLANET MASS DISTRIBUTION: THE NEPTUNE-SATURN DESERT REMAINS AFTER INVERSION

J.L. Bertaux^{1,2}, K. Gizatullin^{1,3}, A. Tavrov¹, V.I. Ananieva¹

¹IKI, Space Research Institute, Moscow, Russia

²LATMOS, Université de Versailles Saint-Quentin, 11 Boulevard d'Alembert, 78280 Guyancourt France

³Moscow Institute of Physics and Technology, Institutsky lane 9, Dolgoprudny, Moscow region, 141700

Keywords:

exo-planets, mass distribution, inversion of $m \sin i$, rocky planets, gaseous giants.

The use of radial velocity (RV) measurements of stars has proven very successful at the indirect detection of planets orbiting other stars, since both the planet (unseen) and the star are orbiting around their common center of mass. Unfortunately the mass m of the exo-planet cannot be retrieved: only the product $m \sin i$ is derived from the amplitude of the RV wobble, where i is the inclination of the polar axis of the orbit on the line of sight (LOS) from the observer to the star.

However, when a reasonable number of exo-planets are detected, giving an observed distribution of $m \sin i$ it is possible to retrieve the distribution function of planetary masses $f(m)$ that will give the observed distribution $f_o(m \sin i)$. One has to make the assumption that the orientations of orbital polar axis are isotropically distributed in space, and independent of the distribution $f(m)$.

We have developed a new representation of exo-planets in a 3D space, and established a formally exact solution to the inversion problem, based on spheres and cylinders.

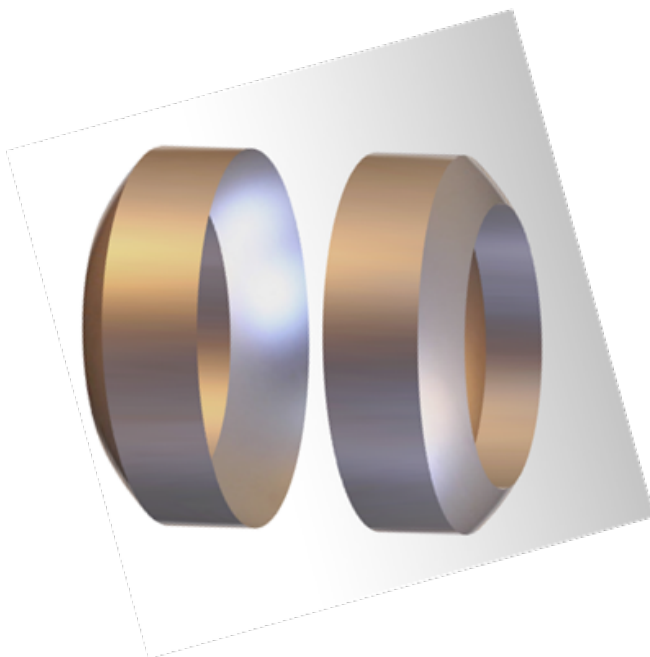


Fig. 1. For the inversion, the elementary volume comprised between two spheres and two cylinders must be computed. It has the shape of a double ring.

We have applied this method to the more than 700 known exo-planets masses. The observed distribution of $m \sin i$ shows two peaks, one around

0.025 M_{jup} (Jupiter mass) and one around 2 M_{jup} . After inversion, the true distribution of masses still present a double peak, showing that this double peak is not an artefact or shortcoming of the RV method. In fact, the first peak is due to a strong bias for non-detection of small-mass planets. The distribution is rather characterized by a trough between the two observed peaks that might be called a “desert” limited by Neptune-Uranus on the low-mass side, and Saturn on the high-mass side.

Our new inversion scheme will be presented and the desert discussed, and compared to theoretical predictions of Mordasini [1]. Other features of the observed distribution will be discussed toward low-mass planets.

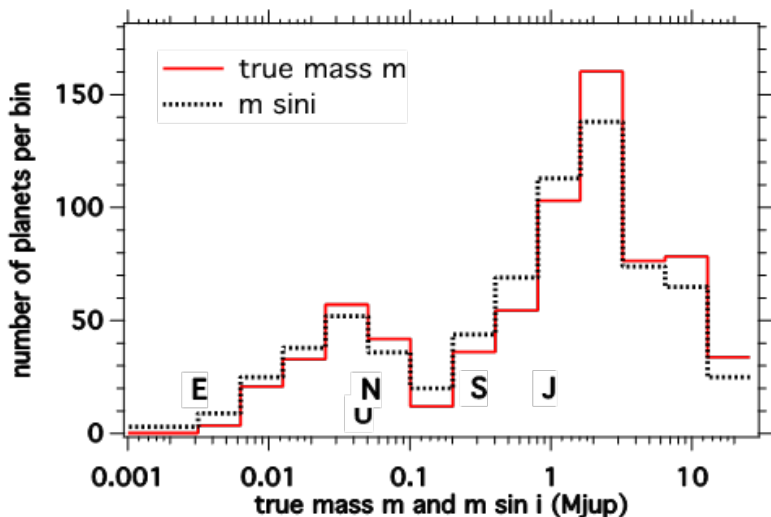


Fig. 2. Distribution of 711 exoplanets for which $m \sin i$ is known, with a geometric progression of the bin size =factor 2. The dotted line is the original $m \sin i$ distribution determined from RV method. The red line is the result of the true mass distribution $f(m)$ determined from our new inversion scheme. The “desert” of planets is still there, with perhaps a reinforcement of the trough in the bin 0.1-0.2 M_{jup} .

References:

- [1] Mordasini C., Planetary Population Synthesis, 2018, invited review accepted for publication in the ‘Handbook of Exoplanets’, planet formation section, section editor: Ralph Pudritz, Springer reference works, Juan Antonio Belmonte and Hans Deeg, Eds

EXOPLANET MASS DISTRIBUTION CONSIDERING THE OBSERVATION SELECTION FACTORS

V. Ananyeva¹, I. Shashkova¹, A. Venkstern¹, and A. Tavrov¹

¹Space Research Institute of the Russian Academy of Sciences;
84/32 Profsoyuznaya Str, Moscow, Russia, 117997

Keywords:

Exoplanets, mass distribution, Kepler Space Telescope.

The problem to retrieve the mass distribution of exoplanets is important e.g. to verify the planet formation mechanisms and to determine the number of planets of various types in the Galaxy. To obtain a true distribution, it is critically important to take into account the factors of observational selection.

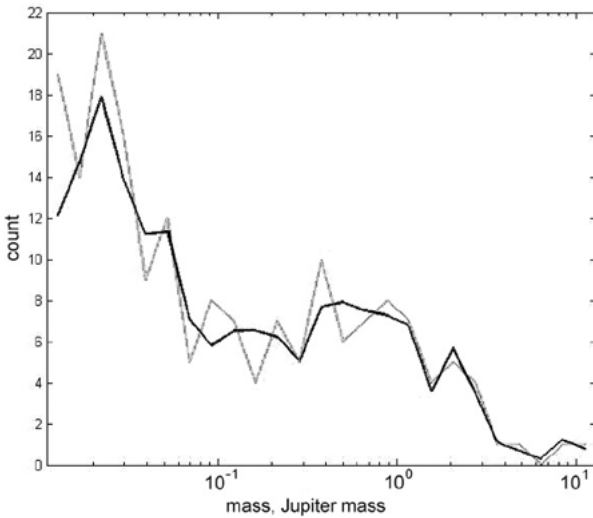


Fig. 1. Distribution by 25 mass intervals of Kepler planets (with the measured mass). Grey line shows not a smoothed distribution, black line is smoothed taking into account errors in the definition of masses.

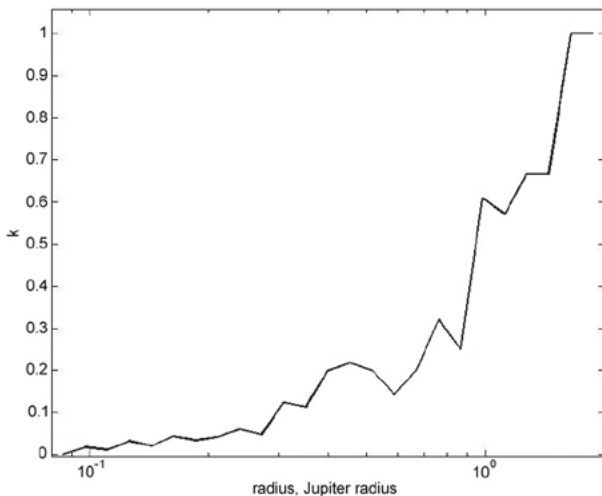


Fig. 2. The “mass measurement coefficient” k is the ratio of the number of Kepler planets with the measured mass to the total number of Kepler planets.

gnoring the observational selection leads to an overestimation of the income of massive planets and an underestimation of the low-massive planets.

To build a distribution of exoplanets by mass, we considered the transit exoplanets discovered by the Kepler Space Telescope. If a planet passes in front the disk of its parent star, i - the inclination of its orbit is known, and it is possible to determine its true mass m from $m \cdot \sin i$ by RV method. Kepler's location outside the earth's atmosphere and its highest accuracy of photometry allow detection of transit planets with radii of up to one Earth radius and even less. It is difficult to detect exoplanets with radii less than 5-6 Earth radii by ground-based transit surveys. 186 Kepler transit planets with a measured mass are known in the mass range from 0.011 to 13 Jupiter masses.

However, the distribution on Fig. 1 is strongly distorted by observational selection. For giants, the mass is easier to measure than for small planets e.g. neptune and super-earth. The proportion of Kepler's planets with a measured mass relative to the total number of Kepler planets is close to 1 in the region of giant planets and falls down to 2-3% in the region of 0.1-0.3 of the radius of Jupiter.

Therefore, for a given range of radii (a histogram bin) we introduced a "mass measurement coefficient" k to describe the ratio of the number of Kepler planets with the measured mass to the total number of Kepler planets.

We have considered each Kepler planet with the measured mass with a statistical weight inversely to k .

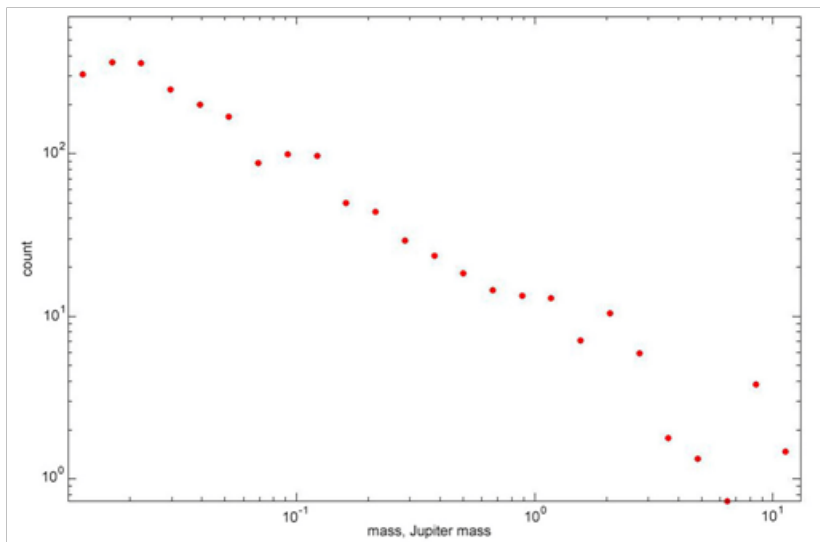


Fig. 3. Distribution of Kepler planets with measured mass taking into account observation selection factors corrected by k . The resulting distribution is well approximated by a power function with exponent -0.9 : $N \sim m^{-0.9}$.

DIFFERENT FACES OF THE MARTIAN MAGNETOSPHERE

E. Dubinin¹, M. Fraenz¹, M. Pätzold², O. Vaisberg³, L. Zelenyi³,
J. McFadden⁴, J. Halekas⁵, J. Connerney⁶, G. DiBraccio⁶

¹Max-Planck-Institute for Solar System Research, Justus-Von-Liebig
Weg, 3 37077 Göttingen, Germany, dubinin@mps.mpg.de,

²Rhenish Institute for Environmental Research, Germany,

³Institute of Space Research, Moscow, Russia,

⁴University of California, Berkeley, United States,

⁵University of Iowa, United States,

⁶NASA Goddard Space Flight Center, United States

Keywords:

Mars, magnetosphere, solar wind, IMF, comet

Introduction:

The interaction of solar wind with Mars starts at large distances from the planet because of the hydrogen atmosphere and the hot oxygen corona which extend many Martian radii. Signatures of such cometary-like interaction are picked-up protons and oxygen ions observed in the upstream solar wind. Charge exchange between incoming solar wind protons and planetary hydrogen also forms a beam of energetic neutral atoms which penetrate deep into the Martian atmosphere where they are partly converted back to energetic positively and negatively charged hydrogen. Because of the small size of Mars as compared to the gyroradius of the picked-up oxygen ions they are deflected toward the hemisphere in which the solar wind motional electric field is pointing away from the Mars. This ion motion provides an excess of transverse momentum in the system which must be balanced by the deflection of the solar wind protons in the opposite direction. All these effects were observed at Churyumov–Gerasimenko (CG) comet by the Rosetta spacecraft. Closer to the planet solar wind interacts with the Martian ionosphere forming the draped induced magnetosphere. The motional electric field also introduces a distinct asymmetry in the upper ionosphere. Such an asymmetry propagates to the night-side and the near plasma wake resembling the features observed at the artificial AMPTE comet. Draped interplanetary magnetic field (IMF) field lines in the wake shape the long tail on the night side with two lobes, the current and plasma sheets. Since the IMF continuously varies the magnetic tail rotates and to see its well-organized structure we need to use the MSE or the modified MSE coordinate system which follows the direction of the cross-flow component of the IMF. Structure of the magnetic tail also occurs very different in the hemispheres defined by the direction of the motional electric field. The existence of strong localized crustal magnetic fields on Mars introduces a lot of new features typical for the intrinsic magnetospheres, adding new classes of field lines—closed field lines and open lines with one end in the solar wind and another one in the collisional atmosphere. When rotating the spacecraft trajectories onto the MSE coordinates and making averaging the effects of the crustal magnetic field are smeared out and therefore to observe these new features we have to use a nonrotating MSO coordinate system. Then a new very interesting phenomenon of a twisting of the magnetic tail appears. The sign of this twist is determined by the orientation of the cross-flow component of the IMF. This result is typical for a combined magnetosphere with elements of the induced and intrinsic magnetospheres giving us a hint of the existence of a weak global magnetic field at Mars.

A MULTISCALE STRUCTURE OF THE CROSS-TAIL CURRENT SHEET AND ITS RELATION TO THE ION COMPOSITION ACCORDING TO MAVEN OBSERVATIONS IN THE MARTIAN MAGNETOTAIL

E. Grigorenko¹, S. Shuvalov¹, H. Malova^{2,1}, L. Zelenyi²

¹Space Research Institute of RAS, Profsoyuznaya str., 84/32, Moscow, 117997, Russia, elenagrigorenko2003@yandex.ru;

²Scobeltsyn Institute of Nuclear Physics, Moscow State University

Keywords:

Martian magnetotail, current sheet, quasi-adiabatic ion dynamics

Introduction:

Multilayered (embedding) Current Sheets (CS) are often observed in the Earth's magnetotail [1]. Simulations based on quasi-adiabatic dynamics of different ion components showed that the observed multiscale structures can be reconstructed by taking into account the net electric currents carried by ions with different masses and, thus, with different gyroradii [2]. The last determines the spatial scales of the corresponding current layers. The embedding can be quantitatively described by the ratio of the magnetic field value at the edges of a thin embedded layer B_1 to the value of the magnetic field outside the CS B_0 [1]. For the Earth's magnetotail it was shown that there is a relation between the B_1/B_0 and the relative densities of heavy and light ion components [2].

The embedding CSs in the Martian magnetotail:

In the Martian magnetotail the embedding feature is also often observed in the cross-tail CS formed by the draping of the IMF field lines [3]. The analysis of ~100 CS crossings by MAVEN spacecraft at $X_{\text{MSO}} < -1 R_M$ (R_M is a radius of Mars) showed that in the Martian magnetotail the relation between the embedding characteristics and ion composition is similar to the one observed in the terrestrial CSs, and the spatial scales of the embedded layers are defined by the gyroradii of the current carrying ion component. This finding confirms that the quasi-equilibrium CS state is supported by universal mechanisms based on general principles of plasma kinetic.

Acknowledgments:

Authors acknowledge the support of Russian Science Foundation (RSF grant Nr. 16-42-01103).

References:

- [1] Petrukovich, A., Artemyev, A., Malova, H., Popov, V., Nakamura, R., Zelenyi, L. Embedded current sheets in the Earth's magnetotail // J. Geophys. Res. 2011. V. 116. A00125. doi:10.1029/2010JA015749.
- [2] Zelenyi, L., Malova, H., Popov, V., Delcourt, D., Ganushkina, N., Sharma, S. "Matreshka" model of multilayered current sheet // Geophys. Res. Lett. 2006. V. 33. L05105. doi:10.1029/2005GL025117.
- [3] Grigorenko, E., Shuvalov, S., Malova, H., Dubinin, E., Popov, V., Zelenyi, L., Espley, J., McFadden. Imprints of quasi-adiabatic ion dynamics on the current sheet structures observed in the Martian magnetotail by MAVEN // J. Geophys. Res. 2017. V. 122. doi:10.1002/2017JA024216.

ANALYSIS OF MARTIAN MAGNETIC BARRIER

V.N. Ermakov¹, L.M. Zelenyi¹, O.L. Vaisberg¹, E.M. Dubinin²

¹*Space Research Institute of the Russian Academy of Sciences (IKI),
Moscow, Russia, vl.n.ermakov@gmail.com;*

²*Max-Planck-Institute for Solar System Research, 37077, Gottingen,
Germany*

Martian magnetic barrier is a thin layer in the magnetosheath, the magnetosphere and topside of the ionosphere, where magnetic pressure dominates other pressure contributes. Martian magnetic barrier originates from magnetic flux tubes of the solar wind during its deceleration due to interaction with the Martian magnetospheric obstacle, mass-loading by the planetary ions and depletion of the solar wind protons. MAVEN spacecraft equipped with instruments for plasma and magnetic field measurements with high temporal resolutions provided a possibility to study magnetic barrier properties.

Magnetic barrier structure and properties depend on the orientation of interplanetary magnetic field it was originated from, in particular, its component transverse to the solar wind flow velocity. We analyzed several months of MAVEN measurements in the northern hemisphere, where crustal field influence is negligible, and used coordinate system based on transverse component of magnetic field. It was shown that distribution of average magnetic field magnitude is asymmetric in this coordinate system, being about 1.5 times higher in the hemisphere with upward motional electric field than in the opposite one. We present an analysis of Martian magnetic barrier properties in the magnetic field aligned coordinate system.

DYNAMICS OF HOT FLOW ANOMALIES AT MARS

S.D. Shuvalov¹, V.O. Zorina², O.L. Vaisberg¹, K.I. Kim³

¹Space Research Institute of the Russian Academy of Sciences (IKI RAS),
shuvalovsergei@gmail.com;

²Moscow Institute of Physics and Technology (MIPT)

³Bauman Moscow State Technical University

Keywords:

hot flow anomaly, current sheet, bow shock, foreshock transient, Mars, solar wind
Hot Flow Anomaly (HFA) is a region in the vicinity of intersection region between interplanetary current sheet (CS) and the planetary bow shock (BS) which is characterized by high temperature and low number density in the core surrounded by relatively thin compression region with high temperature and density.

Being discovered in 1980th [1] HFAs have been quite well studied at Earth. The first probable observation of HFA at Mars was reported by [2] with the use of *Mars Global Surveyor* data. Unfortunately, the spacecraft lacked the ion spectrometer required for the uniquely interpretation of the event, so [2] were cautious in their conclusions regarding the occurrence of HFA at Mars. It was not until November 2014 that the NASA *Mars Atmosphere and Volatile Evolution* (MAVEN) spacecraft carrying comprehensive plasma instrumentation appeared on the Martian orbit and provided an opportunity to make a confident conclusion that this phenomenon indeed occurs on this planet which was reported by [3].

We present a statistical study of propagational characteristics of Hot Flow Anomalies at Mars based on 36 manually selected events registered by the NASA Mars Atmosphere and Volatile Evolution (MAVEN) spacecraft. Based on the amount of registered events we conclude that HFAs are common foreshock transients at Mars with occurrence rate of ~ 1 per day.

The propagation speed of structures was calculated as the speed of intersection line between the interplanetary current sheet and the bow shock. Being detected at solar-zenith angles of 36° - 88° , almost all of the HFAs presented in this study propagate in the anti-sunward direction (see fig. 1) which makes us hypothesize that they tend to form close to subsolar point.

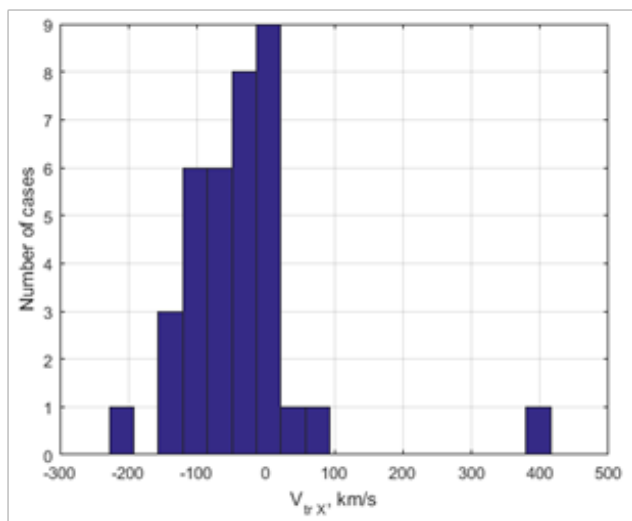


Fig. 1. Distribution of XMSO component of HFA's propagation speed

With the use of HFA's propagation speed and the assumption of their "birth" location we estimated the lifetime of each separate anomaly at the moment of its registration. No visible correlation between HFA's age and size was

found, which is consistent with the previous study proving that these structures can be either expanding, contracting or stable [4].

References:

- [1] Schwartz S.J., Chaloner C.P., Hall D.S., Christiansen P.J., Johnstones A.D., 1985. An active current sheet in the solar wind ISSN0028–0836. *Nature*318,269–271.
- [2] Øieroset, M., D. L. Mitchell, T. D. Phan, R. P. Lin, and M. H. Acuña, Hot diamagnetic cavities upstream of the Martian bow shock // *Geophys.Res.Lett.*, 2001, 28,887–890
- [3] Collinson, G., et al. , A hot flow anomaly at Mars // *Geophys. Res. Lett.*, 2015, 42, 9121–9127, doi:10.1002/2015GL065079
- [4] Xiao T. et al. Propagation characteristics of young hot flow anomalies near the bow shock: Cluster observations, *J. Geophys // Res. Space Physics*, 2015, 120, 4142–4154, doi:10.1002/2015JA021013.

AURORAE AT MARS: MODELING AND COMPARISON WITH OBSERVATIONS

V.I. Shematovich¹, D.V. Bisikalo¹, J.-C. Gérard², B. Hubert²

¹*Institute of Astronomy of the Russian Academy of Sciences, Moscow, Russia, shematov@inasan.ru*

²*Laboratoire de Physique Atmosphérique et Planétaire, STAR Institute, Université de Liège, Belgium*

Keywords:

Mars, solar wind, high-energy proton and hydrogen atom precipitation, auroral phenomena, atmospheric ultraviolet emissions, kinetic Monte Carlo model.

Introduction:

The magnetosphere of Mars is unlike any other in our Solar system, though it has aspects in common with many Solar system objects. Mars has no strong global magnetic field, which allows the solar wind to interact directly with its exosphere and upper atmosphere. However, it has crustal magnetic fields strong enough to perturb the solar wind interaction. Observations with the SPICAM and ASPERA-3 instruments on Mars Express [1,2] and the IUVS spectrograph on board the MAVEN spacecraft [3] have identified three types of aurorae on Mars, two of them (diffuse and proton aurorae) profoundly different from comparable types on Earth and other planets.

The kinetic modeling of different types - discrete, diffuse and proton, - of aurorae on Mars was done [4-6], as well as the comparison of calculations with measured data and observations by the ESA Mars Express and NASA's MAVEN spacecraft were provided [7,8]. It is necessary to mention that the observations by the NASA MAVEN spacecraft are unique, because both fluxes of electrons, protons and hydrogen atoms originated in the solar wind plasma, and induced by their precipitation aurora glows on Mars are measured and observed simultaneously. The using of data from in situ measurements of the solar-wind electron and ion analyzers aboard the NASA MAVEN spacecraft allowed us to calculate the degradation flux of the precipitating electrons and protons and to identify the main mechanisms of formation of the reflected (backscattered by the atmosphere) flux of protons and hydrogen atoms. For proton aurora on Mars such kinetic modeling was performed for the first time. These events appear as strongly correlated with solar wind activity and the population of penetrating solar wind protons in the daytime thermosphere previously identified by the Solar Wind Ion Analyzer (SWIA) on board MAVEN [9]. The interaction of proton and hydrogen atom precipitation into the Martian atmosphere was examined [4,6]. A kinetic Monte Carlo model including all major physical processes combined with in situ measurements [9] of the downward proton fluxes at the upper boundary of the modeled atmosphere was used. Results of the calculations were compared with the observations by the MAVEN/SWIA and IUVS instruments and conclusions about the importance of the backscattered component and the role of the induced magnetic field in the control of the proton aurora were drawn.

The forcing of high-energy electron and proton fluxes measured by the MAVEN/SWEA and MAVEN/SWIA instruments on the middle and lower atmosphere of Mars can be explored using the developed kinetic models. The comparison could be made with measured data by the instrument sets onboard of the MAVEN and ExoMars-TGO (Trace Gas Orbiter) spacecraft and the possibility of monitoring of the atmospheric composition changes caused by the precipitation processes using the ACS (Atmospheric Chemistry Suite) instrument onboard the ExoMars-TGO spacecraft could be estimated.

Acknowledgments:

This work is supported by the RFBR project 18-02-00721 and by the Basic Research Program of the Presidium of the Russian Academy of Sciences (Program No. 28).

References:

- [1] Bertaux, J.-L., et al. // *Nature*. 2005. V.435(7043). P. 790–794.
- [2] Ritter B., et al. // *Geophys. Res. Lett.* 2018. V.45. P. 612-619.
- [3] Schneider N., et al. // *Science*. 2015. V. 350(6261). P. id0313.
- [4] Shematovich V.I., et al. // *J. Geophys. Res.* 2011. V. 116. P. A11320.
- [5] Shematovich V.I., et al. // *Solar Syst. Res.* 2017. V. 52. P. 362-372.
- [6] Bisikalo D.V., et al. // *J. Geophys. Res.* 2018. V. 116 (in press).
- [7] Soret L., et al. // *Icarus*. 2016. V. 264. P. 398-406.
- [8] Bisikalo D.V., et al. // *Icarus*. 2017. V. 282. P. 127-135.
- [9] Halekas C., et al. // *Geophys. Res. Lett.* 2015. V. 42. P. 8901-8909.

SURFACE RELEASE PROCESSES TO POPULATE MERCURY'S EXOSPHERE

P. Wurz¹, D. Gamborino¹, A. Vorburger¹

¹Physics Institute, University of Bern, Sidlerstrasse 5, 3012 Bern, Switzerland, peter.wurz@space.unibe.ch

Keywords:

Mercury exosphere, release processes, magnetospheric plasma composition.

Introduction:

The exosphere of Mercury is mostly the result of external agents acting on the surface to cause release of particles from the surface into the exosphere [1]. The main factors are the illumination of the surface by the Sun causing evaporation of volatile species and photon-desorption of alkali metals. Moreover, the solar wind causes sputtering of regolith material promoting also refractory material into the exosphere. However, Mercury's magnetosphere limits the access of solar wind to the surface to localised regions. Finally, also the bombardment by micro-meteorites adds to the population of exospheric particles. The importance of each of these processes is variable, changing with the activity of the Sun, Mercury's position in its orbit, the longitude and latitude, and the intensity of the micro-meteorite flux.

Comparison between Observation and Modelling:

Measurements done by instruments on the MESSENGER spacecraft allow us to verify our models of Mercury's exosphere. Based on our exosphere calculations we can determine which release processes are responsible for the exosphere as seen in the MESSENGER observations.

An example is shown in Figure 1 where the transversal Na density profile from MASCS/UVVS on MESSENGER observations [2] is compared to the model calculations for the different release processes. The comparison shows that thermal desorption and micro-meteorite impact vaporisation are the main processes for the formation of the Na exosphere at this time.

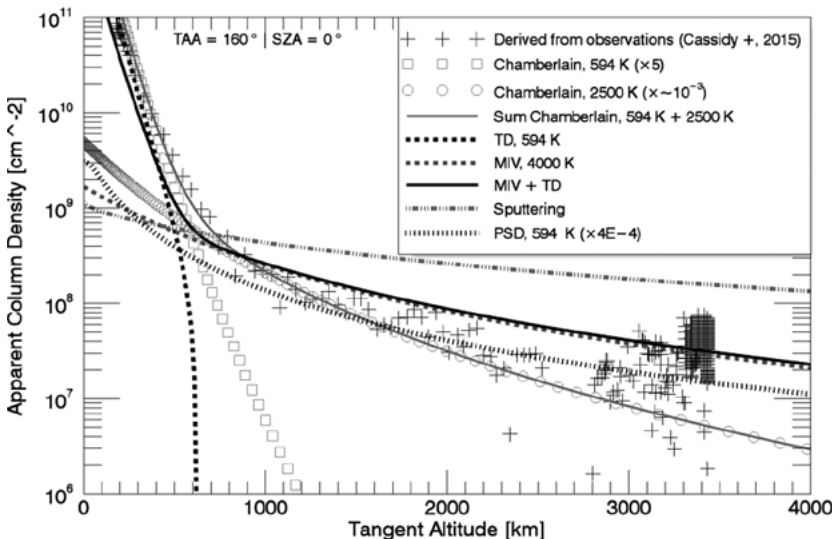


Fig. 1. Measured day-side altitude profile of Na transversal column density from MASCS/UVVS on MESSENGER (cross symbols), and comparison with model calculations (see legend).

Another example is shown in Figure 2 where the ion composition in Mercury's exosphere is compared to the model calculations. Exospheric densities are calculated for all release processes, and these species are subjected to photo-ionisation. Once ionised, these particles become part of the magnetospheric plasma population and are convected to the downwind side,

where they were observed by the FIPS instrument on MESSENGER during the first flyby [3]. Even though the contribution by sputtering to the exosphere is not that large [1], their ionisation is large because of the large scale heights of the sputtered exospheric particles. We find that sputtered refractory particles make a major contribution to the magnetospheric plasma composition of Mercury.

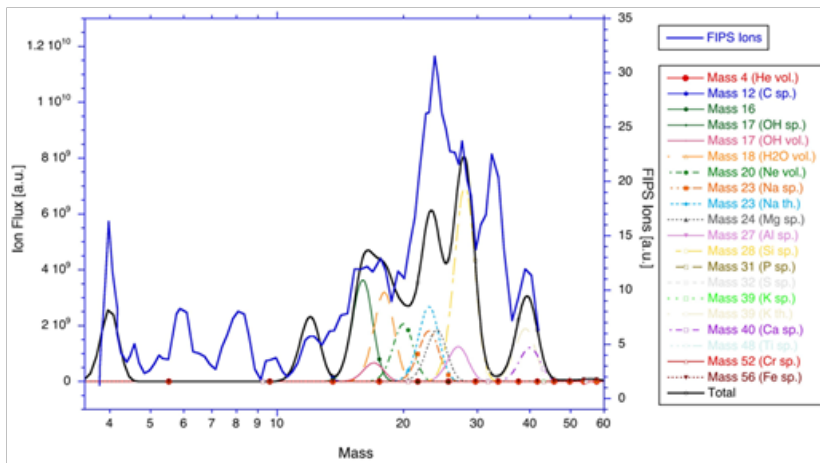


Fig. 2. Measured ion composition from FIPS on MESSENGER (blue solid line) and contribution from the different ion species from photo-ionisation of the exosphere.

Our calculations also allow to project to future measurements of the BepiColombo mission of ESA, which will launch in October 2018 and arrive at Mercury in 2024. The two BepiColombo spacecraft will go into Mercury orbit for at least one year. BepiColombo will have several instruments for remote sensing and for in situ measurements of the exosphere of Mercury allowing for its detailed investigation. Moreover, BepiColombo also has a complete set of particle and fields instruments to fully characterise the plasma environment, and its interaction with the Mercury's surface.

References:

- [1] Wurz, P., J.A. Whitby, U. Rohner, J.A. Martin-Fernandez, H. Lammer, and C. Kolb, Self-consistent modelling of Mercury's exosphere by sputtering, micro-meteorite impact and photon-stimulated desorption, *Planet Space Science*, 58, 1599–1616; Corrigendum: *Planetary and Space Science*, 58, 2051, 2010.
- [2] Cassidy, Timothy A.; Merkel, Aimee W.; Burger, Matthew H.; Sarantos, Menelaos; Killen, Rosemary M.; McClintock, William E.; Vervack, Ronald J.. Mercury's seasonal sodium exosphere: MESSENGER orbital observations. *Icarus*, 248, 547–559, 2015. DOI: 10.1016/j.icarus.2014.10.037.
- [3] Zurbuchen, T.H., J.M. Raines, G. Gloeckler, S.M. Krimigis, J.A. Slavin, P.L. Koehn, R.M. Killen, A.L. Sprague, R.L. McNutt Jr., and S.C. Solomon, MESSENGER Observations of the Composition of Mercury's Ionized Exosphere and Plasma Environment, *Science*, 321, 90–92, 2008.

MOTION OF DUST SUBJECT TO SOLAR WIND AND INTERPLANETARY MAGNETIC FIELDS

C. Lhotka¹, P. Bourdin¹, A. Celletti², C. Gales³, Y. Narita¹

¹Space Research Institute, Schmiedlstr. 6, 8042 Graz, Austria;

²Department of Mathematics, Via d. Ric. Sci. 1, 133 Rome, Italy;

³Department of Mathematics, Bd. Carol I, 11, 7000506 Iasi, Romania.

Keywords:

Dust dynamics, radiation pressure, solar wind, interplanetary magnetic field, Poynting-Robertson effect

Introduction:

Dust in space is subject to various non-gravitational forces. These include radiation pressure, the solar wind drag, and the so-called Poynting-Robertson effect. Additionally, dust in the solar system gets immediately charged due to solar radiation and the interaction with the solar wind. For this reason, dust also experiences the Lorentz force due to the presence of the interplanetary magnetic field (see [1] and references therein). The magnitude of all these forces strongly depend on the size, composition, and charge-to-mass ratios of the dust grains of interest. In our study we investigate the role of these parameters on the orbital stability of dust grains in two distinct scenarios : at the geostationary orbit in the vicinity of the Earth [2] and in the heliosphere [1]. In both cases, we provide suitable conditions for which the orbital stability of dust grains is modified by means of non-gravitational forces, e.g. due to the interaction with solar radiation, the solar wind or the presence of suitable charge-to-mass ratios. Our results are based on numerical simulations and analytical estimates based on averaging theory.

Outlook:

Temporary capture of micron-sized space debris at the geostationary resonance around the Earth may prolong the orbital life-time of dust in Earth-orbit up to several hundreds of years. However, orbital energy is removed by the Poynting-Robertson effect that will finally lead to escape from geostationary orbit. The relation between the drift rates in distance, i.e. semi-major axis, and the physical parameters of the dust grain and the solar wind have been derived in [2]. Solar wind drag and the Poynting-Robertson effect lead to a decrease in semi-major axis of dust grains in the heliosphere, which leads to typical orbital life-times of dust in the solar system of the order of several thousands of years. In [1] the importance of Lorentz force on estimates of the orbital life-times of dust was clearly demonstrated. It was shown, how the presence of specific charge-to-mass ratios may support or counteract the drift in semi-major axis under certain assumptions made on the interplanetary magnetic field.

The talk will review results of [1] and [2] and also provide new insights into the problem of charged dust dynamics in the solar system.

CL acknowledges support of the FWF project P30542.

References:

- [1] Lhotka C., Bourdin, P., Narita Y. Charged Dust Grain Dynamics Subject to Solar Wind, Poynting-Robertson Drag, and the Interplanetary Magnetic Field. *The Astrophysical Journal*, Volume 828, Issue 1, article id. 10, 10 pp., 2016.
- [2] Lhotka C., Gales, C. Celletti A. Poynting-Robertson drag and solar wind in the space debris problem. *Monthly Notices of the Royal Astronomical Society*, Volume 460, Issue 1, 21 July 2016, Pages 802–815, 2016

NUMERICAL SIMULATION OF THERMAL EVOLUTION OF THE COMET 67 P/CHURYUMOV-GERASIMENKO NUCLEUS

M.Ya. Marov, A.V. Rusol, V.A. Dorofeeva

Vernadsky Institute of Geochemistry and Analytical Chemistry RAS, Moscow

Keywords:

comet, nucleus, heat transfer, computer modeling, subsurface layers, insolation, thermal diffusion, evolution.

The results of computer modeling of heat transfer and thermal evolution of comet 67 P/Churyumov-Gerasimenko for the last 130 years corresponding to 20 revolutions in the contemporary heliocentric orbit are presented.

Comets represent extremely interesting objects among the solar system bodies. They are viewed as frozen debris left over from the time of solar system origin. Of great importance is the study of physical properties and chemical composition of these small bodies involving nucleus surface morphology and coma formation and evolution [1]. The great advancement in the study of comets brought space vehicles, specifically Rosetta mission.

The results of numerical simulation of the thermal evolution of the short period comet nucleus of comet 67 P/Churyumov-Gerasimenko in the past 130 years (20 revolutions around the Sun) on its current orbit are discussed. Basically, the goal is to assess how composition of a cometary coma obtained experimentally, depends on how long cometary nucleus resides the orbit and thus to compare the data derived with the results of computer modeling. To solve the task, the hybrid model was developed in which the boundary conditions were defined based on the 3D model of nucleus surface illumination earlier considered in detail by the authors in [2]. The problem of heat propagation in subsurface layers was solved in one-dimensional setting. Such an approach allowed us to find the most efficient rationale combining the virtues of 3D surface illumination model with economic one-dimensional computational scheme, and thereby avoiding requirements for large computing resources. When calculating insolation intensity both nucleus movement in orbit and its intrinsic rotation were taken into account. Heat transfer in subsurface layers of nucleus was described using one-dimensional heat conduction equation for porous stone-and-ice composition with a given dust to ice mass ratio [3,4]. This approach seems justified because heat diffusion in depth considerably less geometrical size of cometary nucleus. It was also assumed that thermophysical properties of cometary nuclei substance were independent on temperature.

Based on the model developed patterns of the temperature distribution in subsurface layer of the comet 67/P nucleus at several selected points of differing modes of insolation within 20 revolutions around the Sun were evaluated. The derived results can be summarized as follows:

1. Temperatures distribution at the inner deep layers number of revolutions around the Sun. It weekly depends on insolation and surface temperature and do not exhibit significant changes tending to a certain limit of asymptotic character. One may conclude that the temperature patterns at depth of the comet nucleus calculated for 20 revolutions keeps generally the same for much extended time.
2. For a short period comet, thermal energy is accumulated in the nucleus subsurface layer of about 10 m depth during prolonged time (at least ~ 100 years) with no quenching. Quasi stationary state of heat storage preserves at such a depth essentially throughout the whole time of comet residing its heliocentric orbit, in contrast to periodic temperature rise and relaxation in a thin surface layer of ~ 0.5 m depth strongly dependent on insolation and surface temperature.
3. As solar radiation progressively absorbed during subsequent nucleus revolutions around the Sun, the heat accumulates in deep layers

of the cometary nucleus giving rise to gradual rise in temperature approaching eventually some stable value at a certain depth, the latter depending on insolation and particular surface morphology and thermophysical properties of the composed matter. This type of thermal energy accumulation provides an opportunity for intensive production of gas/dust coma in the parts of cometary orbit after passing perihelion.

4. Positions of inner layers where sublimation temperature of major volatile components of coma is achieved were figure out. The temperatures are as follows: N₂ (t_{subl.} » 20 k), with (i.e.subl. » 25 k), 2 (i.e.subl. » 90 k) and H₂O (t_{subl.} » 140 k). This allows us to predict the composition of gas jets at different areas of nucleus in the post-perihelium parts of the cometary orbit.

Currently, the results of this study have no analogues in terms of the most detailed assessment of heat transfer in upper layers of nucleus with the account for proper insolation of particular surface elements depending on the comet position in orbit and diurnal variations [5-7]. Other models available mostly dealt with the heat distribution in comet nucleus only for one revolution around the Sun, with an exemption for simulation of thermal energy accumulation in spherically symmetric porous icy-stone body of a given thermal inertia of the matter for less than ten revolutions around the Sun.

Further development of the model is assumed twofold. Firstly, incorporation in the task the dependence of thermophysical properties of the porous icy-stone nucleus matter on temperature. In this more complicated scenario Stefan problem instead of the limited thermal conductivity approach is to be evaluated that requires significant increase in the computing resources. The challenge is to investigate the processes of heat transfer jointly with structural changes and phase transitions in the nucleus matter in the course of orbital/thermal evolution that would result in more accurate predictions about variations of chemical composition of the cometary coma. Secondly, because observational data on the nucleus morphology of 67/P comet are quite good, they are sufficient to build up detailed triangulation model of the surface and hence, different-scaled surface profiles. This will allow us to simulate in more detail some particular regions of interest on the nucleus surface and thus to improve estimates of changing in insolation

This work was performed with partial financial support of the Russian Foundation for basic research (project # 17-02-00319).

References:

- [1] Marov, M.Ya. Physical properties and models of comets. *Astronomicheskii Vestnik // Solar System Research*, 1994. Vol. 28, no. 4-5, p. 5.
- [2] Marov, M.Ya., Rusol A.V., Dorofeeva V.A. Three-dimensional model of insolation of a cometary nucleus // The case of the nucleus of comet 67 p/Churyumov-Gerasimenko, *Dokladi Russian Academy of Science*, 2017, volume 474, no. 1, p. 41-45.
- [3] Karpinos, D.M., Klimenko V.M. Porous materials and their thermal properties // *Znanie*, Kiev., 1978.
- [4] Cheremskoy et al., The pores in a solid body // *Energoatomizdat*, M., 1990.
- [5] Hu, X. et al., Thermal modelling of water activity in comet 67/P Churyumov-Gerasimenko with global dust mantle and plural dust-to-ice ratio // *Monthly Notices of the Royal Astronomical Society*, Volume 469, Issue 2, Suppl. p. S295-S311, 2017,
- [6] Guilbert-Lepoutre, A., Jewitt, D. // 2016,
- [7] Komle et al., Three-dimensional illumination and thermal model of the Abydos region on comet 67P Churyumov-Gerasimenko // *MNRAS* 469, S2-S19, 2017

D/H RATIO IN WATER ICE AND IN SOLID ORGANICS OF COMET 67P : IMPLICATIONS FOR THE FORMATION OF THE SOLAR SYSTEM

J.L. Bertaux^{1,2}, R. Lallement³

¹IKI/RAN, Laboratory for atmospheres of planets and exoplanets, Moscow, jean-loup.bertaux@latmos.ipsl.fr;

²LATMOS/CNRS/UVSQ/IPSL, Guyancourt, France;

³GEPi, Observatoire de Paris, Meudon, France

Keywords:

Deuterium, Hydrogen, water ice, comets, comet 67P, organic solid material,

Introduction

The D/H ratio in solar system bodies is considered as an important clue for the conditions of their formation. Here we will discuss mainly the D/H ratio in water vapor outgassed from comets [1][2] and in the solid organic material from comet 67P as reported recently [3].

Diversity of (D/H) ratio in cometary water

Figure 1 is a summary of measurements of cometary water ice D/H ratio ((D/H)_{H₂O} in the following) in various comets. We argue that this diversity means that interstellar water ice has not been incorporated directly in cometary nucleus under the form of ice, but is rather a signature of different physical local conditions at the birth place of each comet (10-30 AU), dictating the D/H ratio in water when condensing into ice (and never changed since).

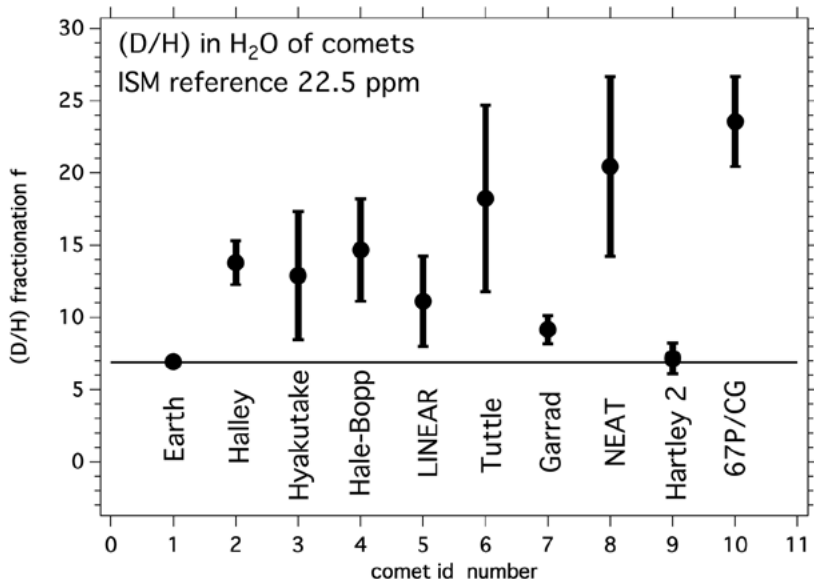


Fig. 1. The measured water (D/H) fractionation factor f in Earth oceans and in various comets w.r.t. the interstellar value as a function of approximate order of publication. The reference (D/H) ratio for the interstellar medium is taken as 22.5 ppm. A horizontal line is drawn at Earth's value ($f=7$). All values of D/H are taken from [1] except for 67P Churyumov-Gerasimenko which value is taken from [2].

The classical view and models (e.g., [4]) start with a highly D enriched water in the proto-solar nebula (factor $f \sim 30$ w.r.t. interstellar value in H_2 gas), inherited from very cold conditions of H_2O ice formation in the pre-solar nebula. Then (D/H)_{H₂O} decreases as a function of time and distance to sun, by isotopic exchange with H_2 (which has the interstellar value). However, this exchange is efficient only at high temperatures (> 500 K) prevailing near the sun, and requires a strong radial mixing of interplanetary material.

But new models [5] include other exchange mechanism through neutral-neutral reactions implying, O, H, D, H₂, HD, OH, OD...which are much more efficient than exchange with H₂. In such a case, the intensity of radial mixing used in previous models [4] is so intense that (D/H)_{H₂O} ratio comes back to the (D/H)_{H₂} interstellar value in a mere 10⁵ years [5], throughout the whole solar system, and new in falling material rich in (D/H)_{H₂O} has to be invoked to explain D-rich comets [5]. As an alternative, we suggested [6] that it is certainly possible to reduce very much the radial mixing to such a point where the effect of neutral-neutral reaction will simply decrease with distance the dilution of originally D-rich H₂O, and replacement by D-poor H₂O coming from the hot central solar region.

The (D/H) ratio in cometary organic material.

The solid material of the comet is made of about 45 % of organic material [6]. We have suggested last year [7] that this organic material is made of coagulated large organic molecules that are detected in the interstellar medium under the form of Diffuse Interstellar Bands (DIB) in absorption on stellar spectra. It was recently reported [3] that the D/H ratio in the comet dust organic part was 2-3 times higher than in water: this means a ratio $f \gg 50$. It would mean that the organic molecules responsible for DIBs are very rich in Deuterium, an important feature that carries a strong message about their formation process in the interstellar medium. This message has still to be fully deciphered. Some inferences will be discussed.

References:

- [1] Bockelée-Morvan D. et al., 2015, Space Sci. Rev 197: 47
- [2] Altwegg K. et al., 2015, Science, 347, A387
- [3] Paquette J.A. et al., Dusty Isotopes, 2018, Rosetta Science Workshop and SWT 49, Rhodes
- [4] Kavelaars J.J. et al. 2011, ApJ Letters, 734:L30
- [5] Yang L., Ciesla F. J., Alexander C. M. O'D., 2013, Icarus 226, 256–267
- [6] Bardyn, A., et al., Carbon-rich dust in comet 67P/Churyumov-Gerasimenko measured by COSIMA/Rosetta, MNRAS 469, S712–S722 (2017)
- [7] Bertaux, J.L., Lallement, R., Diffuse interstellar bands carriers and cometary organic material, MNRAS 469, S646–S660 (2017)

GAS PRODUCTION RATE: MYTHS AND ANALYSIS

Yu. Skorov^{1,2}, H. U. Keller¹, S. Mottola³, L. Rezac², P. Hartogh²

¹*Institute for Geophysics and Extraterrestrial Physics, TU Braunschweig, 38106 Braunschweig, Germany;*

²*Max-Planck Institute for Solar System Research, 37077 Gottingen, Germany;*

³*German Aerospace Center (DLR), Institute of Planetary Research, D 12489 Berlin, Germany*

Keywords:

Comet 67P/Churyumov-Gerasimenko, Space vehicles: Rosetta, Nucleus, Gas Production

Introduction:

In this work we address the nature of discrepancy between heliocentric water production rate estimated from Rosetta and thermophysical transfer models; in short, why does the observed heliocentric dependence differs so strongly from the modeled one. We analyze the models with a constant and uniform desiccated dust layer on top of the ice/dust matrix of the cometary nucleus. The influence of the porosity and heat conductivity including radiation, of the complex shape of the nucleus, and of its rotation are investigated.

Methods and results:

The gas production of comet is studied using numerical as well as analytical models accounting for the relevant microscopic/macrosopic processes. We rely on the thermophysical, compositional and geo-morphological data from the published measurements of respective instruments on board Rosetta.

We analyzed the role of the nucleus shape and its rotation, which is not typically known to such detail for other comets. However, our results pertain to this particular comet and it is not yet certain to which degree our findings can be generalized for other cometary nuclei. At the same time, for comet 67P, the exact data available make our analysis more accurate, and the conclusions more rigorous.

In addition to the role of shape and rotation, we examined the effect of several model assumptions, which are often used in cometary publications, in order to explain the observed accelerated growth of gas production as the comet approaches the perihelion. In particular, we examined the effects of incorporating into consideration: 1) porous surface dust layer, which changes possible channels for utilization of absorbed solar energy; 2) radiative heat conductivity, which can be many times greater than the contact thermal conductivity in the case of dust particles of large size; 3) factor of "ice area fraction", which also modifies the energy balance at the icy interface.

Summarizing the results, we conclude with certainty that the steep increase of the water production rate near perihelion of CG/67P cannot be explained by a two layer model with a constant porous dust cover over the dust/ice matrix. If the physical properties of the dust cover change with approach towards the perihelion, i. e. if the cover becomes thinner or more permeable, a fit to the steep slope of the water production near perihelion could be achieved. Alternatively, if the surface of the nucleus is not homogeneous consisting of regions with different activity levels it may be possible to reproduce the observed course of water production including the shift of its maximum by about 20 days after perihelion passage (Hansen:2016). Our calculations show that the activity level of the nucleus is not homogeneous or it is transient.

SLOW-EJECTED DUST PARTICLES FORMING A CRUST ON A COMETARY NUCLEUS

A. Kochergin^{1,2}, E. Zubko¹, S.I. Popel³, G. Videen⁴

¹*School of Natural Sciences, Far Eastern Federal University, 8 Sukhanova St., Vladivostok 690950, Russia*

²*Ussuriysk Astrophysical Observatory Far Eastern Branch Russian Academy of Science, 21 Solnechnaya St., Gornotayezhnoe 692533, Russia*

³*Space Research Institute of Russian Academy of Science, 84/32 Profsoyuznaya St, Moscow 117997, Russia*

⁴*Space Science Institute, 4750 Walnut Street, Suite 205, Boulder, CO 80301, USA*

Keywords:

Comets, nucleus, crust, gravity, solar-radiation pressure, dust particle, motion

Introduction:

Comets consist of a mixture of refractory materials (silicates, organics, amorphous carbon) and various ices (H₂O, CO, CO₂, N₂, etc). As a comet approaches the Sun, its surface is heated, and volatile species start subliming. Sublimation of ices expel refractory dust particles into a space, forming cometary coma. However, a dust particle lifted off the surface does not necessarily acquire a speed in excess of the escape velocity. Such a particle will resettle back onto the nucleus. In this work we model trajectories of such particles and investigate their transport over the nucleus surface and, their contribution to the formation of a crust refractory layer that may prevent other cometary ices from future heating and sublimation.

Model:

We model the motion of dust particles ejected from a cometary nucleus using an iterative time-domain approach. Such an approach makes it possible to account rigorously for all three forces acting on a small dust particle: gravity of the nucleus F_n , gravity of the Sun F_{Sun} , and the radiation pressure of the solar radiation F_{pr} . It is worth noting that F_{pr} is always directed against F_{Sun} . Their ratio is quantified with the parameter $\beta = F_{pr}/F_{Sun}$ [e.g., 1 and therein], which is a function of microphysical properties of dust particles and, simultaneously, it is independent of the solar distance. In this work we adapt the β parameter previously computed for irregularly shaped *agglomerated debris particles*; we refer the Reader to [2] for more details. We only emphasize that the agglomerated debris particles are capable of reproducing photometric and polarimetric observations of various comets [e.g., 2–4].

A dust particle that is located in a given place on the cometary surface (characterized with the position vector S_0) acquires an initial velocity V_0 at the initial time $t_0 = 0$. Such initial velocity can be attained from expanding cometary gases, for instance. At $t_0 = 0$, we calculate the resultant of all three forces acting on the dust particle. Note, we take into account if the particle is shadowed by the nucleus from the Sun or not. In the former case, we turn off the radiation-pressure effect. During the next increment of time Δt , the resultant force is assumed to remain constant, implying also a constant acceleration of the dust particle a_0 . This assumption significantly simplifies the numerical simulation of dust-particle motion during the increment Δt . In the end of this increment, we update all three forces and their resultant for the current location of the dust particle and repeat the entire procedure. Evidently, at $\Delta t \rightarrow 0$, the model trajectory converges to its exact profile. We experimentally examine different values of Δt and find that $\Delta t = 1$ s yields a very much converged trajectory of dust particles.

In this work we investigate a cometary nucleus of spherical shape that is representative of what was found *in situ* in Comets 9P/Tempel 1, 81P/Wild 2 [5]. In our model, however, the nucleus shape is not necessarily restricted

to a sphere; other, more complicated shapes could also be investigated. The bulk material density of the nucleus is taken to be 0.5 g/cm^3 , which also is consistent with *in situ* findings in comets (e.g., [6]). We set the radius of the nucleus to $R \approx 964.4 \text{ m}$ that yields an escape velocity of $V_e = 0.51 \text{ m/s}$. In this study, we assume no rotation of the nucleus.

Results and Discussion:

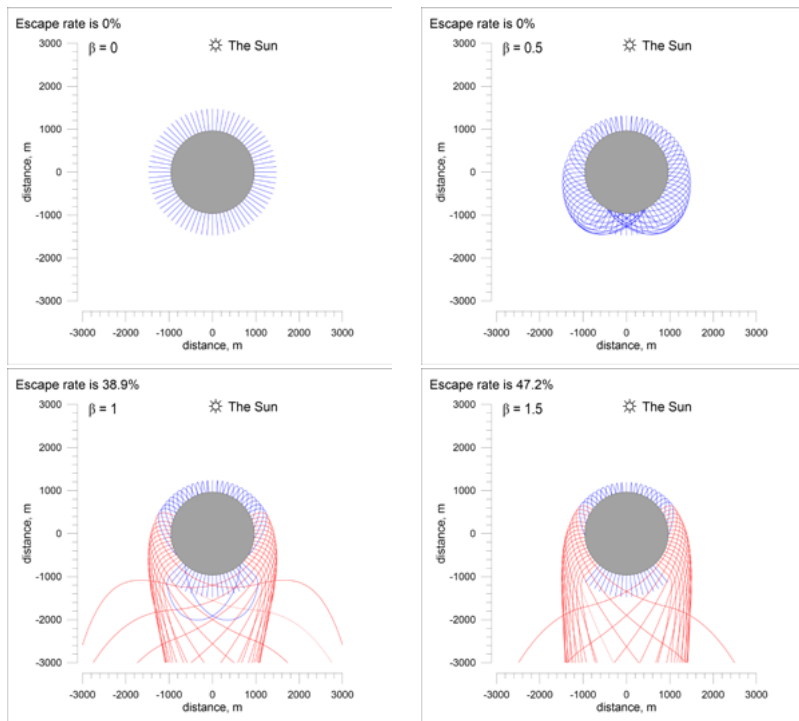


Fig.1 Trajectories of dust particles ejected with velocity of 0.3 m/s from the spherical nucleus located at a heliocentric distance of 10 au .

We consider dust particles at four values of the parameter $\beta = 0, 0.5, 1.0,$ and 1.5 . The first one represents the case of no radiation-pressure effect that is hardly applicable to real submicron and micron-sized dust particles. Nevertheless, this case helps to demonstrate the dramatic importance of the radiation pressure. We consider the radius of dust particles being $0.5 \mu\text{m}$, and $\beta = 0.5$ is representative of weakly absorbing Mg-rich silicate particles; whereas, $\beta = 1 - 1.5$ is compliant with highly absorbing organics and/or amorphous carbon [2]. **Fig.1.** Trajectories of dust particles ejected with velocity of 0.3 m/s from the spherical nucleus located at a heliocentric distance of 10 au .

At each β , we consider 72 places of ejection of dust particles, which are evenly distributed around a great circle of the spherical nucleus. The direction of ejection is oriented along the surface normal. We repeat our modeling at five ejection velocities $V_0 = 0.1 \text{ m/s}, 0.2 \text{ m/s}, 0.3, \text{ m/s}, 0.4 \text{ m/s}$ and 0.5 m/s ; which are less than the escape velocity. In Fig. 1, we demonstrate modeling results obtained at $V_0 = 0.3 \text{ m/s}$ in a comet located at the heliocentric distance of 10 au ; the Sun is located on top.

As one can see on the top-left panel in Fig. 1, at $\beta = 0$, dust particles only jump up to $\sim 510 \text{ m}$ and, then, fall down back exactly to their original location. At $\beta = 0.5$, the particles can get transported a significant angular distance, up to 20° for those ejected from the sunlit side of nucleus (upper half of the circle) and up to 60° for those ejected from the shadowed side (bottom half). Nevertheless, there are no particles escaping from the nucleus into surrounding space. This dramatically changes at $\beta = 1 - 1.5$ (bottom panels in Fig. 1). Here, one can see two types of trajectories, the blue ones correspond to particles returning onto the surface and the red ones to escaping

particles. The escape rate is 38.9% at $\beta = 1$ and 47.2% at $\beta = 1.5$. We stress that these particles escape from the nucleus due to the radiation pressure and despite the fact that their initial velocity is well below $V_e = 0.51$ m/s.

Another important conclusion that can be drawn from Fig. 1 is the evolution of the chemical composition of the surface. While all ejected particles having silicate composition ($\beta = 0.5$) return onto the surface, up to half of carbonaceous particles ($\beta = 1 - 1.5$) are lost. If the particles forming the uppermost layer on cometary nucleus (crust) experience a series of low-velocity ejections, this would quickly lead to depletion of the crust of organics and amorphous carbon. It is worth noting that the imaging polarimetry of various comets reveal a *circumnucleus halo* in the vicinity of their nucleus. Such a halo produces a very strong phenomenon of negative polarization at small phase angles that unambiguously reveals a lack of highly absorbing carbonaceous materials [4]. Thus, our current modeling appears in accordance with the observations of comets.

Finally, we note that at smaller heliocentric distances, 1 au, there is no significant difference in the escape rate over the range of the parameter $\beta = 0.5 - 1.5$. In all cases it is about 40% of the number of ejected particles. On the other hand, in the vicinity of the Sun, cometary ices sublime at much higher temperature and, as a consequence, the resulting gases expand very fast (~ 1 km/s). In such circumstances, slow ejection of dust particles should be a relatively rare phenomenon. This implies that a crust depleted of carbonaceous materials can be formed at long heliocentric distances by slowly ejected dust particles.

References:

- [1] Fulle M. in Comets II, eds. M. C. Festou, H. U. Keller, H. A. Weaver. University of Arizona Press, 2004. 565 p.
- [2] Zubko E., Videen G., Hines D., et al. Comet C/2012 S1 (ISON) coma composition at ~ 4 au from HST observations // Planet. Space Sci. 2015. V. 118, P. 138–163.
- [3] Zubko E., Videen G., Hines D., Shkuratov Yu. The positive-polarization of cometary comae // Planet. Space Sci. 2016. V. 123, P. 63–76. s
- [4] Zubko E., Muinonen K., Shkuratov Yu, Hadamcik E., Levasseur-Regourd A.-C., Videen G. Evaluating the carbon depletion found by the Stardust mission in Comet 81P/Wild 2 // Astron. Astroph. 2012. V. 544, id.L8.
- [5] A'Hearn M. F. Whence Comets? // Science. 2006. V. 314. P. 1708–1709.
- [6] Rickman H. The nucleus of Comet Halley – Surface structure, mean density, gas and dust production // Adv. Space Res. 1989. V. 9. No. 3. P. 59–71.

SOME DYNAMIC CHARACTERISTICS OF THE HALE-BOPP COMET NUCLEUS (BY 1997 OBSERVATIONS)

L.V. Ksanfomality

*Space Research Institute of the Russian Academy of Sciences,
leksanf@gmail.com*

The long-period comet Hale-Bopp C / 1995 O1, or the «Big Comet 1997», was discovered on July 23, 1995 and became the item of numerous observations in the period 1995-1999. It was one of the most watched comets of the XX century, and one of the brightest in the last few decades. Dimensions of the nucleus of the comet are the largest among the known comets (no less than 60 km). By the observations of 1995 it was found that the nucleus of the comet creates radial, slightly curved jets, which could be interpreted as an extremely slow rotation of the nucleus. However, later a typical parabolic coma structure appeared. The period of rotation of the nucleus was estimated as approximately 12 hours. Subsequent measurements gave slightly different results. Observations continued.

In May 1996 the comet Hale-Bopp became visible to the naked eye. Despite the fact that the increase in brightness then slowed somewhat, it was predicted that the comet would be one of the most bright. Because of the proximity of its perihelion to the Sun, in December 1996, observations were discontinued. It again began to be observed in January 1997. The comet was so bright that it could be seen even in the conditions of large cities. Coming closer to the Sun, the comet became brighter: in February it reached the 2nd stellar magnitude, and one could see its extra long tail. On March 23, 1997, the comet passed the minimum distance to the Earth: 1.315 AU. When perihelion passed (April 1, 1997), the comet had an average stellar magnitude of -0.7, and its tail covered 15-20 degrees in the sky. In new observations, the contradictions in estimating the period of rotation of the nucleus persisted. In 1997, a strange paper appeared: that the direction of rotation of the nucleus changed to the opposite. In subsequent observations, other unusual phenomena were recorded and detected, in particular, anti-tail, argon emissions and, presumably, the synthesis of organic substances. There were reports of signs of the double core of the Hale-Bopp comet.

The present report attempts to trace the unusual dynamics and evolution of the nucleus of the comet Hale - Bopp C / 1995 O1 on the basis of the published results of observations.

LINEAMENTS ON THE SURFACE OF CONSOLIDATED MATERIAL OF THE COMET 67P NUCLEUS

A.T. Basilevsky^{1,2}, Yu.V. Skorov^{2,4}, S.F. Hviid³, S.S. Krasilnikov^{1,2},
U. Mall², H.U. Keller⁴

¹Vernadsky Institute, RAN, Kosygin Str., 19, 119991 Moscow, Russia, atbas@geokhi.ru;

²Max-Planck Institute for Solar System Research, 37077 Gottingen, Germany;

³German Aerospace Center (DLR), Institute of Planetary Research, 12489 Berlin, Germany;

⁴Institute for Geophysics and Extraterrestrial Physics, TU Braunschweig, 38106 Braunschweig, Germany

Keywords:

Comet, nucleus, consolidated material, lineament, layer, fracture, spacing.

Introduction:

It has been done the morphologic analysis of lineaments seen on the surface of consolidated material in 18 areas of nucleus of 67P Churyumov-Gerasimenko comet studied by the Rosetta mission [1]. The nucleus is ~4 km across and has a bilobate shape with the lobes informally called Head and Body [2] (Figure 1). We studied images taken by the Osiris camera [3] and tried to select those showing surfaces of both Head and Body because the work [4] suggests that in early time these lobes could be two independent bodies later merged into one in their low-velocity collision. If so their characteristics, including surface textures could be different. However, absence of the difference, if found, does not reject this hypothesis. The areas were selected, first, based on the image availability, and second, trying to select those with view being maximum close to vertical. So in sense of the material nature this selection was rather random. We tried to cover the image resolution from the best available (0.04 m/px) to ~1 m/px showing the surface in a range of details. For analysis we used the 500 x 500 px image fragments. The Rosetta team distinguished on the surface of consolidated material lineaments being probably tension fractures and layer-like features [1]. In our analysis we concentrated on the study of fractures and only shortly mention the layer-like features.

Description and analysis:

The studied 500 x 500 px image fragments are shown in Figure 1. Within each fragment the lineaments have been distinguished, counted, and their apparent lengths were measured. It is seen in Figure 1 that in the first 14 images, which resolution is from 0.04 to 0.34 m/px (study areas are from 400 to 28900 m²) the lineaments look like fractures, and in the last 4 images, having resolution from 0.66 to 1.29 m/px (study areas are from 108900 to 416025 m²), both fracture-like and layer-like features are seen. Below are discussed characteristics of the fracture-like ones only. The latter ones are usually rectilinear, some are arcuate. The fracture-like lineaments are randomly intersecting although sometimes two and even one directions dominate.

Because the lineaments are intersecting to directly measure their spacing (the mean lineament to lineament distance) is not possible. So we calculated a kind of analog of spacing: counting amount of lineaments in the study area, then dividing the area value by the lineament amount and then taking square root from it. In a number of works the tension fracture spacing (S) was found to correlate with their depth of penetration (d) into the fractured material ($d \approx 1/3S$) [e.g., 5, 6].

We did not find any systematic differences in morphology of the fracture-like lineaments among all 18 study areas and in between lineaments of the Body and the Head. We measured the mean length of lineaments within each study area and found that the mean length correlate

with the study area value, which in our case depends with the image resolution (Figure 2(1)) and with the estimates of the depth of penetration of fractures into the nucleus material (Figure 2(2)).

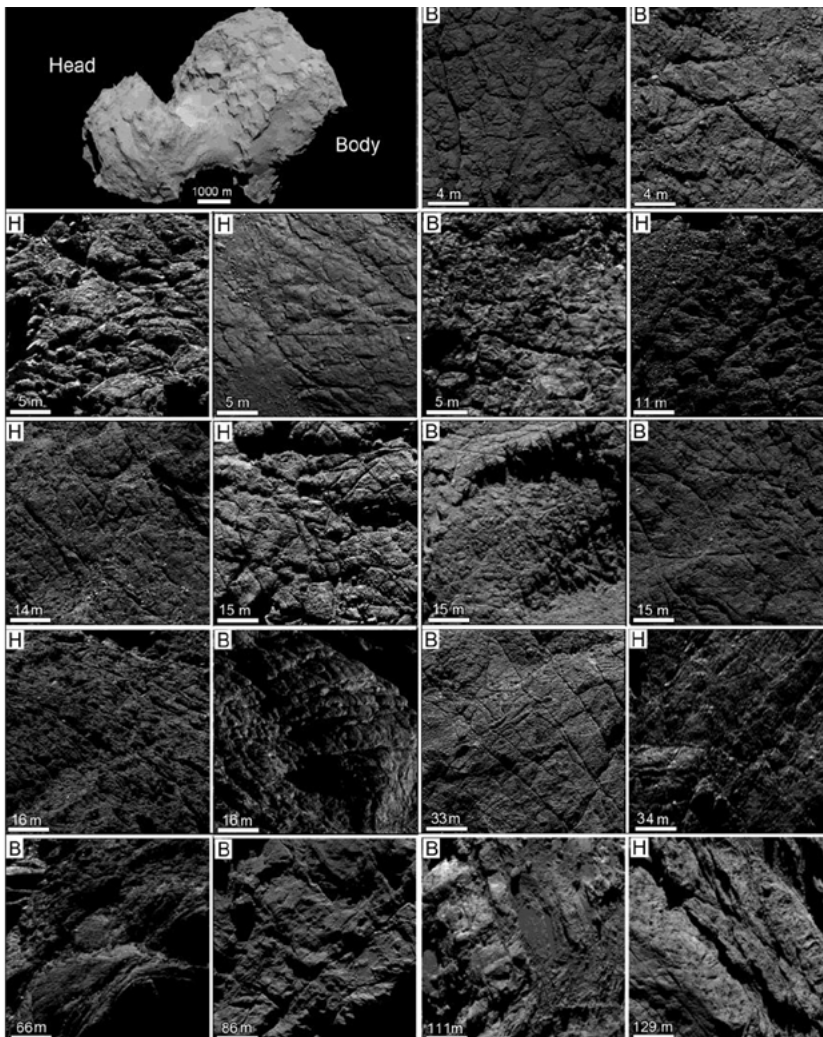


Fig. 1. The 500 x 500 px images of 18 sample areas on the nucleus Body (B) and Head (H). Upper left is the nucleus NavCam image ROS_CAM1_20140815T095218.

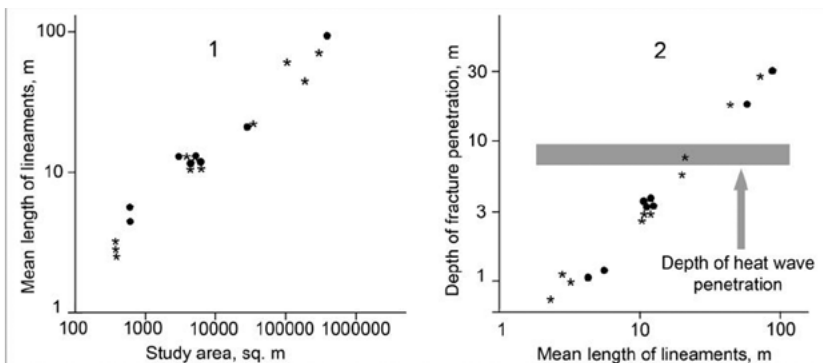


Fig. 2. 1 – Dependence of the mean lineament length on the study area; 2 – Dependence of the depth of fracture penetration on the mean length of lineaments. Black circles – lineaments of Head, stars – of Body.

It was found that in the sequence of images from the higher to lower resolution the amount of distinguished lineaments in the study areas does not systematically change probably because with the resolution decrease the smaller lineaments become to be not reliably visible, while the larger and more prominent ones continue to be visible. In the considered cases along with resolution decrease the observation area increases so the amount of the observed lineaments increases. This is obviously the observational effect. But on the other hand it means that the considered fractures represent a hierarchic population from the smaller (meters long) to larger (decameters and more) features. The considered fractures probably appeared due to diurnal and seasonal temperature changes, which according to [7] reach the several meters depth so only fractures whose depth of penetration was estimated to be smaller than ~10 m (Figure 2 (2)) were formed in this process while the larger and deeper penetrating ones could form due to different factor(s), e.g., in the mentioned low-velocity collision [4].

Acknowledgments:

This work was partly supported by Program I.28 of Presidium of Russian Academy of Sciences, theme 0137-2018-0038, and by Max-Planck Institute for Solar System Research (ATB and SSK) and by DFG grant SK 264/1-1 (Yu.V.S). Discussions with Boris Ivanov were very helpful.

References:

- [1] Taylor G. et al. The Rosetta mission orbiter science overview // *Phil. Trans. Royal. Soc.* 2017. A375: 20160262.
- [2] Sierks H. et al. On the nucleus structure and activity of comet 67P/Churyumov–Gerasimenko // *Science*. 2015. V. 347. No. 6220. P. aaa1044-1-5.
- [3] Keller H.U. et al. OSIRIS – the scientific camera system onboard Rosetta // *Space Science Reviews*, 2007. V. 128. P. 433–506.
- [4] Massironi M. et al. Two independent and primitive envelopes of the bilobate nucleus of comet 67P // *Nature*. 2015. V. 526. P. 402–405.
- [5] Gudmundsson A. Geometry, formation and development of tectonic fractures on the Reykjanes Peninsula, southwest Iceland // *Tectonophysics*, 1987. V. 139. P. 295-308.
- [6] El-Maarry M.R. et al. Potential desiccation cracks on Mars: A synthesis from modeling, analogue-field studies, and global observations // *Icarus*. 2014. V. 241. P. 248–268.
- [7] Skorov Yu.V., et al. A model of short-lived outbursts on the 67P/CG from fractured terrains // *Astronomy & Astrophysics*. 2016. V. 593. A76. P. 10.

SEMI-ANALYTICAL STUDY OF MEAN MOTION RESONANCES WITH APPLICATION TO DYNAMICS OF KUIPER BELT OBJECTS

S.S. Efimov¹, V. V. Sidorenko²

¹Moscow Institute of Physics and Technology, 9 Institutskiy per., 141701 Dolgoprudny, Russia, efimov.ss@phystech.edu;

²Keldysh Institute of Applied Mathematics, 4 Miusskaya sq., 125047 Moscow, Russia

Keywords:

Mean motion resonance, chaotic dynamics, perturbation theory, averaging method, Kuiper belt, plutinos, Kozai-Lidov resonance, trans-Neptunian objects.

Abstract:

We study secular effects in dynamics of minor bodies in mean motion resonance (MMR) within restricted three-body problem (R3BP). Using a system “star-planet-asteroid” MMR can be defined as orbital configuration in which asteroid completes $p+q$ rotations around the star in same amount of time the planet completes p rotations (p and q are integer numbers). Special attention is paid to *first order* MMR ($q = \pm 1$).

It is possible to construct an integrable model of dynamics in first order MMR using perturbation theory by taking into account only dominant term in perturbation [1]. Integrability, however, means the absence of chaotic dynamics found in numerical studies of these resonances [2-5]. This certainly calls for more sophisticated models.

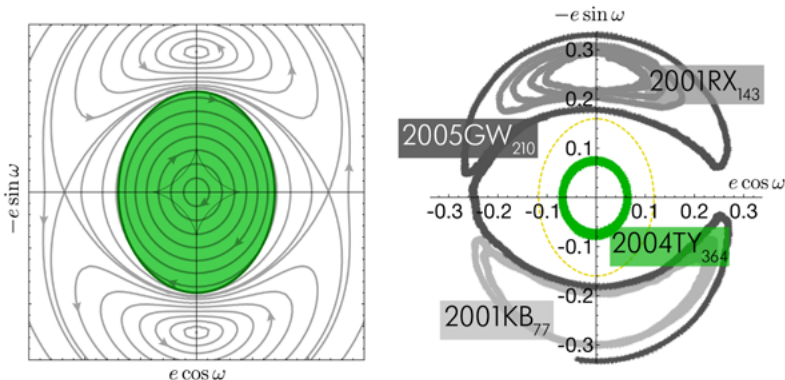


Fig. 1. Topological structure of model phase portrait vs KBO secular evolution

Adopting approach developed in [6] and preserving perturbation terms of higher order compared to [1], we construct an analytical model, which replicates well the general topological structure of secular variables phase space, including argument of periastris ω librations about 90° and 270° (Kozai-Lidov resonance). Figure 1 depicts a model phase portrait side by side with results of numerical integration based on orbital elements of several known plutinos (Kuiper belt objects in 2:3 MMR with Neptune). This model also allows to investigate some mechanisms of chaotization that have not received proper attention in the past. Particularly it reproduces such specific effects as intermittency in resonant angle behavior and chaotic change of secular evolution regimes.

To extend the range of model applicability past the limits of perturbation theory we utilize numerical methods in some intermediate calculations. The result is a semi-analytical model, which can be applied to describe the dynamics of objects with arbitrary values of eccentricity and inclination. At substantially large eccentricities the Kozai-Lidov cycles with oscillations of ω about 0° and 180° are found, which are consistent with trans-Neptunian objects' dynamics discussed in [7].

Acknowledgements:

This work was supported by the Presidium of the Russian Academy of Sciences (Program 28 "Space: investigations of the fundamental processes and their interrelationships").

References:

- [1] Sessin W. and Ferraz-Mello S. Motion of two planets with periods commensurable in the ratio 2:1. Solutions of the Hori auxiliary system // *Celestial Mechanics and Dynamical Astronomy*. 1984. V. 32. P. 307-332.
- [2] Giffen R. A Study of Commensurable Motion in the Asteroid Belt // *Astronomy and Astrophysics*. 1973. V. 23. P. 387-403.
- [3] Sussman G.J. and Wisdom J. Numerical evidence that the motion of Pluto is chaotic // *Bulletin of the American Astronomical Society*. 1988. V. 241. P. 433-437.
- [4] Winter O.C. and Murray C.D. Resonance and chaos. I. First-order interior resonances // *Astronomy and Astrophysics*. 1997. V. 319. P. 290-304.
- [5] Winter O.C. and Murray C.D. Resonance and chaos. II. Exterior resonances and asymmetric libration // *Astronomy and Astrophysics*. 1997. V. 328. P. 399-408.
- [6] Wisdom J. A perturbative treatment of motion near the 3/1 commensurability // *Icarus*. 1985. V. 63. P. 272-289.
- [7] Gallardo T., Hugo G., Pais P. Survey of Kozai dynamics beyond Neptune // *Icarus*. 2012. V. 220. P. 392-403.

CONFIRMATIONS OF ICE SUBLIMATION PROCESS NEAR PERIHELION ON PRIMITIVE MAIN-BELT ASTEROIDS 779 NINA, 704 INTERAMNIA AND 145 ADEONA: A SEARCH FOR COMMON REASONS

V.V. Busarev^{1,2}, M.P. Scherbina¹ S.I. Barabanov², T.R. Irsambetova¹, G.I. Kokhirova³, U.Kh. Khamroev³, I.M. Khamitov^{4,5}, I.F. Bikmaev^{5,6}, R.I. Gumerov^{5,6}, E.N. Irtuganov^{5,6}, S.S. Melnikov^{5,6}

¹*Sternberg State Astronomical Institute, Moscow Lomonosov State University (SAI MSU), 13 Universitetskij av., Moscow 119992, Russian Federation (RF), busarev@sai.msu.ru;*

²*Institute of Astronomy of Russian Academy of Science (IA RAS), 48 Pyatnitskaya str., 109017 Moscow, RF;*

³*Institute of Astrophysics of the Academy of Sciences (IAAS RT), 22 Bukhoro str., 734042 Dushanbe, Republic of Tajikistan (RT);*

⁴*TÜBİTAK National Observatory (TNO), Antalya, Turkey;*

⁵*Kazan Federal University, Kazan, RF;*

⁶*Academy of Sciences of Tatarstan, Kazan, RF*

Keywords:

spectrophotometry of asteroids, mineralogy and ice content in matter, temperature and other conditions, sublimation and sputtering of ices

Introduction:

Spectral signs of a strong simultaneous sublimation activity of the main-belt primitive asteroids 779 Nina, 704 Interamnia, and 145 Adeona were discovered in 2012 near their passage of perihelion [1-3]. We consider light scattering by evaporated micron-sized water ice particles as a main token of the process. According to Mie theory and subsequent numeric modeling [4, 5], intensity of light scattering by particles with refractive index of water ice ($n = 1.33$) is maximal for the dimensionless parameter $x = (2\pi\rho/\lambda) \approx 6$ or $\rho/\lambda \approx 1$, where ρ is the average radius of the particles and λ is the wavelength of light. In other words, ρ and the spectral position of maximum of scattered light (λ) are matching in this case. This is probably the main reason of registered unusual maximum near $0.50 \mu\text{m}$ in asteroid reflectance spectra of mentioned asteroids (Figs 1a, 1b, 1c). A simple suggestion is made that due to eccentricity of the orbits, the asteroids with some content of ice in the matter undergo changes of subsolar temperatures with revolution around the Sun ($\sim 222 \div 257$ K on Adeona, $\sim 206 \div 240$ K on Interamnia, and $\sim 208 \div 262$ K on Nina) [3]. As a consequence, a sublimation process starts to develop or intensify on each of the body with approaching to perihelion. We discuss previous and new observational data and consider possible reasons of the phenomenon.

Previous and new observational results:

Our first spectrophotometric observations of 145 Adeona, 704 Interamnia and 779 Ninawere performed at IARASTerskol Observatory (Mt. Terskol, 3150 m above sea level, Russia) with 2-m telescope and a low resolution CCD-spectrograph of ($R \approx 100$) in the range of $0.38\text{-}0.85 \mu\text{m}$ in September 2012 [1]. A conventional method of asteroid spectral observations (with solar analog stars) and a standard processing procedures (flat-field correction, bias and dark subtraction, etc.) were used. Relative standard deviations in the normalized reflectance spectra (RS) are about 1-3% at $0.40\text{-}0.65 \mu\text{m}$ and rise up to 5-8% at their ends [1]. The RS are compared with nominal SMASSII RS of the asteroids [6 - 8] (Figs 1a, 1b, 1c; Nina's spectra 1-3 on Fig. 1a were registered at different rotational phases within $\sim 40\%$ of asteroid rotational period and shifted arbitrary along the vertical axis [1]).

Very likely, we succeeded to confirm a periodic nature of the sublimation phenomenon on the asteroids at their next perihelion passages in 2016-2018 with the same spectral or similar facilities and *UBVRI*-photometric methods.

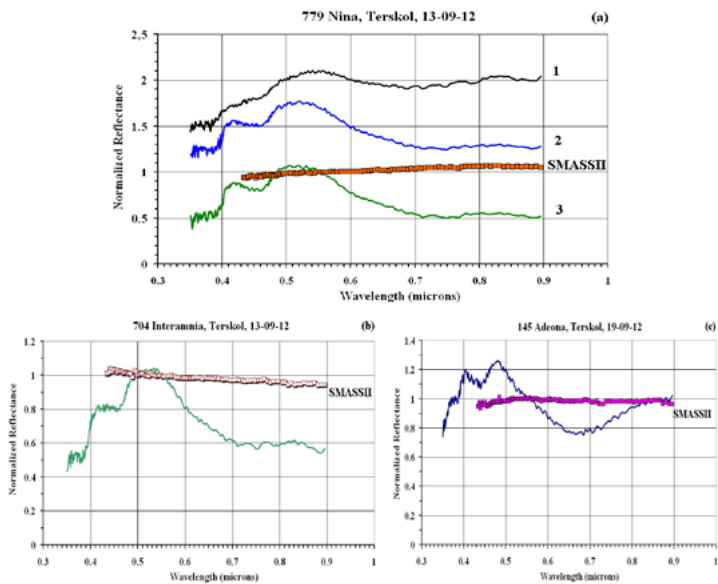


Fig. 1 (a, b, c).

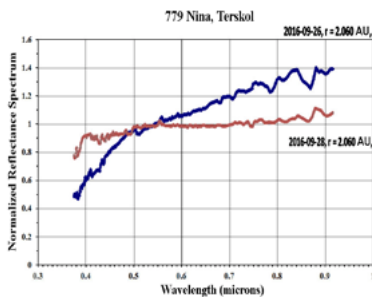


Fig. 2.

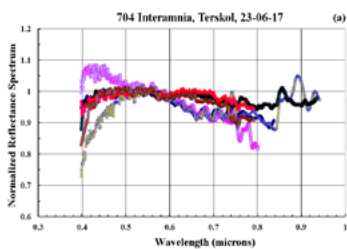


Fig. 3a.

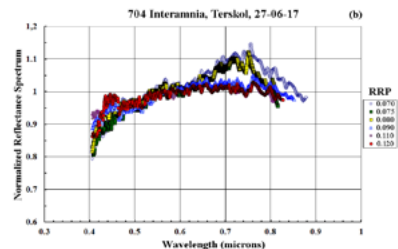


Fig. 3b.

These confirmations are as follows.

- Two reflectance spectra of 779 Nina with a sign of a dust coma (due to observed considerable difference in continuum of the spectra at a change of the asteroid relative rotational phases (RRPs) by only ~ 0.30) were obtained near its perihelion on 26 and 28 September 2016 at IA RAS Terskol Observatory (as solar analogs - HD9986 and HD173071, respectively) (Fig. 2) [3].
- Two sets of 704 Interamnia's RS were obtained on 23 and 27 June 2017 (4 months before the perihelion passage) at the same RRP. They show change the sign of the continuum from negative to positive – also as a mark of a dust coma around of the asteroid (Figs 3a and 3b). Several sets of *UBVRI* (or *BVRI*)- data of Interamnia were made to trace changes in its reflectance with the perihelion passage. To calculate approximations to Interamnia's RS, we performed its *UBVRI*-observations and those of different stable G-class stars as solar analogs (HD 804, HIP 2894, HIP 109931) at SAI MSU Crimea and IAAS RT Sanglok Observatories. The normalized (at

effective wavelength of V-band, $\lambda = 0.545 \mu\text{m}$) *UBVRI* (or *BVRI*) reflectance curves of Interamnia for the perihelion passage in 2017 are given in Figs 4a, 4b, 4c, and 4d.

It is important to note that closest to perihelion curves (on 25-10-17 and 11-11-17) demonstrate the most maxima at $0.55 \mu\text{m}$ as an evidence of reflected light scattering in an icy dust coma around the asteroid.

3) Also we performed *UBVRI*- and repeated spectral observations of 145 Adeona (and some stable stars in the same CCD-frames to control photometric conditions) at its passage of perihelion in February – June 2018 (Figs 5-7).

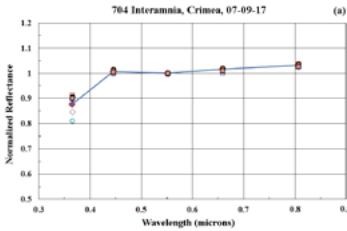


Fig. 4a.

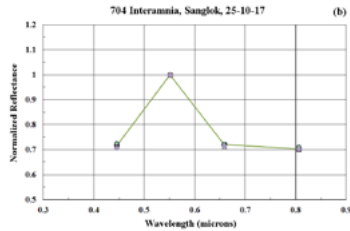


Fig. 4b.

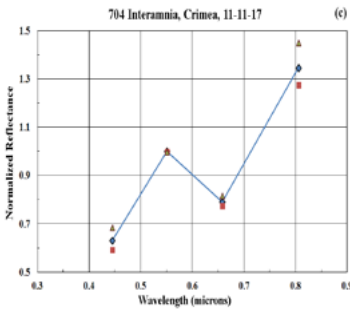


Fig. 4c.

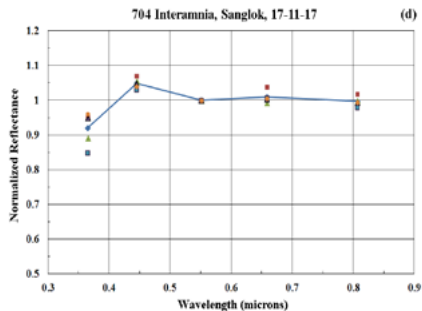


Fig. 4d.

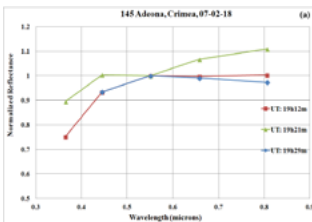


Fig. 5a.

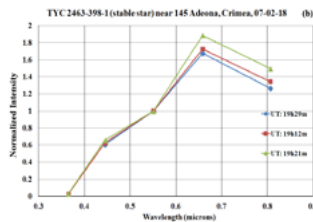


Fig. 5b.

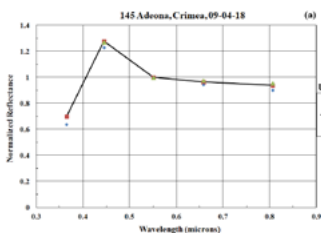


Fig. 6a.

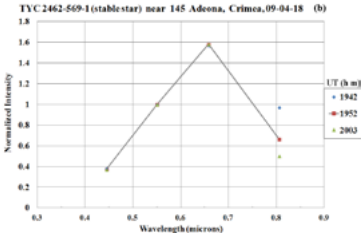


Fig. 6b.

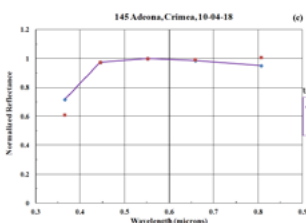


Fig. 6c.

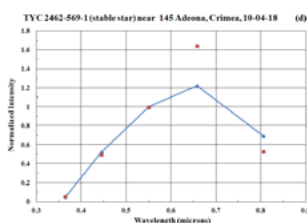


Fig. 6d.

Ten-minute spectral variations in reflectance of Adeona indicative of a coma presence were found (Figs 5a and 5b) on 07-02-18, the closest date to perihelion passage. Also, such changes were absent in normalized spectral intensity of a reference stable star in the same frame. A strong maximum at $0.55 \mu\text{m}$ in Adeona's reflectance and absence of it at close RRP's were observed on 09-04-18 and 10-04-18, respectively (Figs 6a and 6c; Figs 6b and 6c are control of photometric conditions by reference stars). Finally, considerable changes in the shape and continuum slope of Adeona's RS (similar to those of 779 Nina on 26 and 28 September 2016, Fig. 2) were found at small difference in RRP's (~ 0.30) at excellent photometric conditions of TNO (Turkey) on 12-04-18 and 13-06-18 (Fig. 7).

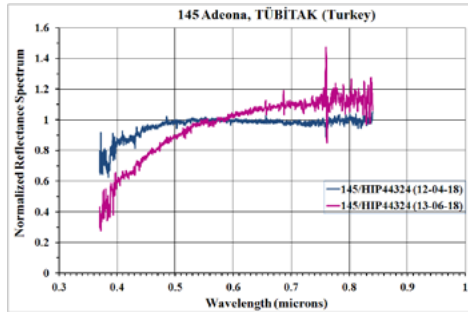


Fig. 7.

Discussion and conclusions:

Along with subsolar temperature changes and supposed average differences in ice content of asteroids, the results point to the other probable factors supporting long-term sublimation activity on primitive main-belt asteroids.

(1) As known from space observations (e. g., [9]), there must be a continuous meteorite/micrometeorite flux resurfacing main-belt asteroids.

(2) The discussed RS of 145 Adeona, 704 Interamnia, and 779 Nina demonstrate striking similarity in their appearance: a high reflectance in all spectral range in 2012 with a $0.5\text{-}\mu\text{m}$ maximum (see Figs 1a, 1b, and 1c) and the lower parameters in 2016-2018 (Figs 2, 3, and 7). Such results correlate with changes of solar activity which was a high in 2012 and declining it in 2016-2018. Influence activity of the Sun and parameters of the solar wind on efficiency of ice sputtering on asteroid surface should be investigated.

References:

- [1] Busarev V.V. et al., *Icarus* 262, 2015, 44-57,
- [2] Busarev V.V. et al., *Sol. Sys. Res.*, 2016, 281-293.
- [3] Busarev V.V. et al. *Icarus* 304, 2018, 83-94.
- [4] Mie G., *Ann. Phys.* 25, 1908, 377-445.
- [5] Hansen J.E., Travis L.D., *Space Sci. Rev.* 16, 1974, 527-610.
- [6] Bus S., Binzel R.P., 779 Nina CCD Spectrum // EAR-A-I0028-4-SBN0001/SMASSII-V1.0: 779_01_TAB. NASA Planetary Data System, 2003a
- [7] Bus S., Binzel R.P., 704 Interamnia CCD Spectrum // EAR-A-I0028-4-SBN0001/SMASSII-V1.0: 704_01_TAB. NASA Planetary Data System, 2003b
- [8] Bus S., Binzel R.P., 145 Adeona CCD Spectrum // EAR-A-I0028-4-SBN0001/SMASSII-V1.0: 145_01_TAB. NASA Planetary Data System, 2003c
- [9] Dermott S.F. et al., *Nature* 312, 1984, 505-509.

LIGHT CURVE ANALYZE OF 50 ASTEROIDS BASED ON THE ALCDEF DATABASE

A. Poro and et al

International Occultation Timing Association Middle East Section (IOTA/ME), iotamiddleeast@yahoo.com

Keywords:

Asteroid, ALCDEF, Light Curve, Analyze

Introduction:

A light curve is the measurement of a celestial body's brightness at certain intervals and over a given period of time. Asteroids shine due to the Sun's light reflecting off their surface, and their brightness might vary due to one or more of the following factors: The asteroid's distance to us is changing (closer objects appear brighter). The asteroid's phase, just like the Moon's, is changing as it orbits around the Sun (the larger the area of the asteroid that is illuminated, as seen from Earth, the brighter it will appear). The asteroid, because of its irregular shape, reflects light differently as it spins. If the orbit of an asteroid is well known, the first two effects can be numerically calculated and their contributions removed from the measured light curve. We are then left with a light curve whose changes are due solely to the spinning of the asteroid.

The International Occultation Timing Association strives to contribute occultation data that will be most useful when combined with other data sources such as light curves and adaptive optics imagery. Light curves analyze and determination of the position of the poles of rotation of an asteroid is a complex process, but the results of carefully analyzed occultations can well assist in making such a determination. As long as asteroids remain the least known population in the solar system, the need will be there to conduct campaigns to intercept occultations of stars by minor planets of all types.

We selected 50 asteroids in this scientific activity based on the ALCDEF database, conducted by some students at the 2018 Summer Astronomy School in Iran (Hold by IOTA/ME and Iranian Space Agency). Then their light curves were plotted and analyzed by using the softwares.

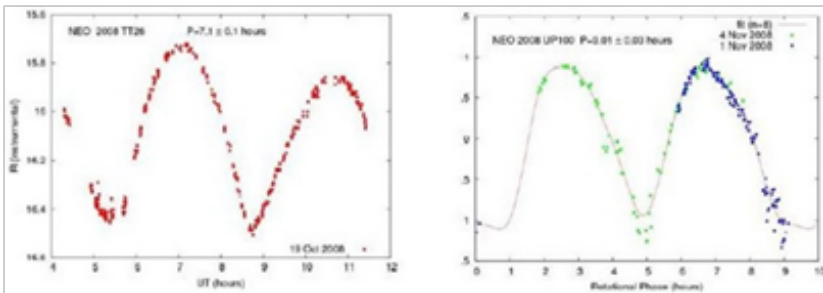


Fig. 1. Example of light curves of two NEO's indicating long rotation periods over 7 hours for small bodies with diameters between 50 and 100 meters.

DYNAMICAL EVOLUTION AND ORIGIN OF METEORITES WITH SHORT COSMIC-RAY EXPOSURE AGES

V.V. Emel'yanenko

Institute of Astronomy, Russian Academy of Sciences, Moscow, Russia, vvemel@inasan.ru

Keywords:

Meteorites, origin, orbits, small perihelion distances.

Introduction:

Very short cosmic-ray exposure (CRE) ages for some meteorites are inconsistent with their origin from catastrophic disruption within the main belt (e.g., [1]). This implies the origin of meteoroids as a free-floating body in the near-Earth region. It is well known from dynamical studies that near-Earth objects evolve frequently to orbits with small perihelion distances [2]. It is estimated that up to 70 percent of near-Earth objects collide with the Sun during their orbital evolution [3]. Recently Granvik et al. [4] concluded that the deficit of near-Earth asteroids on orbits with small perihelion distances arises from the breakup of a substantial fraction of asteroids when they move near the Sun. Thus, disruption of bodies due to the strong solar tide, thermal stresses and interaction with the solar atmosphere at Sun-grazing conditions may play a key role in the origin and modification of small near-Earth objects.

Methods:

Meteorites provide unique possibilities for studies of dynamical aspects of near-Earth asteroids because orbital evolution considerations can be combined with estimates of CRE ages. But among objects with known CRE ages only a handful are appropriate because the accuracy of orbits is often insufficient even for qualitative studies of their long-term motion. We report here results of our dynamical studies of a few objects with measured CRE ages and relatively good orbits. We concentrate our investigation on meteorites with short CRE ages (less than ~ 10 Myr). We consider a large set of test orbits from the confidence region for each meteoroid. We use the symplectic integrator [5] to backward propagate the orbits taking account of perturbations from all planets. We estimate the fraction of particles reaching the near-Sun state (orbits with perihelion distances $q < 0.1$ au) in the past.

Encounters with the Sun:

The study of the Chelyabinsk meteorite shows that 25 percent of test particles reach the near-Sun state in 2 Myr, and more than 50 percent of particles reach the near-Sun state in 5 Myr [6]. This is consistent with the CRE age estimate of 1.2 Myr [7].

The Novato meteorite has a well determined orbit thanks to observations of the CAMS system [8]. According to our integrations 36 percent of test particles reach the near-Sun state in 1 Myr, and 66 percent of particles reach the near-Sun state in 5 Myr. These data are consistent with the conclusion [9] that the change in shielding conditions of this meteoroid occurred during the last few Myr.

The Almahata Sitta meteorite has the most precise orbit among meteorites thanks to pre-atmospheric observations as a small asteroid. Six samples of the meteorite have an average CRE age of 19.2 ± 3.3 Myr, but one sample has a lower CRE age of 11.0 ± 1.4 Myr [10]. Our computations show that 25 percent of test particles reach the near-Sun state in 10 Myr, and 39 percent of particles reach the near-Sun state in 20 Myr.

We also plan to discuss other meteorites with short CRE ages: Lost City, Moravka, Sutters Mill, Košice, etc.

Conclusions:

The probabilities of recent encounters with the Sun are different for the studied meteorites, but they are substantial in all the cases. The times of these encounters are consistent with the estimated CRE ages.

Acknowledgements:

This work was supported by the Russian Foundation for Basic Research (Project 16-02-00805).

References:

- [1] Connolly H.C., et al. Towards understanding the dynamical evolution of asteroid 25143 Itokawa: constraints from sample analysis // *Earth, Planets and Space*. 2015. V. 67. Article id.12, 6 p.
- [2] Farinella P., et al. Asteroids falling into the Sun // *Nature*. 1994. V. 371. P. 314–317.
- [3] Marchi S., et al. Heating of near-Earth objects and meteoroids due to close approaches to the Sun // *Monthly Notices of the Royal Astronomical Society*. 2009. V. 400. P. 147–153.
- [4] Granvik M., et al.: Super-catastrophic disruption of asteroids at small perihelion distances // *Nature*. 2016. V. 530. P. 303–306.
- [5] Emel'yanenko V.V. A method of symplectic integrations with adaptive time-steps for individual Hamiltonians in the planetary N-body problem // *Celestial Mechanics and Dynamical Astronomy*. 2007. V. 98. P. 191–202.
- [6] Emel'yanenko V.V., et al. The orbit and dynamical evolution of the Chelyabinsk object // *Meteoritics and Planetary Science*. 2014. V. 49. P. 2169–2174.
- [7] Popova O.P., et al. Chelyabinsk airburst and damage assessment // *Science*. 2013. V. 342. P. 1069–1073.
- [8] Jenniskens P., et al. CAMS: Cameras for Allsky Meteor Surveillance to establish minor meteor showers // *Icarus*. 2011. V. 216. P. 40-61.
- [9] Jenniskens P., et al. Fall, recovery and characterization of the Novato L6 chondrite breccias // *Meteoritics and Planetary Science*. 2014. V. 49. P. 1388-1425.
- [10] Riebe M.E.I., et al. Cosmic-ray exposure ages of six chondritic Almahata Sitta fragments // *Meteoritics and Planetary Science*. 2017. V. 52. P. 2353-2374.

MIGRATION OF BODIES TO THE EARTH AND THE MOON FROM DIFFERENT DISTANCES FROM THE SUN

S. I. Ipatov

V.I. Vernadsky Institute of Geochemistry and Analytical Chemistry of RAS, Moscow, Russia. siipatov@hotmail.com

Keywords:

Migration, planetesimals, Earth, Moon, probabilities of collisions

Introduction:

Earlier we studied the probability p_E of a collision of a body (during its dynamical lifetime) with the Earth for bodies with orbits close to known Jupiter-family comets [1-5] and for planetesimals from the feeding zone of Jupiter and Saturn (with initial semi-major axes a from 4.5 to 12 AU) [6]. Below I study the probabilities of collisions of bodies migrated to the Earth and the Moon from different distances from the Sun. Studies of such migration allow one to understand better the delivery of water and volatiles to the Earth and the Moon.

Initial data used for calculations:

Using the symplectic code from the Swift integration package [7] I made several series of calculations of migration of bodies under the gravitational influence of $n_{pl}=7$ planets (from Venus to Neptune) or of $n_{pl}=5$ planets (from Venus to Saturn). In some runs, initial semi-major axes varied from a to $a+2.5$ AU with a number of initial planetesimals proportional to $a^{1/2}$. In other runs, initial semi-major axes were the same and equaled to r_f . For different runs, a_o and r_f varied from 2.5 to 40 AU with a step equaled to 2.5 AU. Initial eccentricities e_o and inclinations i_o equaled to 0.3 and 0.15 rad, respectively. Such eccentricities could be reached due to mutual gravitational influence of planetesimals during evolution of a disk of planetesimals in the feeding zone of the giant planets [8-9]. Integrations were made until bodies reached 2000 AU or collided with the Sun. However, some runs with large a_o were stopped after a few tens of millions of years (typically after more than at 100 Myr, up to 500 Myr), if p_E finished increasing during some long time and a small number of bodies was left. In principle, p_E could increase after that stopping time, and so the lower limits of p_E are presented below. Each run was made for 250 initial bodies with different orientations of initial orbits. The values of p_E and p_E/p_M (where p_M is the probability of a collision of a body during its dynamical lifetime with the Moon) for considered runs are presented in Tables 1-3.

Results of calculations:

Some bodies did not reach the Earth's orbit during their dynamical lifetimes. A few migrating bodies could move in Earth-crossing orbits during many millions of years, and they could provide the major contribution to the mean value of p_E calculated for thousands of bodies with close initial orbits. Such results on the role of a few bodies in p_E have been obtained earlier in [1-4] for Jupiter-family comets, and they were also obtained in my new series of runs. The values of p_E could differ by more than a factor of several tens for the runs with the same initial orbits, but with a different step of integration. For example, at the series of runs with $a=5$ AU, p_E varied from 2.4×10^{-7} to 8.5×10^{-6} for different runs, and $p_E=4.1 \times 10^{-6}$ for a series of 8 runs with 2000 bodies. At the series of runs with $a_o=7.5$ AU, in one run $p_E=0$, in another run $p_E=2.64 \times 10^{-3}$, and $p_E=3 \times 10^{-4}$ for a series of 9 runs with 2250 bodies. At $a=12.5$ AU, the mean value of p_E was 1.7×10^{-6} for a series of 3 runs with 750 bodies. The values of p_E were typically greater for smaller a_o , but due to a wide range of possible values of p_E for runs with the same initial data, one needs to consider a greater number of runs for each a_o before making accurate estimates. For most runs with $a_o \geq 20$ AU, it was obtained that $p_E < 10^{-6}$. However, there were runs with greater values of p_E . For example, in some runs $p_E=7.2 \times 10^{-6}$ at $a=22.5$ AU and $p_E=1.4 \times 10^{-6}$ at $a=37.5$ AU. On average, for the region 20-35 AU the value of p_E could exceed 10^{-6} . This region could play a valuable role

in migration of icy bodies to the Earth. In some above runs, p_E continued to grow after 50 Myrs. For runs with $a_o=2$ AU and $r_f=2.5$ AU, the values of p_E were of the order of 10^{-3} , i.e. were much greater than for bodies located at more than 5 AU from the Sun. In two runs with $a_o=2.5$ AU, mean p_E was $5.4 \cdot 10^{-5}$. The values of p_E for such runs could grow after 100 Myrs. The above values of p_E were obtained for $n_{pl}=7$. For $n_{pl}=5$ the mean values of p_E at $a_o=5$ AU and $a_o=7.5$ AU were smaller (see Table 2) than those for $n_{pl}=7$.

Table 1. Probabilities p_E and p_M of collisions with the Earth and the Moon for one body for the run with 250 bodies with semi-major axes from a_o to $a_o+2.5$ AU, $e_o=0.3$, $i_o=0.15$ at $n_{pl}=7$. Mean values of p_E are in parentheses.

a_o	2.	2.5	5.0
p_E	$2.5 \cdot 10^{-3}$	$6.8 \cdot 10^{-5}$, $4.0 \cdot 10^{-5}$ ($5.4 \cdot 10^{-5}$)	$2.4 \cdot 10^{-7}$, $4.0 \cdot 10^{-6}$, $3.1 \cdot 10^{-6}$, $8.5 \cdot 10^{-6}$, $1.2 \cdot 10^{-6}$, $7.6 \cdot 10^{-6}$, $7.3 \cdot 10^{-6}$, $7.8 \cdot 10^{-7}$ ($4.1 \cdot 10^{-6}$)
p_E/p_M	17.6	17.4, 16.8	16.2, 16.4, 17.4, 16.3, 17.0, 16.7, 16.4

a_o	7.5	10	12.5
p_E	$1.2 \cdot 10^{-5}$, $5.2 \cdot 10^{-7}$, $1.1 \cdot 10^{-6}$, 0 , $6.1 \cdot 10^{-7}$, $6.4 \cdot 10^{-7}$, $2.64 \cdot 10^{-3}$, $7.0 \cdot 10^{-6}$ ($2.96 \cdot 10^{-4}$)	$1.1 \cdot 10^{-6}$, $1.6 \cdot 10^{-6}$, $3.1 \cdot 10^{-6}$ ($1.9 \cdot 10^{-6}$)	$1.6 \cdot 10^{-6}$, $2.0 \cdot 10^{-6}$, $1.5 \cdot 10^{-6}$ ($1.7 \cdot 10^{-6}$)
p_E/p_M	16.5, 16.6, 17.0, -, 16.5, 19.1, 16.5	16.1, 16.1, 16.4	16.6, 16.6, 16.6

a_o	15	17.5	20	22.5	25
p_E	$5.5 \cdot 10^{-7}$, $1.4 \cdot 10^{-6}$ ($1.0 \cdot 10^{-6}$)	$5.4 \cdot 10^{-6}$, $3.2 \cdot 10^{-7}$ ($2.9 \cdot 10^{-6}$)	$4.0 \cdot 10^{-7}$, $9.6 \cdot 10^{-7}$, $3.2 \cdot 10^{-7}$ ($5.6 \cdot 10^{-7}$)	$7.2 \cdot 10^{-6}$, $1.7 \cdot 10^{-7}$, $6.8 \cdot 10^{-7}$ ($2.7 \cdot 10^{-6}$)	$3.8 \cdot 10^{-7}$, $6.7 \cdot 10^{-8}$, $4.6 \cdot 10^{-6}$ ($1.7 \cdot 10^{-6}$)
p_E/p_M	16.6, 16.3	16.7, 16.4	16.5, 16.2, 17.1	17.4, 16.3, 16.6	16.4, 16.2, 15.7

a_o	27.5	30	32.5	35	37.5	40
p_E	$2.2 \cdot 10^{-7}$, $1.5 \cdot 10^{-7}$ ($1.8 \cdot 10^{-6}$)	$2.0 \cdot 10^{-7}$, $1.0 \cdot 10^{-6}$ ($6 \cdot 10^{-7}$)	$1.5 \cdot 10^{-7}$, $6.0 \cdot 10^{-7}$ ($3.7 \cdot 10^{-7}$)	$5.0 \cdot 10^{-7}$, $3.3 \cdot 10^{-7}$, $1.8 \cdot 10^{-7}$ ($3.4 \cdot 10^{-7}$)	$1.40 \cdot 10^{-6}$, $6.1 \cdot 10^{-8}$ ($7.3 \cdot 10^{-7}$)	$6.2 \cdot 10^{-7}$, $1.3 \cdot 10^{-6}$ ($9.6 \cdot 10^{-7}$)
p_E/p_M	16.3, 16.5	16.2, 16.0	16.2, 16.2	16.3, 17.4, 16.5	16.5, 16.0	17.3, 16.9

Table 2. Probabilities p_E and p_M of collisions with the Earth and the Moon for one body for the run with 250 bodies with semi-major axes from a_o to $a_o+2.5$ AU, $e_o=0.3$, $i_o=0.15$ at $n_{pl}=5$. Mean values of p_E are in parentheses.

a_o	5.	7.5	10.0
p_E	$7.2 \cdot 10^{-7}$, $2.2 \cdot 10^{-6}$, $2.1 \cdot 10^{-6}$, $1.6 \cdot 10^{-6}$, ($1.7 \cdot 10^{-6}$)	$9.1 \cdot 10^{-7}$, $4.7 \cdot 10^{-6}$, $9.8 \cdot 10^{-7}$, $3.1 \cdot 10^{-7}$ ($1.7 \cdot 10^{-6}$)	$7.7 \cdot 10^{-6}$, $3.5 \cdot 10^{-7}$, $3.0 \cdot 10^{-6}$, $4.2 \cdot 10^{-7}$, ($1.9 \cdot 10^{-6}$)
p_E/p_M	16.7, 16.8, 16.6, 16.4	16.3, 16.8, 16.9, 16.3	16.8, 16.3, 16.8, 16.9

Probabilities of collisions with the Moon for bodies migrated from beyond Jupiter's orbit usually were by about a factor of 16 or 17 smaller than probabilities of collisions with the Earth. Probabilities p_{Sun} of collisions of bodies with the Sun were 0.17 for $a_o=2$ AU, 0.04 for $a_o=2.5$ AU, and 0.76 for $r_f=2.5$ AU. For all other runs presented in Tables 1-3, we have $p_{Sun} < 0.01$, and $p_{Sun} = 0$ for most runs with 250 bodies for a_o or r_f not less than 5 AU.

Table 3. Probabilities p_E and p_M of collisions with the Earth and the Moon for one body for the run with 250 bodies with semi-major axes equal to r_f at $n_{pl}=7$.

r_f	2.5	5.0	7.5	10	12.5	15
p_E	$1.8 \cdot 10^{-3}$	$5.7 \cdot 10^{-7}$	$1.2 \cdot 10^{-6}$	$4.0 \cdot 10^{-7}$	$8.8 \cdot 10^{-6}$	$6.8 \cdot 10^{-7}$
p_E/p_M	13.4	16.8	16.7	16.7	18.0	16.3
r_f	17.5	20.0	22.5	25	30	40
p_E	$2.8 \cdot 10^{-7}$	$1.2 \cdot 10^{-7}$	$7.8 \cdot 10^{-7}$	$3.8 \cdot 10^{-7}$	$5.0 \cdot 10^{-7}$	$4.1 \cdot 10^{-7}$
p_E/p_M	16.8	16.7	16.8	16.5	16.1	14.8

Conclusions:

Probabilities of collisions with the Earth and the Moon for bodies with initial eccentricities equalled to 0.3 and inclinations equalled to 0.15 rad were calculated for initial semi-major axes from 2 to 40 AU. The probabilities calculated for 250 bodies can differ by more than a factor of several tens for different runs with similar orbits. The mean probabilities of collisions of bodies with

the Earth for the region between 5 and 10 AU exceeded 4×10^{-6} . On average, for the region between 20 and 35 AU the probabilities could exceed 10^{-6} . For bodies initially located in the asteroid belt, the probabilities of their collisions with the Earth were about 10^{-4} - 10^{-3} , i.e., were much greater than for bodies initially located beyond Jupiter's orbit. The ratio of the probabilities of collisions of considered planetesimals with the Earth to those with the Moon was mainly in the range from 16 to 17.

The studies of migration of planetesimals to the Earth were supported by the Program of Fundamental Studies of the Presidium of RAS № 17 as a part of Russian state program for GEOKHI N 00137-2018-0030. The studies of migration of planetesimals to the Moon were supported by the grant of Russian Science Foundation N 17-17-01279.

References:

- [1] Ipatov S.I., Mather J.C. Migration of Jupiter-family comets and resonant asteroids to near-Earth space. "Astrodynamics, Space Missions, and Chaos", ed. by E. Belbruno, D. Folta, and P. Gurfil, Annals of the New York Academy of Sciences. 2004. V. 1017. P. 46-65. <http://arXiv.org/format/astro-ph/0308448>.
- [2] Ipatov S.I., Mather J.C. Comet and asteroid hazard to the terrestrial planets, Advances in Space Research. 2004. V. 33. P. 1524-1533. <http://arXiv.org/format/astro-ph/0212177>.
- [3] Ipatov S.I. Mather J.C. Migration of small bodies and dust to near-Earth space. Advances in Space Research. 2006. V. 37. P. 126-137. <http://arXiv.org/format/astro-ph/0411004>.
- [4] Ipatov S.I., Mather J.C. Migration of comets to the terrestrial planets. Proceedings of IAU Symp. No. 236 "Near-Earth Objects, Our Celestial Neighbors: Opportunity and Risk". Cambridge: Cambridge Univ. Press. 2007. P. 55-64. <http://arXiv.org/format/astro-ph/0609721>.
- [5] Ipatov S.I. Collision probabilities of migrating small bodies and dust particles with planets. Proceedings of IAU Symposium S263. Vol. 5, "Icy bodies in the Solar System". Cambridge: Cambridge Univ. Press. 2010. P. 41-44. <http://arxiv.org/abs/0910.3017>.
- [6] Marov M.Ya., Ipatov S.I. Delivery of water and volatiles to the terrestrial planets and the Moon, Solar System Research. 2018. V. 52, N 5, in press.
- [7] Levison H.F., Duncan M.J. The long-term dynamical behavior of short-period comets. Icarus. 1994. V. 108. P. 18-36.
- [8] Ipatov S.I. Accumulation and migration of the bodies from the zones of giant planets. Earth, Moon, and Planets. 1987. V. 39. P. 101-128.
- [9] Ipatov S.I. Migration of celestial bodies in the solar system. Editorial URSS Publishing Company, Moscow. 2000. 320 p., in Russian. http://www.rfbr.ru/rffi/ru/books/o_29239.

MICROFOSSILS, BIOMOLECULES AND BIOELEMENTS IN THE ORGUEIL METEORITE

R.B. Hoover¹, A. Yu. Rozanov²

¹Athens State University, 300 N. Beaty St., Athens, AL 35811, USA, RichardBHoover@iCloud.Com;

²Astrobiology Sector, Laboratory of Radiation Biology, Joint Institute for Nuclear Research, Dubna, Russia, 141980, Aroza@Paleo.ru

Keywords:

Orgueil meteorite, microfossils, biomolecules, bioelements, cyanobacteria

Introduction:

The Orgueil C11 carbonaceous chondrite was observed to fall in southern France on May 14, 1864 and over 20 stones were recovered immediately after the fall. Eyewitness descriptions of the fireball from diverse locations and the initial studies of the physical and chemical properties of the Orgueil meteorite were quickly published. Leymerie [1] found the black stones were soft and easily cut by a knife creating smooth, shiny surfaces indicating a "fine, paste-like matter". This friable micro-regolith breccia was found to disintegrate rapidly in water when salts dissolve releasing insoluble mineral grains and insoluble organic particulates. Cloëz [2,3] found Orgueil contained 5.92% carbon; 5.2-6.9% hygroscopic water and 8-10% indigenous water of hydration (liberated only above 200 °C) along with magnetite, silicic acid and other salts. Primary minerals were replaced by secondary phases indicating extensive aqueous alteration on the Orgueil parent body. Organic chemistry studies revealed complex carbonaceous matter and hydrocarbons analogous to peat and humic substances of ancient biological origin on Earth but very different from recent organic matter [4]. These initial results were confirmed by modern studies using sophisticated instruments and methods. Isotopic analyses [5] revealed the carbon isotopes of the Orgueil carbonates ($d^{13}C \sim +60\text{‰}$) are very different from terrestrial carbonates of precambrian limestones and dolomites ($d^{13}C = +0.4\text{‰}$) [6] or biological carbonates ($d^{13}C = 0\text{‰}$ to -70‰) [7] showing Orgueil carbon is both indigenous and extraterrestrial. Kissin [8] found the Orgueil hydrocarbons were similar to alkanes from thermocracked terrestrial kerogens and bitumens but unlike man-made oils or recent bio-contaminants. Orgueil has been found to contain porphyrins [9] and saturated polyisoprenoid parrifin hydrocarbons- pristane ($C_{19}H_{40}$) and phytane ($C_{20}H_{42}$). These aquatic geochemical biomarkers are found in oil shales and ancient rocks [10,11] and arise mainly from the oxidation and later decarboxylation or reduction of the phytol side chain of the life-critical chlorophyll biomolecule or from degradation of archaeal lipids or tocopherols, that are synthesized exclusively by cyanobacteria and other photosynthetics [12,13]. Orgueil contains only a subset of the 20 protein amino acids and only 3 of the 5 nucleobases of DNA and RNA. Isotopic analyses show these biomolecules were both indigenous and extraterrestrial [14]. Furthermore, if the Orgueil stones were contaminated by modern bacteria or pollen they would contain have to contain all 20 proteinogenic amino acids and all 5 nucleobases. In the early 1960's, researchers reported the detection of organics and possible microfossils in Orgueil, but were not able to prove they were indigenous [15]. After extensive debate, it came to be generally accepted that microfossils in meteorites were either pollen grains or intentional contaminants [14,16] or just "imagination" [17]. Recent studies using sensitive 16S and 18S rRNA PCR amplification (capable of detecting a single cell or pollen grain) have invalidated the hypothesis that the Orgueil stones are contaminated by modern terrestrial pollen grains or bacteria [18].

We present the results of advanced scanning electron microscopy studies carried out in the United States and Russia since 1997. During this research, a great variety of recognizable biological remains have been found, imaged and analyzed in Orgueil and many other carbonaceous chondrites. Energy

Dispersive X-ray Spectroscopy (EDS) analysis of life-critical bioelements contained within these remains provides direct observational evidence that they are microfossils of ancient life forms that died long before the Orgueil meteorite entered the atmosphere of Earth in 1864.

Materials and Methods:

Numerous fragments of different Orgueil samples were provided for this research (to RBH) by the *Natural History Museum*, Montauban; *Planetary Studies Foundation*, Chicago; and *Musée Nationale d'Histoire de Paris*. The samples were fractured using flame sterilized tools and mounted onto SEM stubs with the interior Orgueil surfaces exposed.

Results and Conclusions:

Scanning Electron Microscopy studies of the Orgueil C11 carbonaceous chondrite carried out at NASA/MSFC in the USA and at Joint Institute for Nuclear Research and Paleontology Institute/RAS in Russia have yielded high resolution images (with calibrated scale bars) of microfossils, frambooids and abiotic minerals particulates. Element compositions at selected spots on microfossils and rock matrix and 2D x-ray maps were obtained using Energy Dispersive Fig.

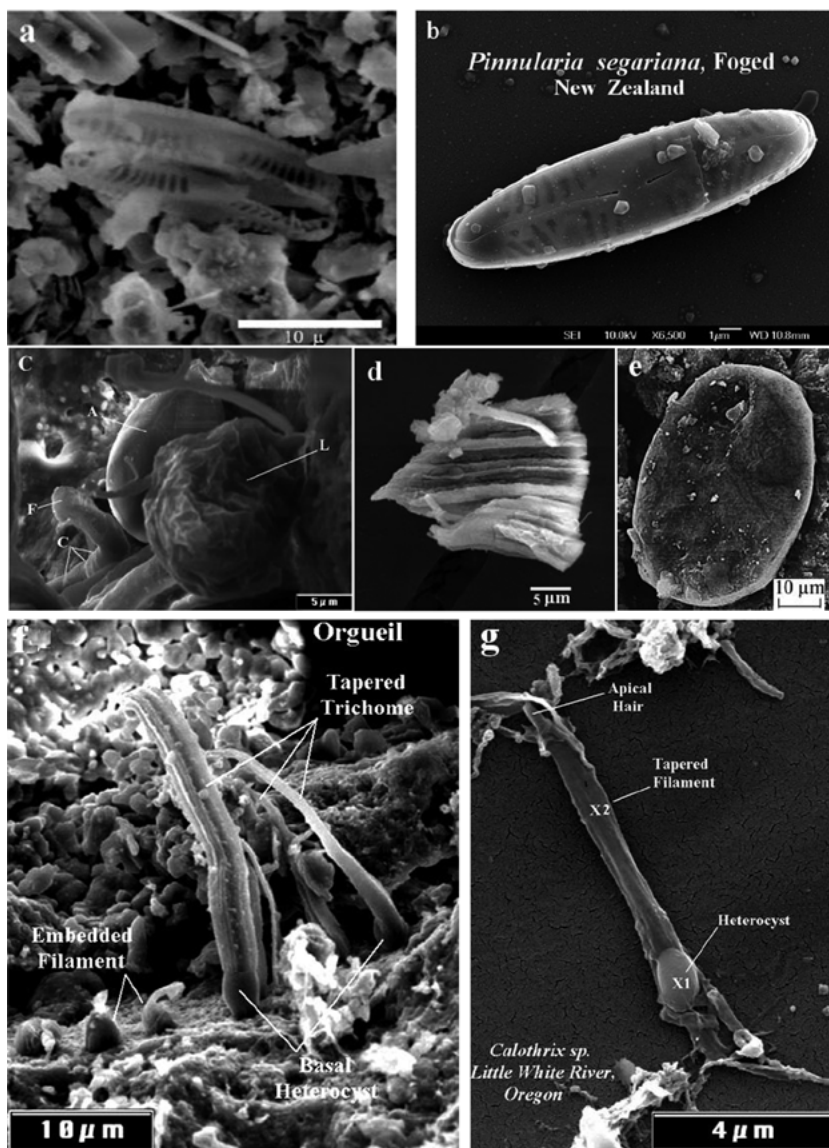


Fig. 1.

1.X-Ray Spectroscopy (EDS). These investigations revealed that the Orgueil meteorite contains a large suite of diverse fossilized (permineralized or kerogenic) remains of cyanobacteria, algae, diatoms, acritarchs and other prokaryotic or eukaryotic aquatic microorganisms. Many exhibit specialized cells used for nitrogen fixation (heterocysts) and show evidence of distinctive reproductive modes (akinetes, hormogonia, and baeocytes). Examples of morphologically diverse and exceptionally well-preserved and recognizable microfossils in the Orgueil C1 carbonaceous chondrite are shown in Plate 1. These include: (a) magnesium sulfate enfused diatom frustules with size and morphology of (b) the terrestrial diatom *Pinnularia segariana* of New Zealand (SEM Image Landcare Research); (c) extinct acritarchs; (d) extinct coiled cyanobacteria ~ *Obruchevella*; protista (e.) alveolata; and (f.) tapered trichomic filaments of embedded heterocystous cyanobacteria with size and morphological characteristics of *g. Calothrix* species from the Little White River of Oregon.

EDS spot data shows the content of the life-critical bioelement nitrogen in most Orgueil microfossils is below the EDS detection limit (< 0.5 % atomic) and C/N; C/O and C/S ratios are very different from living, holocene, or Pleistocene biological remains. Extinct acritarchs, *Obruchevella* and sheaths of trichomic cyanobacteria in Orgueil are consistent with proterozoic biogenic kerogen (O/C < 0.2; C/N ~ 100 to 160)[19-22]. The EDS results and detailed morphologies and sizes of complex cellular and trichomic remains provide direct observational evidence that the Orgueil microfossils represent indigenous and ancient biology rather than modern bio-contaminants. Hence the Orgueil microfossils are interpreted as the remains of ancient algae and cyanobacteria that grew in liquid water regimes within the parent body and died long before the Orgueil bolide entered the atmosphere in 1864.

References:

- [1] Leymerie, M., Sur l'aérolithe d'Orgueil (Tarn-et-Garonne), tombé le 14 Mai, 1864, a huit heures de soir, Lettre de M. Leymerie a M. Daubrée.// Comptes rendus de l'Académie des Sciences, 1864. V. 58. P. 988-990.
- [2] Cloëz, S. Note sur la composition chimique de la pierre météorique d'Orgueil.// Comptes rendus de l'Académie des Sciences. 1864. V. 58. P. 986-988.
- [3] Cloëz, S. Analyse chimique de la pierre météorique d'Orgueil. Note de M. S. Cloëz présentée par M. Daubrée. // Comptes rendus de l'Académie des Sciences. 1864. V. 59. P. 37-40.
- [4] Berthelot M. Sur la matiere charboneuse des meteorites.// Comptes rendus de l'Académie des Sciences, 1868, V. 67. P. 849.
- [5] Clayton, R. N. Carbon isotope abundances in meteoritic carbonates.// Science. 1963, V. 140. No. 3563. P. 192-193.
- [6] Schidlowski, M., Eichman, R., Junge, C. E. Precambrian sedimentary carbonates: carbon and oxygen isotope geochemistry and implications for the terrestrial oxygen budget.// Precambrian Research. 1975. V. 2. No. 1. P. 1-69.
- [7] McConnaughey, T. A., Burdett, J., Whelan J. F., Paull, C. K. Carbon isotopes in biological carbonates: Respiration and photosynthesis.// Geochimica et Cosmochimica Acta. 1997. V. 61. No. 3. P. 611-622.
- [8] Kissin, Y. V. Hydrocarbon components in carbonaceous meteorites. Geochimica et Cosmochimica Acta. 2003. V. 67. 1723-1735.
- [9] Hodgson, G. W. and Baker, B. L. Porphyrins in meteorites: Metal complexes in Orgueil, Murray, Cold Bokkeveld, and Mokoia carbonaceous chondrites.// Geochimica et Cosmochimica Acta. 1969. P. 943-958.
- [10] Oro, J., Nooner, D. W. Zlatkis, A., Wikstrom, S. A. Paraffinic hydrocarbons in the Orgueil, Murray, Mokoia and other meteorites.// Life Science Space Research. 1966. V. 4. P. 63-100.
- [11] Hughes, W. B., Holba, A. G., Dzou, L. I. P. The ratios of dibenzothiophene to phenanthrene and pristane to phytane as indicators of depositional environment and lithology of petroleum source rocks.// Geochimica et Cosmochimica Acta 1995. V. 59. No. 17. P. 3581-3598.
- [12] Goosens, H., de Leeuw, J. W., Schenk, P. A., and Brassell, S. C. Tocopherols as likely precursors of pristane in ancient sediments and crude oils.// Nature. 1984. V. 312. P. 440-442.
- [13] Settler, S. E., Cahoon, E. B., Coughlan, S. J., and Dellapenna, D. Characterization of Topopherol Cyclases from Higher Plants and Cyanobacteria. Evolutionary Implications for Topopherol Synthesis and Function.// Plant Physiology. 2003. V. 132. P. 2184-2195.
- [14] Ehrenfreund, P., Glavin, D. P., Botta, O., Cooper, G., and Bada, J. Extraterrestrial amino acids in Orgueil and Ivuna: Tracing the parent body of CI type carbonaceous

- chondrites.// *Proceedings National Academy of Sciences*. 2001 V. 98. P. 2138-2141.
- [15] Nagy B. *Carbonaceous Meteorites*.// Elsevier. 1975. New York, P. 1-747.
- [16] Anders, E., Dufresne, E. R., Hayatsu, R., Cavaille, A., Dufresne, A. and F. W. Fitch, F. W. *Contaminated meteorite*.// *Science*. 1964. V. 146. No. 3648. P. 1157-1161.
- [17] Gounelle, M. and Zolensky, M. *The Orgueil meteorite: 150 years of history*.// *Meteoritics and Planetary Science*. V. 49. No. 10. P. 1769-1794.
- [18] Aerts J. W., Elsaesser, A., Roling, W. F. M. and Ehrenfreund, P. *A contamination assessment of the CI carbonaceous meteorite Orgueil using a DNA-directed approach*.// *Meteoritics & Planetary Science*. 2016. V. 51. No. 5. P. 920-931.
- [19] Hoover, R. B. *Fossils of prokaryotic microorganisms in the Orgueil meteorite*.// *Proceedings of the SPIE Instruments, Methods, and Missions for Astrobiology IX*. SPIE 6309. 2006. San Diego. USA. P. 1-19.
- [20] Rozanov, A. Yu. *Pseudomorphic microbial structures*.// *Paleontological Journal*. 2010. V. 44. P. 819-826.
- [21] Hoover, R. B. *Ratios of Biogenic Elements for Distinguishing Recent from Fossil Microorganisms*.// *Proceedings of the SPIE Instruments, Methods, and Missions for Astrobiology X*. SPIE. 2007. V. 6694. San Diego. USA. P. 1-12.
- [22] Gallien, J.-P., Orberger, B., Daudin, L., Pinti, D.L. and Pasava, J. *Nitrogen in biogenic and abiogenic minerals from Paleozoic black shales: an NRA study*.// *Nuclear Instruments and Methods in Physics Research*. 2004. V. B217. P. 113-122.

SIGNIFICANT SPATIAL HETEROGENIETY OF REGOLITH ON ASTEROID (3200) PHAETHON

E. Zubko¹, M. Zheltobryukhov², E. Chornaya^{1,2}, A. Kochergin^{1,2}, G. Kornienko², A. Matkin^{1,2}, O.V. Ivanova³, I. Luk'yanyk⁴

¹ Far Eastern Federal University, 8 Sukhanova St., Vladivostok 690950, Russia, evgenij.s.zubko@gamial.com;

² Ussuriysk Astrophysical Observatory of FEB RAS, 21 Solnechnaya St., Gornotaezhnoe 692533, Russia;

³ Astronomical Institute of the Slovak Academy of Sciences, SK-05960 Tatranská Lomnica, Slovak Republic

⁴ Astronomical Observatory, Taras Shevchenko National University of Kyiv, 3 Observatorna St., 04053, Kyiv, Ukraine

Keywords:

Polarimetry, observation, asteroid (3200) Phaethon, regolith, spatial heterogeneity

Introduction:

Asteroid (3200) Phaethon is a near-Earth object. Its perihelion lies at only ~ 0.14 au that suggests systematic strong heating of the surface. Phaethon is long known to be a parent body to the Geminid meteor shower [1] and it indeed was confirmed to reveal a comet-type activity [2]. These features make Phaethon an attractive target for ground-based astronomical observations (e.g., [3–6]). It also is considered as an aim for space-probe exploration.

Observations:

We observe asteroid (3200) Phaethon at the prime focus of the 22-cm telescope that is located at the Ussuriysk Astrophysical Observatory (code C15), which operates within the International Scientific Optical Network (ISON). Weather conditions were favorable for observations on three closest-approach dates, December 14, 16, and 17 of 2017. On the first epoch, we conducted a 2.5-hour series of photometric observations aimed to infer the light curve of Phaethon; whereas, on the two other epochs, we measured the degree of linear polarization $P = (I_{\perp} - I_{\parallel}) / (I_{\perp} + I_{\parallel})$, where I_{\perp} and I_{\parallel} denote intensity of the scattered light that is polarized perpendicular to the scattering plane and within the scattering plane, respectively. Note, when initially unpolarized solar radiation is scattered by asteroid, it acquires a partial linear polarization that is quantified with P .

The telescope was equipped with a commercially available CCD detector, FLI PL09000, which has a resolution of 3056×3056 pixels and pixel size of $12 \mu\text{m}$. The full field of view of the CCD detector is 243×243 arcmin with angular resolution of 4.73×4.73 arcsec per pixel. The CCD detector has a wide range of sensitivity with maximum at $\lambda \approx 0.57 \mu\text{m}$ and FWHM $0.46 \approx \mu\text{m}$ that embraces wavebands in the V and R filters in the *Johnson-Cousins photometric system*. We exploit a relatively small telescope that puts limitations on the use of photometric filters as they significantly reduce the apparent magnitude of the target.

Table 1 gives a summary of our observations showing the epoch of observation (the begin-cycle time, UT), the heliocentric r and geocentric Δ distances, phase angle α of Phaethon, exposure time T_{exp} , number of observations obtained in one night N , the mode of observation, and the obtained degree of linear polarization P with corresponding error bars.

Table 1. Log of observations of asteroid Phaethon

UT Date, 2017	r , au	Δ , au	α , °	T_{exp} , s	N	Mode	P , %
Dec. 14.41	1.05	0.083	33.6	30	526	Image	–
Dec. 16.41	1.02	0.069	57.9	40	18	ImageLP	17.23 ± 2.00
Dec. 17.49	1.00	0.070	73.2	40	30	ImageLP	31.86 ± 2.00

Discussion and Conclusion:

In Fig. 1 we plot the degree of linear polarization P in Phaethon as a function of phase angle α that was measured by four different groups. These four sets of data were obtained on different epochs and at different wavelength λ . Fornaiser et al. measured polarization in 2004 through the Johnson-Cousins V filter [3], Ito et al. in 2016 with the Johnson-Cousins R filter [5], Devogèle et al. in 2017 with the Johnson-Cousins $BVRI$ filters [6], we reproduce in Fig. 1 only the data obtained with the R filter though; whereas, in this work, we report measurements of 2017 with the polarimetric response being integrated over a wide range of wavelength. We also add fourth-degree polynomial fits to observations by Ito et al. and Devogèle et al. that are shown with a brown dashed line and blue solid line, respectively.

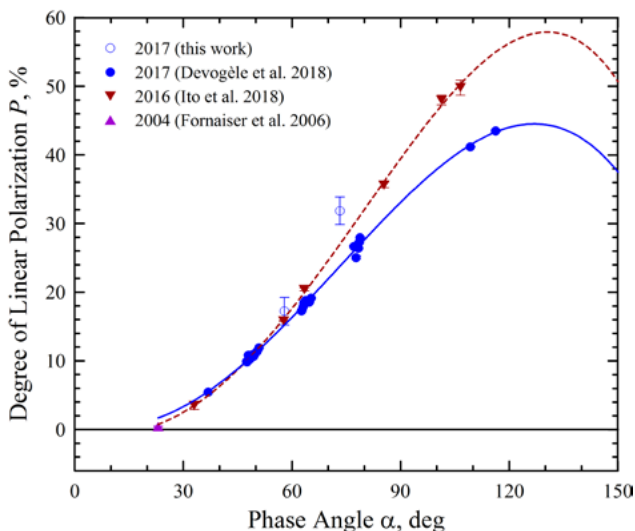


Fig. 1. The degree of linear polarization P in asteroid (3200) Phaethon as a function of phase angle α measured by four different groups.

As one can see in Fig. 1, all four data sets tend to group along a single curve at phase angle $\alpha < 60^\circ$. Interestingly to note, our measurement at $\alpha = 57.9^\circ$ within the error bars ($\sim 2\%$) matches the measurement at $\alpha = 57.7^\circ$ reported by Ito et al. [5]. Such resemblance suggests a weak wavelength dependence of the degree of linear polarization in Phaethon, at least, at this particular α . Note, Devogèle et al. report a wavelength dependence of polarization in Phaethon to be $\sim 1\text{--}2\%$ in the V and R filters at phase-angle range $\alpha \sim 60\text{--}70^\circ$ [6] that is consistent with our finding. We note also that Phaethon reveals no noticeable wavelength dependence in its photometric response [4].

At $\alpha > 60^\circ$, the degree of linear polarization measured by Ito et al. in [5] appears to be systematically higher as compared to what was detected by Devogèle et al. in [6], up to $\sim 10\%$ at $\alpha \sim 110^\circ$. Such a discrepancy could be explained with significant heterogeneity of Phaethon's surface and difference of observation conditions in 2016 and 2017 epochs. However, our observation at $\alpha = 73.2^\circ$ reveals polarization that is $\sim 8\%$ higher than what can be inferred from observations by Devogèle et al. [6] on the same 2017 apparition of Phaethon. Our measurement considerably exceeds ($\sim 5\%$) even that was reported by Ito et al. in [5]. This suggests that Phaethon may have at least three different types of regolith. However, this matter requires further polarimetric study of Phaethon.

Acknowledgment

Authors thank Dr. Gorden Videen, Dr. Yuriy Shkuratov, and Dr. Masateru Ishiguro for valuable comments on this work. OI thanks the SASPRO Programme, the People Programme (Marie Curie Actions) European Union's Seventh Framework Programme under REA grant agreement No. 609427, and the Slovak Academy of Sciences (grant Vega 2/32/14). IL research is supported by the National Scholarship Programme of the Slovak Republic (SAIA).

References:

- [1] Williams I. P., Wu Z. The Geminid meteor stream and asteroid 3200 Phaethon // *Mon. Not. R. Astron. Soc.* 1993. V. 262. No. 1. P. 231–248.
- [2] Jewitt D. The active asteroids // *Astron. J.* 2012. V. 143. No. 3. P. Article ID 66.
- [3] Fornasier S., Belskaya I. N., Shkuratov Yu. G., Pernechele C., Barbieri C., Giro E., Navasardyan H. Polarimetric survey of asteroids with the Asiago telescope // *Astron. & Astroph.* 2006. V. 455. No. 1. P. 371–377.
- [4] Ansdell M., Meech K. J., Hainaut O., Buie M. W., Kaluna H., Bauer J., Dundon L. Refined rotational period, pole solution, and shape model for (3200) Phaethon // *Astroph. J.* 2014. V. 793. No. 1. Article ID 50.
- [5] Ito T., Ishiguro M., Arai T., Imai M., Sekiguchi T., Bach Y. P., Kwon Y. G., Kobayashi M., Ishimaru R., Naito H., Watanabe M., Kuramoto K. Extremely strong polarization of an active asteroid (3200) Phaethon // *Nature Comm.* 2018. V. 9. Article number 2486.
- [6] Devogèle M., Cellino A., Borisov G., Bendjoya Ph., Rivet J.-P., Abe L., Bagnulo S., Christou A., Vernet D., Donchev Z., Belskaya I., Bonev T., Krugly Yu. N. The phase-polarization curve of asteroid (3200) Phaethon // *Mon. Not. R. Astron. Soc.* 2018. V. 479. No. 3. P. 3498-3508.

ASTEROID DISRUPTION BY PLANETS AT NEAR FLYBY

S.A. Voropaev

GEOIKHI RAS, Moscow, Kosygina str. 19, 117991

Keywords:

Asteroid, comet, flyby, tidal, disruption, NEO hazard, planet, Earth, Mars.

Introduction:

One of the most important questions in the NEO hazard context is at what distance from a large planet such a body will split, and how this distance depends on the physical properties. This has been under debate ever since Edouard Roche in the middle nineteenth century drew attention to the problem by calculating his famous expression for the splitting distance as

$$\Delta = 2.45 (\rho_p / \rho)^{1/3} R_p \quad (1)$$

where R_p and ρ_p are the radius and density of the planet, while ρ is the density of the body.

Roche used a homogeneous, self-gravitating liquid satellite on a circular orbit around a solid planet, rotating in a bound, direct fashion around an axis perpendicular to the orbital plane. He only took the effects of self-gravity and tidal forces into account, and the resulting critical breakup distance showed no reference to any other property of the body than its density. Later, ellipsoidal figures of liquid bodies at equilibrium under rotation and self-gravity were studied in detail [1]. An improved model was suggested by Aggarwal and Oberbeck [2], who used a solid, incompressible, homogeneous, elastic, and spherical body. They calculated the effects of tidal forces, material forces, and self-gravity and treated rotation in two different ways. In the first case, the body has no rotation and approaches the planet on a straight line (a *stray* body). In the second case, they treated rotation as Roche had done (a *spin-locked* body). In both cases, the failure plane turned out to be perpendicular to the line intersecting both the planet and the body. They discovered that a stray body (depending on the size, density, and tensile strength), would fracture from the surface and inward, or from the center and outward. When dealing with spin-locked bodies other fracture scenarios were added, e.g., a fracture starting at the surface, spreading inward to the center and then out to the surface again.

Later, triaxial bodies were introduced by Dobrovolskis along with a correction tensor for compressibility [3], but this treatment demands that the planet must lie along a principal axis of the body, which led to the same restraints on orbit and rotation as Roche had used. Although Dobrovolskis' stress tensors are valid for triaxial ellipsoids, he simplified the problem by considering spherical bodies when studying the actual yield behavior for ductile and brittle bodies and the splitting distances. For correct modeling, shapes and rotational period are as important as material properties, and must be treated as free parameters, independent of the orbit. Some of these requirements are met in the model presented by Davidsson for the spherical and two-axial ellipsoidal small bodies [4]. He used a semi-empirical approach in stress calculations however, by introducing a "pressure field" caused by the combination of stretching and compressive forces. One of the goals in this paper is to investigate how shape, rotation, and orientation constraint the tidal splitting distances, by means of the rigorous calculations with the exact analytical methods of elasticity theory. Our equations for the critical breakup distance and orientation of prolate-type asteroid during an planet close encounter as stray body can also be used to derive the density and material strength of other comets and asteroids from observed properties like their sizes, shapes, and rotation periods in similar approaches.

Analytical procedure:

The well-developed theory of gravitational and tidal potential can be used to calculate elastic deformations and stresses of small bodies. The force field strength F is determined by the gradient of the total potential

$$\mathbf{F} = \rho_0 \text{grad}[V(\mathbf{r})], V(\mathbf{r}) = V_g(\mathbf{r}) + V_\omega(\mathbf{r}) + V_t(\mathbf{r}) \quad (2)$$

where ρ_0 is the mean density, while V_g is the gravitational potential, V_ω is the centrifugal potential, and V_t is the tidal potential - of a rock. If the small body has an axis of symmetry, the problem simplifies to an exact analytical solution. In the cylindrical coordinate system, z is an axis of symmetry, and the displacement vector u can be presented as the expansion

$$\mathbf{u} = \mathbf{e}_\rho u_\rho + \mathbf{e}_z u_z \quad (3)$$

where $u_\rho(\rho, z)$, $u_z(\rho, z)$ and $u_\varphi = 0$ are the radial, vertical, and azimuth components of the displacement, respectively. In general, the Cartesian decomposition is appropriate, as in

$$\mathbf{u} = \mathbf{e}_x u_x + \mathbf{e}_y u_y + \mathbf{e}_z u_z \quad (4)$$

Then, the equilibrium equation of an isotropic body in the total (gravitational, tidal and centrifugal) force field takes the form

$$\mu \Delta u + (\lambda + \mu) \text{grad} (\text{div} u) = -\mathbf{F}, \quad (5)$$

where μ , λ are the Lamé constants and

$$\mu = E/2(1+\nu); \lambda = \nu E/(1+\nu)(1-2\nu), \quad (6)$$

where ν is the Poisson ratio, and E is the Young modulus of rock bodies.

Important to evaluate the deformation of a planetary body have the boundary conditions: magnitude and distribution of load on the surface. In general, they are three equations

$$2\mu [e_{11} \cos(n, e_x) + \frac{1}{2} e_{12} \cos(n, e_y) + \frac{1}{2} e_{13} \cos(n, e_z)] + \lambda e \cos(n, e_x) = f_1,$$

$$2\mu [e_{22} \cos(n, e_y) + \frac{1}{2} e_{12} \cos(n, e_x) + \frac{1}{2} e_{23} \cos(n, e_z)] + \lambda e \cos(n, e_y) = f_2,$$

$$2\mu [e_{33} \cos(n, e_z) + \frac{1}{2} e_{13} \cos(n, e_x) + \frac{1}{2} e_{23} \cos(n, e_y)] + \lambda e \cos(n, e_z) = f_3,$$

where e_{ij} are the components of the strain tensor, $e = e_{11} + e_{22} + e_{33}$ is the unit volume change, n - the normal vector to the surface, e_i - unit vectors of the Cartesian coordinate system and f_i - the corresponding projection of the surface forces. If the surface is free of load; as is usually the case for small bodies and asteroids then,

$$f_i = 0, \text{ on the surface} \quad (7)$$

Usually, to analyze the surface deformation of a small body, tension and the maximum stress deviator τ_{\max} are of the most interest. The latter is determined by the difference between the maximum σ_1 and minimum σ_3 main stresses:

$$\tau_{\max} = (\sigma_1 - \sigma_3)/2 \quad (8)$$

When τ_{\max} exceeds a certain limit value, a crack may begin to spread under suitable conditions [26]. Another possible reason for the disruption is stretching. Stone meteorites are unstable with respect to tensile efforts because of the weakening by numerous impacts (presence of microcracks, granular structure, etc.). To consider the internal load, $F_n = (X_n, Y_n, Z_n)$ on an imaginary small site inside the body with the normal vector, n , we apply the following notation

$$l = \cos(e_x, n); m = \cos(e_y, n); p = \cos(e_z, n)$$

In this case, the Cartesian components of the load F_n are

$$X_n = X_x^* l + X_y^* m + X_z^* p,$$

$$Y_n = Y_x^* l + Y_y^* m + Y_z^* p, \quad (9)$$

$$Z_n = Z_x^* l + Z_y^* m + Z_z^* p$$

Thus, for the site under consideration, the normal stress, N_n , will be determined as [27]

$$N_n = X_x^* l^2 + Y_y^* m^2 + Z_z^* p^2 + 2^* X_y^* m l + 2^* Y_z^* p m + 2^* Z_x^* l p \quad (10)$$

Tension is the composition of stretching (rotation and tidal) and pressure (gravity) forces; the final value of which is determined by the ratio of the intensities of the involved potentials:

$$I_g = \rho_0^2 a^2 G 4\pi;$$

$$I_\omega = \rho_0 a^2 \omega^2, \omega = 2\pi/T; \quad (11)$$

$$I_t = \rho_0 a^2 G M/D^3.$$

In which G is gravitational constant, T is the period of rotation, M is the central body mass, D is the distance from the central body to the satellite, and d is the largest semi-axis of the small body.

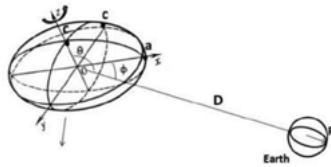


Fig. 1. 'Flyby' orbit of stray body, $d=D/R_p$.

Results:

A flyby when $\theta = \pi/2$ (see Fig.1) is a special case, when most non-diagonal members disappear and stress tensors components can be represented by means of the acting force compositions as

$$\sigma_{ij}(v, t, I_1, I_2, I_3, I_4, x^2/a^2, y^2/c^2, z^2/c^2),$$

where

$$\begin{aligned} I_1 &= I_g * F_1(\epsilon) - I_\omega - I_t * [3 * \cos^2(\phi) - 1], I_2 = -3/2 I_t \sin(2\phi), \\ I_3 &= I_g * F_2(\epsilon) - I_\omega - I_t * [3 * \sin^2(\phi) - 1], I_4 = I_g * F_2(\epsilon) + I_t \end{aligned} \quad (12)$$

Typical example, Eros is one of the most elongated asteroids, a potato-shaped body $\sim 34 \times 12 \times 12$ km. A member of the NEA group known as the Amors, Eros' orbit crosses the path of Mars and could be in future intersect the path of Earth.

For the Eros density, size and eccentricity, and the intensities of the involved potentials (12) are

$$I_g = 1.77 * 10^6 \text{ Pa}, I_\omega = 8.64 * 10^4 \text{ Pa}, I_t = (1/d^3) * 1.21 * 10^6 \text{ Pa}, d = D/R_e$$

where we use mean Earth' radius R_e and density $\rho_e = 5,5 \text{ g/cm}^3$. A simple comparison of these above values show that gravitational compression on Eros prevails and only at small distances from the Earth we can expect local stretching. Also, the eccentricity of Eros, $\epsilon = 0.946$, plays a significant role. To take into account the elastically properties of the rocks, Poisson' ratio will be enough and we assume $\nu \approx 0.2$ as usual for the ordinary chondrites [5]. Finally, the stress' distribution in the asteroid will be determined by the orientation of its main axis towards the central planet (Earth), i.e. angle ϕ

Conclusions:

We study the possible breakup of an prolate-type asteroid during a close flyby with Earth, Mars and other planet. New constraints for the Roche limit for solid biaxial ellipsoids are derived, taking the size, shape, density, material strength, rotation, and orientation of the flyby object into account. Results demonstrate that the shape and orientation have a significant effect on the tidal splitting distance. Therefore, the greatest tensile stresses occur when the prolate body is directed along the largest axis toward the central planet at the nearest point of a flyby. The lowest tensile stresses occur when the prolate body is oriented to the central planet at the same point along the short axis. As important example, this analysis shows that in a worst-case scenario, Eros could fly very close to the Earth and still survive a breakup.

Acknowledgment:

The study was performed by a grant of the Russian Science Foundation (project No. 17-17-01279).

References:

- [1] Chandrasekhar S. Ellipsoidal Figures of Equilibrium. Yale Univ. Press, 1969, 456 p.
- [2] Aggarwal, H. R. , Oberbeck V.R.. Roche limit of a solid body // Astrophys. J., 1974, V. 191, P. 577-588.
- [3] Dobrovolskis, A. R. Tidal disruption of solid bodies // Icarus, 1990, V. 88, P. 24-38.
- [4] Davidsson B. J. Tidal Splitting and Rotational Breakup of Solid Biaxial Ellipsoids // Icarus, 2001, V. 149, P. 375-383.
- [5] Voropaev S.A., Jianguo Y. et al. Features in Constructing a Certificate of Strength of Extraterrestrial Material by the Example of the Chelyabinsk Meteorite // Doklady Astronomy & Mechanics, 2017, V. 62, N 10, P. 486-489.

GRAVITATIONAL DEFORMATION OF SMALL SOLAR SYSTEM BODIES

E. N. Slyuta¹, S. A. Voropaev¹

¹*Vernadsky Institute of Geochemistry and Analytical Chemistry, Moscow, Kosygina str. 19, Russia, slyuta@mail.ru.*

Keywords:

Small bodies, planetary bodies, icy bodies, irregular shape, equilibrium shape, creep, yield strength, stress deviator, gravitational deformation, theory of elasticity.

Introduction:

Small Solar system bodies depending on composition have different irregular shape, which does not depend on the mass and size of the body [1]. In contrast, a sharp transition between small and planetary bodies is observed [2]. There is no creep in small bodies, and, regardless of their composition, all small Solar System bodies are solid elastic bodies having an ultimate strength (tensile and compressive strength) and yield strength [1]. This means that a small body will not deform until deviatoric stresses overcome the yield strength barrier for a solid elastic body and convert its irregular shape into an equilibrium one [3]. Mass of small bodies was not enough to become planetary bodies.

Theory:

If a stress deviator at the given point is more than the yield strength, then gravitational plastic deformation will occur. Gravitational deformation of the irregular figure of a small solid elastic body of the Solar System can be correctly considered in terms of elasticity theory. The modern classical theory of elasticity was mainly developed and used for solving the two-dimensional planar problems in different technical applications [4-6]. The gravitational attraction forces are mass forces (they are active in the volume of a whole body) and influence the final shape of the body itself. Because of this, from the strength of view of mathematical physics, the spatial, or three-dimensional, problem of elasticity theory under the conditions of gravitational compression is a feedback problem, where any change in the shape influences the gravitational potential and vice versa.

To analysis of gravitational deformation of a small body of greatest interest is the maximum stress deviator (τ_{max}), which is defined by the difference between the maximum (σ_1) and the minimum (σ_3) principal stresses [3]

$$\tau_{max} = \frac{\sigma_1 - \sigma_3}{2},$$

or, in the explicit form

$$\tau_{max} = \bar{\tau} \cos(\psi(\chi, \varepsilon, r, \theta)), \quad (1)$$

The obtained universal function (1) allows the gravitational deformation of a small body to be analyzed depending on the chemical and mineralogical composition and the shape parameters. Function is written in the form convenient for calculations [3]

$$T_{max} = \sigma_0 F(\varepsilon, V), \quad (2)$$

where the dimensional factor $\sigma = \frac{9}{8\pi} \frac{G_0 M^2}{a^2 bc}$; G_0 - the gravitational constant;

M – mass of a small body ($M = \frac{4}{3} \pi \rho_0 R_m^3$; R_m – a mean radius of the equal

sphere by volume); a, b and c – main axis of a body; $F(\varepsilon, v)$ – the dimensionless transcendental function.

Small icy bodies:

Mean ratio of the principal semiaxes b/a and c/a of small icy bodies (Fig. 1) is 0.81 and 0.61, respectively, and $a:b:c=1.64:1.33:1$ [1]. All small bodies in the

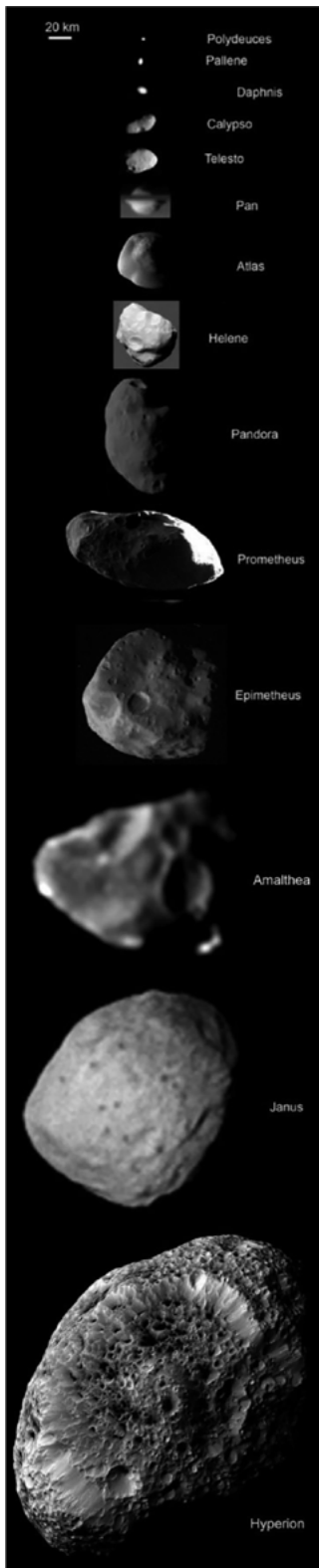


Fig. 1. Small icy bodies shown at the same scale. Photos by “Galileo” and “Cassini” (NASA).

Saturnian system are characterized by a high albedo (0.4 to 1.0) and consist mainly of water ice [7]. Density of small icy bodies ranges from 340 to 857 kg m⁻³ [8], i.e. much less than the density of ice due to high porosity.

Table 1. Stress deviator (τ_{max}) in small icy bodies

Small body	Diameter, km	R_m , km	Density, kg m ⁻³	τ_{max} , MPa
Pandora	104.0×81.0×64.0	40.7	490±60	0.019
Prometheus	135.6×79.4×59.4	43.1	480±90	0.012
Epimetheus	129.8×114×106.2	58.1	640±62	0.026
Amalthea	250×146×128	83.5	857±99	0.130
Janus	203.0×185×152.6	89.5	630±30	0.062
Hyperion	360.2×266×205.4	135	544±50	0.135

Icy Jovian satellite Amalthea is characterized by the highest density (857 kg m⁻³) [9] among icy small bodies (Table 1). It is the largest irregular satellite in the Jupiter system. Low albedo of a satellite (<0.1) is due to the presence on a surface of dust layer [10].

Mimas density is of 1149 kg m⁻³ [8], which is almost in twice higher than the density of porous small icy bodies not subjected to gravitational deformation. Assessing the value of stress deviator in Mimas, we obtain an upper limit of yield stress for the observed transition between the icy small and planetary bodies equal to 0.868 MPa (Fig. 2). The lower limit corresponds to the maximum stress deviator of the largest icy small body, i.e. Hyperion, and is estimated as 0.14 MPa (Table 1). Thus, the range of a yield stress for real composition of icy Solar system bodies, consisting mainly of water ice is 0.14 < σ_p < 0.87 MPa. The obtained value agrees well with the experimental data for pure ice, which define a range of yield strengths at low temperatures of 0.1 < σ_p < 2 MPa [11, references therein].

Using Hyperion parameters (Table 1) in (2) and guided by the maximum stress deviator of Mimas (0.87 MPa), we can estimate the maximum size that had a small porous icy body (ProtoMimas) until its gravitational deformation and turning it into Mimas. ProtoMimas radius is estimated as $R=465 \times 302$ km, and a mean radius is $R_m=349$ km which almost twice present size of Mimas (Fig. 3).

Summary:

The yield strength obtained for icy bodies fits well with available experimental data for pure ice and suggests that the observed transition between the icy small and planetary bodies is probably due to gravitational deformation of solid ice during soft accretion and accumulation, but not by heating and melting ice.

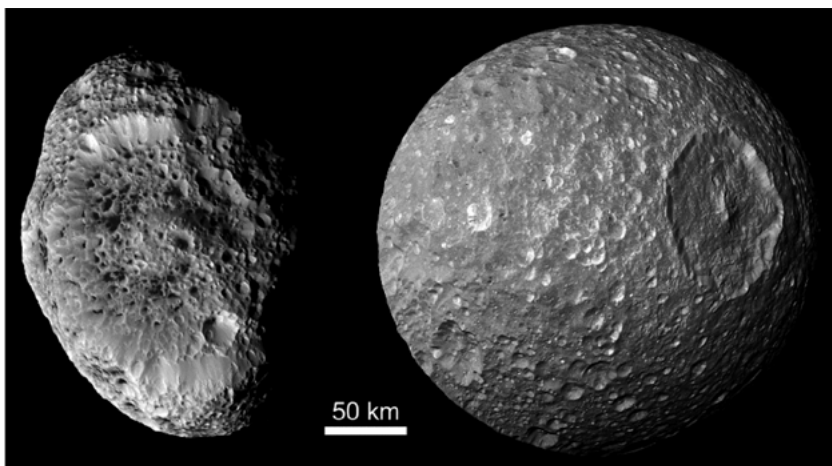


Fig. 2. Icy Saturn's satellites Hyperion (on the left) and Mimas (on the right) are shown at the same scale. Photos by "Cassini" (NASA).

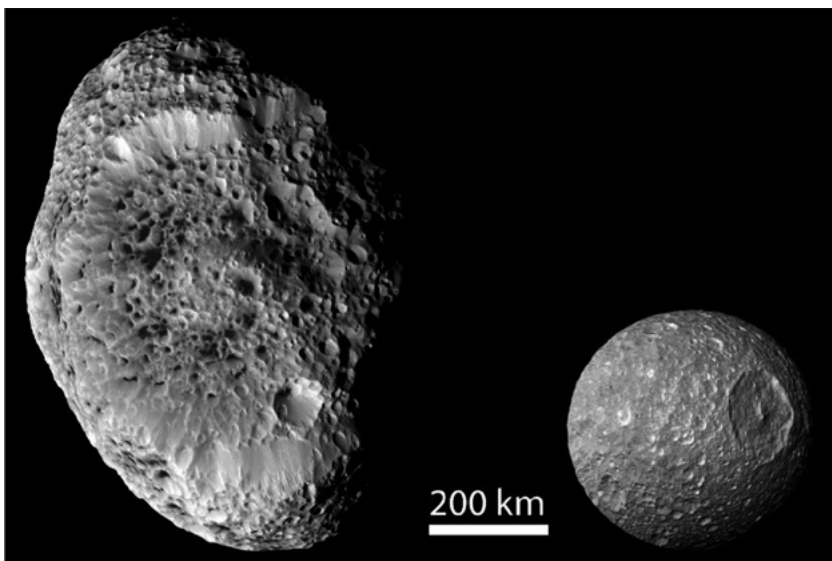


Fig. 3. Hypothetical ProtoMimas (on the left) until to gravitational deformation. To visualize ProtoMimas the image of Saturn's satellite Hyperion was used. Saturn's satellite Mimas (on the right) is shown at the same scale. Photos by "Cassini" (NASA).

References:

- [1] Slyuta E.N. Sol. Sys. Res. 2014. V. 48, №3. P. 217-238. [2] Slyuta E.N. and Voropaev S.A. Icarus. 1997. 129, 401-414. [3] Slyuta E.N., Voropaev S.A. Sol. Sys. Res. 2015. V. 49, №2. P. 123-138. [4] Novozhilov V.V. Theory of elasticity. Sudpromgiz, Leningrad. 1958. [5] Muskhelishvili N.I. Some basic problems of mathematical theory of elasticity. Nauka, Moscow. 1966. [6] Lurie A.I. Theory of elasticity. Moscow, Nauka. 1970. [7] Buratti B.J. et al. Icarus. 2010. 206. 524-536. [8] Thomas P.C. Icarus. 2010. 208. 395-401. [9] Anderson J.D. et al. Science. 2005. 308, 1291-1293. [10] Pasco D. et al. Icarus. 1992. 98, 38-42. [11] Goodman D.J. et al. Philos. Mag. 1981. A43, 665-695.

PRELIMINARY WORK ON PROMOTING ASTERIODS RADIO ASTRONOMICAL STUDY IN CHINA

J. Sun¹, J. Ping¹, S. Han²

¹ *National Astronomical Observatories of the Chinese Academy of Sciences, 20A Datun Road, Chaoyang District, Beijing, China;*

² *Beijing Aerospace Control Center*

Keywords:

Radar astronomy, CVN, NEA, Asteroid, Solar system object

Introduction:

Radar astronomy observations provide information on surface characteristics, orbits, rotations, and polar ices for a wide variety of solar system objects. Measurements of the distribution of echo power in time delay (range) and Doppler frequency (radial velocity) produce two-dimensional images that can provide spatial resolution as fine as a decameter if the echoes are strong enough. With adequate orientational coverage, such images can be used to construct detailed three-dimensional models, define the rotation state precisely, and constrain the object's internal density distribution. Radar signatures have been measured for 2012 TC4 near-Earth asteroids (NEAs) in China. We summarize preliminary results for radar-detected 2012 TC4 asteroid in 2017. Based on Chinese VLBI network (CVN), we present the current and future radar astronomy developments, taking into consideration the possible international joint observations.

References:

- [1] Ipatov A., Bondarenko Yu., Medvedev Yu., Mishina N., Marshalov D., Benner L. Radar observations of the asteroid 2011 UW158 // *Astronomical Letters*. 2016. V. 42. P. 850-855.
- [2] Bondarenko Yu., Medvedev Yu., Vavilov D., Marshalov D. Radar observations of near-Earth Asteroids using the Quasar VLBI Network Telescopes // *European Planetary Science Congress 2017*. 2017. V. 11.
- [3] Ostro S., Rosema K., Jurgens R. The Shape of Eros // *Icarus*. 1990. V. 84. P. 334-351.

THE INTERNATIONAL PHOBOS/DEIMOS SURFACE CHARACTERIZATION AND SITE SELECTION WORKING GROUP: 2018 STATUS

T. Duxbury¹, J.-P. Bibring², M. Fujimoto³, R. Jaumann⁴, D. Titov⁵,
A. Zakharov⁶, N. Seregina¹

¹Physics and Astronomy Department, George Mason University, Fairfax, Virginia, USA, tduxbury@gmu.edu;

²Institut d'Astrophysique Spatiale, University of Paris-South, d'Orsay, France;

³Institute of Space and Aeronautics, Japanese Aerospace Exploration Agency, Tokyo, Japan;

⁴Institute of Planetary Research, German Aerospace Center, Berlin, Germany;

⁵European Space Research and Technology Center, European Space Agency, Noordwijk, Netherlands;

⁶Space Research Institute, Russian Academy of Sciences, Moscow, Russia.

Keywords:

Phobos, Deimos, Mars, MMX, Characterization, Site Selection

2018 Status:

The activities of the working group will be described about its interactions with: international conferences (EGU, EPSC, DPS, COSPAR, 7M-S3); space agency advisory groups (SBAG, MEPAG); flight projects (MMX, MEX, ODY, MRO, MAVEN, UAE Mars) and searchable catalog / level-2 / level-3 data standards (PDS) and orientation / digital terrain models (NAIF SPICE). To characterize the Martian moon surfaces, high spatial and spectral resolution data are needed to be registered (Figure 1) to a precision digital terrain model and then map projected (Figure 2) to produce level-3 products to be analyzed by GIS tools (TREK, PILOT, SBMT, . . .)

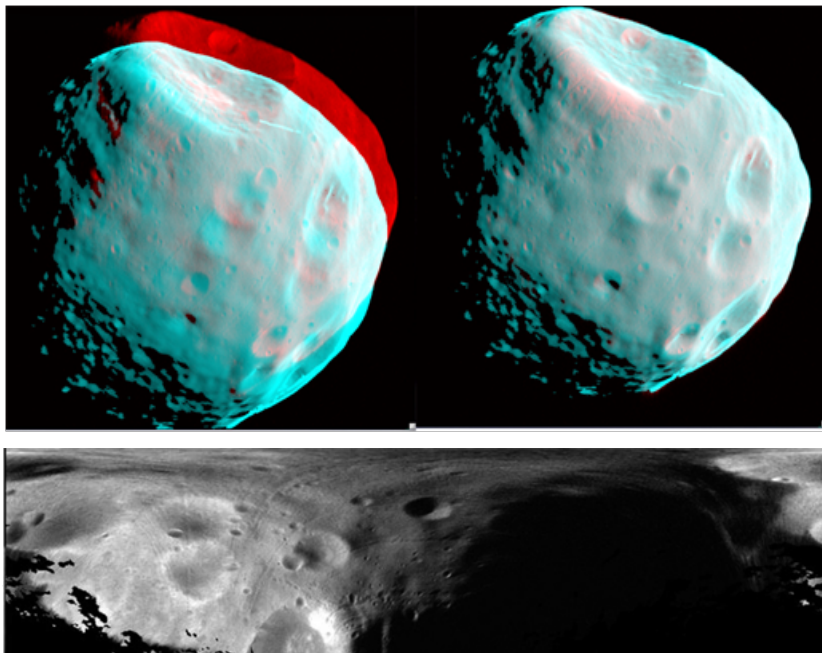


Fig. 1. Top left-unregistered model/image; Top right-registered; Bottom: Map projected.

PROPOSALS TO THE RUSSIAN PROGRAM FOR RESEARCH OF SMALL BODIES OF THE SOLAR SYSTEM

E.N. Slyuta¹, A.E. Shakhanov², R.V. Elnikov³

¹*Vernadsky Institute of Geochemistry and Analytical Chemistry, Moscow, Kosygina str. 19, Russia, slyuta@mail.ru;*

²*Lavochkin Association, Federal Space Agency (ROSCOSMOS), Khimky, Moscow Region, Leningradskaya Str. 24, shakhanov@laspacespace.ru;*

³*Research Institute of Applied Mechanics and Electrodynamics (RIAME), Moscow, Volokolamskoe Sh. 4, Russia, elnikov_rv@mail.ru*

Keywords:

Small bodies, the Main Belt, metallic asteroids, Psyche, Pandora, Hesperia, M-asteroids, stone asteroids, stationary plasma thrusters, spacecraft.

Introduction:

The long-term program for studying small bodies of the Solar System by spacecraft consists of three main stages: 1) flyby of several Near-Earth asteroids by a spacecraft being put into Near-Earth orbit as a payload; 2) flyby and researching of metallic asteroids in the Main Belt; 3) delivery to the Earth of samples from the Main Belt.

Object selection:

On the basis of the analysis of priority scientific problems of studying small bodies at the present stage, and also taking into account the analysis of foreign space missions to small bodies of the Solar system, a decision was made to select metallic asteroids as priority objects for studying by spacecraft (Table 1). The position of the objects in the list reflects their priority for research - from the highest priority to the least priority. The priority list is

Table 1. Priority list of metallic and metal-silicate asteroids.

No	Asteroid	Diameter d, km	Mean d, km	b/a	c/a	Density, g cm ³
1	16 Psyche	279×232×189	226±23	0.77	0.60	4.5±1.4
2	55 Pandora	-	66.7	0.83	0.69	-
3	69 Hesperia	135×106×98	110	0.79	0.70	-
4	129 Antigone	152×109×95	113±17	0.72	0.63	-
5	216 Kleopatra	217×94×81	135±5.8	0.43	0.37	6.92(3.6±0.4)
6	347 Pariana	-	51±5	0.74	0.57	-
7	758 Mancunia	-	85±7	-	-	-
8	779 Nina	-	77±2	-	-	-
9	785 Zwetana	57×46×45	49	0.80	0.79	-
10	872 Holda	-	30	-	-	-
11	22 Kalliope		162±3			3.35
12	77 Frigga	-	69	-	-	-
13	97 Klotho		83±5			
14	92 Undina	-	126	-	-	-
15	110 Lydia		89±9			
16	184 Deiopea	-	66	-	-	-
17	337 Devosa	-	59	-	-	-
18	417 Suevia	-	40	-	-	-
19	1124 Stroobantia	-	25	-	-	-
20	1146 Biarmia	-	31	-	-	-
21	1355 Magoeba	-	13	-	-	-

due to the further selection of the object down the list for ballistic calculations, taking into account the possible launch date of spacecraft in the period 2025-2035 yrs. Metallic asteroids, the composition of which was confirmed by radar data, are shown in bold type (items 1-10) [1].

Stage 1:

In all projected missions, the spacecraft is equipped with an electric propulsion system (ERDU) based on stationary plasma thrusters (SPD). For various variants of space missions, the composition of the ERDU, the starting mass of the spacecraft, etc. are different. To implement the 1st stage of the program, whose mission is the flyby of several near-Earth asteroids, the design appearance of the spacecraft with the marching ERDU with a total mass of 709.18 kg (including fuel of 300 kg and scientific equipment of 39 kg) was developed (Fig. 1).



Fig. 1. The working position of the spacecraft with the ERDU (general view).

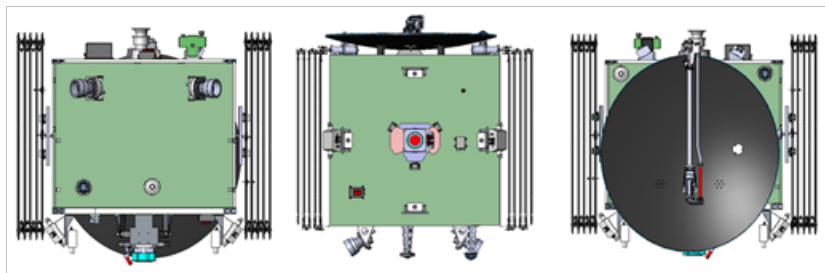


Fig. 2. The transport position of the spacecraft with ERDU (general view).

Flight of the spacecraft in the 2026 era allows ensuring the flyby of five Near-Earth asteroids (Table 2). The mission duration (together with the helical orbit near the Earth) is 2180.6 days (5.97 years). The total fuel consumption of the ERDU is 247.547 kg. The total motor time of the ERDU is 12090.277 h.

Table 2. The main characteristics of the heliocentric section of the mission-1 for the epoch of 2026.

Event	Date	SC mass, kg	Remaining fuel, kg	Flyby velocity, km/s
Exit from the Earth's gravisphere	11.01.2026	526.51279	133.487	--
Entry into the heliocentric orbit of phasing	02.12.2026	481.527	101.527	--
Flyby asteroid 2007 VV6	22.01.2028	477.230	97.230	5.431
Flyby asteroid 2007 UY1	19.02.2029	471.656	91.656	6.391
Flyby asteroid 2011 YD29	03.05.2029	465.918	85.918	7.130
Flyby asteroid 2005 YR3	05.06.2030	461.255	81.255	7.386
Flyby asteroid 2007 RT12	04.04.2031	412.452	32.452	7.289

Stage 2:

For the implementation of the second stage of the program, whose mission is the flyby of several metal asteroids in the Main Belt, a spacecraft was designed with a marching ERDU based on SPD-100VU with a total mass of

1848 kg, including fuel (820 kg) and a scientific equipment package (200 kg) (Fig. 3). The spacecraft is launched as the main (target) payload. As part of the space transportation system used for launching the spacecraft onto the departing hyperbolic trajectory, the Soyuz-2.1b LV is used and the Fregat-MT upper stage.

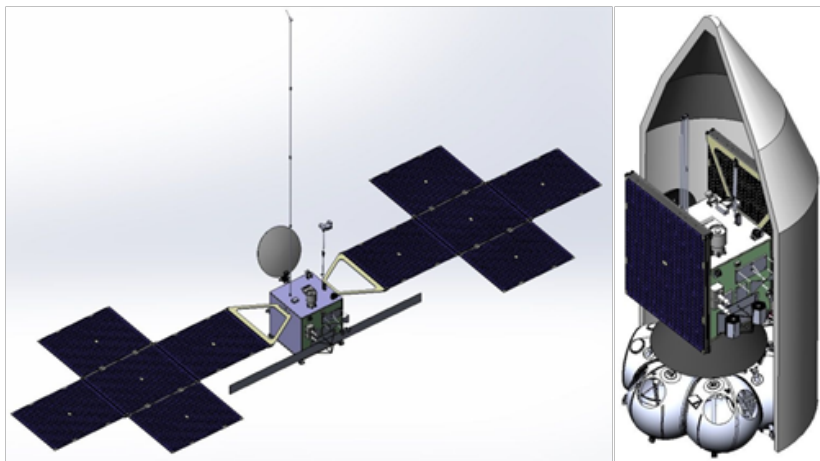


Fig. 3. The working (to left) and transport (to right) position of the spacecraft with the ERDU (general view).

The heliocentric section of the spacecraft trajectory includes one gravity-assist maneuver at the Earth. Different sequences of asteroids flyby from the priority list were analyzed (Table 1). The most economical option from the considered (in terms of fuel consumption) was the route: Earth - Earth - 55 Pandora - 16 Psyche - 69 Hesperia (Table 3). The total fuel consumption of the ERDU for this mission was 715.740 kg. The motor time of the ERDU is 17478.488 h, the total mission duration is 3115.136 days (8.53 years).

Table 3. The main characteristics of heliocentric sections of the mission-2.

Event	Date	SC mass, kg
Exit from the Earth's gravisphere	21.10.2025 04:28:10.970 UTC	1849.928
Gravity-assist at the Earth	03.04.2027 10:29:49.690 UTC	1606.152
Flyby 55 Pandora	22.05.2028 20:39:09.305 UTC	1606.152
Flyby 16 Psyche	03.03.2030 23:24:45.523 UTC	1296.480
Flyby 69 Hesperia	02.07.2034 07:43:48.541 UTC	1134.188

The total fuel consumption of the ERDU for this mission was 715.740 kg. The motor time of the ERDU is 17478.488 h. The total mission duration is 3115.136 days (8.53 years).

Stage 3:

This mission is in the initial stages of development. To assess the energy and time costs for the implementation of a closed Earth-asteroid-Earth mission, the asteroid 10 Hygiea is considered as an example of the mission objective. As a transport system the Soyuz-2 LV the modernization stage 1b and the Fregat-MT are considered. Starting mass of the spacecraft turns out to be equal to about 1533 kg. When using ERDU on the basis of SPD-100D, the total fuel consumption is 550 kg. The total mission duration is 11.5 years.

References:

[1] Slyuta E.N. (2013) Physicomechanical Properties and Gravitational Deformation of Metallic Asteroids. Sol. Sys. Res. V. 47, №2. P. 109-126.

JUNO'S SURPRISING RESULTS AT JUPITER

S.J. Bolton¹, J.Connerney²

¹*Southwest Research Institute, San Antonio, TX, USA,
sbolton@swri.edu;*

²*Space Research Corporation, Annapolis, MD, United States,
jack.connerney@nasa.gov*

Keywords:

Overview of Juno's results at Jupiter

Introduction:

NASA's Juno mission to Jupiter launched in 2011 and arrived at Jupiter on July 4, 2016. Juno's scientific objectives include the study of Jupiter's interior, atmosphere and magnetosphere with the goal of understanding Jupiter's origin, formation and evolution. An extensive campaign of Earth based observations of Jupiter and the solar wind were orchestrated to complement Juno measurements during Juno's approach to Jupiter and during its orbital mission around Jupiter. This presentation provides an overview of results from the Juno measurements and the collaborative campaign during the early phases of Juno's prime mission. Scientific results include Jupiter's interior structure, magnetic field, deep atmospheric dynamics and composition, and the first in-situ exploration of Jupiter's polar magnetosphere and aurorae.

A SHORT INTRODUCTION TO MAGNETOSPHERE-IONOSPHERE-THERMOSPHERE STUDIES AT JUPITER WITH JUNO

M. Blanc¹, S.J. Bolton², J. Connerney³, F. Bagenal⁴, B. Mauk⁵ and the Juno Magnetosphere Working Group

¹*IRAP, Toulouse, France*

²*SwRI, San Antonio, TX, USA*

³*NASA/Goddard Space Flight Center, Greenbelt, MD, USA*

⁴*LASP, Boulder, CO, USA*

⁵*APL-JHU, Laurel, MD, USA*

Keywords:

Jupiter exploration; Planetary magnetospheres; Magnetosphere-Ionosphere-Thermosphere coupling; Space Science missions.

We will present the exceptional potential offered by the Juno mission, currently in orbital operations at Jupiter, for an in-depth study of magnetosphere-ionosphere-thermosphere coupling processes at Jupiter. We will place a special emphasis on the specific role played by the auroral magnetic field lines and the—largely unknown—transport processes taking place therein in the exchange of momentum between the Jovian upper atmosphere and the magnetodisk and in the establishment of their imperfect rotational coupling.

We will illustrate this subject by preliminary measurements and results from the outstanding suite of Juno instruments, which altogether provide access to fields (FGM and WAVES), particles (JEDI and JADE) and to the structure and dynamics of the Jovian auroras on the two polar caps (JIRAM and UVS).

This presentation will be prepared under the guidance of the Magnetosphere Working Group of the Juno mission and will essentially reflect its work.

JUNO MAGNETOMETER OBSERVATIONS OF JUPITER'S MAGNETIC FIELD AND MAGNETOSPHERE

J.E.P. Connerney^{1,2}, D.J. Gershman², S. Kotsiaros^{2,3}, J.L. Joergensen⁴, P.S. Joergensen⁴, J.M.G. Merayo⁴, J. Bloxham⁵, K.M. Moore⁵, S.J. Bolton⁶, S.M. Levin⁷

¹*Space Research Corporation, Annapolis, MD, United States, jack.connerney@nasa.gov;*

²*NASA Goddard Space Flight Center, Greenbelt, MD, United States;*

³*University of Maryland College Park, College Park, Maryland, United States;*

⁴*Technical University of Denmark (DTU), Lyngby, Denmark;*

⁵*Harvard University, Cambridge, MA, United States;*

⁶*Southwest Research Institute, San Antonio, TX, United States;*

⁷*Jet Propulsion Laboratory (JPL), Pasadena, CA, United States*

Keywords:

Jupiter's magnetic field; magnetosphere; magnetodisc;

Introduction:

The Juno spacecraft, in orbit about Jupiter since July 4, 2016, is mapping Jupiter's magnetic and gravitational potential fields and probing its deep atmosphere in search of clues to the planet's formation and evolution [1]. Juno is also instrumented to conduct the first exploration of the polar magnetosphere [2] and to acquire images and spectra of its polar auroras and atmosphere.

Juno is equipped with two magnetometer sensor suites [3], located 10 and 12 m from the center of the spacecraft at the end of one of Juno's three solar panel wings. Each contains a very accurate (100 ppm absolute vector accuracy) fluxgate magnetometer (FGM) sensor and a pair of co-located non-magnetic star tracker camera heads, providing accurate attitude determination for the FGM sensors. The co-located star cameras monitor the attitude of the magnetometer sensors continuously (providing up to 4 quaternions/s), correcting for the slight deformation of the spacecraft solar array experienced during maneuvers and perijove passes. Such deformations, if not measured and corrected, would otherwise compromise measurement vector accuracy.

Juno's 53.5-day orbit trajectory carries her science instruments from pole to pole in approximately 2 hours, with a closest approach to within $\sim 1.05 R_J$ of the center of the planet (one $R_J = 71,492$ km, Jupiter's equatorial radius), just a few thousand km above the clouds. Repeated periapsis passes will eventually encircle the planet with a dense net of observations equally spaced in longitude ($< 12^\circ$ at the equator) and optimized for characterization of the Jovian dynamo [3]. Such close passages are sensitive to small spatial scale variations in the magnetic field and therefore many such passes are required to bring the magnetic field into sharp focus. Nevertheless, a dramatically detailed model ("JRM09", for Juno Reference Model after 9 orbits) can be extracted from a partial solution to a more complicated model representation (e.g., 20 degree/order), providing the first new information about Jupiter's magnetic field in decades. This model is a degree 10 spherical harmonic representation of the internal field.

Jupiter's internal magnetic field exhibits a dramatic hemispheric asymmetry, with a very non-dipolar northern hemisphere contrasting a southern hemisphere that appears very dipolar [4]. An equatorial belt of positive radial flux is interrupted by an isolated reverse-polarity patch situated near the equator at about 90 degrees system III west longitude. These features make for an interesting environment for charged particle motion on drift shells with equatorial field strengths above about 2 Gauss. Comparison with earlier magnetic field models is suggestive of secular variation [5,6] but inconsistencies among prior analyses call for caution in interpretation. We present

an overview of the magnetometer observations obtained during Juno's first two years in orbit [7,8] in context with prior observations and those acquired by Juno's other science instruments.

References:

- [1] Bolton, S. J. and the Juno Science Team (2010) // The Juno mission. Proceedings of the International Astronomical Union Symposium, No. **269**: 92-100.
- [2] Bagenal, F., Adriani, A., Allegrini, F., et al. // Magnetospheric science objectives of the Juno mission, Space Sci. Rev., doi 10.1007/s11214-014-0036-8.
- [3] Connerney, J. E. P., Benn, M., Bjarno, et al. The Juno Magnetic Field Investigation, Space Sci. Rev., doi: 10.1007/s11214-017-0334-z, 2017.
- [4] Connerney, J.E.P., Kotsiaros, S., Oliverson, R.J., Espley, J.R., Joergensen, J.L., Joergensen, P.S. et al., A new model of Jupiter's magnetic field from Juno's first nine orbits. Geophys Res. Lett., 45, 2018, doi: 10.1002/2018GL077312.
- [5] Connerney, J.E.P., & Açuna, M.H.. Jovimagnetic secular variation // Nature, 297, 313 - 315, 1982.
- [6] Ridley, V. A., and Holme, R.. Modeling the Jovian magnetic field and its secular variation using all available magnetic field observations // J. Geophys. Res. Planets, 121, doi:10.1002/2015JE004951, 2016.
- [7] Bolton, S. J., Adriani, A., Adumitroaie, V., et al.: Jupiter's interior and deep atmosphere: the first pole-to-pole pass with the Juno spacecraft // Science, doi: 10.1126/science.aal2108, 2017.
- [8] Connerney, J. E. P., Adriani, A., Allegrini, F., et al., Jupiter's Magnetosphere and Aurorae Observed by the Juno Spacecraft During its First Polar Orbits // Science, 10.1126/science.aam5928, 2017.

THE AURORAL FOOTPRINTS OF GALILEAN MOONS AT JUPITER

A. Mura, A. Adriani

National Institute for Astrophysics, Italy

JIRAM, the Jovian InfraRed Auroral Mapper on board NASA/Juno mission, is an infrared camera and a spectrometer working in the infrared spectral range 2-5 μm . One of the primary scientific objectives of the instrument are the study of the infrared aurora emitted from H_3^+ excited by electron precipitation. The instrument was able to get its observations during the PJ1 and from PJ4 to PJ 15 passes, resulting in an almost complete coverage of the auroral emission from the planet. Here we present a highlights from the results obtained from those observations, with particular emphasis on the auroral footprints. The spectral analysis of the emission from these features is also presented

MULTI-INSTRUMENT INVESTIGATION FOR JUPITER LIGHTNING-INDUCED WHISTLER AND SFERIC EVENTS USING JUNO

M. Imai¹, O. Santolík^{2,3}, S.T. Brown⁴, I. Kolmašová^{2,3}, W.S. Kurth¹, M.A. Janssen⁴, G. B. Hospodarsky¹, D. A. Gurnett¹, S.J. Bolton⁵, S.M. Levin⁴

¹*Department of Physics and Astronomy, University of Iowa, Iowa City, Iowa, USA;*

²*Department of Space Physics, Institute of Atmospheric Physics, The Czech Academy of Sciences, Prague, Czechia;*

³*Faculty of Mathematics and Physics, Charles University, Prague, Czechia;*

⁴*Jet Propulsion Laboratory, California Institute of Technology, Pasadena, California, USA;*

⁵*Space Science Department, Southwest Research Institute, San Antonio, Texas, USA*

Keywords:

Jupiter, Juno, Waves, MWR, whistler, sferic

Introduction:

The discovery of Jupiter's lightning was made independently by the Voyager 1 plasma wave instrument recording Jovian low-frequency whistler waves [1] and images of Jovian optical flashes [2]. Jupiter's whistlers were observed in a frequency range of a few tens of Hz to 7 kHz [3], having the restriction of propagation below either the local electron cyclotron frequency or local electron plasma frequency, whichever is lower. Clouds illuminated from below by lightning were visible in optical wavelengths from Voyager 1 [2], Voyager 2 [4], Galileo [5], Cassini [6], and New Horizons [7]. However, none of the Jovian lightning observations were carried out simultaneously by two or more instruments onboard a spacecraft. Another opportunity to examine the nature of Jupiter lightning is provided by the Juno polar-orbiting spacecraft that arrived at Jupiter on 5 July, 2016. Since then, Juno has maintained a 53-day eccentric polar orbit about Jupiter, collecting data during seven perijove passes from PJ1 on 27 August, 2016, through PJ8 on 1 September, 2017 [8]. The perijove lightning observations were made at radial distances between $1.05 R_J$ and $5 R_J$, where $R_J = 71,492$ km. During these perijove passes, the Juno Microwave Radiometer (MWR) instrument [9] originally recorded 377 lightning radio pulses called "sferics" in a narrowband channel at 600 MHz within 100-ms integration intervals [10]. More recently, the compiled catalogue was updated to a total of 383 sferic detections. The radio and plasma wave (Waves) instrument [11] has recorded 1627 Jovian low-dispersion whistlers on the time scale of one to tens of milliseconds and at frequencies below 20 kHz, revealing that Jupiter's lightning flashes are more frequent than previously detected, with lightning rates similar to Earth [12]. Here, we report the first multi-instrument investigation of Jupiter lightning by examining whistler and sferic events obtained by the Waves and MWR instruments onboard Juno [10, 12]. We found 71 overlapping Waves and MWR observations during which a sferic was detected. Eleven of these also included whistler detections. By measuring distances between the MWR boresight and the whistler exit point, we estimated the distance whistlers propagate below the ionosphere before exiting to the magnetosphere, called the coupling distance, to be typically one to several thousand of km with a possibility of no sub-ionospheric propagation. We present the details of whistler and sferic event analysis and show a new constraint on the atmospheric whistler propagation.

References:

- [1] Gurnett D.A., et al. Whistlers observed by Voyager 1: Detection of lightning on Jupiter // *Geophys. Res. Lett.* 1979. V. 6(6) P. 511-514.
- [2] Cook A.F., Duxbury T.C., Hunt G.E. First results on Jovian lightning // *Nature* 1979. V. 280 P. 794.

- [3] Kurth W.S., et al. A summary of whistlers observed by Voyager 1 at Jupiter // *Icarus* 1985. V. 61(3) P. 497-507.
- [4] Borucki W.J., Magalhães J.A. Analysis of Voyager 2 images of Jovian lightning // *Icarus* 1992. V. 96(1) P. 1-14.
- [5] Little B., et al. Galileo images of lightning on Jupiter // *Icarus* 1999. V. 142(2) P. 306-323.
- [6] Dyudina U.A., et al. Lightning on Jupiter observed in the H α line by the Cassini imaging science subsystem // *Icarus* 2004. V. 172(1) P. 24-36.
- [7] Baines K.H., et al. Polar lightning and decadal-scale cloud variability on Jupiter // *Science* 2007. V. 318(5848) P. 226-229.
- [8] Bolton S.J., et al. The Juno mission // *Space Sci. Rev.* 2017. V. 213(1) P. 5-37.
- [9] Janssen M.A., et al. MWR: microwave radiometer for the Juno mission to Jupiter // *Space Sci. Rev.* 2017. V. 213 P. 139-185.
- [10] Brown S., et al. Prevalent lightning sferics at 600 megahertz near Jupiter's poles // *Nature* 2018. V. 558(7708) P. 87-90.
- [11] Kurth W.S., et al. The Juno Waves investigation // *Space Sci. Rev.* 2017. V. 213 P. 347-392.
- [12] Kolmašová I., et al. Discovery of rapid whistlers close to Jupiter implying similar lightning rates to those on Earth // *Nat. Astron.* 2018. V. 2 P. 544-548.

ELECTRON ACCELERATION TO HIGH ENERGIES VIA WHISTLER-MODE WAVE-PARTICLE INTERACTIONS IN THE JOVIAN POLAR REGIONS

S.S. Elliott¹, D.A. Gurnett¹, W.S. Kurth¹, B.H. Mauk², R.W. Ebert³, G.Clark², P. Valek³, F. Allegrini^{3,4}, S.J. Bolton³

¹University of Iowa, Iowa City, IA, 52242, USA;

²The Johns Hopkins University Applied Physics Laboratory, Laurel, MD, 20723, USA;

³Southwest Research Institute, San Antonio, TX, 78238, USA;

⁴Department of Physics and Astronomy, University of Texas at San Antonio, San Antonio, TX, 78249, USA

Keywords:

Jupiter, electron acceleration, wave-particle interactions, whistler-mode waves, Landau resonance, solitons, Hamiltonian chaos

Introduction:

One discovery recently made by the Juno spacecraft was the observation of upward-traveling energetic electrons (from tens of keV to several MeV) over the Jovian polar cap [1, 2, 3]. The electrons have nearly power law energy distributions (Figure 1), indicative of a stochastic acceleration process.

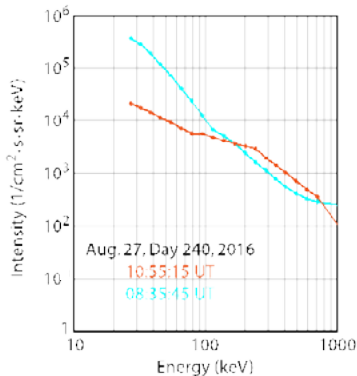


Fig. 1. Example energy spectra for upward-traveling electrons over the polar cap during perijove 1, demonstrating power law-like energy distributions (adapted from [2]).

Intense upward-propagating broadband whistler-mode waves were also observed over the entire Jovian polar cap region [4]. These whistler-mode waves are analogous to auroral hiss at Earth, which is known to be generated by beams of electrons called inverted-Vs [5, 6]. However, the Jovian whistler-mode waves are propagating nearly along the magnetic field, not near the resonance cone, which causes the waves to be more electromagnetic than typical terrestrial auroral hiss. This electromagnetic property may be due to the very strong planetary magnetic field and higher electron beam velocities that caused the whistler-mode waves. The energy flux of the upward-propagating whistler-mode waves is comparable to and strongly correlated with the energy flux of the upward-traveling energetic electrons, suggesting that the whistler-mode waves may be accelerating the electrons. Here, we propose a theory for the acceleration of upward-traveling polar cap electrons that involves a mechanism similar to the wave-particle interactions that occur in a linear accelerator. We believe that a downward field-aligned current over the polar cap generates strong downward parallel electric fields and upward electron beams in the low-density regions of Jupiter's upper ionosphere. This mechanism is similar to the formation of inverted-Vs in Earth's auroral regions [7, 8]. The Jovian upward-traveling electron beams produce intense upward-propagating broadband whistler-mode waves, similar to auroral hiss at Earth, via the Landau resonance. As the whistler-mode waves propagate upward out of the inverted-V

source region, the waves are absorbed by the plasma, thereby accelerating the electrons. The growth and damping of the whistler-mode waves can be analyzed by looking at the growth rate equation for a simple Maxwellian electron velocity distribution function (Figure 2). Where the growth rate switches from positive (wave growth) to negative (wave damping) depends on the wave phase velocity relative to the electron beam velocity (Figure 3).

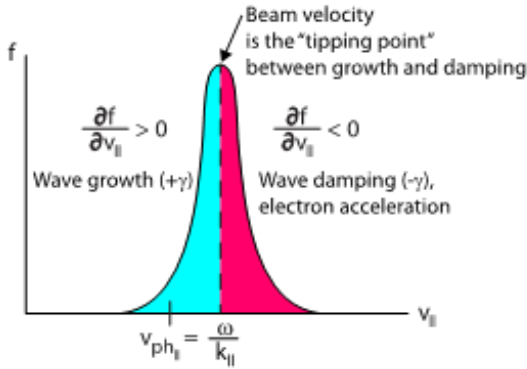


Fig. 2. Maxwellian distribution function for an electron beam in the parallel direction. The blue region indicates wave growth and pink indicates wave damping and electron acceleration. The electron beam velocity relative to the wave phase velocity determines the “tipping point”.

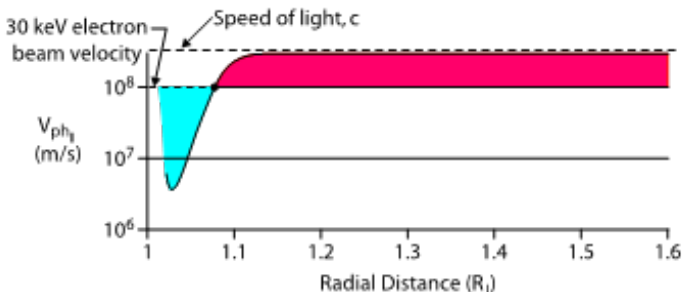


Fig. 3. Whistler-mode wave phase velocity as a function of radial distance. A beam velocity for a 30 keV electron beam and the speed of light are represented by dashed lines. Blue and pink colors indicate wave growth and wave damping respectively (as in Figure 2). This phase velocity model was created using an ionospheric density model, a magnetospheric density model, and a magnetic field model.

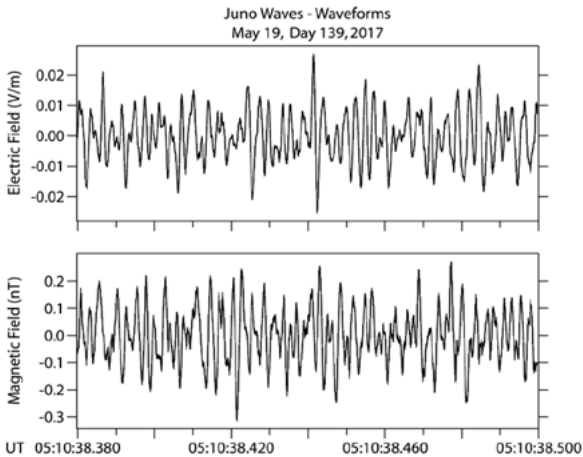


Fig. 4. Example electric (top) and magnetic (bottom) waveforms for the northern polar region on perijove 6. The waves are electromagnetic, and show signatures similar to solitons. The irregularity in the electric field suggests possible stochastic electron acceleration.

We attribute the stochastic power law-like energy spectrum (Figure 1) of the accelerated electrons to the development of Hamiltonian chaos (velocity space diffusion), the signature of which is indicated by the occurrence of spiky soliton-like variations in the whistler-mode electric fields [9] (Figure 4). Another mechanism that contributes to electron acceleration to high energies is the rapid increase in the phase velocity of the whistler-mode waves with increasing altitude (Figure 3), which could accelerate some of the electrons trapped in the wave field to very high relativistic energies. On auroral field lines, the whistler-mode waves are more intense and the waves and electrons are both up- and down-going. This paper will discuss our proposed electron acceleration mechanism for the Jovian polar cap upward-traveling electrons in detail and its applications to the electrons and waves observed on auroral field lines.

References:

- [1] J.E.P. Connerney, A. Adriani, F. Bagenal, S. J. Bolton, S. Cowley, J.-C. Gerard, G.R. Gladstone, D. Grodent, G. Hospodarsky, et al., Jupiter's magnetosphere and aurora observed by the Juno spacecraft during its first polar pass // *Science*, 2017, doi:10.1126/science.aam5928.
- [2] B.H. Mauk et al., Juno observations of energetic charged particles over Jupiter's polar regions: analysis of mono- and bi-directional electron beams // *Geophys. Res. Lett.*, 2017, 44, 4410-4418, doi:10.1002/2016GL072286.
- [3] F. Allegrini et al., Electron beams and loss cones in the auroral regions of Jupiter // *Geophys. Res. Lett.*, 2017, 44, 7131-7139, doi:10.1002/2017GL073180.
- [4] S.S. Tetrack, D.A. Gurnett, W.S. Kurth, M. Imai, G.B. Hospodarsky, S.J. Bolton, J.E.P. Connerney, S.M. Levin, and B.H. Mauk, Plasma waves in Jupiter's high latitude regions // *Observations from the Juno spacecraft*, *Geophys. Res. Lett.*, 2017, 44, 4447-4454, doi:10.1002/2017GL073073.
- [5] L.A. Frank, K.L. Ackerson, Observations of charged particle precipitation into the auroral zone // *J. Geophys. Res.*, 1971, 76(16), 3612-3643, doi: 10.1029/JA076i016p03612.
- [6] D.A. Gurnett, Electric field and plasma observations in the magnetosphere, in *Critical Problems of Magnetospheric Physics* // *Proceedings of the Symposium Jointly Sponsored by COSPAR, IAGA, and URSI, May 11-13, 1972 in Madrid, Spain*, ed. By E. R. Dyer, Washington, DC: National Academy of Sciences, 1972, pp. 123-138.
- [7] Gurnett, D. A., and L. A. Frank, VLF hiss and related plasma observations in the polar magnetosphere // *J. Geophys. Res.*, 1972, 77(1), 172-1190, <https://doi.org/10.1029/JA077i001p00172>.
- [8] D.A. Gurnett, S.D. Shawhan, and R R. Shaw, Auroral hiss, Z more radiation, and auroral kilometric radiation in the polar magnetosphere // *DE 1 observations*, *J. Geophys. Res.*, 1983, 88(A1), 329-340, doi:10.1029/JA088iA01p00329.
- [9] H. Matsumoto, H. Kojima, T. Miyatake, Y. Omura, M. Okada, I. Nagano, M. Tsutsui, Electrostatic solitary waves (ESW) in the magnetotail: BEN wave forms observed by Geotai // *Geophys. Res. Lett.*, 1994, 21, 2915-2918

JUPITER'S GRAVITY FIELD DETERMINATION FROM DOPPLER TRACKING OF THE JUNO SPACECRAFT

P. Racioppa¹, D. Durante¹, L. Iess¹, V. Notaro¹, W.M. Folkner², M. Parisi², Y. Kaspi³, E. Galanti³, T. Guillot⁴, W. B. Hubbard⁵, D.J. Stevenson⁶, J.D. Anderson⁷, D. R. Buccino², L. Gomez Casajus⁸, A. Milani⁹, R. Park², D. Serra⁹, P. Tortora⁸, M. Zannoni⁸, H. Cao⁶, R. Helled¹⁰, J.I. Lunine¹¹, Y. Miguel⁴, B. Militzer¹², S. Wahl¹², J.E.P. Connerney¹³, S.M. Levin², S.J. Bolton⁷

¹*Sapienza Università di Roma, 00184 Rome, Italy;*

²*Jet Propulsion Laboratory/Caltech, Pasadena, CA 91109, USA;*

³*Weizmann Institute of Science, Rehovot 76100, Israel;*

⁴*Observatoire de la Côte d'Azur, 06304 Nice, France;*

⁵*Lunar and Planetary Laboratory, University of Arizona, Tucson, AZ 85721, USA;*

⁶*California Institute of Technology, Pasadena, CA 91125, USA;*

⁷*Southwest Research Institute, San Antonio, TX 78238, USA;*

⁸*Università di Bologna, 47100 Forlì, Italy;*

⁹*Università di Pisa, 56127 Pisa, Italy;*

¹⁰*University of Zurich, 8057 Zurich, Switzerland;*

¹¹*Cornell University, Ithaca, NY 14853, USA;*

¹²*University of California, Berkeley, CA 94720, USA;*

¹³*NASA Goddard Space Flight Center, Greenbelt, MD 20771, USA.*

Keywords:

Jupiter, Juno, gravity, Doppler, orbit determination, zonal winds, differential rotation.

On July 4, 2016, the Juno spacecraft completed the Jupiter orbit insertion maneuver, entering into a highly eccentric polar orbit around the gas giant with a period of about 53 days and a pericentre at an altitude of 4500 km above the cloud tops and a latitude of 3° N. As of July 2018, Juno completed its 14th orbit, 6 of which were dedicated to gravity investigation.

A prime scientific goal of the mission is the accurate determination of the Jupiter gravity field enabled by a very accurate tracking system. The spacecraft is equipped with an advanced telecommunication system that includes a Ka-band frequency translator (KaT) enabling a large reduction of the noise and systematic effects from charged particles, such as solar plasma and the Io torus (generated by Io's volcanic activity). The telecommunication radio link at X-band can be operated simultaneously with the radio science link at Ka band and may be used during gravity orbits to further reduce dispersive noises. The tracking system is augmented by an advanced water vapor radiometer located at the Goldstone DSN complex, near the DSS 25 antenna, allowing a strong reduction of the noise from Earth's wet troposphere. With this configuration, used for the first time in a planetary gravity field determination, the tracking system provides range rate data accurate to 10 $\mu\text{m/s}$ at 60s integration time.

We report here on the latest result from the analysis of all available gravity orbits and comment on the implications for models of Jupiter's internal structure [1]. Although limited to six pericenter passes, the current data set already provides a very good estimation of the zonal coefficients of Jupiter's gravity field. The observed north-south asymmetry described by the odd harmonics offers a strong evidence for zonal winds extending from the cloud level down to 2000-3000 km deep into the planet [2]. The observed values of the even harmonics (J8 and J10 in particular) reveal that the differential rotation below the wind depth, if present, shall be much weaker, at least by an order of magnitude [3]. The observed coefficients also suggest that the Jupiter's core is diluted over a large volume [4].

Juno will continue its mission at Jupiter until 2021, completing 25 gravity orbits and enabling the measurement of the planet's precession constant. Simulations shows that if the mission could be extended, it will be possible to attain sensitivity to smaller gravitational signatures that are currently undetectable. Those may include a non-zonal component of the gravity field induced by meridional flows, frequency-dependent tides, and a time-variable gravity associated to acoustic oscillations.

References:

- [1] Iess, L., Folkner W.M., Durante D., Parisi M., Kaspi Y., Galanti E., Guillot T., Hubbard W.B., Stevenson D.J., Anderson J.D., Buccino D.R., Casajus L., Milani A., Park R., Racioppa P., Serra D., Tortora P., Zannoni M., Cao H., Helled R., Lunine J.I., Miguel Y., Militzer B., Wahl S., Connerney J.E.P., Levin S.M., Bolton S.J. The measurement of Jupiter's asymmetric gravity field // *Nature*. 2018, 555, 220-222.
- [2] Kaspi, Y., Galanti E., Hubbard W.B., Stevenson D.J., Iess L., Guillot T., Bloxham J., Cao H., Durante D., Folkner W.M., Helled R., Ingersoll A.P., Lunine J.I., Miguel Y., Militzer B., Parisi M., Wahl S., Connerney J.E.P., Levin S.M., Bolton S.J. The extension of Jupiter's jet to a depth of thousands of kilometers. *Nature* // 2018, 555, 223-226.
- [3] Guillot, T., Miguel Y., Militzer B., Hubbard W.B., Galanti E., Kaspi Y., Cao H., Wahl S., Iess L., Folkner W.M., Helled R., Stevenson D.J., Lunine J.I., Reese D., Biekman A., Parisi M., Durante D., Connerney J.E.P., Levin S.M., Bolton S.J. A suppression of differential rotation in Jupiter's deep interior // *Nature*. 2018, 555, 227-230.
- [4] Wahl, S. M., Hubbard, W. B., Militzer, B., Guillot, T., Miguel, Y., Movshovitz, N., Kaspi, Y., Helled, R., Reese, D., Galanti, E., Levin, S., Connerney, J. E., Bolton, S. J. Comparing Jupiter interior structure models to Juno gravity measurements and the role of a dilute core // *Geophysical Research Letters*. 2017, 44(10), 4649-4659.

SATURN'S GRAVITY FIELD DETERMINATION FROM DOPPLER TRACKING OF THE CASSINI SPACECRAFT

P. Racioppa¹, D. Durante¹, L. Iess¹, B. Militzer², Y. Kaspi³, P. Nicholson⁴, W.B. Hubbard⁵, E. Galanti³, S. Wahl²

¹*Sapienza Università di Roma, 00184 Rome, Italy;*

²*University of California, Berkeley, CA 94720, USA;*

³*Weizmann Institute of Science, Rehovot 76100, Israel;*

⁴*Cornell University, Ithaca, NY 14853, United States;*

⁵*Lunar and Planetary Laboratory, University of Arizona, Tucson, AZ 85721, USA*

Keywords:

Saturn, Cassini, gravity, Doppler, orbit determination, zonal winds, differential rotation.

Cassini completed its mission on September 2017 by diving into Saturn's atmosphere. In the last phase of the mission, the Grand Finale, Cassini completed 22 highly eccentric orbits passing between the planet and the inner edge of the rings. Six of those orbits were dedicated to analysis of the planet's gravity field and have been planned to have extensive coverage from both NASA-DSN and ESA-ESTRACK ground stations. Range rate data, accurate up to about 20 $\mu\text{m/s}$ (for a count time of 30s) have been acquired for a time span of 1-1.5 days around each closest approach, located about 5 degrees below Saturn's equator.

We report here on the latest results from the analysis of the data set. Range rate observables from the six gravity Grand Finale orbits have been fitted in a multiarc weighted least square filter to obtain an accurate estimate of the Saturn's gravity field. The model for Saturn's gravitation potential includes even and odd zonal spherical harmonics up to a degree 20 and is completed with additional potential from the three most massive rings (A, B, and C rings). We measured values of J_8 and J_{10} zonal harmonics far from the predictions of interior models that assume a uniform rotation of the planet. This deviation can be explained by strong differential rotation and zonal winds extending very deep into the planet.

In addition, the spacecraft orbit, with pericenters between Saturn and its rings, allowed for the first time to separate the gravitational signature of the rings from that of the planet's oblateness. Although the acquired data do not allow an estimate of the mass of each ring, they provide enough accuracy on the total ring mass to contribute to the fundamental debate on the age and origin of the rings.

ON THE CARBON ISOTOPE RATIO IN TITAN'S ATMOSPHERE AND INTERIOR

V.A. Krasnopolsky

Moscow Institute of Physics and Technology (PhySTech), Moscow, Russia, vlad.krasn@verizon.net

Keywords:

Titan, atmosphere, carbon isotopes, evolution, photochemistry.

Introduction:

Carbon has two natural isotopes with $^{12}\text{C}/^{13}\text{C} = 89.4$ on the Earth. Methane is the parent carbon species on Titan with mixing ratio decreasing from 5.7% near the surface to 1.5% above the tropopause at 75 km. Averaging a few measurements, the weighted-mean $^{12}\text{C}/^{13}\text{C} = 89.7 \pm 1.0$ in methane on Titan (Nixon et al. [1]). The methane lifetime is rather short on Titan, ≈ 30 Myr. Nixon et al. [1] compared $^{12}\text{C}/^{13}\text{C}$ in methane with that in the outer Solar System and evaluated the isotope fractionation in the loss of methane on Titan. Using data of three photochemical models, they concluded that methane was delivered into Titan's atmosphere 60-1600 Myr ago and its amount exceeded the present value by a factor 4-70. Mandt et al. [2] established an upper limit of 0.5 Byr to the outgassing timescale. Here we will use photochemical products to calculate the carbon isotope fractionation on Titan.

Initial data and models

$^{12}\text{C}/^{13}\text{C}$ in methane on Titan were measured using mass spectrometers at the Huygens probe [3] and the Cassini flybys [2] as well as the CIRS spectra of the CH_4 bands:

Table 1. $^{12}\text{C}/^{13}\text{C}$ in methane on Titan

$^{12}\text{C}/^{13}\text{C}$	Instrument	Reference
91.1 ± 1.4	Huygens/GCMS	Niemann et al. [3]
88.5 ± 1.4	Cassini/INMS	Mandt et al. [2]
86.5 ± 8.2	Cassini/CIRS	Nixon et al. [1]
89.7 ± 1.0	Weighted-mean	

From Nixon et al. [1].

$^{12}\text{C}/^{13}\text{C}$ ratios in the outer Solar System are equal to

Table 2. $^{12}\text{C}/^{13}\text{C}$ in the outer Solar System

$^{12}\text{C}/^{13}\text{C}$	Species	Object	Reference
92.6 ± 4.3	CH_4	Jupiter	Niemann et al. [4]
91.8 ± 8.1	CH_4	Saturn	Fletcher et al. [5]
90 ± 4	CN	comets	Hutsemekers et al. [6]
91.3 ± 2.7	all	weighted-mean	
<u>92.4 ± 5.4</u>	<u>CH_4</u>	<u>weighted-mean</u>	

Fractionation of carbon k_{12}/k_{13} was calculated by Nair et al. [8] for photolysis of methane and by Nixon et al. [1] for the reaction $\text{C}_2\text{H} + \text{CH}_4 \rightarrow \text{C}_2\text{H}_2 + \text{CH}_3$. Nixon et al. [1] adopted no fractionation in all other processes. Their calculations are based on comparison of $^{12}\text{C}/^{13}\text{C}$ on Titan with that in the outer Solar System using the above reaction as the only fractionation process. Mandt et al. [2] analyzed 30 Cassini/INMS flybys and obtained the isotope fractionation factor of methane escape at 0.736 ± 0.045 . Using the Cassini/INMS observations, De la Haye et al. [9] evaluated the total loss of carbon from Titan by sputtering and ion escape at $(2.8 \pm 2.1) \times 10^7 \text{ cm}^{-2} \text{ s}^{-1}$.

Budget of methane in Titan's atmosphere is given in Table 3 based on our photochemical model [7]:

Table 3. Budget of methane on Titan [7]

Loss by photolysis	2.69+9	$k_{12}/k_{13} = 0$
Loss by $C_2H + CH_4$	1.62+9	1.019
Other loss	5.29+9	?
Total loss	9.60+9	
Production	1.13+9	?
Flow from surface	8.47+9	
	7.09 kg cm ⁻² Byr ⁻¹	
<u>Residence time</u>	<u>32.4 Myr</u>	

$$2.69 + 9 = 2.69 \times 10^9 \text{ cm}^{-2} \text{ s}^{-1}.$$

Our model

The basic idea of our approach is to use $^{12}C/^{13}C$ measured in photochemical products of methane (Table 4) as a tool to understand the carbon isotope fractionation.

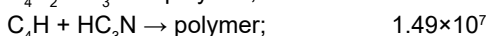
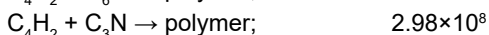
Table 4. $^{12}C/^{13}C$ in photochemical products on Titan

<u>Species</u> $^{12}C/^{13}C$	<u>Instrument</u>	<u>C + P^a</u>	
CO	89.9 ± 3.4	ALMA [10]	-
C2H2	84.8 ± 3.2	CIRS [11]	3.12+8b
C2H6	89.8 ± 7.3	CIRS [11]	2.05+9
C4H2	90 ± 8	CIRS [12]	1.98+9
HCN	89.8 ± 2.8	ALMA [13]	1.47+8
HC3N	79 ± 17	CIRS [14]	1.13+9
CO2	84 ± 17	CIRS [15]	1.78+6
All	88.3 ± 1.8	weighted-mean (uncertainties)	
All	88.3 ± 3.0	wieght-ed-mean	

^aCondensation plus polymerization from table 1 and 4 in [7], in numbers of carbon atoms.

$$^b 3.12+8 = 3.12 \times 10^8 \text{ cm}^{-2} \text{ s}^{-1}.$$

Usually the measured isotope ratios are weighted by their uncertainties, and the weighted-mean $^{12}C/^{13}C$ is 88.3 ± 1.8 . However, another important factor is the contribution of each species to production of the haze by condensation and polymerization. These data are taken from the photochemical model [7]. The most significant reactions of polymerization in the model are



Here CR is the column rate, and we adopt that $^{12}C/^{13}C$ in C_4H and C_3N are equal to those in C_4H_2 and HC_3N , respectively. The calculated weighted-mean carbon isotope ratio is 88.3 ± 3.0 in the haze on Titan. Comparing with the isotope ratio of methane, the haze is slightly enriched in heavy carbon. This conclusion is opposite to that in [1] and agrees with the recent laboratory simulations of Titan's haze (Sebree et al. [16]).

A minor correction for sputtering and ion escape results is $^{12}C/^{13}C = 88.5 \pm 3.0$ for a source of methane that compensate for its loss. That may be outgas-

sing and/or cryovolcanism of, say, methane clathrate hydrate $\text{CH}_4 \cdot 5.75\text{H}_2\text{O}$. However, there are some difficulties associated with this explanation (see for example [1]).

Another scenario with injection of, e.g., ten times the present methane abundance ≈ 300 Myr ago and its gradual decrease by the photochemistry, results in $^{12}\text{C}/^{13}\text{C} = 87.1 \pm 7$ for the injected methane. Compared with the permanent outgassing, this scenario is less favorable in both the assumption and the result (the greater difference between the isotope ratio and that in the outer Solar System). Another scenario with a constant outgassing that started some time ago is an intermediate case. Evidently its result is intermediate as well.

Acknowledgement.

This work is supported by a grant of Russian Science Foundation to Moscow Institute of Physics and Technology (PhysTech) and V.A. Krasnopolsky.

References

- [1] Nixon C.A. et al. *Astrophys. J.* 759, 159, 2012.
- [2] Mandt K. et al. *Astrophys. J.* 759, 160, 2012.
- [3] Niemann H.B. et al. *JGR* 115E, E12006, 2010.
- [4] Niemann H.B. et al. *JGR* 103, 22831, 1998.
- [5] Fletcher L.N. et al. *Icarus* 199, 351, 2009.
- [6] Hutsemekers H. et al. *Astron. Astrophys.* 440, L21, 2005.
- [7] Krasnopolsky V.A. *Icarus* 236, 83, 2014.
- [8] Nair H. et al. *Icarus* 175, 32, 2005.
- [9] De la Haye V. et al. *JGR* 112, A07309, 2007.
- [10] Serigano J. et al. *Astrophys. J. Lett.* 821, L8, 2016.
- [11] Nixon C.A. et al. *Icarus* 195, 778, 2008.
- [12] Jolly A. et al. *Astrophys. J.* 714, 852, 2010.
- [13] Molter E.M. et al. *Astron. J.* 152, 42, 2016.
- [14] Jennings D.E. et al. *Astrophys. J. Lett.* 681, L109, 2008.
- [15] Nixon C.A. et al. *Astrophys. J. Lett.* 681, L101, 2008.
- [16] Sebree J.A. et al. *Icarus* 270, 421, 2016.

THE MULTI-SHELL MODELS OF CELESTIAL BODIES WITH AN INTERMEDIATE LAYER OF FLUID: DYNAMICS IN THE CASE OF THE LARGE VALUES OF THE EKMAN NUMBER

V.V. Sidorenko¹, S.M. Ramodanov²

¹*Keldysh Institute of Applied Mathematics, Miusskaya sq., 4, 125047 Moscow, Russia, sidorenk@keldysh.ru;*

²*Mechanical Engineering Research Institute, Malyi Kharitonievskiy s-st., 4, 101990 Moscow, Russia*

Keywords:

Rotational motion, inner core, ice shell

The structure of celestial bodies can often be described as a set of three components: an internal solid core, an intermediate liquid layer, and an outer solid shell. The contribution of these components to the total mass of the body is significantly different in objects of different nature. For example, for planets, the mass of the inner core is much less than the mass of the outer solid shell, called the mantle in planetary physics (Figure 1a). For some satellites of Jupiter and Saturn, the outer shell is an ice layer whose thickness is substantially less than the radius of these objects (Figure 1b). Depending on which component is dominant, the reference frame in the studies of rotational motion of such multi-shell models is connected either with the outer shell and then the relative motion of the liquid and inner core is considered, or with a massive inner component and then the relative displacements of the outer shell are investigated.

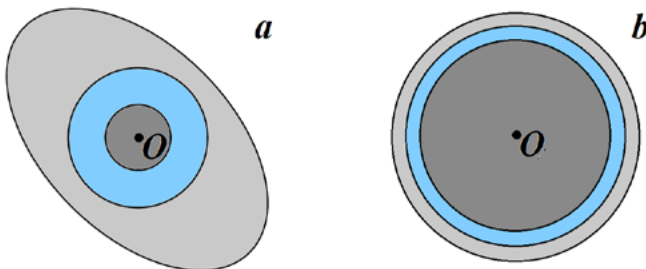


Fig. 1. Examples of celestial bodies described by multi-shell models with an intermediate liquid layer: a – “planet” (small solid inner core), b – satellite with a thin outer ice shell.

One of the key parameters in the theory of rotating fluids is the Ekman number [1]

$$E = \frac{\mu}{\rho_l \omega_{rot} R_c^2}$$

where μ and ρ_l are the viscosity and the density of the liquid, ω_{rot} is the characteristic angular velocity, R_c is the outer radius of the cavity filled with liquid. If $E \gg 1$, then the motion of the liquid in the cavity is characterized as creeping one. Approximate formulas describing the velocity field in the case of creeping flow can be obtained by omitting the relative accelerations in the Navier-Stokes equation.

Following [2], we show that under the condition $E \gg 1$ the consideration of the rotational motion of a multi-shell system can be reduced to studying the rotation of a rigid body under the action of a torque of a special form.

Acknowledgments:

Our investigations were supported by RFBR (grant 17-01-00902).

References:

- [1] Greenspan, H.P. The Theory of Rotating Fluids. Cambridge University Press // 1968.
- [2] Chernousko, F.L. Motion of a Rigid Body with Cavities Containing a Viscous Fluid // NASA Technical Translations, 1972.

PLANETARY EXPLORATION, HORIZON 2061: FROM KEY QUESTIONS TO REPRESENTATIVE SPACE MISSIONS AND ENABLING TECHNOLOGIES

The Planetary Exploration Horizon 2061 team¹: M. Blanc, A.M. Hari, N. Krupp, R. Rodrigo, K. Szego, J. Zarnecki, M.F. A'Hearn, M. Anand, W. Benz, S. Bolton, P. Bousquet, E. Bunce, M.T. Capria, A. Coustenis, D. Daou, V. Dehant, J.F. Démonet, B. Foing, M. Fujimoto, H. Hammel, A. Ivanov, S. Jacobson, J.P.Kneib, O. Korablev, M. Lambrechts, H. Lammer, J. Lasue, J.P. Lebreton, S. Mackwell, N. Mangold, B. Marty, N. Mason, A. Masters, S. Maurice, L. Prockter, H. Rauer, D.A. Senske, C. Sotin, T. Spohn, V. Sterken, F. Tian, N. Tosi, F. Westall, P. Wurtz, L. Zelenyi, P. Beauchamp, H. Boithias, J. Broquet, A. Ferri, P. Falkner, M. Grande, L. Guo, G. Preti, D. Lebleu, Y. Tsuda
The Horizon 2061 W.G.², Air and Space Academy: M.Blanc, A.M. Mainguy, J.P. Lebreton, J.L. Bertaux, J. Broquet, M.A. Perino, R. Somma, M. Bouffard, A. Hauchecorne, W. Kofman, A. de Leffe, M. Heppener

¹The Planetary Exploration Horizon 2061 Team;

²The Horizon 2061 W.G., Air and Space Academy

Keywords:

Planetary exploration; Solar System; Origins of Planets and Life; Habitability; Planetary Systems; Space missions; Space technologies.

We will present the results of the first two steps of a foresight exercise to produce a community Vision of Planetary Exploration up to the 2061 horizon, named H2061 for short. 2061 is a symbolic date corresponding to the return of Halley's comet into the inner Solar System and to the centennial of the first Human space flight. This Vision is progressively built on the basis of a concurrent analysis of the four "pillars" of planetary exploration: (1) The key priority questions to be addressed in Solar System science; (2) The representative planetary missions that need to be flown to address these questions; (3) The enabling technologies needed to fly this set of ambitious missions; (4) The supporting infrastructures, both space-based and ground-based, to be made available.

Starting from a concept formulated by the H2061 Working Group of the Air and Space Academy, this exercise is currently implemented in three successive steps: the first step, accomplished in September 2016 in the framework of an ISSI-Europlanet forum held in Bern on September 13-15, 2016, addressed the connection between pillars 1 and 2. The second one, accomplished at the EPFL in Lausanne on April 23 to 25, 2018 as a community workshop, focused mainly on pillars 3 and 4.

We will present the initial results of these first two steps to the international planetary science community assembled at the 9M-3S Symposium and will invite all its participants to join the preparation and implementation of step 3, to be hosted in Toulouse in 2019, which will work on establishing a synthetic view of the four pillars via a critical confrontation of the "scientific wishes" and of the technical capacities, both projected to the 2061 Horizon.

JUNO AND THE NEW RENAISSANCE

T.C. Clarke

*Mission Juno, 5000 Risinghill Road, Altadena, California, USA,
tccclarke@earthlink.net*

Keywords:

Renaissance; Convergence of art and science; spectrum of human creativity.

Introduction:

There is an intangible societal need to connect with the universe. This is why the space program is so popular. Through the space program the people of the world can touch the universe, touch infinity.

Spacecraft reconnaissance of our solar system continues a legacy of exploration ingrained in our psyches. As a human race, we explore. We ask, Who am I and where do I come from? In the process of this exploration the aura and soul of NASA's Juno mission to the planet Jupiter, like the Medici of the Renaissance, has inspired, facilitated and embodied a broad spectrum of human creativity, including not only science and technology, but also history and literature, art and music, and visualization and public engagement. Indeed, through Juno the world is witness to a remarkable convergence of art and science, witness to a New Renaissance. Juno is an ambassador to the universe of this New Renaissance.

In my presentation I will unveil the Juno mission at Jupiter, the Earth encounter that slung it to Jupiter, and the amazing cultural connections that define its mission. I will speak of Juno's public engagement program called Science in a Fishbowl. The Science in a Fishbowl program encourages public participation in processing, in often artistic ways, imaging data taken of Jupiter by JunoCam, the camera on Juno. I will show the best of these citizen scientist works of art. I will also assemble and describe a 3-D scale model of the orbital mission of Juno at Jupiter. The scale of the model is $1'' = 2 R_J$.



Fig. 1. Juno Trajectory Model and Poster Paper at AOGS 2018

In summary, I will unveil a dimension of the Juno mission to the planet Jupiter that will appeal to a broad sector of the global public.

MIGRATION OF INTERPLANETARY DUST PARTICLES TO THE EARTH AND THE MOON

S. I. Ipatov

V.I. Vernadsky Institute of Geochemistry and Analytical Chemistry of RAS, Moscow, Russia, siipatov@hotmail.com

Keywords:

Migration, dust, Earth, Moon, probabilities of collisions

Introduction:

Earlier (e.g., in [1-4]) I studied the probabilities of collisions of migrating dust particles produced by different small bodies with planets. Below I compare the probabilities of collisions of such particles with the Earth and the Moon and with the embryos of the Earth and the Moon. The probabilities were also calculated based on results of new calculations of migration of dust particles from test initial orbits of planetesimals located at different distances from the Sun.

Integration of motion of dust particles and the calculations of probabilities of their collisions with celestial bodies:

The orbital evolution of ~20,000 dust particles with initial orbits close to orbits of various asteroids and comets was studied in [1-4] during dynamical lifetimes of particles (until all particles reached 2000 AU from the Sun or collided with the Sun). The BULSTO code from the integration package [5] was used for such integration. The gravitational influence of planets, the Poynting-Robertson drag, radiation pressure, and solar wind drag were taken into account. The influence of Mercury was omitted in most runs (exclusive for orbits close to that of Comet 2P/Encke). For particles started from small bodies, the ratio β between the radiation pressure force and the gravitational force varied from ≤ 0.0004 to 0.4. For silicates, such values of β correspond to particle diameters d between ≥ 1000 and 1 microns; d is proportional to $1/\beta$. New calculations of migration of dust particles were made for particles initially located at different distances from the Sun. For such particles, I considered β equal to 0.04 and 0.004. Diameters of such silicate particles were about 12 and 120 microns, respectively.

Based on the orbital elements of particles during their dynamical lifetimes I calculated the probability of collisions of dust particles with the Earth (p_E), with the Moon (p_M), and with the embryos of the Earth and the Moon (p_{E01} and p_{M01}) which masses were smaller by a factor of 10 than masses of the Earth and the Moon, respectively. The algorithm of calculations of the probabilities was described in [6], and later it was improved in [7]. In Table 1 the probabilities of collisions at different values of β are presented for particles launched from asteroids with numbers from 1 to 500 (runs marked as *ast*), discovered trans-Neptunian objects (*tno*), Comet 10P/Tempel 2 (10P, $a \approx 3.1$ AU, $e \approx 0.53$, $i \approx 12^\circ$), Comet 39P/Oterma (39P, $a \approx 7.25$ AU, $e \approx 0.25$, $i \approx 2^\circ$), Comet 2P/Encke at perihelion (2Pper, $a \approx 2.2$ AU, $e \approx 0.85$, $i \approx 12^\circ$), test long-period comets (*lp*) at eccentricity $e=0.995$ and perihelion distance $q=0.9$ AU, and test Halley-type comets (*ht*) at $e=0.975$ and $q=a(1-e)=0.5$ AU (for *lp* and *ht* runs, initial inclinations i were from 0 to 180° , and particles were launched near perihelia).

Probabilities of collisions of migrating dust particles with the Earth, the Moon, and their embryos for dust particles produced by asteroids and comets:

For dust particles produced by asteroids and comets, p_E was found typically to have a maximum ($\sim 0.001-0.02$) at $0.002 \leq \beta \leq 0.01$, i.e., at $d \sim 100$ microns (this value of d is in accordance with observational data). However, for trans-Neptunian particles p_E has maximum at $\beta=0.2$. The maximum values of p_E for dust particles were usually (exclusive for Comet 2P/Encke) greater by at least an order of magnitude than the values for parental comets. For the same β , values of $p_E/p_{M'}$, p_E/p_{E01} and p_M/p_{M01} typically were greater for greater p_E . For initial orbits with greater e , the ratio p_E/p_M is typically smaller. The maximum values of p_E and $p_{M'}$ and the intervals of values of $p_E/p_{M'}$, p_E/p_{E01} and p_M/p_{M01} are presented

in Table 1. Note for comparison that the square of the ratio of radii of the Earth and the Moon is 13.48, and the square of the ratio of radii of bodies differed in mass by a factor of 10 is 4.64.

Table 1. Migration of dust particles produced by asteroids and comets to the Earth and the Moon

	<i>ast</i>	<i>tno</i>	C39	C10	2Pper	<i>ht</i>	<i>Lp</i>
$\max\{\rho_E\}$	$1.7 \cdot 10^{-2}$	$1.5 \cdot 10^{-4}$	$1.1 \cdot 10^{-3}$	$1.6 \cdot 10^{-3}$	$2.0 \cdot 10^{-4}$	$1.6 \cdot 10^{-4}$	$9.3 \cdot 10^{-7}$
$\max\{\rho_M\}$	$5.1 \cdot 10^{-4}$	$2.9 \cdot 10^{-6}$	$5.3 \cdot 10^{-5}$	$6.5 \cdot 10^{-5}$	$1.1 \cdot 10^{-5}$	$1.8 \cdot 10^{-6}$	$9.8 \cdot 10^{-8}$
β for $\max\{\rho_E\}$	0.005	0.2	10^{-4}	0.01	0.002	0.001	0.001
ρ_E/ρ_M	16-33	16-52	16-32	16-30	15-23	10-18	9.5-14
ρ_E/ρ_{E01}	5.6-9.2	5.3-7.6	5.5-8.3	5.6-8.6	5.2-6.6	4.4-5.0	3.9-4.8
ρ_M/ρ_{M01}	3.5-5.4	4.6-8.0	4.2-5.2	4.2-4.8	4.2-5.3	4.5-4.7	4.2-4.6

Probabilities of collisions of migrating dust particles with the Earth, the Moon, and their embryos for dust particles migrated from different distances from the Sun:

For recent calculations of migration of dust particles from different distances from the Sun, in each run I considered 250 particles with initial semi-major axes from a_o to $a_o + 2.5$ AU, eccentricities $e_o = 0.3$, inclinations $i_o = 0.15$ rad. Such eccentricities and inclinations could be acquired by planetesimals due to gravitational influence of planets and planetesimals [8]. At $n_{pl} = 7$ the gravitational influence of all planets, excluding Mercury, was taken into account, and at $n_{pl} = 5$ the gravitational influence of 5 planets from Venus to Jupiter was

Table 2. Migration of dust particles to the Earth and the Moon from different distances from the Sun at $\beta = 0.04$.

a_o	5	5	5	5	7.5
n_{pl}	7	7	5	5	7
ρ_E	$4.9 \cdot 10^{-4}$	$1.6 \cdot 10^{-4}$	$1.1 \cdot 10^{-4}$	$1.2 \cdot 10^{-4}$	$3.0 \cdot 10^{-5}$
ρ_M	$1.6 \cdot 10^{-5}$	$6.2 \cdot 10^{-6}$	$4.8 \cdot 10^{-6}$	$4.7 \cdot 10^{-6}$	$1.8 \cdot 10^{-6}$
ρ_E/ρ_M	31.0	26.0	22.8	25.6	16.0
ρ_E/ρ_{E01}	7.9	7.4	7.0	7.6	5.5
ρ_M/ρ_{M01}	4.8	4.6	4.6	4.6	4.4
r_{Sun}	0.33	0.31	0.29	0.26	0.27
a_o	7.5	7.5	7.5	10	10
n_{pl}	7	5	5	7	5
ρ_E	$2.3 \cdot 10^{-4}$	$6.5 \cdot 10^{-5}$	$1.8 \cdot 10^{-4}$	$1.4 \cdot 10^{-4}$	$2.8 \cdot 10^{-4}$
ρ_M	$7.7 \cdot 10^{-6}$	$3.3 \cdot 10^{-6}$	$6.5 \cdot 10^{-6}$	$5.6 \cdot 10^{-6}$	$1.5 \cdot 10^{-5}$
ρ_E/ρ_M	29.4	19.6	28.0	25.3	28.4
ρ_E/ρ_{E01}	7.9	6.0	7.5	7.2	8.0
ρ_M/ρ_{M01}	4.7	4.8	4.7	5.0	4.5
r_{Sun}	0.20	0.26	0.26	0.24	0.25

Table 3. Migration of dust particles to the Earth and the Moon from different distances from the Sun at $\beta = 0.004$.

a_o	5	5	5	5
n_{pl}	7	7	5	5
ρ_E	$2.1 \cdot 10^{-6}$	$1.3 \cdot 10^{-4}$	$4.9 \cdot 10^{-4}$	$1.4 \cdot 10^{-4}$
ρ_M	$1.2 \cdot 10^{-7}$	$6.1 \cdot 10^{-6}$	$2.2 \cdot 10^{-5}$	$6.7 \cdot 10^{-6}$
ρ_E/ρ_M	16.9	20.6	22.5	21.0
ρ_E/ρ_{E01}	5.6	6.4	7.4	6.8
ρ_M/ρ_{M01}	4.7	4.7	4.5	4.4
r_{Sun}	0.008	0.02	0.016	0.03

a_o	7.5	7.5	10	10
n_{pl}	7	5	7	5
p_E	$5.7 \cdot 10^{-7}$	$4.2 \cdot 10^{-6}$	$2.1 \cdot 10^{-5}$	$7.3 \cdot 10^{-5}$
p_M	$3.5 \cdot 10^{-8}$	$2.6 \cdot 10^{-7}$	$1.2 \cdot 10^{-6}$	$5.2 \cdot 10^{-6}$
p_E/p_M	21.0	16.1	17.0	14.0
p_E/p_{E01}	5.5	5.4	5.6	4.8
p_M/p_{M01}	4.4	4.7	4.7	4.6
r_{Sun}	0.004	0.008	0.022	0.025

taking into account. Some results are presented in Tables 2 and 3 for $\beta=0.04$ and $\beta=0.004$, respectively. The values of a_o in the tables were between 5 and 10 AU. The fraction of particles collided with the Sun is denoted by p_{Sun} . At $\beta=0.04$ the values of p_{Sun} were in the range from 0.20 to 0.33 and were typically a little smaller for greater a_o . At $\beta=0.004$ the values of p_{Sun} did not exceed 0.03. For $\beta=0.04$ the values of p_E and p_M were greater by up to two orders of magnitude than the values (which on average are about $(2-4) \cdot 10^{-6}$) for bodies in similar initial orbits. As it was earlier obtained for bodies, for $\beta=0.004$ the values of p_E (and p_M) could differ by up to two orders of magnitude for different runs with the same a_o . They were smaller than at $\beta=0.04$, but for a_o equal to 5 and 10 AU were greater than for bodies. For $\beta=0.004$ the values of p_E (and p_M) were greater at $n_{pl}=5$ than at $n_{pl}=7$. For $\beta=0.04$, the values of p_E (and p_M) for different runs differed less (both at $n_{pl}=5$ and $n_{pl}=7$) than for $\beta=0.004$. The values of p_E/p_M were in the range from 16 to 31 for $\beta=0.04$ and in the range from 14 to 22.5 for $\beta=0.004$. The ratio p_E/p_{E01} was in the range from 4.8 to 8, and p_M/p_{M01} was in the range from 4.4 to 5.

Conclusions:

Probabilities of collisions of migrating dust particles with the Earth and the Moon were studied for various sizes of particles. Particles launched from different asteroids, comets and planetesimals were considered.

Acknowledgements:

The work was supported by the grant of Russian Science Foundation N 17-17-01279.

References:

- [1] Ipatov S.I., Mather J.C., Taylor P.A., Migration of interplanetary dust, "Astrodynamics, Space Missions, and Chaos", ed. by E. Belbruno, D. Folta, and P. Gurfil, Annals of the New York Academy of Sciences // 2004. V. 1017. P. 66-80. <http://arXiv.org/format/astro-ph/0308450>.
- [2] Marov, M. Ya. and Ipatov, S.I., Migration of dust particles and volatiles delivery to the terrestrial planets, Solar System Research. 2005. V. 39. N 5. P. 374-380.
- [3] Ipatov S.I. Mather J.C. Migration of small bodies and dust to near-Earth space. Advances in Space Research. 2006. V. 37. P. 126-137. <http://arXiv.org/format/astro-ph/0411004>.
- [4] Ipatov S.I. Collision probabilities of migrating small bodies and dust particles with planets. Proceedings of the International Astronomical Union, vol. 5, Symposium S263 "Icy bodies in the Solar System", Cambridge University Press. 2010. P. 41-44. <http://arxiv.org/abs/0910.3017>.
- [5] Levison H.F., Duncan M.J. The long-term dynamical behavior of short-period comets, Icarus. 1994. V. 108. P. 18-36.
- [6] Ipatov S.I. Evolution times for disks of planetesimals. Soviet Astronomy. 1988. V. 65. P. 1075-1085.
- [7] Ipatov, S.I. and Mather, J.C., Migration of trans-Neptunian objects to the terrestrial planets, Earth, Moon, and Planets. 2003. V. 92. P. 89-98. <http://arXiv.org/format/astro-ph/0305519>.
- [8] Ipatov S.I. Accumulation and migration of the bodies from the zones of giant planets, Earth, Moon, and Planets. 1987. V. 39. P. 101-128.

FORMATION OF TWO DUSTY PLASMA CLOUDS AS A RESULT OF A METEOROID IMPACT ONTO THE MOON

S.I. Popel¹, A.P. Golub¹, A.V. Zakharov¹, L.M. Zelenyi¹, A.A. Berezhnoy², E. Zubko³, M. Iten⁴, R. Lena⁵, S. Sposetti⁶, Yu.I. Velikodsky⁷, A.A. Tereshchenko⁷, B. Atamaniuk⁸

¹Space Research Institute of the Russian Academy of Sciences, Profsoyuznaya 84/32, Moscow 117997, Russia;

²Sternberg Astronomical Institute, Moscow State University, Universitetsky pr. 13, Moscow 119234, Russia;

³Far Eastern Federal University, Sukhanova St. 8, Vladivostok 690090, Russia;

⁴Garden Observatory, Gordola CH-6596, Switzerland;

⁵Geologic Lunar Research (GLR) group, Rome 00137, Italy;

⁶Gnosca Observatory, Gnosca CH-6525, Switzerland;

⁷National Aviation University, Kosmonavta Komarova 1, Kiev 03058, Ukraine;

⁸Space Research Centre of the Polish Academy of Sciences, Bartycza 18A, Warsaw 00-716, Poland

Keywords:

Dusty plasma cloud, meteoroid impact, the Moon, shock wave, lunar regolith.

Introduction:

Origin of an appearance of two dusty plasma clouds as a result of a meteoroid impact onto the Moon is considered. It is shown that the first of the clouds is formed by particles (or debris) of lunar regolith ejected from the lunar surface

by shock wave of meteoroid impact, while the second one is collected by solidified drops of melt. Calculations of basic characteristics of these clouds are performed including the speeds of expansion of the clouds, characteristic sizes of particles in each of the clouds, number densities of the particles, their charges, etc. Qualitative agreement of the calculated speeds of cloud expansion with observational data is shown.

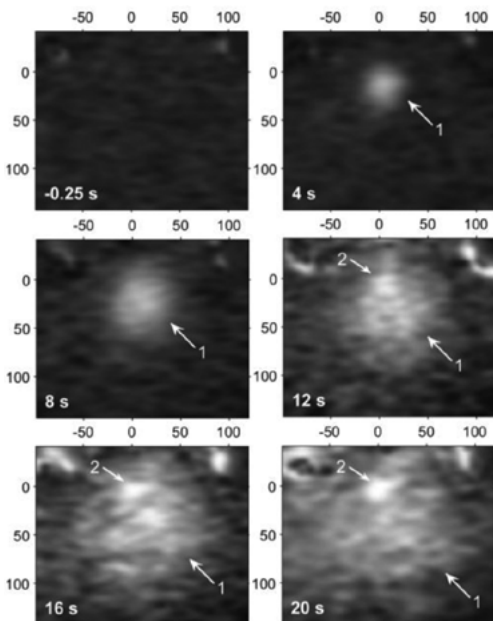


Fig. 1. Photopictures of the region where meteoroid impact onto the Moon occurred in February 26, 2015. They correspond to the points of time 0.25 s before the impact and 4, 8, 12, 16, 20 s after the impact. The coordinates (0, 0) characterize the impact point. The distances along the axes are calculated in km. A large fast cloud (1) and a small slow cloud (2) are shown.

Observations in February 26, 2015:

Optical flash produced on the shadowed lunar surface near the terminator was detected at 21h 35m 22.871s \pm 0.010s UT, February 26, 2015. The flash was registered by M. Iten using a 125-mm refractor equipped with the Watec 902H2 Ultimate videocam in Gordola (Switzerland). While the flash itself resulted from the thermal emission, the successive glow (see Fig. 1) clearly was caused by sunlight scattering from dust particles

that got ejected from the surface by a meteoroid impact. It is seen in Fig. 1 that two dust clouds arose after the impact: a small slow cloud and a large fast cloud.

Meteoroid impacts and dusty plasma clouds formation:

We consider the impact of a large fast meteoroid with the lunar surface. For estimation of the kinetic energy of the impactor we use the technique [1] based on the consideration of maximum brightness of flashes. We find the range of possible kinetic energies of the impactor from $6 \cdot 10^8$ J to $1.7 \cdot 10^9$ J. We carry out our calculations for the impactor mass $m_i = 4.7$ kg and its speed $u_i = 27$ km/s which correspond to the upper border of the above range, namely, $1.7 \cdot 10^9$ J. Consideration of the impactor parameters fitting the lower border ($6 \cdot 10^8$ J) does not allow us to explain an appearance of the two dusty plasma clouds. Furthermore, the calculations are performed for the case where the incident meteoroid and target consist of continuous and porous gabbroid anorthosite, respectively.

The impact of a fast meteoroid on the lunar surface leads to the formation of zones around the equivalent center of the meteoroid [2]. These zones are (I) material evaporation zone; (II) material melting zone; (III) destruction zone of lunar regolith particles and their irreversible deformations; and (IV) zone of nonlinear elastic deformations of regolith material, where pressures in a non-linear acoustic wave are lower than the dynamic elasticity limit. In zone V of linear elastic deformations, which is formed behind zone IV, the acoustic wave can be considered as linear.

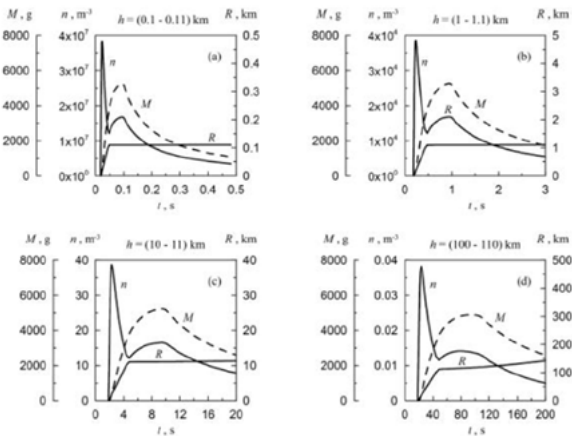


Fig. 2. Dynamics of different layers of dusty plasma cloud formed by solidified drops of melt. The curves describe the time dependencies of the layer radius R , the total mass of dust particles in the layer M , and the averaged over the volume of the layer number density of dust particles n .

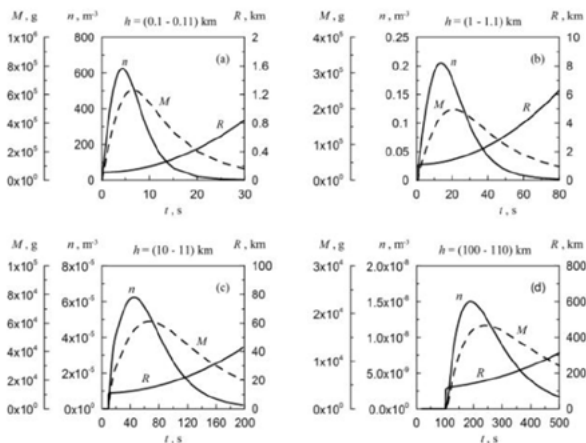


Fig. 3. Dynamics of different layers of dusty plasma cloud formed by particles (or debris) of lunar regolith ejected from the lunar surface by shock wave of meteoroid impact.

Zones III-V are the sources of dust particles over the lunar surface which are the particles of regolith or their debris. Zones I-II are the sources of evaporated and melted substance of impactor and regolith. The material ejected by the shock wave into free space from the material melting zone II is a liquid decaying into fragments. Equilibrium drops are formed when the volume occupied by vapor in the drop-vapor flux becomes comparable to the volume of the liquid. Rising over the lunar surface, liquid drops are solidified and acquire electric charges owing to their interaction, in particular, with electrons of the solar wind, as well as with solar radiation. Finally, two dusty plasma clouds are formed due to the meteoroid impact onto the Moon, the first of the clouds is collected by particles (or debris) of lunar regolith ejected from the lunar surface by shock wave of meteoroid impact, while the second one is formed by solidified drops of melt. The clouds have different characteristics (see Figs. 2 and 3).

The typical magnitude of the charge numbers in the cloud formed by particles (or debris) of lunar regolith is $Z_d \sim 2 \cdot 10^5$ (for the typical dust particle size of $a \approx 70 \mu\text{m}$) while that for the cloud formed by solidified drops of melt is $Z_d \sim 1 \cdot 10^4$ (for $a \approx 4 \mu\text{m}$).

The calculated value of the speed of expansion of the cloud formed by solidified drops of melt is about 2 km/s while that of the cloud formed by particles (or debris) of lunar regolith is approximately equal to 1 km/s. This fact shows the qualitative agreement of the calculated speeds of cloud expansion with observational data (see Fig. 1).

Events similar to that occurred in February 26, 2015 change significantly the properties of the dusty-plasma system at the Moon. In particular, during such events tangible amount of micron-sized particles appears in the lunar exosphere. Usually, the number of micron-sized particles in the lunar exosphere is very small [3].

Acknowledgements:

This work was supported by the Russian Science Foundation (project no. 17-12-01458).

References:

- [1] Ortiz J.L., Madiedo J.M., Morales N., et al. Lunar impact flashes from Geminids, analysis of luminous efficiencies and the flux of large meteoroids on Earth // MNRAS. 2015. V. 454. No. 1. P. 344-352.
- [2] Popel S.I., Golub' A.P., Zelenyi L.M., Horányi M. Impacts of fast meteoroids and a plasma-dust cloud over the lunar surface // JETP Lett. 2017. V. 105. P. 635-640.
- [3] Popel S.I., Golub' A.P., Lisin E.A., et al. Impacts of fast meteoroids and the separation of dust particles from the surface of the Moon // JETP Lett. 2016. V. 103. P. 563-567.

THE 10- μM SILICATE FEATURE IN SUB-MILLIMETER COMPACT OLIVINE PARTICLES

E. Chornaya^{1,2}, A.M. Zakharenko¹, E. Zubko¹, A. Kuchmizhak^{1,3},
K.S. Golokhvast¹, G. Videen⁴

¹Far Eastern Federal University, 8 Sukhanova St., Vladivostok 690950, Russia (rainu13rainu@gmail.com);

²Ussuriysk Astrophysical Observatory of FEB RAS, 21 Solnechnaya St., Gornotaezhnoe 692533, Russia;

³Institute of Automation and Control Processes FEB RAS, 5 Radio St., Vladivostok 690041, Russia

⁴Space Science Institute, 4750 Walnut Street, Boulder Suite 205, CO 80301, USA

Keywords:

Comets, cometary dust, 10- μm silicate feature, mid-IR spectroscopy, olivine

Introduction:

Cosmic dust particles having silicate composition could be detected with the help of the 10- μm silicate feature. This phenomenon appears in mid-IR spectra of comets and protoplanetary disks as a series of five peaks located at wavelength λ of $\sim 10 \mu\text{m}$. Fig. 1 gives an example of the 10- μm silicate feature in comets 1P/Halley and C/1995 O1 (Hale-Bopp) [1,2]. The positions and shapes of these peaks correspond with specific chemical composition and crystalline/amorphous structure of silicate species of dust particles [2]. It is long believed that the presence of the 10- μm silicate feature itself places a constraint on size of dust particles and their morphology. Namely, using the Mie theory, it was demonstrated that the silicate feature appears only if the radius of a perfect silicate sphere does not exceed $\sim 1 \mu\text{m}$ [3].

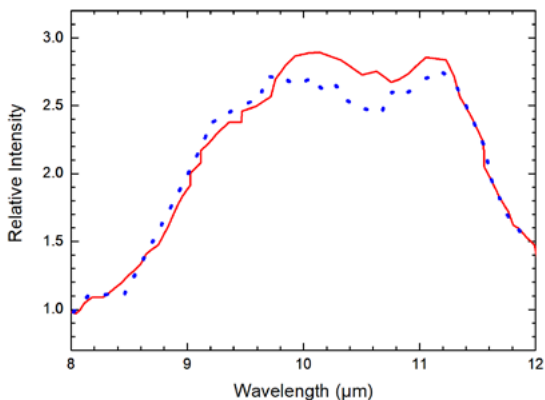


Fig.1. The 10- μm silicate feature in comets 1P/Halley (blue dots) [1] and C/1995 O1 (Hale-Bopp) (red line) [2]. The Halley spectrum is stretched by a factor of 3.

Such a limitation has had a significant impact on physics of comets, despite the obvious fact that the ideal sphere has nothing in common with the irregular morphology of cometary dust particles. This size limit of compact dust particles (or constituent grains of fluffy aggregates) hardly matches *in situ* findings in comets. This could indicate that the size limit is inaccurate itself. Using a mid-IR spectrometer, we experimentally investigate the 10- μm silicate feature in sub-millimeter compact particles made of olivine that is an abundant species of comets. Thus, our sample particles are $\sim 10^3$ bigger compared to the size limit of $\sim 1 \mu\text{m}$. Unlike theoretical Mie theory, the experimental approach does not place restrictions on the shape of target particles, making it possible to study irregularly shaped particles which are a more realistic model of true cometary dust.

Samples preparation and laboratory measurements:

The initial sample was about 1 cm in diameter, and has a complex morphology. It consists of numerous sub-millimeter and millimeter-sized irregularly shaped grains that cohered together in random orientations. The grains can be detached from the sample with a little effort; whereas, each grain is quite hard. The bulk sample is light green in appearance. Separated grains are almost colorless and appear transparent. We investigate 15 different grains that were detached from the main sample. All the grains are approximately equal sized with average size of about 0.5 mm. As one can see in Fig. 2, the grains have a solid structure with no significant surface roughness. The surface of one of these grains was examined at high spatial resolution, $\sim 0.1 \mu\text{m}$, and it was found to be very much smoothed.

Micro-FTIR measurements of the mid-IR spectra were performed with fouriertransform infrared (FTIR) spectrometer (*IRTracer-100, Shimadzu, Japan*) and additional facility connected to the microscope (*AIM 8800, Shimadzu, Japan*). This instrument measures a relative reflectance spectrum that is converted to a relative absorption spectrum by subtraction it from 1.

Using an optical microscope *Morphology G3-ID (Malvern Instruments Ltd, UK)* combined with the Raman spectrometer *Rnx1 (Kaiser Optical Systems, Inc., USA)*, we examined chemical composition of all 15 sample particles and found that they predominantly consist of forsterite (Mg_2SiO_4). There also was found some small contamination with other materials, presumably organics; they are difficult to discriminate within the available Raman-spectrum databases. They unlikely belong to silicates as such materials are well described in the Raman-spectrum databases.

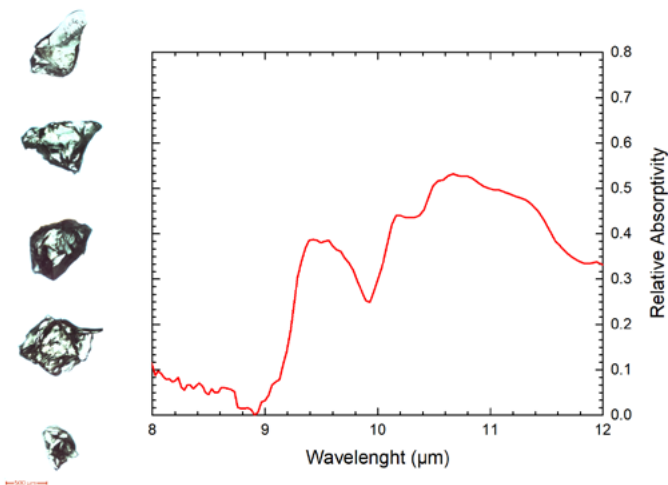


Fig. 2. Five examples of sub-millimeter olivine compact particles investigated in this work (left) and the mid-IR spectrum average of all 15 olivine compact particles.

Results and conclusion:

For analysis, we measure spectra of all 15 sample particles and take their average. The resulting spectrum over the range of $\lambda = 8 - 12 \mu\text{m}$ is shown in Fig. 2. While we measure crystals of olivine, the dust in comets always has a much more complex chemical composition that involves various types of olivine with different Mg/Fe composition and crystalline/amorphous structure. For instance, the breakdown of the 10- μm silicate feature in Comet C/1995 O1 (Hale-Bopp) yields 6 species [2]. The spectra of some of those qualitatively resemble what is shown in Fig. 2.

Our experiment clearly shows that sub-millimeter compact olivine particles are capable of producing the 10- μm silicate feature. It suggests that the 1- μm limit on radius of compact grains in comets should be revisited.

References:

- [1] Gehrz, R. D., Ney, E. P. 0.7- to 23- μm photometric observations of P/Halley 1986 III

and six recent bright comets // *Icarus*. 1992. V. 100. P. 162-186.

- [2] Hayward T. L., Hanner M. S., Sekanina Z. Thermal Infrared Imaging and Spectroscopy of Comet Hale-Bopp (C/1995 O1) // *Astroph. J.* 2000. V. 538. P. 428-455.
- [3] Hanner M. S., Bradley J. P. in *Comets II*, eds. M. C. Festou, H. U. Keller, H. A. Weaver. University of Arizona Press, 2004. 555 p.

COSMIC DUST STUDIED BY THE MOSS ANALYSIS

M.V. Frontasyeva¹, S.S. Pavlov¹, V. A. Tselmovich², E. Steinnes³

¹Joint Institute for Nuclear Research (JINR), str. Joliot-Curie, 6, Dubna, 141980, Moscow Region, Russian Federation, marina@nf.jinr.ru;

²Borok Geophysical Observatory, branch of Shmidt's Institute of Physics of the Earth, RAS, Russia, 152742, Borok, Nekouz, Yaroslavl Region, tselm@mail.ru;

³Norwegian University of Science and Technology, Trondheim, Norway, eiliv.steinnes@ntnu.no

Keywords:

Cosmic dust, moss biomonitor, scanning electron microscopy (SEM), neutron activation analysis (NAA).

Introduction:

It is a well-established phenomenon that extraterrestrial dust particles (micrometeorites) survive atmospheric entry and reach the Earth's surface. Collection of extraterrestrial dust for research focuses on the environments where terrestrial sedimentation rates and input of artificial particles of anthropogenic origin is minimal, including deep-sea sediments, Antarctic ice and snow, as well as natural planchettes of mosses and peat-bog cores.

Materials and Methods:

Experimental observations of particles considered as cosmic dust in moss samples (*San-ionia uncinata*) collected in King George Island [1], highlands of Georgia [2], lowlands of Belarus and Tver Region of Russia are presented. Microanalysis of moss samples using scanning electron microscopy (SEM) showed the presence of clastic, anthropogenic particles and particles of cosmic dust. The results from Georgia are compared with those for moss samples collected in pristine areas of Norway [3]. The identification of particles as micrometeorites is achieved on the basis of their compositional, mineralogical, and texture analyses using SEM microscopy with EDAX techniques and epithermal neutron activation analysis (ENAA) carried out at the reactor IBR-2 of the Frank Laboratory of Neutron Physics, JINR [4].

Results and conclusion:

The majority of particles undergo melting during their passage through the atmosphere. Most abundantly, particularly at large sizes, cosmic spherules, i.e. completely melted droplets, were observed. These spherical particles provide a useful proxy for the total flux of dust because they are relatively easy to identify. They are the background magnetic component of cosmic dust, mainly microspheres and particles of native metals. Most often, it was possible to detect native Fe, Fe-Ni and Fe-Cr minerals.

Acknowledgement:

The work was partially supported by the Russian Foundation for Basic Research, project 16-05-00703.

References:

- [1] Mróz T., Szufa K., Frontasyeva M.V., Tselmovich V.A., Ostrovnaya T.M., Kornaś A., Olech M., Mietelski J.W., Brudecki K. Determination of atmospheric deposition of trace elements across King George Island (Antarctica) using reactor neutron activation analysis and scanning electron microscopy // *Environ Sci Pollut Res Int.*, 2018. V. 25: P. 436-446. <https://link.springer.com/article/10.1007%2Fs11356-017-0431-2>
- [2] Sh. Shetekauri, O. Chaligava, T. Shetekauri, A. Kvlividze, T. Kalabegishvili, E. Kirkesali, M.V. Frontasyeva, O.E. Chepurchenko, V.A. Tselmovich. Bbiomonitoring air pollution with moss in Georgia.// *Polish Journal of Environmental Studies*, 2018. 2018. V. 27. No. 5. P. 2259–2266. DOI: <https://doi.org/10.15244/pjoes/73798>
- [3] M. V. Frontasyeva, E. Steinnes and H. Harmens. Monitoring long-term and large-scale deposition of air pollutants based on moss analysis. Chapter in a book "Biomonitoring of Air Pollution Using Mosses and Lichens: Passive and Active Approach – State of the Art and Perspectives", Edts. M. Aničić Urošević, G. Vuković, M. Tomašević, Nova Science Publishers, New-York, USA, 2016. P. 1-20.
- [4] Frontasyeva M.V. Neutron activation analysis for the Life Sciences. A review // *Physics of Particles and Nuclei*, 2011. V. 42, No. 2, P. 332-378. <http://www.springerlink.com/content/f836723234434m27/>

ON THE DUST CHARGED PARTICLES AS A PART OF KORDYLEWSKI CLOUDS

T.V. Salnikova¹, S.Ya. Stepanov²

¹Lomonosov Moscow State University, GSP-1, Leninskie Gory 119991 Moscow, Russia & Peoples' Friendship University of Russia, 6 Miklukho-Maklaya Street, Moscow, 117198, Russia; tatiana.salnikova@gmail.com;

²Dorodnitsyn Computing Center, FRC CSC RAS, Vavilov str. 40, 119333 Moscow, Russia & Lomonosov Moscow State University, GSP-1, Leninskie Gory 119991 Moscow, Russia, stepsj@ya.ru

Keywords:

Dust clouds, charged particles, Coulomb interaction, Vlasov-Poisson equations.

Introduction:

Triangle libration points of the Earth-Moon system are stable in Lyapunov sense. So, many astronomers were looking for Trojan moons of the Earth, similarly the Trojan asteroids of the Sun-Jupiter system. Priority in the discovery of these new moons belongs to Kazimierz Kordylewski. Now we call the dust clouds in the vicinity of the Lagrange libration points of the Earth-Moon system as Kordylewski dust clouds.

Nevertheless, the existence of these clouds is still disputed. On the contrary to the observations, there are theoretical arguments of impossibility of existence of the Kordylewski clouds. Taking under consideration gravitational influence of the Sun, we obtain, that Lagrange libration points are not the points of relative equilibrium of the Earth-Moon system: the mass point with zero-velocity in Lagrange point on the rotating frame immediately leave the surrounding of this point.

It is shown existence of the stable periodic solutions, capturing the Lagrange libration points [1-2]. Each of the Lagrangian libration points is captured by the two stable periodical orbits. Stability of the periodic solution implies that, in the case of small deviations of coordinates and velocities from periodic motion, we should see an ensemble of particles, moving in the vicinity of this periodic motion. These particles possibly represent the dust cloud, moving around the Lagrange libration point.

Problem setting:

Taking into account the light pressure of the Sun, one get a family of periodical orbits, which rises from the mentioned periodic solutions. It is shown a dependence of the light pressure on the characteristic size of the particles [3]. It is clear, that for negligible small masses of the particles the perturbation of the Sun can be excluded. So, we return to the classical unperturbed three-body problem Earth - Moon - Particle, but for the small enough masses of the particles.

Now we study a behaviour of the charged dust particles in the small vicinity of the Lagrange libration points of the Earth-Moon system. Let's consider a plasma, consisting of dust particles with individual electric charge $-q$. We assume that the particles initial distribution is maxwellian on the velocities, centered at zero, and uniform on the coordinates in the small surrounding of the Lagrange libration point on the rotating plane. To analyze the possibility of existence of stable configuration, consisting of the charged dust particles in the small surrounding of the Lagrange point, we use the equations of characteristics for the Vlasov equation. It turned out that for some values of the parameters our initial cloud of the dust charged particles has periodically changing stable configuration [4].

This investigation enlarges the clarification of the phenomenon of the Kordylewski cosmic dust clouds.

References:

- [1] Salnikova T.V., Stepanov S.Ya. On the Lagrange libration points of the perturbed Earth-Moon system. // Proceeding of the International Astronomical Union, 2014. V. 9. No. 310. P. 192-193.

- [2] Salnikova T.V., Stepanov S.Ya. Mathematical Model of Formation of Kordylewski Cosmic Dust Clouds. // Doklady Physics. Maik Nauka/Interperiodica Publishing, 2015. V.60, No 7, P. 323-326.
- [3] Salnikova T., Stepanov S., Shuvalova A. Periodic trajectories of the particles in the Earth vicinity. // Proceedings of 2016 International Conference «Stability and Oscillations of Nonlinear Control Systems» IEEE Catalog Number CFP16E79-ART RUSSIA, P.1-4.
- [4] Salnikova T.V., Stepanov S.Ya. Probabilistic Model of Kordylewski Clouds. // AIP Conference Proceeding, 2018. V.1959, No 1, P. 020004-1-020004-6

TRANSFORMATIVE LUNAR SCIENCE

C. Pieters¹, R. Canup², D. Kring³, J. Head¹, D. Scott¹

¹*Department of Earth, Environmental and Planetary Science, Brown University, Providence, RI 02912 USA, carle_pieters@brown.edu;*

²*Southwest Research Institute, 1050 Walnut Street, Suite 300 Boulder, CO 80302 USA;*

³*USRA Lunar and Planetary Institute, 3600 Bay Area Boulevard, Houston, TX 77058 USA.*

Keywords:

Moon, impact, planet migration, interior, space weather, chronology, plasma, commercial, infrastructure, human and robotic exploration.

The foundation of Apollo and Luna programs implemented 50 years ago combined with more recent results from the renaissance of international lunar exploration over the last 15 years has provided humanity a deeper and more intimate view of the Moon. It has also opened enormous opportunity for accomplishing Transformative Lunar Science (TLS), which are the next major breakthroughs in understanding the origin and early habitability of our Earth-Moon system as well as fundamental constraints on events that control the evolution of our Solar System. A few examples of TLS topics include: a) Establish the period of early giant planet migration and its effects in our Solar System, b) Provide an absolute chronology for Solar System events over 4 billion years, c) Understand and utilize the recently recognized water cycle of the Moon and other airless bodies, d) Characterize the Moon's interior to reveal how this differentiated cousin of Earth formed and evolved, e) Use the accessible vantage from the lunar farside to view the universe, f) Evaluate the extended record of space weather and fundamental processes of plasma interactions with surfaces. As human/robotic partnerships are developed further for space exploration, the next era of significant lunar exploration is a broad international undertaking, including commercial involvement. An enabling element for such Transformative Lunar Science is joint development of a stable infrastructure for efficient integrated activities.

LUNAR POLAR REGIONS OF INTEREST FOR FUTURE EXPLORATION

J. Flahaut¹, J. Carpenter², E. Sefton-Nash², M. Anand³, J.-P. Williams⁴, L. Xiao⁵, S. Zhao⁵, E. Füre¹, B. Marty¹

¹CRPG, CNRS/Université de Lorraine, 15 rue Notre Dame des Pauvres, 54500 Vandœuvre-lès-Nancy, France (flahaut@crpg.cnrs-nancy.fr).

²ESA-ESTEC, Noordwijk, The Netherlands

³Dept of Physical Sciences, The Open University, Milton Keynes, UK

⁴Dept of Earth and Space Sciences, University of California, USA

⁵Planet. Sci. Inst., China Univ. of Geosci., Wuhan, 430074, China

Keywords:

Lunar poles, landing sites, volatiles, cold trap, ISRU, lunar exploration

Introduction and scope:

The last decades have been marked by increasing evidence for cold trapped volatiles at the lunar poles [1-3]. Orbital measurements reveal an enhancement in hydrogen at both poles, which is interpreted as evidence for surface or subsurface water ice [4]. In addition, recent Moon Mineralogy Mapper (M3) data reveal hydroxylation of the lunar surface [5]. Lunar hydroxyl and water are targets of interest both as scientific repositories and for exploration purposes. Determining the exact nature, extent and origin of the volatiles at and near the surface of the lunar poles requires in situ analyses via lander or rover missions. A number of upcoming projects and missions will address these by obtaining new in situ data or return of lunar surface or shallow subsurface samples, and hence rely on the selection of optimal landing sites (e.g., [6]).

Identifying Regions of Interest:

Several recent studies have focused on the identification of regions of interest (ROI) in the vicinity of both lunar poles, in preparation for future missions (e.g., [7,8]). ROI are accessible regions where water ice and other volatiles should be present and could be extracted and analyzed on site, but where

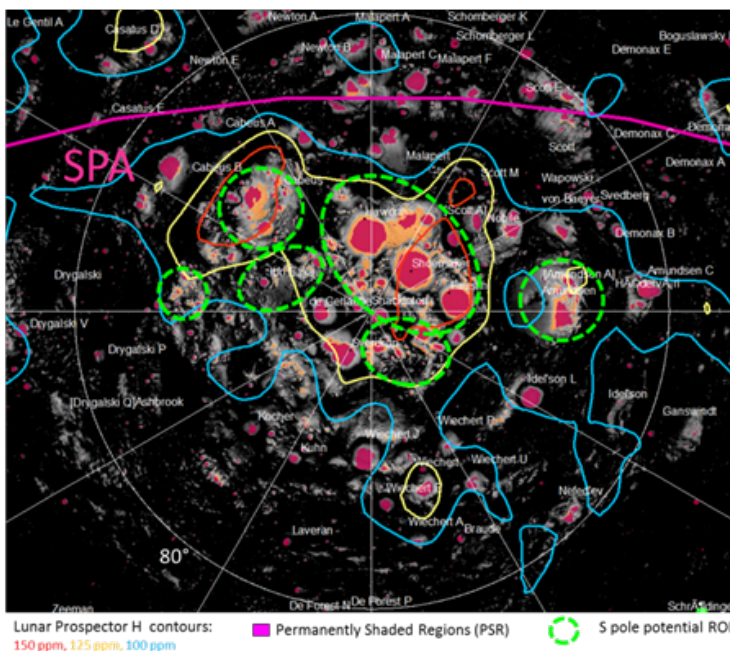


Fig. 1. South pole ROI for volatile investigations above 80° in latitude (green circles). Background: Diviner average temperature map (white = low). Blackened areas = Diviner avg T >110K, Orange areas = Diviner avg T <54K, South Pole stereographic projection.

additional science benefits have also been identified. Of particular interest are highly illuminated areas that would provide almost continuous power supply for lunar landers or permanent bases (e.g., [9-12]). We will show however, that finding and extracting volatiles such as water ice is probably not possible at those sites, given their high temperatures. In the present paper, we will establish a list of possible ROI at both poles based on various selection criteria, including illumination, enhanced detection of volatiles, surface temperature, proximity of cold traps, terrain characteristics and the presence of geological features of interest. We will also discuss the available datasets for remote characterization and existing knowledge gaps. An example of ROI for the south pole is given in figure 1. Downselecting from ROI to candidate landing sites is specific to a mission; examples based on given scenarios (e.g., a Luna-27 solar-powered lander type mission) will be presented.

References:

- [1] Keller J. W. et al. (2016), *Icarus*, 273, 2-24.
- [2] Lawrence D.J. (2018) In: Cudnik B. (eds) *Encyclopedia of Lunar Science*.
- [3] Paige D. A. et al. (2010), *Science*, 479-82.
- [4] Feldman W. C. et al. (1998), *Science*, 281, 1496-1500.
- [5] Pieters C. M. et al. (2009a), *Science*, 326, 568-572.
- [6] Flahaut J. et al. (2012), *ASR*, 50(12).
- [7] Lemelin M. et al. (2014), *PSS*, 101, 149-161.
- [8] Flahaut J. et al. (2016), 4th ELS, #004.
- [9] Bussey D.B.J. et al. (1999), *GRL*, 30, 1278.
- [10] Mazarico E. et al. (2011), *Icarus*, 211, 1066-1081.
- [11] De Rosa D. et al. (2012), *PSS*, 74, 224-246.
- [12] Gläser P. et al. (2017) *PSS*.

ANALYSIS OF SUBSURFACE IMPACT AND VOLCANIC STRUCTURES ON THE MOON WITH GRAVITY RECOVERY AND INTERIOR LABORATORY (GRAIL)

A.N. Deutsch¹, G.A. Neumann², J.W. Head¹

¹Department of Earth, Environmental, and Planetary Sciences, Brown University, Providence, RI 02912, USA, ariel_deutsch@brown.edu;

²NASA Goddard Space Flight Center, Greenbelt, MD 20771, USA

Keywords:

Moon; Geology; Volcanism; Impact cratering; Gravity.

Introduction:

Oceanus Procellarum on the Moon hosts four distinctive positive Bouguer gravity anomalies (PBGAs): *Southern Aristarchus Plateau*, *Northern and Southern Marius Hills*, and *Northern Flamsteed* (Fig. 1). These four PBGAs span a region ~700 km in N-S extent, and are all similar in diameter (~90–190 km), gravitational amplitude (>100 mGal contrast), and shape (approximately circular in planform). However, the four PBGAs can be distinguished due to their unique geologic settings. These four spatially associated PBGAs are important in understanding the impact and volcanic/plutonic history of the nearside maria, in a region of elevated temperatures characteristic of the Procellarum

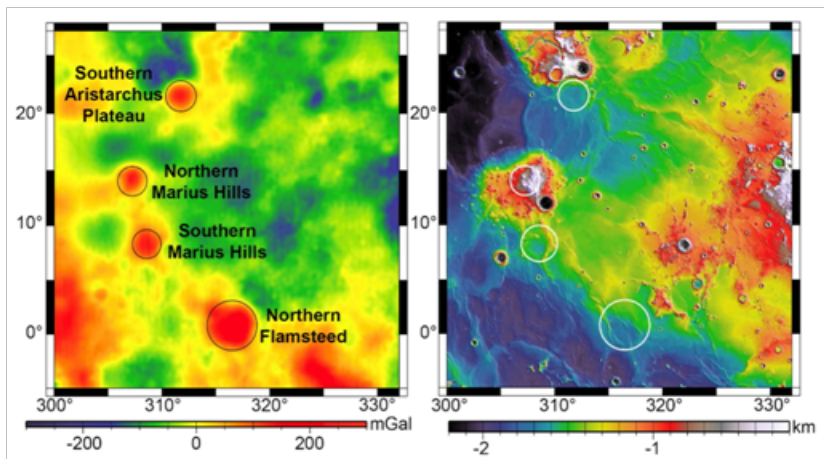


Fig. 1. Four positive Bouguer gravity anomalies in Oceanus Procellarum. GRAIL-derived GRGM900c [2] Bouguer spherical harmonic solution to degree 6-660 is displayed on the left, and surface elevations, measured from the Lunar Orbiter Laser Altimeter (LOLA) [3], are shown on the right.

Here we explore six geologic endmember scenarios (Fig. 2) to model possible subsurface structures that may produce the four PBGAs. The endmembers represent variations of lava-filled crater scenarios [e.g., 4-6] and variations of volcanic/magmatic intrusion scenarios [e.g., 7-9]. By coupling these geologic analyses with forward modeling of high-resolution GRAIL gravity data, we constrain subsurface structures that may contribute to the four PBGAs (*Southern Aristarchus Plateau*, *Northern and Southern Marius Hills*, and *Northern Flamsteed*). Previous work on the Marius Hills anomalies was restricted to lower resolution Lunar Prospector [7] and GRAIL [4] gravity data, which is likely to have resulted in an underestimation of the mass anomaly magnitudes. Using our new modeling results of GRAIL data, we discuss regional impact and volcanic histories, and implications for the evolution of the lunar crust in the central Oceanus Procellarum region.

Methods:

We consider six geologic endmembers (Fig. 2) when modeling various density contrast scenarios that may contribute to the GRAIL-derived PBGAs within central Oceanus Procellarum. The first three scenarios are variations of lava-flooded impact craters: filled and buried impact craters [e.g., 4] (Fig. 2.1), buried craters with combined floor-fractured crater (FFC) intrusions and surface mare fill [e.g., 5] (Fig. 2.2), and buried craters associated with mantle upwelling at the crust-mantle boundary (Fig. 2.3). We fill each crater with dense mare material, exploring density contrasts between 300 and 600 kg/m³. The explored density contrast between the mare fill and the surrounding crust is at the lower end of ranges considered by others [4], appropriate to the less heavily cratered and lower-porosity mare regions. For each PBGA, we estimate reasonable thicknesses for mare fill of a buried crater using depth-to-diameter relationships for complex craters derived from altimetry data [10] (Table 1). The mare thickness is modeled as the topographic difference between the measured height of the surrounding terrain and the estimated depth of the crater floor.

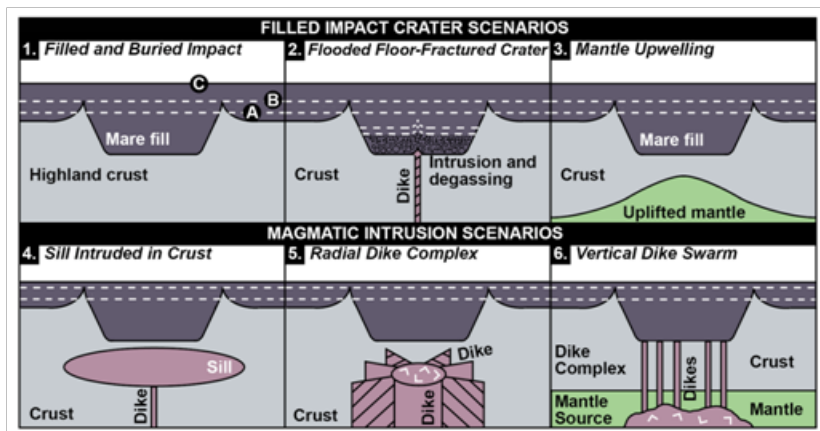


Fig. 2. Interpretive endmember scenarios. Cases 1–3 are variations of filled craters, which are associated with (A) identifiable crater rim crests when filled below the rim, (B) wrinkle ridges when lavas flooded to near the rim crest, or (C) no topographic expression when completely flooded over. Cases 4–6 are variations of magmatic intrusions. Schematics are not to scale.

The following three geologic endmembers are variations of subsurface volcanic/magmatic intrusions: an intruded volcanic sill or shallow magma reservoir [7] (Fig. 2.4), a swarm of radial dikes surrounding or above a magma source region [8] (Fig. 2.5), and a concentration of vertical dikes over a deeper mantle source region [9] (Fig. 2.6). Here we model sills with a mare basalt-like density (3150 kg/m³) and explore a density contrast between 150 and 600 kg/m³ for the dikes. Density contributions from mantle source regions are not included because we assume that the diapirs, which are no longer generating dikes in the lunar crust, have reached neutral buoyancy in the mantle through cooling. Initial modeling explores the resulting gravity disturbance from 2-km-thick sills, on the basis of previous modeling and analysis of lunar intrusions [11]. We model radial (Fig. 2.5) and vertical (Fig. 2.6) dike complexes as occupying up to 50% of the volume of the crust. The upper limit for the fraction of crust occupied by dikes is 37–50% by volume, but the crust is likely to be occupied by much less [12].

Conclusions:

The GRAIL data presented here, at spherical harmonic degrees 6–660, permit higher resolution analyses of these anomalies than previously, and reveal new information about subsurface structures. We find that ancient craters buried by 2.8–3.5 km of surface mare fill (as expected from crater depth-to-diameter relationships) alone do not correspond to, and are below the magnitude of, the GRAIL-derived Bouguer anomalies. Therefore, an additional density contrast is required to explain the high-amplitude

PBGAs. For *Southern Aristarchus Plateau* and *Northern Flamsteed*, two anomalies with crater-related topographic structures, the additional density contrast may be provided by ~5.6–7 km of impact-related mantle uplift. For the *Northern* and *Southern Marius Hills* anomalies, the additional density contrast is consistent with a crustal complex of vertical dikes that occupies up to 50% of the region's crust, fed by a magmatic/volcanic mantle reservoir. It is unlikely that the Marius Hills complex overlies a single intrusion or sill [7], given that ~10 km of volcanic material in the shallow subsurface is required to produce the magnitude of the GRAIL-derived signals. The four PBGAs analyzed here are important in understanding the impact and volcanic/plutonic history of the Moon, specifically in a region of thin crust and elevated temperatures characteristic of the Procellarum KREEP Terrane.

References:

- [1] Wieczorek, M. A., Phillips, R. J., 2000. *J. Geophys. Res.* 105, 20417–20430.
<https://doi.org/10.1029/1999JE001092>.
- [2] Lemoine, F. G. et al., 2014. *Geophys. Res. Lett.* 41, 3382–3389.
<https://doi.org/10.1002/2014GL060027>.
- [3] Smith, D. E., et al., 2010. *Geophys. Res. Lett.* 37, L18204.
<https://doi.org/10.1029/2010GL043751>.
- [4] Evans, A. J. et al., 2016. *Geophys. Res. Lett.* 43, 2015GL067394.
<https://doi.org/10.1002/2015GL067394>.
- [5] Jozwiak, L.M. et al., 2017. *Icarus* 283, 224–231.
<https://doi.org/10.1016/j.icarus.2016.04.020>.
- [6] Baker, D.M.H. et al., 2017. *Icarus* 292, 54–73.
<https://doi.org/10.1016/j.icarus.2017.03.024>.
- [7] Kiefer, W.S., 2013. *J. Geophys. Res. Planets* 118, 733–745.
<https://doi.org/10.1029/2012JE004111>.
- [8] Wilson L., Head, J. W., 2002. *J. Geophys. Res.: Planets* 107, 1–1.
<https://doi.org/10.1029/2001JE001593>.
- [9] Head, J.W., Wilson, L., 2017. *Icarus* 283, 176–223.
<https://doi.org/10.1016/j.icarus.2016.05.031>.
- [10] Kalynn, J. et al., 2013. *Geophys. Res. Lett.* 40, 38–42.
<https://doi.org/10.1029/2012GL053608>.
- [11] Wilson L., Head, J. W., 2017. *Icarus* 283, 146–175.
<https://doi.org/10.1016/j.icarus.2015.12.039>.
- [12] Head, J.W., Wilson, L., 1992. *Geochimica et Cosmochimica Acta* 56, 2155–2175.
[https://doi.org/10.1016/0016-7037\(92\)90183-J](https://doi.org/10.1016/0016-7037(92)90183-J).

THE DISTRIBUTION OF THE CONCENTRATIONS (ANOMALIES) OF THE WATER EQUIVALENT OF HYDROGEN AS A FUNCTION OF THE RELIEF AT THE POLAR REGIONS OF THE MOON REGARDING THE LRO DATA

M.A. Sundeeva, O.S. Tretyukhina, E.N. Slyuta

*Vernadsky Institute, Moscow, Kosygina street 19, 119334,
mari.al.zakharova@gmail.com*

Keywords:

WEH, Moon, Lunar poles, GIS, LRO, LOLA, LEND

Introduction:

The correlation between the distribution of the water equivalent hydrogen (WEH) and lunar relief configuration is a widely discussed question nowadays. We can't say for sure that all the anomalies are located at the crater bottoms or permanently shadowed regions of the lunar surface. The main issue of the research is to figure out if there any relation between WEH concentrations and such relief elements as relative heights, slopes, exposition, shades and landforms.

Data and area of research:

In this research we consider both South and North Lunar poles between 70 and 90 northing degrees. The source of the relief data is LOLA LRO DEMs with several hundred-meter spatial resolution. To obtain the information about spatial distribution of the WEH at the polar regions we used the LEND data which is also obtained by the Lunar Reconnaissance Orbiter. The full research is based on the GIS analytics methods to prove or oppositely refute the WEH spatial distribution as a function of lunar relief.

References:

- [1] Sanin A.B., Mitrofanov I.G., Litvak M.L., Bakhtin B.N., Bodnarik J., Boynton W., Chin G., Evans L., Harshman K., Fedosov F., Golovin D.V., Kozyrev A.S., Livengood T., Malakhov A.V., McClanahan T., Mokrousov M.I., Starr R.D., Sagdeev R.Z., Tret'yakov V.I., Vostrukhin A.A, Hydrogen Distribution in the Lunar Polar Regions // Icarus. 2017. 283. 10.1016/j.icarus.2016.06.002.

SO MANY DISCOVERIES OF WATER ON THE MOON

I.G. Mitrofanov

Space Research Institute, Moscow, Russia, 117997, Profsouznaya st 84/32, litvak@mx.iki.rssi.ru.

Keywords:

Moon, lunar water, polar volatiles

There are known to be several times in the history of Moon space investigations, when the discovery was announced of detection of water on the Moon. The different forms of lunar water are reviewed in this presentation, and distinct processes are also considered for water appearance on the Moon or for its delivery to the Moon. The concepts of future space missions are discussed for studying lunar water, as witness of past evolution of the Earth-Moon binary system, and also as useful natural resource for future Moon exploration.

LUNAR BASALTIC VOLCANIC ERUPTIONS: GAS RELEASE PATTERNS AND VARIATIONS IN LAVA VESICULARITY: FISSURES, MARE FLOWS, AND RING MOAT DOME STRUCTURE (RMDS) MORPHOLOGY

J.W. Head¹, L. Wilson²,

¹*Department of Earth, Environmental and Planetary Sciences, Brown University, Providence, RI 02912, U.S.A. james_head@brown.edu*

²*Lancaster Environment Centre, Lancaster University, Lancaster LA1 4YQ, U.K. l.wilson@lancaster.ac.uk*

Keywords:

Volcanism, maria, basalts, second boiling, RMDS, IMPs.

Introduction:

In a recent paper [1] we outline 4 phases expected to have occurred during a typical lunar volcanic eruption. These are Phase 1: arrival of a dike from the deep mantle which releases gas and magmatic foam in a transient but vigorous explosive eruption forming regional pyroclastic deposits; Phase 2: a high volume flux, hawaiian-style eruption forming an at least partly optically dense fire-fountain from which pyroclasts efficiently lose volatiles and accumulate to form non-vesicular lava. This phase continues until the dike reaches a buoyancy equilibrium between the crust and mantle densities and ceases to ascend. Phase 3 begins as the dike is squeezed by relaxation of the internal excess pressure holding the dike open, forcing magma to the surface at a decreasing volume flux. With a stable internal pressure gradient in the dike, magma volatile exsolution deep in the dike becomes negligible and gas bubbles rise and coalesce to produce strombolian activity until all of the deep-sourced CO₂ gas has been lost. Phase 4 now involves release of H₂O and S compounds in shallow magma as it is forced upward. Surface tension stabilizes small (~20 mm) gas bubbles against exploding into the overlying vacuum and a stable crust forms on lava leaving the vent. This phase continues at an exponentially decreasing volume flux until dike stresses are completely relaxed. This outline of the sequence of events expected in basaltic lunar eruptions is generic: all phases should have occurred in all eruptions. However, the relative importance and duration of the various phases varied significantly, being dictated by the total magma volatile inventory, the global state of stress in the lithosphere, and the consequent way in which the erupted magma volume flux changed with time.

In [1] we identified four different configurations that commonly result from eruptions: 1 - Summit pit craters on shield volcanoes (e.g., Ina); 2 - Caldeiras associated with intersecting dikes (e.g., Hyginus); 3 - Linear depressions above dikes (e.g., Sosigenes); and 4 - Topographically uncontained linear vents above fissure eruptions in the maria (e.g., most mare IMPs). Also, in [1] we addressed the first two of these configurations, in which all three of the magma volatile content driving explosive activity, the active length of the fissure vent, and the erupted magma volume flux were relatively small. Low volatile content and short fissure length caused pyroclasts to be ejected approximately radially to only a few km, producing optically dense fire fountains from which uncooled pyroclasts accumulated to form lava ponds at magmatic temperatures. The ponds overflowed to feed lava flows, and the low magma volume fluxes ensured that these were short, cooling-limited flows that accumulated to form small shield volcanoes with summit pits. Fractures in the crusts of the lava ponds allowed underlying extremely vesicular foam to erupt to form low domes [2, 3], these being one sub-set of the features called irregular mare patches (IMPs) [4]. We now consider configurations 3 and 4, involving the longer fissure vent outcrops and higher magma volume fluxes needed to explain the properties of large-scale mare lava flows.

Mare volcanism:

The low viscosities of lunar basalts coupled with typical thicknesses of 20-50 m [5] for large >100 km long mare lava flows emplaced on surface slopes of order 10^{-3} imply typical flow speeds of $10\text{-}20\text{ m s}^{-1}$ and inevitably require turbulent rather than laminar motion in the proximal parts of flows [6, 7]. Turbulence inhibits formation of a stable surface crust and maximizes radiative heat loss. Even so, analyses of turbulent lavas eroding lunar sinuous rille channels show that turbulence will persist in such thick flows until the lava has traveled for at least $\sim 100\text{ km}$ [8]. This implies that the lengths of most large mare flows were limited by the volume of magma available to be erupted rather than by cooling [5]. Vents feeding the larger mare flows are commonly hard to identify, but the $\sim 30\text{ km}$ widths of the flows suggest that their fissure vents had outcrop lengths of $\sim 10\text{ km}$. Volume fluxes consistent with thicknesses, widths and flow speeds of lavas range from 10^4 to $10^6\text{ m}^3\text{ s}^{-1}$. We now assess how the successive eruptive phases outlined above influenced the lava emplacement process.

Phase 1.

The very transient release of gas and foam concentration would have had minimal consequences, mainly depositing a thin layer of sub-mm pyroclasts over a large area around the vent.

Phase 2.

This would have involved the formation of a relatively steady, largely optically dense hawaiian fire fountain within which sub-mm sized pyroclastic droplets would have lost gas efficiently and accumulated with negligible cooling in a linear zone a few to 10 km wide on either side of the fissure to form vesicle-free lava. This lava would have flowed away in an initially turbulent manner to form the distal part of the eventual lava flow deposit. This phase would have continued until the rising dike had established a neutral buoyancy configuration relative to the crust-mantle boundary. The relative vertical extents of typical mantle dikes ($50\text{-}90\text{ km}$ [5]) and the crust ($\sim 30\text{ km}$ [9]) imply that 40% to 70% of the total dike magma volume would have been erupted during this phase.

Phase 3.

A decrease would now have occurred in magma rise speed and volume eruption rate as the dike ceased rising *en masse* towards the surface and instead began to shrink in thickness as the internal excess pressure holding the dike open was lost. There is no evidence in the morphologies of flows for a dramatic and abrupt decrease in eruption rate as this transition took place and to maintain the 10^4 to $10^6\text{ m}^3\text{ s}^{-1}$ effusion rates the time constant for the presumably roughly exponential decrease in discharge is of order a few weeks. The low magma rise speed towards the end of this period would have allowed bubbles of exsolved CO gas formed at great depths [10] to move at an appreciable speed relative to the magmatic liquid being squeezed out of the dike and so coalescence of bubbles should have occurred, causing a change from hawaiian to strombolian explosive activity at the surface. The stabilization of the dike magma pressure distribution meant that no additional CO was released at depth and minimal amounts were released near the surface [10].

Phase 4.

With minimal explosive release of CO gas now taking place, and a significantly reduced volume flux allowing laminar flow, a stable crust would have formed on the lava near the vent. The magma being erupted would have consisted of liquid containing bubbles of H_2O and sulphur species released over the last $<500\text{ m}$ of magma rise [10]. These bubbles would have nucleated with diameters of $\sim 10\text{-}20\text{ mm}$ and would have grown to $\sim 20\text{-}30\text{ mm}$ at the surface, remaining stable as surface tension forces [2] imposed a pressure of $\sim 70\text{ kPa}$. Lunar basalts exsolving $\sim 1000\text{ ppm}$ of H_2O and sulphur species would have left the fissure vent as lava foams with vesicularities up to 96% by volume.

Implications for vent areas:

It is difficult to predict what fraction of the original volume of magma in a dike would have been erupted as foam, because both the extent and speed of the dike closure process would have been functions of the lithosphere stress regime, likely compressive late in the history of mare volcanism [11], and upper mantle rheology. Nevertheless, the lava closest to the

vent is likely to have been the most vesicular. The very last stages of activity at a vent would involve a competition between (i) cooling of un-erupted magma in the dike causing a reduction in volume and allowing drain-back of the last-erupted lava into the fissure and (ii) the final total relaxation of stresses forcing foam magma upward, possibly fracturing the crust on lava in the vent and extruding small foam flows as at Sosigenes [12] (Fig. 1). Alternatively, these processes may have essentially cancelled one another out, leaving no clear topographic marker of the vent location, other than modification of the most vesicular lava near the vent by thermal and impact processes to form clusters of IMPs.

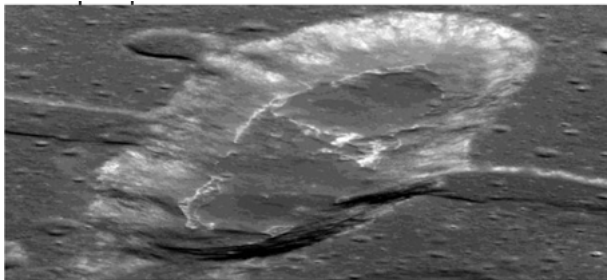


Fig. 1. Oblique view of Sosigenes IMP. Modified from NASA LROC image NAC M1108117962LR.

Post-eruption changes in flows:

After the main phases of an eruption are complete and all motion has ceased, changes still occur. Cooling of lava takes place at all boundaries, causing contraction stresses in the surface crust. Shrinkage of the lava as its density increases, being greatest where lava has infilled pre-eruption depressions, adds differential stresses. Crystallization due to cooling increases the concentration of residual volatiles in the magmatic liquid causing supersaturation and additional gas bubble nucleation. Where this process occurs in regions of a flow that already contain a foam core, expansion of the foam and extrusion of foam through cracks onto the lava flow surface can occur. This is a likely explanation of the ring moat dome structures [RMDs, 13, 14] found in large numbers on many mare flows (Fig. 2). The moat surrounding the low dome structure represents loading and conservation of volume as the extrusion occurs.



Fig. 2. Ring moat dome structures in Mare Tranquillitatis, typically 4-6 m high. From Fig. 1E of [13].

References:

- [1] Wilson L. & Head J.W. (2018) *GRL*, 45, 5852-5859.
- [2] Wilson, L. & Head, J.W. (2017) *JVGR*, 335, 113-127.
- [3] Qiao, L. et al. (2017) *Geology*, 45, 455-458.
- [4] Braden S.E. et al. (2014) *Nature Geosci.*, 7, 787-791.
- [5] Hiesinger H. et al. (2002) *GRL*, 29, 1248, 4 pp.
- [6] Wilson L. & Head J.W. (2017) *Icarus*, 283, 146-175.
- [7] Head J.W. & Wilson L. (2017) *Icarus*, 283, 176-223.
- [8] Williams D. A. et al. (2000) *JGR*, 105, 20189-20205.
- [9] Wieczorek M. A. et al. (2013) *Science*, 339, 671-675.
- [10] Rutherford M. J. et al. (2017) *Amer. Mineral.*, 102, 20145-2053.
- [11] Solomon S. C. & Head J. W. (1980) *Rev. Geophys. Space Phys.*, 18, 107-141.
- [12] Qiao L. et al. (2017) *MAPS*, doi:10.1111/maps.13003.

GEOLOGY OF THE NORTHERN PORTION OF THE SPA BASIN ON THE MOON: EVIDENCE FOR COMPOSITIONAL STRATIFICATION OF THE ANCIENT LUNAR CRUST

M. A. Ivanov^{1,2}, H. Hiesinger², C. Orgel³, J. H. Pasckert²,
C. H. van der Bogert², J. W. Head⁴

¹*Vernadsky Institute, RAS, 119991, Kosygin St. 19, Moscow, Russia;*

²*Westfälische Wilhelms-Universität Münster, Germany*

³*Freie Universität, Berlin, Germany;*

⁴*Brown University, Providence, USA*

Keywords:

Please suggest 5–10 keywords that describe the content of the abstract. If possible, each keyword should appear in the accompanying abstract.

Introduction:

We studied a region between 10–60° S and 125–175° W that encompasses the northern portion of the South Pole-Aitken basin (SPA, Fig. 1a), which is the largest known [1-5] and likely the oldest, ~4.2 Ga, impact structure on the Moon [6,7]. The SPA basin is a huge topographic feature [1,8,9], formed within a solid crust. The detailed photogeological investigation of the basin is motivated by the need for additional constraints on the structure and composition of the ancient lunar crust.

The SPA iron anomaly:

The SPA region displays a distinct iron anomaly [10-11], although it is significantly weaker than those in typical maria. The floor of the basin shows a limited extent of obvious volcanic plains. So, what could have caused the SPA iron-rich region? Is the anomaly linked to the presence of extensive cryptomare deposits on the floor [12] or does it reflect vertical compositional stratification of the ancient crust?

Goals of the study:

We approached this question via detailed photogeological/stratigraphic analysis of the study area. We compiled a geological map (Fig. 1a) based on LROC WAC mosaics and LOLA topography, and analyzed the FeO abundancies in units with different ages using the Clementine FeO abundance map [13].

General topography of the study area:

The hypsogram of the study area is bimodal (Fig. 1b) indicating that this region consists of two topographic domains (SPA-floor and SPA-rim). The mean difference between the domains is ~8.5 km.

Morphology and stratigraphy of map units:

Two major classes of landforms occur in the study area: (1) impact craters and related features, and (2) plains-forming terrains of volcanic and impact origin.

The crater-related landforms include the following stratigraphic units (Fig. 1a,c): Copernican craters with prominent rays and ejecta (Cc), Eratosthenian sharp-crested craters without rays (Ec), and large craters with ejecta and surrounding fields of secondary craters. Determination of the absolute model ages of these craters shows that they vary in age from the Lower to Upper Imbrian (Llc, Ulc) epochs. Additional crater-related units include: ejecta from the Orientale basin of the Lower Imbrian age (Llo), craters with complete rims but without ejecta.

These craters formed during the Nectarian and pre-Nectarian epochs (NpNc). Also present are massifs of the Apollo (pNrnAPL) and SPA (pNrnSPA) basin rims of the pre-Nectarian age. Finally, strongly degraded crater materials of the pre-Nectarian age occur within both SPA topographic domains, predate unit NpNc, and show no lower stratigraphic limit. We interpret these units as those displaced to form the SPA rim (pNmSPAr) and exposed on the floor (pNmSPAf) of the basin due to the SPA event.

Plains-forming units include dark and light plains of the Upper Imbrian age [14] (Uldp, Ullp) and low-relief rugged terrain. This unit occurs in two areas where it has different ages. Near the SW corner of the map area, this unit is of the Lower

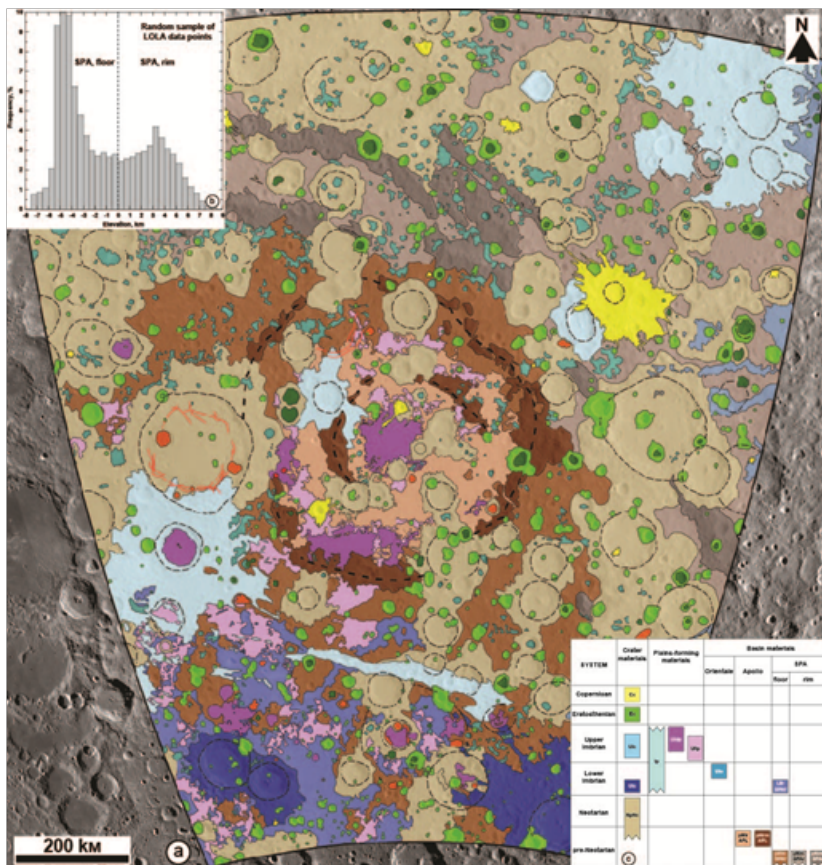


Fig. 1.

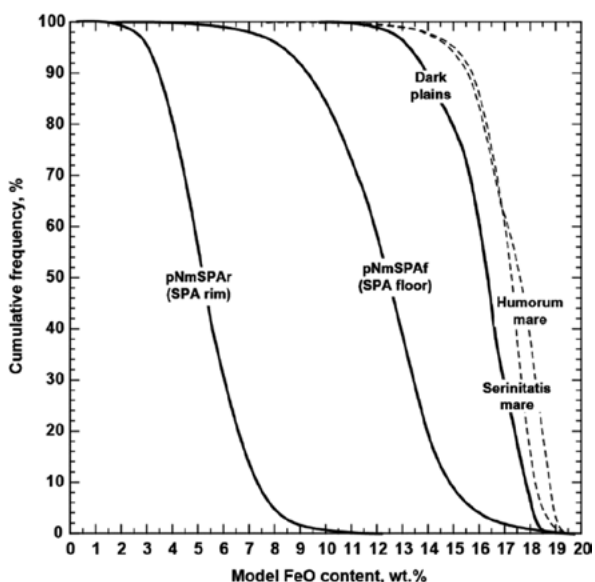


Fig. 2. Cumulative distribution of FeO in materials in the SPA basin and Humorum and Serenitatis maria.

Imbrian age (LlIr), associate with the other plains-forming units and likely represent older volcanic plains. Within the Apollo basin, this unit (pNlrAPL) has the same age as the basin itself and probably represents its impact melts.

Discussion:

In order to assess possible sources of Fe inside SPA, we collected data on the FeO content for the Upper Imbrian dark plains and the pre-Nectarian materials on the SPA rim and floor, and compare the concentration of Fe in these units with those in materials of the Serenitatis and Humorum mare. The dark plains have the highest FeO abundance comparable with that of typical mare materials (Fig. 2), which is in agreement with the volcanic nature of the dark plains. The oldest units in the map area (pNmSPAf and pNmSPAr) represent rugged terrains whose morphology is inconsistent with their interpretation as possible ancient volcanic plains. In addition, the Fe content in these materials is significantly lower than in typical mare units (Fig. 2).

The oldest materials on the basin floor have typical Fe content of ~11-13.5 wt % (Fig. 2), which accounts for the absolute majority of the SPA iron anomaly; materials on the basin rim are significantly Fe-poorer (Fig. 2). The large difference in the Fe abundance between the SPA floor and rim primordial materials suggests that by the time of the SPA event the lunar crust was stratified in respect to the iron content. The oblique SPA impact [5,15,16] likely stripped away the upper (Fe-poorer) portion of the crust, the materials of which were re-deposited in the SPA rim, and exposed the lower (Fe-richer) portion of the crust on the basin floor. The characteristic difference between the SPA topographic domains (~8.5 km) provide the upper estimate of the thickness of the upper, Fe-poorer portion of the crust.

Acknowledgements:

This work was supported by Russian Science Foundation (grant 17-17-01149) to MAI.

References:

- [1] Stuart-Alexander D.E., USGS Map I-1047. 1978
- [2] Spudis P. et al. Ancient multiring basins on the Moon revealed by Clementine laser altimetry // *Science*. 1994. V. 266. P. 1848-1851.
- [3] Hiesinger H, Head J.W. Lunar South Pole - Aitken impact basin: Topography and mineralogy // *Proceedings of the 34th Lunar and Planetary Science Conference, 2004*. Abstract 1164.
- [4] Shevchenko et al. Structure of the South Pole-Aitken lunar basin // *Solar System Research*. 2007 V. 41, P. 447-462.
- [5] Garrick-Bethell I, Zuber M.T. Elliptical structure of the lunar South Pole-Aitken basin // *Icarus*. 2009. V. 204. P. 399-408.
- [6] Wilhelms D.E., USGS Map I-1348. 1987
- [7] Hiesinger H. et al. New crater size-frequency distribution measurements of the South Pole Aitken basin // *Proceedings of the 43th Lunar and Planetary Science Conference, 2004*. Abstract 2863.
- [8] Wilhelms D.E., USGS Map I-1192. 1979
- [9] Zuber M.T. et al. A sharper view of impact craters from Clementine data // *Science*. 1994. V. 266. P. 1839-1843.
- [10] Pieters C.M. et al. The shape and internal structure of the Moon from the Clementine mission // *Science*. 1994. V. 266. P. 1844-1848.
- [11] Lawrence D.J. et al. Iron abundances on the lunar surface as measured by the Lunar Prospector gamma-ray and neutron spectrometers // *Journal of Geophysical Research*. 2002. V. 107. 5130. doi:10.1029/2001JE001530.
- [12] Gibson K.E., Jolliff B.L. Correlation of surface units and FeO concentrations in the South Pole - Aitken basin interior // *Proceedings of the 42nd Lunar and Planetary Science Conference, 2011*. Abstract 2326.
- [13] Lucey P.G. et al. Lunar iron and titanium abundance algorithms based on final processing of Clementine ultraviolet-visible images // *Journal of Geophysical Research*. 2000. V. 105. P. 20297-20305.
- [14] Pasckert J.H. et al. Lunar farside volcanism in and around the South Pole-Aitken basin // *Icarus*. 2018. V. 299. P. 538-562.
- [15] Schultz P.H. Forming the South-Pole Aitken basin: The extreme games // *Proceedings of the 28th Lunar and Planetary Science Conference, 1997*. P. 1259-1260.
- [16] Schultz P.H., Origin of nearside structural and geochemical anomalies on the Moon. *Geological Society of America Special Paper 477, 2011*. P. 141-159.

KINETIC MODELING OF SODIUM POPULATION IN THE LUNAR EXOSPHERE

V. Tenishev

University of Michigan, vtenishe@umich.edu

Our knowledge about the lunar environment is based on a large volume of ground-based, remote, and in situ observations. These observations have been conducted at different times and sampled different pieces of such a complex system as the surface-bound exosphere of the Moon. Numerical modeling is the tool that can link the results of these separate observations into a single picture. Being validated against previous measurements, models can be used for predictions and interpretation of future observations results.

In this paper, we present a kinetic model of the sodium exosphere of the Moon as well as results of its validation against a set of ground-based and remote sensing observations. The unique characteristic of the model is that it takes the orbital motion of the Moon and the Earth into consideration and simulates both the exosphere as well as the sodium tail self-consistently. The extended computational domain covers the part of the Earth's orbit at new Moon, which allows us to study the effect of Earth's gravity on the lunar sodium tail.

The model is fitted to a set of ground-based and remote sensing observations by tuning the sodium source rate as well as values of sticking, and accommodation coefficients. The best agreement of the model results with the observations is reached when all sodium atoms returning from the exosphere stick to the surface and the net sodium escape rate is about $5.3 \cdot 10^5 \text{ s}^{-1}$.

SOME PRE-STUDIES ABOUT THE CANDIDATE LANDING AREA FOR CHANG'E-4 PROJECT

J. Ping¹, M. Wang¹, Z. Meng^{1,2}, Y. Lian^{1,3}

¹ National Astronomical Observatories, CAS, Datun Rd. 20A, Chaoyang District, Beijing, 100101, China. jsping@bao.ac.cn;

² College of Geo-exploration Science and Technology, Jilin University Changchun 130026, China, mengzg@jlu.edu.cn;

³ Tianjin Normal University, Tianjin 300387, China, fishlice@163.com

Keywords:

Lunar mission, lunar farside, ChangE-4, lunar lander, lunar rover.

Introduction:

Chang'E-4 lunar exploration project is composed of relay communication satellite, a lander and a rover. Where, the lander and the rover are the backup of the Chang'E-3 lunar explorer. The relay satellite has been launched and is flying at the mission orbit. The lander and the rover are estimated to be launched by the end of 2018, may be at the southern pole Aitken Basin. This mission will carry out the in-situ detection and reconnaissance at the farside of the moon. The scientific objectives of Chang'E-4 lunar mission are to do the moon-based low frequency radio astronomical observations, to explore the shallow structure of the roving area at the farside of moon, and to investigate the morphology and mineral composition of the landing and roving area. Chang'E-4 mission has been planned to install six kinds of scientific payloads to complete the corresponding tasks, with three kinds of payloads on the lander and with three kinds of payloads on the rover. Also, some international joint collaboration payloads to be installed on the Chang'E-4 explorer(s).

The candidate landing area is tentatively fixed in Von Karman impact crater which is inside the South Pole-Aitken basin. In view of the lack of field analysis of microwave radiation brightness temperature, the research which is based on the field and the penetrability of Chang'e Microwave radiometer analyzed the brightness temperature's temporal and spatial distribution characteristics of Von Karman impact crater. The results showed that there is a significant couple mode between 3GHz diurnal brightness temperature field and 37GHz diurnal brightness temperature field, on top of that, the trend of brightness temperature appeared consistent in the crater. It also turned out that the area with high FeO+TiO₂ content has a closer connection which is the key area of brightness temperature changes. Nevertheless, the FeO+TiO₂ content does not have significant impact on the density of contours.

Also, in this area, a mascon anomaly may indicate historical complicated evolution of dynamics, and fruitful material composition. The lunar mascon distribution is usually obtained by means of satellite gravity method. The obtained gravity field information is combined with the lunar topography information both from CE-1 lunar orbital mission. From the analysis, a middle scale mascon just under the south half part of the Von Kármán Crater is identified newly. This means that Von Kármán Crater is a younger crater follow the older one. The discovery of this hidden middle scale mascon will benefit the study of lunar evolution, and will benefit the exploration of Von Kármán Crater in future Chang'E mission.

LANDING SITE SELECTION PROCESS FOR FUTURE MOON POLAR MISSIONS

M.V. Djachkova, I.G. Mitrofanov, M.L. Litvak, A.B. Sanin, V.I. Tretiyakov
*Space Research Institute of the Russian Academy of Sciences (IKI),
84/32 Profsoyuznaya Str, Moscow, Russia, 117997*

Keywords:

Moon, Luna-25, Luna-27, lunar polar lander, landing site

Introduction:

The landing site selection method developed by our team primarily for Luna-25 mission allowed us to select the main and reserved landing sites in the South Polar Region of the Moon. Furthermore, the performed analysis of the Moon polar surface indicated an extensive area suitable for landing (with the 1 km precision) and surface operations in both North and South Polar Regions of the Moon. Several locations in this area can be considered as possible landing and operation sites for future lunar lander missions including Luna-27.

NEUTRAL GAS MASS SPECTROMETER FOR THE LUNA-RESURS MISSION: STATUS, PERFORMANCE AND SCIENTIFIC IMPLICATIONS

R. G. Fausch¹, P. Wurz¹, M. Tulej¹, D. Lasi¹, L. Hofer¹, A. Buch², M. Cabane³, P. Coll⁴, D. Coscia³, S. Aseev⁵, M. Zaitsev⁵, M. Gerasimov⁵, A. Saggir⁵, C. Szopa³

¹ *Physics Institute, University of Bern, Sidlerstrasse 5, 3012 Bern, Switzerland, rico.fausch@space.unibe.ch;*

² *LGPM, Ecole Centrale Paris, 92295 Châtenay-Malabry, France;*

³ *LATMOS, Université Pierre et Marie Curie, 75252 Paris, France;*

⁴ *LISA, Université Paris-Est Créteil, Université Denis Diderot & CNRS, 94010 Créteil, France;*

⁵ *Space Research Institute, 117997 Moscow, Russia*

Keywords:

In situ mass spectrometry; Gas chromatography mass spectrometry; Luna-Resurs; Lunar volatiles; Lunar regolith analysis

Introduction:

Lunar polar volatiles could hold key information about the origin and evolution of solar system bodies. Moreover, they might be a valuable resource for manned exploration of the Moon. Assessing their chemical composition with in situ measurements is a scientific goal of the Russian Luna-Resurs mission. The mission plan foresees landing near a lunar pole to investigate chemical composition of volatiles trapped in the icy lunar surface by a Gas Chromatograph (GC) and Neutral Gas Mass Spectrometer (NGMS) [1]. NGMS will analyze the tenuous lunar exosphere additionally.

Instrumentation:

The NGMS instrument, pyrolysis cells and the GC with a Thermal Differential Analyzer (TDA) constitute the Gas Analytical Package (GAP) which performs detailed lunar regolith measurements of the volatile content (GC mode). In addition, NGMS can operate stand-alone to perform exosphere measurements (exosphere mode). For GC-mode, the pyrolysis oven releases the volatile species from the collected samples with a temperature range of up to 1000°C followed by both a chemical pre-separation and detection of the GC and mass spectrometric analysis by the NGMS instrument. As the NGMS is a time-of-flight instrument containing an ion storage source [2], it is capable to examine the continuous output of the GC allowing for highly sensitive measurements of chemical composition including CHON and noble gases, their isotopes, organics and water fraction.



Fig. 1. The NGMS flight model consumes < 25 W at a total mass of < 3.5 kg and size of 18 x 26 x 15 cm³.

Results and discussion:

Measurements conducted with our two flight units of the NGMS instrument (Figure 1) are comparable with the earlier prototype measurements [3] where sensitivities of hydrocarbons in the soil sample of about $2 \cdot 10^{-10}$ by mass and of about $2 \cdot 10^{-9}$ by mass for noble gases are demonstrated. Environmental testing and stand-alone scientific measurements with different calibration gas mixtures indicate that the flight instrument will comply with its requirements (i.e. dynamic range of up to 10^6 within 1 second integration time, mass resolution $M/\Delta M$ up to 1200), when coupled to the GC.

References:

- [1] Wurz P., Abplanalp D., Tulej M., Lammer H. A Neutral Gas Mass Spectrometer for the Investigation of Lunar Volatiles, *Planet. Space Sci.* 2012. V. 74. 264–269.
- [2] Abplanalp D., Wurz P., Huber L., Leya I. An optimised compact electron impact ion storage source for a time-of-flight mass spectrometer, *Int. J. Mass Spectrom.* 2010. V. 294. 33–39.
- [3] Hofer L., Wurz P., Buch A., Cabane M., Coll P., Coscia D., Gerasimov M., Lasi D., Saggir A., Szopa C., Tulej M. Prototype of the gas chromatograph–mass spectrometer to investigate volatile species in the lunar soil for the Luna-Resurs mission, *Planet. Space Sci.* 2015. V. 111. 126–133.

LUNAR IONOSPHERE AND PLANETARY RADIO EMISSIONS DETECTION BASED ON RADIO EXPERIMENTS OF CHINESE SPACE MISSION

M-Y. Wang¹, J. Ping¹, M. Wang², L-J. Chen¹, S-T. Han²

¹*National Astronomical Observatories, Chinese Academy of Sciences, Beijing, China, wangmy@nao.cas.cn;*

²*Key Laboratory of Science and Technology on Aerospace Flight Dynamics, Beijing, China*

Keywords:

Lunar Ionosphere; TEC; Chang'E-4; Planetary Radio Emissions; Radio Experiments.

Introduction:

The radio experiments of the service module of circumlunar return and reentry spacecraft indicate that lunar ionosphere is obvious than people expected. The maximums of lunar electron density is more than 3000 el/cm^3 and there is a strong correlation between lunar ionosphere density and solar azimuth. In order to explore the lunar ionosphere and planetary radio emission, two low frequency radio astronomical payloads has been placed on Chang'E-4 mission. One is onboard ChangE-4 relay satellite and the other will be sent to the surface of lunar far-side by the Chinese Chang'E-4 lunar lander mission. These payloads will record the information from the Type II solar burst and radio emissions of Earth, Jupiter and Saturn and help the understanding of lunar and planetary space environment.

Acknowledgements

This work was supported in by the NSFC No. 41604150.

EUROMOONMARS PILOT PROGRAMME FOR RESEARCH, TECHNOLOGY, TRAINING AND FIELD SIMULATIONS

B.H. Foing¹, A. Sitnikova², G. van der Sanden¹ & EuroMoonMars Team

¹ESA/ESTEC, ILEWG & VU Amsterdam, ESTEC postbus 299 2200 AG
Noordwijk, Bernard.Foing@esa.int;

²ABK The Hague, ILEWG & ESA/ESTEC

Keywords:

Moon, Mars, research, planetary, astrobiology, technology, instruments, lander, habitat, laboratory, training, analogue, field simulations, outreach

Introduction:

ILEWG developed EuroMoonMars [1-12], an evolving pilot research programme starting with a Robotic Test Bench (ExoGeoLab) and a Mobile Laboratory Habitat (ExoHab) at ESTEC, & ExoLaboratory (ExoLab). They can be used to validate concepts and external instruments from partner institutes. Field campaigns have been conducted in ESTEC, EAC, at Utah MDRS station, Eifel, Rio Tinto, Iceland, La Reunion, LunAres base at Pila Poland, and Hawaii (HiSeas, PISCES and upcoming MoonBase Alliance). We shall report on latest activities with application to Moon and Mars.

We integrated instruments on an ExoGeoLab test bench, with methodic hands-on approach: 1) We adapted instruments on a small ExoGeoLab demo lander, a small Rover, or field site campaigns; 2) This terrestrial payload (instruments, sensors, data handling) was deployed, transported, operated; 3) it was used for collaborative research ; 4) We implemented remote control of instruments from adjacent mobile laboratory, and remote science desks; 5) The suite of measurements includes a comprehensive set with telescopic imaging reconnaissance and monitoring, geophysical studies, general geology and morphology context, geochemistry (minerals, volatiles, organics), subsurface probe, sample extraction and retrieval, sample spectroscopy analysis; 6) We reproduced some simulation of diverse soil and rocks conditions and diagnostics; 7) We used these instrument packages to characterize geological context and properties; 8) Science investigations include geology, geochemistry, mineral and organics diagnostics; 9) Collaborators provided additional guest instruments, and investigations; 10) We use the ExoHab for logistics support and local operations. It was upgraded with some shield and origami structures supporting research and EVAs; 11) An ExoBiology Laboratory module (ExoLab) supporting related technical research was upgraded in 2017; 12) From ExoGeoLab instruments, we can help in preparing future lander/rover missions on the Moon, Mars, asteroids; 13) we developed EuroMoonMars activities with designers & artists expanding awareness of Moon-Mars benefits to the society at large.

This research can benefit Science, Exploration or Application programmes, and International Tasks Groups (space agencies, and research partners, ILEWG, IMEWG, ISECG, SSERVI, etc...).

References:

- [1] Foing BH () LPI/LPSC // 2009, 40, 2567 ;
- [2] Groemer G & ILEWG Eifel team // 2010, LPI/LPSC 41, 1680 ;
- [3] Foing B. H. et al. () Special Issue MoonMars // 2011, 10, IJA, 10;
- [4] Ehrenfreund et al. IJA // 2011, 10 (3), 239;
- [5] Stoker C. et al, IJA // 2011, 10 (3), 269;
- [6] Kotler et al. IJA // 2011., 10 (3), 221;
- [7] Foing BH. et al., LPI/LPSC// 2014, 45, 2675 ;
- [8] Foing BH et al., LPI/LPSC // 2016 47, 2719 ;
- [9] Offringa M et al, LPI/LPSC// 2016, 47, 2522;
- [10] Kamps OM et al, LPI/LPSC // 2016, 47, 2508;
- [11] Harasymczuk, M et al, LPI // 2017, 48, 2997;
- [12] Foing B. et al, LPICo2041 // 2017, 5073

BIBLIOMETRIC ANALYSIS OF SOLAR SYSTEM EXPLORATION MISSIONS

W. Fan¹, L. Han¹

¹*Institutes of Science and Development, Chinese Academy of Sciences, 33 Beisihuan Xilu, Zhongguancun, Beijing P.R.China, 100190, fanweiwei@casipm.ac.cn*

Keywords:

solar system exploration mission, bibliometric analysis, scientific outputs

Introduction:

The international trends of solar system exploration researches are depicted and analyzed by bibliometrics and text mining method based on solar system exploration missions. The overall situation and development trends of robotic solar system exploration missions and their scientific outputs are emphatically analysed and estimated. The analysis of solar system exploration missions shows that Mars and the moon will continue as top-priority exploration targets, meanwhile asteroids, giant planets and their satellites and Venus are also attracting targets. The boom of solar system exploration since 1990s is reflected in scientific papers. Bibliometric analysis based on solar system exploration missions shows that the volume of papers had been increasing rapidly since 1990s, and kept relatively steady after 2008. The United States is in the absolute leading position, the volume of papers and ESI papers and citations are way ahead of the other countries. France and Germany are on the second tier, outstanding in the above three aspects. China started late, but has made considerable progress in the volume of papers in recent years. Most countries have made extensive international cooperation. Among the top 10 countries, only the United States, Japan and Chinese have published more independent research papers than international cooperation papers. The proportion of international cooperation papers of France, Germany, Britain, Holland and Spain is over 70%. At the institutional level, the U.S. research institutions performance is outstanding, with NASA, Caltech, and University of California being the Top 3.

Digital formats for figures:

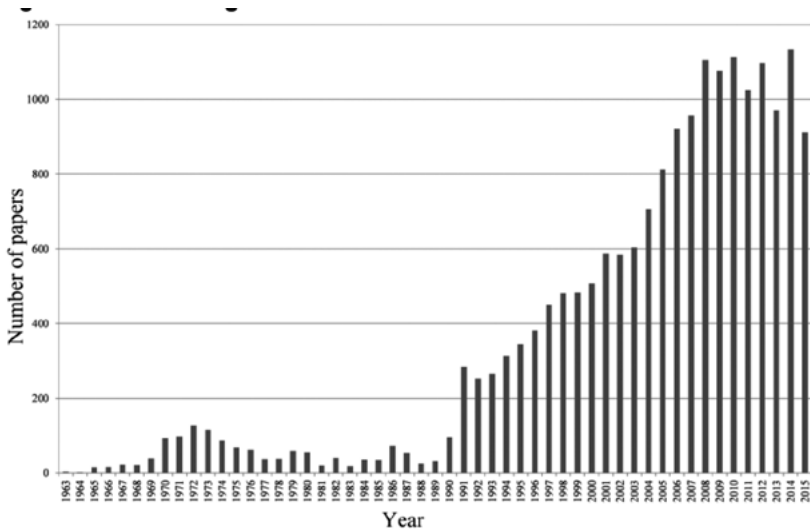


Fig. 1.

References:

- [1] NRC. Vision and Voyages for Planetary Science in the Decade 2013-2022 // <http://www.nap.edu/catalog/13117/vision-and-voyages-for-planetary-science-in-the-decade-2013-2022>
- [2] ISECG. The Global Exploration Roadmap 2013
- [3] 日本内閣府. 宇宙基本計画. // <http://www8.cao.go.jp/space/plan/plan2/plan2.pdf>

LUNAR ROUND-TRIP MISSION: OBJECTIVES

M.L. Litvak, I.G. Mitrofanov , V.I. Tretyakov

Space Research Institute, Moscow, Russia, 117997, Profsovnaya st 84/32, litvak@mx.iki.rssi.ru

Keywords:

Moon, lunar exploration program, lunar resources

Introduction:

We would like to present our vision of future phase of Russian lunar exploration program which could be implemented right after the completion of Luna 25-27 robotic missions and after initial attempt of lunar polar sample return (Luna-28). It is expected that the next step will be based on a close interaction between robotic and manned missions and should be focused on further exploration of the Moon polar regions, developing resource utilization technologies, biological experiments and site selection for future lunar base. The main task for robotic surface operations is to develop concept of multiple and sophisticated sample return involving mobility operations, sample collection across wide area and subsurface depths, preliminary sample screening/selection and sample transport to ascent module with further delivery for detailed study aboard lunar manned orbital station. The exploration activities should be combined with testing key technologies (for example, H and O production from the lunar regolith and water ice), required for the permanent presence of astronauts on the Moon surface. The list of primary goals should also include the so called round trip concept when some Earth materials (for example, medical staff, biological species, electronic components and etc) are temporarily delivered to the Moon surface to expose them in the lunar environment and then return back to the Earth for examination.

THE MODULAR MOBILE LUNAR BASE CONCEPT THE MOST REDUNDANT APPROACH FOR HABITAT ARCHITECTURE [HAB-ROB]

N.K. Pradhan

*Moscow Aviation Institute National Research University,
4, Volkolamskoe Shosse, GSP-3, A-80, Moscow, 125993, Russia, Faculty
No 6, Department of Aerospace Engg, pradhanneeraj97@gamil.com*

Keywords:

lunar base formed by a group of several independent lunar rovers.

Introduction:

This paper describes three innovative concepts for a mobile lunar base. These concepts combine design research for habitat architecture, mobility systems, habitability, radiation protection, human factors, and living and working environments on the lunar surface. The mobile lunar base presents several key advantages over conventional static base notions. These advantages concern landing zone safety, the requirement to move modules over the lunar surface, and the ability to stage mobile reconnaissance with effective systemic redundancy. All of these concerns lead to the consideration of a mobile walking habitat module and base design. The key issues involve landing zone safety, the ability to transport habitat modules across the surface, and providing reliability and redundancy to exploration traverses in pressurized vehicles. With self-ambulating lunar base modules, it will be feasible to have each module separate itself from its retro-rocket thruster unit, and walk 5 to 10 km away from the LZ (launch zone) to a pre-selected site. These mobile modules can operate in an autonomous or tele-operated mode to navigate the lunar surface.

Modular Integrated Lunar Outpost “MILO

The mobile lunar base presents several advantages over conventional static base notions. These advantages concern landing zone safety, the requirement to move modules over the lunar surface, and the ability to stage mobile reconnaissance with effective systemic redundancy. All of these concerns lead to the consideration of a mobile habitat module and base design. The key issues that the design of a mobile base must resolve include automated assembly and deployment, the configuration and methods for connecting modules, radiation protection and mission duration. The principal advantage of the stationary base is that it affords the build-up of infrastructure and resources in one location, which can lead to economies of scale and of agglomeration, without added the transportation costs of making it all mobile. One leading prospect of infrastructure build-up is to provide radiation shielding by burying the modules under 1 meter or more of lunar regolith.

Concept

1. In this concept, the rovers would travel together as individual units “wagon train” style.
2. At a likely site they would join together to form a temporary base.
3. There is a central “core module” with two lateral docking ports on either side.
4. At the end showing in the picture is an EVA airlock exiting to a deployable platform and stair.
5. The driver’s position is presumably at the distal end of the core module, although perhaps it could be towed.
6. The two modules docked on each side of the core would “back into” the docking ports.
7. The driver’s station appears on the right as a large gold-coated lens.
8. While the pressurized modules are docked together, they afford a continuous atmosphere among the three vehicles.
9. While the rovers are docked, the crew would employ the small, unpressurized rover on the left for local mobility.
10. The HAB-ROB modules land on six articulated legs, and then take double advantage of the legs by using them to walk away robotically from the landing zone.
11. The pressure vessels are hexagonal insofar as they require three cross-axes separated equally at 60° of arc.
12. They cluster together automatically to form a temporary base.
13. The possible module size ranges from about 3 to 5m diameter.
14. The crew arrive and depart the surface of the moon in a separate Descent/Ascent vehicle that may share some hardware commonality with

the HAB-ROB units, but is optimized for transporting the crew through cis-lunar space, landing and taking off from the lunar surface. 15. With self-ambulating lunar base modules, it would be feasible to have each module separate itself from its retro-rocket thruster unit, and walk five to ten km away from the LZ to a pre-selected site. 16. These walking modules can operate in an autonomous or tele-operated mode to navigate the lunar surface. 17. At the site of the base, the walking modules can combine together; make pressure port connections among themselves, to create a multi-module pressurized lunar base. 18. With exposed joints, the articulated legs would be vulnerable to dust and grit in the mechanisms, so the legs would need to be covered with dust-tight "stockings. 19. At the site of the base, the mobile modules can combine together; make pressure port connections among themselves, to create a multi-module pressurized lunar base.

Landing Zone

The landing zone (LZ) poses the problem that once a habitat lands on the moon, it is not prudent to land another vehicle within several kilometers because of safety concerns from ejecta in a normal landing and in case of an explosive failure on impact. Therefore, if the lunar mission intends to create a well-established approach range and LZ, it is necessary to move the landed habitats and payloads well away from the LZ, much in the manner that aircraft taxi off the runway after landing at an airport. So what is the best way to move the module?

Exploration Mobility Approach

Approach A further advantage of the mobile lunar base concerns exploration traverses of the lunar surface. The conventional model of exploration is that a crew of two or more astronauts travel in a pressurized or unpressurized rover to a remote site, perform an EVA, collect some rock, soil and regolith samples, and then return to the base. An unpressurized rover is limited to a traverse measured in hours. If the rover is pressurized, then the crew can make a longer traverse, under some scenarios lasting days (sols) or weeks.

Reliability, Redundancy and Availability

The problem with this conventional rover scenario is one of reliability and redundancy. If the rover should experience a failure that prevents its return to base or that otherwise compromises safety or is life threatening, how will other astronauts at the lunar base rescue them? The usual answer is to have a second rover that can perform the rescue. But what if it runs into a problem too – the same or a different problem? Well, that means a third rover. Following this chain of reasoning, fairly soon, most or all of the landed mass resources of the lunar mission becomes devoted to ensuring the safety of a pressurized traverse mission. So, why not make the entire base mobile, so that all the resources, reliability and redundancy of the lunar mission move with the exploration crew? This approach means that the laboratory facility will travel with the explorers, affording them the capability to conduct complex and sophisticated scientific assays and analyses on site, without a need to return to the base. Once the lunar exploration concept transcends the convention of a rover as a delivery truck for rocks, vast new potentialities open up. The Mobile Lunar base allows the explorers to bring the base to the sites of scientific interest to make the most complete investigation, without the severe constraints and limitations to traverses and EVA sortie time. A further advantage of the Mobile Base system is availability. With the versatility of the Mobile Base approach, it is possible to land new mobile modules with new equipment, supplies or logistical support in the path of the moving ensemble. These new units could then join the "wagon train" to continue on the journey, or simply provide a cache of supplies for the crew to pick up along the way.

Mission Activities

Once enough mobile base units arrive to form the lunar base, they cluster together at a site of scientific or technical interest, and make the vital connections for pressurized access, communications, data, life support, etc. After these modules have completed joining together to form the lunar base, it becomes possible for the first lunar expedition crew to arrive. After the crew completes their mission at that particular site, they return

to the Earth, in a separate, dedicated vehicle. In the following weeks or months, the mobile units separate from one another, and move across the lunar surface to a new location of scientific interest, and a second crew arrives. It is also possible for the crew to travel with the mobile base units. The crewmembers will also use individual mobile units as pressurized rovers to explore the lunar environment.

Lunar Missions Habitats to support lunar missions were considered for locations in the lunar DRO, EML1(EarthMoon Lagrangian point 1), and EML2(Earth-Moon Lagrangian point 2) orbits. The missions of interest included more direct control of lunar surface robotic systems, service for reusable robotic and human Lander systems, initial analysis and collection of lunar sample materials collected from the surface of the moon, and assistance with setting up and serving of ISRU(insitu resources utilization) systems on the moon and in a laboratory inside the habitat using lunar materials. Although initial missions might use an MPCV (Multi purpose crew vehicle)and an expendable Lander in a low lunar orbit, as done in the Apollo Program, a habitat at the higher orbits could support human-tended missions for 4-crew up to 180 days, provide global access to the lunar surface, and support Lander reusability with the required servicing functions. It was found that these systems could be developed as an expansion of the capabilities described for the current asteroid retrieval missions.

Key HAB-ROB parameters The fundamental idea is that the Habitat + Robotic mobility (HAB-ROB) is a combination of a human habitat and a robot. The Hab-Rob lands autonomously on the Moon on a set of articulated legs. The Hab-Rob then uses those legs or wheels mounted on the legs to move itself away from the designated landing zone so that more Hab-Rob can land. Once enough Hab-Rob arrive to form the lunar base, they cluster together at a site of scientific or technical interest, and make the vital connections for pressurized access.

Robotic Habitat Deployment and primery mission Verification

Once enough mobile base units arrive to form the lunar base, they cluster together at a site of scientific or technical interest, and make the vital connections for pressurized access, communications, data, life support, etc. After these modules have completed joining together to form the lunar base, it becomes possible for the first lunar expedition crew to arrive. After

the crew completes their mission at that particular site, they return to the Earth, in a separate, dedicated vehicle. In the following weeks or months, the mobile units separate from one another, and move across the lunar surface to a new location of scientific interest, and a second crew arrives. It is also possible for the crew to travel with the mobile base units. The crewmembers will also use individual mobile units as pressurized rovers to explore the lunar environment. In FIGURE 2 the articulated legs carry manipulator devices that can pick up rocks. A hexagonal cluster appears in the middle ground at the right.

Mobility System Modular Integrated Lunar Outpost [MILO]

This study does not presuppose any specific mobility system. Only after analyzing all of the necessary functions and components of the mobile habitat and base configurations, will it be reasonable to develop requirements for the mobility system. Never the less, since the HAB-ROB is closely associated with the walking model, it is appropriate to describe the candidate walking aspect. The HAB-ROB will have a very modest walking speed that need not exceed 5 km/hour. There is no advantage in designing it to move "fast" if that translates into a huge energy burden that will be used for only short periods of time. The baseline is a maximum of 2 km/hr with a crew driver over smooth, level terrain. On rough terrain, the speed will be reduced to whatever is safe, perhaps as slow as .5 km/hr on slopes or rough terrain. The baseline speed without a crew on board is .5 km/hr.

All HAB-ROB will land un-crewed. They will walk or roll themselves about 10km away from the LZ to a base deployment site. There, the HAB-ROB will dock together and await the arrival of the crew. When the crew land in the descent/ascent vehicle, they travel on the same walking system to the base deployment site. There, the crew transfers via a docking tunnel

in a shirtsleeve environment to the united base. As a contingency, the descent/ascent vehicle will carry EVA suits the crew can use to make the transfer. Additional contingencies if the descent/ascent vehicle is unable to walk, a HAB-ROB from the base will come to the LZ and pick up the crew. The final fallback is that the crew can walk the 10 km EVA to the base.

6 HAB-ROB modules that form the Modular Integrated Lunar Outpost "MILO" cluster.

These modules would all derive from the same basic pressure vessel, platform and chassis, comprising the complete living and working environment

Table 1.

Living Environment/Habitability Support	Working Environment & Operational Systems
Crew "Cabin" (Sleeping Quarters).	EVA Access: Airlock and Stowage, including the, EVA suit Stowage and maintenance NASA "Robonaut" a) master-slave tele-robot b) heavy-duty space truck (hexa-pod system) ATHLETE [All-Terrain Hex-Limbed Extra Terrestrial Explorer]
Ward Room (back-up Command and Communications Center)	Command and Communications Center
Logistics Module	Laboratory1- Life Sciences.
Health Maintenance, Exercise, Recreation	Laboratory 2-Physical Sciences (Cupola and Observatory).

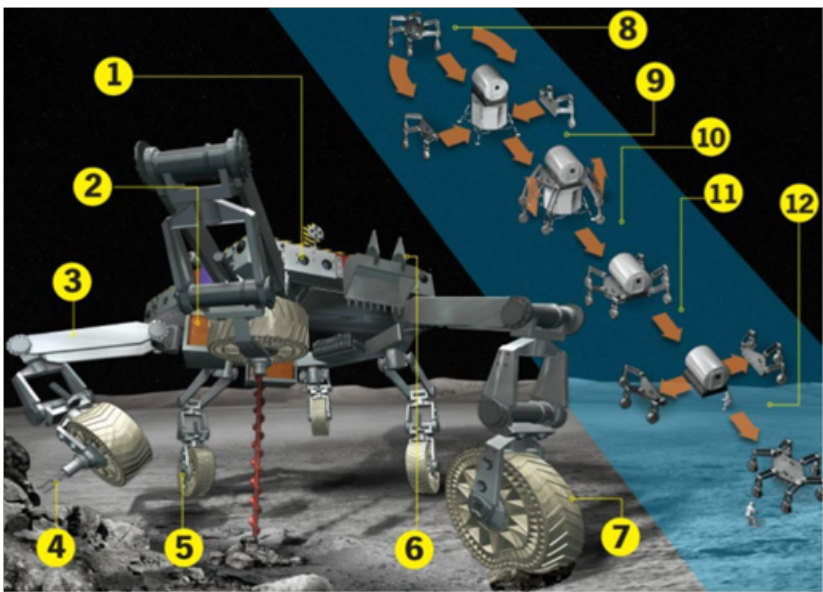


Fig.1.

- 1) The ATHLETE moon rover has 48 stereo cameras, which stream 3-D video from its limbs, frame, and wheels to human operators on Earth or the moon, allowing them to look for hazards and maneuver tools. ATHLETE will have more cameras than any previous rover. (Curiosity has 17)
- 2) The rover can refill its hydrogen fuel cells at a solar-powered station that splits water into hydrogen and oxygen (for astronauts to breathe).
- 3) ATHLETE's wheeled limbs let it walk, drive, or climb, depending on the environment. Each has seven motorized joints that bend and twist. ATHLETE controls each leg separately so that it can keep cargo level even while climbing uneven terrain.
- 4) Drills, scoops, and grippers collect rock and soil samples for analysis. One set of motors operates both the wheels and tools, which saves weight

and makes the rover cheaper to launch into space.

- 5) Clamps on the wheels hold interchangeable tools.
- 6) A tool belt stores gear when not in use.
- 7) Airless tires can't burst or go flat.
- 8) Drive: People in mission control (on Earth or on the moon) tell the ATHLETE rover to drive to a lander that has just touched down, carrying a cargo pallet. Incoming supplies must land far from the astronauts' base to prevent jagged moondust from damaging equipment.
- 9) Split: ATHLETE divides into two identical, three-legged rovers, called _Tri-ATHLETE_s, by lifting motorized hooks that latch across its center.
- 10) Stretch: The rovers straighten their legs until they're 27 feet tall—high enough to reach above the lander to the cargo pallet—and use their motorized hooks to grab pins on either side of the cargo.
- 11) Walk: If the rovers travel over rocky terrain too uneven for driving, they can walk while keeping the cargo level.
- 12) Deliver: The rovers crouch down until the pallet is on the ground and then release it.



Fig.2.

Energy System

The energy system incorporates several elements. A cylindrical tower atop the module carries photovoltaic cells to provide constant "lifeline" power during the lunar day. At the top of this tower sits a parabolic dish antenna to receive beamed microwave or laser power. A possible back-up option for "lifeline" power would be to install a radio-thermal generator (RTG) at the base of the tower. Safe disposal of spent nuclear fuel will be required to make this concept viable. However, providing sufficient and reliable energy throughout the lunar day/night cycle remains one of the technological "tall poles" to make any mobile base concept succeed, and will demand much more research and development. In addition to the HAB-ROB approaches to energy systems are two possible alternatives using beamed energy, and by RTG

- 1] Beamed micro wave or Laser Power
- 2] Radio Isotope Thermo Electric Generator

Beamed micro wave or Laser Power scheme to power a lunar rover by beaming laser power from a solar power satellite to a parabolic receiver on a pressurized rover. The primary source of this power will be a space solar power satellite in a lunar-synchronous orbit that would keep the satellite above the rover at all

times which would provide power in the 100 to 300 KW range. However, it is not clear how it would supply power when in the shadow of the moon. Such a concept might be more viable in combination with solar power satellites at the lunar L1 or L2 point or both. The large laser beam antenna is mounted in the center of the cylindrical portion and the small antenna to the front is for communications.

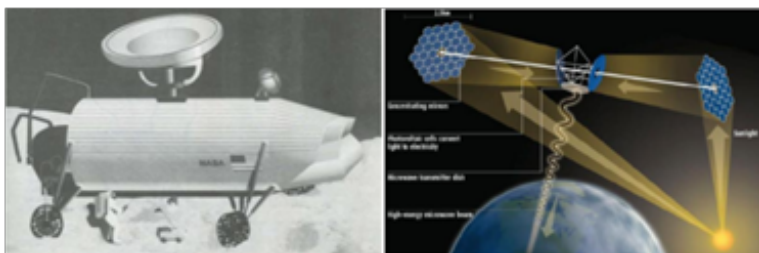


Fig.3.

A second power alternative would be a nuclear reactor (RTG) mounted on a HAB-ROB, Rover or Mobitat chassis. Mobile Lunar Reactor concept, following and powering a pressurized rover. This "Powerbot" would follow the Habots from a distance of several kilometers away, and beam power in the 100 to 150 KW range by microwave to the same antenna that would serve for solar satellite power.

is an electrical generator that uses an array of thermocouples to convert the heat released by the decay of a suitable radioactive material into electricity by the Seebeck effect. This generator has no moving parts. A thermocouple is a thermoelectric device that can convert thermal energy directly into electrical energy, using the Seebeck effect. It is made of two kinds of metal (or semiconductors) that can both conduct electricity. They are connected to each other in a closed loop. If the two junctions are at different temperatures, an electric current will flow in the loop.

The design of an RTG is simple by the standards of nuclear technology: the main component is a sturdy container of a radioactive material (the fuel). Thermocouples are placed in the walls of the container, with the outer end of each thermocouple connected to a heat sink. Radioactive decay of the fuel produces heat. It is the temperature difference between the fuel and the heat sink that allows the thermocouples to generate electricity.

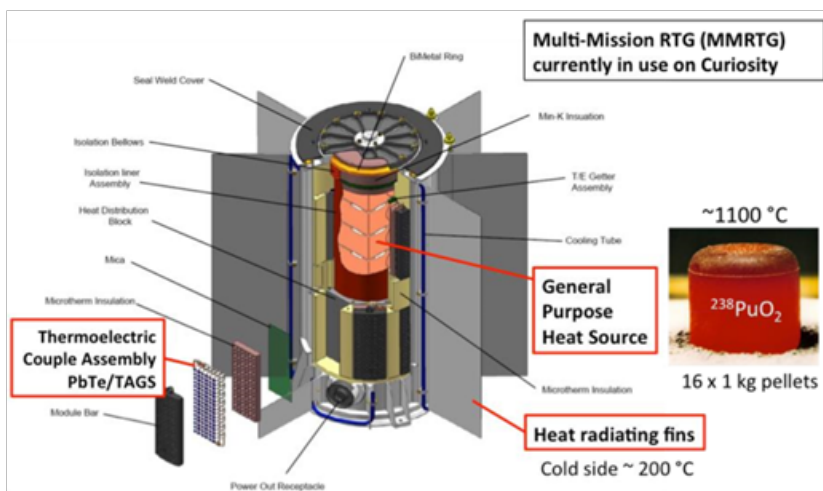


Fig.4.

The original concept for the Habot aimed for a mass budget per unit of 3 to 5 mTons. This mass limit would be very convenient for launch by existing conventional expendable rockets. However, as a preliminary analysis the

5 mTon mass budget per unit has small margin and overall is extremely tight for a nominal 100-sol mission by the crew of 4. A more realistic Hobot mass budget baseline may be closer to 10 mTon (10,000kg), separate from the descent engine unit. TABLE 2 presents a preliminary mass budget for this Hobot unit, working with the range of masses that Mankins envisions. These bounding values appear in the top line for the pressurized habitat and its contents, including outfitting. However, these mass values are simply too small to provide the complete system for one Hobot with a crew of 4 over 100 days. The lines below the pressurized habitat indicate the additional elements that would be needed.

Table 2. Preliminary Mass Estimate

Component	Min Mass, mTon	Max Mass, mTon	Remarks
Pressurized Habitat: Pressure Vessel Structure, Life Support & Thermal Control, Habitability Accommodations, Operational Systems	3.0	5.0	Habitat is fully pre integrated before launch.
Exterior Protection Radiation Shielding, Thermal Protection, Micrometeoroid Protection	.8	1.0	Mobility system require more study
Mobility System Hobot "Unibody" consisting of Base frame, 6 legs, motors and mechanisms	.5	.8	
Energy Systems Solar Cells, batteries, SSP/"Powerbot" Microwave Antenna, Possible RTG	1.0 7.3	.4 10.0	

Conclusion

The most significant development is the reliance upon automation and robotics assembly to move the mobile units across the lunar terrain and then to assemble them and verify the readiness of the base for the arrival of the crew. A major challenge emerges as allocation of resources and distribution of capabilities among the Hobot modules. Radiation protection remains a challenge and a potential showstopper, as it does for all Lunar Base and rover concepts. The energy systems stand out as a technological tall pole for all mobile base concepts. The architecture for combining the pressurized modules – the habitats – into the base cluster will play a substantive role in facilitating the use of resources and application of capabilities of all types.

Reference

- [1] <https://www-robotics.jpl.nasa.gov/systems/system.cfm?System=11>
- [2] <https://athlete.jpl.nasa.gov/>
- [3] <https://www.space.com/39985-nasa-lunar-orbital-platform-gateway-science-plan.html>
- [4] Systems Engineering Principles And Practice, Alexander Kossiakoff William N. Sweet Samuel J. Seymour Steven M. Biemer
- [5] Space Mission Analysis and Design // Third Edition Wiley J. Larson United States Air Force Academy and James R. Wertz Microcosm, Inc. Coordination by Douglas Kirkpatrick, United States Air Force Academy Donna Klungle, Microcosm, Inc
- [6] file:///D:/3rd%20semester%20MASTERS/nasa_systems_engineering_handbook_0.pdf

ON EVE OF THE GLORIOUS JUBILEE: 60 YEARS OF THE MOON'S EXPLORATION BY SPACECRAFTS

A. Gusev¹, H. Hanada², A. Kosov³, Zh. Meng⁴, J. Ping⁵

¹*Kazan Federal University, Kazan, Russia;*

²*National Astronomical observatory of Japan, Oshu, Japan;*

³*IKI RAS, Moscow, Russia;*

⁴*College of Geoexploration Science and Technology, Jilin University, Changchun, China;*

⁵*National Astronomical Observatory of China CAS, Beijing, China;*
agusev33@gmail.com

Keywords:

Moon, rotation, libration, liquid core, tidal - librational dissipations, lunar navigation, long-term lunar bases.

Introduction:

The implementation of modern long-term programs for the exploration of the Moon in the framework of LLR projects, Kaguya, SELENE-X (JAXA, Japan), LRO, GRAIL, LADEE (NASA, USA), Chang'E-1/2,3/4,5/6 (China), Chandrayaan-2 (India), Luna-Glob-Resource (Roscosmos, Russia) is aimed both at creating long-term lunar bases, and on obtaining a wide range of information about the lunar gravitational field, the exact position of the Moon in the inertial coordinate system, the dynamic and geometric figure of the Moon and its internal structure.

This review [1,2,3] shows results of investigation for features of multilayer celestial bodies rotation: 1. Study of physical libration effect in multilayered Moon's rotation, associated with the presence of two-layer hot core; 2. Analysis of free and forced librations for multilayered Moon with tidal and librational dissipation, modeling of three-layered Moon's internal structure with a liquid core. 3. Preparation of navigational, geodetic and geophysical justifications and recommendations for program on studying the inner structure of the Moon in framework of future Russian and international space missions.

Fundamental answers:

What would we like to know about the Moon? Why is the visible and reverse side of the Moon so different in relief, tectonic formations, gravitational, geochemical, mineralogical and magnetic distributions and anomalies? Is there water ice in the polar regions of the Moon and is it possible for it to be developed and used for lunar bases? What is the nature and origin of the largest crater (more than 2500 km in diameter, up to 12 km deep) in the Solar System located at the south pole of the Moon? What are the sizes and geochemical composition of the liquid core, viscoelastic mantle and solid crust of the thin marine and thick continental parts of the Moon? What is the source of the paleomagnetic field of the Moon found in the investigation of lunar samples? What is the future of the Moon-Earth system?

The answer to the scientific questions may be information from a whole fleet of new and planned spacecraft to the Moon - the European technical satellite "SMART-1" (ESA, 2003-2006), the Japanese mission to farside of the Moon "SELENE" (JAXA, 2007- 2009), the Indian probe "Chandrayaan-1" (2007), the Chinese probes "CHANG'E-1,2,3" (2007-2012 +), the American scouts of the polar ice "LRO" (NASA, 2009-2015), gravity field "GRAIL"(2011-2012), lunar exosphere LADEE (2013-2014). The question of choosing the best place for long-term lunar bases for earthlings along the whole range of life support and industrial development of the Moon also ripens on the agenda of the data of this space armada. Due to its proximity to the Earth, the Moon is being investigated by space vehicles on a circumlunar orbit and devices located on the lunar surface for almost 60 years (January 2, 1959) already. The richest volume of data and a wide range of research methods of geophysics led to the creation of a new scientific discipline – lunar astrometry,

selenodesy, selenophysics and others. The knowledge of the fine effects of rotation, physical libration and nutation of the Moon allows us to look convincingly into the internal structure of our natural satellite.

It is assumed that 4.5 billion years ago the celestial body of Mars's size and mass, with a speed of 11 km per second, collided with the proto-Earth, formed only 95% of the protoplanetary disk around the Sun, heated and sprayed a significant piece of the upper mantle of proto-Earth in near-earth orbit for several hours of contact [1]. Later, from the formed hot disk of particles and debris in vicinity of the Earth for several millennia, a hot Moon was formed due to the accretion and coalescence of planetesimals at distance of several Earth's radii from the Earth and with a rotation period of only 4-5 hours! For comparison, at present time, the Moon rotates already at distance of about 58 radii of the Earth and with a period of 27 days and moves away from the Earth at a speed of 3.8 cm per year due to solar-terrestrial tidal-librational dissipation!

Lunar research in 21st century:

The beginning of the new millennium is marked by a big number of theoretical papers that review the results and problems in this area (Kuskov, Kronrod, 1998-2016, Gusev, Petrova, Hanada, 1996-2017; Williams et al., 2001-2016; "New Views of the Moon", 2006) [1]. Studying the rotation of celestial body opens a possibility to penetrate in the complex internal structure of the celestial body, especially in cases when other (geophysical) methods are inaccessible. It is shown [1] that the determination of periods and amplitudes of free libration will make it possible to conclude that there is a liquid core of the Moon and planets, to estimate the dimensions, composition and thermal profile, as well as a periods of Chandler Wobbles of inner solid core and Free Core Nutation of outer liquid core of the Moon.

The authors of the review [1] for the first time calculated the spectrum of free libration and carried out structural and parametric modeling of the internal structure of the Moon. A simulation was performed to determine the dependence of the obtained periods of free rotation on the radius, density, chemical composition of the core, and the dissipative characteristics of the core-mantle zone. A geophysical, thermal, temperature and mineral section of the Moon and structural detailing of the lunar two-layer core based on the latest data of lunar observations, experiments and computer modeling are proposed. A draft of estimates and recommendations for observing the physical libration of a multilayered Moon for the Japanese robotic program ILOM at the south pole of the Moon for the period 2020+ is proposed.

In the new millennium, a series of space experiments aimed at the global exploration of the Moon, started with the **SMART-1** project (Foing et al, 2006), which opened new technological capabilities of lunar experiments providing a wide range of data on the Moon. 2007 is the year of triumphant inclusion in the lunar exploration of space agencies in Japan, China, and India. First of all, it concerns the Japanese mission **SELENE (Kaguya)**, which for the first time provided high-accuracy topographic and gravitational mapping of the entire lunar surface, including the previously inaccessible areas of the invisible side and the limb zone of the Moon (Araki et al., 2009; Namiki et al., 2009, [1]). With the help of the on-board laser altimeter Kaguya, heights of 6.8 million points were determined on the entire surface of the Moon, including the polar zones, with an error within 4 meters. It is established that the difference between the highest and the lowest points on the lunar surface is 19.8 km, which is 2 km more than previously thought. The highest point of the Moon is at the edge of the Dirichlet-Jackson crater and rises above the surface for 11 km. The deepest depression on the Moon is the bottom of the Antoniadi crater near the south pole, submerged on 9 km from the average surface of the Moon.

In October 2007, China launched the automatic interplanetary station "**ChangE-1**" to the Moon [1]. The spacecraft accomplished several tasks: 1) Construction of a three-dimensional topographic map of the Moon - for scientific purposes and for determining the location of planting of future probes. 2) Mapping the distribution of chemical elements such as titanium

and iron. It is necessary for an estimation of an opportunity of industrial working out of deposits. 3) Evaluation of the deep distribution of elements using microwave radiation - will help clarify how helium-3 is distributed and whether its content is large. 4) The study of the environment between the Earth and the Moon, for example, the "tail" region of the Earth's magnetosphere, plasma in the solar wind. Chang'E-1 generated the most accurate and highest resolution 3-D map ever of the lunar surface, until it was surpassed by the LRO and conducted world's first passive, multi-channel, microwave remote sensing of the Moon.

The main objectives of **Chandrayaan-1** probe (India, Nov. 2008) included 1) the search for minerals and ice reserves in the polar regions of the Moon, and 2) the compilation of a three-dimensional surface map of the Moon. Indian scientists were able to detect water at the bottom of the lunar craters. For the first time such information was obtained by remote sensing observations from the Moon's orbit. Earlier studies of samples of lunar soil, delivered by expeditions of the Apollo, also showed the presence of water on the Moon [1].

The LRO - LCROSS lunar probe (NASA, USA) launched in June 2009, from the very first days of its operation in the lunar orbit, delivers to Earth unique high resolution images of the lunar surface. Lunar modul LCROSS in Oct. 2009 collided with the surface of the Earth satellite, found evidence of the presence there of a significant amount of water ice! LRO also found the coldest point of the Solar System. It located in shaded craters near the southern pole of the Moon. The temperature inside the craters reaches minus 240 degrees Celsius. It's only 33 degrees above absolute zero. The LRO mission is the first serious step in the implementation of a long-term program for the installation of habitable lunar bases, planned by many countries in the 2020+. The task of LRO is to find the most suitable place for the deployment of the base. To do this, he will have to find water and energy sources, "to find out" how dangerous the radiation situation in the near-moon space is for a person. These tasks are solved with the help of six scientific tools LRO. To date (2018) four sets of databases have been created on basis of the whole complex of observations: 1) topographic (6.4 billion altitude measurements, top-chart models take in account spherical harmonics up to 2500 degree and order); 2) surface slope data; 3) data of surface irregularities (accuracy reaches 5 m); 4) albedo data in the zero phase. According to the results of data analysis in the polar region, the greatest brightness is observed in the Shackleton crater. At the south pole of the Moon, as the most interesting area of future scientific research, a landing area 2 km x 1.5 km was recommended for future international missions (Smith et al., 2015).

In October 2010, China launched the "ChangE-2" probe to the Moon, which underwent significant improvements, so the device can be assigned to the next generation of lunar probes: it was equipped with a digital camera that allowed to obtain images of higher resolution in different frequency bands [1].

All 2012 was held for the study of the Moon under the sign of the American unique mission "**GRAIL**" (NASA, USA, Zuber et al., 2013), which resulted in the construction of models of the gravitational field of the Moon in the beginning up to 600 order, and within the extended mission, up to 1200 order accuracy! The accuracy of the model of the Moon's gravity field was improved by three to four orders of magnitude in comparison with the previous models of the Moon's gravity field! The surface resolution of the gravity reaches on a linear scale of 5 km and there is a high correlation between the gravity field and the lunar topography of the LRO probe. According to the results of the research, the average thickness of the crust on the visible side of the Moon is 35 km (less than estimated earlier), the porosity of the lunar crust on the visible and invisible sides reaches up to 5% - 20% [1]. The density of the cortex was less than expected. Additional arguments appeared on the two-layer structure of the lunar core: external liquid FeS and internal solid Fe.

2013 was opened by the new American lunar mission "**LADEE**", (Noble et al. 2014) the main purpose of which was to study the exosphere of the Moon, its dust and gas components, at altitudes of 30-100 km. It was found that the daytime temperature on the surface reaches plus +107°C,

and the night temperature drops to -173°C , the temperature difference is $+280^{\circ}\text{C}$. The structure of the atmosphere of the moon varies with its phases [1]. The atmosphere of the Moon contains numerous very simple molecules of very low concentration, its dust component is inhomogeneous and is formed when many micrometeorites fall. During the operation of this probe, up to 10 thousand drops of micrometeorites were observed.

In December 2013 the Chinese landing module “**ChangE-3**” with a mini rover “**Yutu**” successfully landed on the Moon. The highly stable beacon placed on the platform was actively engaged for two years with the onset of each lunar day and gave a unique in accuracy and volume information on the motion and rotation of the Moon with an accuracy of 0.5 mm on a linear scale! After the two year of observations using the Lunar Radio Ranging (LRR), the volume and accuracy of the information obtained about the spin-orbit motion of the Moon already exceeds the array of data obtained by the Lunar Laser Ranging (LLR) for 48 years of its observations (Ping et al., 2014, [1]).

Conclusions:

On basis of the high-accuracy theory and observations, it is possible to include the searching for the new modes in libration series – Free Core Nutation (FCN), Free Inner Core Nutation (FICN) and Inner Chandler Wobble (ICW) in the programs of the future Chinese, EU, Russian, Japanese space geodesy experiments, which will provide the direct determination of the Moon orientation in space. Differential radio and optical technologies have been proposed for measurements of Lunar physical librations and lunar tides. A new big size corner cubes reflectors (CCR) and a stable long-lived radio beacons would be desirable experiments on future lunar landers. Sensitivities to physical libration and tidal displacements would be enhanced by a broad geographical spread of the CCR, radio beacons, seismometers at Chang'E - 4/5/6 (China), Luna - 25, 26, 27 (Russia) projects.

References:

- [1] Gusev A., Hanada H., Petrova N., Kosov A., Kuskov O., Kronrod V., Kronrod E., Rotation, physical librations and interior structure of the active and multi-layer Moon, // Monograph, Kazan University Publishing Co., Kazan, 328pp. (Russian+English), 2015
- [2] Hanada H., Gusev A., et al., “Development of a Small Telescope like PZT and Results of Experiments on the Ground”. // Gyroscopy and Navigation, v.8(4), Issue 4, p.304-319. [3] Gusev A. Hanada N., Ping J., (2018), “Moon 2020+”, Educational and scientific booklet, Kazan University Publishing House, 4 p., 2017

CLOSED DEPRESSIONS IN ARABIA TERRA, MARS: IMPLICATIONS FOR SUBSURFACE MASS REMOVAL

C.A. Denton, J.W. Head

Brown University, Providence RI 02912, USA, camille_denton@brown.edu

Keywords:

Mars, Late-Noachian-Early Hesperian, geomorphology, fretted terrain, climate, groundwater,

Introduction:

The Arabia Terra plateau of Mars hosts numerous unusual geologic features whose formation mechanisms remain unexplained. An understanding of the modes of formation for these features, as well as their relationship to the presence or absence of surface water, is crucial to unraveling the complex geologic history of the planet during the Late Noachian-Early Hesperian. We address this question through an in-depth geomorphologic analysis to document morphology/morphometry, assess previously proposed formation mechanisms, and develop new hypotheses for their formation in the context of Arabia Terra and the morphologically similar fretted terrain to the north [1].

Geologic Background:

The Arabia Terra (AT) plateau ($\sim 2.6 \times 10^6$ km² in size) contains a record of key geologic and climatic changes during the early history of Mars (Fig. 1); its surface is defined by emplacement of lava flows in the Mid and Late Noachian [2]. Subsequently during the Late Noachian and Early Hesperian (LN-EH) valley networks formed and a thin veneer of sediments was emplaced, producing a complex series of fluvial landforms [2-4]. The AT plateau is associated with the fretted terrain to the north, a broad region of plateaus, and mesas in complex configurations whose formation has been attributed to the removal of intervening plateau and substrate material [1-2, 5-6]. Within the plateau itself, the three main unusual feature classes are: (1) the *fretted channels*, wide, sinuous, flat-floored channels, (2), *chaos-floored craters*, whose floors have been heavily fractured and disrupted, and (3) *closed depressions*, wide, flat, linear to curvilinear depressions ~ 30 -200 km long, ~ 5 -15 km wide, and ~ 0.3 -1 km deep. Each of these shares diagnostic morphologic features with each other as well as the fretted terrain, and each remains poorly understood. Here we focus on the nature of the closed depressions (Fig. 1), and the insights that their characteristics provide for the history of the AT plateau during the LN-EH.

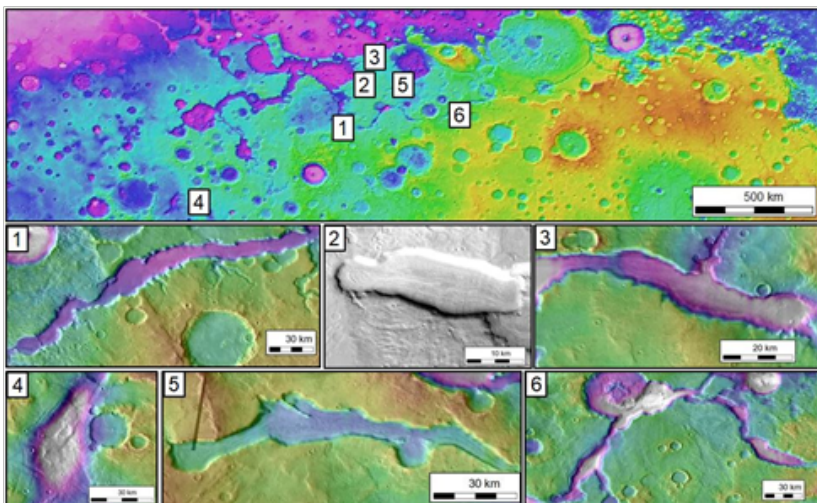


Fig. 1. Top: Locations of individual closed depressions within the AT plateau are numbered. Below: higher-resolution images of each closed depression. The depression described in more detail here is #5.

Figure 1 indicates the location of the six observed closed depressions in the AT plateau. Most closed depressions are isolated in the interior; they lack inlet channels or outlet channel mouths and are instead bounded by amphitheater-shaped headwalls. Further, the walls and flat floors of most closed depressions are occupied by Amazonian debris-covered glaciers [7,8], obscuring the true depth profile of the channel. The majority of closed depressions are oriented subparallel to the dichotomy boundary between the northern lowlands and southern highlands, and thus do not follow regional topographic trends [2]. Here we focus on a specific closed depression (Fig. 1, #5) for detailed description and in-depth morphologic analysis. We utilized MOLA topography and THEMIS daytime imagery (Fig. 2) [9-10] in our general analysis and as well as that of #5.

The selected closed depression is ~127 km in length and covers an area of $\sim 1.28 \times 10^3$ km². While the closed depression is at its narrowest in the east (~5-7 km wide) and widest in the center (~15-19 km wide), the majority of the channel is ~10 km wide on average, and is ~350-500 m deep. The formation process(es) for the closed depression denuded multiple ~10-20 km-diameter craters during formation of the depression far beyond what is typical for Noachian-aged craters [11], removing crater rims within the path of the depression, including the crater-like feature which forms the western head of the depression, the circular feature covered by the B-B' profile, and the partially denuded crater between profiles B and C along the southern wall (Fig. 2).

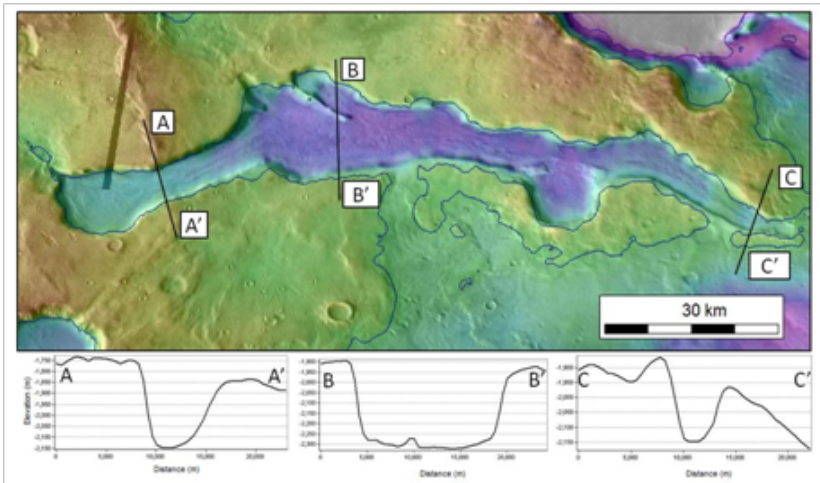


Fig. 2. MOLA global gridded topography [9] overlain by THEMIS daytime imagery [10] of the selected closed depression. Three topographic profiles perpendicular to the channel are shown below from west to east.

Mass wasting and debris shedding from the steep scarps bounding the depression obscure stratigraphic variations in the wall stratigraphy beyond first-order observations; a cliff-building upper unit is clearly visible, consistent with the volcanic capping unit in AT. Glaciation of the walls and floor of the depression prevents measurement of true depression topography as well as identification of any preexisting flow paths or collapse features. We find that the apparent volume of material removed to produce the closed depression is ~ 470 km³, approximately the volume of Lake Erie; however, due to the presence of debris-covered glaciers this volume is a minimum estimate.

Discussion and Implications:

The lack of inlet channels into the closed depression appears to preclude overland flow as a mechanism for depression formation. Multiple ridges and local topographic uplifts can be observed to terminate along the northern wall, perpendicular to the main depression; these are morphologically similar to wrinkle ridges observed elsewhere in AT [2] and imply contractional tectonic deformation of the plateau following volcanic plains emplacement. There are multiple possibilities for removal of the estimated >470 km³ of material from the subsurface to produce the closed depression. Overland water

flow seems unlikely as no inlet channels are observed. Glacial activity within the depression significantly post-dates the formation of the feature. The circulation of liquid groundwater in a warm and wet LN-EH climate scenario, the melting of snow, ice, or ice-cemented soil in a colder LN-EH climate scenario, or chemical dissolution of a soluble subsurface unit may all provide mechanisms for collapse and removal of material from the system. However, for such a large volume to be removed from the system without an observable sink for material, a large proportion of the missing volume must be sublimated, melted, and otherwise transported water. Such a process converts existing volume to void space in the subsurface, requiring lateral transport of a minimum volume of sediment relative to the total volume of missing material. Thus, we suggest that melting of buried ice and/or ice-cemented soil is the most volumetrically efficient mechanism.

Conclusions:

The closed depressions observed in the AT plateau record a process of subsurface volume loss at the edge of the southern highlands, in which massive quantities of material (ranging from $2.8 \times 10^3 \text{ km}^3$ to $3.4 \times 10^3 \text{ km}^3$), including sediment and H_2O , were mobilized and removed from the subsurface. The proximity and similarity in age, scale and morphology between closed depressions, fretted channels, and the fretted terrain suggests that their origins may be related; we speculate that the closed depressions may represent the initial stages of fretted channels. We conclude that the observed morphology appears to be most consistent with removal of material through disruption of the subsurface, in which a preexisting reservoir was removed, weakening and collapsing overlying material, and removal of that material from the system through unidentified vertical and lateral modes of transport.

References:

- [1] Sharp R.P. Mars: Fretted and chaotic terrains. // JGR. 1973. V. 7. No. 20. P. 4073-4083.
- [2] McGill G.E. Crustal history of north central Arabia Terra, Mars. // JGR. 2000. Vol. 105. No. E3. P. 6945-6959.
- [3] Carr M.H. The martian drainage system and the origin of valley networks and fretted channels // JGR Planets. 1995. V. 100. No. E4. P. 7479-7507.
- [4] Davis, J.E. et al. Extensive Noachian fluvial systems in Arabia Terra: Implications for early Martian climate // Geology. 2016. V. 44. No. 10. P. 847-850.
- [5] Carr M.H. Water on Mars. Oxford University Press. 1996.
- [6] Irwin R.P. et al. Sedimentary resurfacing and fretted terrain development along the crustal dichotomy boundary, Aeolis Mensae, Mars // JGR. 2004. V. 109.
- [7] Morgan, G.A. et al. Lineated valley fill (LVF), and lobate debris aprons (LDA) in the Deuteronilus Mensae northern dichotomy boundary region, Mars: Constraints on the extent, age, and episodicity of Amazonian glacial events // Icarus. 2009. V. 202. No. 1. P. 22-38.
- [8] Head J.W., et al. Northern mid-latitude glaciation in the Late Amazonian period of Mars: Criteria for the recognition of debris-covered glacier and valley glacier landsystem deposits // Earth Planet. Sci. Lett. 2010. V. 294. P. 306-320.
- [9] Smith, D.E. et al. Mars Orbiter Laser Altimeter: Experiment summary and the first year of global mapping of Mars // JGR. 2001. V. 106. No. E10. P. 23689-23722.
- [10] Christensen, P.R. et al. The Thermal Emission Imaging System (THEMIS) for the Mars 2001 Odyssey Mission // 2004. Space Sci. Rev. V. 110. No. 1-2. P. 85-130.
- [11] Mangold, N. et al. A chronology of early Mars climatic evolution from impact crater degradation // JGR. 2012. V. 117.

EARLY MARS CLIMATE HISTORY: CHARACTERIZING A “WARM AND WET” MARTIAN CLIMATE WITH A 3D GLOBAL CLIMATE MODEL AND TESTING GEOLOGICAL PREDICTIONS

A.M. Palumbo¹, J.W. Head¹

¹*Department of Earth, Environmental and Planetary Sciences, Brown University, Providence RI 02912, USA, Ashley_Palumbo@Brown.edu*

Keywords:

Mars climate, valley networks, climate model, rainfall, ocean, fluvial activity

Introduction:

The surface of Mars contains abundant geomorphological and mineralogical evidence that liquid water was stable at the surface during the Late Noachian and Early Hesperian [e.g. 1–3], including widespread valley networks (VNs) [4], lakes [5,6], and aqueous alteration products [7]. Further, Noachian-aged craters have degraded rims and no visible ejecta deposits [8], characteristics which have been attributed to rainsplash-related erosion [6].

Despite this evidence for abundant liquid water activity at the surface, climate models have been unsuccessful in reproducing the continuous “warm and wet” conditions presumed to be necessary for the formation of these features when considering the influence of the faint young Sun [9] and reasonable greenhouse gas concentrations [10–13]. Instead, the models predict a “cold and icy” climate, characterized by mean annual temperature (MAT) far below the melting point of water [14,15], an adiabatic cooling effect [16], and ice distributed across the highlands. In this “cold and icy” climate scenario, the formation of the VNs and lakes may be explained through transient or punctuated ice melting, surface runoff, and ponding [e.g. 16–18], instead of rainfall.

In this work, we assume that a “warm and wet” climate was plausible, based on the overwhelming geologic evidence, and force these climatic conditions in a 3D climate model. The combination of our model results and the distributions of the VNs and lakes provides useful insight into the possible formation conditions of these features.

Methods:

We employ the 3D Laboratoire de Météorologie Dynamique General Circulation Model (LMD GCM) for early Mars to simulate a “warm and wet” climate. We consider a 1 bar CO₂ atmosphere, 25° and 45° obliquity (probable lower limit and most likely obliquity values for the past 5 Gy; [19]), a circular orbit, and 75% the present solar luminosity [9]. Because a plausible combination of greenhouse gases that can continuously increase MAT to or above 273 K has not yet been identified [15], we focus on the lowest temperature end of a “warm and wet” climate and we artificially warm the planet by introducing a gray gas into the model atmosphere. A gray gas characteristically absorbs at all wavelengths with a defined absorption coefficient, κ . We choose $\kappa = 7.5 \times 10^{-5} \text{ m}^2 \text{ kg}^{-1}$ for the 25° obliquity simulation and $\kappa = 7.5 \times 10^{-5} \text{ m}^2 \text{ kg}^{-1}$ for 45° obliquity, which produces the desired climate, with MAT ~ 273 K in near-equatorial regions where VNs and lakes are abundant and global MAT ~ 275 K (Fig. 1).

Our goal is to better understand the characteristics of a “warm and wet” climate. In this analysis, we highlight multiple characteristics of this climate and discuss how these characteristics are consistent or inconsistent with the distribution of the VNs and lakes. We analyze the climate on the basis of the factors deemed necessary to explain the formation of the VNs and lakes. Among these factors are temperatures >273 K and rainfall. We determine regions of the planet that experience temperatures >273 K and rainfall and how these patterns vary seasonally. Then, we perform a spatial

correlation between areas with temperatures >273 K and the distributions of the VNs/lakes, and areas with rainfall and the distributions of the VNs/lakes. The goal of this analysis is to determine if the fluvial and lacustrine features could have been formed in a “warm and wet” climate, or if they appear inconsistent with this climate scenario. In the latter case, we consider that the formation of these features may have required even warmer and wetter conditions or that they formed through punctuated ice melting and runoff in a predominantly “cold and icy” climate.

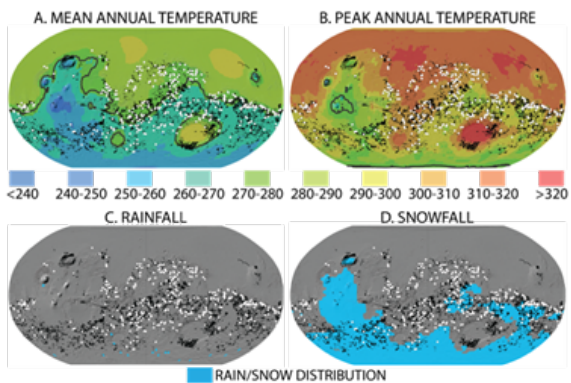


Fig. 1. Results from simulations for 25° obliquity (45° obliquity is not shown). (A) MAT and (B) Peak annual temperature maps. Locations where (C) rainfall and (D) snowfall occur at some point in the year are shown in blue. VNs are black lines and lakes are white circles. The black line is the 273 K isotherm.

Results and Discussion:

Under the influence of an atmosphere much thicker than current, the atmosphere and surface thermally couple and temperature becomes dominantly altitude dependent [14,17]. Thus, higher altitudes act as cold traps for water and ice becomes stable at high altitudes year-round. In the typical “cold and icy” climate scenario, ice is distributed across the highlands because of this effect. In this “warm and wet” simulation, the highest altitude region, the Tharsis rise, and the south polar region are consistently below 273 K and some water is trapped in these regions as ice (Fig. 1). The global MAT is above the melting point of water (~ 275 K), but the altitude dependence of temperature leaves vast portions of the southern highlands with MAT <273 K (Fig. 1). Areas with abundant VNs and lakes and MAT >273 K include Arabia Terra and regions near the dichotomy boundary. In total, $\sim 33\%$ of the VNs mapped by [4] are located in regions with MAT ≥ 273 K.

Seasonal temperature variations increase temperatures above 273 K in the warmest parts of the summer season, producing peak annual temperatures >273 K for most of the planet (Fig. 1). However, these temperatures are relatively short-lived. As a result, most precipitation occurs as snowfall instead of rainfall. The distribution of locations that experience rainfall is very limited, with only a few locations in the southern highlands (Fig. 1), and none of these regions are correlated with areas with MAT >273 K, where a significant percentage of the VNs are located. Thus, the distribution of VNs and lakes is inconsistent with rainfall in this “warm and wet” climate. However, widespread snowfall occurs across most of the southern highlands. In low latitudes and near-equatorial regions, the snowfall distribution is consistent with many VNs and lakes. Specifically, $\sim 41\%$ of the VNs mapped by [4] are located in regions where snowfall occurs at some point in the year (Fig. 1). When temperatures increase above 273 K in the summer season, melting of the snow accumulation and subsequent runoff and ponding would be expected. It is possible that snow melting and runoff could have been responsible for incision of VNs and filling of lakes, instead of rainfall.

Thus, based on temperature and precipitation distributions, the formation of the VNs and lakes appears broadly inconsistent with rainfall in the simulated “warm and wet” climate, but may be explained through seasonal snow/

ice accumulation and melting in the southern highlands. Further, the climate produced in this study is inconsistent with rainfall as the driving mechanism for crater degradation [6] due to the fact that snowfall dominates precipitation. Thus, the observed crater degradation requires an alternate explanation, possibly transient flooding [20].

In summary, despite the “warm” MAT (~ 273 K), the widespread fluvial and lacustrine features and observed crater degradation cannot be explained through rainfall in this climate scenario. We have offered possible alternative explanations for the formation these features and characteristics, but the explanations are inconsistent with formation through rainfall and rainfall-related processes [6,19].

How much higher would MAT need to be to induce more widespread rainfall? [16] simulated a warmer climate (~ 283 K) with a (forced) stable northern ocean and found that precipitation is dominated by rainfall, not snowfall. The widespread rainfall is consistent with a rainsplash-related explanation for degraded crater rims and aqueous mineral alteration at the surface in the highlands [16], in contrast to the simulations done in this study. However, the distribution of VNs and lakes is inconsistent with the distribution of rainfall in many regions [16]. Thus, increasing temperatures even further leads to more areas that experience rainfall, but does not appear to offer a rainfall-related explanation for VN/lake formation. Further, snowfall in a “cold and icy” climate, and seasonal or punctuated melting, is better correlated with the VN distribution than rainfall in a “warm and wet” climate [16].

Conclusions:

Using the 3D LMD GCM, we have simulated a “warm and wet” climate, characterized by global MAT ~ 275 K and equatorial MAT ~ 273 K. Rainfall is limited, precipitation is dominated by snowfall, and temperatures in the highlands are < 273 K for the majority of the year. The vast majority of VNs, lakes, and degraded craters, occur in areas of snowfall, not rainfall, and the global distribution of water is dominated by ice in the highlands and near Tharsis, not by an ocean or global liquid water that might form surface channels.

The transition from a snowfall-dominated to a rainfall-dominated climate [16] occurs at global MAT > 275 K and < 283 K. Even at MAT 283 K, the distribution of VNs is not well-correlated with predicted rainfall patterns [16]. We suggest that detailed analysis of shorter-term transient warm temperature phases in an otherwise “cold and icy” background climate [16,17] might be more likely to explain the formation of the VNs and lakes, the most robust evidence for “warm and wet” Late Noachian conditions.

Acknowledgements:

This work was supported by NASA Headquarters under the NASA Earth and Space Science Fellowship Program for AMP (Grant 90NSSC17K0487). The authors thank Robin Wordsworth for continued guidance for use of the GCM.

References:

- [1] Craddock and Howard, *JGR Planets*, 2002, 107, 5111.
- [2] Ramirez, *Icarus*, 2017, 297, 71–82.
- [3] Ramirez and Craddock, *Nat. Geosci. Perspect.*, 2018, 11, 230–237.
- [4] Hynek et al., *JGR Planets*, 2010, 115, E09008.
- [5] Fassett and Head, *Icarus*, 2008, 198, 37–56.
- [6] Goudge et al., *Icarus*, 2015, 260, 346–367.
- [7] Bibring et al., *Science*, 2006, 312, 400–404.
- [8] Jones, *JGR*, 1974, 79, 3917–3931.
- [9] Gough, *Sol. Phys.*, 1981, 74, 21–34.
- [10] Johnson et al., *JGR Planets*, 2009, 114, E11011.
- [11] Mischna et al., *JGR Planets*, 2013, 118, 560–576.
- [12] Kuhn and Atreya, *Icarus*, 1979, 37, 207–213.
- [13] Postawko and Kuhn, *JGR Solid Earth*, 1986, 91, 431–438.
- [14] Wordsworth et al., *Icarus*, 2013 222, 1–19.
- [15] Forget et al., *Icarus*, 2013, 222, 81–99.
- [16] Wordsworth et al., *JGR Planets*, 2015, 120, 1201–1219.
- [17] Head and Marchant, *Antarct. Sci.*, 2014, 26, 774–800.
- [18] Palumbo et al., *Icarus*, 2018, 300, 261–286.
- [19] Laskar et al., *Icarus*, 2004, 170, 343–364.
- [20] Palumbo and Head, *MAPS*, 2017, 1–39.

RETRIEVAL OF AEROSOL PROPERTIES FROM TIRVIM SOLAR OCCULTATIONS ONBOARD EXOMARS/TGO

M. Luginin¹, N. Ignatiev¹, A. Fedorova¹, A. Grigoriev¹, A. Shakun¹, A. Trokhimovsky², F. Montmessin², and O. Korabiev²

¹Space Research Institute (IKI), Moscow, Russia, mikhail.luginin@phystech.edu;

²LATMOS/IPSL, Guyancourt, France

Keywords:

Please suggest 5–10 keywords that describe the content of the abstract. If possible, each keyword should appear in the accompanying abstract.

The ExoMars Trace Gas Orbiter (TGO) is a joint ESA-Roscosmos mission to Mars that has been launched in March 2016. The aerobreaking phase has ended in February 2018 followed by the start of nominal scientific work on the near-circular 400 km orbit in April 2018. The Atmospheric Chemistry Suite (ACS) is a set of three spectrometers (NIR, MIR, and TIRVIM), capable to observe Mars atmosphere in solar occultation, nadir and limb geometry [1]. TIRVIM instrument is a Fourier-spectrometer operating in the 1.7 to 17 μm spectral range in solar occultation and nadir operation modes.

The main constituent of aerosols on Mars is mineral dust, while ice crystals of H_2O and CO_2 are also present at some seasons and locations. Wide spectral range of TIRVIM makes possible to distinguish dust and H_2O ice particles.

20 wavenumbers in the spectral range 1500–4500 cm^{-1} outside of strong gas absorption bands are used to retrieve aerosol properties from TIRVIM solar occultation data. The algorithm used for aerosol properties retrievals is standard for all solar occultation experiments. The reference solar spectrum I_0 is obtained when observing the Sun out of the atmosphere. Inside the atmosphere, solar radiance I is attenuated by extinction of aerosols integrated over the line of sight L . The ratio of I to the I_0 gives a spectrum of atmospheric transmission at a target altitude: $T_v(L) = I_v(L)/I_0$. Slant optical depth of aerosols is calculated as $\tau_v(L) = -\ln(T(L))$.

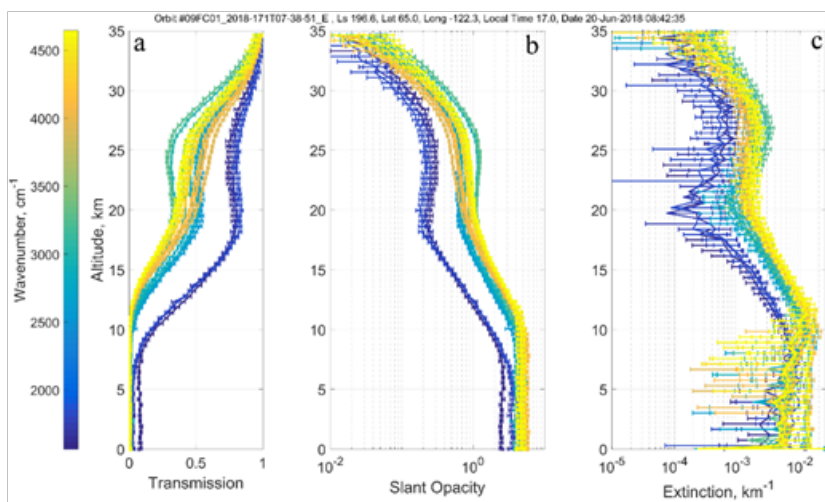


Fig. 1. Retrieved vertical profiles of transmission (a), slant opacity (b), and extinction coefficient (c) from orbit #9FC (recorded on 20 June 2018, latitude = 65N, $L_s = 197$, egress) for 20 wavenumbers in 1500–4500 cm^{-1} .

The procedure for the retrieval of the extinction vertical profiles ('onion peeling') is identical to the one used for SPICAM solar occultations on Mars [2, 3]. Example of retrieved vertical profiles of transmission, slant opacity, and extinction coefficient for orbit #9FC is presented in Figure. Analysis of the

spectral dependence of extinction coefficient reveals presence of two types of aerosols: dust at altitudes 10–18 km and water ice crystals at 20–30 km. Modelling of extinction coefficient spectral dependence and its fitting to the experimental extinction provide information on vertical size distribution and number density of the aerosols.

Acknowledgements

ExoMars is the space mission of ESA and Roscosmos. The ACS experiment is led by IKI Space Research Institute in Moscow. The project acknowledges funding by Roscosmos and CNES. Science operations of ACS are funded by Roscosmos and ESA. M. Luginin acknowledges the support from the Ministry of Science and Higher Education of the Russian Federation, grant №14.W03.31.0017.

References:

- [1] Korablev, O. et al. The Atmospheric Chemistry Suite (ACS) of Three Spectrometers for the ExoMars 2016 Trace Gas Orbiter // *Space Science Reviews*. 2018. V. 214(1). No 7.
- [2] Fedorova, A. et al. Solar infrared occultation observations by SPICAM experiment on Mars-Express: Simultaneous measurements of the vertical distributions of H₂O, CO₂ and aerosol // *Icarus*. 2009. V. 200(1). Pp. 96–117.
- [3] Fedorova, A. et al. Evidence for a bimodal size distribution for the suspended aerosol particles on Mars // *Icarus*. 2014. V. 231. Pp 239–260.

ON THE LOCATION OF POTENTIAL MARSQUAKES' SOURCES

A.V. Batov^{1,2}, T.V. Gudkova², V.N. Zharkov²

¹*Institute of Control Sciences of RAS, 65 Profsoyuznaya street, Moscow, Russia, batov@ipu.ru;*

²*Schmidt Institute Physics of the Earth RAS, B.Gruzinskaya, 10, Moscow, Russia, gudkova@ifz.ru, zharkov@ifz.ru*

Keywords:

Mars, tension-compression stresses, shear stresses, gravity, topography

Introduction:

Studying of stress field in the Martian interior is of importance for the seismic exploration of Mars. It's assumed to place a seismometer on Mars at the end of November 2018 (mission InSight of NASA) to determine the present level of tectonic activity and get information on its deep interior. We perform the stress field analysis in the lithosphere of Mars in order to reveal the areas of maximum shear and extensional stresses as potential marsquakes' sources.

Interior structure model:

As a benchmark real model for the planetary interior we use a trial model of Mars M_50 from [1], which satisfies currently available geophysical and geochemical data. The mean density of the crust is 2900 kg m^{-3} , the thickness of the crust is 50 km, the density contrast at the crust-mantle boundary is 360 kg m^{-3} . For stress field calculations the rheological cross section of Mars is of importance, but it is not well known. We consider models with 1) an elastic, 150-500 km thick lithosphere, overlying a sublithosphere low rigidity layer – a weakened layer, which partly lost elastic properties (shear modulus is ten times lower). Weakened layer is assumed to extend down to the core-mantle boundary or the olivine-wadsleyite phase transition; 2) 300 km thick lithosphere with some partly melting zones in it at the depth of 100-150 km or 100-200 km.

Method:

A planet is modeled as an elastic, self-gravitational spherical body. It is assumed, that deformations and stresses which obey Hooke's law are caused by the pressure of relief on the surface of the planet and anomalous density, distributed by a certain way in the crust and the mantle. Numerical simulation is based on a static approach (the loading factors technique or the Green's functions method) [2–5]. Recent data of gravitational field from [6] is used.

There is no a unique criterion for defining zones of maximum probability of rock strength failure when one considers the lithosphere of a planet extending for hundreds of kilometers. As potential marsquakes' sources we have identified the zones in which maximum shear stresses occur along the extensional stresses in the lithosphere of Mars.

Results:

We find that the zones of large shear stresses occur along with extensional stresses beneath Hellas Planitia, Argyre Planitia, Mare Acidalia, Arcadia Planitia and Valles Marineris (fig. 1). Changing of principle directions of stresses is an additional criterion for determining focuses of possible masquakes.

The landing zone of InSight mission spacecraft is at the eastern part of Elysium Planitia, where extensional stresses occur simultaneously with the maximum shear stresses (fig. 2).

Large non-hydrostatic stresses may lead to relatively increased seismic activity for these regions.

Acknowledgements:

This work is partly financially supported by RFFR (project 18-32-00875) and the Programme of Presidium RAS 28.

References:

[1] Zharkov, V.N., Gudkova, T.V., Batov, A.V. 2017. On estimating the dissipative factor of the Martian interior. *Sol. Syst. Res.* 51, 6, 479-490.

- [2] Marchenkov K.I., Lyubimov V.M., Zharkov V.N. Calculation of load factors for deeply buried density anomalies // Doklady Earth Science Sections. V.279.1984. P.14-16.
- [3] Zharkov V.N. Marchenkov K.I., Lyubimov V.M. On long-waves shear stresses in the lithosphere and the mantle of Venus // Sol. Syst. Res. 1986. V.20. P.202-211.
- [4] Marchenkov K.I., Zharkov V.N. Stresses in the Venus crust and the topography of the mantle boundary // Sol. Astron. Lett. 1989. T.16. № 1. P.77-81.
- [5] Zharkov V.N., Koshlyakov E.M., Marchenkov K.I. Composition, structure and gravitational field of Mars // Sol. Syst. Res.1991. V.25. P.515-547.
- [6] Konopliv A.S., Park R.S., Folkner W.M. An improved JPL Mars gravity field and orientation from Mars orbiter and lander tracking data // Icarus. 2016. V. 274.P. 253260.

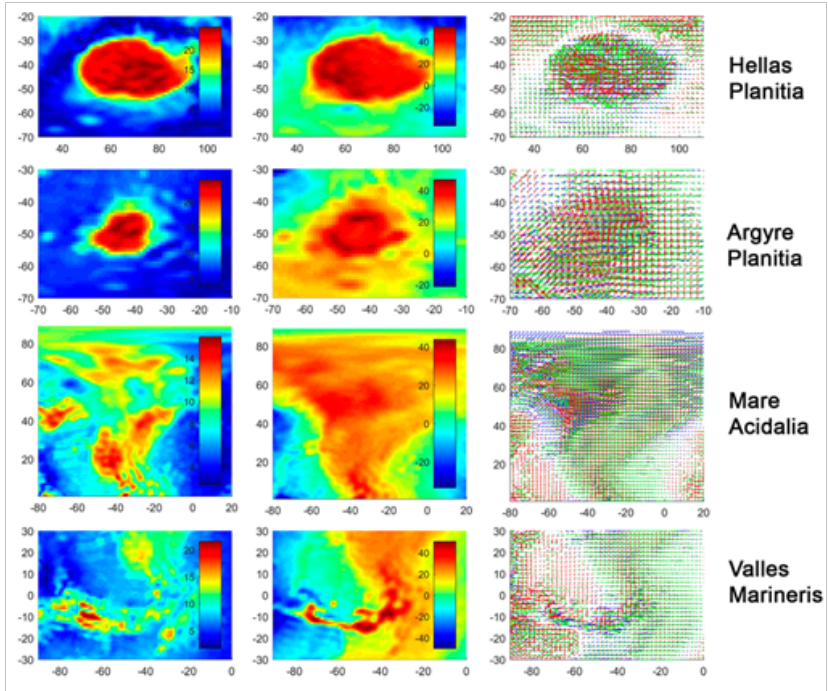


Fig. 1. Shear stresses (left), tension-compression stresses (center) and principle directions σ_1 (blue), σ_2 (green), σ_3 (red) (horizontal plane projection) at the depth of 25 km. The length of the vector is proportional to the magnitude of stress.

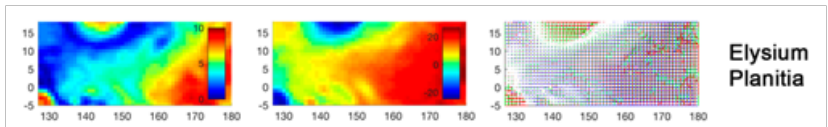


Fig. 2. Shear stresses (left), tension-compression stresses (center) and principle directions σ_1 (blue), σ_2 (green), σ_3 (red) (horizontal plane projection) at the depth of 5 km. The length of the vector is proportional to the magnitude of stress.

MODEL ESTIMATES OF STRESS STATE IN MARS FOR THREE-LEVEL LOADING

T.V. Gudkova¹, A.V. Batov^{1,2}, V.N. Zharkov¹

¹Schmidt Institute Physics of the Earth RAS, B.Gruzinskaya, 10, Russia;

²Institute of Control Sciences of RAS, 65 Profsoyuznaya street;

Moscow, Russia, gudkova@ifz.ru, batov@ipu.ru, zharkov@ifz.ru

Keywords:

tension-compression stresses, shear stresses, gravity and topography data, interior structure, Mars

Introduction:

In order to calculate the stresses, the set of equations is solved that includes the elastic equilibrium equation of the gravitating planet, and the Poisson equation that relates the anomalous gravitational potential to the density distribution. The Green's function method (or loading numbers method) allows us to find boundary conditions based on the data on topography and the gravitational field of the planet [1-4]. Relief and density anomalies distributed in special ways in the planetary interior are the sources of the anomalous gravitational field. In the stress calculation in [5], for the sake of definiteness of the problem, an assumption was made that there were two sources of the Martian anomalous gravitational field: non-equilibrium relief and density anomalies at the crust-mantle boundary (two-level compensation model). In this study, an exploration of zones of maximum shear stresses and tension-compression stresses in the Martian interior is proposed for a three-level compensation model (the non-equilibrium relief, density anomalies at the crust-mantle boundary, and density anomalies at the base of the lithosphere).

Calculation of stresses for three-level model:

Density anomalies in the planet interior $\delta\rho(r, \varphi, \lambda)$ can be presented in the form of infinitely thin layers located at levels r_i . It is known that it is impossible to determine unambiguously $\delta\rho(r, \varphi, \lambda)$ using the planet's gravitational field parameters. Therefore, to make the problem definite, we suppose that there are three levels of density anomalies concentration inside Mars: the planet's surface $r=R$; the crust-mantle boundary $r=R_1=R-l$, where l is the crust thickness; and the base of the lithosphere $r=R_2=R-h$, where h is the lithosphere thickness. Then, coefficients of expansion in Legendre polynomials of the anomalous density on surface R , on crust-mantle boundary R_1 , and at the base of the lithosphere R_2 ($R_{i,n,m}^1(\varphi, \lambda)$, $R_{i,n,m}^2(\varphi, \lambda)$, $R_{i,n,m}^3(\varphi, \lambda)$, respectively) are related to expansion coefficients of the anomalous gravitational field and topography by the following expressions:

$$C_{ginm} = \frac{R_{innm}^1(\phi, \lambda) 3(1+k_n(R))}{R\rho_0 (2n+1)} + \frac{R_{innm}^2(\phi, \lambda) 3(1+k_n(R_1))}{R\rho_0 (2n+1)} \left(\frac{R_1}{R}\right)^{n+2} + \frac{R_{innm}^3(\phi, \lambda) 3(1+k_n(R_2))}{R\rho_0 (2n+1)} \left(\frac{R_2}{R}\right)^{n+2}$$

$$C_{tinm} = \frac{R_{innm}^1(\phi, \lambda)}{R\rho_c} + \frac{R_{innm}^1(\phi, \lambda) 3(1+h_n(R))}{R\rho_0 (2n+1)} + \frac{R_{innm}^2(\phi, \lambda) 3(1+h_n(R_1))}{R\rho_0 (2n+1)} \left(\frac{R_1}{R}\right)^{n+2} + \frac{R_{innm}^3(\phi, \lambda) 3(1+h_n(R_2))}{R\rho_0 (2n+1)} \left(\frac{R_2}{R}\right)^{n+2}$$

where ρ_0 and ρ_c are mean density of Mars and its crust density, k_n and h_n are loading Love numbers, calculated for the interior structure model from [6].

We assume that $R_{i,n,m}^2(\varphi, \lambda) = R_{i,n,m}^3(\varphi, \lambda)$. The coefficients $R_{i,n,m}^1(\varphi, \lambda)$, $R_{i,n,m}^2(\varphi, \lambda)$, $R_{i,n,m}^3(\varphi, \lambda)$ are selected so to obtain the observed non-equilibrium values of gravitational field C_{ginm} [7] and topography C_{tinm} [8] coefficients, which are determined relative to the reference surface that is assumed to be an equilibrium spheroid [9]. The data on topography and the gravitational field are used in the form of coefficients of expansion in Legendre polynomials up

to the degree and order of 90.

These parameters are set as the boundary conditions to solve elastic equilibrium equations for a gravitating planet for each of n and m harmonics. Then, the harmonic series are summarized, and symmetric tensor is reduced to the diagonal form with principal stresses $\sigma_3 \leq \sigma_2 \leq \sigma_1$. Tension-compression stresses and maximum shear stresses are defined as $p = (\sigma_1 + \sigma_2 + \sigma_3)/3$ and $\tau = \max|\sigma_i - \sigma_k|/2$, ($i, k = 1, 2, 3; i \neq k$), respectively.

Calculations of tension-compression stresses and maximum shear stresses are performed for the models with elastic lithosphere of various thicknesses (150–500 km) overlying the weakened layer that has partially lost its elastic properties. The weakening is simulated by a tenfold reduced shear modulus μ of the layer located beneath the lithosphere and it is assumed spreading down to the core.

Results:

The general stress distribution pattern for the three-level compensation model differs from the stress field in the two-level model described in [5]. Maximum shear stresses and tension-compression stresses differ by 5–10%; however, their behavior is the same as those discovered by the two-level compensation model. The mean levels of stresses for the models with crust thickness of 50 and 100 km differ by 10% on the average, the same as for the two-level compensation model. The stress distribution of tension-compression stresses and maximum shear stresses in the Martian lithosphere displays precise correlation with the surface structures of the planet.

The stresses obtained for the three-level compensation model were calculated in particular Martian regions under such structures as Olympus Volcano, Hellas Planitia, Argyre Planitia, Acidalium Planitia, Arcadia Planitia and Valles Marineris.

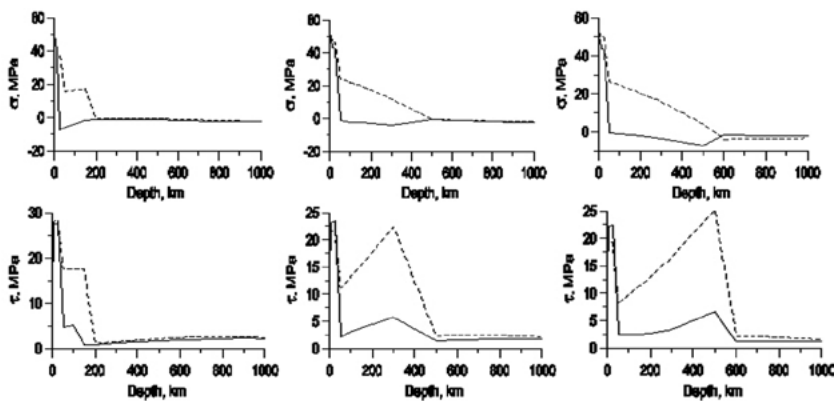


Fig.1. The distribution of tension-compression stresses (upper panel) and maximum shear stresses (lower panel) along the depth beneath the Hellas for the interior structure model from [6] with 50 km thick crust. The thickness of the lithosphere is varied (from the left to the right): 150, 300 and 500 km). Two-level compensation model (solid lines), three-level compensation model (dashed lines). The lines represent the values obtained for the depth of 0, 5, 10, 25, 50, 100, 150, 200, 300, 500, 600, 700, 800, 900 и 1000 km.

Under the Olympus Volcano, shear stresses reach 30–80 MPa in the crust, and simultaneously compression stresses reach values of 200–400 MPa depending on the lithosphere thickness. High tensions reaching 10–80 MPa are formed at the lithosphere lower boundary. The thinner is the lithosphere, the higher are the tensions in this zone. Under such structures as Hellas Planitia, Argyre Planitia, Acidalium Planitia, Arcadia Planitia and Valles Marineris, high tensions are formed reaching 20–30 MPa in the lithosphere, simultaneously with high shear stresses.

The essential difference between stress distributions over depth for the two- and three-level compensation models has been discovered under Hellas Planitia and Argyre Planitia. The stress distributions over depth plotted for

Hellas region is presented in the Figure. High stresses in the two-level compensation model located under the compensated structure of Hellas Plateau concentrated in the crust, sharply fading after the compensation level assumed for any of the considered models of non-uniform elasticity. Upon application of loading to the base of the lithosphere, the stress distribution pattern in the lithosphere has sharply changed. Distribution of anomalous masses under the shock basins can be a consequence of the crust extrusion and displacement (elevation) of the crust–mantle boundary.

Conclusion:

In general, the stresses for the three-level compensation model (non-equilibrium relief, density anomalies at the crust–mantle boundary and at the base of the lithosphere are the sources of the anomalous gravitational field) differ from the values obtained for the two-level model (non-equilibrium relief and density anomalies at the crust–mantle boundary are the sources of the anomalous gravitational field) by 5–10%. A considerable difference between the two- and three-level compensation models has been revealed under two largest shock craters of Hellas and Argyre, which requires further ample exploration of the stress distribution pattern under these regions not only over depth, but also laterally. Stress state patterns in Mars are of importance for the determination of possible marsquake sources, the seismic experiment on the planet is expected to be started at the end of November 2018 [10].

This work is partly financially supported by RFFR (project 18-32-00875) and the Programme of Presidium RAS 28.

References:

- [1] Marchenkov K.I., Lyubimov V.M., Zharkov V.N. Calculation of load factors for deeply buried density anomalies // *Doklady Earth Science Sections*. V.279.1984. P.14-16.
- [2] Zharkov V.N. Marchenkov K.I., Lyubimov V.M. On long-waves shear stresses in the lithosphere and the mantle of Venus // *Sol. Syst. Res.* 1986. V.20. P.202-211.
- [3] Marchenkov K.I., Zharkov V.N. Stresses in the Venus crust and the topography of the mantle boundary // *Sol. Astron. Lett.* 1989. T.16. № 1. P.77-81.
- [4] Zharkov V.N., Koshlyakov E.M., Marchenkov K.I. Composition, structure and gravitational field of Mars // *Sol. Syst. Res.*1991. V.25. P.515-547).
- [5] Gudkova T. V., Batov A. V., Zharkov V.N. Model estimates of non-hydrostatic stresses in the Martian crust and mantle: 1. Two-level model // *Solar Syst. Res.* 2017. V. 51 (6), P. 457-478.
- [6] Zharkov V.N., Gudkova T. V., Batov A. V. On estimating the dissipative factor of the Martian interior // *Sol. Syst. Res.* 2017. V. 51, N 6, P.479-490.
- [7] Konopliv A.S., Park R.S., Folkner W.M. An improved JPL Mars gravity field and 253-260.
- [8] Smith D.E., Zuber M.T., Frey H.V., et al. Mars Orbiter Laser Altimeter: Experimental summary after the first year of global mapping of Mars // *J.Geophys.Res.* 2001. V.106 (E10). P. 23689-23722.
- [9] Zharkov V.N., Gudkova T.V. On model structure of gravity field of Mars // *Sol. Syst. Res.* 2016. V.50. P.250-267.
- [10] Panning M.P., Lognonne Ph., Banerdt W.B., et al. Planned products of the Mars structure service for the InSight mission to Mars // *Space Science Rev.* 2017. V. 211, N 1-4, P. 611-650.

THE STUDY OF INFLUENCE OF MARS CLIMATE ON SLOPE STREAKS FORMATION PROCESS

E. Brusnikin, A. Dubovitskaia

Moscow State University of Geodesy and Cartography

The goal of this project is studying of active geomorphological processes on the Mars surface that are connected with origin of Slope streaks and have signs of influence of water brine. Nowadays, we have several theories about their origin, but neither of them can fully describe all observed features. We will investigate the influence of changes of atmospheric parameters on the periods of new Slope streaks origins. For the goals of the project remote sensing data of high and ultra-high resolution will be used. With the help of overlapping images we will identify new slope streaks which appeared between the dates of images. A database of new Slope streaks will be created in GIS. In the work we will use data about climate and parameters of Mars atmosphere and special developed program algorithms for preliminary processing of remote sensing data and valuation of climate conditions on Mars surface. Usage of remote sensing data and products of their processing (DTM, morphometric characteristics) and catalog of new Slope streaks will allow us to determine patterns in changes of climate conditions, local features of relief and their influence on the Slope streaks origin process. Results of the project can be used to study water cycle on the Mars surface and for future investigations like ExoMars-2020 and planning human space missions.

EXOMARS - 2020 PROGRAM: ON THE CONCEPT OF THE MARSOKHOD LOCOMOTION SYSTEM

M.I. Malenkov¹, V.N. Nazarov¹, R.R. Nazirov¹, D.S. Rodionov¹,
V.A. Volov²

¹Space Research Institute Russian Academy of Sciences. 117997,
Profsoyuznaya 84/32, GSP-7, Moscow, Russia,
vnazarov@romance.iki.rssi.ru;

²Gesellschaft für Innovative Marktforschung. Goldschmid str., 4-6,
Heidelberg, Germany

Keywords:

locomotion system, mars rover, (marsokhod), self-propelled chassis, wheel-walking propulsor, walking mechanism, flexible wheel, simple bogie.

Introduction:

Actual production history of the mars rover, like the history of the program ExoMars, dates back almost two decades. During this time, various concepts of the locomotion system were proposed. The results of design developments, testing of the prototypes of self-propelled chassis in the ground channels and testing ground have been reflected in numerous published papers by European and Canadian specialists, primarily at ESA/ESTEC meetings, ASTRA and *i*-SAIRAS conferences [1, 2, 3, 4]. Whether it can be said that the optimal concept can be decided on?

Evolution of the Concept of the Marsokhod Self-propelled Chassis:

Formulation of the concept includes justification and selection of the type, design, and preliminary parameters of all components of the locomotion system (LS), which is often called "self-propelled chassis (SC)" or "Rover", including the undercarriage, including propulsion and suspension; traction and other drives that ensure locomotion; supporting structure; automation block, and sensors of the locomotion safety subsystem, providing the implementation of automatic control algorithms. When choosing the wheel propulsion, the wheel formula and type of wheels should be substantiated. The main conceptual quality criterion is compliance with the tasks of the scientific program ExoMars on a hostile terrain and loosely connected sandy soils.

At the start of the project, experts from ESA/ESTEC, when developing the concept of the LS Mars rover, adopted the wheel formula of the Sojourner rover 6x6x4. The first dimension means the number of wheels, the second is the number of drive wheels, and the third one denotes the number of wheels equipped with steering drives. During these years, communication and discussions between European experts and Russian scientists from the Space Research Institute of the Russian Academy of Sciences, specialists of VNIITRANSMASH, and Lavochkin Association concerned with the creation of automatic instruments and robotic equipment for studying the Moon, planets, and small celestial bodies of the Solar system, began. In cooperation of different kinds, several scale-models and full-scale SC prototypes, including with a wheel-walking propulsors (WWP) and three-point parallelogram suspension, were developed and delivered to Noordwijk and Toulouse. ESTEC and CNES have appreciated a high level of WWP performance [5] for the soils with low bearing capacity. As a result, by 2004, the wheel formula had taken on 6x6x4 + 6W, where the last digit means the number of motor wheels equipped with walking mechanisms (WM).

European experts have revealed by experiment and by theory a shortcoming in the suspensions with parallelogram arms, i.e. a decreased resistance to overturning. Therefore, the developers switched to so-called simple bogies (with single rockers) [6]: two longitudinal bogies and one transverse bogie are connected to the supporting structure (frame or container) by means of free joints (Fig. 1). In addition, in order to increase the maneuverability of the rover, it was decided to install the steering drives on middle wheels drives. Thus, in 2018, the wheel formula 6x6x6 + 6W and flexible cylindrical wheels of small diameter are relevant.

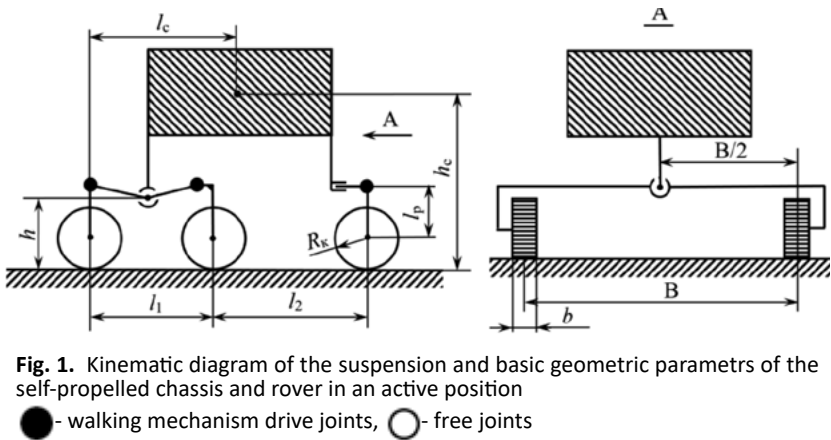


Fig. 1. Kinematic diagram of the suspension and basic geometric parameters of the self-propelled chassis and rover in an active position

● - walking mechanism drive joints, ○ - free joints

Design Requirements to a Self-Propelled Chassis:

Design within the “terrain-machine” framework requires, first, considering the properties of all the above listed components of SC that affect physical process of locomotion, and, second, taking into account interrelations between operating conditions and driving characteristics of the self-propelled chassis at all stages of creating a new form of transport starting from the technical specification.

Currently, European and Russian scientists have identified two zones the landing module on Mars: the plateau of Oxia and the Mawrth valley [7], which are promising in terms of exobiological research. Both zones are in the most dangerous in terms of loss of performance areas, possibly covered with a sufficiently thick layer of loose and dusty material. Both areas are located in the latitudes 10° S to 40° N, where sections of various types of dry regolith from eolian deposits with grain size (0.001-0.01) mm to sand dunes with grain sizes (0.06-0.2) mm can be encountered [8].

Therefore, the Mars rover, in our opinion, should ensure overcoming of the following elevation angles along the route:

- at least 32° on a cohesive soil of a semi-rocky and rocky type,
- at least 32° on a slightly cohesive soil with crust, and on lumpy soil with bearing capacity of 34-200 kPa,
- at least 17° on eolian deposits with an abnormally low bearing capacity of a dusty soil with particle size from 0.001 to 0.01 mm and bearing capacity from 5 to 34 kPa.

Strength of the wheels should be ensured when the rover drives across the sand and gravel materials with a bearing capacity of more than 200 kPa, with medium (0.05 – 0.3 m) and fine (0.05 m or less) strong stones with sharp edges scattered on the surface.

The SC should retain mobility when overcoming single stones at least 250 mm high under the wheels and bottom.

Methods of Analysis of the Concept and Some Conclusions:

For a comparative analysis of the level of development, the report uses both the results of the operation of American rovers and the results of Russian of the SC prototypes. In addition, the authors repeated the static calculations that needed to be performed to justify and select the type and parameters of electric motors, reducers, traction drive brakes, and the walking mechanism drive.

The main design parameters of the rover were borrowed from published papers and, therefore, are indicative. This applies to the following data: gross weight, mass of the SC, wheel track (B), wheelbase (+), clearance, coordinates of the center of mass (\cdot), arm of WM (\cdot), wheel radius (\cdot), modes and speeds of locomotion, ways of maneuvering, ways of stop and parking braking, ways of laying and unfolding the running gear from the transportation position.

Below are the main findings of the comparative and computational analysis, with the techniques and results presented on the report presentation slides. Analytical study of static stability of the SC with simple bogies showed an increase in the critical angles by 20% -25%, compared with the SC with parallelogram suspension.

Traction-dynamic calculation of the wheel drive mode has revealed an unused reserve of electric motor power, which is sufficient to increase the rated speed of locomotion up to the speed of the MER mission rovers.

Assessment of the wheel-walking mode of motion has revealed a kinematic discrepancy between the nominal speeds of wheeling of the wheels and of the arms of the walking mechanisms during when carryover of the wheels. The difference between the lengths of the levers WM of medium and external wheels makes it difficult to move the housing.

In publications there are no results of working out automatic algorithms for switching the operating modes of the SC from wheeled to wheel-walking mode and vice versa. There is no data on the development of algorithms for realizing the most effective uniform discontinuous gait. Against the background of exceeding the SC weight, the use of flexible wheels, as well as the use of steering mechanisms, is insufficiently well-founded.

In general, the concept of the locomotion system, in our opinion, has certain reserves for increasing the mobility of the rover ExoMars compared with the MER mission rovers. There are also reserves for increasing the reliability of the self-propelled chassis.

References:

- [1] J.L. Vago, A. Santovincenzo, B. Gardini. Pasteur: The Search for Signs of Life on Mars // Proceedings of the Workshop ASTRA - 2002. ESTEC (NL). 2002.
- [2] V. Koutcherenko¹, A. Bogatchev¹, M. van Wiennendael². Chassis Concepts for ExoMars Rover. Proceedings of the Workshop ASTRA - 2004. ESTEC (NL), November 2 – 4, 2004. Vol. c. pp. 1 – 8.
- [3] Design and Manufacture of a full Size Breadboard ExoMars Rover Shassis. Lee C. G-Y, Dalcolmo J, Klinkner S et. al. // Proceedings of the Workshop ASTRA - 2006. ESTEC (NL), November 28 – 30, 2006.
- [4] ExoMars Suspension and Locomotion. R. McCoubrey, J. Smith, A. Cernusco et al. Proceedings of the Workshop i-SAIRAS – 2008.
- [5] Kazhukalo, I.F., Wheel-walking propulsor, in Planetokhody (Planetary Rovers), Kemurdzhian, A.L., Ed., Moscow: Mashinostroenie, 1982, pp. 84–107 (rus.).
- [6] Development of the ExoMars Chassis and Locomotion Subsystem. S. Michaud, A. Gibbesch, T. Thueer, et. al. Proceedings of the Workshop i-SAIRAS – 2010
- [7] <http://www.bbc.com/news/science-environment-39420971>.
- [8] Demidov, N.E., Bazilwevsky, A.T., Kuzmin, R.O. Martian Soil: Kinds, Structure, Composition, Physical Properties, Drilling Capacity, and Danger for Landing Systems. Astronomic Bulletin. – 2015. – Vol. 49. – 4. – pp. 243 – 261 (rus.).

AMR INSTRUMENT FOR EXOMARS' 2020 SURFACE PLATFORM. DEVELOPMENT STATUS, CALIBRATION AND QUALIFICATION

D.R. Díaz¹, J. Vicente-López¹, J. García-Martínez¹, R. Sanz¹,
A.A. Ordóñez², V. González², J. Pazos¹, R. Kilian², M.A. Rivero¹,
J. de Frutos¹, M.C. Parrondo¹, M. Díaz Michelena¹

¹INTA Crta. Torrejón-Ajalvir km 4, 28850 Torrejón de Ardoz, Madrid, Spain;

²Geology Department, University of Trier, Behringstrasse, 54286 Trier, Germany

Keywords:

ExoMars 2020, Surface Platform, METEO, Anisotropic MagnetoResistance-AMR, 3-axis vector magnetometer, magnetic cleanliness, deployment system, qualification campaign.

Introduction:

AMR instrument is part of the scientific payload included on the ExoMars 2020 Surface Platform. The scientific goals of AMR instrument are the determination of local crustal magnetic signatures at the landing site and the measurement of the variations of the magnetic field on the surface, the latter comprising short term daily variations and superimposed anomalies due to the interaction with the solar wind along the duration of the mission. These measurements will be analyzed and compared with measurements from orbiters missions, e.g. MAVEN data to improve the interpretation and extent of the events.

The AMR instrument consists of two main units, the E-BOX, whose main tasks are the power distribution, control and data processing, and serves as physical interface for communications with METEO (METEOrological instrumentation module within the SP); and the S-BOX Deployment Assembly Unit, which is the deploying sensor head of the instrument that comprises a 3-axis vector magnetometer based on AMR technology, a tilt angle sensor and temperature sensors (PT-1000). The S-BOX is linked to the E-BOX through a SPI communications I/F that will operate as a slave unit in charge of collecting the scientific data.

The mechanical architecture of the AMR instrument has been designed as a balanced trade-off and optimization between: i) compactness, ii) magnetic cleanliness at the sensing head (S-BOX), iii) limited power consumption, iv) reduced mass envelope. In addition, it includes a newly designed and developed deployment system which allows the S-BOX Unit to be ejected from the edge of its location (a solar panel on the SP) to a maximum of 2-meter range on Mars surface in order to minimize the magnetic noise produced by the SP.

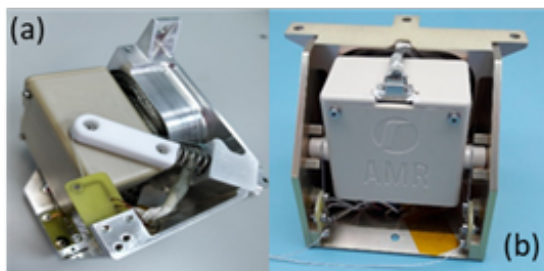


Fig. 1.-(a) S-BOX Deployment Assembly Unit Thermal Model side view, (b) S-BOX Deployment Assembly Unit Qualification Model.

The deployment system has been qualified through extensive qualification tests ensuring its performance under the expected Mars' surface conditions for the

mission. This specific qualification campaign involved material characterization for retention wires, overall system configuration and over 30 deployments.

The magnetic characterization and calibration of the AMR instrument (S-BOX Deployment Assembly Unit and E-BOX Unit) has been performed at INTA's magnetic singular facility. This singular facility has been designed and built as a magnetically clean environment.



Fig. 2. Magnetic singular facility at INTA.

This work describes the AMR instrument and summarizes the process of characterization and calibration of AMR. Additionally, we give an insight in the qualification campaign performed entirely at INTA's premises.

References:

- [1] M. Díaz Michelena, R. Sanz, M.F. Cerdán, and A.B. Fernández. Calibration of QM-MOURA three-axis magnetometer and gradiometer // *Geosci. Instrum. Method. Data Syst.*, 4, P. 1–18, 2015.
- [2] M. Díaz Michelena, R. Sanz, A.B. Fernández, V. de Manuel, M.F. Cerdán, V. Apéstigue, I. Arruego, J. Azcue, J.A. Domínguez, M. González, H. Guerrero, M.D. Sabau, R. Kilian, O. Baeza, F. Ríos, M. Herráiz, L. Vázquez, J.M. Tordesillas, P. Covisa, J. Aguado. MOURA magnetometer for Mars MetNet Precursor Mission // *Its potential for an in situ magnetic environment and surface characterization. Física de la Tierra Vol. 28 (2016). P. 65-82.*

THE USE OF THE EO GAS STERILIZATION PROCESS FOR THE PLANETARY PROTECTION REQUIREMENTS FULFILLMENT ON THE «EXOMARS-2020» MISSION

M.A. Zaitsev¹, S.V. Poddubko², A.A. Guridov², S.V. Fialkina²,
L.N. Moukhamedieva², D.S. Tsarkov², A.A. Pakhomova², V.N. Sychev²,
E.A. Deshevaya²

¹ *Space Research Institute of the Russian Academy of Sciences, 84/32 Profsoyuznaya St., Moscow 117997, Russia, mzaitsev@iki.rssi.ru;*

² *RF SRC – Institute of Biomedical Problems of the Russian Academy of Sciences, 76 A Khoroshevskoye Shosse, Moscow 123007, Russia, poddubko@imbp.ru*

Keywords:

Gas sterilization, ethylene oxide (EO), bioburden reduction, Planetary Protection (PP), flight hardware, ExoMars-2020, descent module (DM).

Introduction:

During the «ExoMars 2020» mission realization the Planetary Protection (PP) requirements shall be met in order to prevent technogeneous panspermia – the biological contamination of the Mars with terrestrial organisms, which can jeopardize its subsequent scientific exploration. In part of landing on the surface of Mars this mission relates to the IV category (IVa for the Surface Platform and VIb for the Rover) according to the COSPAR classification. There are stringent limitations on quantitative content of spores on the surfaces of the Descent Module (DM) at the end of its assembly and the overall the DM surface bioburden before launch. Therefore it's required in particular to reduce the bioburden using effective decontamination methods, which are fully compatible with the structural materials and units of the DM.

The use of ethylene oxide (EO) gas sterilization method for decontamination of the DM scientific instruments was studied in scope of this work.

EO sterilization has been considered for use during the early development of interplanetary spacecrafts for their microbial reduction. But due to inherent health and explosive hazards it has not found widespread use for PP purposes, and development for terminal bioburden reduction has focused on dry heat microbial reduction (DHMR) and vapor-phase hydrogen peroxide (VHP). EO sterilization may be proposed for specific uses, but this should be weighed against existing alternatives and the advantages of standardizing procedures on an agency and interagency levels [1].

Application of exactly EO sterilization, which performs within the temperature range of 35-55°C, for materials and instruments is relevant and valid in cases for example, when the application of DHMR which requires long-term exposure at the $t \geq 110^\circ\text{C}$ is not possible due to the materials/unit incompatibility (thermolability and/or requirements to storage temperature range of the optical, electronic and radio-electronic equipment, plastic items, etc.). The other advantage of EO is that it's not an oxidant like for example hydrogen peroxide and in the gaseous state it doesn't cause corrosion of metals and doesn't change the integrity of plastics and rubber items [2, 3]. But at the same time the toxicity of EO and possible organic contamination that it can cause requires to perform the control under EO and by-products abundances in the treated hardware and development of the techniques for their proper removing from it.

Experiments:

The experiments were performed on the base of «SteriPak Service» (Moscow) using a functionally operative mockup of a flight scientific instrument and bio-indicators in the gas sterilizer/aerator «3M™ Steri-Vac™ 5XL» with application of two types of the standard sterilization cycles: «warm» (55°C) and «cold» (37°C). The specified sterilizer operates with preliminary vacuumizing, using 100% EO, and the whole sterilization cycle is conducted under negative pressure [3].

The two types of experiments were conducted – microbiological ones and toxicological ones. The microbiological experiments were intended to the determination of the possible degree of the bioburden reduction which could be reached during the EO treatment. For that purpose, the bioindicators were developed using high concentration of sporous forms mix of the different *Bacillus* wild strains ($10^5 - 10^{10}$ spores per a bioindicator) and at the same time the flight hardware mockup was artificially contaminated (on internal and external opened and mated metallic and nonmetallic surfaces) with these spores at high surface density ($10^6 - 10^7$ spores/cm²). Both the mockup and bioindicators were packed into the biobarrier packages – double bags «КЛИНИПАК» combined of Tyvek™ and PET/PE-film and thermally sealed and then subjected to the «warm» and «cold» sterilization cycles and subsequent vacuum outgassing.

The toxicological experiments were aimed to the qualitative assessment and quantification of the possible EO and other volatile organics residues in the flight hardware mockup after sterilization/aeration/vacuum outgassing and to the determination of the aeration time and subsequent vacuum outgassing duration ($t = 45-50^\circ\text{C}$ and $P \leq 10^{-4}$ mm Hg) required for proper removal of EO and other organics from the sterilized and packed hardware. For that purpose the mockup packed as described above was subjected to the «warm» and «cold» sterilization cycles with different aeration time and within and without subsequent vacuum outgassing which also had different duration. After each experiment the mockup was packed into the gas tightened bag for 24 h and the analysis of the air from the bag was performed according to ISO 16000-6:2011 and after it the mockup was fully unpacked and tested according to the ISO 14624-3:2005. The final concentration of the EO in the air of the test chamber using after 50°C and 72 h of exposition shall not be more than 1 mg per the nominal m³ (according to the ГИ 2.2.5.1313-03 its time-weighted average threshold limit value stated in Russia is 1mg/m³).

Results and their discussion:

The reduction of the mockup and bioindicators initial bioburden was very significant – at least nine orders of magnitude. At the same time functional capacity of the mockup is fully preserved even after multiple sterilization cycles (>10 cycles). The necessary aeration time and subsequent vacuum outgassing duration of the scientific instruments in order to meet the toxicological requirements was determined.

As a result the following protocol can be recommended. After sterilization at 37 or 55°C (EO exposure time is 3 h and 1 h respectively) under controlled humidity (50-80%) and aeration of no less than 96 h at 37°C and 48 h at 55°C the vacuum outgassing performs ($t = 45-50^\circ\text{C}$ and $P \leq 10^{-4}$ mm Hg) for a period of no less than 120 hours after «cold» cycle and no less than 72 hours after «warm» cycle. At the end of the sequence the treated unit is placed in the gas tightened bag for a period of no less than 24 h, and assay of the EO concentration in the air from the bag is conducted by portable gas analyzers or GC. It shall not be more than 3 mg/m³ (according to the ГИ 2.2.5.1313-03 its short-term average threshold limit value stated in Russia is 3 mg/m³). If not – the additional vacuum outgassing performs until this requirement will be met.

Conclusion:

The EO sterilization method for the PP requirements fulfillment is possible to apply during the DM scientific payload production according to the developed protocol.

It should be noted that contemporary level of development of EO sterilization equipment and techniques for healthcare products treatment can eliminate the limitations which prevented the wide spread of EO process application for the PP purposes.

Acknowledgments:

The authors are deeply grateful to the developers of the instrument «ADRON-RM» of the «ExoMars-2020» mission, provided «ADRON-RM» engineering model for the experiments, and to the «SteriPak Service» (Moscow) for packing of the test objects and for conducting of the EO test sterilization cycles.

References:

- [1] Frick A., Mogul R., Stabekis P., Conley C.A., Ehrenfreund P. Overview of current capabilities and research and technology development for planetary protection // *Advances in Space Research*. 2014. V. 54. No 1. P. 221-240.
- [2] Shintani H. Ethylene Oxide Gas Sterilization of Medical Devices // *Biocontrol Science*. 2017. V. 22. No. 1. P. 1-16.
- [3] Kornev I.I., Logvinov N.L., Kornev A.I. Gas sterilization of healthcare products products with the use of ethylene oxide in medical and preventive treatment facilities (In Russian). «Chelovek», Sankt-Peterburg, 2014. 126 p.

INVESTIGATION OF MARTIAN DUST WITH DUST COMPLEX ONBOARD THE EXOMARS-2020 LANDING PLATFORM

G. Dolnikov¹, A. Zakharov¹, I. Kuznetsov¹, A. Lyash¹, I. Shashkova¹, V. Gotlib¹, E. Seran², M. Godefroy², F. Esposito³, C. Molfese³, F. Cozzolino³, F. Cortecchia⁴, D. Scaccabarozzi⁵, B. Saggin⁵, A. Martin Ortega Rico⁶

¹IKI RAN, Moscow, Russia, kia@iki.rssi.ru;

²LATMOS, Paris, France;

³INAF - Osservatorio Astronomico di Capodimonte, Napoli, Italy

⁴INAF – Osservatorio Astronomico di Bologna, Bologna, Italy;

⁵Politecnico di Milano, Milano, Italy;

⁶INTA, Madrid, Spain

Keywords:

mars, dust, in-situ measurements, dust instrument, dust suit, dust complex

The load of suspended dust in the Martian atmosphere varies dramatically but never drops entirely to zero. Effects of airborne dust contribute to the dynamic and thermodynamic evolution of the atmosphere and its large-scale circulation processes on diurnal, seasonal and annual timescales. Suspended dust plays a key role in determining the present climate of Mars and probably influenced the past climatic conditions and surface evolution. Atmosphere dust and windblown dust are responsible for erosion, redistribution of dust on the surface, and surface weathering.

The mechanisms for dust entrainment in the atmosphere are not completely understood, as the current data available so far do not allow us to identify the efficiency of the various processes. Dust-grain transport on the surface of Mars has never been directly measured despite great interest in and high scientific and technological ramifications of the associated phenomena. This paper describes planned, future investigations of the Martian dust environment made possible by the scientific payload Dust Complex (DC) of the ExoMars-2020 mission's landing platform.

The Dust Complex is a suite of sensors devoted to the study of Aeolian processes on Mars. It includes four units: an Impact Sensor, the MicroMED sensor, Conductive sensor and a Mast. The Impact Sensor contains the main electronics of the DC and two different elements: a piezoelectric based sensor, for the detection of the saltating sand grain flux and momentum, and a Charge-Sensitive Grid for the measurement of the grains' electric charges. MicroMED is an optical particle counter for the measurement of airborne dust size distribution and number density. The Mast accommodates the following sensors: 1) a second Impact Sensor, with the same sensors of the first one, 2) two Electric Probes for the measurement of the atmospheric electric field, 3) a Conductive Sensor, for the measurement of the electric conductivity of the Martian atmosphere and 4) an EM Sensor (antenna), which scans the atmosphere at frequencies up to 1 MHz to monitor electric discharges in the atmosphere.

The Dust Suit primary scientific goal is to monitor the dust cycle by direct measurements of dust flux at the surface of Mars. This has never been performed on Mars. Indeed, the dust cycle and the resulting feedback on atmospheric circulation are still poorly known for Mars. The unpredictability of the global dust storms on Mars is one of the most evident consequences of this lack of understanding.

ExoMars 2020 mission will offer a unique opportunity to study these processes by monitoring dust dynamics for one Martian year. This will allow spanning from periods of relatively clear sky to more dusty periods, where an important load of dust is expected to be injected into the atmosphere.

The presentation reviews outlining design and characteristics of DC, various dust effects and dust phenomena that are anticipated to occur

in the near-surface environment on Mars and that are possible to observe by DC as well as the instrument developing status.

Scientific outcomes of DC have future meteorological and environmental applications on Mars, for example, for the study of the evolution dynamics of the atmospheric aerosols and near-ground stratification.

M-DLS EXPERIMENT FOR THE EXOMARS-2020 STATIONERY LANDING PLATFORM

I.I. Vinogradov¹, V.V. Barke¹, V.A. Kazakov^{1,2}, A.Yu. Klimchuk¹, T.O. Kozlova¹, Yu.V. Lebedev¹, A.V. Rodin^{2,1}, O.Z. Roste¹, M.V. Spiridonov³, A.A. Venkster¹, S.G. Zenevich², J. Cousin⁴, G. Durry⁴, M. Ghysels-Dubois⁴, L. Joly⁴

¹Space Research Institute of the Russian Academy of Sciences (IKI RAS), 117997, 84/32 Profsoyuznaya Str., Moscow, Russia, imant@iki.rssi.ru;

²Moscow Institute of Physics and Technology (MIPT), 141701, Institutsky Dr. 9, Dolgoprudny, Moscow Region, Russia, alexander.rodin@phystech.edu;

³Prokhorov General Physics Institute of the Russian Academy of Sciences (GPI RAS), 119991, Vavilov Str., 38, Moscow, Russia;

⁴GSMA, UMR CNRS 7331, Université de Reims, BP 1039, 51687 Reims, Cedex 2, France.

Keywords:

ExoMars-2020; Martian atmosphere; chemical and isotopic composition variations; tunable diode laser absorption spectroscopy; integrated cavity output spectroscopy.

Introduction:

An application of tunable diode laser absorption spectroscopy (TDLAS) in combination with integrated cavity output spectroscopy (ICOS) was proposed for Martian atmosphere study as a Martian multichannel diode laser spectrometer, or M-DLS experiment. M-DLS instrument has been designed as a compact and lightweight device for continuous *in situ* study of chemical and isotopic composition variations of atmosphere near the Martian surface at the ExoMars-2020 mission stationery Landing Platform.

Measurement method:

In the M-DLS experiment, Martian atmosphere will be studied by optical measurements of molecular absorption spectrum of ambient gas sample, taken from close location of the stationery Landing Platform. Flexibility of TDLAS and radical optical path enhancement of ICOS will be combined in the M-DLS instrument for fine measurements of weak absorption at low pressure of Martian atmosphere sample. H₂O and CO₂ molecular content and isotopic ratio variations will be retrieved from absorption data, which will be continuously stored during one Martian year.

Gas sample will be sounded inside the ICOS optical cell by two highly monochromatic tuneable DFB-lasers, emitting at the NIR range. Measurements will be carried out sequentially within $\sim 1 \text{ cm}^{-1}$ intervals at 2.65 μm for H₂O and at 2.81 μm for CO₂ with spectral resolution of $\sim 10 \text{ MHz}$ ($\sim 0.0003 \text{ cm}^{-1}$), providing for fine recording of molecular absorption line contours of H₂O and CO₂ main molecules and their isotopologues HDO, HO¹⁸O, ¹³CO₂, CO¹⁷O, CO¹⁸O.

Highly reflective R=99.9% mirrors of the compact ICOS cell correspond to $\sim 220 \text{ m}$ effective optical path at 2.65 μm . Slightly lower reflection of the mirrors at 2.81 μm will result in $\sim 50 \text{ m}$ effective optical path for specially selected weak absorption lines at this range.

Modelling of the absorption spectra has shown noticeable temperature dependence of the line amplitudes, demanding for sub-degree precision of the gas sample temperature control in the optical cell, corresponding to molecular concentration retrieval and isotopic ratio measurement accuracy of: D/H < 2%, ¹⁸O/O < 2% (H₂O), ¹⁸O/¹⁷O/O < 0.3% (CO₂), ¹³C/C < 0.3%.

Ambient gas sampling system will connect the ICOS cell analytical volume to the Martian atmosphere. Gas inlet will be raised $\sim 20 \text{ cm}$ up over the Landing Platform top point, or $\sim 2 \text{ m}$ above the Martian surface. Better measurement accuracy will be optionally provided by increasing ~ 5 times up of sampled gas pressure in the ICOS cell analytical volume.

Following the M-DLS experiment idea, industrial design of a flight instrument is now under way, in compliance with its definite location on board of the ExoMars-2020 Landing Platform [1–3].

Summary:

The idea of M-DLS experiment, combining TDLAS and ICOS methods, was proposed for continuous study of atmosphere near the Martian surface. Compact and lightweight M-DLS instrument, aiming for *in situ* measurements of H₂O and CO₂ content and of D/H, ¹⁸O/¹⁷O/¹⁶O, ¹³C/¹²C isotopic ratio variations is now under industrial design for the ExoMars-2020 mission stationery Landing Platform scientific payload.

References:

- [1] Vinogradov I., Klimchuk A., Alexandrov K., Barke V, Benderov O., Fedorova A., Gerasimov M., Ignatiev N., Kazakov V., Kozlova T., Lebedev Yu., Patsaeva M., Rodin A., Roste O., Sapgir A., Semenov V., Spiridonov M., Venkstern A., A multichannel diode laser spectrometer for in situ study of atmosphere near the Martian surface for the ExoMars-2020 mission Landing Platform // European Planetary Science Congress (EPSC 2017) Abstracts, Vol. 11, EPSC2017-23, Riga, Latvia, 17–22 September 2017.
- [2] Vinogradov I., Klimchuk A., Barke V, Fedorova A., Gerasimov M., Kazakov V., Kozlova T., Lebedev Yu., Patsaeva M., Rodin A., Roste O., Semenov V., Spiridonov M., Venkstern A., A multichannel diode laser spectrometer experiment on board of the ExoMars-2020 mission Landing Platform for in situ study of atmosphere near the Martian surface // The Eighth Moscow Solar System Symposium (8M-S3), 8MS3-PS-66, Moscow, 9-13 October, 2017.
- [3] Vinogradov I.I., Barke V.V., Kazakov V.A., Lebedev Yu.V., Rodin A.V., Roste O.Z., Venkstern A.A., Klimchuk A.Yu., Semenov V.M., Spiridonov V.V., Cousin J., Durry G., Ghysels-Dubois M., Joly L., Diode laser spectroscopy instrument design for in situ study of atmosphere near the Martian surface // 18th International Conference on Laser Optics (ICLO 2018), DOI: 10.1109/LO.2018.8435269, St. Petersburg, Russia, 4-8 June, 2018.

THE MARTIAN GAS ANALYTICAL PACKAGE (EXOMARS MISSION, 2020)

**M. Gerasimov, K. Alexandrov, M. Zaitsev, A. Saggir, A. Vasileva,
T. Yukhnevich, , A. Stepanov, U. Lebedev, S. Podkolzin, A. Nosov,
P. Bocharnikov**

Space Research Institute of the Russian Academy of Sciences

Keywords:

Gas chromatography, mass spectrometry, analysis of Martian atmosphere.

Introduction:

The Martian Gas Analytical Package (MGAP) is an analytical laboratory for direct precise gas analysis of Martian atmosphere. It is a part of scientific payload of the surface platform of the mission ExoMars 2020. The main scientific aim of the package is to investigate dynamics of minor components in the near-surface layer of atmosphere and atmosphere-surface interaction.

Composition of Martian atmosphere is mostly defined by two factors: ultraviolet (UV) photo-chemistry and interaction of gases with planetary surface. Transparency of the Martian atmosphere to UV solar radiation provides significant effect of UV radiation in physicochemical processes during the daytime [1,2,3]. Volatile compounds of the subsurface atmosphere can interact with the regolith in a physical (freezing and adsorption of volatiles at night into the cooled regolith and releasing them from the regolith during the day warming) and chemical way (various chemical reactions) [4,5].

Thus, the tasks of the MGAK are:

- chemical analysis of the atmosphere;
- determination of the isotopic composition of elements forming the atmosphere;
- determination of composition and isotopy of noble gases;
- investigation of the atmospheric minor components dynamics near the surface;
- investigation of the atmosphere-surface interaction.

MGAP consists of two instruments, made in the form of monoblocks: Gas Chromatograph (GCM) and Neutral Gas Mass-Spectrometer (NGMS), and three gas connectors.

The prototype of the GCM instrument is the GC-L instrument of the Luna-Resource project. The prototype of the NGMS mass spectrometer is the mass spectrometer of the Ptolemy device of landing platform Philae of the Rosetta mission.

The main function of the GCM instrument is separation of a complex sample gas mixture into individual gas components with measurement of their quantity and transfer of separated gases to the mass spectrometer. Depending on the chosen measurement mode, analyzed gas sample is sent from the sample volume directly to the chromatographic columns or pre-accumulated in adsorption traps for further analysis. The GCM uses two chromatographic columns optimized for measurement of low-boiling and high-boiling gases, thus providing measurement in the targeted range of compositions. The choice of types of adsorbents in two adsorption traps allows separating of the gas mixture for analysis with respective columns. The gases coming out from the GCM pass through the connecting capillary tube to the NGMS mass spectrometer synchronously with the chromatographic analysis. Mass spectra of pure components provide reliable identification of these gases and, in addition, measuring isotope composition of incoming elements. The NGMS operates on the principle of a quadrupole ion trap. The NGMS can also autonomously analyze samples of the atmospheric gases.

The strategy of the complex operation is the mutual addition of the analytical capabilities of the devices included in the complex. The complex operates only on the surface of Mars after the departure of the rover in the single-cycle measurement mode.

References:

- [1] Gerasimov M.V., Kosheev A.P., Gutman E.E UV- decomposition of Martian sulphates and chlorides as a possible source of Cl- and S- containing gases to the Martian atmosphere // *Annales Geophysicae. Suppl.* 1993. III to V. 11. P. 483.
- [2] Mukhin L.M., Koscheev A.P., Dikov Yu.P, Huth J., Waenke H. Experimental simulations of the photodecomposition of carbonates and sulphates on Mars // *Nature.* 1996. V. 379. P. 141-143.
- [3] Kounaves S.P., Hecht M. H, Kapit J., Gospodinova K., DeFlores L., Quinn R.C, Boynton W.V., Clark B.C., Catling D.C., Hredzak P., Ming D.W., Moore Q., Shusterman J, Stroble S., West S.J, and Young S.M.M. Wet Chemistry experiments on the 2007 Phoenix Mars Scout Lander mission: Data analysis and results // *J. Geophys. Res.* 2010. V. 115. E00E10. doi:10.1029/2009JE003424
- [4] Navarro-Gonzalez R., Vargas E., de la Rosa J., Raga A.C., McKay C.P. Reanalysis of the Viking results suggests perchlorate and organics at midlatitudes on Mars. // *J. Geophys. Res.* 2010. P. 115
- [5] Clancy R.T., Sandor B.J., Moriarty-Schieven G.H., A measurement of the 362 GHz absorption line of Mars atmospheric H₂O₂// *Icarus.* 2004. № 168. P. 116–121.

MARS: ELECTROMAGNETIC SURVEY AT THE LANDING PLATFORM

S.V. Kulikov, A. A. Skalsky

Space Research Institute of RAS, Moscow, Russia, kulikov@rx24.ru

Keywords:

Mars, solar wind, dust devil, ULF waves, ionosphere, MAIGRET

Introduction:

Mars is the highly interesting object for survey due to the lack of a global magnetic field and the presence of the strongly magnetized areas on its surface. Martian magnetosphere combines both electromagnetic phenomena that are typical for the induced magnetosphere and those known for planets possessing intrinsic magnetic field. Dust devils and the related electrification of the dust particles can cause the electrostatic discharges in the atmosphere near the planet's surface.

To date, measurements of the electromagnetic field on the surface of Mars have not been ever carried out.

The MAIGRET instrument installed onboard the landing platform and actually developed in the scope of EXOMARS 2020 project will provide an opportunity for first monitoring of electromagnetic activity on the Martian surface. The present paper is aimed to overview the known wave phenomena occurring in the magnetosphere and ionosphere of Mars, as well as estimates of electromagnetic fields in the atmosphere generated by dust storms and tornadoes.

LARA (LANDER RADIOSCIENCE) ON THE EXOMARS 2020 SURFACE PLATFORM – ROTATION OF MARS AND POSITIONING OF THE SURFACE PLATFORM

**A. Kosov¹, S.L. Maistre², V. Dehant^{2,3}, R.M. Baland², Ö.Karatekin²,
M. Mitrovic², M.J. Péters², A. Rivoldini², T.V. Hoolst², B.V. Hove²,
M. Yseboodt²**

¹*Space Research Institute Russian Academy of Sciences (IKI);*

²*Royal Observatory of Belgium, Brussels, Belgium;*

³*Université catholique de Louvain, Louvain-la-Neuve, Belgium*

The LaRa experiment is designed to obtain coherent two-way Doppler measurements from the radio link between the 2020 ExoMars lander (the Surface Platform, SP) and the Earth over at least one Martian year. The Doppler measurements will be used to observe the orientation and rotation of Mars in space (precession, nutations, and length-of-day variations), as well as polar motion. The ultimate objective is to obtain information on the Martian interior and on the sublimation/condensation cycle of atmospheric CO₂. Rotational variations will allow us to constrain the moment of inertia of the entire planet, including its mantle and core, the moment of inertia of the core, and seasonal mass transfer between the atmosphere and the ice caps.

Besides, LaRa could allow to accurately determine the position of the SP within a very short time after the starting of operations. An early estimate of the lander location will certainly improve the quality of the science analysis (for instance by making easier the recognition of the geological features seen on the lander's pictures) and allow high-resolution cameras from spacecraft like MRO to correctly target the lander. The classical technique using Delta DOR measurements for obtaining the SP position has an accuracy in the plane of sky of 200-900m (depending on the Earth-Mars distance), while our estimation combining LaRa Doppler data and local terrain maps is about 10 m. Such an early precise estimate of the lander location will also certainly improve the quality of the science analysis.

MARTIAN SOIL SIMULANT FOR LARGE-SCALE FIELD EXPERIMENTAL RESEARCH

E.A. Grishakina¹, A.A. Dmitrovskii¹, M.A. Ivanov¹, E.M. Sorokin¹, V.Y. Makovchuk¹, A.V. Uvarova^{1,2}, E.A. Voznesensky², M.S. Nikitin², E.A. Sentsova², and E.N. Slyuta¹

¹Vernadsky Institute of Geochemistry and Analytical Chemistry, RAS, Moscow, Russia; grishakina@geokhi.ru

²Lomonosov Moscow State University, Moscow, Russia; eugene@geol.msu.ru

Keywords

Martian soil simulant, physical and mechanical soil properties, triaxial tests, grain-size distribution, ExoMars.

Introduction

According to Roskosmos and ESA plans, 2020 mission of ExoMars programme consists of rover and surface platform. Preliminary research on martian surface of supposed target areas (*Oxia Planum* and *Mawrth Vallis*) is necessary for successful landing of the module. This investigation includes exploration of *physical and mechanical* soil properties which is based on *new martian soil simulant*.

Materials and methods

Spirit, Opportunity, Pathfinder, Viking missions provide in-situ data on physical and mechanical properties of martian soils which became a basis of our research [1]. We created 4 mixtures of easy-to-find desintegrated components such as quartz sand, fly-ash and ash-slag waste (ASW) based on quantitative estimates of the prevalence of different types of terrain (Tables 1a, 1b). Table 1a. Martian soil properties (density and particle size distribution) expected at the landing sites of Oxia Planum and Mawrth Vallis. Chemical composition of all components (except clay) are basalt-like. The percentage of soil components was estimated by analysis of high-resolution images of the sites [2]

Table 1a.

Soil components	Density, g/cm ³	Grain size, mm	Percentage, %		Cohesion, kPa	Angle of internal friction, degree
			Oxia	Mawrth		
Silt	1-1.3	0.001-0.01	2-7	2-7	0-3	15-21
Sand	1.1-1.3	0.06-0.2	22-27	8-13	0-1	30
Crusty to Cloddy	1.1-1.6	0.005-0.5	32-37	22-27	0-4	30-40
Blocky	1.2-2.0	0.05-3	26-31	20-25	3-11	25-33
Pebbles	2.6-2.8	2.0-2000	5-10	13-18	1000-10000	40-60
Clay	1.5-1.6	<0.001	0-3	20-25	-	-

Table 1b. Composition of soil simulants, %

	Quartz sand 0.5-1.2 mm	Quartz sand 0.19-0.23 mm	Fly-ash	Ash-slag waste (ASW)
1	33	28	7	32
2	25	15	30	30
3	40	40	10	10
4	-	50	20	30

Data on other physical and mechanical properties of real martian soil were used as requirements for appropriate soil simulant:

Table 2a. Physical properties of components and soil imitators (grain-size distribution)

	Grain-size distribution in soil simulants in weight %											
	Cob- ble	Pebble		Sand					Dust			
	>10	10-5	5-2	2-1	1-0.5	0.5- 0.25	0.25- 0.1	0.1- 0.05	0.05- 0.01	0.01- 0.005	0.005- 0.002	<0.002
Compo- nents												
Coarse quartz- sand	0.0	0.0	0.0	24.0	72.0	2.6	0.8	0.5	0.1	0.0	0.0	0.0
Fine quartz- sand	0.0	0.0	0.0	0.0	1.0	36.0	62.3	0.6	0.1	0.0	0.0	0.0
Fly-ash	0.0	0.0	0.0	0.0	0.0	0.6	5.9	42.7	48.0	1.7	1.1	0.0
Ash-slag waste (ASW)	2.2	1.6	2.1	1.9	1.4	1.7	5.0	22.5	45.6	10.6	5.0	0.6
Mixtures												
1	0.0	0.0	0.3	11.2	25.2	8.1	22.0	7.9	18.5	5.4	1.5	0.0
2	0.0	0.0	0.2	7.4	21.2	4.6	16.9	12.5	35.1	1.0	1.0	0.0
3	0.0	0.0	0.1	9.6	33.2	11.6	26.6	8.3	7.8	2.0	1.0	0.0
4	0.0	0.0	0.1	0.8	1.2	12.7	36.0	10.7	33.6	4.4	0.6	0.0

Table 2b. Physical and mechanical properties of components and soil imitators

	Moisture content, %	Particle density, g/cm ³	Dry bulk density, g/cm ³		Cohesion, MPa	Angle of internal friction, degree	Stiffness modulus (in stress range 0.1-0.2 MPa), MPa	Elastic modulus, MPa	Bearing capacity, MPa	Dynamic elastic modulus, MPa	Frictional coefficient	Dynamic modulus, MPa
			Comp-act	Loose								
			W	ρ_s								
Compo- nents												
Coarse quartz sand	0.0	2.65	1.44	1.20	-	-	-	-	-	-	-	-
Fine quartz sand	0.1	2.65	1.58	1.38	-	-	-	-	-	-	-	-
Fly-ash	0.1	2.48	1.47	1.12	-	-	-	-	-	-	-	-
Ash-slag waste (ASW)	14.3	2.24	1.24	0.98	-	-	-	-	-	-	-	-
Mixtures												
1	0.5	2.54	1.69	1.44	0.011	24	12.7	-	0.385	115.2	0.445	77.6
2	0.4	2.48	1.55	1.30	0.007	25	5.6	57.3	0.332	248.9	0.458	52.5
3	0.2	2.61	1.85	1.59	0.036	28	18.7	-	0.384	117.6	0.525	68.6
4	0.5	2.50	1.57	1.32	0.031	25	10.6	67.5	0.451	148.5	0.472	57.2

- Grain-size distribution
- Dry and particle density
- Cohesion
- Angle of internal friction
- Moisture content

Mechanical properties were obtained in triaxial and direct shear tests.

Results

According to results of our experiments, mixture #2 (Table 1b) seems physico-mechanically similar to martian soil. Its density in loose state is 1.3 g/cm^3 (Table 2b), that is close to upper bound of martian silt and sand soils' density estimations ($\sim 1.3 \text{ g/cm}^3$) (Table 1a). The mixture's density in compact state is 1.55 g/cm^3 (Table 2b), which corresponds to the density range for clay, crusty to cloddy and blocky martian soil density intervals (Table 1a). Low moisture of the mixture is typical for upper part of martian soil in ExoMars mission's target areas [3]. Besides, stiffness modulus, elastic modulus, bearing capacity, dynamic elastic modulus, dynamic modulus were measured, but there are no estimates of these properties of real martian soil.

We propose Mixture #2 for throwing tests of ExoMars landing module.

References

- [1] Golombek M.P., Haldemann A.F.C., Simpson R.A., Fergason R.L., Putzig N.E., Arvidson R.E., Bell III J.F., Mellon M.T. Martian surface properties from joint analysis of orbital, Earth-based, and surface observations // *The Martian surface: Composition, mineralogy and physical properties* / Ed. Bell III J.F. Cambridge Univ. Press, 2008. P. 468–498.
- [2] Ivanov M.A., E.A. Grishakina, A.A. Dmitrovskii, E.M. Sorokin, V.Y. Makovchuk, A.V. Uvarova, E.A. Voznesensky, M.S. Nikitin, E.A. Sentsova, and E.N. Slyuta. ExoMars landing sites in OxiaPalus and MawrthVallis: geological characterization // *This issue*
- [3] Mitrofanov I.G., Litvak M.L., Kozyrev A.S., Sanin A.B., Tret'yakov V.I., Grin'kov V.Yu., Boynton W.V., Shinohara C., Hamara D., Saunders S. Soil water content on Mars as estimated from neutron measurements by the HEND instrument on board the 2001 Mars Odyssey spacecraft // *Sol. Syst. Res.* 2004. V. 38. № 4. P. 253–265.)

EXOMARS LANDING SITES IN OXIA PALUS AND MAWRTH VALLIS: GEOLOGICAL CHARACTERIZATION

M.A. Ivanov¹, E.A. Grishakina¹, A.A. Dmitrovskii¹, E.N. Slyuta¹, V.Y. Makovchuk¹, E.M. Sorokin¹, A.V. Uvarova¹, E.A. Voznesensky², M.S. Nikitin²

¹*Vernadsky Institute of Geochemistry and Analytical Chemistry, RAS, 119991, Kosygin St. 19, Moscow, Russia;*

²*Moscow State University, Moscow, Russia*

Keywords:

Mars, ExoMars, landing sites, Oxia Planum, Mawrth Vallis.

Introduction:

Two regions on Mars were selected for the lander phase of the ExoMars mission. Here we report on the topography and geology of both sites investigated with the use of the MOLA and HiRISE digital elevation models (DEM) and mosaics of the CTX images with resolution ~ 6 m/px.

Oxia Planum landing site, topography and slopes:

The HiRISE-based, high-resolution DEMs are absent for the Oxia Planum site and topographic information for this area is provided by the MOLA DEM with the spatial resolution ~ 463 m/px. Two major Martian provinces, the lowlands and highlands compose the Oxia Planum site. Lowlands are flat with minor topographic variations (~ 100 - 150 m over the distance of ~ 80 km). The major topographic features within this province are low hills with gentle slopes and relicts of impact craters. The long (463 m)-baseline slopes in this province are predominantly small ($< 2^\circ$) and occupy $\sim 90\%$ of the landing site area. The elevated highlands are characterized by more contrast topographic variations and the most prominent features in this area are the system of the fluvial channels Coogoon Valles, which are 50-60 m deep, and rough ejecta deposits that can be many tens of meters high.

Oxia Planum landing site, morphological units:

The oldest units in the Oxia landing region occur within the highland domain and correspond to ejecta of an ancient impact crater (unit uem) and old, morphologically smooth plains with wrinkle ridges (unit ups). Unit uem consists of poorly sorted and rough materials of the Noachian highlands and unit ups likely represent the Hesperian lava plains. Bright mantles with the etched surface and very sinuous boundaries (unit bem) overlay the units uem and ups within the highlands. The HiRISE images show that the unit bem consists of numerous angular blocks several meters across. The high albedo and specific texture of the unit bem suggest that its material may include a significant amount of clay components.

The terminal channel of Coogoon Valles (unit cd) cuts the older terrains (uem and ups) and opens to the vast lowlands with flat surface. At the edge of the channel, there are terminal deposits (unit dd) that form elongated fan- and lens-like bodies about 10-15 km long and a few kilometers wide. The formation of these deposits indicate the change of the fluvial regime from erosional (within the highlands) to depositional within the lowlands. The surface of unit dd is morphologically smooth and gently undulating; the units apparently consists of several layer. The HiRISE images show the absence of large boulders at the edges of the layers and their surface show the presence of dune-like fields. These observations indicate that sand deposits formed by low-power flows through the Coogoon Valles terminal channel compose the major portion of the unit dd.

Within the lowlands, light-toned plains form the most abundant unit (unit lbp). In places, narrow (10-20 m wide) and low (a few meters high) ridges complicate the gently undulating surface of the unit lbp. The ridges are often merging to form individual dunes and dune fields that preferentially occur in local topographic depressions, e.g., within the degraded impact craters.

The abundant dunes suggest that the major portion of unit lbp consists of sands. However, the surface of the unit does not represent a contiguous dune field suggesting that some cementing materials bond the sand components of the unit. In some places within unit lbp, there are small (a few meters across) areas of bright polygonal materials resembling the clay deposits discovered elsewhere on Mars.

The unit of dark, hummocky materials (dpi) is less abundant within the lowlands but comprises ~18% of its surface. Exposures of this unit are usually seen within local topographic depressions (e.g., floors of degraded impact craters) and at continuation of the channels of Coogoon Valles near the highlands. The surface of unit dpi is rugged and consists of numerous short (a few tens of meters long) chaotic ridges; the unit edges often represent low scarps. The HiRISE images show that abundant large (>1 m) boulders and fine-grained (sand) materials are important components of unit dpi. The mixture of rough and fine components of this unit indicates that its material is poorly sorted and typical association of this unit with local lows suggest that the unit formed by high-power flows through Coogoon Valles that transported and deposited unsorted highland materials within the adjacent lowlands.

The other units within the lowland domain make up negligible fraction of its surface and include erosional remnants of the highlands (unit me) and impact craters (unit ed), and fresh crater ejecta (unit ejd). It is important to note that all fresh-looking craters have small diameter (several hundred meters and smaller) and their ejecta have low albedo. This means that at the shallow subsurface (~1/10 of the crater diameters) below the plains complexes of the lowlands, there is a dark materials typical of the lava flows. Thus, it is likely that lava plains exposed within the highland domain underlie the brighter and darker plains units that compose the majority of the lowlands within the Oxia landing region.

Mawrth Vallis landing site, topography and slopes:

There are two types of the DEMs for the Mawrth Vallis landing region constructed based on the MOLA data (463 m/px) and derived from stereo pairs of the HiRISE images (~1 m/px). In our study, we used both types of DEMs to characterize the long- and short-baseline components of relief.

Variations of the long-baseline relief can reach many tens-several hundred meters and are most pronounced within the NW portion of the landing region where topography is changed for ~300-400 m over the distance of 20-22 km. About 90% of the Mawrth Vallis landing region show small (<30) long-baseline slopes. The HiRISE-based DEMs, however indicate that the landing area is characterized by numerous small topographic features with large amplitudes. These landforms cause appearance of abundant steep (>100) slopes. For example, the slopes steeper than 90 on a 1-m-baseline comprise ~24% of the landing site region.

Mawrth Vallis landing site, morphological units:

Bright plains (unit bp) form the most abundant unit within the landing region. The surface of the plains is morphologically smooth at the CTX resolution (~6 m/px). At the higher resolution of the HiRISE images (0.25 m/px), however, the surface of the plains shows very abundant short (several tens of meters long) and low (a few meters up to a few tens of meters high) chaotically oriented ridges with rounded crest area. Very often, the surface of the plains consists of numerous polygonal blocks or plates. In some places, there are dunes on the surface of the plains. The dunes have the same albedo as the surrounding surface, which suggests that they represent materials of the plains re-distributed by wind. Boulders are absent at the edges of low scarps within the plains. The lack of the boulders suggests that mostly fine-grained materials compose the bright plains.

The bright surface of the plains, their polygonal texture, and virtual lack of boulders suggest that materials of the plains to large extent consist of clay minerals. The bright plains not only make up the surface within the landing region, but also are exposed in the walls of larger impact craters and the Mawrth Vallis channel at low hypsometric levels. This means that the total thickness of the bright, clay-bearing material is at least several hundred

meters and the emplacement of this materials predated formation of the fluvial structures of Mawrth Vallis.

The next areally important unit of the Mawrth Vallis landing region is dark plains (unit dp). The plains form extensive mesas that are many hundred meters - a few kilometers wide. The extremely sinuous scarps, which typically are several tens of meters high, bound the mesas. The surface of the dark plains are gently rolling and morphologically smooth. Almost everywhere, talus aprons overlay the walls of the mesas. At the highest available resolution, the taluses appear to be fine-grained without boulders and evidence for internal layering. This implies that the dark plains represent massive accumulations of fine-grained materials. In all places where the dark plains are exposed, they overlay the bright plains and, thus, are younger.

The dark plains is are heavily eroded and in many places on the landing region they have been mapped as a specific unit of degraded dark plains (unit dpd). The surface of the unit dpd is rugged and consists of chaotically oriented ridges, small (tens of meters across) mesas, and large blocks. Zones of unit dpd surround larger occurrences of the dark plains.

The less widespread units in the study area are units of dark mantles (dm), talus aprons (unit ta), and dune fields (unit df). These materials represent the result of degradation and redeposition of the bright and dark plains. Although the walls of the Mawrth Vallis tributaries have been mapped as a specific unit (cd), they mostly expose the layers of the bright plains covered by a veneer of the apron-forming materials.

EXOMARS LANDING SITES IN OXIA PALUS AND MAWRTH VALLIS: SMALL CRATERS AND BOULDERS

M.A. Ivanov¹, E.A. Grishakina¹, A.A. Dmitrovskii¹, E.N. Slyuta¹, V.Y. Makovchuk¹, E.M. Sorokin¹, A.V. Uvarova¹, E.A. Voznesensky², M.S. Nikitin²

¹*Vernadsky Institute of Geochemistry and Analytical Chemistry, RAS, 119991, Kosygin St. 19, Moscow, Russia;*

²*Moscow State University, Moscow, Russia*

Keywords:

Mars, ExoMars, landing sites, Oxia Planum, Mawrth Vallis.

Introduction:

Small impact craters and boulders present a serious threat to landers. Impact craters are the most abundant landforms in both ExoMars landing region and boulders usually occur in the spatial association with the craters. In order to estimate the size-frequency distribution (SFD) of craters and boulders we used the HiRISE images with the highest available spatial resolution (~0.25 m/px).

Oxia Planum landing site, craters:

Impact craters significantly contribute to the variations of both long- and short-wavelength components of the landing sites topography. In the Oxia Planum region, the crater diameters vary from the HiRISE resolution limit (~1-1.5 m) up to 5 km. In order to assess the SFD of the craters we have mapped them in three randomly selected areas. Their total area is 2.88 km² and the total number of the craters within these areas is 2390.

All crater are bowl-shaped and, thus, are similar to each other by their general shape but their depth/diameter (d/D) ratio depends upon the preservation state of the craters. In our study, we define three morphological classes of the craters, A, B, and C. Craters of class A have distinct ejecta/ray system and are the deepest; d/D is ~0.200; the A-craters comprise ~3% of the crater population in the study area. Craters of class B lack ejecta, but their rim is still prominent (d/D is ~0.109, ~31% of the population), craters of class C represent shallow topographic depressions without discernible rim (d/D is ~0.052, ~66% of the population).

Impact craters in the study area are distributed randomly. The null hypothesis of their non-random distribution is rejected at the 95% confidential level. The SFD of the craters is described by two power laws:

$$N_{(>D)} = 6.62 * D^{-1.45}, \text{ for craters 6-44 m}$$

$$N_{(>D)} = 12.07 * D^{-2.92}, \text{ for craters 44-200 m}$$

The shallower slope of the curve for the smaller craters indicates that they were erased preferentially and, thus, the larger diameter of these craters (~40 m) provides an estimate of the thickness (~4 m, i.e., 1/10 of the larger crater diameter) of the surficial layer removed/degraded in the area of the study.

Oxia Planum landing site, boulders:

We define boulders as equidimensional, self-standing (or clustered), positive landforms in the diameter interval from 1 to 10 m. In contrast to the craters, boulders are distributed over the surface in the non-random fashion and preferentially occur at the base of the steeper slopes and in the ejecta of the fresher impact craters (A-craters).

In the Oxia Planum region, we investigated the spatial and size-frequency distribution of boulders within two most abundant units from the lowland domain, the light-toned plains (lbp) and the dark, hummocky materials (dpi). Within unit dpi, boulders (1-6 m diameter) are more abundant and their density is ~737 km⁻² or ~0.018 boulders in a 5x5 m area. The spatial distribution of boulders significantly varies and they form distinct clusters where their density rapidly increases up to ~0.4-0.6 in a 5x5 m area.

Within the bright plains, boulders are rare and their mean density about an order of magnitude smaller than within unit dpi: $\sim 65 \text{ km}^{-2}$ or 0.002 boulders in a 5×5 area. The spatial distribution of boulders on the bright plains is also uneven and they form clusters near impact craters. Within the clusters, the mean density of boulders is increased up to 0.3-0.4 boulders in a 5×5 m area.

The SFD of boulders is described by the power law and within both units the distribution is approximated by at least two curves. For the dark hummocky material, the approximating curves are:

$$N_{(>D)} = 6.2 * D^{-2.31}, \text{ for boulders } 2.5\text{-}4 \text{ m}$$

$$N_{(>D)} = 11.5 * D^{-6.33}, \text{ for boulders } 4\text{-}6.65 \text{ m}$$

For the bright plains, the approximating curves are:

$$N_{(>D)} = 11.3 * D^{-5.64}, \text{ интервал диаметров } 2.5\text{-}4 \text{ m}$$

$$N_{(>D)} = 18.2 * D^{-10.69}, \text{ интервал диаметров } 4\text{-}6.65 \text{ m}$$

In both cases, the break of slope of the approximating functions occurs for the ~ 4 m diameter boulders.

Mawrth Vallis landing site, craters:

Within this region, diameters of impact craters vary from ~ 1 m (the resolution limit) to ~ 600 m. In order to assess the SFD of the craters we have mapped them in three randomly selected areas. Their total area is 12 km^2 and the total number of the craters within these areas is 4421.

All crater are bowl-shaped and, thus, are similar to each other by their general shape but their depth/diameter (d/D) ratio depends upon the preservation state of the craters. In our study, we define three morphological classes of the craters, A, B, and C. Craters of class A have distinct ejecta/ray system and are the deepest; d/D is ~ 0.180 ; the A-craters comprise $\sim 6\%$ of the crater population in the study area. Craters of class B lack ejecta, but their rim is still prominent (d/D is ~ 0.100 , $\sim 34\%$ of the population), craters of class C represent shallow topographic depressions without discernible rim (d/D is ~ 0.054 , $\sim 60\%$ of the population).

Impact craters in the study area are distributed randomly. The null hypothesis of their non-random distribution is rejected at the 95% confidential level. The SFD of the craters is approximated by a single curve:

$$N_{(>D)} = 9.1 * D^{-1.85}, \text{ for craters } 10\text{-}600 \text{ m}$$

For the smaller craters, the curves rolls-off, which is the resolution effect.

Mawrth Vallis landing site, boulders:

In the Mawrth Vallis region, we defined boulders in a similar manner as in the Oxia Planum area. Within the bright plains (unit bp), some boulders formed due to maturation of the polygonal network typical of the plains. In contrast to the craters, boulders are distributed spatially non-randomly within the bright (unit bp) and dark (unit dp) plains. The other units within the Mawrth Vallis landing region show no boulders recognizable at resolution of the HiRISE images.

Within the bright plains, boulders are more abundant and their density is $\sim 3200 \text{ km}^{-2}$ or ~ 0.08 boulders in a 5×5 m area. The spatial distribution of boulders strongly varies and they form clusters where their density rapidly increases up to $\sim 1\text{-}1.5$ boulders in a 5×5 m area.

Within the dark plains, boulders are less frequent and their mean density is: $\sim 824 \text{ km}^{-2}$ or 0.02 boulders in a 5×5 area. The spatial distribution of boulders on the dark plains is also uneven and they form clusters where the mean density of boulders is increased up to 0.3-0.5 boulders in a 5×5 m area.

The SFD of boulders is described by the power law and within both units the distribution is approximated by a single curve. For the bright plains, the approximating curve is:

$$N_{(>D)} = 11.0 * D^{-4.67}, \text{ for boulders } 1.5\text{-}3 \text{ m},$$

For the dark plains, the approximating curve is:

$$N_{(>D)} = 8.1 * D^{-4.94}, \text{ интервал диаметров } 2.5\text{-}7 \text{ m}.$$

A MINIATURIZED 3D WIND SENSOR FOR PLANETARY EXPLORATION

M. Dominguez-Pumar, L. Kowalski, S. Gorreta, M.T. Atienza, S. Bermejo, V. Jimenez, L. Castañer

Micro and NanoTechnologies Group. Technical University of Catalonia. UPC-Campus Nord, Ed. C4. Jordi Girona, 1-3. 08034 Barcelona, SPAIN, manuel.dominguez@upc.edu

Keywords:

Wind sensor, meteorology, planetary exploration, Mars, Venus, Titan, miniature sensor.

Introduction:

Meteorological stations in planetary exploration are key instruments to analyze atmosphere dynamics. Wind Sensors have been incorporated to several missions to Mars (Viking, Mars Pathfinder, MSL, InSight) or are planned for the near future (Exomars, Mars2020). Additionally, wind sensors are key instruments in planetary exploration such as in the case of Venus and Titan.

The aim of this paper is to present a miniaturized 3D wind anemometer which is a good candidate for all these target scenarios: Mars, Venus and Titan. The sensor structure consists of a 10mm-diameter sphere divided in 4 sectors clamped to a thin supporting structure made of 2 Printed Circuit Boards (PCBs) placed back-to-back. The current prototypes have been designed and tested for Mars atmosphere. However, the robustness and simplicity of the design make this new concept a good candidate for Venus and Titan challenging atmospheres.

The experimental results presented in this paper have been obtained for Mars atmosphere. The sensor has been extensively tested at the Aarhus Wind Tunnel Simulator II (AWTSII) showing that solid angle and wind speed can be easily recovered.

Sensor description:

The sensor is composed of 4 sectors, conforming a 10 mm diameter sphere, that are placed on two superimposed PCBs, which act as supporting structure and provide signal routing (see Figure 1). A customized silicon die which includes a Pt resistor is attached to each sector in order to sense temperature and dissipate heat. Finally, two additional resistors are placed on the supporting PCBs in order to be able to control the temperature at the core of the sphere, on the PCBs. A diagram of the heat fluxes on the sensor structure can be seen in Figure 1.

The sensor is operated at the same constant temperature in the sectors and core. Conduction losses from the sectors to the supporting structure are thus minimized, since all parts are at the same temperature. The output signals are the heating powers injected on the 4 resistors within the sectors. Table I, summarizes the weight and volume of the sensor.

Table I. Summary of weight and dimensions of the sensor.

Unit	Mass	Size
Sensor head	3g	10mm diameter
2 x half PCB	12g (6g each)	230 x 35 mm ²
PCB connector	7g	55 x 25 x 8 mm ³

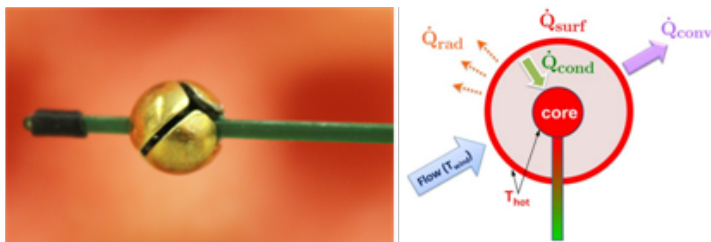


Fig. 1. Left: Photograph of the prototype of the spherical sensor anemometer. Right: Diagram of heat fluxes on the sphere.

Power depends on planned overheat but typically is below 300mW for the whole sphere (6 resistors). Typical ASIC consumption is below 200mW.

Results at the AWTsII wind tunnel of the Mars Simulation Laboratory at Aarhus University.

The targeted environmental conditions are: CO₂ atmosphere, 7-8 mbar, temperatures from -25°C to -15°C. In order to test the invariability of the results to the operating temperature two constant operating temperatures have been used: $T_{hot}=20^{\circ}\text{C}$ and $T_{hot}=10^{\circ}\text{C}$. The tested wind velocities span the range 0 – 16 m/s, whereas the angle span is 0-360° full yaw rotation, and pitches from -45° to +45°. The pressure and ambient temperature in the chamber were continuously monitored during the experiments.

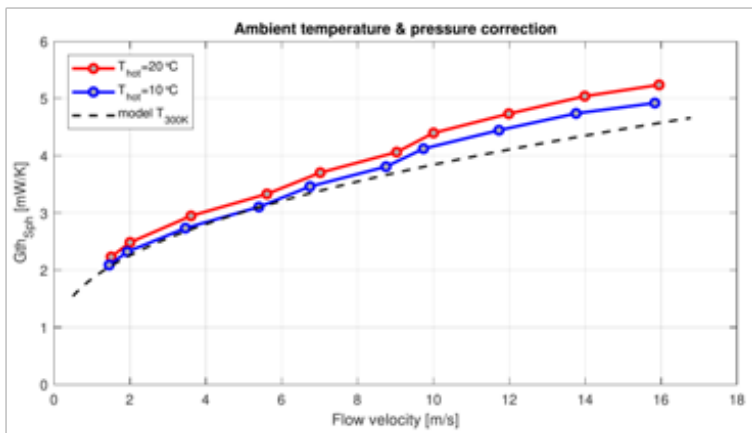


Fig. 2. Thermal conductance in the experiments obtained from the total power in the sectors, ambient temperature and pressure. Very good agreement with the model in [3].

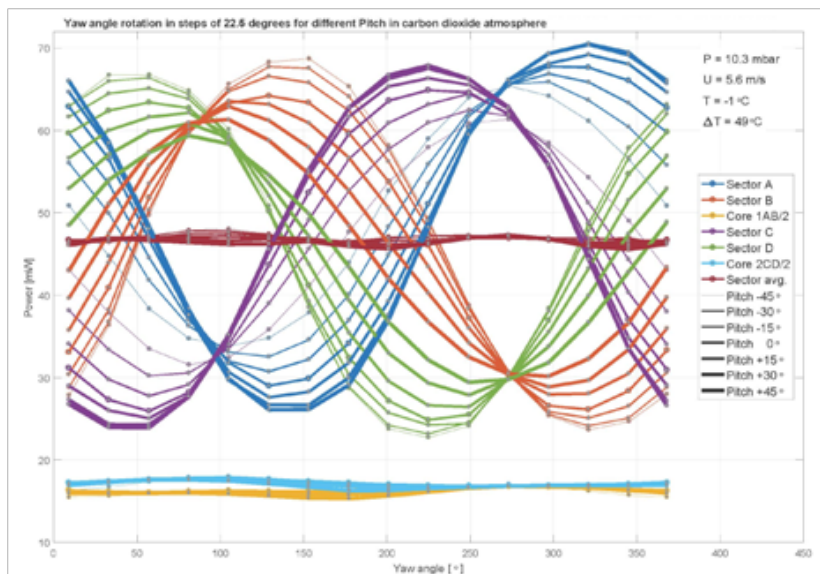


Fig. 3. Power delivered to all Pt resistors (sector A,B,C,D and 2 cores) in a experiment in which 0-360° yaw angles were swept for different pitch angles (-45°, -30°, -15°, 0, 15°, 30° and 45°), at constant wind speed (5.6 m/s)

Figure 2 shows the calculated thermal conductance of the whole sphere, taking into account the heating power delivered to the sectors, ambient temperature and pressure variations. Superimposed is the comparison with the model in [3]. As it can be observed the thermal conductance is practically independent of the overheat and very close to the expected thermal models.

Figure 3 shows the powers injected in all resistors for a long-time experiment in which many different yaw and pitch angles were swept. As it can be observed in Figures 2 and 3, wind speed and angle recovery is possible: high individual sector variations for different yaw and pitch angles, whereas the sum of power of four sectors remains constant, and depends only on wind speed.

Sensor dynamics:

Figure 4 shows the time response of the powers injected into the heaters as a result of a sudden change of angle. As it can be observed a time response of 1-2s is achieved. This closed-loop dynamics, which is much faster than the open-loop time response, is ensured by an accurate thermal design of the sensor that guarantees that only one time constant is relevant. Sliding mode analysis then shows that the time response can be reduced much beyond the limit imposed by the open-loop time constants [2,4].

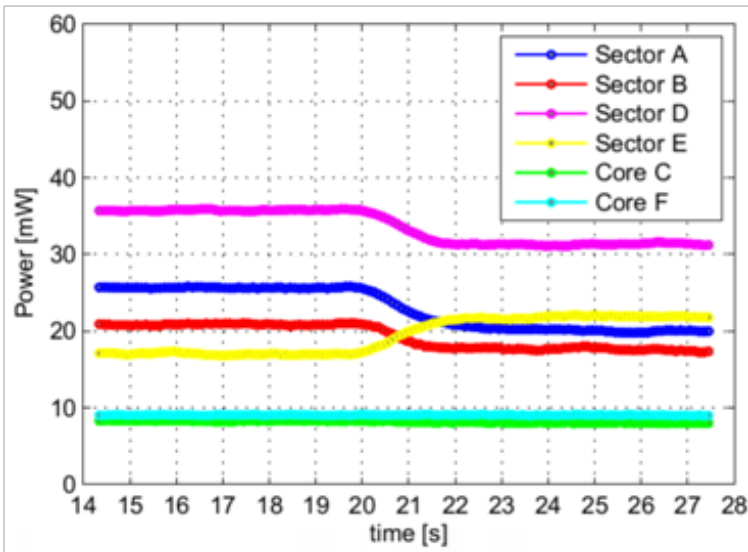


Fig. 4. Time evolution of the powers in the heaters of the sensor when a sudden change in angle is made (at $t=20s$). Time response: 1-2s.

Conclusions:

A miniaturized, simple and robust 3D wind sensor has been presented. The current prototypes are optimized for Mars atmosphere. Results obtained at the AWTSII Martian wind tunnel have been presented. The simple spherical structure makes this sensor a good candidate for other environments such as Venus and Titan.

References:

- [1] L. Kowalski, M.T. Atienza, S. Gorreta, V. Jiménez, M. Dominguez-Pumar, S. Silvestre, L.M. Castaner, Spherical wind sensor for the atmosphere of mars // IEEE Sensors Journal. 2016. V. 16. P. 1887-1897.
- [2] MT Atienza, L Kowalski, S Gorreta, V Jiménez, LM Castaner, M. Dominguez-Pumar, Sliding mode analysis applied to improve the dynamical response of a spherical 3D wind sensor for Mars atmosphere // Sensors and Actuators A. 2017. V. 267. P. 342-350.
- [3] Zhi-Gang Feng, Efstathios E. Michaelides, A numerical study on the transient heat transfer from a sphere at high Reynolds and Peclet numbers // International Journal of Heat and Mass Transfer. 2000. V. 43. N. 2. P. 219-229.
- [4] M. Dominguez-Pumar, M.T. Atienza, L. Kowalski, S. Novio, S. Gorreta, V. Jimenez, Heat Flow Dynamics in Thermal Systems Described by Diffusive Representation. // IEEE Transactions on Industrial Electronics. V. 64. N. 1 P. 664-673. 2017

NEXT-GEN LASER RETROREFLECTORS FOR MARS (EXOMARS 2016-2020, MARS 2020, INSIGHT 2018)

S. Dell'Agnello¹, G. Delle Monache¹, R. Vittori¹, M. Tibuzzi¹, L. Salvatori¹, L. Porcelli¹, C. Mondaini¹, M. Muccino¹, L. Ioppi¹, O. Luongo², M. Tantalò¹, M. Di Paolo Emilio¹, G. Bianco², R. Mugnuolo², C. Benedetto², F. Pasquali²

¹INFN-LNF (National Institute for Nuclear Physics-Frascati National Labs, via E. Fermi 40, Frascati (RM), 00044, Italy, simone.dellagnello@lnf.infn.it)

²ASI-CGS (Italian Space Agency-Space Geodesy Center), Matera (MT), Italy

Keywords:

Laser retroreflectors, ExoMars 2020, Mars 2020, InSight, Mars Geophysical Network, general relativity.

Introduction:

There are laser retroreflectors on the Moon and no laser retroreflectors on Mars, except for the Italian micropayload on the ExoMars 2016 Schiaparelli lander. These instruments are positioned by time-of-flight measurements of short laser pulses, the so-called "laser ranging" technique (see the website of the reference international community, ILRS: <https://ilrs.gsfc.nasa.gov>). For example, this is performed by MLRO, the Matera Laser Ranging Observatory of the Italian Space Agency. INFN-LNF and ASI-CGS work as a synergetic Joint Lab on laser retroreflectors, satellite laser ranging, lunar laser ranging and their extension for Mars exploration and science.

Since 1969 Lunar Laser Ranging (LLR) to Apollo/Lunokhod laser retro-reflector (CCR) arrays supplied accurate tests of General Relativity (GR) and new gravitational physics: possible changes of the gravitational constant G and \dot{G} , weak and strong equivalence principle, gravitational self-energy (Parametrized Post Newtonian parameter β), geodetic precession, inverse-square force-law; it also constrains gravitomagnetism [1][2][3]. LLR has also provided significant information on the composition of the deep interior of the Moon. In fact, LLR first provided evidence of the existence of a fluid component of the deep lunar interior, confirmed also by lunar seismometry data [1]. Therefore, Apollo/Lunokhod CCRs form a Lunar Geophysical Network (LGN) for lunar science, exploration and test of GR.

For the Moon, in collaboration with D. Currie at the Univ. of Maryland (MD, USA), we have developed a next-generation CCR payload. In 1969 CCR arrays contributed a negligible fraction of the LLR error budget. Since laser station range accuracy improved by more than a factor 100, now, because of lunar librations, the Apollo/Lunokhod CCR payloads dominate the error due to their multi-CCR geometry. We developed a next-generation, single, large CCR, MoonLIGHT (Moon Laser Instrumentation for General relativity high-accuracy test) unaffected by librations that supports an improvement up to a factor 100 of the space segment of the LLR accuracy.

Activity for Mars (subject of the presentation):

Here we describe next-generation, optimized laser retroreflectors for imminent deployment on Mars. By deploying CCRs on the Mars surface, we can build a Mars Geophysical Network (MGN), which can be an analogous to the LGN, in order to get ready for future laser-equipped orbiters (like on the Mars Global Surveyor).

For Mars (but also for the Moon) we also developed INRRI (INstrument for landing-Roving laser Retro-reflector Investigations), a microreflector to be laser-ranged by orbiters. The performance of CCR payloads is characterized at the SCF_Lab (Satellite/Lunar laser ranging Characterization Facilities Lab at INFN-LNF [4]) in environmental conditions representative for their deployment at their respective destinations. They will be used to accurately position of landers, rovers, hoppers, orbiters, space stations, etc.

Following two ESA-ASI agreements, INRRI was first launched in 2016 with the ESA mission ExoMars (Exobiology on Mars) EDM (Entry, descent and landing Demonstration Module), deployed on the Schiaparelli lander [5] and it will be also deployed on the ExoMars 2020 mission.

Based on an agreement between NASA and ASI, another microreflector, LaRRI (Laser Retro-Reflector for InSight), was delivered to JPL (Jet Propulsion Laboratory) and integrated on NASA's InSight Mars Lander successfully launched to Mars on May 5, 2018 [6]. A fourth microreflector, LaRA (Laser Retro-reflector Array) will be delivered to JPL for deployment on the NASA Mars 2020 Rover.

INRRI, LaRRI and LaRA will form the basis of a passive, long-lived, maintenance free, positioning MGN for future Mars exploration and science, extending the space program which is being carried out with the LGN (and that will also continue in the future).

References:

- [1] Williams, J. G. et al., *Adv. Space Res.* 37(1), 67-71 (2006).
- [2] M. Martini, S. Dell'Agnello, in *Springer DOI 10.1007/978-3-319-20224-2_5*, R. Peron et al. (eds.) (2016).
- [3] D. Currie, S. Dell'Agnello, G. Delle Monache, B. Behr, J. Williams, *Nucl. Phys. B (Proc. Suppl.)* 243-244 (2013) 218-228.
- [4] S. Dell'Agnello et al., *Adv. Space Res.* 47, 822-842 (2011).
- [5] S. Dell'Agnello, et al., *J. Adv. in Space Res.*, 9 (2017) 645-655.
- [6] S. Dell'Agnello et al., *Space Research Today N. 200*, 25-32, December 2017.

SERVERLESS ON-DEMAND MARSIS IONOGRAM PROCESSING ON A PUBLIC CLOUD COMPUTING INFRASTRUCTURE

J.L. Vázquez-Poletti¹, I.M. Llorente¹, P.J. Pascual², M. Ramírez-Nicolás¹, S. Jiménez³, D. Usero¹, L. Vázquez¹

¹Universidad Complutense de Madrid (UCM), Spain;

²Universidad Autónoma de Madrid (UAM), Spain;

³Universidad Politécnica de Madrid (UAM), Spain;

jlvazquez@fdi.ucm.es

Keywords:

Mars, cloud computing, ionogram, serverless, optimization

Introduction:

Cloud computing [1] has been postulated as a powerful solution for fulfilling needs of dynamic, elastic and on-demand resources in many application areas, including Space Exploration. Many of these applications have different computational aspects that prevent the use of in-house solutions (such as supercomputers) due to budget restrictions or the inexistence of dedicated environments.

During the 8th Moscow Solar System Symposium an architecture for processing MARSIS (ESA Mars Express) data was introduced. This architecture, based on Amazon Elastic Compute Cloud (EC2), was presented along with an optimization model expressed by means of virtual machine type and number. This is because we have focused in public cloud infrastructures, which follow a “pay as you go” basis. Estimating an optimal computing setup based on the offerings of these providers increases the level of complexity [2,3].

In the present contribution we refactor this work using a totally different cloud execution model: serverless computing. Its architecture, based on Amazon Lambda [4], will be described and compared with the previous solution, showing clear improvements.

MARSIS data process.

The objective of the proposed architecture is to process data of the MARSIS radar instrument from the ESA Mars Express mission. This is accomplished in two steps: first, AIS datasets are converted into images and then, the magnetic field is calculated with an algorithm that reads them [5].

This process is to be performed every time a data file becomes available. The whole dataset used in this work corresponds to that retrieved by the instrument between 2008 and 2016. Its total size is 92GB.

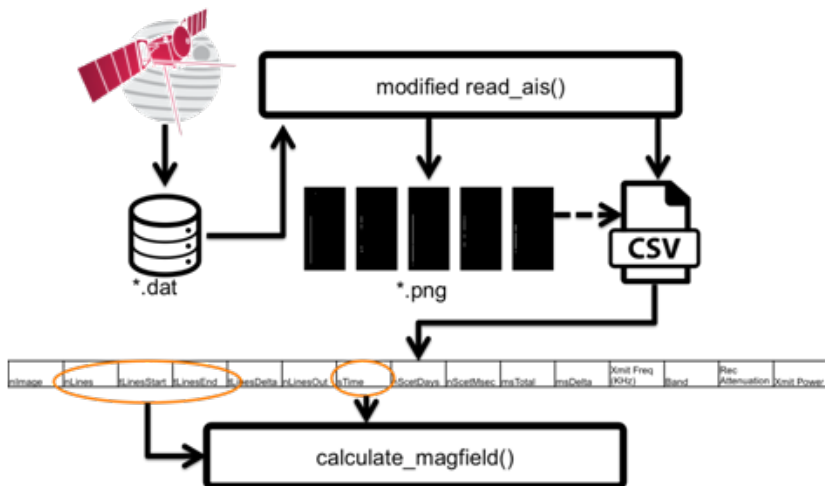


Fig. 1.

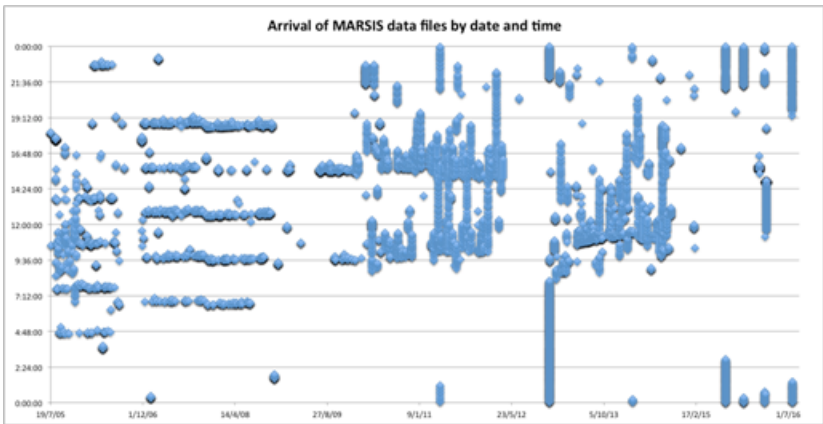


Fig. 2.

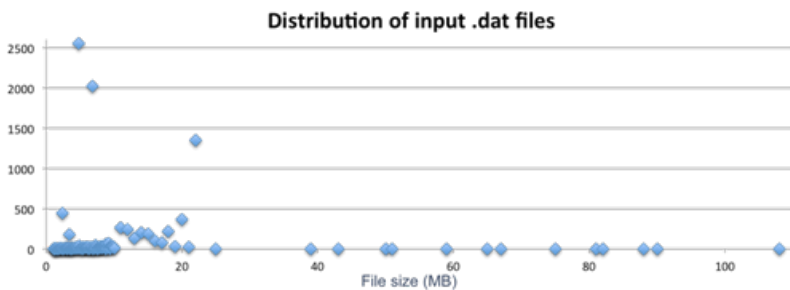


Fig. 3.

Serverless computing with AWS Lambda.

The new solution allows forgetting about the virtual machine aspect of the architecture, as code is directly uploaded and its execution is declared as a service (named “Lambda function” by Amazon Web Services). This service can be programmed using a variety of bindings. In our case, the MARSIS data processing code was produced using Node.js.

Lambda functions can be triggered on different events. In the present case, the event is the upload of data files on an AWS Simple Storage Service (S3) bucket. Output files are then deposited into another S3 bucket.

MARSIS data process on Lambda Vs. EC2.

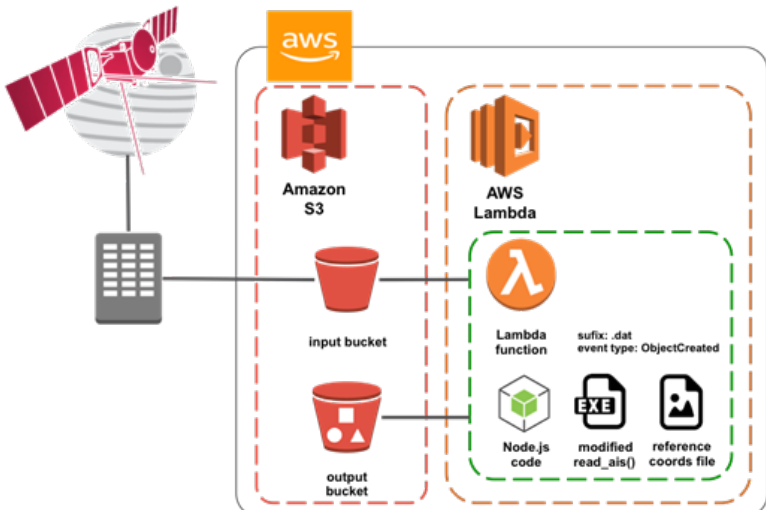


Fig. 4.

Despite its limitations (CPU, memory), Lambda proved to be a valid solution for the present scientific data stream use case.

For this reason, we performed a comparison between both architectures by means of execution time (processing delay) and cost. In the experiments the arrival of new data from the original dataset was simulated but execution times were taken from real processing.

Results showed a great improvement in both execution time and cost for the AWS Lambda based architecture. The MARSIS data process function is triggered only when needed with lower delays than in the EC2 architecture, as there is no need of starting up a virtual machine. Considering storage, eliminating the need of Elastic Block Store (EBS) volumes from EC2 and relying only on S3 buckets, resulted in a dramatic cost reduction.

Acknowledgments:

Authors would like to thank the support of the Ministerio de Economía y Competitividad (Spain) under the project TIN2015-65469-P.

References:

- [1] Peter M. Mell, Timothy Grance, The NIST Definition of Cloud Computing // Technical Report SP 800-145, NIST, 2011.
- [2] J.L. Vazquez-Poletti, M.P. Velasco, S. Jimenez, D. Usero, I.M. Llorente, L. Vazquez, O. Korablev, D. Belyaev, M.V. Patsaeva, I.V. Khatuntsev, Public “cloud” provisioning for Venus Express VMC image processing // Communication on Applied Mathematics and Computation, 2019, in press.
- [3] J.L. Vazquez-Poletti, S. Santos-Muñoz, I.M. Llorente, F. Valero, A Cloud for Clouds: Weather Research and Forecasting on a Public // Cloud Infrastructure, Cloud Computing and Services Sciences, Volume 512, 2015, Pages 3-11.
- [4] Amazon Web Services Lambda. <https://aws.amazon.com/es/lambda/>.
- [5] M. Ramírez-Nicolás, B. Sánchez-Cano, O. Witasse, P.-L. Blelly, L. Vázquez, M. Lester, The effect of the induced magnetic field on the electron density vertical profile of the Mars’ ionosphere // A Mars Express MARSIS radar data analysis and interpretation, a case study, Planetary and Space Science, Volume 126, 2016, Pages 49-62.

FRACTIONAL MODELS TO SIMULATE THE MARTIAN ATMOSPHERIC DUST DYNAMICS

M.P. Velasco¹, D. Usero², S. Jiménez¹, J.L. Vázquez-Poletti², L. Vázquez²

¹Universidad Politécnica de Madrid, mp.velasco@upm.es, s.jimenez@upm.es;

²Universidad Complutense de Madrid, umdavid@mat.ucm.es, jl vazquez@fdi.ucm.es, lvazquez@fdi.ucm.es

Keywords:

Dust, Solar Radiation, Fractional Calculus, Mittag-Leffler functions, Fractional Ordinary and Partial Differential Equations, Cloud Computing.

Introduction:

The dust storms are very frequently seen features of Mars. They play an important role in governing the climate of Mars [1]-[2]. For instance, the global storms alter the planet's total heat balance, promote variations in seasonal frost formation and dissipation, and greatly affect the distribution of water vapour. One of the effects of the atmospheric dust is the solar radiation scattering. This is a complex phenomenon, which depends on many space and time scales associated to the concentration, distribution and size of the dust as well as the radiation wavelength.

In the study of this challenging dynamics, we have as basic references the Rayleigh scattering associated to the elastic scattering of light from atomic and molecular particles whose diameter is less than about one-tenth the wavelength of the incident light. Mie scattering refers primarily to the elastic scattering of light from atomic and molecular particles whose diameter is larger than about the wavelength of the incident light.

At the same time, the theory of radiative transfer establishes that the dust aerosols cause an attenuation of the solar radiation traversing the atmosphere. This attenuation is modeled by the Lambert-Beer-Bouguer law, where the aerosol optical thickness plays an important role and, through Angstrom law, the aerosol optical thickness can be approximated [3]. However, the classical model often does not fit to the reality since the propagation of the solar radiation in the atmosphere is more complex than a simple diffusive process associated to a Brownian motion. This dynamic is governed by different time/space scales and, thus, it is natural to think about integro-differential equations to describe a better modeling [4]-[6].

In this work, we continue the study started in [7]-[9] and, on the basis of the Angstrom exponent properties we present a panoramic view of possible fractional models to describe the above context where we have the competition of many space / time scales. We define both one and three dimensional wavelength-fractional diffusion equations to obtain a more accurate model of the attenuation of the solar radiation traversing the atmosphere:

- Classical diffusion model: $\frac{\partial \varphi}{\partial \lambda} = C \frac{\partial^2 \varphi}{\partial^2 x}$

whose second order moment is $\langle X^2 \rangle = 2ct$.

- 1-space dimensional fractional diffusion model $\frac{\partial^\alpha \varphi}{\partial^\alpha \lambda} = C \frac{\partial^2 \varphi}{\partial^2 x}$:

whose second order moment is $\langle X^2 \rangle = 2ct^\alpha$.

- 3-space dimensional fractional diffusion model:

$$\frac{\partial^\alpha \varphi}{\partial^\alpha \lambda} = C \left(C_1 \frac{\partial^2 \varphi}{\partial^2 x} + C_2 \frac{\partial^2 \varphi}{\partial^2 y} + C_3 \frac{\partial^2 \varphi}{\partial^2 z} \right).$$

With this fractional model, we obtain a generalization of the classical Angstrom law, through the second order moment of the fractional equation. Also, the fractional model provides information of higher order moments,

which is relevant to understand the atmospheric dynamic. We discuss some questions of the model: interpretation of variables, statement of initial and boundary conditions, analytic and numerical solutions in one and three space dimensions, and computational simulations vs observational data. Furthermore, our objective is to apply these models in the context of the development of the sensors of Universidad Carlos III de Madrid, and to deal possible experiments in the Planetary Atmosphere and Surface Chamber of the Astrobiology Center.

Acknowledgements:

The authors thank to the support of MINECO of Spain, through the projects ESP2016-79135-R, TIN2015-65469-P

References:

- [1] Cachorro V.E., de Frutos A.M., Casanova J.L. Determination of the Angstrom turbidity parameters // *Applied Optics*. 1987. V. 26. No. 15. P. 3069-3076.
- [2] Córdoba C., Vázquez L. Characterization of atmospheric aerosols by an in-situ photometric technique in planetary environments // In Bearman G.H., Beauchamp P.M. (eds.). *First Jet Propulsion Laboratory In Situ Instruments Workshop*. SPIE. 2003. V. 4878.
- [3] Angstrom A. On the atmospheric transmission of sun radiation and on dust in the air // *Geografiska Annaler*. 1929. V. 11. P. 156-166.
- [4] Diethelm K. *The analysis of fractional differential equations*. Springer, 2010.
- [5] Kilbas A.A., Srivastava H.M., Trujillo J.J. *Theory and Applications of Fractional Differential Equations*. Elsevier, 2006.
- [6] Zaslavsky G.M., Baleanu D., Tenreiro J.A. *Fractional Differentiation and its Applications*. Physica Scripta, 2009.
- [7] Velasco M.P., Usero D., Jiménez S., Aguirre C., Vázquez L. Mathematics and Mars Exploration // *Pure and Applied Geophysics*. 2015. V. 172. No. 1. P. 33-47.
- [8] Velasco M.P., Usero D., Jiménez S., Vázquez-Poletti J.L., Vázquez L. Modeling and simulation of the atmospheric dust dynamic: Fractional Calculus and Cloud Computing // *International Journal of Numerical Analysis and Modeling*. 2018. V. 15. No. 1-2. P. 74-85.
- [9] Velasco M.P., Usero D., Jiménez S., Vázquez-Poletti J.L., Vázquez L. Fractional diffusion models for the atmosphere of Mars // *Fractal and Fractional*. 2018. V. 2. No. 1.

THE NEW WAVE PLANETOLOGY SHOWN IN THE MARTIAN SATELLITES: SHRINKING PHOBOS AND SWELLING DEIMOS

G.G. Kochemasov

*IGEM of the Russian Academy of Sciences, 35 Staromonetny, 119017
Moscow, RF, kochem.36@mail.ru*

Keywords:

Phobos, Deimos, modulated structures, grooves, dust, craters, rocky blocks

As all cosmic bodies in Universe move in several periodic orbits of wave nature with very different orbiting frequencies they are affected by modulated waves. They appear as predicted by radio wave physics. The modulation is division and multiplication of the higher frequency by the lower one. As a result, along with main frequencies appear two side frequencies with corresponding them tectonic granules. Examples are on surfaces of Saturn, Jupiter (cloudy covers) Pluto, the Moon, Titan, Ceres, Churyumov-Gerasimenko comet core [2, 3]. Now we show the modulation effects on Phobos and Deimos.

On Phobos a series of crossing troughs and crater chains is well presented.



Fig.1. (up) Phobos. ESA/DLR/FU Berlin (G. Neukum). Radii 14 x 11 x 10 km



Fig.2. Deimos. PIA11826-Deimos.jpg. Radii 8 x 6 x 6 km.

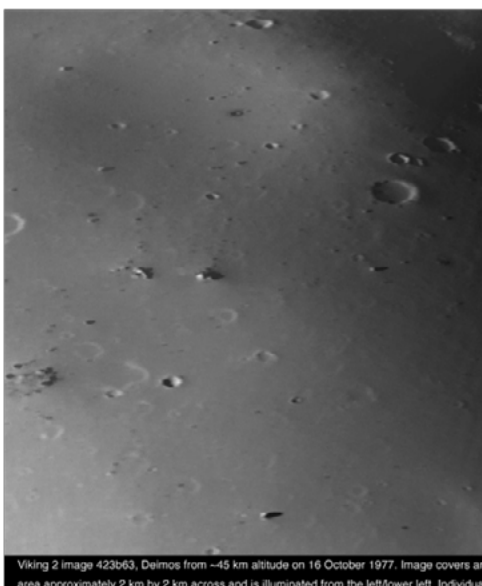


Fig. 3,

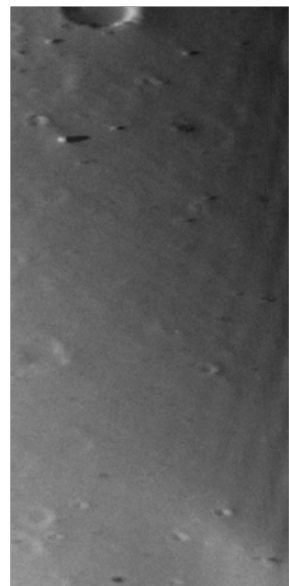


Fig. 4. an enlarged portion of Fig. 3

They cover the entire satellite surface by a kind of wavy cloak – a drying apple (Fig. 1). This shrinkage of the gaining speed falling on Mars satellite is due to necessity to keep the angular momentum [4]. Thus, the body's radius must diminish and the body shrinks and abundantly degases (numerous craters witness this). This occurs not chaotically but in form of regular crossing in four directions waves inscribed in a drying diminishing its surface sphere. Smallest wave forms concordant with the highest orbital frequency of the satellite (1/7.65 hours) still are not visible. However, modulated side waves and corresponding them forms (troughs and "craters «chains) are visible. $1/7.65 : 1/16488$ (circummartian frequency) gives the side frequency $1/2155$ and corresponding granule size 16.5 m (the scale is the Earth with the orbital frequency 1/1 year and the corresponding wave length $\pi R/2$ or the granule size $\pi R/4$). The smallest visible features (troughs and "craters") in Fig.1 are about 15 m. Along with them also are numerous wider troughs marking earlier more distant orbits of the satellite with the lower frequencies.

Two modulated frequencies of Deimos are interesting in that the corresponding them granules are: for the smallest (0.038 m), too fine and making smooth surface and, for the large (34.6 m), hardly visible as grids under the soft damping cover of fine dust material and blocks (Fig. 2, 3, 4). These grids are better visible along brinks of the image (Fig. 2-4). Presence of mainly two sizes of fragments (dust and blocks-bifurcation of sizes) also proves an action of two distinct modulated structuring frequencies. The dust cover is mainly discarded on shrinking Phobos and grows on Deimos. The first diminishes orbit radius, the second, in contrast, keeps it or slowly increases (different tendencies of angular momenta development).

Phobos diminishes the radius of its orbit eventually crossing the Roche limit for the "liquid" (actually porous dusty) cover and losing it. The squeezed folded peeled bedrock outcrops (Fig. 1). Deimos, on the contrary, far from the limit, keeps its dusty cover (Fig. 2).

References:

- [1] Duxbury T.C., Veverka J. Viking imaging of Phobos and Deimos: An overview of the primary mission // *J. Geophys. Res.*, 1977, v. 82, # 28, p. 4203-4211.
- [2] Kochemasov G.G. Wave modulation in the Solar system bodies and their radio emissions // *Geophya. Res. Abstr.*, v. 10, EGU2008A-01272, 2008. SRef-ID: 1607-7962/gra/EGU-2008-A-01272; EGU General Assembly 2008.
- [3] Kochemasov G.G. A wave modulation nature of the 3D structural lattice of the Churyumov-Gerasimenko comet icy core // 46th LPSC, 2015, Abstr. # 1088.
- [4] Kochemasov G.G. (2016) The Moon and Phobos: specific responses of two satellites moving off and nearer their respective planets // DPS 48/EPSC 11, Pasadena, Oct. 16-21, 2016, Bulletin of the American Astronomical Society, 2016, vol. 48, # 7, p. 175, Abstract 318.08, Session 318: Formation and Evolution of Planets and Satellites Posters.
- [5] Veverka J., Duxbury T.C. Viking observations of Phobos and Deimos: preliminary results // *J. Geophys. Res.*, 1977, v. 82, # 28, p. 4213-4223.

POTENTIAL OF NANOPARTICLE SELF-ASSEMBLED LAYER FOR OPTICAL INSTRUMENTS

S. Bermejo¹, M. Garin, M. Dominguez-Pumar, J. Pons, L. Castañer

¹Universitat Politècnica de Catalunya (UPC) Campus Nord, C/Jordi Girona 1-3, 08034, Barcelona, Spain, sandra.bermejo@upc.edu

Keywords:

Metamaterial, nanospheres, colloidal crystal, inverse opal, electro spray

Introduction:

The advent of optical metamaterials has empowered us with new and exciting ways to control and manipulate light [1]. Furthermore, it enables to engineer materials that exhibit unusual optical properties not found in nature such as, for instance, negative index of refraction [2]. However, optical metamaterials require a three-dimensional sculpting of the material at the nanoscale, which is still challenging nowadays. Top-down approaches based on standard microelectronic techniques [3] can be complex, slow and expensive. On the other hand, bottom-up approaches, such as self-assembly of nanospheres [4], are simpler, faster and inexpensive, although the crystal quality might be inferior. In this work we present the electro-spray technique as a suitable technique to fabricate high-quality large-scale (up to 50 cm²) colloidal nanostructures with good optical behavior and that can be produced in just minutes with a largely simplified set-up [5-7]. Changing the deposition conditions, different metamaterials can be fabricated: from scattered monolayers of polystyrene nanospheres to self-assembled three dimensional ordered nanolayers forming colloidal crystals (opals) that can also be turned into inverse opals. All these structures exhibit interesting structural and optical properties that can be applied to a broad range of applications. Some of them benefit from the high surface-to-volume ratio of the nanostructure fostering, for instance, a new generation of ultrafast bulk battery electrodes [8], scaffolds of macroporous materials [9]. Other applications benefit from the good 3D nanostructuring making, them suitable for photonic applications in the visible or terahertz [10] range. All this feasibility will position these metamaterials as potential devices for space applications as the instruments needed to find out if there has been past life or to support human life in manned missions will surely need systems in these wavelength bands.

Experimental:

The electro spray set-up consists on an infusion pump from B. Braun SA., an OMNI-FIX 5ml syringe, a Hamilton needle (600 μm outer and 130 μm inner diameter), an Ultravolt high voltage bipolar source. The deposition area is placed inside a glove box with a controlled N₂ atmosphere. Figure 2 shows schematically the experimental set-up. The formation of the ordered nanostructures is based in the so-called self-assembly process. There is a dielectrophoretic force (DEP force) that is originated by the electric field created by the electro spray gun and by the distortion of the field created by the effective dipole of each nanoparticle. The directional nature of DEP in the wet phase chain nanoparticles aligned with the main electric field direction and is responsible for the final ordered configuration [11].

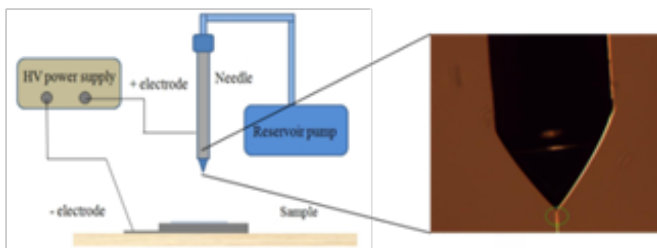


Fig. 1. Schematic view of the experimental set-up and a zoom of the tip of the needle with a Taylor cone and a jet of 4 μm .

Applying the suitable conditions (e.g. 10KV of potential difference, 2.2 ml/h of pumping rate and an off-the-shelf distilled water dissolution with the dielectric nanospheres) perfectly arranged 3D structures are met. Surface and

in-depth SEM observations have been performed. Figure 2 a) a view of the surface milled at two angles: normally to the top surface (shown at the left and bottom of Figure 2(a)) and at an angle of 54.7° between the normal of the surface and the FIB axis (shown at the right in Figure 2(a)). A closer view of the orthogonal corner is shown in Figure 2(b) where the (100) order of the top surface and of the two orthogonal planes etched by the FIB can be seen.

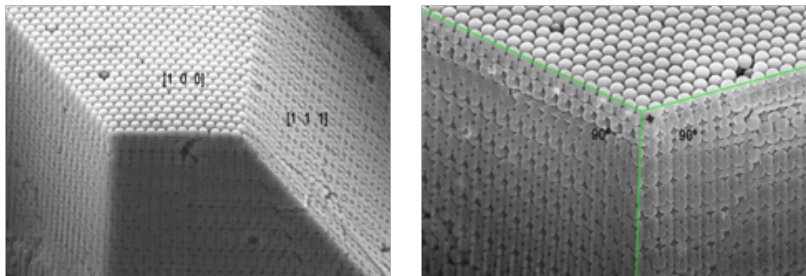


Fig. 2: SEM pictures of 360-nm-diameter polystyrene nanosphere layers. (a) Cut surface showing [1 0 0] and [1 1 1] ordered facets, (b) close view of the perpendicular cut.

Figure 2 shows a perfect opal, but the technology also allows to develop inverse opals. Inverse opals have specific optical properties giving freedom to more precisely tune the reflected peak. Inverse opals can be created using colloidal crystals as templates to build close packed assemblies of air spheres. Our technology is pioneer in using $\text{Al}_2\text{O}_3 / \text{TiO}_2$ as structural layer infiltrated through the voids. This is a two steps atomic layer deposition (ALD) process in which the polymeric template is eliminated after the deposition of the alumina layer and before the ALD deposition of the titania layer. Figure 3 shows SEM pictures of the resulting inverse opals.

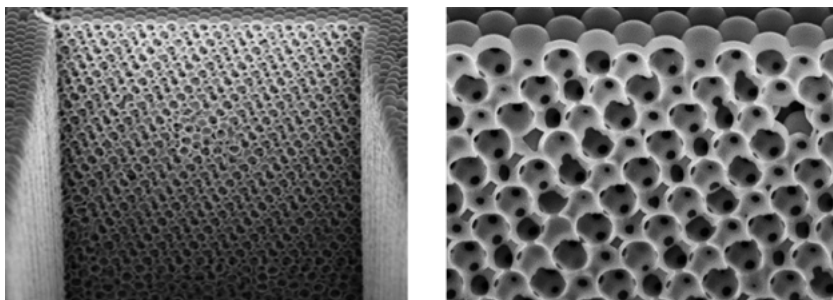


Fig. 3: a) SEM images of an $\text{Al}_2\text{O}_3 / \text{TiO}_2$ inverse opal, b) close view.

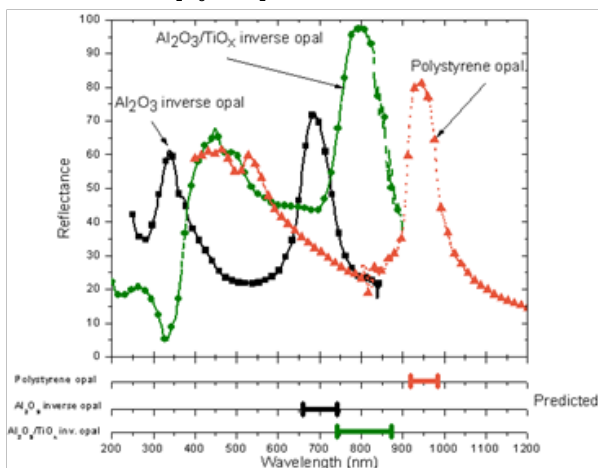


Fig. 4. Reflectance measurements of a colloidal crystal (red) an Al_2O_3 inverse opal (black) and an $\text{Al}_2\text{O}_3 / \text{TiO}_2$ inverse opal (green). The measurements exhibit high reflection bands closely centered with expected bands due to simulation (in the lower part of the figure).

Optical measurements were performed using a spectrophotometer equipped with an integrating sphere. Figure 4 shows reflectance values as a function of the wavelength at three different stages: (i) colloidal crystal, (ii) after depositing the alumina layer and burning the nanospheres and (iii) after deposition of the titania layer onto the alumina carcass. Looking to the plot corresponding to the colloidal crystal measurement, a broad peak of 81% reflectance located around 940 nm can be seen. The peak is blue-shifted and varies its magnitude due to the formation of the inverse opal, allowing this optical tunability of the device. The value of the center wavelengths of the reflection peaks is consistent with the predicted theoretical calculations.

References:

- [1] Joannopoulos J.D., Villeneuve P.R., Fan S. Photonic crystals: putting a new twist on light // *Nature*. 1997. V. 386. P. 143-149.
- [2] Smith D.R., Pendry J.B., Wiltshire, M.C.K. Metamaterials and negative refractive index // *Science*. 2004. V. 305. P. 788-792.
- [3] Noda S., Tomoda K., Yamamoto N., Chutinan A. Full three-dimensional photonic bandgap crystals at near-infrared wavelengths // *Science*. 2000. V. 289. P. 604-606.
- [4] Blanco A. et al. Large-scale synthesis of a silicon photonic crystal with a complete three-dimensional bandgap near 1.5 micrometres // *Nature*. 2000. V. 405. P. 437-440.
- [5] Coll A., Bermejo S., Hernández D., Castañer L. Colloidal crystals by electro spraying polystyrene nanofluids // *Nanoscale Research Letters*. 2013. P. 1-8.
- [6] Coll A., Bermejo S., Hernández D., Castañer L. Al₂O₃/TiO₂ inverse opals from electro sprayed self-assembled templates // *Beilstein J. Nanotechnol.* 2018 V. 9. P. 216–223.
- [7] Véliz B., Bermejo S., Vives J., Castañer L. Large area deposition of ordered nanoparticle layers by electro spray // *Colloid and Interface Science Communications*. 2018. V. 25 P. 16–21
- [8] Zhang H. G., Yu X. D., Braun P. V. Three-dimensional bicontinuous ultrafast-charge and -discharge bulk battery electrodes // *Nature Nanotech.* 2011. V. 6. P. 277-281.
- [9] Velev O. D., Jede T. A., Lobo R. F., Lenhoff A. M. Porous silica via colloidal crystallization // *Nature*. 1997. V. 389. P. 447-448.
- [10] Hubert H. W. Terahertz technology: Towards THz integrated photonics // *Nature Photon.* 2010. V. 4. P. 503-504.
- [11] Castañer L., Bermejo S., Dominguez-Pumar M. Effect of dielectrophoretic force in the self-assembly process of electro sprayed nanoparticles // *Journal of Electrostatics*. 2017. V. 87. P. 257-262.

VIABILITY OF DESERT SOIL MICROBIAL COMMUNITY AFTER IRRADIATION WITH ACCELERATED ELECTRONS UNDER SIMULATED EXTRATERRESTRIAL CONDITIONS

V. S. Cheptsov^{1,2}, E. A. Vorobyova^{1,2}, A. A. Belov¹, A. K. Pavlov³,
D. Tsurkov³, V. N. Lomasov⁴

¹Lomonosov Moscow State University, GSP-1, Leninskie Gory 1-12, Moscow, 119991, Russia;

²Space Research Institute of Russian Academy of Sciences, 84/32 Profsoyuznaya Str, Moscow, 117997, Russia;

³Ioffe Physical-Technical Institute of the Russian Academy of Sciences, Polytechnicheskaya street, 26, Saint-Petersburg, 194021, Russia,

⁴Saint-Petersburg State Polytechnical University, Polytechnicheskaya street, 29, Saint-Petersburg, 195251, Russia.

cheptcov.vladimir@gmail.com

Keywords:

Astrobiology, Mars, accelerated electrons, microbial communities, soil, radioresistance, Martian conditions.

Introduction:

The survivability of microorganisms under impact of extraterrestrial factors is one of the priority issues of modern astrobiological studies. Much attention is paid to ionizing radiation being considered as one of the main factors that can prevent the preservation and spread of life outside the Earth. It has been proved that the conditions under which irradiation occurs (temperature, pressure, etc.) substantially correct radiation effects. Therefore, in order to correctly assess the radioresistance of terrestrial microorganisms in the extraterrestrial regolith or other habitat, the closest possible reproduction of the relevant physicochemical factors is necessary, while preserving the natural environmental model, to which microbial communities are adapted. The aim of this research was to study the effect of accelerated electrons as a component of cosmic radiation at high doses of 10 kGy and 100 kGy on microbial community in its natural habitat – arid soil, as well as on pure bacterial cultures that were isolated from this biotope. Irradiation was carried out under low pressure (~0.01 Torr) and low temperature (-130 °C) conditions, to simulate Martian and outer space environments.

Materials and Methods:

An arid soil sample (SN2) from the Negev desert as well as pure cultures of bacteria *Arthrobacter polychromogenes* SN_T61 and *Kocuria rosea* SN_T60 were used for the study. Pure bacterial cultures were immobilized on montmorillonite for irradiation.

The samples were irradiated with accelerated electrons (~1MeV) under ~1 Torr pressure and -130°C temperature. For the extraterrestrial conditions simulation an original climatic chamber was used [1]. The samples were irradiated with 10 kGy and 100 kGy doses at 0.28 kGy/s and 2.8 kGy/s radiation intensity, respectively. Some samples were exposed only to temperature and pressure without any irradiation. After irradiation the samples were stored at -18°C.

Determination of the number of culturable heterotrophic bacteria in the samples was carried out by plating on glucose-peptone-yeast (GPY) agar. The total numbers of prokaryotic cells in the samples were determined using epifluorescence microscopy (EFM) with acridine orange dye. Potential metabolic activity and the functional diversity of microbial communities have been investigated by the multisubstrate testing method. Pure bacterial cultures isolated from arid soil and permafrost samples were identified by sequencing of the 16S rRNA genes. The physiological properties of the isolated strains were studied by inoculation into 96-well immunoassay plates with liquid GPY medium supple-

mented with triphenyltetrazolium chloride as an indicator of metabolic activity. Phosphate (pH 2–6) and carbonate (pH 7–12) buffer systems were used to determine the range of pH values that are suitable for growth. Resistance to salts presence was analyzed using liquid GPY nutrient media with the addition of NaCl, KCl, $MgSO_4$, or $NaHCO_3$ at concentrations of 2, 5, 10, 15, or 20%. The temperature limits of growth were determined by incubating cultures in liquid GPY nutrient media at temperatures of +2, +4, +10, +25, +37, +45, or +50 °C.

Results and Discussion:

Exposure to low temperature and low pressure did not affect the number of colony forming units (CFU) and the total number of prokaryotes in the soil sample. Irradiation with accelerated electrons led to a decrease in the CFU number in the arid soil by a one order of magnitude. The total number of prokaryotic cells (EFM) in desert soil decreased 1.5 and 20 times after irradiation with doses of 10 kGy and 100 kGy, respectively. Irradiation with even a minimal dose (10 kGy) led to a sharp suppression of the potential metabolic activity: microbial communities of all the irradiated samples consumed only one substrate – peptone.

Representatives of the genera *Arthrobacter*, *Bacillus*, *Cryobacterium*, *Microbacterium*, *Micrococcus*, *Phenyllobacterium*, *Saccharothrix*, *Sphingoaureticus*, and *Streptomyces* were found in the sample exposed at low pressure and temperature without irradiation. After irradiation with 10 kGy, bacteria belonging to the genera *Arthrobacter*, *Massilia*, *Micrococcus*, *Planomicrobium*, *Rufibacter*, and *Spirosoma* were cultured from the same arid soil, and after irradiation with a dose of 100 kGy the genera *Arthrobacter*, *Microvirga*, *Pontibacter*, *Rufibacter*, and *Spirosoma* were revealed. Most of the isolated strains showed facultative-psychrophilic (psychotropic) properties, that is, they could grow in the temperature range extended to the low-temperature. This can be both a manifestation of adaptation to storage and exposure of samples at low temperatures, and the increased resistance of psychrophiles to oxidative stress, and, consequently, to radiation. According to the data on resistance to pH, neutrophiles with wide pH-ranges of growth (4–12), alkalophiles (8–12), and acid-tolerant alkalophiles (4–8, 5–9) were found among isolates. The variety of pH-ranges of growth probably reflects the heterogeneity of the soil environment. However, it is noteworthy that most of the isolated strains are resistant to the acidity of the medium and grow in a wide pH range. Some strains were sensitive to the presence of salts in the medium, others were halotolerant and grew with a content of up to 20% NaCl or $MgSO_4$ and up to 15% KCl in the medium. Bacterial strains practically did not grow on media containing $NaHCO_3$, even in small concentrations. Correlations between resistance to the studied physical and chemical factors (T, pH, salts) and radioresistance were not observed.

Low temperature and low-pressure conditions had practically no impact on the number of CFU of *A. polychromogenes* SN_T61 and *K. rosea* SN_T60. After irradiation with a dose of 10 kGy, the number of CFUs of *A. polychromogenes* SN_T61 and *K. rosea* SN_T60 decreased by three and four orders of magnitude, respectively. After irradiation with a dose of 100 kGy, no cultured cells were detected. Pure cultures showed significantly less resistance to radiation than microbial communities *in situ*. Such a result can be caused by features of a heterogeneous soil environment, as well as by interactions of microorganisms within the community.

Conclusion:

It is shown that irradiation with electrons with 100 kGy dose in the model conditions of Mars and open space did not sterilize the samples of arid soils. Considering the radiation intensity on the different space bodies [2-5], the data obtained suggest that viable microorganisms can be viably cryopreserved for at least 1.3 and 20 million years in the Mars regolith in the shallow surface layer and at 5 m depth, respectively; for at least ~170 years in the ice of Europa at 10 cm depth; for at least 400 thousand years in the open space inside the meteorites. We found that bacteria have a much higher radioresistance as a part of microbial communities *in situ* in the natural habitat when compared to their stability in pure culture. Due to the protective function of the

natural environment and possibly due to the intra- and interpopulation interactions of organisms, even radiosensitive microorganisms being part of natural microbial communities are able to withstand the effects of high doses of ionizing radiation.

Acknowledgements:

This work was supported by RSF grant No. 17-12-01184 and by RFBR grant No. 18-34-00331 (in part of physiological characteristic of bacterial isolates).

References:

- [1] Cheptsov V., Vorobyova E., Belov A. et al. Survivability of soil and permafrost microbial communities after Irradiation with accelerated electrons under simulated Martian and open space conditions // *Geosciences*. 2018. V. 8. No. 8. P. 298.
- [2] Baumstark-Khan C., Facius R. Life under conditions of ionizing radiation // In: Horneck G., Baumstark-Khan C. (eds.) *Astrobiology: The Quest for the Conditions of Life*. Springer, Berlin, Germany, 2002. P. 261–284.
- [3] Dartnell L.R., Desorgher L., Ward J.M., Coates A.J. Martian sub-surface ionising radiation: Biosignatures and geology // *Biogeosciences Discussion*. 2007. V. 4. P. 455–492.
- [4] Hassler D.M., Zeitlin C., Wimmer-Schweingruber R.F. et al. Mars' surface radiation environment measured with the Mars Science Laboratory's Curiosity rover // *Science*. 2014. V. 343. P. 1244797.
- [5] Horneck G., Mileikowsky C., Melosh H.J. et al. Viable transfer of microorganisms in the solar system and beyond // In: Horneck G., Baumstark-Khan C. (eds.) *Astrobiology: The Quest for the Conditions of Life*. Springer, Berlin, Germany, 2002. P. 57–76.

HALOTOLERANCE OF BACTERIA FROM EXTREME ECOSYSTEMS: IMPLICATIONS FOR ASTROBIOLOGY

A.A. Belov¹, V.S. Cheptsov^{1,2}, E.A. Vorobyova^{1,2}

¹Lomonosov Moscow State University, Soil Science Faculty, Moscow, GSP-1, Leninskie Gory 1/12, 119991, Russia, a.a.belov@ecostudy.org;

²Space Research Institute, Russian Academy of Sciences, Moscow, 84/32 Profsoyuznaya str., 117997, Russia

Keywords:

Bacteria, stress-tolerance, Mars, astrobiology, halotolerance, perchlorate

Introduction:

Defining of living organisms' stress-tolerance and life limits is one of the most important current astrobiological tasks. Laboratory modeling of extraterrestrial conditions and investigation of their impact on living cells is a common approach in astrobiological studies. Different xero-arid and cryo-arid ecosystems and organisms inhabiting it are frequently used in astrobiological experiments as a model objects. They are considered like terrestrial analogues of putative ecosystems of some planets and satellites in the Solar System due to similarity of some physicochemical properties characteristic for the ecotopes [1,2].

It has long been known [3] and confirmed by subsequent research [4,5] that Martian regolith contains different water-soluble salts, in particular, chlorides, sulfates and perchlorates. At the same time, it is necessary to consider that microbial cells are inhabit in micro volumes and, therefore, in heterophase systems such as soil and regolith they exists in conditions of high water-soluble compound concentrations due to cell adhesion on the solid particle surfaces [6], where, in its turn, all soluble molecules are concentrate because of colloid interactions [7]. Consequently, one of the important factors, which should determine potential viability of microbial cells in extraterrestrial regolith conditions, is the presence of different water-soluble salts.

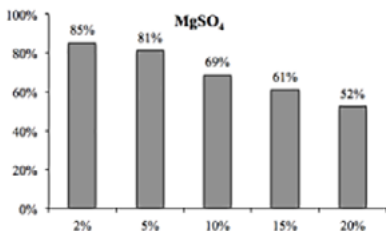


Fig. 1. Magnesium sulfate resistance diagram

in concentrations gradient was conducted. As mentioned above, sulfates and perchlorates were found in Martian regolith [8], sodium and potassium chlorides are frequently found in terrestrial soils [1]; soda is a high toxic compound for the most bacteria and other organisms [9,10].

To study the bacteria tolerance to salt the strains were cultured in 96-well microplates on the same media on which they were isolated but with addition of 2, 5, 10, 15, or 20% of NaCl, KCl, NaHCO₃, or MgSO₄, or 0.5, 1, 2, 5, 10, or 15% of Mg(ClO₄)₂. Triphenyltetrazolium chloride (TTC) was added to the media as a marker of metabolic activity. The culturing was performed for 14 days. Metabolic activity was estimated by means of visually detectable dyeing [11].

Minimal inhibitory effect of magnesium sulfate (Fig.1) and potassium chloride (Fig.2a) on examined strains was detected – more than half of strains were able to proliferate on nutrient media with addition of 20% of MgSO₄. Probably, it is related with cations' and/or anions' assimilation as an elements of mineral nutrition.

In this study we have analyzed 731 aerobic heterotrophic bacteria strains of Astrobiological collection of the National Depository Bank of Living Systems "Noah's Ark" (*depo.msu.ru*), which were isolated from different xerophytic habitats. The strains were isolated on non-saline media. Analysis of ability to reproduce *in vitro* in presence of different water-soluble salts (NaCl, KCl, NaHCO₃, MgSO₄, and Mg(ClO₄)₂)

Addition of potassium chloride to the nutrient media had less inhibitory action compared to sodium chloride (Fig.2b). Predominantly moderate halotolerant properties of examined bacteria were revealed.

Significant inhibitory effect on bacterial growth was detected on media containing 5% of magnesium perchlorate (Fig. 3a) and already all strains were inhibited on the media containing 10% of this salt. But perchlorate in concentrations close to the ones found in Martian regolith [8] had inhibitory effect only for small part of bacterial strains isolated from extreme habitats.

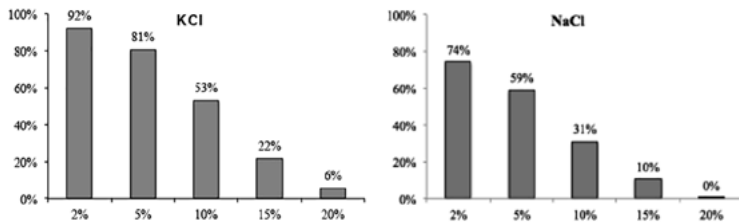


Fig.2. Potassium chloride (a) and sodium chloride (b) resistance diagrams

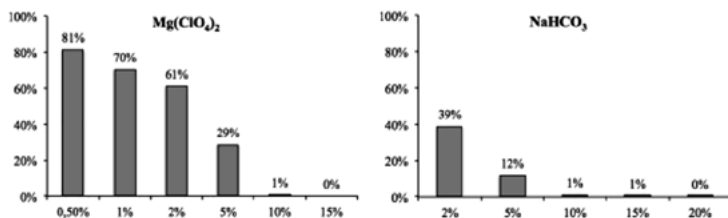


Fig.3. Magnesium perchlorate (a) and sodium hydrocarbonate (b) resistance diagrams

Main point for understanding of limiting or non-limiting perchlorate role for bacteria functioning apparently is the degree of soil or regolith saturation by water. This process determines the perchlorate concentration in the solution contacting with cells – the less sample saturated by water the higher concentrated perchlorate solution (up to maximum solubility) is in contact with bacterial cells. Study on viability of bacterial communities in perchlorate containing soils under different saturation with water is planned in future research.

Maximal inhibition of bacteria was observed on media with addition of low soda (Fig. 2b) concentrations (2%), which is due to Na⁺-ions cytotoxicity and cell-membrane permeability increasing in alkaline conditions [10]. Nevertheless, a few strains, which were able to growth in 15% soda containing media, were found.

The study performed testify that the most of bacteria of extreme habitats are well adapted to salt stress and are able to withstand the effects of various salts in high concentrations. Combined with data on bacteria resistance to the impact of a number of other extreme factors, the data obtained support the possibility of survival of Earth-like bacteria in an extraterrestrial environment. At the same time it should be noted that assessment of habitability of any space body should include study on microorganisms' survivability under synergetic impact of the complex of physicochemical factors characteristic for the target space object.

Acknowledgments

The reported study was funded by RFBR according to the research project № 18-34-00331.

References:

- [1] Dion P. Microbiology of extreme soils. – 2008.
- [2] Makhalanyane T. P. et al. Microbial ecology of hot desert edaphic systems //FEMS mi-crobiology reviews. – 2015. – V. 39. – №. 2. – pp. 203-221
- [3] Clark B. C., Van Hart D. C. The salts of Mars //Icarus. – 1981. – V. 45. – №. 2. – pp. 370-378.

- [4] Chevrier V. F., Hanley J., Altheide T. S. Stability of perchlorate hydrates and their liquid solutions at the Phoenix landing site, Mars //Geophysical Research Letters. – 2009. – V. 36. – №. 10
- [5] Fox A. C. et al. The Effect of Gamma Radiation on Mars Mineral Matrices: Implications for Perchlorate Formation on Mars //AGU Fall Meeting Abstracts. – 2017
- [6] Zvyagintsev D. G. Interaction between microorganisms and solid surface – Moscow State University, 1973 (Book in Russian)
- [7] Shein E.V. et al., Soil physics course – Moscow State University, 2005 (Book in Russian)
- [8] Navarro-González R. et al. Reanalysis of the Viking results suggests perchlorate and organics at midlatitudes on Mars //Journal of Geophysical Research: Planets. – 2010. – V. 115. – №. E12.
- [9] Sorokin I. D. et al. *Bacillus alkalidiazotrophicus* sp. nov., a diazotrophic, low salt-tolerant alkaliphile isolated from Mongolian soda soil //International journal of systematic and evolutionary microbiology. – 2008. – V. 58. – №. 10. – pp. 2459-2464.
- [10] Padan E. et al. Alkaline pH homeostasis in bacteria: new insights // Biochimica et bio-physica acta (BBA)-biomembranes. – 2005. – V. 1717. – №. 2. – pp. 67-88
- [11] Paul E. A. Soil microbiology, ecology and biochemistry. – Academic press, 2014.

THE INFLUENCE OF HIGH ENERGY ELECTRONS (HEE) ON FUNGAL COMMUNITY FROM DESERT SOIL

M.O. Kriuchkova¹, A.E. Ivanova², E.A. Vorobyova^{1,2}, V.S. Cheptsov^{1,2},
A.K. Pavlov³, V.N. Lomasov⁴

¹Lomonosov Moscow State University, GSP-1, Leninskie Gory 1-12,
Moscow, 119991, Russia;

²Space Research Institute of Russian Academy of Sciences, 84/32
Profsoyuznaya Str, Moscow, 117997, Russia;

³Ioffe Physical-Technical Institute of the Russian Academy of Sciences,
Polytechnicheskaya street, 26, Saint-Petersburg, 194021, Russia,

⁴Saint-Petersburg State Polytechnical University, Polytechnicheskaya
street, 29, Saint-Petersburg, 195251, Russia,
margo_kruchkova@mail.ru

Keywords:

Astrobiology, HEE, fungi, fungal communities, desert soils, high doses, Martian conditions.

Introduction:

An useful approach in astrobiology is modeling extraterrestrial environments using extreme habitats of the Earth as the objects of investigation.

The impact of high energy electrons (HEE) is one of the factors that can limit existence of biological life on Mars. In this research we have studied the impact of simulated Martian conditions, viz. HEE radiation with low temperature and pressure, on the structure of culturable microfungi communities and fungal biomass in desert soil.

Materials and Methods:

The samples from the upper humic horizon of Aridic Calcisol soil (Negev desert, Israel) were the objects of research.

Samples were irradiated by high-energy electrons (HEE) in the climatic chamber allowing to maintaining pressure of $8-9 \times 10^{-3}$ Torr and temperature of -130°C during the whole time of irradiation. Radiation intensity was 2,8 kGy/s. The samples were irradiated with 0,05 MGy; 1 MGy; 2 MGy total doses. Some samples were affected only by temperature and pressure without any irradiation. Before irradiation the samples were activated by wetting and incubating during 10 days at temperature 28°C , and then they were dried to air-dry state. After irradiation the samples were stored at -18°C .

For culturing of fungi solid Czapek medium [3] and alkaline agar [1] were inoculated with soil suspensions which were warmed before the inoculation (52°C , 2 min) [2]. The fungi were cultivated at temperature 5°C , 25°C , 37°C . The amount of fungal biomass *in situ* and its morphological structure were evaluated by direct fluorescent microscopy with calcofluor white dye [3].

Results and Discussion:

The average number of fungal propagules in control sample was $1-5 \times 10^4$ colony forming units (CFU) per gram of soil. Low temperature and low pressure had no significant effect on CFU numbers. However, after the irradiation with doses 0,05 MGy and 1 MGy CFU numbers increased fivefold ($11-20 \times 10^4$), and after the irradiation with 2 MGr dose the number of culturable fungi increased to 7×10^4 CFUs per gram.

The changes in the numbers of species isolated from the soil had an opposite relation to the dose of irradiation. The highest diversity, 35 species, was observed in control samples. The influence of low temperature and pressure resulted in reduction of up to 25 species. After the irradiation with doses 0,05 MGy and 1 MGy the quantity of species isolated were almost the same (11-13). The impact of the irradiation with 2 MGr dose led to decreasing of the fungal isolates numbers up to 20 species, i.e the biodiversity was higher than that one after more lower doses.

The structure of soil fungal communities also changed after the exposure. Some species that were quite rare in control samples became dominants in irradiated samples (*Penicillium*, *Aspergillus*, *Trichoderma*), the number of yeasts increased significantly.

There was a negative correlation between fungal biomass content in soil samples and doses of irradiation.

Conclusion:

It was shown that fungal communities from desert soil could survive after the influence of high doses of irradiation with HEE under low temperature and low pressure conditions. The irradiation led to increasing of CFUs and decreasing of biodiversity at the same time. The obtained results testify to the possibility of prolonged survival of eukaryotic natural communities in conditions of Mars regolith, and also in the space environment inside of small bodies.

Acknowledgements:

This work was supported by RSF grant No. 17-12-01184 and by RSF grant No. 14-50-00029 (in part of culturing and identification of fungi).

References:

- [1] Bilanenko E.N., Georgieva M.L. Micromycetes of saline in South Siberia (Kulunda steppe) // Mycology and Phytopathology. 2005. P.39, № 4, pp. 6-13.
- [2] Kochkina G.A., Ivanushkina N.E., Karasev S.G. et al. The survival of micromycetes and actinobacteria under conditions of long natural crioconservation // Microbiology. 2001. P.70, № 3, pp. 412-420.
- [3] The methods of soil microbiology and biochemistry.: Schoolbook/ Edited by D.G. Zvyagintsev. M.: MSU, 1991. 304 p.

SUBGLACIAL ANTARCTIC LAKE VOSTOK VS. SUBGLACIAL SOUTH POLE MARTIAN LAKE AND HYPERSALINE CANADIAN ARCTIC LAKES – PROSPECTS FOR LIFE

S. Bulat

NRC 'Kurchatov Institute' - Petersburg Nuclear Physics Institute,
St. Petersburg-Gatchina, Russia, bulat@omrb.pnpi.spb.ru

Keywords:

Antarctica, subglacial Lake Vostok, Mars, subglacial South Pole ice cap lake, subglacial hypersaline Canadian lakes, Lake Vostok unsealing, frozen water, life, extremophiles, bacteria, 16S rRNA genes, astrobiology

Introduction:

The objective was to search for microbial life in the subglacial freshwater Antarctic Lake Vostok by analyzing the uppermost water layer entered the borehole following successful lake unsealing at the depth 3769m from the surface. The samples included the drillbit frozen and re-cored borehole-frozen water ice. The study aimed to explore the Earth's subglacial Antarctic lake and use the results to prospect the life potential in recently discovered subglacial very likely hypersaline South Pole ice cap Martian lake (liquid water reservoir) [1] as well as similar subglacial hypersaline lakes (reservoirs) in Canadian Arctic [2].

The Lake Vostok is a giant (270 x 70 km, 15800 km² area), deep (up to 1.3km) freshwater liquid body buried in a graben beneath 4-km thick East Antarctic Ice Sheet with the temperature near ice melting point (around -2.5°C) under 400 bar pressure. It is extremely oligotrophic and poor in major chemical ions contents (comparable with surface snow), under the high dissolved oxygen tension (in the range of 320 – 1300 mg/L), with no light and sealed from the surface biota about 15 Ma ago [3].

The water frozen samples studied showed very dilute cell concentrations - from 167 to 38 cells per ml. The 16S rRNA gene sequencing came up with total 53 bacterial phylotypes. Of them, only three phylotypes passed all contamination criteria. Two phylotypes were reported before [4] - hitherto-unknown and phylogenetically unclassified phylotype w123-10 likely belonging to *Parcubacteria* Candidatus *Adlerbacteria* and 3429v3-4 showing below-genus level (93.5%) similarity with *Herminiimonas glaciei* of *Oxalobacteraceae* (*Beta-Proteobacteria*) – water-inhabited ultramicrobacterium isolated from a deep Greenland ice core. The new third finding (the phylotype 3698v46-27) proved to be conspecific with several species of *Marinilactobacillus* of *Carnobacteriaceae* (*Firmicutes*). All three bacterial phylotypes may represent ingenious microbial communities in the subglacial Lake Vostok.

Two newly discovered (RES) subglacial hypersaline lakes (5 and 8.3km² areas) in the Canadian Arctic are settled in bedrock throughs beneath 560 and 740m ice cap with modeled temperature below -10.5°C [2] and isolated by a glacier for at least 120 Ky ago. The biology is not yet studied (lakes are not unsealed), but the life potential is rather high (while dissimilar to the Lake Vostok). Their estimated salinity (140-160 psu) is in a range of that observed for brine-rich water body beneath Taylor Glacier (-7.8°C, 125 psu) and the ice-covered Lake Vida (-13°C, 200 psu) in Antarctica, both inhabited by active unique microbial communities.

The just discovered (RES) 20km-wide subglacial lake beneath the South Pole ice cap on Mars [1] should be ultra-hypersaline because it is buried beneath 1.5km water ice cap with modeled temperature -68°C. It is well below known low-temperature limits supporting terrestrial microbial cell propagation and metabolism as well (-18°C and -33°C, respectively [5]). Such conditions may indicate zero-level life potential for this lake from the Earth-bound point of view, but its exploration may give us surprises.

In general, all three subglacial lakes (complexes) – two Earth-bound and one Martian, may host unique life forms never met before but their exploration (unsealing) is challenging as it happened with the Lake Vostok.

References:

[1] Orosei et al 2018 Science 361_490-3

[2] Rutishauser et al 2018 Sci Adv 4_eaar4353

[3] Bulat et Petit 2015 Encyclopedia of Astrobiology, Vol 1, pp.1-6 (Ch. 1765-2)

[4] Bulat 2016 Phil Trans Royal Soc A Math Phys Eng Sci 374 (2059)_20140292

[5] Rummel et al 2014 Astrobiology 14_887-968

VENERA-D: FROM SCIENCE OBJECTIVES TO MISSION ARCHITECTURE

L. Zasova¹, T. Gregg², A. Burdanov³, T. Economou⁴, N. Eismont¹, M. Gerasimov¹, D. Gorinov¹, J. Hall⁵, N. Ignatiev¹, M. Ivanov⁶, K. Lea Jessup⁷, I. Khatuntsev¹, O. Korablev¹, T. Kremic⁸, S. Limaye⁹, I. Lomakin¹⁰, M. Martynov¹⁰, A. Ocampo¹¹, S. Teselkin¹⁰, O. Vaisberg¹, V. Vorontsov¹⁰

¹Space Research Institute RAS, Russia;

²University Buffalo, USA;

³TSNIIMASH, Russia;

⁴Enrico Fermi Institute, USA;

⁵Jet Propulsion Laboratory, USA;

⁶Vernadsky Inst. RAS, Russia;

⁷Southwest Research Institute, USA;

⁸NASA Glenn Research Center, USA;

⁹Univ. of Wisconsin, USA;

¹⁰Lavochkin Assoc., Russia;

¹¹NASA Headquarters, USA

Keywords:

Venera-D, JSDT, Orbiter, Lander, LLISSSE, aerial platform, sub-satellite

Introduction:

Building on the results of the highly successful Soviet Venera and VEGA missions [1], along with the Pioneer, Magellan [2,3], and more recent Venus Express and Akatsuki missions [4,5], a joint NASA-IKI/Roscosmos Science Definition Team (JSDT) was established in 2015. Within the overarching goal of understanding why Venus and the Earth took divergent evolutionary paths, the JSDT has the task of defining the science and architecture of a comprehensive Venera-D (Venera-Dolgozhivuschaya (long-lasting)) mission. The baseline Venera-D concept includes two elements, orbiter and a lander, with potential contributions consisting of an aerial platform/balloon, small long-lived surface stations, (LLISSE) or a sub-satellite. LLISSSE is studied to be included as a Lander payload element even in baseline concept. In January of 2017, the JSDT completed the first phase and generated a report to NASA - IKI/Roscosmos of its findings [6]. The second phase of the JSDT activities is currently underway with a focus on refining the science investigations, undertaking a compressive development of the core orbiter and Lander mission architecture, a detailed examination of contributed elements and aerial platforms that could address key Venus science [7, 8]

Venera-D science goals:

Venera-D investigations would address the dynamics of the atmosphere with emphasis on atmospheric superrotation, the origin and evolution of the atmosphere, and the geological processes that have formed and modified the surface with emphasis on the mineralogical and elemental composition of surface materials, and the chemical processes related to the interaction of the surface and the atmosphere and the solar wind and plasma environment.

Venera-D mission concept architecture:

The JSDT members from Lavochkin Association are leading the mission concept architecture development [6]. This assessment includes: (1) Development of the general configuration for both the orbiter and the lander; (2) Accommodation of systems and subsystems within the orbiter and lander; (3) Assessment of orbit options along with the strategy for descent and landing and long term observation of LLISSSE; (4) Evaluation of telecommunication options from the spacecraft to Earth and from the lander and LLISSSE to the orbiter; (5) Accommodation of an aerial vehicle in its own delivery system. Launch dates between 2026 and 2031 have been evaluated.

Venus Aerial Platforms:

The JSDT concluded that *in situ* atmospheric measurements over an extended period of time (days to months) would be scientifically enabling. Thus,

a high priority augmentation to the core concept would be an aerial platform to address science focused on atmospheric superrotation, chemistry, and trace species in the middle cloud layer.

Ongoing activities of the Venera-D JSDT:

The current phase of activity of the Venera-D JSDT will result in a report to be delivered to NASA-IKI/Roscosmos in late January of 2019. The tasks of the group will concentrate on (1) science refinement and evaluation of payload elements, specifically notional instruments; (2) development and refinement of the mission concept architecture including mission operations and risk assessment; (3) evaluation of potential landing sites within the context of the evolving lander engineering concept; and (4) incorporation of the results from the aerial platform study in the evaluation of a potential contributed element(s).

Venus Modelling workshops:

As the important resource to the JSDT two Venus modeling workshop were organized: one took place at the NASA Glenn Research Center located in Cleveland, Ohio, USA in the month of May 2017, with the participation of the wide community of Venus scientists, a second workshop was organized by NASA and IKI/Roscosmos in Moscow Space Research Institute in October, 2017. It has focused on the limitation and needs of current models (e.g., General Circulation Models or GCMs and interior structure models), landing site selection, and the types of measurements needed to more adequately constrain parameters in the models and experiments of the mission "Venera-D". Findings and results of modelling workshops are used by JSDT for concept of "Venera-D" elaboration.

References:

- [1] Sagdeev, R. V., *et al.* *Science*, 1986, 231, 1407-1408.
- [2] Colin, L., *et al.* (1980), *JGR*, 85, A13,
- [3] Saunders, R. S. *et al.* *JGR*, 1992, 97, 13067.
- [4] Svedhem, H. *et al.*, *JGR*, 2009, 114, E00B33. [
- 5] Nakamura, M. *et al.* *Earth, Planets and Space*, 2011, 63, 443.
- [6] Venera-D JSDT, 2017,
https://solarsystem.nasa.gov/docs/Venera-D_Final_Report_170213.pdf.
- [7] Cutts, J. *et al.*, Planetary Science Vision 2050 Workshop, 2017, 1989.
- [8] Cutts, J., 15th Meeting of the Venus Exploration Analysis Group (VEXAG), 2017, 8015.

CIRCULATION OF VENUSIAN ATMOSPHERE AT 90-110 KM BASED ON APPARENT MOTIONS OF THE O_2 1.27 μM NIGHTGLOW FROM VIRTIS-M (VENUS EXPRESS) DATA

D.A. Gorinov¹, I.V. Khatuntsev¹, L.V. Zasova¹, A.V. Turin¹
¹Space Research Institute of RAS, Moscow, Russia;

Keywords:

Venus, nightglow, mesosphere, dynamics, gravity waves

Introduction:

In the atmosphere of Venus at the altitudes of 90-110 km - the transition region between the superrotation and the subsolar-antisolar modes of circulation [1], tracking of the O_2 ($a^1\Delta_g$) 1.27 μm nightglow is one of the few possible methods of studying the dynamics [2]. The horizontal wind speed can be retrieved by tracking the displacement of the bright morphological features at given pairs of images. The nightglow images used in this study were obtained by VIRTIS-M on Venus Express from 2006 to 2008. This amount of data allowed to retrieve ~9000 velocity vectors.

Results:

The resulting global mean velocity vector field covers the nightside between latitudes 75°S – 0°N and local time 19 h – 5 h. The mean zonal and meridional components are asymmetrical between the morning and the evening side in terms of direction and magnitude. The zonal wind speed in the eastward direction from the morning side exceeds the westward (evening) by 20-30 m/s, and the streams “meet” at 22±1 h. The meridional component is predominantly poleward on the morning side, ranging from 0 to -50 m/s, and changes to equatorward at mid-latitudes. The influence of underlying topography via generated gravity waves was suggested in some cases: above mountainous regions flows behave as if they encounter an “obstacle” and “wrap around” highlands. Instances of circular motion were discovered, encompassing areas of 500-4000 km.

References:

- [1] Sánchez-Lavega A., Lebonnois S., Imamura T., Read, P., Luz D. The atmospheric dynamics of Venus. *Venus III*, 2017. 1541–1616.
- [2] Hueso R., Sanchez-Lavega A., Piccioni G., Drossart P., Gérard J.-C., Khatuntsev I., et al. Morphology and dynamics of Venus oxygen airglow from Venus Express/VIRTIS observations // *Journal of Geophysical Research*. 2008. V. 113. <https://doi.org/10.1029/2008JE003081>

GRAVITY WAVE ACTIVITY AS POSSIBLE CAUSE OF IONOSPHERIC LAYERS REGISTERED AT 90-115KM ON VENUS

M.I. Bondarenko, A.L. Gavrik

Institute of Radio Engineering (RAS); 1, Academician Vvedensky square, Fryazino, Moscow Region, Russian Federation

Keywords:

Venus, occultation, ionosphere, VEX, VENERA-15,16, meteoric layers, gravity waves, GWs

Introduction:

In the context of studies of ionosphere on Venus, the USSR VENERA-9,10 and 15,16 missions' (V15,16) occultation results – besides reporting correctly and fully on the layered structure of night and day ionosphere [6,7] (daytime: F, E layers at appr. 142, 130km and possible F2 at 190km) – which was not obvious to researchers at the time according to [1] – were also important in producing the first evidence of ionization between 85-90 and 115-120km altitude, i.e. in the possible daytime “Venusian D layer” (vD) ionospheric region.

Later many researchers began to note small irregular peaks (usually one or two) at the bottom of the main electron density profile (N_e) curve in data from many missions. Some used a parallel with the Earth ionospheric studies to interpret them as “sporadic layers of meteoric origin”.

Today we may be in a position to provide an alternative interpretation of the V-15,16 lower ionospheric plasma observations and we propose that what is perceived as small irregular maxima are traces from Gravity Wave (GW) activity on Venus (partially remaining on the processed N_e profiles) – which happens to be fully registered in occultation experiments from V-15,16 – and is a generic mechanism for many planetary atmospheres.

Observations:

The proposed hypothesis is based on a series of day-time (close to midday) series of 8 occultations spanning 58-85 deg south latitude and obtained in a closest Earth to Venus occultation season in October 1983. Two-frequency occultations used 32cm L-band and 8cm X-band signals, sampled at 17 Hz (in “level 2” preprocessed data). The data processing sequence was different from that in more recent studies (e.g. those for Venus Express, VEX 2006-2014), and included comparing received signal power of the 32cm channel with “calculated power” (a derivative of the differential Doppler frequency, which excludes non-plasma effects) to reveal poss. vD ionization.

This form of data makes it immediately obvious that oscillatory phenomena are present, superimposed on the basic “two-valley” form of the signal corresponding to the vF, vE layers of N_e profiles after processing. Further processing with Wavelet transform (Morlet) and wavelet filtration separated the signals into two parts, the lower-frequency component, which becomes the main curve of the N_e profile, and the higher-frequency oscillatory components with 5-8km vertical wavelengths, with bell-shaped envelopes and maxima at varying altitudes – in contrast with the fixed altitudes of the vF, vE maxima.

If the signal “separates” into two differently behaving parts, it is reasonable to seek a separate physical process to interpret the higher-frequency oscillatory component, and we propose that these high-resolution data from V-15, 16 occultations registered Venusian GW activity at these heights.

While it is known that the ionospheric part of the occultation signal can register GWs (the general mechanism of electron and ion perturbation by propagating GWs has been studied, used and modelled e.g. for tsunami-generated GWs on Earth), the possibility of existence of GWs on Venus with parameters and at altitudes of our signal components was considered using theory in [2],[5] (using pressure, density and temperature profiles at ionospheric altitudes obtained by the VEX mission in a similar part of solar activity cycle).

Supporting evidence in results from the VEX mission:

There exist direct observations of actual GWs with similar parameters at similar altitudes in the VEX mission. Work of Garsia et al (2009) [3] studied images from non-LTE CO₂ emissions with VEX VIRTIS-M tool at altitudes of 125-135km (4,277 um) and 115-120km (4.315 um) with horizontal wavelengths of 90-400km. Secondly, Peralta et al (2008) [4] studied daytime images from VIRTIS-M at the top of the cloud layer (66 +/- 4 km) with horizontal wavelengths of 95-210 km and vertical wavelengths of 5 and 15 km. Our estimates according to [2] also show that GWs observed by Peralta would reach the altitudes, at which components of our signals are observed, if propagating upwards. Therefore GWs with such parameters are present in reality at these ionospheric altitudes, and if we are right, might even reflect horizontal views of the same phenomenon we observe vertically on V-15,16 occultation signals, or be secondary GWs generated by the dissipation of rising GWs at 120-140km.

Another estimation in support of our scenario can be seen in the theoretical work by Peralta et al [5], which reviewed all wave phenomena possible in the Venus atmosphere. Dispersion graphs of estimated GWs permitted by the environment include GW parameter ranges of the oscillations in V-15,16 data and those directly observed in VEX photographic data (mentioned above).

In conclusion:

We propose that (a) lower altitude peaks on N_e profiles from many missions might reflect traces of GW activity (b) an example of which was fully registered in V-15,16 high resolution occultation data, and (c) itself reveals ionization of the possible analogue of the D layer of the Venusian ionosphere.

References:

- [1] "Aeronomy of the Venus Upper Atmosphere" J.-C. Gérard · S.W. Bougher · M.A. López-Valverde · M. Pätzold · P. Drossart · G. Piccioni, 2017
- [2] Thermospheric Responses to Gravity Waves: Influences of Increasing Viscosity and Thermal Diffusivity Sharon L. Vadas and David C. Fritts, 2008
- [3] R. F. Garcia, P. Drossart, G. Piccioni, M. Lopez-Valverde, and G. Occhipinti "Gravity waves in the upper atmosphere of Venus revealed by CO₂ nonlocal thermodynamic equilibrium emissions", 2009
- [4] [J. Peralta, R. Hueso, A. Sanchez-Lavega, G. Piccioni, O. Lanciano, and P. Drossart "Characterization of mesoscale gravity waves in the upper and lower clouds of Venus from VEX-VIRTIS images", 2008
- [5] "Analytical Solution For Waves In Planets With Atmospheric Superrotation. Part I. Acoustic And Inertia-Gravity Waves" J. Peralta, T. Imamura, P. L. Read, D. Luz, A. Piccialli, and M. A. Lopez-Valverde, 2013
- [6] Savich N.A., Gavrik A.L., Samoznaev L.N. The analysis of diffusion processes in the daytime ionosphere of Venus from the "Venera-9,10" radio occultation data // 1983
- [7] Gavrik A.L., Pavelyev A.G., Gavrik Yu.A. Detection of ionospheric layers in the Daytime Ionosphere of Venus at Altitudes of 80-120 km from VENERA-15 and -16 Two-Frequency Radio-Occultation Results // 2009.

WAVE-LIKE STRUCTURES IN THE VENUS IONOSPHERE DURING RADIO OCCULTATION

A.L. Gavrik

*Kotelnikov Institute of Radio Engineering and Electronics of RAS,
Fryazino, Russia, alg248@hotmail.com*

Keywords:

occultation, radio wave, data processing, ionosphere, wave-like structure.

Introduction:

The high informativity of radio occultation, which was proved during sensing of planets' envelopes [1,2], and implementation of this method for monitoring of the near-Earth space on satellite-to-satellite radio path [3] have raised the problem of comprehensive theoretical analysis of regular variations in the probing radio wave parameters. Studying the invariants of radio occultation experiment will open prospects for the development of better methods of data processing [4,5], which will enable one to extract new information from the data of radio occultation experiments of completed missions. The aim of the report is the analysis of the possibility of detecting wave phenomena in the atmosphere-ionosphere system from perturbations of radio signals in radio occultation experiments.

Occultation experiment:

The Venera-15 and Venera-16 spacecraft radiated monochromatic decimeter and centimeter wave signals at the frequencies $f_0 = 938$ MHz and $f_c = 4f_0$ with the wavelengths $\lambda = 32$ and 8 cm. A ground-based complex determined variations of phase $\varphi(t)$ and power $P(t)$ of coherent probing signals. Variations in the power $X(t) = P(t)/P_0$ were normalized by power level P_0 that was detected in the absence of the studied ionosphere. The measuring device enables one to determine the phase increment observed during time $0.47 < \tau < 0.06$ s. These variations should be summarized in order to find function $\varphi(t)$, which can lead to accumulation of the error due to random failures of the equipment. In the radio occultation experiments, it is appropriate to use another signal characteristic: the instant frequency $f_0(t) = (2\pi)^{-1} d\varphi(t)/dt$, which is obtained by dividing the phase increment observed during time τ by τ . In the solution of the inverse problem, it is the function $f(t)$ that is coupled with the radial profile of the refractive index $n(h)$ of the medium via an integral relationship [4,5].

A method for diagnostics of layered structures:

The receiver determined the residual frequency $\delta f(t)$. From $\delta f(t)$, we exclude the influence of the neutral atmosphere, the instability of reference oscillators, and the Doppler frequency shifts caused by the mutual motion of the transmitter and receiver [4,5]. The quantity $\delta f(t)$ is determined by the total electron concentration on the radio line. A method for reconstructing the variation in the frequency $f(t)$ of the DM-wave signal in plasma from variations $\delta f(t)$ has been developed and tested [4,5]. Solving the inverse problem makes it possible to determine from the function $f(t)$ the electron density profile. But near the lower boundary of the Venus ionosphere, in a region with a length of ~ 30 km (in the altitude interval 85–115 km), the large error of determining the atmospheric and ionospheric characteristics distorts the information on the variations in refractive index $n(h)$, which restricts the possibilities of studying the density waves propagating in the atmosphere-ionosphere system.

The theoretical interrelationship between the power $X(t)$ variation and frequency $f(t)$ variation is obtained $X(t) = \text{const} * df(t)/dt$ which indicates the presence of a linear relationship between the cross section area of a ray tube and the rate of the change in the beam refraction angle observed during the radio wave transmission probing of a spherically symmetric medium. The noise sources for energy parameter $X(t)$ and signal frequency $f(t)$ are different, so the correlation between the noise components of experimental function $X(t)$ and calculated function $X_c(t) = \text{const} * df(t)/dt$ is absent and the

revealed correlation between functions $X(t)$ and $X_f(t)$ will indicate the probing of stratified structures of the medium under study. The comparison between experimental function $X(t)$ and calculated function $X_f(t)$ is the main instrument for separating (on the background of noise) small variations of $n(h)$ making it possible to analyze the fine structure of radial perturbations in the atmosphere-ionosphere system. The correlation under consideration of $X(t)$ and $X_f(t)$ indicates the influence of the ionosphere. The absence of correlation between variations $X(t)$ and $X_f(t)$ evidences the dominating influence of atmosphere or noise and the inapplicability of the employed approximations. Reliable criteria for detection of stratified structures in the ionosphere are the coincidences of the variations in functions $X(t)$ and $X_f(t)$. The disagreement in the magnitudes of the corresponding effects are caused by the influence of disturbing factors, which include an insufficiently small data sampling interval, significant fluctuation of the signal caused by the instrumental noise or the turbulence of the medium, scattering or absorption of the signal power, violation of the applicability of the ray approximations or spherical symmetry, etc.

The results of the radio wave probing:

The procedure under consideration reliably separates the effects of the atmosphere, ionosphere, and noise. This circumstance is of particular importance in studying low-altitude and nighttime low-density plasma layers, for which these effects are comparable with noise in magnitude. Figure shows the results of a comparison between $X(t)$ and $X_f(t)$ for the measurement time interval $\tau = 0.058$ s.

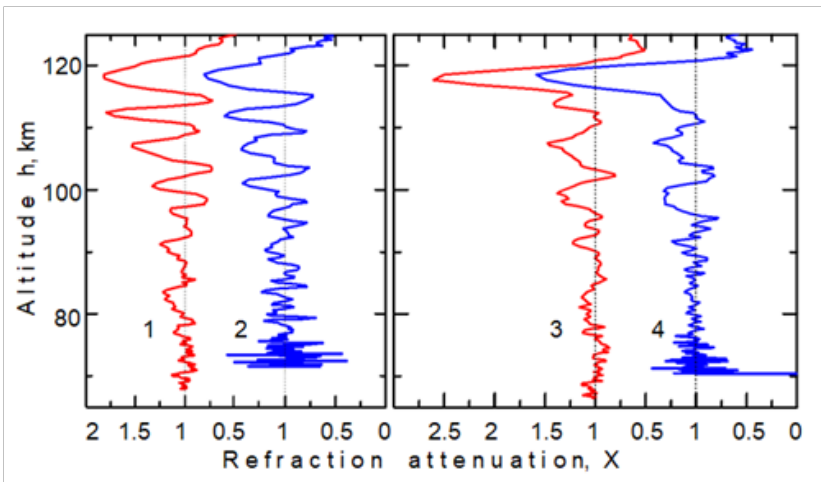


Fig. 1. Comparison of the refractive variation in the power $X(h)$ of the signal ($\lambda = 32$ cm) with the variation in $X_f(h)$ calculated from the frequency $f(t)$ in two Venera-15 sessions of radio occultation lower day-side ionosphere for $\tau = 0.058$ s: (curves 1,2) 25.10.1983 ($Z_0=73^\circ$), (curves 3,4) 14.10.1983 ($Z_0=58^\circ$). The ordinate axis is the altitude of the radio beam over the Venus surface.

Oscillations of signal power $X(h)$ are observed in the atmosphere below 85 km and in the ionosphere above 85 km (curves 1 and 3). The difference between the variations in $X(h)$ (curves 1 and 3) and the variations in $X_f(h)$ (curves 2 and 4) indicates the absence of correlation between $X(h)$ and $X_f(h)$ below 85 km, which evidences the absence of the influence of stratified plasma layers. Starting from the altitude of 85 km, a correlation between $X(h)$ and $X_f(h)$ is observed, the amplitudes of variations in $X(h)$ and $X_f(h)$ coincide, which indicates the influence of the plasma, and the difference between the functions $X(h)$ and $X_f(h)$ decreases with increasing altitude, because the refractive attenuation of the signal in a neutral atmosphere decreases. In the lower region of the ionosphere, at altitudes of 85–115 km, the amplitude of oscillations of $X(h)$ and $X_f(h)$ increases as the beam moves upward by ~ 30 km. The regular increase in the amplitude of oscillations of $X(h)$ and $X_f(h)$ with a

decrease in the atmospheric density directly indicates the wave nature of stratified periodic perturbations in the ionosphere refractive index.

Conclusion:

Vertical oscillations of the electron concentration near the lower boundary of the Venus atmosphere were never observed earlier. Moreover, the position of the lower boundary of the ionosphere was assumed to be at the altitude of 110–120 km. This uncertainty of the structure of the atmosphere–ionosphere system is due to the absence of direct measurements in the range 75–120 km and the low accuracy of the medium parameters determined during the solution of the inverse problem of electromagnetic transmission probing. The new results of processing the radio occultation data of the Venera-15 and Venera-16 spacecraft have lowered the boundary of ionization by 20–30 km.

The lower ionized region exists only in the daytime and, after the sunset, due to the comparatively high density of the atmosphere, positively and negatively charged particles recombine and the electron concentration at low altitudes drops practically to zero. The sources of ionization of the lower ionosphere of Venus, as well as the D regions of the Earth ionosphere, are rather difficult to reveal because of the limited amount of experimental data in the region of the lower boundary of the ionosphere, hardly accessible for direct measurements. The effects of the periodically oscillating signal power that have been observed in the process of probing when the amplitude of perturbations increases with an increase in the altitude over the surface directly indicate the wave activity in the daytime atmosphere and ionosphere, forming stratified periodic structures with the vertical scale of 6–10 km.

Acknowledgments:

The work is partially supported by the RAS Presidium Program № 28.

References:

- [1] L.H. Brace. A.J. Kliore. The structure of the Venus ionosphere // *Space Science Reviews*. 1991. V. 55. P. 81-163.
- [2] M. Pätzold et al. Mars Express 10 years at Mars: Observations by the Mars Express Radio Science Experiment (MaRS) // *Planetary and Space Sci.* 2016. V. 127 P. 44-90.
- [3] A. Steiner et al. (eds.). *New Horizons in Occultation Research*. Springer-Verlag Berlin Heidelberg. 2009. 315 p.
- [4] A.L. Gavrik, et al. Amplitude and Frequency Variations of Coherent Radio Signals during Probing of the Daytime Venusian Ionosphere // *Journal of Communications Technology and Electronics*. 2010. V. 55. № 3. P. 256-262.
- [5] A.L. Gavrik, et al. Oscillations Detected near the Lower Boundary of the Venus Ionosphere from the Radio Occultation Measurements of the Venera-15 and Venera-16 Satellites // *Journal of Communications Technology and Electronics*. 2013. V. 58. No. 10. P. 985–995.

MAIN GLOBAL EXTENSIONAL REGIMES ON VENUS

E.N. Guseva

*Vernadsky Institute of Geochemistry and Analytical Chemistry,
119991, Kosygin st., 19, Moscow, Russia, guseva-evgeniya@ya.ru*

Keywords:

The Venus, rift zones, groove belts, morphology of fractures, spacing.

Introduction:

The groove belts and the rift zones are extensive structural zones that have formed at different period of the geological history of Venus [1-2]. The groove belts are older and characterize the global tectonic regime of resurfacing [1,3]. The rift zones are typical of the youngest rifting-volcanism regime [3]. The groove belts are represented by series of closely spaced linear and curvilinear fractures and graben. They occur in many areas of Venus and occupy about 8% of the Venus surface [2] (Fig. 1).

The rift zones are extended belts of closely spaced graben/troughs, which are distinctly wider than the structures of the groove belts [3-6]. Rift zones form systems with a total length of about 40,000-55,000 km [4, 7-9] and occupy ~ 5% of the surface of Venus [2] (Fig. 1).

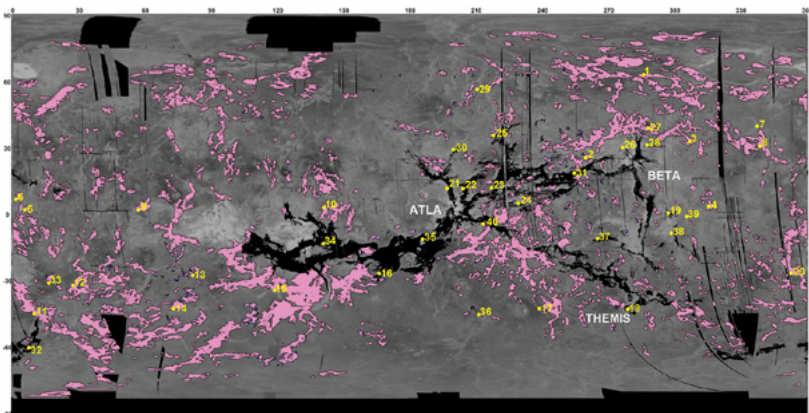


Fig. 1. Distribution of the rift zones (black) and the groove belts (pink). The base map is the SAR image in a simple cylindrical projection; boundaries of units by [2]. Numbers show areas of the spacing measurements.

The goal of the study was to compare the distance between the structural elements (spacing) within the groove belts and the rift zones to assess the possible changes of the thickness of the deformed layer through time.

The work was performed using traditional methods of photogeological analysis of images with a spatial resolution of ~ 100 m/px [<https://www.mapaplanet.org/explorer/venus.html>].

Results and discussion:

The groove belts are distributed much wider than the rift zones (Fig. 1). In some regions, the rift zones inherit the structural trend of the groove belts, but more often they form their own trends. The spatial distribution and orientation of the groove belts and the rift zones may indicate that the directions of the extension axes in the lithosphere changed with time. Probably, this is due to a change of the thickness of lithosphere and/or of the nature of mantle convection in the formation of the groove belts and the rift zones.

The morphology of fractures within the rifts and the groove belts was studied and characterized within randomly chosen areas (20 for the groove belts and 20 for the rift zones) in order to assess the possible changes on the thickness of deformed layer.

The groove belts consist of a series of closely spaced fractures; the width of individual fractures is a few hundred meters. The total width of the groove

belts is often hundreds of kilometers. Fractures of the groove belts are dense, linear or slightly sinuous; the mean length of fractures is ~ 285 km, and individual fractures reach ~ 700 km in length. The rift fractures are less dense and more sinuous; the structures of the rifts are longer; their average length reaches ~ 490 km, some fractures can be as long as ~ 900 km.

We measured the distance between the structural elements (spacing) within the rift zones and the groove belts in randomly selected areas. The average spacing within the groove belts is about 1.2 ± 0.2 km (1σ) and for the rift zones it is about 1.8 ± 0.4 km (1σ). Thus, the morphometric characteristics of the rift zones and the groove belts show that they form two different populations of extensional zones.

Conclusions:

(1) Individual segments of the rift zones are longer comparing with the segments of the groove belts [10-12]. However, the rifts are more compact zones that are concentrated mainly in the equatorial area of Venus. The groove belts, although are less expressive in topography, are found almost everywhere on Venus and form a branching system of deformational zones of a global scale. Thus, over time, the extension zones on Venus became more localized. This may indicate changes in the mantle convection regime as a function of time. (2) The rift zones have a more contrasting relief, formed by alternating deep graben/trough and horsts. The total amplitude of the relief within the rift zones can reach several kilometers [13]. The groove belts are topographically less contrasting, their relief amplitude, as rule, does not exceed several hundred meters. The increase in the topographical contrast of the rift zones probably indicates an increase in the thickness of the deformed layer of the lithosphere at the later stages of geological history. (3) The structures of rifts differ from the structures of groove belts by the morphology of the fractures. The rift fractures are less density spaced and are sinuous in plan view. The groove belts fractures are denser and more linear or slightly sinuous. The higher density of structures in the groove belts indicates a higher degree of deformation of the surface. The morphology of the fractures indicates the difference in the kinematics of the formation of structures, i.e. possible involvement of shear stresses during formation of the groove belts structures. (4) The results of measurements of the spacing within the rift zones and the groove belts show systematically lower average values of spacing. The increase of the spacing values suggests a systematic increase of the thickness of the deformed lithosphere over time [3, 14].

Acknowledgments:

This research was supported in part by the Russian Academy of Science program P-28.

References:

- [1] Basilevsky A.T., Head J.W. The geologic history of Venus: a stratigraphic view // *J. Geophys. Res.* 1998. V.103. 8531–8544;
- [2] Ivanov M.A., Head J.W. Global geological map of Venus // *Planet. Space Sci.* V. 59. 2011. P. 1559–1600;
- [3] Ivanov M.A., Head J.W. The history of tectonism on Venus: A stratigraphic analysis // *Planetary and Space Science.* 2015. V. 113-114. P. 10-32;
- [4] Masursky H.E., Eliason E., Ford P.G., McGill G.E., Pettengill G.H., Schaber G.G., Schubert G. Pioneer Venus Radar Results: Geology from Images and Altimetry // *J. Geophys. Res.* V.85. N. A13. 1980. P.8232-8260;
- [5] Campbell D.B., Head J.W., Harmon J.K. and Hine A.A. Venus Volcanism and Rift Formation in Beta Regio // *Science.* 1984. V.226. P.167-170;
- [6] Stofan E.R., Head J.W., Campbell D.B. et al. Geology of a rift zone on Venus: Beta Regio and Devana Chasma // *GSA Bull.* 1989. V.101. P.143-156;
- [7] McGill G.E., Steenstrup S.J., Barton C., Ford P.G. Continental rifting and the origin of Beta Regio, Venus // *Geophys. Res. Lett.* 1981. V.8. No.7. P. 737-740;
- [8] Schaber G.G. Venus: limited extension and volcanism along zones of lithospheric weakness // *Geophys. Res. Lett.* 1982. V.9. P.499-502;
- [9] Jurdy D.M., Stefanick M. Correlation of Venus surface features and geoid // *Icarus.* 1999. V.139. P.93-99;
- [10] Ivanov M.A., Head J.W. Geology of Venus. Mapping of a global geotraverse at 30N latitude // *J. Geophys. Res.* 2001. V.106. E8. P.17,515-17,566;
- [11] Basilevsky A.T., Head J.W. Rifts and large volcanoes on Venus: Global assessment of their age relations with regional plains // *J. Geophys. Res.* 2000. V.105. P.24.583-24.611;

- [12] Cherkashina O.S., Guseva E.N., Krassilnikov A.S. Mapping of Rift Zones on Venus, Preliminary Results: Spatial Distribution, Relationship with Regional Plains, Morphology of Fracturing, Topography and Style of Volcanism // *35th Lunar and Planetary Science Conference. 2004. Abst. 1525.*
- [13] Guseva E. N. Classification of the Rift Zones of Venus: Rift Valleys and Graben Belts // *Solar System Research. V. 50 № 3. 2016. P. 184-196.*
- [14] Brown C.D, Grimm R.E. Tectonics of Artemis Chasma: a Venusian "plate" boundary // *Icarus. 1999. V. 117. P. 219-249.*

ON THE ESTIMATE OF PRECESSION CONSTANT FOR VENUS

V.N. Zharkov, T.V. Gudkova

Schmidt Institute Physics of the Earth RAS, B.Gruzinskaya, 10, Russia, zharkov@ifz.ru, gudkova@ifz.ru

Keywords:

Venus, precession constant, moment of inertia, period of rotation, small parameter of the theory of figure

Introduction:

By its mechanical parameters – mass M , mean radius R , and mean density ρ_0 – Venus is reminiscence of Earth. Analysis of available observational data is performed. By using Venusian gravity field data the parameters and the precession constant of the earth-like model of Venus are estimated.

Analysis of observational data:

Observational data for Venus are summarized in the Table 1, where, for comparison, analogous parameters for Earth are given. The Table 1 lists the mass M , the first coefficients for expansion of the gravitational potential into spherical functions [1], the period of rotation τ , the equatorial R_e and mean R radii, the mean density ρ_0 , the nondimensional moment of inertia I/MR^2 .

The value of a small parameter of the theory of figure q , the dynamic flattening (the flattening of the outer equipotential surface of the gravitational potential of the planet) α , and the geometrical flattening e , given by

$$q = \frac{\omega^2 R_e}{GM} = \frac{4\pi^2 R_e^3}{GM\tau^2}, \quad \alpha = \frac{3}{2}J_2 + \frac{1}{2}q, \quad e = \frac{R_e - R_p}{R_e}, \quad (1)$$

where ω is the angular speed of rotation, G is the gravitational constant, and R_p is the polar radius.

For planets close to hydrostatic equilibrium, the mean radius R to a first approximation is expressed by R_e in the formula $R = (1 - \alpha/3)R_e$. As is known [2, 3], for an equilibrium planet the values of q and J_2 are of the same order of smallness. Referring to the Table 1, we find out that, for Venus, J_2 is 72 times larger than q . Consequently, we may assert that Venus is the most nonequibrated planetary body in the solar system. This fact is evidently not random, since the rotation of Venus in the past was greatly retarded by tidal friction. If we take the ratio of J_2/q for an effectively equilibrated Venus about 0.3 (i.e., the same as for the Earth, see the Table 1), then it is possible to determine the dynamic flattening for equilibrated Venus $\alpha_0 = 1.5J_2 + 0.5q_0 \sim 3.17J_2 \sim 13.9 \times 10^{-6}$. The corresponding equatorial radius R_e for Venus is shown in the Table 1. Thus, we see that, for Venus, R_e should practically coincide with R . The usual method of determining the moment of inertia of a planet close to a hydrostatic equilibrium from given J_2 and q is based on the formula of Radau-Darwin [2]

$$\frac{1}{MR^2} = \frac{2}{3} \left\{ 1 - \frac{2}{5} \left[5 \left(1 - \frac{3J_2}{2\alpha_0} \right) - 1 \right]^{1/2} \right\} \quad (2)$$

The scale of disequilibrium of Venus prevents us from finding out their moments of inertia in this manner. The constant of precession

$$H = (C - A)/C,$$

where C and $A \approx B$ are the polar and equatorial moments of inertia, which are also unknown for Venus and it is not clear whether H can be determined in the foreseeable future. As seen from the Table 1 the model value of H is very small. Hence, apparently, it is not possible to obtain the moment of inertia of Venus from such observations in the near future. The young Venus, at an early epoch – when its rotation was not yet retarded by tidal friction – rotated much more quickly with a period of ~ 10 hr [2]. Thus, the small parameter of the theory of figure, inversely proportional to the square of the rotation period ($q \sim \tau^{-2}$),

Table 1. Observational data and parameters of the figures of the Venus and Earth

Parameters	Venus	Earth
Mass M , 10^{24} kg	4.869	5.974
J_2 , 10^{-6}	4.40	1082.64
C_{22} , 10^{-6}	0.8578	1.565
S_{22} , 10^{-6}	-0.0955	-0.894
Period of rotation τ , days	243.16	1.00
Equatorial radius R_e , km	6051.53*	6376
Mean radius R , km	6051.5	6371
Mean density ρ , kg m^{-3}	5250	5514
Mean moment of inertia	0.334*	0.33076
	0.326**	
Small parameter of the theory of figure q		
J_2/q	6.1×10^{-8}	3.47×10^{-3}
f , 10^{-6}	72	0.31
precession constant H	3.45	7.2
	$\sim 2 \times 10^{-5}$ *	0.00327

*Values calculated theoretically for the interior structure model, see the text

**Value calculated with the help of formula (2), see the text

was much larger (roughly 4 orders of magnitude) for the young planet, than the present value. The observed value of J_2 for Venus approximately 70 times greater than q , which may be regarded as certain relic value of this quantity, pertaining to the early and much larger values of q , when the rotation of the planet was not yet retarded by tidal friction to the present extent. Since the shells of Venus had been able to cool considerably and become excessively rigid (or excessively viscous), the planetary figure 'froze', as it was, at a certain remote epoch and therefore does not conform to the present angular speed of rotation of the planet. If we solve the formula of Radau-Darwin with respect to the period of rotation, we have

$$\tau_{J_2} = \left\{ \frac{\pi}{\rho_0 G J_2} \left[\frac{5}{6.25(1-1.5I)^2 + 1} - 1 \right] \right\}^{1/2}, \quad (3)$$

then we are able to estimate for the epoch when the corresponding equilibrium figure of the planet was 'fixed', as well as the value of J_2 , which has been retained to the present day. Assuming for the moment of inertia of Venus $I^* = 0.334$ (the value obtained from interior structure model calculations) or $I^{**} = 0.326$ (the value obtained with the help of formula (2)) (see the Table 1), we can find a certain paleoperiod of rotation of Venus, $\tau_0 = \tau_{J_2} \approx 15.7$ days. The obtained result suggests that Venus rotated more rapidly in the past. The rotation period of the young Venus was probably even less and equal to ~ 10 hr, although the disequilibrium of the planet, corresponding to such a rapid rotation, was apparently lost from the 'memory' of Venus due the 'ductility' of its mantle and core long ago.

The idea, that it is reasonable in the zero approximation to use earth-like interior structure model of Venus, and that the estimated values of the parameters H , A , B , C were built when the planet was close to the hydrostatic state at the end of tidal evolution process, let us to obtain estimates H .

Table 2. Model values of the mean moment inertia, major moments of inertia and precession constant.

	I/MR^2	A/MR^2	B/MR^2	C/MR^2	H
1	0.334	0.333997	0.334000	0.334003	1.834×10^{-5}
2	0.326	0.325997	0.326000	0.326003	1.879×10^{-5}

The polar moment of inertia C , equatorial moments A and B , and constant precession are related by [4]

$$H = 1 - \frac{I - 2\sqrt{C_{22}^2 + S_{22}^2} - J_2 / 3}{I + 2/3 * J_2} \quad (4)$$

$$C = MR^2 \frac{J_2 + \sqrt{5/3(C_{22}^2 + S_{22}^2)}}{H} \quad (5)$$

$$A = (1 - H) / C \quad (5)$$

$$B = \left(1 - \frac{J_2 - \sqrt{5/3(C_{22}^2 + S_{22}^2)}}{J_2 + \sqrt{5/3(C_{22}^2 + S_{22}^2)}} H \right) C \quad (5)$$

Conclusion

Since the interior of the planets of the Earth group deviate from the state of hydrostatic equilibrium, the difference between their major moments of inertia with respect to the axes in the equatorial plane, is not equal to zero. This difference can be calculated from the formula [2]

$$f = \frac{B - A}{MR^2} = 4\sqrt{C_{22}^2 + S_{22}^2} \cdot \quad (8)$$

The parameters are shown in the Table 1. We see that the value f for Venus is small and it is smaller than for Earth. This indicates that the density distribution in both planets is close to the axisymmetrical, with good accuracy. Moreover, this fact strengthens the idea that the large nonequilibrium value of J_2 for the planet represents a relict value which corresponds to more rapid rotation of Venus in a certain earlier epoch, as we have mentioned above.

Acknowledgements

This work is partly financially supported by the Programme of Presidium RAS 28.

References:

- [1] Konopliv, A.S., Banerdt, W.B., Sjogren, W.L. Venus gravity: a 180th degree and order model // Icarus. 1999. V.139. No. 1. P. 3-18.
- [2] Zharkov, V. Models of the internal structure of Venus // The moon and the Planets. 1983. V. 29. P. 139-175.
- [3] Zharkov, V., Trubitsyn, V. 1978. Physics of planetary interiors. Tucson, AZ // Pachart. 1978.
- [4] Zharkov V.N., Molodensky S.M., Brzezinski A., Groten E., Varga P. The Earth and its rotation: low frequency geodynamics. Heidelberg // Herbert Wichman Verlag, 1996. 501p.

IMPROVED RETRIEVAL OF GASEOUS CONCENTRATION PROFILES IN VENUS MESOSPHERE USING SPICAV-UV/VEX STELLAR OCCULTATION DATA

D.G. Evdokimova^{1,2}, D.A. Belyaev¹, F. Montmessin², L. Baggio², J.-L. Bertaux^{1,2}

¹Space Research Institute of the RAS (IKI), 84/32 Profsoyuznaya Str., Moscow 117997, Russia. evd.dar@yandex.ru

²LATMOS, CNRS/UVSQ/IPSL, 11 Boulevard d'Alembert, Guyancourt 78280, France.

Keywords:

Venus, night mesosphere, stellar occultation, SPICAV UV

Introduction:

The occultation technique is a powerful method to investigate vertical structure of a planetary atmosphere. During one occultation a light source is tracked while it is ascending or descending behind a planet. Spectra of light partly absorbing in the atmosphere were measuring. There are both stellar and solar occultations depending on a type of a tracking object. If the star is chosen as a light source the night atmosphere is able to be probed. In case of Venus stellar occultation data containing the information about the night mesosphere species was accumulated for the first time in 2006-2015 by the SPICAV-UV instrument onboard the Venus Express orbiter [1]. The spectrometer's wavelength range extended from 120 to 320 nm and covered absorption bands of CO₂, SO₂, SO and O₃ molecules.

Contamination of the SPICAV stellar occultation spectra:

Besides of the stellar spectrum there were UV emissions produced by different sources registered by the spectrometer. These sources were an airglow of the nitric oxide, the Lyman-alpha line and the solar light reflected from the Venus crescent. The NO emission was the most intense and represented in the whole dataset of the SPICAV-UV. On Venus it is forming at altitudes about 115 km and was observed in stellar occultations [2] and night limb observations [3] within a wavelength range of 190-270 nm. The Lyman-alpha emission observed at 121.6 nm is a combination of photons of the outer space and scattered from the Venus day side. It was much weaker than the nitric oxide one with the intensity values in range of 1-3 kR [4]. The lower intensity allowed neglecting this emission at bright stars observations. The reflected at the cloud tops sunlight overlapped the range of 200-300 nm similarly to nitric oxide airglow.

Improved retrieval of gaseous profiles:

The gaseous profiles retrieval is an inverse problem which is resolved by fitting a synthetic spectrum with a set of parameters to an experimental one. This task requires good quality atmospheric transmission spectra. Their preparation combines a precise wavelength to pixel assignment and additional illumination extraction. Previously, the wavelength to pixel assignment was established by a CO₂ band alignment. This method was used for stellar occultation data of the SPICAM-UV/MEX [5] which was a precursor of the SPICAV-UV. The improved quality of the wavelength to pixel assignment is achieved by matching the stellar lines between the catalog and experimental stellar spectra. To resolve the extraction problem of the contaminating emission two approaches were investigated [2, 6]. Therefore, one of them was chosen as the most accurate to apply for the whole dataset of the SPICAV stellar occultations.

Acknowledgments:

D. G. Evdokimova and D. A. Belyaev acknowledge a support of the RSF grant #16-12-10453.

References:

- [1] J.-L. Bertaux et al. SPICAV on Venus Express: Three spectrometers to study the global structure and composition of the Venus atmosphere. *Planet. Space Sci.*, 2007. V. 55. P. 1673–1700.

- [2] E. Royer et al. NO emissions as observed by SPICAV during stellar occultations. *Planet. Space Sci.* 2010. V. 58. P. 1314–1326.
- [3] A. Stiepen et al., Venus nitric oxide nightglow mapping from SPICAV nadir observations. *Icarus*, 2013. V. 226. P. 428–436.
- [4] J.-Y. Chaufray et al. Observations of the nightside venusian hydrogen corona with SPICAV/VEX. *Icarus*, 2015. V. 262. P. 1–8.
- [5] E. Quemerais et al. “Stellar occultations observed by SPICAM on Mars Express” *J. Geophys. Res.* 111, E09S04 (2006).
- [6] D. Belyaev et al. Night side distribution of SO₂ content in Venus’ upper mesosphere. *Icarus*, 2017. V. 294. P. 58–71.

AN ACCURACY OF THE RETRIEVING OF VENUSIAN ATMOSPHERIC DATA FROM THE RADIOMETER INSTRUMENT IN THE VENERAD MISSION

V.D. Gromov, A.S. Kosov

IKI RAS, 84/32 Profsovnaya, Moscow, Russia, 117997,

vgromov@iki.rssi.ru

Keywords:

Venusian Atmosphere; Microwave Radiometer; Remote Sensing; Temperature Profile; Sulfur Dioxide; Sulfuric Acid vapor; Venusian Cloud layer; Weight-Functions; Inverse Problem; Regularization Techniques.

Introduction:

The recent progress in laboratory measurements of microwave absorption at Venus simulating conditions [1-3] provide a good basis for investigations of Venusian atmosphere with the microwave radiometer on board of the Venera-D orbiter. This radiometer [4] was developed for detection of thermal radiation of Venusian atmosphere in frequency range from 20 to 90 GHz with fluctuation threshold of sensitivity ≤ 0.03 K for integration time 1 s.

A thermal radiation at these frequencies is generated at atmospheric heights from Venus surface to about 60 km. High pressure of the sub cloud atmosphere produces broadening and full overlapping of the microwave molecular lines. It doesn't permit directly separate spectral absorption of different species and, therefore, need special techniques for retrieving atmospheric parameters from radiometric data. A correct use of retrieving techniques could give benefit in accuracy of atmospheric parameters in orders of magnitudes.

Weight functions:

A contribution of different atmospheric layers to a measured brightness temperature could be characterized by the weight function $W(h)$:

$$T_b(\nu, \vartheta) = \int_0^{\infty} T(h)W(h)dh, \quad W(h) = \alpha(h, \nu)e^{-\tau(h)} / \cos \vartheta, \quad (1)$$

where T_b is a radiometric brightness temperature, $T(h)$ is an atmospheric temperature profile, $\alpha(h, \nu)$ is a microwave absorption profile, depending on a frequency ν . In approximation of plane layers, optical depth is:

$$\tau = \int_h^{\infty} \alpha(\eta)d\eta / \cos \vartheta, \quad \alpha(h, \nu) = \alpha_{CIA} + q_1 k_{SO_2} + q_2 k_{H_2SO_4} + q_3 k_{cloud}, \quad (2)$$

where $\alpha_{CIA}(T, p, \nu)$ is the coefficient of the collision induced absorption [5] by molecules CO_2 and N_2 ; $q_1(h)$ and $q_2(h)$ are volume mixing ratios (VMR) of molecules SO_2 and H_2SO_4 vapor, correspondingly; $k_{SO_2}(T, p, \nu)$ and $k_{H_2SO_4}(T, p, \nu)$ are the coefficients of the absorption by these molecules; $q_3(h)$ is a mass content of liquid sulfuric acid in clouds, $k_{cloud}(T, p, \nu)$ is the coefficient of the absorption by acid drops, with T and p related to a local altitude h .

Coefficient α_{CIA} represents a dominant microwave absorption in sub-cloud region. It is produced by nonpolar, but most abundant molecules CO_2 and N_2 . Main microwave absorbers within minor constituents of Venus atmosphere are polar molecules SO_2 and H_2SO_4 , and a condensed sulfuric acid in clouds.

System of Eq. (1, 2) has no general solution for determination of unknown profiles $T(h), q_1(h), q_2(h), q_3(h)$ from measured $T_b(\nu, \vartheta)$. A numerical solution could be obtained by linearization of this equation and use of iteration technique. Its linearized form is:

$$\Delta T_b(\nu, \vartheta) = \int_0^{\infty} \Delta T(h)W(h, \vartheta)dh + \sum_{i=1}^3 \int_0^{\infty} \Delta q_i(h)W_i(h, \vartheta)dh, \quad (3)$$

where W_i , ($i = 1, 2, 3$) are the weight functions of the minor constituents:

$$W_i(h, \nu, \vartheta) = k_i(T_0(h), p_0(h)) \cos \vartheta^{-1} e^{-\tau_0(h, \vartheta)} [T_0(h) - \int_0^h T_0(\eta)W(\eta, \vartheta)d\eta], \quad (4)$$

The index 0 relates to profiles of the previous iteration. In first approximation it could be reference atmosphere profiles along with the absence of minor constituents, so $\Delta q_i = q_i$. The weight functions are shown on Fig. 1 - 4.

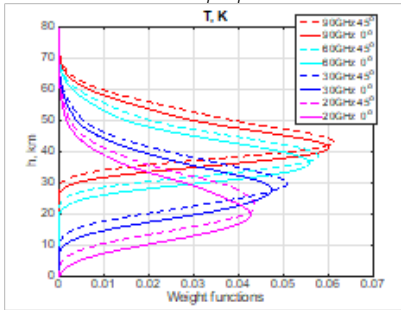


Fig. 1. Weight functions for Venus atmosphere thermal emission. Frequencies and nadir angles ϑ are shown at right.

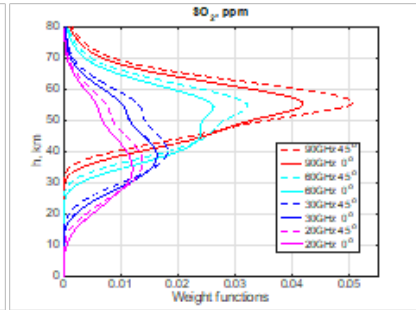


Fig. 2. Weight functions for sulfur dioxide in Venus atmosphere. Frequencies and nadir angles ϑ are shown at right.

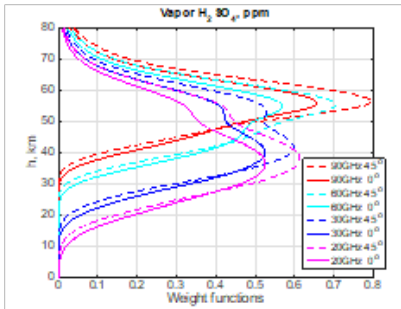


Fig. 3. Weight functions for sulfuric acid vapor, and ϑ - as in Fig. 1.

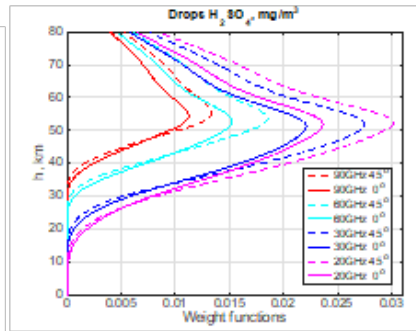


Fig. 4. Weight functions for liquid sulfuric acid in clouds, and ϑ - as in Fig. 1.

Data retrieving:

A result of one radiometric measurement could be represented by a set of $\Delta T_{b_j}(v, \theta_j)$ ($j=1, \dots, n$) including full set of frequencies and nadir angles. Atmospheric profiles of temperature and minor constituents could be represented by linear combination of some elementary profiles $g_k(h)$ with unknown coefficients to be determined, $x_k, k=1, \dots, m, m \leq n$. A system of linear equations to be solved is:

$$\mathbf{d} = \mathbf{B}\mathbf{x}, \quad (\mathbf{d} = \|\Delta T_{b_j}\|, \quad \mathbf{x} = \|x_k\| \text{ are column vectors, matrix } \mathbf{B} = \|B_{jk}\|) \quad (5)$$

Elements of the matrix \mathbf{B} are integrals of the corresponding functions $W(h)$ and $g_k(h)$. The matrix is bad-conditioned due to large overlapping of weight functions. In this case, a simple solution of Eq. (5) using the inverse matrix, $\mathbf{x} = \mathbf{B}^{-1}\mathbf{d}$, ($m=n$) has too large errors. If a matrix of measurement errors (noise) is

$$N(d_j, d_i) = \langle (d_j - \langle d_j \rangle)(d_i - \langle d_i \rangle) \rangle = \sigma^2 \delta_{ij} \text{ then, for example, for a}$$

temperature profile $N(\Delta T(h), \Delta T(h)) \gg \sigma^2$. Therefore a restricted number of parameters should be used ($m < n$) along with a pseudoinverse matrix, minimizing resulting errors (generalized inverse). This matrix could be calculated using a standard procedure of the singular value decomposition (SVD), or using Tikhonov regularization [6].

A numerical simulation of the data retrieval was done for the radiometer, characterized by weight functions given above ($n=8$). The atmospheric model included piece-wise linear temperature profile, thick layers of gaseous H_2SO_4 and SO_2 with constant VMR, and a thin cloud layer. It was defined by functions $g_k(h)$ ($m=7$). A SVD pseudoinverse matrix was used in data retrieving procedure. Some results of the simulation are given in conclusions.

Conclusions:

Low layers of Venusian atmosphere are sufficiently transparent for micro-

wave radiation, opening a unique possibility to collect data about processes in sub-cloud atmosphere, using orbital radiometer. High pressure in the low layers restricts spectral resolution of microwave radiometry and seriously reduces accuracy of the retrieving of profiles of atmospheric temperature and concentrations of minor constituents.

The numerical simulation shows that main atmospheric parameters are determinable by means of the radiometric measurements. It shows also, that stochastic errors of the parameters are strongly correlated, and some defined linear combination of parameters could be retrieved with higher accuracy. These data could be used in physical models of the atmosphere.

Note: The applications of the radiometers proposed by [6] in Russian and US meteorological services demonstrated their efficiency in detecting important meteo-events in spite of a restricted accuracy in a direct determination of temperature profiles.

References:

- [1] Steffes P.G., Shahan P., Barisich, C.G., Bellotti A. Laboratory measurements of the 3.7-20 cm wavelength opacity of sulfur dioxide and carbon dioxide under simulated conditions for the deep atmosphere of Venus // *Icarus*. 2015. V. 245. P. 153-161.
- [2] Akins A.B., Steffes P.G. Laboratory Measurements of Sulfuric Acid Vapor Opacity at Millimeter Wavelengths Under Venus Conditions // *AAS Division for Planetary Sciences Meeting Abstracts*. 2017. V. 49. P. 417.04.
- [3] Akins A.B., Steffes P.G. Millimeter Wavelength Opacity of H₂SO₄ Vapor at Venus: Initial Results // *Lunar and Planetary Science Conference*. 2018. V. 349. P. 2306.
- [4] Gromov V.D., Kosov A.S. The radiometer for thermal sounding of low atmosphere and sulfur compound detection. *Proceedings of the Venera-D Modeling Workshop*. Moscow, Russia. 5 – 7 October 2017.
- [5] Richard C., Gordon I.E., Rothman L.S., et al. New section of the HITRAN database: Collision-induced absorption (CIA) // *JQSRT*. 2012. V. 113. P. 1276-1285.
- [6] Troitsky A.V., Gajkovich K.P., Gromov V.D., Kadygrov E.N., Kosov A.S. Thermal sounding of the atmospheric boundary layer in the oxygen absorption band center at 60 GHz // *IEEE Transactions on Geoscience and Remote Sensing*. 1993. V. 31. P. 116-120.

NONLINEAR THEORY OF STABILITY OF NANOCRAFT EQUIPPED WITH A SAIL ACCELERATED BY AN INTENSE LASER BEAM

Popova E.^{1,2},

¹*Skobel'syn Institute of Nuclear Physics, Lomonosov Moscow State University, GSP-1, Leninskie Gory, Moscow, 119991, Russian Federation;*

²*The Schmidt Institute of Physics of the Earth of the Russian Academy of Sciences (IPE RAS), Bolshaya Gruzinskaya str., 10-1, Moscow 123242, Russia, popovaelp@mail.ru*

Keywords:

Breakthrough Starshot, light sail, light-propelled nanocraft

Breakthrough Starshot is engineering program aiming to demonstrate proof of concept for light-propelled nanocrafts. These could fly at 20 percent of light speed and capture images of possible planets and other scientific data in our nearest star system, Alpha Centauri, just over 20 years after their launch.

In this project nanocrafts are gram-scale robotic spacecrafts comprising two main parts: StarChip and Lightsail. The StarChip is gram-scale wafer, carrying cameras, photon thrusters, power supply, navigation and communication equipment, and constituting a fully functional space probe. The Lightsail is made of increasingly thin (no more than a few hundred atoms thick) and light-weight (gram-scale mass) metamaterial.

It is also assumed that the Breakthrough Starshot components can be used to fly other comets devices in the Solar System and beyond, that is, for shorter distances.

To achieve goal of the project it is necessary to solve a lot of complex scientific and engineering problems. One of these tasks is investigation stability nanocraft orientation in intense laser beam which should accelerate it up 60,000 km/s during 2 minutes.

We considered a problem of stability nanocraft orientation while illuminated by intense laser beam. In our model the nanocraft driven by intense laser beam pressure acting on its lightsail is sensitive to the torques and lateral forces reacting on surface of sail. This forces influence the orientation and lateral displacement of spacecraft. We consider stability of its position inside laser illuminated column.

The assumptions in choosing the model: 1. concave (part of the sphere) circular sail; 2. configuration of nanocraft is treated as solid body (applicability of Euler equations); 3. mirror reflection of laser beam from surface of the lightsail; 4. Gaussian profile of the laser beam.

In [1] we discussed how sail shape and profile of the laser beam can affect stability of nanocraft position provided that surface of the sail has a small curvature.

In this work we have constructed a nonlinear theory of stability of nanocraft orientation taking into account arbitrary curvature of surface of the sail. We obtained conditions for the case of a stable orientation of the sail. We estimated the threshold value of the disturbing force, at which the position of the sail in the beam is still preserved.

For ground-based planned experiments, we evaluated the stability of nanocraft orientation under the action of a laser beam in a gravitational field.

References:

- [1] Popova E., Efendiev M., Gabitov I. On the stability of a space vehicle riding on an intense laser beam// *Mathematical Methods in the Applied Sciences*. 2017. V. 40. No. 4. P. 1346-1354.

NUMERICAL STUDY OF THE PLANETARY ATMOSPHERE OF GLIESE 436B

A.G. Berezhitskiy¹, I.F. Shaikhislamov¹, M.L. Khodachenko^{2,3},
I.B. Miroshnichenko^{1,4}, M.S. Rumenskikh¹

¹*Institute of Laser Physics, Siberian Branch Russian Academy of Science, Novosibirsk, Russia;*

²*Space Research Institute, Austrian Academy of Science, Graz, Austria;*

³*Skobeltsyn Institute of Nuclear Physics, Moscow State University, Moscow, Russia*

⁴*Novosibirsk State Technical University, Novosibirsk, Russia*
a.berezuckiy@yandex.ru

Keywords:

Exoplanet; stellar wind; planetary atmosphere; numerical simulation.

Introduction:

We study a plasmasphere of a Neptune-size exoplanet Gliese 436b, orbiting the red dwarf at an extremely close distance (0.028 au), taking into account its interaction with the stellar wind plasma flow. The modelled planet Gliese 436b has a mass $M_p=0.07M_J$, radius $R=0.38R_J$ and an estimated surface temperature 700 K. To describe the physical processes in the planetary upper atmosphere, we use a 2D self-consistent multi-fluid hydrodynamic aeronomy model. In our simulations we investigated basic properties of exosphere during interaction with stellar plasma.

Methods:

To describe the expanding atmosphere of Gliese 436b and its interaction with the stellar wind plasma, we use a 2D axisymmetric multi-fluid hydrodynamic model [1, 2]. Each fluid describes the hydrogen and helium components of the planetary origin (H, H⁺, H₂, H₂⁺, H₃⁺, He, He⁺) and the stellar wind protons. The planetary plasma is regarded as a quasineutral fluid with thermal equilibrium: $T_i = T_e$. The model takes into account the basic photo-chemical processes in the hydrogen-dominated atmosphere, allowing to describe in a self-consistent way its heating and ionization due to absorption of the stellar XUV radiation. An approximated spectrum of Gliese 436 in the range of 10-912 Å with a total flux of $F_{XUV} = 0.8 \text{ erg cm}^{-2}\text{s}^{-1}$ at a distance of 1 a.u. is used in the simulations. The tidal forces acting on the streams of the escaping planetary upper atmospheric material are also taken into account.

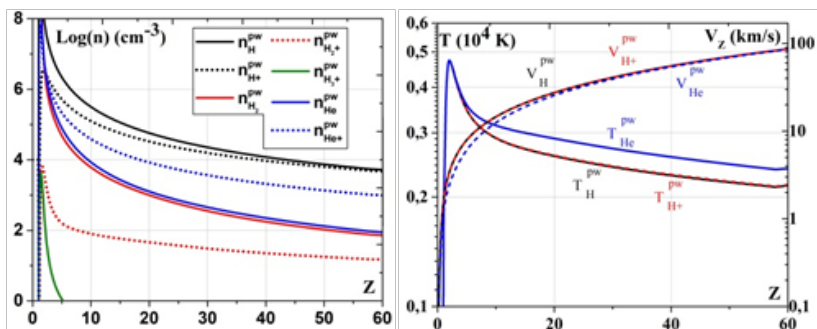


Fig.1. Distribution of density, temperature and velocity of the species in the PW along the planet-star line.

Results:

At the initial state of the simulations, the atmosphere of Gliese 436b is assumed to consist of the molecular hydrogen and helium atoms at a ratio $N_{\text{He}} / N_{\text{H}_2} = 1/5$ with a temperature of 750 K. We consider the case of a weak stellar wind (SW) with $n_{\text{sw}} = 100 \text{ cm}^{-3}$, $T_{\text{sw}} = 1 \text{ MK}$, $V_{\text{sw}} = 70 \text{ km/s}$, which is much less intense than the solar wind. Because of this, we did not consider gener-

ation of Energetic Neutral Atoms (ENAs). The planetary wind (PW) streams, moving towards and away from the star, are formed, driven by the stellar XUV energy input and the stellar gravity. They propagate within the SW plasma, separated from it by a sharp boundary. The structure of the expanding PW of Gliese 436 b is shown in Figure 1, which gives the profiles of density, velocity, and temperature for hydrogen atoms, protons and helium atoms along the planet-star line. A strong collisional coupling between atoms and protons in the PW region is indicated by the velocity and temperature profiles, which are rather close to each other. The velocity rapidly increases and at the distance of 50-60 Rp from the planet it reaches ~ 90 km/s, while the temperature after having a maximum of about 5000 K decreases smoothly down to ~ 2200 K. These results are in good agreement with the one-dimensional aeronomy calculation of Gliese 436 b, performed in [3].

Acknowledgements

This work was supported by the Russian Science Foundation, project 18-12-00080, and the Austrian Science Foundation FW, projects I2939-N27, S11606-N16, S11607-N16. Parallel computing simulations have been performed at Computation Center of Novosibirsk State University, SB RAS Siberian Supercomputer Center, and Supercomputing Center of the Lomonosov Moscow State University.

References:

- [1] I. F. Shaikhislamov, M. L. Khodachenko, H. Lammer, et al. 2016, *ApJ*, 832,173
- [2] M. L. Khodachenko, I. F. Shaikhislamov, H. Lammer, et al. 2017, *ApJ*, 847,126
- [3] Loyd R. O. P. Koskinen, T. T., France, K., et al. 2017, the *Astrophysical Journal Letters*, 834, 2

MARINILACTOBACILLUS SP AND TWO MORE BACTERIA IN THE SUBGLACIAL ANTARCTIC LAKE VOSTOK

S. Bulat¹, M. Doronin¹, E. Rudaya¹, E. Karaevskaya¹, D. Marie²

¹NRC 'Kurchatov Institute' - Petersburg Nuclear Physics Institute, St. Petersburg-Gatchina, Russia;

²Station Biologique de Roscoff, Roscoff Cedex, France, bulat@omrb.pnpi.spb.ru

Keywords:

Antarctica, subglacial Lake Vostok, lake unsealing, ice cores, life, extremophiles, bacteria, 16S rRNA genes, contamination, astrobiology

Introduction:

The objective was to search for microbial life in the subglacial Antarctic Lake Vostok by analyzing the uppermost water layer entered the borehole and shortly got frozen within following three lake unsealing (February 5, 2012; January 25, 2015, and February 03, 2015). The samples included the drillbit frozen and re-cored borehole-frozen water ice.

All the lake water frozen samples proved to be contaminated to a different extent with the kerosene-based drill fluid. The cell concentrations measured by flow cytometry varied from 167 (drillbit frozen water) until 5.5 – 38 cells per ml in different borehole-frozen samples. The comprehensive DNA analyses came up with total 53 bacterial phylotypes discovered by sequencing of different regions of 16S rRNA genes. Of them, only 3 phylotypes successfully passed all contamination criteria. Two phylotypes detected after the 1st lake unsealing were reported before [1] - hitherto-unknown and phylogenetically unclassified phylotype w123-10 showing less than 86% similarity with known taxa and likely belonging to *Parcubacteria* Candidatus *Adlerbacteria* featured by unusual biology and 3429v3-4 showing 93.5% similarity with *Hermiimonas glaciei* of *Oxalobacteraceae* (*Beta-Proteobacteria*) – water-inhabited ultramicrobacterium isolated from deep Greenland GISP2 ice core. The borehole-frozen water samples after the 2nd lake unsealing gave nothing of confident while the new finding just recently came from the samples after the 3rd lake unsealing. The phylotype 3698v46-27 proved to be conspecific with several species of *Marinilactobacillus* of *Carnobacteriaceae* (*Firmicutes*) sharing very similar 16S rRNA genes. Among them is *M. piezotolerans* isolated from 4.15m deep sub-seafloor sediment core collected at 4790.7m deep Nankai Trough. No archaea were detected in any samples.

Thus, 3 discovered bacterial phylotypes might represent ingenious cell populations in the subglacial Lake Vostok.

References:

- [1] Bulat S.A. Microbiology of the subglacial Lake Vostok: first results of borehole-frozen lake water analysis and prospects for searching for lake inhabitants // Philosophical Transactions of The Royal Society A Mathematical Physical and Engineering Sciences. 2016. V. 374(2059) 20140292.

THEORETICAL MODEL OF HYDROGEN LINE EMISSION FROM ACCRETING GAS GIANTS

Y. Aoyama¹, M. Ikoma¹, T. Tanigawa²

¹*The University of Tokyo, Department of Earth and Planetary Science, yaoyama@eps.s.u-tokyo.ac.jp;*

²*National Institute of Technology, Ichinoseki College*

Keywords:

Hydrogen Lines, Gas Accretion, Planet Formation, Direct Imaging, LkCa15b

Introduction:

Observation of growing protoplanets is key to understand planet formation. While few planets detected so far are young enough to provide us with constraints to planet formation, an important object is LkCa15b. This planet is reported to be bright not only in the infra-red, but also in H α [1]. Hydrogen line emission such as H α needs hot hydrogen gas with temperature higher than $\sim 10^5$ K. Such a high temperature is unlikely to be realized in the protoplanet nor circum-planetary disk. The physical mechanism for the H α emission is poorly understood in planet formation context.

Method:

In this study, we focus on the accreting flow from a circumstellar disk (often termed a protoplanetary disk) onto a circumplanetary disk. According to recent high-resolution 3D hydrodynamic simulations, the accreting gas almost vertically onto and collides with the surface of the circumplanetary disk at a super-sonic velocity [2]. Then, the gas passes through a strong shock wave and becomes hot enough to emit hydrogen lines. Here, we have developed a 1D radiative hydrodynamic model of the flow after the shock with detailed calculations of chemical reactions and electron transitions in hydrogen atoms. Then, we quantify the hydrogen line emission from the shock surface.

Results and Conclusion:

Comparing our theoretical H α intensity with the observed one from LkCa15b, we constrain the protoplanet mass and the disk gas density. Observation of hydrogen line emission from protoplanets is highly encouraged to obtain direct constraints of accreting gas giants, which will be key in understanding the formation of gas giants.

References:

- [1] Sallum, S., Follette, K. B., Eisner, J. A., et al. Accreting protoplanets in the LkCa 15 transition disk // *Nature*. 2015. vol. 527, p. 342-344, <https://arxiv.org/abs/1112.3706>
- [2] Tanigawa, T., Ohtsuki, K., and Machida, M. N. Distribution of accreting gas and angular momentum onto circumplanetary disks // *The Astrophysical Journal*, vol. 747, 47 (<https://arxiv.org/abs/1511.07456>)

SUPERFAST EXOPLANETS AND 9600 SECONDS

V. A. Kotov

*Crimean Astrophysical Observatory, Nauchny, Crimea 298409, Russia;
vkotov@craocrimea.ru*

We show the motion of the superfast exoplanets (with periods < 2 d, and with the $\pi/2$ factor accounted for) is modulated by the timescale 9603(90) s, coinciding with the «solar» period 9600.606(12) s (confidence 99.9%). It is supposed the exoplanet resonance reflects some new property of gravitation.

INTERFERENCE CORONAGRAPH WITH ROTATIONAL SHEAR FOR GROUND-BASED AND SPACE TELESCOPES

A. V. Yudaev¹, D. Bahur², I. Shashkova³, A. Tavrov⁴

¹Moscow institute of physics and technology, yudaev@phystech.edu;

²Moscow institute of physics and technology,

³Russian Space Research Institute, shi@iki.rssi.ru;

⁴Russian Space Research Institute, tavrov@iki.rssi.ru

Keywords:

Coronagraph, exponents, rotation shear, direct imaging, space telescope

Introduction:

At the last time, significant growth of interest in exoplanetary research are observed. Commonly, more than 3500 exoplanets are known. This progress is defined by comprehensive development of indirect searching techniques like transit and radial velocity methods. These methods are not able to observe exoplanets whose orbital plane lays orthogonal to the line of observation.

Direct imaging methods have practical complexity of implementation. The main problem is crucial brightness difference between an exoplanet and its parent star. The irradiance contrast requires 9 orders of magnitude for exoplanet like Jupiter. In case of contrasting to an acceptable range Lyot coronagraph type is conventionally used. However, a Lyot coronagraph is critically sensitive to wave front distortions due to atmospheric turbulence and/or due to optical system fabrication errors. Proposed here is an interference coronagraph with rotation shear. Its main advantage is much less sensitivity to wave front errors.

Numerical investigation was made for WSO-UV space telescope, taking into account known mid- and low spatial frequencies aberrations for the primary and secondary telescope mirrors. Achievable contrasts are shown on fig. 1 for 10 deg rotation shear interfero-coronagraph for different micro roughness PSD exponents.

Choosing the rotation shear angle smaller, it becomes principally possible to increase contrast and effectively maintain the sensitivity to fabrication errors by expense of spatial resolution (IWA).

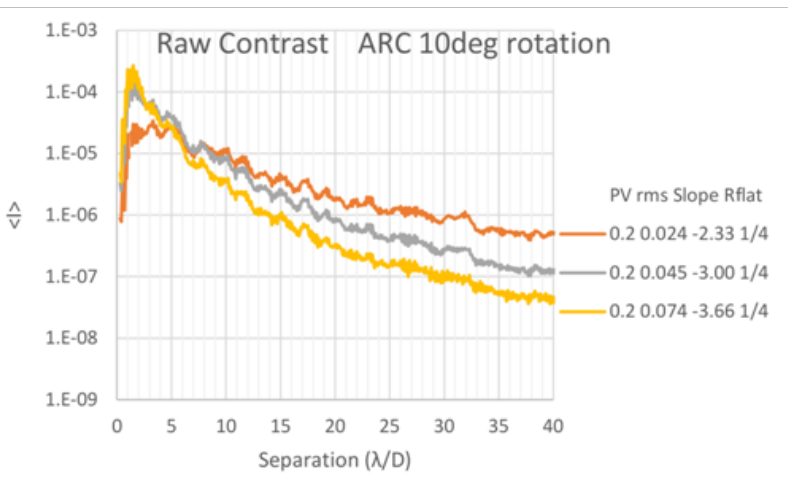


Fig. 1. Relative contrast for WSO-UV based null coronagraph with different mirror sharpness

The model of rotation shear interfero-coronagraph was studied by numerical calculations. Experimental set-up is started. Experimental facility consists of two lasers and collimating systems, to emulate light sources of a host star and

an exoplanet. Two beams are mixed with small angle that represents apparent separation between star and exoplanet. Mixed beams are re-directed to coronagraph input optics by means of adjustable mirror. CCD camera records interference on the dark output. Input beam (star component) needs to be exactly coincident with a coronagraph rejection axis. This is achieved by piezo-adjustable mirror on the input. When it occurs, CCD camera records dark field and the stars light strongly suppressed. Planet component does not suppressed because of two images of a planet have sheared in different positions on a CCD and therefore they do not interfere with each other. As a result, CCD records residual star light and two copies of planet displaced each to other in a double rotation shear angle.

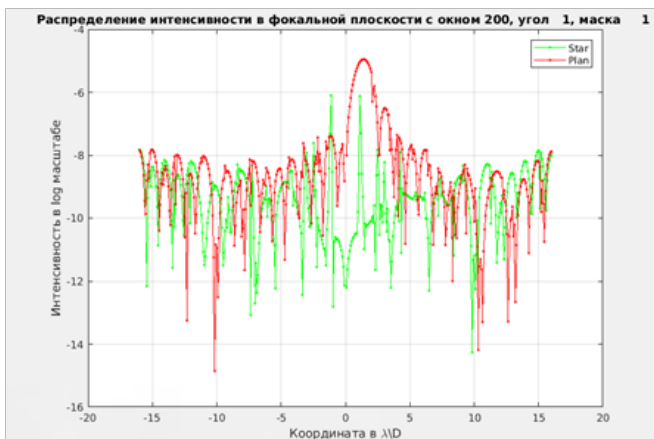


Fig. 2. Relative contrast for WSO-UV based null coronagraph with 1 degree rotation shear.

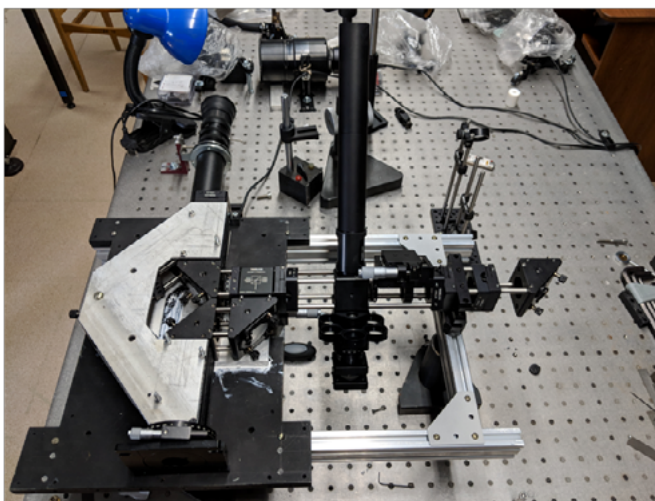


Fig. 3. The experimental model of null coronagraph with variable

References:

- [1] Sachkov, M., Shustov, B., Savanov, I., & Gómez de Castro, A.I., «WSO-UV project for high-resolution spectroscopy and imaging» *Astronomische Nachrichten* 335, 46 -50, 2014.
- [2] www.exoplanets.eu (accessed 29/05/2017).
- [3] P. Frolov, I. Shashkova, Yu. Bezymyannikova, A. Kiselev and A. Tavrov, "Achromatic interfero-coronagraph with variable rotational shear: reducing of star leakage effect, white light nulling with lab prototype", *J. Astronomical Telescopes, Instruments, and Systems*, Vol. 2, Issue 1, p. 011002-1, 2016, doi: 10.1117/1.JATIS.2.1.011002.
- [4] Murty M. V. R. K. and E. C. Hagerott, "Rotational Shearing Interferometry," *Appl. Opt.*, 5, 615 (1966).

CHANDLER'S PRECACE, SUN PROCESSES: SPECTRAL ANALYSIS

O.B. Khavroshkin, A.B. Khrustalev

IPhE RAS, khavole@ifz.ru

Keywords:

Earth pole, pole shift, global mass movements, solar activity, statistical analysis.

Introduction.

The nature of the Chandler's precession has not been finally established, several global processes are attracting its explanation: the displacement of the Earth's atmosphere and the water masses of the world ocean; dynamics of the inner core of the Earth; effects of astrophysical nature.

Each of these mechanisms is quite real, but to assess the depth of influence of each of these factors it is necessary to estimate its relative contribution to the motion of the pole. Therefore, an attempt was made to create a methodology for assessing the significance of various factors associated with the motion of the pole. When studying the role of solar activity, the latest achievements in studying the Sun and its radiations were used.[1,2].

Statistical analysis.

Daily data on the motion of the Earth's poles have been considered since 1962. to the present with a sampling frequency of 1 day; Accordingly, the trajectories of the motion of the Earth's pole and one of the coordinates of the pole are constructed. Next, amplitude spectra and SWAN diagrams of pole motion, resonance diagrams were constructed with subsequent evaluation of the significance of peaks using the histogram method. Two periods are clearly distinguished: $T_1 = 365.08$ days, which corresponds to the period of the Earth's rotation around the Sun (annual period) and $T_2 = 432.84$ days, which corresponds to the Chandler's precession. New methods were also used: resonance diagrams and a histogram method for determining resonance frequencies. The distribution of the resonance amplitudes and the spectrum of the main resonance periods were obtained.

The obtained periodicity is of considerable interest, especially $\sim 28s$. which coincides with the period of the Sun's own rotation (for different zones, more accurately the depths, the Sun, the period of rotation is different). In all likelihood, the influence of the Sun on the Chandler's precession is more profound and has its own mechanisms of influence. In this respect, an open HENRI-effect can play a significant role when exposed to a neutrino solar flux with radioactive structures of the Earth [3-6].

Conclusions

1. Spectral analysis allows us to identify the most significant periods of the Chandler's precession.
2. The histogram method has made it possible to reliably estimate the contribution of one or another process that affects the motion of the pole.
3. Using the resonance method, a table of new periods of the Chandler's precession has been obtained, which previously were not detected by the usual spectral analysis.
4. Anomalous neutrino radio isotope (ANRI) absorption explains the effect of the appearance of solar periods in the spectrum of the Chandler's precession.

References:

- [1] Avsyuk Yu. N. Tidal forces and natural processes. - Moscow: OIFZ RAS, 1996. - 188 p.
- [2] Yu. N. Avsyuk. On the motion of the inner core of the Earth, Dokl. AN SSSR. - 1973. - No. 5. - P. 1103-1104.
- [3] Khavroshkin O.B., Tsyplakov V.V. Radioactivity ore sample: monitoring. *Engineering Physics*. 2013. № 8. Pp. 53...62.
- [4] Khavroshkin O., Tsyplakov V. Sun, Earth, radioactive ore: common periodicity. *The Natural Science (NS)*. 2013. Vol. 5. № 9. Pp. 1001...1005.
- [5] Khavroshkin O.B., Tsyplakov V.V. Anomalous neutrino radio-isotope (ANRI) uptake

- and nuclear reactor. *Engineering Physics*. 2016. № 10. Pp. 3...8] (in Russian).
- [6] [Rukhadze A.A., Khavroshkin O.B., Tsyplakov V.V. Periodicity of natural radioactivity. *Engineering Physics*. 2015. № 6. Pp. 26...36 (in Russian).
- [7] Nicolaev A.V., Khavroshkin O.B., Tsyplakov V.V. The structure of astrophysical component seismic emissions and noise. *Engineering Physics*. 2016. № 9. Pp. 68...74 (in Russian).

SUN AND TEMPERATURE FIELDS OF THE EARTH

O.B. Khavroshkin, V.V. Tsyplakov

IPhE RAS, khavole @ ifz.ru

Keywords:

Sun, solar neutrino streams, anomalous neutrino radioisotope absorption, nuclear power station.

Introduction

The problems of the Earth's heat and possible connections with other processes are becoming increasingly urgent [1-5]. The earth loses about 0.06 watts per square meter of surface, or about 30 trillion watts for the entire planet, from the heat flow from the interior. The main sources of the Earth's internal heat are: the decay of long-lived radioactive isotopes (uranium-235 and uranium-238, thorium-232, potassium-40), gravitational differentiation of matter, tidal friction, metamorphism, phase transitions [1]. The spectrum of long-period oscillations of the Earth, which are longer than their own, contains peaks that coincide in value with an accuracy of 1 ... 3% with peaks of the Sun's own oscillations [1]. The mechanism of excitation of these vibrations and variations in the activity of a radioactive sample of ore with a strong difference in scale has practically one mechanism. The observed effects, together with other periodicities, underlie the interaction in the Earth-Sun systems [3, 4] and affect the volcanism, seismicity and energy of seismic fields [5]. Naturally, variations in solar neutrino fluxes with subsequent changes in radioactive substance activity are accompanied by temporary variations of temperature fields everywhere.

Temperature fields and solar neutrino stream.

The Earth's thermal fields and temperature fields of radioactive substances have a common periodicity, determined by the cyclical of solar processes and, accordingly, the latent periodicity of neutrino solar fluxes. Temperature variations of all types are determined by anomalous neutrino radioisotope (ANRI) absorption or by the effect of neutrino flux interaction with radioactive structures of the Earth. The statement that the influence of the cyclical of solar activity can be neglected below the zone of constant temperatures (at depths above 40 m), and the temperature regime of the rocks is determined by the depth flow of heat and the specific features of the thermal properties of the rocks, incorrectly: at a depth of 40 m there can exist a thermal component due to muons (K_p -index), and at any and large depths - heat from the interaction of the solar neutrino flux with radioactive structures. When estimating the heat flux, it is necessary to introduce the factor $S(\omega)$, which represents the spectrum of the natural oscillations of the Sun. Perhaps there is a relationship between global warming and the heat fluxes of the Earth, taking into account the ANRI effect. New unknown data on long-period wave processes on the Sun are also obtained. The power of nuclear power plants, their prevalence is increasing. Therefore, it should be borne in mind that if ~ 10% of the reactor capacity is an antineutrino flux, the nearest station zone will be a source of increased heat flux and local seismicity and warming. In the case of Japan, a general increase in seismicity is possible. Since extraterrestrial neutrinos play an important role in the thermal history of the Earth and the safety of nuclear reactors, in the future it is necessary to create an observational neutrino safety monitoring network.

References:

- [1] Khavroshkin O., Tsyplakov V. Sun, Earth, radioactive ore: common periodicity. The Natural Science (NS). 2013. Vol. 5. № 9. Pp. 1001...1005.
- [2] Khavroshkin OB, Tsyplakov VV Anomalous neutrino radioisotope (ANRI) absorption and nuclear reactor // Engineering Physics. 2016. № 10. With. 3 ... 8.
- [3] Fedotov SA, Khavroshkin OB, Tsyplakov VV, Boyko A.N. Solar and astrophysical factor, Z-variations of GPS data of calderas and volcanoes: the mechanism of their interaction. Applied Physics and Mathematics, No. 6, 2016, 57-64.
- [4] Rukhadze AA, Khavroshkin OB, Tsyplakov VV Periodicity of natural radioactivity // Engineering Physics. 2015. № 6. P. 26 ... 36
- [5] Nikolaev AV, Khavroshkin OB, Tsyplakov VV Structure of the Strophysical Component of Seismic Emission and Noise // Engineering Physics. 2016. № 9. With. 68 ... 74

STEPWISE DEGASSING OF THE ORIGINAL GRAY MATTER OF THE METEORITE CHELYABINSK (LL5)

V.S. Fedulov¹, S.A. Voropaev¹, O.I. Yakovlev¹, N.V. Dushenko¹, S.G. Naimushin¹

¹*Vernadsky Institute of Geochemistry and Analytical Chemistry RAS
119991 Moscow, Kosygina 19, Russia, voropaev@geokhi.ru ;*

Keywords:

Small bodies, Chelyabinsk meteorite, stepwise heating, primary crust, atmospheres of the terrestrial planets, thermal metamorphism of meteorites.

Introduction:

It is known that the planets of the terrestrial group have a secondary atmosphere due to the degassing of the volatile components during and/or after the planetary accretion [1-3], the nature of the early terrestrial atmosphere being of particular interest, because it was in this atmosphere that the first life forms arose between 4.5 and 3.8 billion years ago [4]. But, unfortunately, the process of degassing of volatile from chondrites is largely unexplored. This process is important in the formation of the planetary crust, the thermal metamorphism of meteorites, the chemistry and mineralogy of asteroids, the discovery of exoplanets and many other modern problems of geo- and cosmochemistry [1] Thus, our experimental work was begun with the study of degassing of ordinary chondrites.

Experimental:

We performed a stepwise heating of the meteorite Chelyabinsk (LL5) and the study of the evolved gases by gas chromatography (GC), typical chromatogram on Fig. 1.

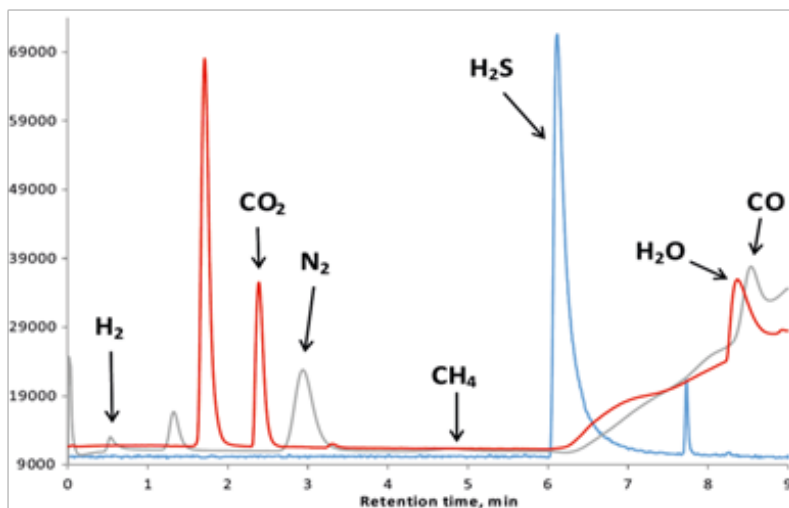


Fig. 1. Typical chromatogram in the study of degassing meteorite Chelyabinsk

To carry out this experiments and to ensure the conditions of a closed system, we created a device for burning small amounts of various samples shown. This furnace allows annealing of small quantities of samples with linear programming of temperatures from 25.0°C (room) to 1100.0°C in 25.0°C increments. A quartz high-temperature reactor allows us to supply any gas, as well as create vacuum conditions controlled by a manometer and a system of bypass valves.

We determined some simple volatile, such as: H₂, H₂O, N₂, CO, CO₂, CH₄ and H₂S. According to calculations from the work [5], these gases were in our temperature range. Step heating was carried out from 200°C to 800°C in steps of 100°C; at each heating stage, samples were taken for analysis

from 0 to 90 minutes in steps of 15 minutes to assess the features of thermal degassing. For the step degassing, 8 samples of the original gray matter of the meteorite Chelyabinsk were prepared. For all samples, the time and temperature dependences were also studied (Fig. 2).

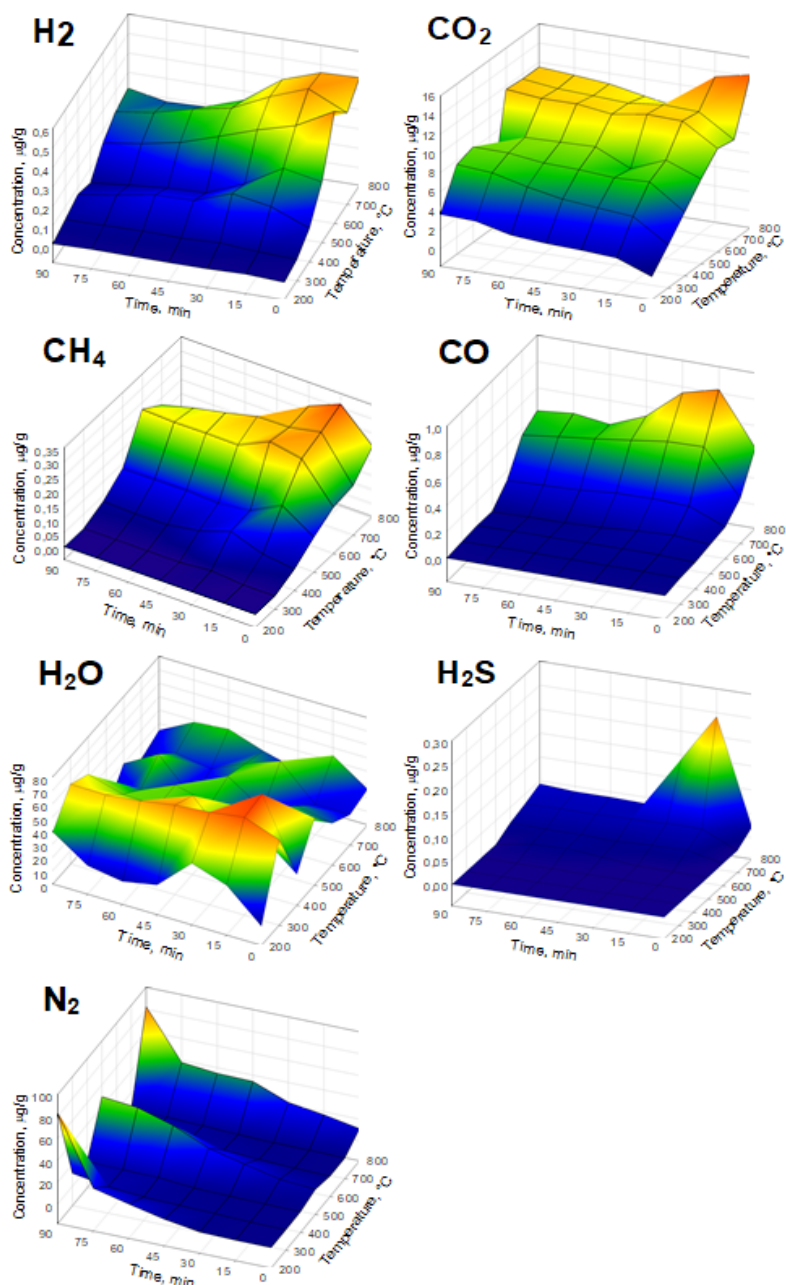


Fig. 2. Dependence of volatiles concentration on time degassing and temperature

Based on the experimental conditions, we made an assumption about the reactions taking place in this system. Based on this hypothesis, a thermodynamic calculation of 20 hypothetical reactions was carried out (in fact, there may be more of them). The calculation was based on the conditions for the search for a criterion for the reaction ($\Delta G < 0$) in the equilibrium state (Table 2).

Summary:

Because gases enter the surface of the cosmic body from the heated subsoil,

Table 2. Some possible reactions taking place in a closed system

No	Reaction	Notation*
1	$\text{CO}_2 + \text{H}_2 = \text{CO} + \text{H}_2\text{O}$	It is possible from 625°C
2	$\text{CH}_4 + 2\text{O}_2 = \text{CO}_2 + 2\text{H}_2\text{O}$	
3	$2\text{CO} + \text{O}_2 = 2\text{CO}_2$	
4	$2\text{H}_2 + \text{O}_2 = 2\text{H}_2\text{O}$	
5	$\text{CO} + \text{H}_2\text{O} = \text{H}_2 + \text{CO}_2$	It is possible to 850°C.
6	$2\text{CH}_4 + \text{O}_2 = 2\text{CH}_3\text{OH}$	In the wide temperature range, the formation of the first homologues of complex organic substances is possible!!!
7	$\text{CH}_4 + \text{O}_2 = \text{HCOH} + \text{H}_2\text{O}$	In the wide temperature range, the formation of the first homologues of complex organic substances is possible!!!
8	$\text{CH}_4 + \text{O}_2 = \text{HCOOH} + \text{H}_2$	In the wide temperature range, the formation of the first homologues of complex organic substances is possible!!!
9	$\text{CO}_2 + 4\text{H}_2 = \text{CH}_4 + 2\text{H}_2\text{O}$	It is possible to 600°C.
10	$\text{CO} + 3\text{H}_2 = \text{CH}_4 + \text{H}_2\text{O}$	It is possible to 625°C.
11	$2\text{CO} + 3\text{H}_2 = \text{HCOOH} + \text{CH}_4$	It is possible to 375°C.

*An empty cell indicates that this reaction can take place over a wider temperature range than 200-800°C. The oxygen involved in the calculated reactions most likely enters the closed system from oxides that decompose at a given temperature in the matrix of meteoritic matter (for example, P2O5).

we assume that this kind of “barbotage” of gases determined the conditions for the formation of the primary crust of planets of the Earth group and small bodies, thereby lowering its density. Also, during the cooling of the crust near the surface, the formation of a primary atmosphere and the first homologues of oxygen-containing organic substances (alcohols, aldehydes, acids) could occur.

Acknowledgment:

This work was supported by a Russian Science Foundation (RSF) grant, project № 17-17-01279

References:

- [1] Prinn, R.G., Fegley Jr., B. The atmospheres of Venus, Earth, and Mars: A critical comparison // *Ann. Rev. Earth Planet. Sci.* 1987. V. 15. P. 171–212.
- [2] Lange, M.A., Ahrens, T.J. The evolution of an impact-generated atmosphere // *Icarus*. 1982. V. 51. P. 96–120.
- [3] Lewis, J.S., Prinn, R.G. *Planets and Their Atmospheres: Origin and Evolution*. Academic Press, New York. 1983. 480 p.
- [4] Oró, J., Miller, S.L., Lazcano, A. The origin and early evolution of life on Earth // *Annu. Rev. Earth Planet. Sci.* 1990. V. 18. P. 317–356.
- [5] Schaefer L., Fegley B. Jr. Outgassing of ordinary chondritic material and some of its implications for the chemistry of asteroids, planets, and satellites // *Icarus*. 2007. V. 186. P. 462-483.

ACCESSING ICY MOON'S OCEAN WITH THERMONUCLEAR REACTOR

P.E. Laine

Departments of Physics and Computer Science and Information Systems, P.O. Box 35, FI-40014 University of Jyväskylä, Finland, pauli.e.laine@jyu.fi;

Keywords:

Icy moons, subsurface ocean, astrobiology, extraterrestrial life, thermonuclear reactor.

Introduction:

The icy moons (e.g. Europa and Enceladus) present some of the promising examples of extended habitable locations in our Solar System. Some of them seem to have potential ocean that could support life.

The primary goal for astrobiology is to find life somewhere else in the Universe. How could we detect biosignatures on icy moons, if we cannot find them on the hostile surface or water plumes? The only solution is to go somehow under the ice and explore the ocean beneath.

Challenges in Accessing the Ocean:

Accessing ocean under ice in remote moon to explore possible biosignatures seems overwhelmingly difficult. We don't even know how thick the icy shells are. It is estimated, that in e.g. Europa the ice is around 15 to 25 km thick [1]. It takes 35 to 52 minutes to send radio signals from Europa to Earth, so any exploration vehicle should be autonomous in all its activities. As these icy moons are in high priority for astrobiology, all vehicles flying-by or landing them should be extremely sterilized in order not to contaminate the target.

Using Thermonuclear Penetrator:

One obvious way to penetrate ice is to melt it. And that would need a lot of energy. On the remote moon, there is only one adequate energy source available today: fission. Thermonuclear reactors are relatively simple nuclear reactors that could be used for providing needed energy to get to ocean. For this purpose, we can do rough estimates about the size of the reactor by using information and estimates about the thickness of the ice cover, diameter of the penetrator (these give us the amount the ice), and the temperature of the ice.

Nuclear reactors have already flown in space. For example, Soviet TOPAZ reactors demonstrated that nuclear reactors could provide steady power for years.

In this presentation, I will present general model of thermonuclear penetrator for accessing oceans beneath icy shells, and also some existing plans and test results of using nuclear energy for ice drilling.

References:

[1] NASA Frequently Asked Questions about Europa // 2012, <http://solarsystem.nasa.gov/europa/faq>.

RETRIEVAL OF SURFACE PROPERTIES USING POLARIZATION AND INTENSITY OF LIGHT REFLECTED BY ATMOSPHERELESS CELESTIAL BODIES

E.V. Petrova¹, V.P. Tishkovets^{2,3}

¹Space Research Institute, Moscow, Russia, epetrova@iki.rssi.ru

²Institute of Radioastronomy, Kharkiv, Ukraine, tishkovets@rian.kharkov.ua

³V.N. Karazin Kharkiv National University, Kharkiv, Ukraine

Keywords:

atmosphereless celestial bodies, polarimetry, photometry, radiative transfer, coherent backscattering, shadow hiding

Introduction:

A potential of the reflectance model developed in [1-4] for interpreting polarimetric and photometric observations of atmosphereless celestial bodies is demonstrated by the example of Saturn's moon Rhea. In the model, the noncoherent (diffuse) and coherent components of radiation scattered by a random discrete medium are considered. These components are calculated within the theories of vector radiative transfer and weak localization, respectively. To take the near-field effects into account, randomly oriented clusters of spherical particles are considered as an elementary volume of the medium. As shown in [1, 2] by comparison to laboratory measurements, such an approach works correctly for non-absorbing or weakly absorbing media. Though a range of phase angles available for observations of Saturn from the Earth is very narrow (less than 6°), some surface properties of its ice moons, Rhea and Enceladus, were estimated from the measured phase profiles of polarization: the concentration of scatterers in the medium, their smallest size, and the portion of the surface area generating the negative branch of polarization [4]. The main disadvantage of the proposed model is that it cannot take into account the macroscopic shadow-hiding effect, contributing to the brightness surge at small phase angles especially in low-albedo surfaces. Consequently, to check how adequately the proposed model may describe the phase profiles and spectra of the media composed of absorbing particles is of key importance.

Photometric observations:

For this purpose, we used the data obtained for Rhea in a wavelength range of 0.9 to 5 μm with the VIMS instrument onboard the Cassini spacecraft [5, 6] (Fig. 1). Our earlier estimates obtained for the surface of Rhea [4] from polarimetric ground-based measurements were also invoked for modeling.

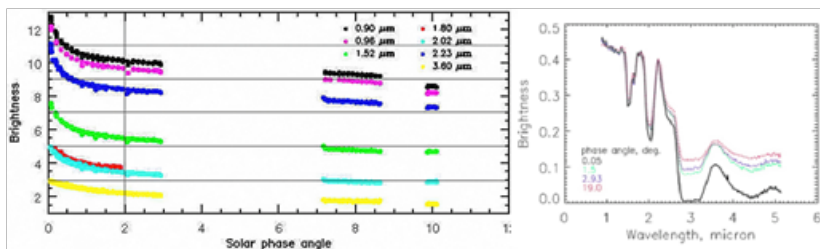


Fig. 1. The phase profiles of brightness (at several wavelengths) (left) [5] and the spectra (at several phase angles, shifted to match the continuum at the short wavelengths) (right) [6] of Rhea measured by the VIMS/Cassini instrument.

It is clearly seen from Fig. 1 that the depth of the absorption bands decreases as the phase angle increases from 0.05° to 19°, which is consistent with the expectations from the coherent-backscattering (CB) effect [6]: the brightness curve becomes steeper, as phase angles get smaller, and the difference between the results for the wavelengths outside the absorption bands (more influenced by this effect) and those inside the absorption bands gets larger.

Simulations for the spectra and phase profiles:

Our numerical simulations (Fig. 2) showed that the agreement between the measured and modeled spectra of Rhea is qualitative rather than quantitative and the spectra, as well the phase profiles (see below), are more sensitive to the scatterers' concentration in the medium rather than to the clusters' properties.

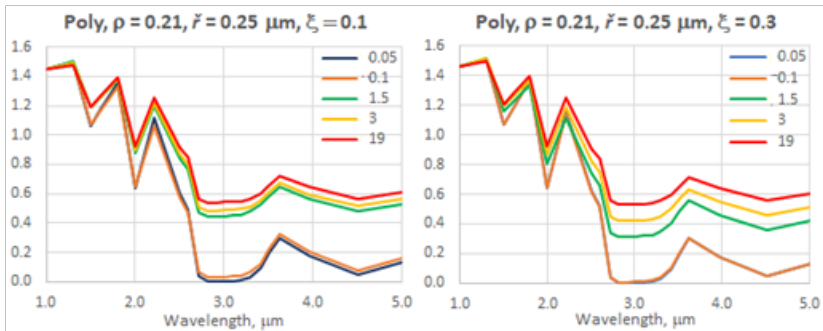


Fig. 2. Examples of the modeled spectra of Rhea for several phase angles (see legend). The mean concentration of scatterers in the medium is 0.1 (left) and 0.3 (right). Polydisperse water-ice clusters with the mean radius of constituents $0.25 \mu\text{m}$ and the packing density 0.21 were used in these simulations.

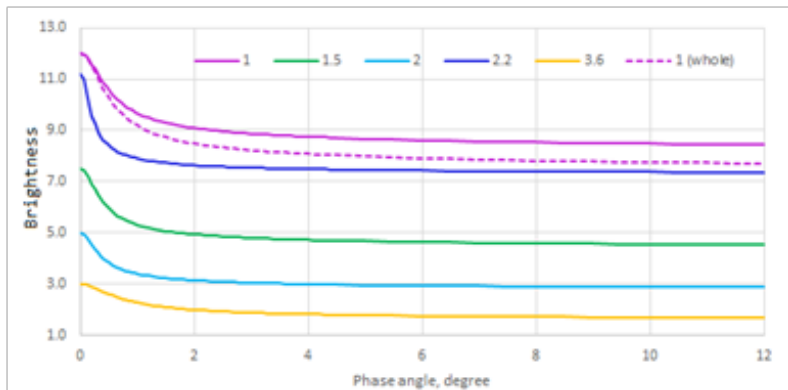


Fig. 3. Examples of the modeled phase profiles of Rhea for several wavelengths (see legend). The mean concentration of scatterers in the medium is 0.15. Only a portion of the surface (22%) is assumed to participate in the coherent backscattering. The model shown dashed ($\lambda=1 \mu\text{m}$) considers the whole surface of Rhea as participating in CB.

From modeling the phase profiles of brightness of Rhea, it was found that, to fit the low-absorption profiles, it is important to take into account the fact that only a portion of the satellite's surface is dispersed enough to participate in CB (Fig. 3). For this, we used the estimate of this portion (22%) obtained earlier from modeling the polarization phase profiles measured from the Earth [4]. At the same time, the model satisfactorily describes the profiles with higher absorption, for which CB is not important. The agreement between the measured and modeled phase profiles remains not perfect due to the shadow-hiding (SH) effect that is beyond this model. However, if the disperse surface portion is known, the relative contribution of the SH effect to the brightness at opposition can be estimated from the simulations. This contribution was determined as almost half the CB input at the wavelengths with low absorption, while these effects are comparable for darker surfaces.

Polarimetry of dark surfaces:

To verify whether the proposed model can adequately describe the phase profiles of polarization for the medium composed of absorbing particles, we calculated such profiles and compared them to the data of astronomical observations. It turned out that the increase in absorption and packing density yields the phase profiles of polarization resembling those of low-albedo surfaces (Fig. 4).

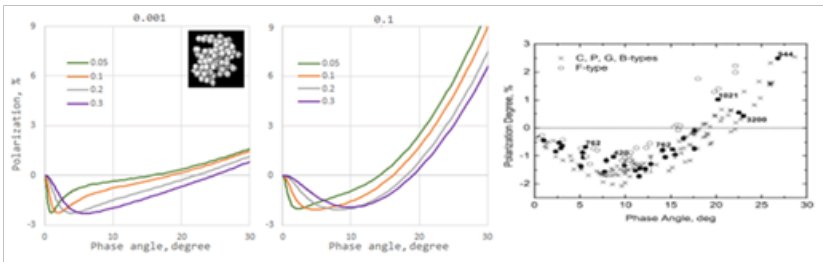


Fig. 4. Examples of the polarization phase profiles calculated for the medium composed of absorbing clusters (the imaginary part of the refractive index is 0.001 and 0.1; the structure is shown in the inset) for several values of the mean concentration of scatterers in the medium (see legend). The size parameter of the cluster's constituents is 1.5, their number is 100, and the real part of the refractive index is 1.55. The polarization measured in low-albedo asteroids versus the phase angle [7] (right) is shown for comparison.

Summary:

The proposed model can be successfully applied to retrieving the primordial parameters of high-albedo surfaces from the polarization phase profiles and shows a good potential in interpreting the polarization data of low-albedo objects. To estimate reliably the surface properties of celestial bodies, the fact that only a portion of the surface participates in CB should be taken into account.

Since the model ignores the SH effect, which is important for the brightness phase profiles, only qualitative rather than quantitative agreement can be obtained for the intensity profiles and spectra (especially for relatively compact media). However, the relative contribution of the SH effect to the brightness at opposition can be estimated from the phase profiles, if the disperse surface portion is known.

The absence of laboratory measurements of characteristics of light reflected by low-albedo samples with reliably controlled parameters (the shape, size, refractive index, and packing density of particles) does not allow us to specify the limits of applicability of the described model. At the same time, we suppose that observations of mid-albedo objects can be interpreted with this approach at least at qualitative level.

References:

- [1] Tishkovets V.P. et al. Scattering of electromagnetic waves by ensembles of particles and discrete random media // JQSRT. 2011. V. 112. P. 2095-2127.
- [2] Tishkovets V.P., Petrova E.V. Coherent backscattering by discrete random media composed of clusters of spherical particles // JQSRT 2013. V. 127. P. 192-206.
- [3] Tishkovets V.P., Petrova E.V. On applicability of the far-field approximation to the analysis of light scattering by particulate media // JQSRT 2016. V. 182. P. 24-34.
- [4] Tishkovets V.P., Petrova E.V. Reflectance model for densely packed media: estimates of the surface properties of the high-albedo satellites of Saturn // Sol. Syst. Res. 2017. V. 51. P. 277-293.
- [5] Buratti B.J. et al. Opposition surges of the satellites of Saturn from the Cassini Visual Infrared Mapping Spectrometer (VIMS) // Proceedings of the 40th LPSC. 2009. P. 1738.
- [6] Kolokolova L. et al. Impact of coherent backscattering on the spectra of icy satellites of Saturn and the implications of its effects for remote sensing // Astrophys. Journal Letters. 2010. V. 711. L71-L74.
- [7] Fornasier S. et al. Polarimetric survey of asteroids with the Asiago telescope // Astron. Astrophys. 2006. V. 455, P. 371-377.

ASTEROIDS: SPECTRAL PROPERTIES OF POLARIZATION DEGREE

L. F. Golubeva, D.I. Shestopalov

Shemakha Astrophysical Observatory, Shemakha AZ-3243, Azerbaijan

Keywords:

Asteroids, polarization degree, spectral dependences

In the early twentieth century, Russian physicist N. A. Umov found that the partial polarization resulting from the reflection of non-polarized light has the largest value at the maximum absorption [1, 2]. In planetary physics, inverse correlation between polarization degree and albedo in visible light is well-known for the Moon and asteroids and highly likely for other atmosphereless Solar System bodies. At the same time, there is opinion that the Umov effect can sometimes be violated for asteroid surfaces when varying the polarization degree with a wavelength. As noted in [3] asteroids of S and M types reveal a deeper negative branch with increasing wavelength. The same asteroids exhibit reddish reflectance spectra (i.e. albedo rises when wavelength increases), and so the spectral behavior of negative polarization appears to contradict the inverse correlation of P_{min} and albedo. For low-albedo asteroids, polarization decreases with increasing wavelength, "breaking" Umov law too, because the spectra of these asteroids are "flat", and it would seem polarization should not depend on the wavelength. Since spectral variations of negative polarization in the range of 0.37 – 0.83 μm are a subtle effect (no more than 0.5%), it is not surprising that various groups of researchers come to ambivalent conclusions. For instance, the authors [3] claim that the wavelength dependence of asteroid polarization has a tendency to become more pronounced for increasing phase angles up to 30–40°. Whereas in the works [4, 5], it is stated that the slope of the spectral dependence of asteroid polarization changes its sign upon transition from a negative branch of polarization phase curve to a positive one. The general circumstance, which unites above-cited works, is that the spectral slopes of polarization degree were investigated only at several phase angles, which correspond to the moments of observations. In other words, these phase angles were established not by investigator but by a case, and the same case can affect the final conclusions.

In order to see the big picture, the polarization spectral slope distribution by the phase angles needs to be taken into account in analyzing the polarization spectral behavior. We use $\Delta|P|/\Delta\lambda = (|P(\lambda_1, \alpha)| - |P(\lambda_2, \alpha)|)/(\lambda_1 - \lambda_2)$ as a characteristic of the spectral slope of polarization degree in the range of $\Delta\lambda$, $\lambda_1 > \lambda_2$, against the phase angle α . In fact, the problem is reduced to investigating the difference between the phase polarization curves of asteroids obtained at different wavelengths. To calculate these polarimetric curves, we use the approximating function [6], which has proved to be a good tool to operate with asteroids and comets [7, 8]. The approximating function at phase angles $\alpha < 30\text{--}40^\circ$ depends on three parameters (Eq.(5) in [7]). They are the inversion angle α_{inv} (i.e. the phase angle, where the polarization degree changes sign); the polarimetric slope $h = dP/d\alpha$ at $\alpha = \alpha_{inv}$; power exponent m , which describes the asymmetry of the negative branch of the polarimetric curve.

Figure 1 shows the calculation of the phase dependencies of $\Delta|P|/\Delta\lambda$ using the average parameters $\langle h \rangle$, $\langle \alpha \rangle$, and $\langle m \rangle$ at different wavelengths for E, S, M, and C asteroid optical types. All the necessary data for such calculations are concentrated in Table 1 published in [7]. The spectral range in this approach is limited by the conditions of selecting the most reliable polarimetric observational data.

E-type (BGV bandpasses). The positive slope (+slope) of the polarization spectral dependence has a maximum in the P_{min} region. For $\alpha > 20^\circ$ the polarization degree is weakly dependent on the wavelength, i.e. the spectral slope of polarization is about zero. The inversion angles of the function of the spectral slope are close to α_{inv} of the initial polarimetric curves. **S-type**

(*UBGV bandpasses*). The “+slope” occurs in the range of negative polarization branch, whereas the polarization spectral slope changes sign for $\alpha > 20^\circ$. In this part we confirm the conclusion about the variations of polarization spectral slope obtained earlier [4, 5]. *M-type (UBGV bandpasses)*. There are a weak “+slope” near $\alpha \approx 5^\circ$ and the slope \sim zero near α_{min} . The polarization spectral slope becomes negative and begins to grow at $\alpha \rightarrow 20^\circ$. The slope again becomes positive in the range of $20\text{--}25^\circ$. *C-type (UBGV bandpasses)*. The most complicated $\Delta|P|/\Delta\lambda$ curve of the presented. There are several regions of inversion of the polarization spectral slope: the “+slope” with a maximum near 5° , and the “-slope” with a maximum near 18° . Then again, the “+slope” with a peak near 20° and the “-slope” for $\alpha > 26^\circ$. Three inversion angles of spectral slopes are present, and two of them (close to 10 and 26°) do not coincide with the inversion angles of the polarization phase curves.

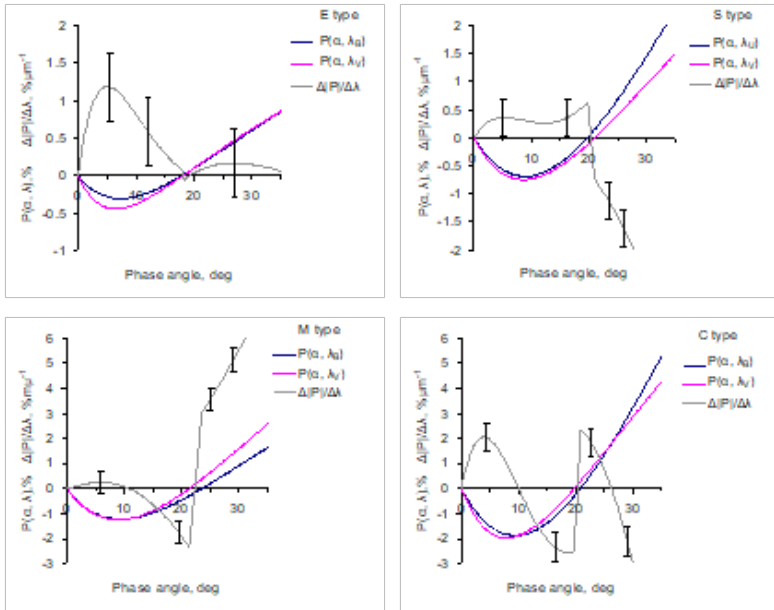


Fig.1.

We conclude that (i) the shape of the curves of polarization spectral slope is distinct for different asteroid optical types and strongly depends on the parameters of “monochromatic” polarimetric functions (h, α_{inv}, m) and (h, α_{inv}, m); (ii) the phase curves of the spectral slope may have several inversion sign, at which the slope changes sign. One of the angles necessarily lies in the interval $(\alpha_{inv})_i - (\alpha_{inv})_j$, others correspond to the angles of intersection of the “monochromatic” phase polarization functions; (iii) in the case of spectral polarization, there is a violation of the tendency “the higher polarization the lower albedo” since the slopes of asteroid spectrum reflectivity curves (unpolarized light) slightly monotonically grow with increasing the phase angle and is not accompanied by a change in the sign.

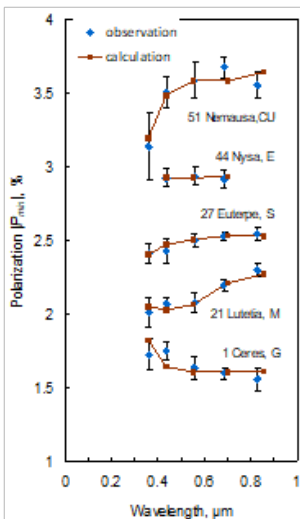


Fig.2.

To understand the latter assertion, let us take into account that the polarimetric color index $P_{min}(\lambda/\lambda_0) = P_{min}(\lambda)/P_{min}(\lambda_0)$ and spectral

color index $C(\lambda/\lambda_0) = R(\lambda)/R(\lambda_0)$ are inversely connected variables [9]: $P_{min}(\lambda/\lambda_0) = a + b/C(\lambda/\lambda_0)$, where $R(\lambda)$ is reflectance and $\lambda_0 = 0.55 \mu\text{m}$. For a number of asteroids with known $P_{min}(\lambda_0)$ and $C(\lambda/\lambda_0)$, we was able to estimate a and b parameters in order to calculate $P_{min}(\lambda)$. As shown in Fig.2, the calculations are in a good agreement with the observation data. This supports the fact that a main cause of changing $P_{min}(\lambda)$ is spectral variation of color index $C(\lambda/\lambda_0)$ rather than spectral albedo. If so, the spectral analog of Umov effect can actually be violated for asteroid regoliths at least in the range of phase angles corresponding to the negative polarization degree.

References:

- [1] Shpol'skij E.V. Nikolaj Alekseevich Umov (1846 – 1915) // Phys. Usp. 1947. V. XXXI. No. 1. P. 129–146.
- [2] Umov N. A. Chromatische depolarisation durch Lichtzerstreuung // Physik. Z. 1905. V. 6. P. 674–676.
- [3] Belskaya I.N., Levasseur-Regourd A-Ch., Cellino A. et al. Polarimetry of main belt asteroids: Wavelength dependence // Icarus 2009. V.199. P. 97–105.
- [4] Gil-Hutton R., Cellino A., Bendjoy Ph. Polarimetric survey of main-belt asteroids. IV. New results from the first epoch of the CASLEO survey // Astron. and Astrophys. 2014. V. 569. Id.A122. P. 1–6.
- [5] Lupishko D.F., Shkuratov Yu.G. On spectral dependence of polarization of asteroids // Solar Sys. Res. 2016. V. 50. No. 5. P. 329–336.
- [6] Shestopalov D. Approximation formula for polarization of the light scattered by particulate surfaces: an application to asteroids // J. Quant. Spectrosc. Radiat. Transfer 2004. V. 88. P. 351–356.
- [7] Shestopalov D.I., Golubeva L.F. Polarimetric properties of asteroids // Adv. in Space Res. 2015. V. 56. P. 2254–2274.
- [8] Shestopalov D.I., Golubeva L.F. About a linear polarization of comets: The phase-angle dependences of polarization degree // Adv. in Space Res. 2017. V. 59. P. 2658–2274.
- [9] Golubeva L.F., Shestopalov D.I. Polarized light scattered from asteroid surfaces. VII. New insight into the effect of the wavelength dependence of negative polarization degree // 47th Lunar Planet. Sci. Conf. 2016. Abstr. # 1069.

OBSERVATIONAL EVIDENCES AND POSSIBLE DYNAMICAL REASONS OF SUBLIMATION ACTIVITY OF PRIMITIVE ASTEROIDS IN THE MAIN-BELT

V.V. Busarev¹, S.I. Ipatov²

¹*Sternberg State Astronomical Institute, Moscow Lomonosov State University (SAI MSU), 13 Universitetskij av., Moscow 119992, Russian Federation (RF), busarev@sai.msu.ru;*

²*Vernadsky Institute of Geochemistry and Analytical Chemistry of RAS, Moscow, RF, siipatov@hotmail.com*

Keywords:

spectrophotometry of asteroids, ice content in the matter, temperature and other conditions, sublimation of ices, origin and dynamical evolution of asteroids and their parental bodies

Introduction:

We have discovered spectral signs of a strong simultaneous sublimation activity of main-belt primitive asteroids 779 Nina, 704 Interamnia, and 145 Adeona at their passages of perihelion in 2012 (Figs 1-3) [1-3]. The main features is unusual shape of their reflectance spectra with a maximum near 0.50 μm as a manifestation of reflected light scattering in a coma of micron-size icy dust particles [2, 3]. The periodic nature of the process on the asteroids is confirmed at their next passages of perihelion in 2016-2018 with the same spectral and *UBVRI*-photometric methods [3, 4]. Due to eccentricity of the orbits, the asteroids undergo changes of subsolar temperatures with revolution around the Sun ($\sim 222\div 257$ K on Adeona, $\sim 206\div 240$ K on Interamnia, and $\sim 208\div 262$ K on Nina) and elevated water ice content in the matter is probably a source of the sublimation activity [3]. We suggest that it may be a widespread phenomenon among primitive asteroids and is explained by their common origin. However, it contradicts previous notions that primitive asteroids include water only in a bound state (e. g., [5]).

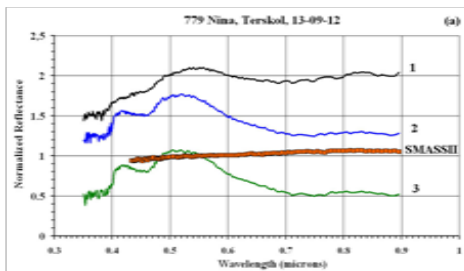


Fig. 1.

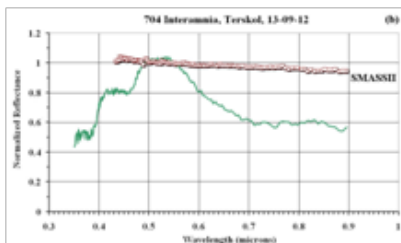


Fig. 2.

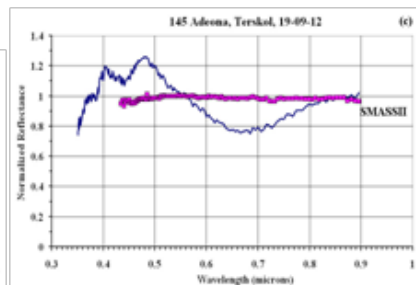


Fig. 3.

A background:

For asteroids of primitive types (with low-temperature mineralogy), the

question of the ice content in the composition of their matter has so far been poorly studied due to a number of limitations. At heliocentric distances, possibly from 3 to 5 AU, there were significant variations of volatile compounds' content in the matter of planetesimals and parent bodies of asteroids. Physico-chemical conditions in the zone corresponding to the periphery of the present main asteroid belt (MBA) might have been influenced by not only the temperature gradient in the protoplanetary disk but also on the luminosity variations of the early Sun (e. g., [6, 7]). On the other hand, as it was shown by V. S. Safronov [8], at the process of growth of proto-Jupiter, when its mass exceeded several masses of the Earth, inevitably there was ejection of smaller rock ice bodies from its formation zone in different directions, including MBA [8]. So, another mechanism could be delivery of ice compounds from the periphery of our planetary system. On this basis, we have proposed a hypothesis about the origin of C-types asteroids and close to them bodies as fragments of stone ice pre-planetary bodies from the accumulation zone of Jupiter and other giant planets [9]. To verify the suggestion, as a first step we performed numeric modeling of migration of planetesimals from the outer Solar system and estimate probability of their collisions with asteroid parent bodies and delivery of ice material to MAB.

Probabilities of collisions of planetesimals with asteroids:

Several series of calculations of migration of planetesimals under the gravitational influence of planets (from Venus to Neptune) have been made. The symplectic code from the Swift integration package [10] was used. Integrations were made until planetesimals reached 2000 AU or collided with the Sun. In the Table we present the values of the probability p_a of a collision of one planetesimal with an asteroid with a semi-major axis a_{ast} equal to 2.3, 2.5, 2.8, or 3.1 AU for the run with 250 planetesimals with initial semi-major axes from a_o to $a_o+2.5$ AU. A diameter of an asteroid equaled to 1000 km, and a density equaled to that of Ceres ($2.16 \text{ kg}\cdot\text{dm}^{-3}$). The eccentricity and inclination of the orbit of an asteroid were close to those for Ceres: 0.1 and 10° , respectively. For different runs, a_o varied from 5 to 40 AU. Initial eccentricities e_o and i_o inclinations equaled to 0.3 and 0.15 rad, respectively. Such eccentricities could be reached due to mutual gravitational influence of planetesimals during evolution of a disk of planetesimals in the feeding zone of the giant planets [11]. The algorithms of calculations of p_a based on arrays of orbital elements of migrating bodies were discussed in [12] and corrections made in [13].

Table 1. Values of $10^8 p_a$, where p_a is the probability of a collision with an asteroid with semi-major axis a_{ast} equal to 2.5, 2.8, or 3.2 AU for one planetesimal for the run with planetesimals with semi-major axes from a_o to $a_o+2.5$ AU, $e_o=0.3$, $i_o=0.15$ rad. Two series of runs are for the same a_{ast} .

$a_{ast} \setminus a_o$	5.	7.5	10.	15.	20.	25.	30.	35	40
2.3	0.48	0.34	0.88	0.94	0.57	0.09	0.10	0.17	0.33
2.3	2.1	0.18	0.82	0.49	0.08	0.06	0.18		
2.5	0.51	0.85	1.9	1.4	1.1	0.09	0.14	0.56	0.73
2.5	2.3	0.42	0.56	0.39	0.20	0.13	0.14		
2.8	0.49	1.1	1.6	0.66	1.1	0.09	0.15	0.70	0.84
2.8	5.4	0.77	0.76	0.88	0.23	0.15	0.11		
3.1	0.82	0.98	1.9	4.0	1.3	0.21	0.11	0.31	1.0
3.1	3.3	0.49	1.2	0.72	0.21	0.17	0.17		

For runs with 250 initial bodies differed by only initial orientations of their orbits there could be differences in the values of p_a due to that a few bodies in a run could have higher probabilities than most other bodies. The values of p_a presented in the Table were of the order of 10^{-8} at $a_o \leq 15$ AU, were on average about 10^{-9} - $2 \cdot 10^{-9}$ at $25 \leq a_o \leq 30$ AU, and were a few 10^{-9} at a_o equal to 20, 35

and 40 AU. Typically p_a was smaller at $a_{\text{ast}}=2.3$ AU than for greater considered values of a_{ast} . At $p_a=10^{-8}$ and the total mass of planetesimals migrated from beyond Jupiter's orbit equal to $100M_E$ (where M_E is the Earth mass), the total mass of planetesimals collided with an asteroid of a diameter of 1000 km will be $10^{-6}M_E$, i.e. two orders of magnitude smaller than the mass of the asteroid ($1.89 \cdot 10^{-4}M_E$). The total mass of planetesimals delivered to the asteroid belt from the feeding zones of Uranus and Neptune could be smaller by a factor of several than that from the feeding zone of Jupiter and Saturn. For large eccentricities of planetesimals reaching the asteroid belt, the effective radius of an asteroid of mass m_a is proportional to the asteroid radius, and p_a is proportional to $m_a^{2/3}$. Such dependence was also obtained in our calculations. If diameters of asteroids differ by a factor of 10, then p_a differ by a factor of 100. However, for such model, the value of p_a for a 1000 km asteroid will be smaller by a factor of 10 than the total probability of 100 km asteroids of the same mass.

Conclusions:

Thus, our calculations confirm delivery of ice material to the outer MAB from heliocentric distances corresponding mainly to the formation zone of Jupiter and Saturn (see Table, last three lines with highest values of $10^6 p_a$).

References:

- [1] Busarev V.V. et al. *Icarus*. 2015. V. 262. P. 44-57.
- [2] Busarev V.V. et al. *Solar Sys. Res.* 2016. V. 50. P. 281–293.
- [3] Busarev V.V. et al. *Icarus*. 2018. V. 304. P. 83-94.
- [4] Busarev V.V. et al. 2018. This book of abstracts.
- [5] Gaffey M.J., et al. In: *Asteroids II* / Eds Binzel R. P. et al. Tucson: Univ. of Arizona Press. 1989. P. 98-127.
- [6] Lewis J. S. *Science*. 1974. V. 186. P. 440-442.
- [7] Makalkin A.B., Dorofeeva V.A. *Solar Sys. Res.* 2009. V. 43. P. 508–532.
- [8] Safronov V.S. *Evolution of the protoplanetary cloud and the formation of the Earth and planets*, M: Nauka. 1969. 244 p. (in Russian) [NASA TTF-667 Engl. transl., 1972].
- [9] Busarev V.V. Proc. of the conf. "ACM 2012" Niigata, Japan. 2012. Abs. #6017 (<https://arxiv.org/ftp/arxiv/papers/1211/1211.3042.pdf>).
- [10] Levison H. F., Duncan M.J. *Icarus*. 1994. V. 108. P. 18-36.
- [11] Ipatov S.I. *Earth, Moon, and Planets*. 1987. V. 39. P. 101-128.
- [12] Ipatov S.I. *Soviet Astron.* 1988. V. 65. P. 1075-1085.
- [13] Ipatov S.I., Mather J.C. *Earth, Moon, and Planets*. 2003. V. 92. P. 89-98 (<http://arXiv.org/format/astro-ph/0305519>).

COMPARATIVE STUDY OF ORBITAL PARAMETERS AND MAGNITUDE OF SHORT AND LONG PERIOD COMETS

D. Asgarian

International Occultation Timing Association Middle East Section (IOTA/ME), dorsaasgarian@gmail.com

Keywords:

Comets, Short period, Long period, Magnitude, Phase

Introduction:

We use several parameters to compare short and long period comets. Short-period comets with perihelion distance greater than 2 AU have a magnitude distribution index of about 2.3, similar to that of the long period comets.

In this research, the relevance between the Cometary phase and magnitude is examined and we used Occult4 to extract data.

Since the orbit of the long period is higher, we expect it to be lighter and the short period is dimmer.

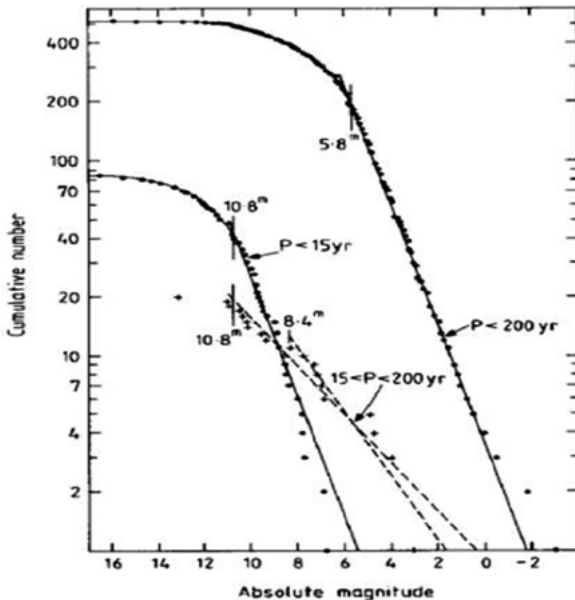


Fig. 1. The cumulative number (log scale) of short period.

The cumulative number (log scale) of short period and long-period comets plotted as a function of their absolute magnitudes, H_t0 (see Fig. 1). The line through the $P < 15$ -year data has purposefully been chosen to have the same gradient as the line through the $P > 200$ -year data. The fit is good. The magnitude at which the curves break away from linearity is clearly different. The intermediate-period comets (+) have a much lower a value than the previous two groups and the position of the break from linearity is less distinct [2].

References:

- [1] David W. Hughes, The magnitude distribution and evolution of short-period comets, 2002
- [2] DAVID W. HUGHES, Cometary Magnitude Distribution and the Ratio between the Numbers of Long- and Short-Period Comets, 1987

MODELS OF THE JOVIAN MAGNETODISC VS. JUNO MAGNETOMETER DATA

I.A. Pensionerov¹, E.S. Belenkaya¹, I.I. Alexeev¹

¹Lomonosov Moscow State University, Skobeltsyn Institute of Nuclear Physics (SINP MSU), 1(2), Leninskie gory, GSP-1, Moscow 119991, Russian Federation

Keywords:

Planetary magnetospheres, magnetodisc, Jupiter, Juno mission.

Introduction:

A noticeable feature of the largest in the solar system magnetosphere of the Jupiter is its disk-like plasma sheet located near the magnetic equator of the planet. It contains azimuthal and radial currents related to dynamic of the plasma inside the sheet and magnetosphere-ionosphere coupling.

Many models describing structure of the magnetodisc were constructed to date. In the paper [1] Connerney et al. proposed empirical model of the magnetodisc. In that model a disc was located in the magnetic equator, had an inner and outer radii and fixed thickness. The current density was proportional to r^{-1} , where r is a distance from the magnetic dipole axis. Semi-empirical global magnetic model of the Jovian magnetosphere by Alexeev and Belenkaya [2] included its own model of the magnetodisc with infinitesimal thickness and current proportional to r^{-1} . In the present work we also use modified version of [1] model with combined r^{-1} and r^{-2} current density dependency.

Model proposed by Goertz et al. in [3] was constructed by an Euler potential approach. This model incorporated the sweep-back of the magnetic field lines. In the work [4] Khurana introduced a description of the current sheet warping and proposed [5] the model taking the warp into account, based on the [3] model.

Caudal in the work [6] presented a self-consistent force-balance based model, taking into account centrifugal force and isotropic plasma pressure. In the [7,8] researches Nichols et al. included anisotropic plasma pressure in the Caudal model.

A large amount of new data was collected by Juno mission. We use Juno magnetometer data to test different models of Jovian magnetodisc and find their strengths and weaknesses.

Acknowledgements.

The MAG data was obtained from Planetary Data System (PDS). Instrument scientist of FGM – J. E. P. Connerney. Principal investigator of Juno mission – Scott J. Bolton.

Work was partially supported by the Ministry of Education and Science of the Russian Federation (grant RFMEFI61617X0084).

References:

- [1] Connerney, J. E. P., Acuña, M. H., and Ness, N. F.: Modeling the Jovian current sheet and inner magnetosphere // *Journal of Geophysical Research: Space Physics*. 1981. 86, 8370–8384
- [2] Alexeev, I. I. and Belenkaya, E. S.: Modeling of the Jovian Magnetosphere // *Annales Geophysicae*. 2005. 23, 809–826
- [3] Goertz, C. K.: The current sheet in Jupiter's magnetosphere, *J. Geophys. Res.* 1976. 81(19), 3368–3372
- [4] Khurana, K. K.: A generalized hinged-magnetodisc model of Jupiter's nightside current sheet // *J. Geophys. Res.* 1992. 97, 6269
- [5] Khurana, K. K.: Euler potential models of Jupiter's magnetospheric field // *Journal of Geophysical Research: Space Physics*. 1997. 102, 11 295–11 306
- [6] Caudal, G.: A self-consistent model of Jupiter's magnetodisc including the effects of centrifugal force and pressure // *Journal of Geophysical Research*. 1986. 91, 4201
- [7] Nichols J. D.: Magnetosphere-ionosphere coupling in Jupiter's middle magnetosphere: Computations including a self-consistent current sheet magnetic field model // *Journal of Geophysical Research: Space Physics*. 2011.
- [8] Nichols, J. D., Achilleos, N., and Cowley, S. W. H.: A model of force balance in Jupiter's magnetodisc including hot plasma pressure anisotropy, *Journal of Geophysical Research: Space Physics*. 2015. 120, 10,185–10,206

THE AMMONIA ABSORPTION IN THE JOVIAN GREAT RED SPOT

V.G. Tejfel, V.D. Vdovichenko, G.A. Kirienko, A.M. Karimov, P. G. Lysenko,
V.A. Filippov, G.A. Kharitonova, A.P. Khozhenetz
Fesenkov Astrophysical Institute, Almaty, Kazakhstan

Keywords:

Jupiter, Great Red Spot, atmosphere, clouds, spectrophotometry, ammonia, methane, absorption bands, thermal emission

Introduction:

We investigated the behavior of the 645 and 787 nm ammonia (NH_3) absorption bands in the Great Red Spot (GRS) region. We found that these ammonia bands are visibly weakened in the GRS in comparison with the surrounding regions. In terms of magnitude, this depletion is comparable to the previously observed [1] depression of the 787 nm NH_3 band intensity in the Northern Equatorial Belt (NEB). However, a comparison with the results of observations of Jupiter in the thermal IR, optical and millimeter radio emission of Jupiter, showed that the mechanism of ammonia depletion in GRS and in the NEB is not the same, but is determined by very different causes.

It is known from the infrared studies that the brightness temperature in the Spot at 4.8 μm is lower in comparison with the surrounding regions, which may indicate a higher density of clouds in it and the opacity for thermal infrared radiation coming from deeper layers. When observing Jupiter in the spectral ranges with strong methane absorption bands, the Great Red Spot looks like the brightest formation on the planet. The GRS special properties are also manifested in ammonia absorption in comparison with other regions of Jupiter.

The NH_3 absorption bands measurements

The main attention was paid to measurements of the profiles of the two (645 and 787 nm) NH_3 absorption bands and their intensities. Figure 1 shows the examples of the both ammonia band profiles obtained when processing one spectrogram of the Jupiter central meridian for all points of the meridian from the South Pole to the North one.

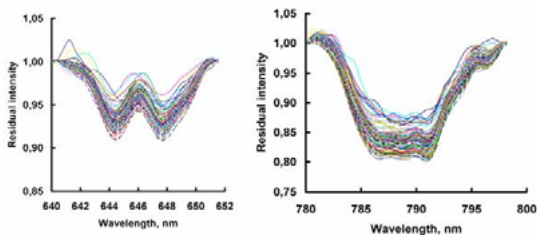


Fig. 1. The 645 and 787 nm NH_3 absorption band profiles, isolated from all the lines of the Jupiter central meridian spectrum.

According to the results of the spectrogram measurements of each cycle of observations during the GRS passage through the Jupiter central meridian, the graphs of latitudinal variations in the ammonia absorption band intensities are plotted. Figure 2 shows the graphs of the 645 and 787 nm NH_3 absorption band intensities along the central meridian from the measurements on April 19, 2017. The absorption profiles obtained in the longitudinal range of 240-310 degrees are averaged. The graphs separately show the profiles for the longitude of 272 degrees, corresponding to the middle of the Great Red Spot. The ammonia absorption depletion in the GRS stands out clearly.

To illustrate the differences in the meridional variations of the NH_3 absorption at different longitudes, the equivalent-width profiles of the 787-nm band are shown in Fig. 3 with a vertical shift per the scale unit. One can see that the absorption depression in the northern hemisphere extends over all longitudes, whereas in the southern hemisphere only the GRS region is manifested.

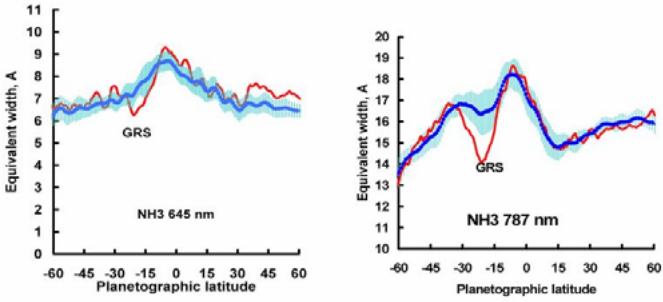


Fig. 2. Latitudinal variations in the 645 and 787 nm NH_3 absorption bands.

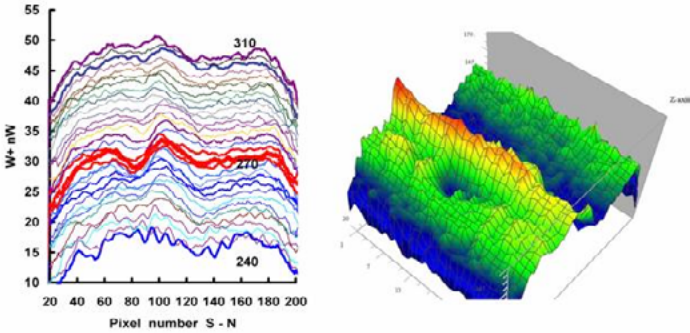


Fig. 3. Variations in the equivalent widths of the 787 nm NH_3 band (left); the 3D representation of the latitude-longitudinal variations of ammonia absorption (right).

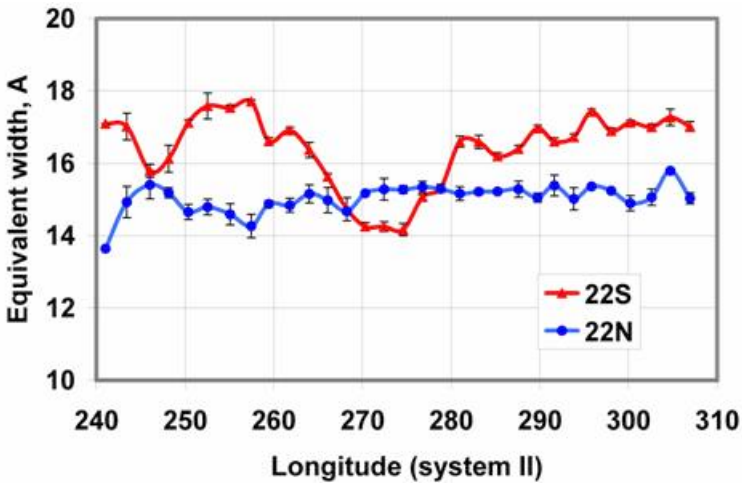


Fig. 4. Longitudinal variations of ammonia absorption at symmetrical latitudes in the SEB and NEB regions.

Figure 4 shows a systematic difference in the equivalent widths of the 787 nm NH_3 absorption band in these belts - depletion in the NEB, with the exception of the GRS, where the absorption is even smaller than in the NEB.

Discussion

Unlike the GRS, the NEB does not show an abnormal increase in brightness in the 887 nm CH_4 absorption band, while the depletion of ammonia absorption in the 645 and 787 nm NH_3 bands observed in the NEB [1], is comparable to that obtained for the GRS. The reason for this discrepancy, apparently, should be found in the difference in the structural features of the atmosphere and the clouds in these regions. For example, the radio measurements

[2] do not show such an increase in the brightness temperature in the GRS, as in the NEB, which is associated with a decrease in the ammonia gas abundance. Observations in the optical infrared range of Jupiter's thermal radiation also show a similar difference [3]. In the strong 887 nm CH_4 band, the absorption in the atmosphere above the clouds can play an even greater role than that is inside the clouds, since the number of acts in multiple scattering decreases with increasing the absorption coefficient. A sharp methane absorption decrease in the GRS is most likely due to that the upper boundary of the cloudiness in the Spot is higher than in its surroundings. The formation of the ammonia absorption bands occurs practically only within the cloud layer, since the NH_3 concentration above it becomes smaller by several orders of magnitude. It follows that the decrease in the intensity of the NH_3 absorption bands in the GRS occurs mainly because of the increased bulk density of the clouds inside it.

Acknowledgements

This research was carried out in accordance with the grants of MES RK 0073 / GF4 and AP05131266

References

- [1] Tejfel V.G., Karimov A.M., Vdovichenko V.D. Strange latitudinal variations of the ammonia absorption on Jupiter, Bulletin Amer // Astron. Soc., 37(3): 682 , 2005
- [2] Pater I., de Sault R.J., Butler B., de Boer D., Wong M.H. Peering through Jupiter's clouds with radio spectral imaging // Research Reports Gas Giant Planets, Science, 352: 1198-1201, ISSUE 6290 ,2016
- [3] Fletcher L.N., Orton G.S., Mousis O., Yanamandra-Fisher P., Parrish P.D., Irwin P.G.J., Edkins E., Baines K.H., Line M.R., Vanzi L., Fujiyoshi T., Fuse T. Jupiter's Great Red Spot // High-resolution thermal imaging from 1995 to 2008, Icarus, 208: 306-328 , 2010.

SUBMILLIMETER WAVE RADIOMETRY OF THE JOVIAN ICY MOONS' CRUST: NUMERICAL SIMULATIONS

Y.A. Ilyushin^{1,2,3}, P. Hartogh³

¹Moscow State University, 119992 Russia, ilyushin@phys.msu.ru;

²Institute of Radio-engineering and Electronics of RAS, Mokhovaya 11/7, Moscow, 125009, Russia ;

³Max-Planck-Institut für Sonnensystemforschung Justus-von-Liebig-Weg 3, Göttingen 37077 Germany hartogh@mps.mpg.de

Keywords:

Submillimeter waves, SWI, radiometry, radiative transfer, Ganymede

Introduction:

Galilean icy moons differ from most objects of the Solar System in several respects. Except of remarkably high reflectance in the optical [1] and microwave [2] spectrum, they exhibit anomalous polarization signatures of radar echoes [2], not typical for most planetary surfaces. Due to that, many studies address issues of their structure, composition and thermal regime.

Disk-integrated and disk-resolved measurements in a broad wavelength range [3] provided information on the surface temperature and its changes over the diurnal cycle.

The Submillimeter Wave Instrument (SWI) is a spectrometer and radiometer with two channels working in frequency bands around 600 and 1200 GHz. It will register the radio brightness temperatures of the icy surface at these frequencies. This will give a possibility to study the global structure of icy crust and tectonic and resurfacing processes. In the Jovian icy moons' crust, volume scattering should be expected to be relatively more significant, due to probably lower absorption in comparison to the lunar regolith.

For the correct interpretation of microwave radiometry observational data, relevant radiative transfer models, adequately treating transport of the electromagnetic radiation in millimeter and submillimeter microwave bands, should be elaborated as well as the approaches for retrieval of the physical quantities of interest.

In this study, thermal radiation of the icy moons' surfaces is simulated by numerical solution of the radiative transfer equation. A Bayesian retrieval procedure for thermal and electrical properties of the surface has been tested with the simulated radiometry data.

The study is partially supported by the Max-Planck-Institut für Sonnensystemforschung. Support from Russian Science Foundation with the grant 17-77-20087 is also kindly acknowledged.

References:

- [1] Buratti B.J. Application of a radiative transfer model to bright icy satellites. // *Icarus*. 1985. V.61. P.208-217.
- [2] Black G.J., Campbell D.B., Nicholson P.D. Icy Galilean satellites: Modeling radar reflectivities as a coherent backscatter effect. // *Icarus*. 2001. V.151. P.167-180.
- [3] Orton G.S., Spencer J.R., Travis L.D., et al. Galileo photopolarimeter-radiometer observations of Jupiter and the Galilean satellites. // *Science*. 1996. V.274. P.389-391.

HYDRATED PHASES IN THE TITAN'S CORE

A.N. Dunaeva, V.A. Kronrod, O.L. Kuskov

V.I. Vernadsky Institute of Geochemistry and Analytical Chemistry
RAS, Moscow, dunaeva.an@gmail.com

Keywords:

Satellites of gas giant planets, Titan, hydrous silicates, water content

Introduction:

Simulated results of Jupiter and Saturn regular satellites formation revealed that satellites like Titan and Callisto were accreted at 4-8 Myr after meteoritic CAI inclusions occurrence, from the small (less than 10-15 m) rock-ice particles (planetesimals) consisting of H₂O ice and rock-iron components [1, 2]. Models of the large icy satellites' internal structure [3-5] impose the restrictions on the satellites rock composition in accordance with the substance of ordinary (L/LL) or carbonaceous (CI) chondrites. The rock-iron meteorites substance can be partially or completely hydrated. Hydration/serpentinization reactions relatively quickly occur, both on the scale of geological time and in comparison with the rate of satellites' accretion [5]. These reactions can occur at different stages of evolution of the rocky-ice objects, leading to formation of low-density hydrated phases (hydrous silicates). Given the fact that both small particles and large volumes of planetary bodies can be involved in the hydration reaction, hydrous silicates become a significant component in their composition. The presence of hydrated minerals affects the density of the chondritic substance, and also imposes certain limitations on the satellites thermal history, which should be taken into account during constructing models of their composition and internal structure. The main task of this paper aims to determine the region of hydrated phases' stability in Saturn large ice satellite Titan.

Model description and results:

Titan accretion from small rock-ice particles occurred for a continuous period of time $\approx 10^6$ years, which has made it possible to form Titan, initially consisting of a homogeneous ice and rock mixture [6]. During the last stages of accretion, as a result of impactors action, the temperature of the near-surface Titan's regions increased sufficiently to initiate the ice melting. This leads to the separation of the rock-iron component and its migration to the satellite center accompanied by formation of inner rock-iron (silicate-iron) core. Surface water and ice formed an outer water-ice shell. Between the water-ice shell and the inner core a homogeneous rock-ice mixture (the rock-ice mantle) remains.

Radiogenic heating of the Titan silicate rocks may lead to the temperature increasing to the level at which the reverse reactions of hydrous silicates dehydration occurs. Such reactions are irreversible as it is assumed that water released from dehydration is rapidly removed. The temperature line of the hydrous silicates stability (the boundary of the hydrous silicates to silicates phase transition) under Titan conditions is equal to about 900K. This thermal boundary is achieved at the satellite central core and divides it into two parts: outer hydrated part (the region of hydrous minerals stability) and innermost dehydrated part composed with pure anhydrous silicates.

In this paper, degree of the Titan silicate core hydration is assessed, depending on the satellite core size and type of chondritic substance. For this purpose the non-steady-state thermal model [7] was used to calculate the temperature/depth profile changes in the Titan's core over geological time:

$$T = \frac{\chi \cdot A_0}{k \cdot \lambda} e^{-\chi t} \left\{ \frac{R_c \cdot \sin r \left(\frac{\lambda}{\chi} \right)^{\frac{1}{2}}}{r \cdot \sin R_c \left(\frac{\lambda}{\chi} \right)^{\frac{1}{2}}} - 1 \right\} + \frac{2R_c^3 A_0}{r \cdot \pi^3 k} \sum_{n=1}^{\infty} \frac{(-1)^n}{n \left(n^2 - \frac{\lambda R_c^2}{\chi \pi^2} \right)} \sin \frac{n\pi r}{R_c} \exp \left(-\frac{\chi n^2 \pi^2 t}{R_c^2} \right)$$

where: T is the temperature, K; t is the time after Titan's core formation, s; A_0 - the initial radiogenic heat production rate of radioactive isotopes per unit

volume of chondrite, W/m^3 ; R_c and r – are the core radius and the current distance from the Titan's center, m ; λ - the mean decay constant for chondritic material; k - thermal conductivity; $\chi = k/(\rho \cdot c_p)$ is the coefficient of temperature diffusion, m^2/s ; ρ is the density; c_p is the specific heat.

Under calculations the following values of required parameters were used: $\lambda = 1.4016 \cdot 10^{-17} s^{-1}$; for silicate and hydrous silicate material respectively ρ was equal to 3620 and 2800 kg/m^3 , c_p - 920 and 1360 $J/kg \cdot K$. Thermal conductivity coefficient k was 4.2 $W/m \cdot K$ and 2.95 $W/m \cdot K$, representing pure silicate and antigorite minerals.

As the start point of time countdown and determination of initial value of A_0 the 500 My after CAI was chosen. By this time the inner core of Titan had already formed, and its temperature was enough to melt the core ice (ice-VII) and its removing to the upper layers. Under the core pressure (50-60 kbar) the ice melting temperature lies at 550-600 K [8].

The calculations of Titan core thermal evolution were done both for L/LL-chondritic core (with a small amount 1-2% of hydrous minerals) and for CI-chondritic core corresponding to the maximum initial hydration of the core substance. Examples of calculations are shown in Fig. 1.

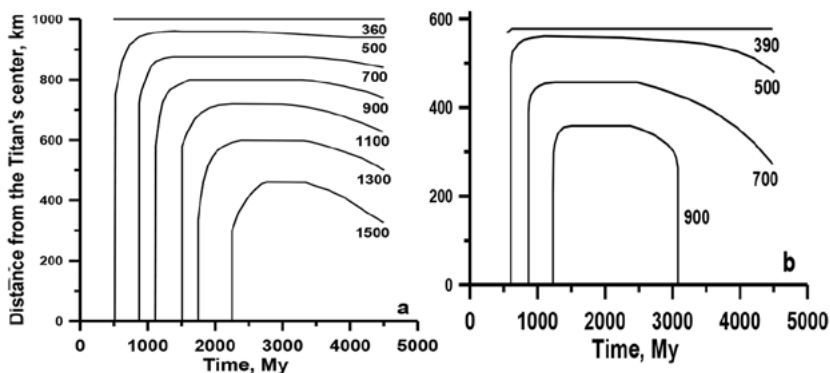


Fig. 1. Radiogenic heating of L/LL-chondritic Titan's core. The results for core radii of 1000 km (a) and 600 km (b) are shown. Lines and numbers indicate positions of heating isotherms over the time.

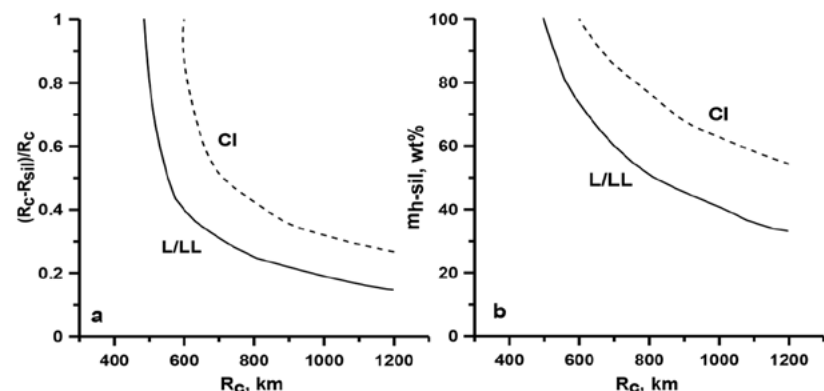


Fig. 2. The region of Titan's core hydration, depending on core size (R_c) and type of meteorite substance. The results are presented as a proportion of Titan radius (a) and as mass fractions of the core (b). The solid and dotted lines correspond to the L/LL-chondritic core (with a small fraction of hydrated minerals) and to the CI-chondritic core, respectively.

As can be seen from Fig. 1, for the large ($R_c = 1000$ km) L/LL-cores with a minor degree of substance hydration, the phase boundary of hydrous/anhydrous silicates ($T=900$ K) lies at the radius of innermost silicate Titan core (R_{sil}) equal to 800 km. This means that the size of overlying region of hydrated

silicate phases stability in the core is equal to 0.2 R_c (mass of hydrated layer in the core (m_{h-sil}) is ~ 40 wt%). For the small cores ($R_c = 600$ km), the radius of inner silicates is 360 km, i.e. the cores are hydrated by 0.4 R_c ($\sim 70\%$ of their mass).

The summarized results on the determination of hydrated phases stability region in Titan core for various core's composition are shown in Fig. 2. Assuming that in the given Titan model the size of satellite's core is equal to ~ 1000 - 1100 km, i.e. small sized cores are unlikely, the expected sizes of the hydrated part of the L/LL-cores are ~ 35 - 40 wt%. The CI-cores remain hydrated up to 50-60% of their mass.

Acknowledgments.

This research was supported by the RFBR grant (№ 18-05-00685).

References:

- [1] Makalkin A.B., Dorofeeva V.A. Accretion disks around Jupiter and Saturn at the stage of regular satellite formation // *Solar System Research*. 2014. V. 48(1). P. 62-78.
- [2] Kronrod V.A., Makalkin A.B. Capture of material by the protosatellite disks of Jupiter and Saturn due to interaction of the in falling planetesimals with the gaseous medium of the disks // *Experiment in GeoSciences*. 2015. in russian.
- [3] Kuskov O.L., Kronrod V.A. Core sizes and internal structure of the Earth's and Jupiter's satellites // *Icarus*. 2001. V. 151. P. 204-227.
- [4] Kuskov O.L., Kronrod V.A. Internal structure of Europa and Callisto // *Icarus*. 2005. V. 177. P.550–569.
- [5] Castillo-Rogez J.C., Lunine J.I. Evolution of Titan's rocky core constrained by Cassini observations // *Geophys. Res. Lett.* 2010. V. 37. L20205.
- [6] Barr A.C., Citron R.I., Canup R.M. Origin of a partially differentiated Titan // *Icarus*. 2010. V. 209. No. 2. P. 858-862.
- [7] Carslaw H.S., Jaeger J.C. *Conduction of heat in solids*: Oxford Science Publications. – Oxford, England, 1959. 510 p.
- [8] Dunaeva A.N., Antsyshkin D.V., Kuskov O.L. Phase Diagram of H₂O: Thermodynamic Functions of Phase Transitions of High-Pressure Ices // *Solar Syst. Res.* 2010. V. 44. P. 202–222.

DEPENDENCE OF THE PLANETESIMALS MASS CAPTURED IN GIANT PLANETS ACCRETION DISKS FROM ABLATION PROCESSES

V.A. Kronrod¹, A.B. Makalkin², A.N. Dunaeva¹

¹*V.I. Vernadsky Institute of Geochemistry and Analytical Chemistry RAS, Moscow, va_kronrod@mail.ru;*

²*O.Y. Schmidt Institute of Physics of the Earth RAS, Moscow*

Keywords:

Jupiter, Saturn, Ganymede, Callisto, Titan, circumplanetary disk, planetesimals, aerodynamic braking, ablation.

We simulated planetesimals passing through the circumplanetary disks of Jupiter and Saturn and capture of their material into the disks with consideration of combined processes of aerodynamic braking, and ablation of planetesimals in the disk's gas medium. In the following calculation the planetesimals substance is modeled by comet material. We estimated the maximum size which the planetesimals should have when passing through the disk to keep them inside the disk after losing their mass and velocity due to gas drag and ablation.

There is a significant dependence of the amount of material captured by the disk on the ablation coefficients. For ablation factors $<0.01 \text{ s}^2\text{km}^{-2}$, the contribution of ablation to the captured mass can be ignored, however, for planetesimals from cometary material, ablation can supply 20-30% of planetesimals mass in the Ganymede and Callisto feeding area and 10%-20% planetesimals mass in the feeding area of Titan.

Introduction:

There are two kinds of processes of solid material entering the protoplanetary disk. If the solid particles are small enough, they form a single whole with the gas stream and could be contributed into the protoplanetary disk with a gas stream [1]. The second mechanism is the capture material of planetesimals by an accretion disk. In the present study, to address the problem of planetesimals and gas interaction in the disk medium the well-known semiempirical methods of meteoric physics [2-5] have been used for calculation of the substance amount captured in accretion disk. A problem statement and the solution method are described in [6,7]. In this work, the processes of planetesimals ablation during their passing through the disk's gas medium and their influence on the substance mass captured by disk are discussed.

The motion and loss of mass of the bodies in the accretion disk:

We simulated passing planetesimals through the circumplanetary disks of Jupiter and Saturn and capture of their material into the disks with consideration of combined processes: aerodynamic braking and ablation of planetesimals in the disk's gas medium. We estimated maximum planetesimal size (radius $R_{1,\text{max}}$) which the body should have at the entrance to the disk in order to stay in the disk after mass and velocity loss due to gas drag and ablation. The maximum radius of captured planetesimal $R_{1,\text{max}}$ is obtained as a function of distances from the central planet. For the planetesimals with radii $R > R_{1,\text{max}}$, which were able to escape the disk, the velocities at the exit after crossing the disk should be higher than the escape velocity from the Hill (gravitational) sphere of the planet.

Ablation of planetesimals:

The calculation of the equations of motion and ablation of planetesimals is performed assuming the constancy of the coefficients of strength, heat transfer, ablation and the shape factor. In this case, the solutions of the meteoric physics equations admit simple self-similar solutions. A large experimental material, accumulated in meteor physics, allows specifying these coefficients depending on the velocity, body material and density of the gaseous medium. The ablation coefficient σ is a semi-empirical value which is determined from

the numerous observational data on meteoritic falls by solving the meteoric physics equations [2, 4, 5]. In this study, the material of planetesimals is modeled by comet material. The ablation coefficient for comet material varies over a wide range of values. Comets in accordance with the classification [8] belong to the type IIIA-IIIIB with the observed ablation coefficient (reconstructed from the equations of meteoric physics) of 0.1-0.2 s²km⁻². It should be noted that the observed or "effective" ablation coefficient apparently includes the processes of fragmentation of the surface layers of the meteorite and the drift of particles of small mass. The "proper" ablation coefficient (without the effect of fragmentation processes) is much smaller, almost independent on the types of meteorites, and lies within the range of (0.004 - 0.008 s²km⁻²) [2]. Since it is impossible to calculate the density and the shape of a meteorite from the results of observations within the constructed model [4], it is difficult to relate the results to specific types of meteorites.

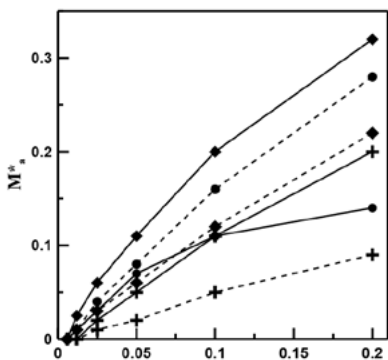


Fig. 1. Dependence of the M^* parameter from the ablation coefficient σ . M^* is the M_a/M_f ratio, where M_a - ablated mass captured into the disk and M_f - the total mass of bodies with radii $0 < R < R_0$.

Circles, diamonds, crosses - distances from the central planets Ganymede, Callisto, Titan, respectively.

$R_0 = 100$ m - solid line, $R_0 = 1000$ m - dashed line.

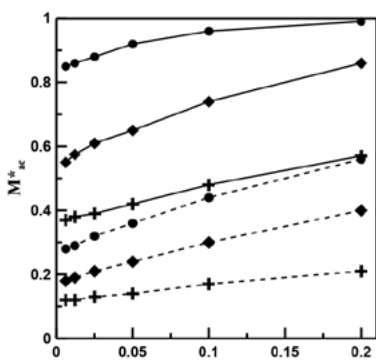


Fig. 2. Dependence of the parameter M^* (the ratio of the whole mass sized of $0 < R < R_0$ captured into the disk, including the small bodies (with the radii $R < R_{1,max}$) trapped into the disk and ablated mass) from the ablation coefficient σ .

Circles, diamonds, crosses - distances from the central planets Ganymede, Callisto, Titan, respectively.

$R_0 = 100$ m - solid line, $R_0 = 1000$ m - dashed line.

Results:

Simulations of aerodynamic braking, fragmentation, and ablation (a comet substance) integrated processes in the gas medium of the Jupiter and Saturn accretion disks were carried out.

To estimate the mass of a substance captured by a disk, a degree-law distribution of bodies by mass was assumed [6, 9]. The following relations were estimated: $M^*_{ac} = (M_c + M_a) / M_t$, $M^*_a = M_a / M_t$ (fig. 1, fig. 2) and $M^*_{a+} = (M_c + M_a) / M_t$ [6]. The first ratio characterizes the mass fraction of the substance trapped in the disk as a result of mass capture (M_c) and mass ablation (M_a) from the total mass of the planetesimals (M_t) with radii $R < R_0$ passing through the disk. The second one shows the mass fraction of the substance (M^*_a) captured in the disk with partial evaporation of the planetesimals crossing the disk. The maximum radius of planetesimals R_0 in our calculations was set at 100 m and 1000 m.

Thus, there is a significant dependence of the amount of matter captured by the accretion disks in the feeding region of the regular ice satellites of Ganymede, Callisto and Titan on the ablation coefficients. For ablation factors < 0.01 s²km⁻², the contribution of ablation to the captured mass (the maximum radius of planetesimals is 100-1000 m) can be ignored, however, for planetesimals from cometary material, ablation can supply ~ 20-30% planetesimals mass in the feeding region of Ganymede and Callisto and ~ 10% - 20% planetesimals mass in the feeding region of Titan.

Acknowledgments:

This work was supported in part by the Russian Foundation for Basic Research (RFBR) under Grant 18-05-00685, Program 28 of the Presidium of the Russian Academy of Sciences.

References:

- [1] Canup R.M., Ward W.R. Formation of the Galilean satellites: Condition of accretion // *Astronom. J.* 2002.V.124. P. 3404–3423.
- [2] Ceplecha A.Z., Revelle D.O. Fragmentation model of meteoroid motion, mass loss, and radiation in the atmosphere. *Meteoritics & Planetary Science*. 2005. V. 40. № 1. P. 35–54.
- [3] Stulov, V.P., Mirskii, V.N., Vislyi, A.I. *Fireball Aerodynamics* // Nauka, Moscow.1995. (in Russian).
- [4] Gritsevich M.I. Determination of parameters of meteor bodies based on flight observational data// *Advances in Space Research*.2009. V. 44. P. 323–334.
- [5] Gritsevich, M., and Koschny, D. Constraining the luminous efficiency of meteors // *Icarus*. 2011, V. 212(2).P. 877-884.
- [6] Kronrod V.A., Makalkin A.B. Capture of material by the protosatellite disks of Jupiter and Saturn due to interaction of the infalling planetesimals with the gaseous medium of the disks // *Proceedings of russian annual seminar on experimental mineralogy, petrology and geochemistry (RASEMPG - 2015)*, 282-286 (in Russian).
- [7] Makalkin A.B., Dorofeeva V.A. 2014. Accretion disks around Jupiter and Saturn at the stage of regular satellite formation // *Solar System Research*, 48(1), 62-78.
- [8] Revelle D.O. Recent advances in bolide entry modeling: a bolid potpourri. *Earth, Moon, and Planets*. 2005.V. 97.P. 1–35. DOI 10.1007/s11038-005-2876-4.
- [9] Safronov V.S. 1969. Evolution of protoplanetary cloud and formation of the Earth and planets. M.: Nauka, 244 p., NASA, F-677, 1972, transl., Washington D.C.

TERRESTRIAL CATASTROPHIC ATMOSPHERIC PHENOMENA OF THE WAVE NATURE (EL-NINO, CYCLON, TORNADO) AND COMPARISON OF CYCLONES ON EARTH AND JUPITER

G.G. Kochemasov

IGEM of the Russian Academy of Sciences, 35 Staromonetny, 119017 Moscow, RF, kochem.36@mail.ru

Keywords:

Atmosphere, catastrophic phenomena, El-Nino, cyclones, tornado, Earth, Jupiter, wave nature

Atmosphere is one of the outer geographical envelopes occurring under influence of the tectonics of the solid Earth [2]. In its structure is the first order feature – global tectonic dichotomy made by the fundamental wave long $2\pi R$. The uplifted continental hemisphere opposes to the subsided Pacific one. This global structure is complicated by superimposed sectors due to the first overtone wave2 (long πR). Corresponding to the Earth's orbit tectonic granulation has size $\pi R/4$ due to the wave $\pi R/2$. Characteristic tectonic formation of this size (~ 5000 km in diameter) is a Precambrian platform or a craton with its folded frame. Eight such granules are placed in the great planetary ring – equator.

To the tectonic dichotomy in the atmosphere correspond two global cells: one with the lower pressure with a center of constant measurements in Darwin (Australia) on the continental hemisphere and the second with the higher pressure with a center in the Easter Island in the Pacific hemisphere (Fig. 1). From the point of view keeping the angular momentum such opposition of atmospheric pressures is understandable: to the uplifting eastern hemisphere with increased radius corresponds the lower pressure, to the subsided oceanic western hemisphere with diminished radius corresponds the higher pressure. Periodic changes of this stable configuration of pressures- increasing pressure in Darwin and lowering over Easter Island – leads to a change of oceanic current in the Pacific, increasing water temperature and origin of unfavorable often catastrophic conditions in the environment (Fig. 2).

Cyclones or typhoons with diameters up to several thousand km – cells of the lower pressure – arise normally in the tropics (Fig. 3). Their sizes are typically rather smaller than calculated for tectonic granules (5000 km). One might explain this by a tendency of diminishing sizes of objects in the tropical and equatorial belts for the purpose of diminishing their angular momentum. This process of diminishing is characteristic also for other geospheres. For example, in the lithosphere (crust) there is subsidence of platform bases, in the anthroposphere there is a global phenomenon of pygmeoidness. According to the Le Chatelier principle, diminishing sizes of atmospheric cells (granules) are compensated by increasing speed of their rotation for keeping their angular momentum. Such rapidly rotating objects, and also taking in moisture for increasing their mass, come down to coasts and inlands with downpours and hurricanes.

Tornado – smaller rotating objects possess huge destructive force. Their sizes are connected with atmospheric cells made by rotating atmosphere. Under rotating frequency $1/1$ day their theoretical size is $\pi R/1460$ or ~ 14 km in diameter. In fact, their size is smaller, reaches about 8 km. This decrease also can be connected with their occurrence in the tropical zones with increased radius demanding decrease of sizes and masses of objects for decreasing the angular momentum. A consequence of this is increase of rotating speed with catastrophic results (Fig. 5).

Recently discovered with help of infrared device (Yuno project, 2018, [1]) cyclonic chains around both poles of Jupiter might be compared with famous catastrophic terrestrial cyclones. Jovian cyclones make chains of 8 around the North Pole and 5 around the South Pole. In case of Earth 8 tectonic granules of the wave nature and $\pi R/4$ size encircle the planet along the equator (grand planet's ring). At the western Pacific hemisphere four of these granules

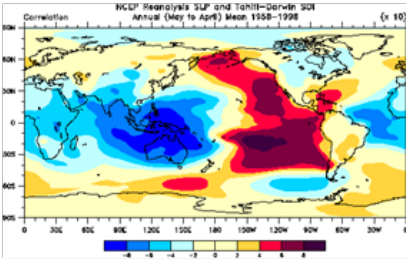


Fig. 1. High and low atmospheric pressures (many years' observations) [3].

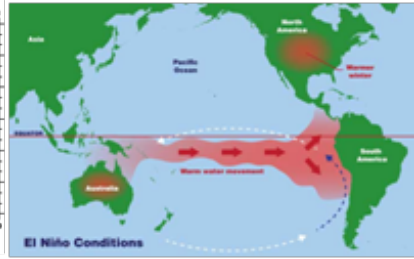


Fig. 2. Origin of El-Niño.



Fig. 3. Cyclones on Earth. (over the Pacific).

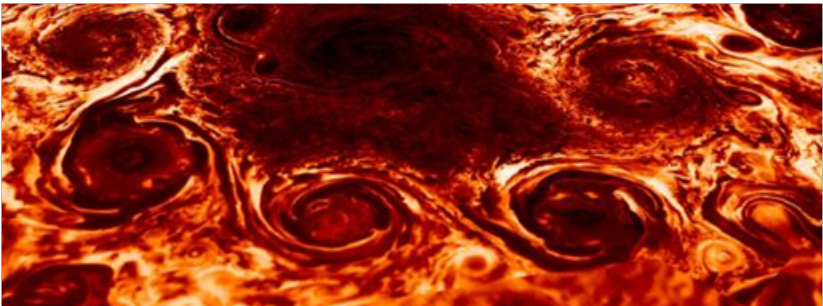


Fig. 4. Cyclones on Jupiter (North Pole) [1]



Fig. 5. Tornado in USA

are presented by a chain of cyclones in the atmosphere (Fig.3). An essential difference of the Jovian and terrestrial chains is in their positions: on Earth it belongs to the longest equatorial ring, on Jupiter to a much shorter ring in high latitudes near to the North Pole(Fig.4). Another important difference is in relative sizes of the storms. On Earth they are smaller (as if, squeezed), on Jupiter they are larger, more massive. The positions of both chains should explain this taking into account difference of their angular momentum. The equatorial belt with the larger angular momentum requires squeezing objects to diminish momentum, the high latitude zones with smaller radius and momentum require more massive objects. All this for equilibration of momenta in various zones of a rotating body. Significantly squeezed terres-

trial equatorial cyclones are catastrophically rapidly rotating.

References:

- [1] Adriani A., Muru A., Orton G., Hansen C., Altieri F et al Clusters of cyclones encircling Jupiter's poles // *Nature*, 2018, v. 555, # 7695, 216-219. doi:10.1038/nature25491.
- [2] Kochemasov G.G. Reflection of the Earth's tectonic dichotomy in the atmosphere, dendrosphere, and anthroposphere (the geospheres coupling of the two-faced Earth) // 'Planet Earth' system, Moscow, LENAND, 2016, 496 pp.(p. 179-181) (In Russian).
- [3] Trenberth K.E., P.D.Jones, P. Ambenje, R. Bojariu et al. Observations: Surface and Atmospheric Climate Change. In: *Climate Change // The Physical Science Basis. Contribution of Working Group I to the Fourth Assessment Report of the Intergovernmental Panel on Climate Change*, 2007
- [4] Solomon S., D. Qin, M. Manning, Z. Chen, M. Marquis, K.B. Averyt, M. Tignor and M.L. Miller (eds.) // *Cambridge University Press, Cambridge, United Kingdom and New York, NY. USA. 2007*

DETECTOR OF COSMIC DUST «METEOR-L»

A.I. Demyanov¹, V.V. Vysochkin²

¹*Institute for Geochemistry and Analytical Chemistry (GEOKHI) RAS
119991 Moscow, Kosygina 19, Russia, demyanovalexey@mail.ru;*

²*Institute for Geochemistry and Analytical Chemistry (GEOKHI) RAS
119991 Moscow, Kosygina 19, Russia, vvisochkin@mail.ru*

Keywords:

Cosmic dust, meteor, the Moon.

Assignment and application area

Meteoritic material in the Solar System is multitude of solids with diameter range of dozens of kilometers to part of micron. Such a large range of mass of meteoroids requires the use of different methods while studying them. The research of meteoroids with masses greater than about g is carried out by ground optical and radar methods. Information about individual bodies with smaller mass up to about g for different areas of interplanetary space are given by measurement from spacecraft.

The "METEOR-L" device is being developed within the "LUNA-RESURS-1" project.

Purpose of the «METEOR-L» device:

1. The study of meteoric material;
2. The determination of the meteoric flow density on the path of the Earth–Moon flight;
3. The revealing of the dust envelope on the Moon;
4. The obtaining of data on the physical-dynamic parameters (mass, speed) of meteoric particles.

Device design

The "METEOR-L" detector of cosmic dust structurally made as a single block of cylindrical shape (Fig.1). There is a detector in the upper part of the device and there are electronic devices installed on 3 boards in the lower part.



Fig.1. Meteor-L Detector of Cosmic Dust

The operational principle of the apparatus

The operational principle of the instrument is based on the phenomenon of the ionization of high-speed particle material during its interaction with a barrier (Fig. 2). The plasma dust formed as a result of the evaporation and ionization of the meteoric particle material and some of the target material enters the electrostatic dividing field between the ion collector and the target, being an electron collector at the same time. The signals induced by plasma on the collector and the target are fed into amplifying-converting device, where charge-sensitive amplifiers are amplified and amplitude-time parameters of signals which containing information about physical-dynamic properties of meteoric particle are determining. As this takes place, the total charge of the ions or electrons of the plasma (Q) formed due to the impact is proportional to the mass and impact speed of the meteoric particle, and

the duration of the first front of the current impulse (t) is proportional to the particle speed.

The measured parameters of the meteoric particles, namely, the mass (m) and speed (V), as well as the registered parameters of electrical signals (Q, t), are related by

$$Q = k \cdot m \cdot V^{\beta}, t = V^{\alpha}$$

where k and α are the coefficients depending on the geometry and constructive solutions of the detector of the apparatus. The values of the coefficients are determined by the results of model experiments on the microparticle amplifier during the development of the apparatus and its calibration [1].

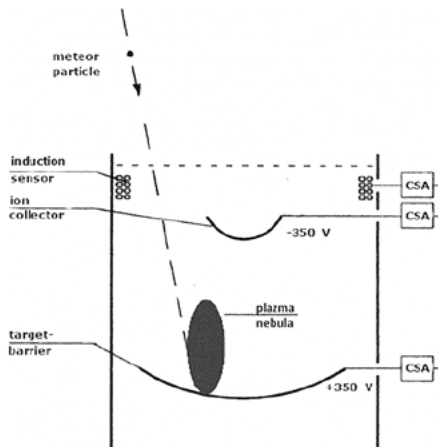


Fig.2. Physical scheme of the experiment

The main device's technical characteristics

Since the mass of the meteoric particle is determined from the measured value of the total charge of ions or electrons, the range of the determined masses depends on the value of the shock speed of the particle.

The range of speeds registered by the instrument (3–35 km/s) was determined with accounting for the distribution of meteor bodies in the Solar System by speeds; this allows us to register particles within the mass range of g .

The technical characteristics are given in the table 1.

Table 1.

Measurement range	Mass: from 3×10^{-15} to $10^{-6}g$ Speed: from 1,5 to 35 km/s
Accuracy of measurements	Mass: $\pm 30\%$ Speed: $\pm 10\%$ in the range of 10 km/s $\pm 30\%$ in the range of 10 to 35 km/s
Dimensions of the device, mm	$\varnothing 252 \times 380$
Instrument mass, kg	$2,9 \pm 0,3$
Power consumption, W	5,5
Supply voltage, V	27

The constructed instrument is applied not only for solving the tasks on the study of the space distribution of meteoric matter and obtaining the data on the physical-dynamic parameters of individual particles, but for the estimation of meteor danger for flights of spacecraft in that area of cosmic space [1].

References:

- [1] Vysochkin V.V., Korolev S.A., Andreenkov V.B. Meteor-F Detector of Space Dust // *Astronomicheskii Vestnik*. 2011. Vol. 45. No. 1. P. 81–84.

LOWER-HYBRID TURBULENCE IN DUSTY PLASMAS OVER THE MOON

Yu.N. Izvekova^{1,2}, T.I. Morozova^{1,2}, S.I. Popel^{1,2,3}

¹Space Research Institute of the Russian Academy of Sciences, 84/32 Profsoyuznaya Str, Moscow, Russia, 117997 (popel@iki.rssi.ru);

²Moscow Institute of Physics and Technology, Dolgoprudny, Moscow region, 141700 Russia;

³National Research University Higher School of Economics, Moscow, 101000 Russia

Keywords:

Lower-hybrid turbulence, dusty plasmas, dust over the Moon, magnetosphere.

The interaction of the lunar plasma-dust system with the magnetosphere of the Earth is considered. Near-moon plasma is represented mainly by charged particles of regolith and photoelectrons, magnetospheric plasma consists of electrons and ions. The dynamics of the wave processes depends substantially on the parameters of the plasma-dust system. The plasma parameters near the lunar surface were calculated using the model [1], according to which the characteristic concentrations of dust particles of the order of 100 nm in the lunar surface are 10^3 cm^{-3} . The concentrations and temperatures of the electrons in the plasma of the tail of the Earth's magnetosphere near the Moon were measured by the ARTEMIS spacecraft [2]. According to these data, the electron and ion concentrations of the magnetosphere are two or three orders of magnitude smaller than the corresponding parameters of the solar wind, the ion temperature increases by two orders of magnitude compared with the temperature of the solar wind, the temperature of the electrons varies insignificantly. It is shown that generation of lower hybrid waves is possible along with ion-acoustic and dust sound instability in the presence of a magnetic field, taking into account the magnetic field of the magnetosphere and the lunar magnetic anomalies. Dispersion relations and instability rates of lower hybrid waves are obtained taking into account the motion of the near-moon plasma relative to the terrestrial magnetosphere. In all cases, instabilities develop due to the relative motion of magnetospheric ions and charged dust grains. Due to the relatively long growth time of instabilities, well-developed plasma turbulence has time to be established in these situations. We have found the effective collision frequency characterizing the anomalous loss of momentum due to particle-wave interaction for the case of lower-hybrid instability. The obtained effective collision frequency should be taken into account when deriving hydrodynamic equations for dusty plasma ions with allowance for their turbulent heating.

Acknowledgements:

The work is supported by the Russian Science Foundation (project No 17-12-01458).

References:

- [1] Popel, S. I., Kopnin, S. I., Dol'nikov, G. G., Zakharov, A. V., Zelenyi, L. M., and Izvekova, Y. N. Dusty plasma at the surface of the moon. // *Solar System Research*, 2013. V. 47(6). P. 419.
- [2] Vaverka, J., Richterová I., Pavlů J., Šafránková J., and Němeček Z. Lunar surface and dust grain potentials during the earth's magnetosphere crossing. // *Astrophys. J.*, 2016. V. 825. P. 133.

DUSTY PLASMAS AND VORTEX MOTIONS IN THE ATMOSPHERE OF MARS

Yu.N. Izvekova^{1,2}, S.I. Popel^{1,2,3}

¹ *Space Research Institute of the Russian Academy of Sciences, 84/32 Profsoyuznaya Str, Moscow, Russia, 117997 (popel@iki.rssi.ru);*

² *Moscow Institute of Physics and Technology, Dolgoprudny, Moscow region, 141700 Russia;*

³ *National Research University Higher School of Economics, Moscow, 101000 Russia*

Keywords:

Martian atmosphere, dust grains, ionosphere, dusty plasmas, dust devils

Introduction:

Plasma–dust effects in the Martian atmosphere are discussed. A specific feature of the Martian atmosphere is the presence of dust grains in a wide range of altitudes. Taking into account the presence of the Martian ionosphere and the high conductivity of the medium at lower altitudes, the appearance of plasma systems in the Martian atmosphere can be considered quite a common phenomenon. Special attention is paid to dust devils that frequently form in the Martian atmosphere and can efficiently lift dust grains. The processes of dust grain charging as a result of tribocharging and generation of electric fields in a dust devil are discussed. The dynamics of dust grains in such a vortex is simulated with allowance for their charging and the generated electric field.

Martian atmosphere:

The density and pressure on the Martian surface amount to about 1/100 of those on the Earth's surface, the main gaseous component (95%) of the Martian atmosphere being carbon dioxide. The altitude profile of the temperature allows one to distinguish between the troposphere (from the surface to altitudes of 50–60 km), middle atmosphere (from the troposphere to an altitude of 110 km), and thermosphere (above 110 km). The average surface temperature is 210 K, the temperature profile experiences considerable daily and seasonal variations, especially, in the troposphere. There is an ionosphere on Mars with the maximum electron density of up to 10^5 cm^{-3} at altitudes of 135–140 km (Fig. 1). The lower boundary of the ionosphere lies at 80 km; however, it can come down to 65 km in some cases. In addition, the conductivity of the atmosphere near the Martian surface is very high (it exceeds the air conductivity near the Earth's surface by nearly two orders of magnitude) and, according to estimates, lies in the range between $2.8 \cdot 10^{-12} \text{ S/m}$ and $10\text{--}11 \text{ S/m}$. The daytime values of the electron and ion densities near the Martian surface reach about 1 and 10^3 cm^{-3} , respectively.

Dust grains at different altitudes in the Martian atmosphere:

High dust density in Martian atmosphere is observed only during dust storms or other events that lift dust from the Martian surface. The data on the presence of dust in the Martian atmosphere were obtained from Mars rovers and instruments installed on orbital stations. However, estimates made by different methods yield somewhat different values of the main physical parameters of dust grains. These discrepancies can be explained, e.g., by the presence of clouds of condensed grains. At altitudes of 100 km in the mesosphere, where the temperature is sufficiently low for carbon dioxide freezing, clouds formed of dust grains with a size of about 100 nm (similar to noctilucent clouds in the Earth's atmosphere) were observed by means of the SPICAM infrared spectrometer installed on Mars Express orbiter. In addition, clouds of micron-size grains were observed at altitudes of about 80 km by means of the OMEGA spectrometer onboard Mars Express. The mechanisms of formation of such clouds are still unclear. There are also regions near the surface and at an altitude of about 4 km, where clouds consisting of frozen water were observed in the nighttime. Polar clouds are usually located relatively low above the surface (at altitudes below 10 km) and, according to the data obtained by the

Mars Climate Sounder installed on Mars Reconnaissance orbiter, represent thin formations consisting of H_2O ice in summer and at CO_2 ice in winter. The altitudes at which the formation of clouds was observed are marked in Fig. 1. Estimates of the lifetime with allowance for coagulation of small grains yield substantially lower values, which means that there may be additional sources of such grains altitudes of 20–70 km. According to estimates made in [1], the material flux provided by meteor showers is one order of magnitude smaller than that required to maintain the observed parameters of dust grains. Lifting of dust from the Martian surface seems to be a more probable source. Another explanation of stability against coagulation can be charging of fine-dispersed grains in the Martian atmosphere. Thus, dust grains or grains of frozen carbon dioxide or water can be present in the Martian atmosphere at nearly all altitudes of up to 100 km. Taking into account the presence of electrons and ions at different altitudes (starting from the surface), as well as the photoelectric effect in the day time, we can speak of the presence of plasma–dust systems in the Martian atmosphere.

Dust devils:

Plasma–dust systems can form just near the Martian surface. Strong heating of the Martian surface by the Sun leads to the formation of layers in which the temperature decreases with altitude. Such stratification is unstable and leads to gas convection. According to recent findings, dust devils are generated due to convective instability of internal gravity waves. Vortex formation begins with the onset of vortical motion in the vertical plane, followed by the generation of horizontal rotation, i.e., vertically directed toroidal vorticity.

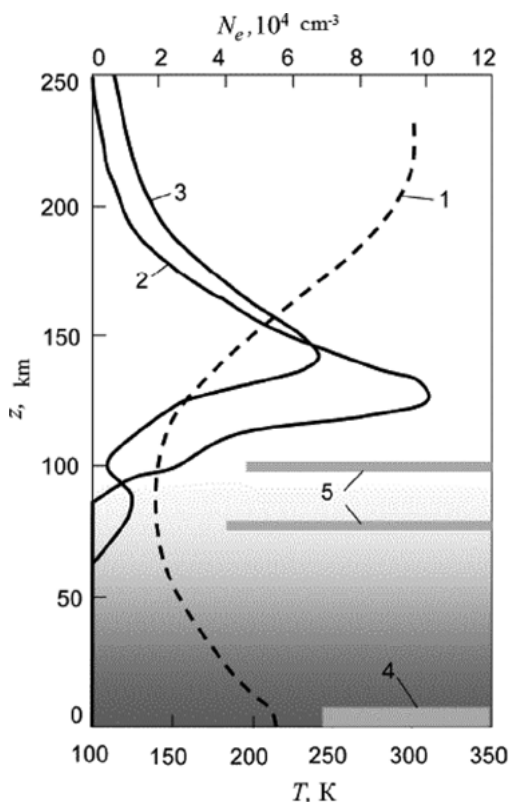


Fig. 1. Altitude profiles of the (1) temperature, (2) electron density in the daytime ionosphere (below 80 km, the number density of charged grains drops to $\sim 1 \text{ cm}^{-3}$), and (3) density of ionospheric electrons at the time of sporadic layer formation at altitudes of 65–100 km. Stripes 4 and 5 show the positions of the layers of clouds consisting of frozen carbon dioxide and water ice. According to observations [1,2], dust grains with number densities depending substantially on the latitude and time can be present at altitudes of up to 100 km.

According to numerous observations in the Earth's atmosphere, substantial electric fields are present in dust devils. The generally accepted mechanism of field generation is spatial separation of charges caused by the motion of charged grains in an ascending air flow. The main mechanism of grain charging in dust devils and dust storms is the tribocharging, i.e., dust grains get charged due to their friction with one another. The charges acquired by grains in the near-surface layer of the Martian atmosphere in the absence of the tribocharging do not exceed 10–20 electron charges, while the charges acquired due to the tribocharging can be two to three orders of magnitude larger. In this regard, we will assume below that the dominant mechanism of dust grain charging is the tribocharging. Collisions of dust grains of different size lead to their charge exchange. As a rule, small grains acquire a negative charge, while large grains acquire a positive charge. We analyze the motion of dust grains in a dust devil with allowance for the electric fields generated due to charge separation. In the calculations, we used the electric field configuration calculated taking into account charging of dust grains and spatial charge separation. For comparison, we also present the result obtained for the lower part of the vortex for which the electric field was replaced by that of a point dipole located at one-half the vortex height. The calculations show that the point-dipole approximation is sufficiently accurate to investigate the lower part of the trajectory. At high altitudes, the field changes its direction and this approximation becomes invalid. The influence of charges and fields in the region where dust grains are entrapped is substantial. In general, entrapped dust grains are efficiently lifted by the dust devil to altitudes reached by the vortex. Dust devils are important sources of dust in Martian atmosphere.

Acknowledgements:

The work is supported by the Russian Science Foundation (project No 18-72-00119).

References:

- [1] Fedorova A.A, Montmessin F., Rodin A. V., Korablev O. I., Määttänen A., Maltagliati L., and Bertaux J. L., Evidence for a bimodal size distribution for the suspended aerosol particles on Mars // *Icarus*. 2014. V.231. P. 239.
- [2] Määttänen A., Listowski C., Montmessin F., Maltagliati L., Reberac A., Joly L., and Bertaux J. L., A complete climatology of the aerosol vertical distribution on Mars from MEx/SPICAM UV solar occultations. // *Icarus*. 2013. V. 223. P.892.

SURVIVABILITY OF BACTERIA IN AN IMPACT-TYPE PLASMA TORCH

V.S. Cheptsov^{1,2}, G.G. Managadze¹, A.E. Chumikov¹

¹Space Research Institute of RAS, 117997, Russian Federation, Moscow, Profsoyuznaya Street, 84/32, cheptcov.vladimir@gmail.com;

²Lomonosov Moscow State University, 119991, Russian Federation, Moscow, Leninskie Gory, 1

Keywords:

Panspermia, survivability of bacteria, meteorite impact, plasma, transport of microorganisms.

Introduction:

The possibility of interplanetary transfer of life has been studied extensively for several decades. It was shown that microorganisms are capable to survive all stages of such transfer – ejection from the planetary crust, travel in open space, and landing onto the surface of another planet [1, 2]. However, a number of impact events may involve the formation of a plasma torch [3, 4]. So far, no studies have addressed the problem of survivability of microorganisms in impacts involving the formation of plasma. It may be expected that microorganisms located inside large fragments of ejected crust rock should be well protected against plasma exposure, however, plasma may affect rather small soil particles (which make up the bulk of the ejecta [5]) and individual microbial cells. In this connection, we analyzed the survivability of *Methylobacterium sp.* bacteria after exposure to a ~ 7 ns long $\sim 10^{10}$ W/cm² laser pulse producing an impact-type plasma torch and simulating impact effects.

Materials and Methods:

The bacterial biomass was mixed with JSC Mars-1 analog of Martian regolith [6]. The resulting sample was applied to the target of a camera specially designed for the experiment (Fig. 1). The camera hosted a round aluminum target with tungsten supports located above it. The camera was placed into LASMA device [4], and more than 1000 laser shoots were made with energy $\sim 10^{10}$ W/cm². In the shooting process fragments of target flew at various directions at angles reaching 180°, and part of the target material moved to the supports (Fig. 1).

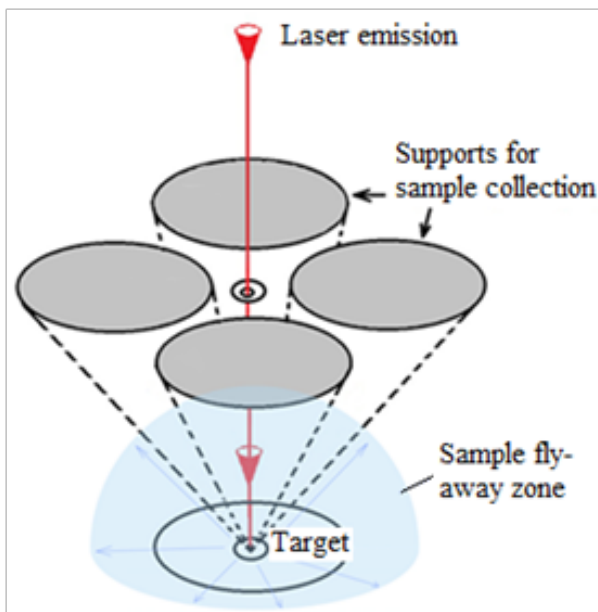


Fig. 1. Scheme of experimental camera.

After the experiment the target was inspected with microscope in order to determine the size of the crater produced by the laser beam. Detection of microorganisms on supports was carried out using several methods. The supports were analyzed on two independent LASMA mass spectrometers using the earlier described technique [7]. At least 300 spectra on each mass spectrometer were analyzed. The principal criterion for interpreting the spectra as «microorganism spectra» was based on the K/Ca, P/S, and N/C ratios [7]. The number of culturable bacteria was determined by plating onto a solid glucose-peptone-yeast media [8]. The total number of bacterial cells on supports was determined using epifluorescence microscopy (EFM) method with acridine orange dye [8]. 16S rRNA gene nucleotide sequences of the *Methylobacterium sp.* IKI-1 strain and five bacterial colonies obtained by culturing from supports after the experiment was analyzed [9] to confirm that bacterial colonies cultured from the support belong to the IKI-1 strain.

Results and Discussion:

Laser beam shots produced a 2-3- μm deep 180- μm diameter crater. According to theoretical computations, a total of about 1.6×10^5 bacterial cells should have been transferred to the entire surface of supports ($\sim 2.3 \times 10^4$ cells per 1 cm^2 of the support). In mass-spectrometric analyses of the supports $\sim 30\%$ of the spectra were classified as «microorganism spectra». Considering the diameter of the laser spot (50 microns), the result obtained suggests that the support contained at least 1.5×10^4 cells/ cm^2 . The bacterial count on supports determined by EFM was $3.8\text{-}8 \times 10^3$ cells/ cm^2 , which was somewhat less than the computed value. The difference between the theoretically estimated number of cells and experimental EFM data could be explained both by the low accuracy of the computations and by the destruction of a part of the cells by the impact-produced plasma torch. The fact that fewer cells were found via EFM compared to mass-spectrometric measurements can be explained by the transfer to the supports of destroyed cells, which are detected by mass spectrometry but are not observed by EFM. The number of culturable cells proved to be 49 colony-forming units (CFU) per 1 cm^2 of supports, which amounts to 0.8% of the total number of cells determined using the EFM and 0.2% of the total number of cells transferred to the supports according to computations. Part of the cells may have died in the process of exposure to laser beam and during the transfer of the target matter to the support. At the same time, part of the population may have passed to viable but nonculturable state as a result of stress [10].

The nucleotide sequences of 16S rRNA gene of IKI-1 strain and of bacterial colonies cultured from supports proved to be 100% similar. This result confirms that colonies obtained from supports are indeed IKI-1 strain colonies and not a result of contamination in process of the experiment.

Thus at first time it was shown experimentally that formation of impact-produced plasma does not limit the survivability of microorganisms. The survival of a large number of living cells could be explained both by the possibility of presence of regions which remained unaffected by the plasma, and by the short duration of exposure to effects of the plasma and its fast cooling in the process of adiabatic expansion [11], which prevents overheating and death of microorganisms. The results obtained combined with the data of other authors concerning the survival of microorganisms in impact processes occurring without the formation of plasma (e.g., [1, 2, 5, 12]) show that viable microorganisms could be preserved and transported in the material ejected in impact events accompanied by the formation of a plasma torch.

We also assume that meteorite impact plasma not only does not limit the survivability of microorganisms during a meteorite impact, but, on the contrary, that it may contribute to interplanetary transport of finely dispersed material including material carrying microbial cells. Plasma flows are known to be capable of carrying rather large dust grains [13-15]. The velocity of plasma in a meteorite impact is substantially higher than the velocities of the debris [3, 4]. It is therefore likely that in the cases of impact events involving the formation of plasma torch, dust grains and, possibly, individual cells may leave their planets moving at speeds of several tens km/s. Hence given their higher

velocities microorganisms should cover greater distances before being killed by the effects of exposure to factors of space environment. In addition, having a high speed, the dust particles carrying microorganisms probably could leave the planets with massive atmospheres, or might rise to the high layers of their atmospheres. In particular, through this mechanism, microorganisms feasibly could rise from the crust of Venus (if they inhabit the crust in the past or present) into potentially inhabited areas [16] of its atmosphere.

References:

- [1] Horneck G. et al. Viable transfer of microorganisms in the solar system and beyond // In: Horneck G., Baumstark-Khan C. (eds.) *Astrobiology: The Quest for the Conditions of Life*. Springer, Berlin, 2002. P. 57-76.
- [2] Mileikowsky C. et al. Natural transfer of viable microbes in space: 1. From Mars to Earth and Earth to Mars // *Icarus*. 2000. V. 145. No 2. P. 391–427.
- [3] Kovalev A.T. et al. Ionospheric and magnetospheric effects // In: Adushkin V.V., Nemchinov I.V. (eds.) *Catastrophic impacts of cosmic bodies*. Moscow, ECC, Akademkniga, 2005. P. 236-250 (in Russian).
- [4] Managadze G. *Plasma of Meteorite Impact and Prehistory of Life*. Nova Science Publishers Inc., New York, 2011. 291 p.
- [5] Moreno M.A. Microorganism transport from Earth to Mars // *Nature*. 1988. V. 336. P. 209.
- [6] Allen C.C. et al. Martian soil simulant available for scientific, educational study // *Eos, Transactions American Geophysical Union*. 1998. V. 79. No. 34. P. 405-409.
- [7] Managadze G. G. et al. A New Method and Mass-Spectrometric Instrument for Extraterrestrial Microbial Life Detection Using the Elemental Composition Analyses of Martian Regolith and Permafrost/Ice // *Astrobiology*. 2017. V. 17. No. 5. P. 448-458.
- [8] Cheptsov V.S. et al. Impact of gamma irradiation under Martian conditions on the viability of soil microbial community // *Paleontological Journal*. 2017. In Press.
- [9] Chutko E.A. et al. Laser microsampling of soil microbial community // *Soil Biology and Biochemistry*. In Press.
- [10] El-Registan G.I. et al. Adaptogenic functions of extracellular autoregulators of microorganisms // *Microbiology*. 2006. V. 75. No. 4. P. 380-389.
- [11] Bykovskii Yu.A., Nevolin V.N. *Laser Mass Spectroscopy*. Moscow, Energoatomizdat, 1985. 128 p. (in Russian).
- [12] Burchell M.J. et al. Survivability of bacteria ejected from icy surfaces after hypervelocity impact // *Origins of Life and Evolution of Biospheres*. 2003. V. 33. No. 1. P. 53-74.
- [13] Choudhary M. et al. Transport and trapping of dust particles in a potential well created by inductively coupled diffused plasmas // *Review of Scientific Instruments*. 2016. V. 87. No. 5. P. 053505.
- [14] Norris B. R. M. et al. A close halo of large transparent grains around extreme red giant stars // *Nature*. 2012. V. 484. No. 7393. P. 220-222.
- [15] Hanslmeier A. (ed.). *Astrobiology, the Search for Life in the Universe*. Bentham Science Publishers, 2013. 214 p.
- [16] Schulze-Makuch D., Irwin L.N. Reassessing the possibility of life on Venus: proposal for an astrobiology mission // *Astrobiology*. 2002. V. 2. No. 2. P. 197-202.

INVESTIGATION OF LUNAR DUSTY EXOSPHERE WITH FUTURE RUSSIAN LUNAR MISSIONS: DEVELOPMENT OF THE INSTRUMENT & SIMULATION CONTROL

A.V. Zakharov, G.G. Dolnikov, I.A. Kuznetsov, A.N Lyash, I.A. Shashkova, S.I. Popel

Space Research Institute of the RAS, Moscow, Russian Federation, kia@iki.rssi.ru

One of the complicating factors of the future robotic and human lunar landing missions is the influence of the dust. Meteorites bombardment has accompanied by shock-explosive phenomena, disintegration and mix of the lunar soil in depth and on area simultaneously. As a consequence, the lunar soil has undergone melting, physical and chemical transformations.

Recently we have the some reemergence for interest of Moon investigation. The prospects in current century declare USA, China, India, and European Union. In Russia also prepare two missions: Luna-Glob and Luna-Resource. Not last part of investigation of Moon surface is reviewing the dust condition near the ground of landers. Studying the properties of lunar dust is important both for scientific purposes to investigation the lunar exosphere component and for the technical safety of lunar robotic and manned missions.

The absence of an atmosphere on the Moon's surface is leading to greater compaction and sintering. Properties of regolith and dust particles (density, temperature, composition, etc.) as well as near-surface lunar exosphere depend on solar activity, lunar local time and position of the Moon relative to the Earth's magneto tail. Upper layers of regolith are an insulator, which is charging as a result of solar UV radiation and the constant bombardment of charged particles, creates a charge distribution on the surface of the moon: positive on the illuminated side and negative on the night side. Charge distribution depends on the local lunar time, latitude and the electrical properties of the regolith (the presence of water in the regolith can influence the local distribution of charge).

On the day side of Moon near surface layer there exists possibility formation dusty plasma system. Altitude of levitation is depending from size of dust particle and Moon latitude. The distribution dust particle by size and altitude has estimated with taking into account photoelectrons, electrons and ions of solar wind, solar emission. Dust analyzer instrument PmL for future Russian lender missions intends for investigation the dynamics of dusty plasma near lunar surface. PmL consists of three parts: Impact Sensor and two Electric Field Sensors.

Dust Experiment goals are:

- 1) Impact sensor to investigate the dynamics of dust particles near the lunar surface (speed, charge, mass, vectors of a fluxes) a) high speed micrometeorites b) secondary particles after micrometeorites soil bombardment c) levitating dust particles due to electrostatic fields. PmL instrument will measure dust particle impulses. Also Impact Sensor will measure the charges of dust particles. In case the charge and impulse of a dust particle are measured we can obtain velocity and mass of them.
- 2) Electric field Sensor will measure the value and dynamics of the electric fields near the lunar surface. Two Electric Field Sensors both are measured the concentration and temperature of charged particles (electrons, ions, dust particles). Electric Field Sensors contain of Langmuir probes. Using Langmuir probes near the surface through the lunar day and night, we can obtain the energy spectra photoelectrons in various periods of time.

PmL instrument is developing, working out and manufacturing in IKI.

These days the engineering model of PmL for LG-mission is finished. We obtained first practical results from the simulating chambers with

dust particles injectors and plasma inside. All the important achievements are presented in this report as well as the roadmap for further development of PmL instruments in both of Russian lunar missions.

Acknowledgements:

This work was supported by the Russian Scientific Foundation (the grant № 17-12-01458).

DEVELOPMENT OF THE EXPERIMENTAL SET-UP FOR LUNAR DUST PARTICLES INVESTIGATION AND INSTRUMENTS CALIBRATIONS

A.N. Lyash, I.A. Kuznetsov, A.V. Zakharov, G.G. Dolnikov, I.A. Shashkova
Space Research Institute of the RAS, Moscow, Russia, kia@iki.rssi.ru

Introduction:

The complex of scientific instruments of the Lander "Luna-Glob" included device PML. This instrument is designed to study the dust component, its dynamics in the near-surface exosphere of the moon, the registration of micro-meteorites and secondary particles of the lunar regolith, impact by micrometeorites and the measurement of their physical characteristics. The device directly measured momentum, velocity, mass and charge of the particles.

For the purpose of conducting physical experiments on modeling of the dusty environment conditions in the surface layer was created an experimental setup. This unit is designed for carrying out functional tests, adjustments and calibrations of the instrument. The installation is carried out testing of the methodology of space experiment. It is planned to hold correction of the coefficients of relative sensitivity and verification of the scientific data obtained during the mission.

Experimental set-up:

The experimental set-up is realized on the base of the vacuum chamber and includes a system of supply and control of vacuum, the injector (generator) of charged particles. The setup includes the control system for measuring the speed of the charge of particles and the system to measuring and control electrical signals and instrument parameters. Vacuum system provides vacuum with a residual pressure sufficient to operate the injector of the dust particles and simulate the conditions of the dust of the atmosphere. Injector (generator) of dust, charged particles produces a stream of metallic, charged particles with dimensions from units to hundreds of microns with flow rates from units to tens of meters per second with a charge of not less than 1000 electrons per the particle. The measuring system for the control of the speed and charge of particles consists of the induction sensor and charge sensitive amplifiers that allow to display and measure the signal. Method of measuring charge is based on the measurement of the induced mirror charge from the moving particles in the metallic electrode of the induction sensor. The geometry data of the placement of the induction sensors is used to measure the speed of particles by time delays of signals.

The voltage applied to the injector governs the speed and charge of the injected particles. In the experiments are used different in size and mass of particles loaded into the injector.

Since the process of injection and the detection of particles are random, the statistical methods to handle the large volume of accumulated data are used.

Results:

The set-up made it possible to realize the streams of charged particles with velocities in the range of 2 to 60 m/sec for the metalized particles with sizes from 10 μm to 200 μm .

On the installation was carried out calibration of the engineering sample PML device, had allowed to determine the sensitivity of the sensors of the device. Threshold sensitivity for the charge is amounted to 2 000 the charge of the electron. The threshold sensitivity of the momentum is amounted to the value of $3 \cdot 10^{-12}$ Newton*sec.

Acknowledgements:

This work was supported by the Russian Scientific Foundation (the grant № 17-12-01458).

COUPLING BETWEEN THE INTERNAL ATMOSPHERIC WAVES AND TILTED SPORADIC E-LAYERS IN THE EARTH'S IONOSPHERE

V.N. Gubenko¹, I.A. Kirillovich¹, Y.-A. Liou²

¹*Kotel'nikov Institute of Radio Engineering and Electronics RAS, Vvedenskii Square 1, Fryazino, Moscow Region, 141190, vngubenko@gmail.com;*

²*Center for Space and Remote Sensing Research, National Central University, Taoyuan City, 32001, yueian@csrsr.ncu.edu.tw*

Keywords:

Earth's ionosphere, radio occultation, inclined plasma layers, internal gravity waves.

Introduction:

We have used the radio occultation (RO) satellite data for studying the ionosphere of the Earth. A method for deriving the parameters of ionospheric structures is based on an analysis of the RO signal variations in the phase path and intensity. This method allows one to estimate the spatial displacement of a plasma layer with respect to the ray perigee, and to determine the layer inclination and height correction values [1, 2]. In this work, we focus on the case study of inclined sporadic (E_s) E-layers in the high-latitude ionosphere based on available CHAMP (Challenging Minisatellite Payload/Global Positioning System) RO data. Assuming that the internal gravity waves (IGWs) with the phase-fronts parallel to the ionization layer surfaces are responsible for the tilt angles of sporadic plasma layers, we have developed a new technique for determining the parameters of IGWs linked with the inclined E_s -structures [3]. A small-scale internal wave may be modulating initially horizontal E_s -layer in height and causing a direction of the plasma density gradient to be rotated and aligned with that of the wave propagation vector k . We have shown that the magnitudes of intrinsic frequency and period can be directly determined based on the values of Brunt-Vaisala frequency and angle between the local vertical and wave propagation vector, only. It was found that the analyzed internal waves have the intrinsic periods from 35 to 46 min and intrinsic vertical phase speeds from 1.4 to 2.0 m/s. These values correspond to a period of 30 min in the ground-based frame and downward wind speed of 2.0 m/s at a height of 100 km found for a model of the Polar cap Sporadic-E layers [4]. The developed technique extends capabilities of the RO method for studying the atmospheres and ionospheres of the Earth and planets. The results of determination of the intrinsic wave frequency and period, vertical and horizontal wavelengths, intrinsic vertical and horizontal phase speeds, angle between the local vertical and wave propagation vector, and other characteristics of IGWs under study are presented and discussed.

This work was partially supported by the RAS Presidium Program 28.

References:

- [1] Pavelyev, A.G., Liou, Y.A., Zhang, K., Wang, C.S., Wickert, J., Schmidt, T., Gubenko, V.N., Pavelyev, A.A., Kuleshov, Y. Identification and localization of layers in the ionosphere using the eikonal and amplitude of radio occultation signals // *Atmos. Meas. Tech.* 2012. V. 5. No. 1. P. 1–16. DOI: 10.5194/amt-5-1-2012.
- [2] Pavelyev, A.G., Liou, Y.A., Matyugov, S.S., Pavelyev, A.A., Gubenko, V.N., Zhang, K., Kuleshov, Y. Application of the locality principle to radio occultation studies of the Earth's atmosphere and ionosphere // *Atmos. Meas. Tech.* 2015. V. 8. No. 7. P. 2885–2899. DOI: 10.5194/amt-8-2885-2015.
- [3] Gubenko, V.N., Pavelyev, A.G., Kirillovich, I.A., Liou, Y.-A. Case study of inclined sporadic E layers in the Earth's ionosphere observed by CHAMP/GPS radio occultations: Coupling between the tilted plasma layers and internal waves // *Advances in Space Research.* 2018. V. 61. No. 7. P. 1702–1716. DOI: 10.1016/j.asr.2017.10.001.
- [4] MacDougall, J.W., Plane, J.M.C., Jayachandran, P.T. Polar cap Sporadic-E: part 2, modeling // *J. Atmos. Sol.-Terr. Phys.* 2000. V. 62. P. 1169–1176.

A HIGH RESOLUTION UV SPECTROGRAPH TO STUDY LUNAR AND PLANETARY ATMOSPHERES AND THE INTERPLANETARY MEDIUM

J.T. Clarke¹, M. Mayyasi¹, V. Izmodenov², E. Quemerais³, W. McClintock⁴, D. Alexashov², I. Balyukin², J.-L. Bertaux³, O. Katushkina², R. Lallement³, A. Petrukovich²

¹*Center for Space Physics, Boston University, 725 Commonwealth Ave, Boston MA 02215 USA, jclarke@bu.edu;*

²*IKI – Russian Academy of Science, Moscow, Russia;*

³*LATMOS - CNRS, Guyancourt, France;*

⁴*LASP - University of Colorado, Boulder CO, USA*

Keywords:

UV instrumentation; Moon; Planetary Atmospheres; Geocorona; Interplanetary Hydrogen.

Introduction:

This presentation will describe a high spectral resolution UV airglow instrument for remote observations of the thin lunar atmosphere, the Earth's geocorona, comets, the interplanetary medium, and the atmospheres of other planets. The instrument is being designed to be accommodated on the Luna-26 mission, which will be placed into a low lunar orbit in the 2020's. The instrument is based on the echelle channel of the MAVEN IUVS instrument, which is presently returning similar data from orbit about Mars. The optical design includes an echelle grating for high spectral resolution (a few km/sec) and is optimized for the detection of faint diffuse emission lines in the absence of continuum emission. On MAVEN it is used to separately detect emissions from D and H Lyman-alpha from resonant scattering of solar emission, and can also be used to study emissions from oxygen, carbon, and nitrogen. The spectral format on the detector is a series of well separated emissions, each consisting of the image of a long, narrow aperture. The high spectral resolution also provides emission line profile measurements at the quoted velocity resolution.

The science that can be achieved by these observations covers several areas of solar system science:

- the thin and variable lunar atmosphere can be observed along a slant column through the lunar exosphere, and when sufficiently dense the emission line profiles will indicate the velocity distribution and thus the source of the material (most effective for atomic hydrogen)
- the Earth's extended geocorona is sufficiently bright that it can be mapped across the sky, the D/H ratio can be measured, and the velocity profile of the bright H emission will show the presence of any superthermal atoms with velocities of a few km/sec
- the extended hydrogen and oxygen atmospheres of comets can be observed, also toward the goals of determining the D/H ratio and the velocity distributions of outflowing atoms
- the interplanetary hydrogen flowing through the solar system from the interstellar medium (ISM) can be observed and the emission line profiles spectrally resolved to determine the velocity distribution of the atoms along different lines of sight, providing key information about the interaction of the ISM with the solar wind at the boundary of the heliosphere
- while expected to underfill the aperture field of view, the UV emission lines from the atmospheres of other planets can also be observed with unprecedented high spectral resolution.

The presentation will describe in more detail the design and expected characteristics of the instrument.

THE GAS ANALYTICAL COMPLEX FOR STUDY OF THE LUNAR SUBPOLAR REGOLITH VOLATILES

M. Gerasimov¹, E. Safonova¹, Y. Lebedev¹, A. Stepanov^{1,2}, A. Sapgir¹, O. Kozlov¹, I. Vinogradov¹, M. Zaitsev¹, A. Vasileva¹, T. Yukhnevich¹, A. Tumbakov¹, A. Nosov¹, V. Makarenko¹, S. Aseev¹, A. Kalyujnii³, P. Wurz⁴, D. Lasi⁴, L. Hofer⁴, M. Cabane⁵, D. Coscia⁵

¹Space Research Institute of the Russian Academy of Sciences

²Lomonosov Moscow State University, Physics Faculty

³SKB KP IKI RAS, Russia

⁴University of Bern, Switzerland

⁵Université Pierre et Marie Curie (France)

Keywords:

Gas chromatography, mass spectrometry, thermal analysis, lunar subpolar regolith volatiles.

Introduction:

The study of the Lunar subpolar regolith will help the scientific community to identify the origin of Lunar subpolar volatiles more confidently, ascertain their quantitative characteristics and also imagine their possible utilization during the future exploration of the Moon.

For this research, the international team of specialists has developed the Gas Analytical Complex, consisting of four integrated instruments: Gas chromatograph (GH-L), Neutral Gas Mass Spectrometer (NGMS), Tunable Diode Laser Spectrometer (TDLAS) and Differential Thermal Analyzer (TAL).

This complex is designed for installation onboard the Luna-Resource landing module, which should descent at the Moon's subpolar region in 2021. It is intended for the different in-situ measurement.

The general scientific goals of Gas Analytical complex are:

- Qualitative and quantitative measurements of near-surface volatile deposits and their behavior during the Moon day

Mineral component analysis of the Moon's subpolar regolith

Near-surface exosphere probing and monitoring of exosphere variation during the Moon day.

GHL (Gas Chromatograph), was engineered by Space Research Institute, Moscow. The main function of this instrument is the separation of gas mixture, obtained as a result of pyrolysis (thermal decomposition) of the Lunar soil sample performed by the **TAL** instrument, allowing mass spectrometer **NGMS** to measure all the gas components separately. The joint operation of NGMS, GHL and TAL is guaranteed by designed software as well as by electrical communicated interfaces.

Furthermore, separation and transferring of the gas sample is not the only feature of **GHL**. It is supplied with the thermal conductivity detector (TCD), giving this instrument the sensitivity of ppmv order. It can measure the wide range of gas components: noble gases, CO₂, H₂O, hydrocarbones.

Another important property of **GHL** is the embedded laser spectrometer, **TDLAS**.

NGMS was designed at the University of Bern and possesses very high-fidelity characteristics. **NGMS** is a time-of-flight mass spectrometer. This device provides for the whole instrument's complex a very high level of sensitivity of order 2.00E-09 for organic components and 2.00E-10 for noble gases.

NGMS has two principal modes of operation:

- GC-MS mode is meaning the measurement of the separated by GHL gas mixture, obtained during the thermal decomposition of the soil probe or during the thermal evolving of volatiles from the frozen soil
- Exosphere mode is meaning direct sensing of Lunar exosphere in the vicinity of spacecraft landing site.

The remarkable features of **NGMS** are the configurable integration time (from 100 ms up to 1 s) and dynamic range up to $1.00E+06$.

Working synchronously, **GHL** and **NGMS** provide more exact and simple interpretation of obtained data.

TDLAS was designed at Space Research Institute. The whole instrument, including laser emitters, receivers, electronics and optical cell, is incorporated into **GHL** case, thus lowering the total complex's mass and dimensions.

The optical cell of **TDLAS**, containing the measured gas probe, is built in the gas capillary system of **GHL**, so **TDLAS** is able to measure its target molecules in dynamic mode, following the thermal decomposition process.

TDLAS primary intention is the estimation of isotope ratios for H_2O and CO_2 molecules, because this information is very valuable for understanding of the Lunar volatiles nature. Besides this, **TDLAS** is capable of measurement of "usual" molecules, providing very high (comparing to TCD) sensitivity. For plain data interpretation, **TDLAS** equipped with the reference optical cell.

TAL was designed at Space Research Institute. Unlike other instrument of described complex, **TAL** contains many moving mechanical parts necessary for preparation of Lunar soil probe for thermal decomposition. Using about 8 drive units, it receives the soil probe from the descent module manipulator, then seals it within one of the pyrolytic oven and became ready for pyrolysis.

TAL equipped with two types of pyrolytic ovens:

- Multidesorption mid-temperature oven (up to $250^{\circ}C$), purposed for the evolving of volatiles from frozen Lunar soil
- Single-use high-temperature ovens, allowing the heating of a regolith sample up to $1000^{\circ}C$.

For both types of ovens, the heating results in release of volatile compounds which are transferred via a system of capillaries into the GC-L and the **NGMS** for chemical analysis).

TAL also performs direct measurements of endothermic and exothermic effects, caused by phase transitions and chemical reactions in soil probe during the given heating process.

NUMERICAL MODELLING OF THE LUNAR EXOSPHERE AND LUNAR LANDER INTERACTIONS WITH SPIS-DUST

I.A. Kuznetsov^{*1}, A.V. Zakharov¹, S.I. Popel¹, G.G. Dolnikov¹, A.N. Lyash¹, I.A. Shashkova¹, S.L.G. Hess², E. Seran³, F. Cipriani⁴

¹Space Research Institute of the RAS, Moscow, Russia, kia@iki.rssi.ru;

²French Aerosp. Lab., ONERA, Toulouse, France;

³Laboratoire Atmospheres, Milieux, Observations Spatiales/UVSQ/UPMC, Paris, France;

⁴ESTEC/TEC-EES, Noordwijk, The Netherlands;

Introduction:

One of the complicating factors of the future robotic and human lunar landing missions is the influence of the dust. Meteorites bombardment has accompanied by shock explosive phenomena, disintegration and mix of the lunar soil in depth and on area simultaneously. As a consequence, the lunar soil has undergone melting, physical and chemical transformations. Recently we have the some reemergence for interest of Moon investigation. The prospects in current century declare USA, China, India, and European Union. In Russia also prepare two missions: Luna-Glob and Luna-Resource. Not last part of investigation of Moon surface is reviewing the dust condition near the ground of landers. Studying the properties of lunar dust is important both for scientific purposes to investigation the lunar exosphere component and for the technical safety of lunar robotic and manned missions. The absence of an atmosphere on the Moon's surface is leading to greater compaction and sintering. Properties of regolith and dust particles (density, temperature, composition, etc.) as well as near-surface lunar exosphere depend on solar activity, lunar local time and position of the Moon relative to the Earth's magneto tail. Upper layers of regolith are an insulator, which is charging as a result of solar UV radiation and the constant bombardment of charged particles, creates a charge distribution on the surface of the moon: positive on the illuminated side and negative on the night side. Charge distribution depends on the local lunar time, latitude and the electrical properties of the regolith (the presence of water in the regolith can influence the local distribution of charge). On the day side of Moon near surface layer there exists possibility formation dusty plasma system. Altitude of levitation is depending from size of dust particle and Moon latitude. The distribution dust particle by size and altitude has estimated with taking into account photoelectrons, electrons and ions of solar wind, solar emission. Dust analyzer instrument PmL for future Russian lander missions intends for investigation the dynamics of dusty plasma near lunar surface. PmL consists of three parts: Impact Sensor and two Electric Field Sensors. One of the tools, which allows to simulate the dust emission from the Moon and asteroids, its transport, deposition and its interaction with a lander, is the SPISDUST (Spacecraft Plasma Interaction Software) code which based on Particle-in-Cell (PiC) method. This paper presents results of SPIS-DUST modelling of the interaction between the lunar plasma environment, regolith and a lander. The model takes into account the geometry of the Luna-Glob lander, the electric properties of materials used on the lander surface, as well as Luna-Glob landing place. Initial conditions were chosen based on the current theoretical models of formation of dusty plasma exosphere and levitating charged dust particles.

Acknowledgements:

The research was carried out using funds of the Russian science foundation (project №17-12- 01458).

IMPACT OF ASTEROIDS AND METEORITES ON THE LUNAR SURFACE

S.G. Pugacheva, E.A. Feoktistova, V.V. Shevchenko

Sternberg Astronomical Institute, Moscow State University,

Universitetsky 13, Moscow 119992, Russia, sve-pugacheva@yandex.ru

Keywords:

Slow moving asteroids, meteorites, the Moon, impact craters, water, natural resources

Introduction:

A huge amount of asteroids have been discovered in recent years by ground-based telescopes and by WISE - the infrared orbital observatory. For the purposes of improvement of special meteorites and asteroids observations in near-Earth space, as well as in order to study the impact traces of even the smallest objects on the lunar surface, the European Space Agency launched the NELIOTA project. Under the project, a 1.2-meter telescope with superfast high-resolution cameras was installed in the Kryoneri Observatory in Greece. Meteorites and asteroids strike the lunar surface and surface of other planets and form some circular morphological structures which can be subdivided into impact craters with a diameter of less than 100 m and explosion craters of more than 100 m in diameter. Due to impact of small cosmic bodies the impact craters are getting crushed when they collide with the surface of planets causing partial ejection of targets. Explosion craters are formed out of cosmic bodies that entry into the target rocks so that 70% explosive energy is transferred to heat, and the impactor body evaporates completely. Collisions of asteroids with the Moon cause powerful flares observed by astronomers on its surface already for several hundred years.

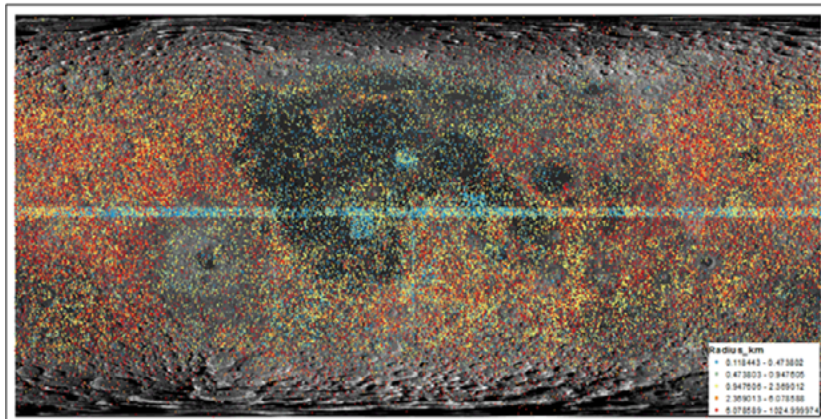


Fig.1. The distribution of 78287 lunar craters of the LI78 catalog. The dots denote the dimensions of the radii of the craters: blue - 0.112 - 0.478 km; Green - 0,478 - 0,947km; yellow - 0,947 - 2,389 km; orange - 2,389 - 6,078 km; red - 6,078 - 1024,559 km [4].

Water of ice asteroids and comets:

Simulating Comet Impacts on the Moon by the SOVA algorithm shows that the ice comets lose 95 to 99.9% of the total cometary water during the impact process. Short-period comets have speed 8-10 km per second, with the impact of such low-speed comets, 1% of water remains after evaporation. The low-speed comets account only for 1.5% of lunar craters. Unlike ice comets, the water in the asteroids is in a chemically bound state. The water is blocked in the crystal lattice of minerals and will separate out of the composition only when heated up to 300-1200 degrees (depending on type of minerals). At impact speed of 14 kilometers per second and impact angle of about 45 degrees, about half the mass of the asteroid does not even reach the melting point and remains in the solid state. A third of all asteroids impacting on the Moon before collision has speed less than 14 kilometers per second. In this case, most of substance of the impacted body remains in the crater - from 30% - 40% at oblique impact,

and up to 60-70% - at the vertical one. Scientists founded out that asteroids containing water when impacted could create "reserves" of chemically bound water inside some lunar craters. Based on Scientists' estimates between 2% and 4.5% of lunar craters can contain substantial water reserves in form of hydrated minerals which are sufficiently stable to hold water even in sunlit places [1,7].

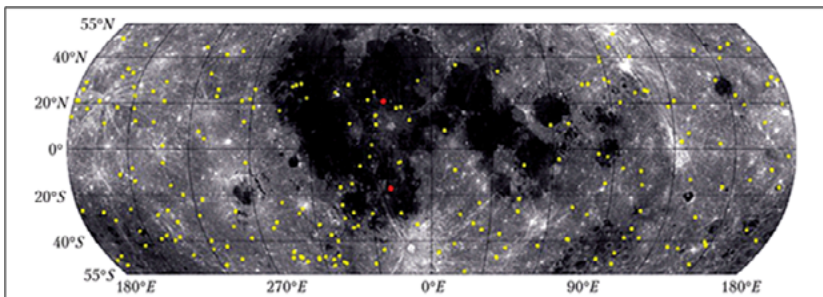


Fig. 2. Distribution of 222 new craters on the lunar surface, the appearance of which was detected from the images obtained Lunar Reconnaissance Orbiter (photo NASA [6]). The red dots denote observations from the Earth.

Natural resources in craters of slow moving asteroids:

Based on the data of 222 craters, it was found out that craters formed by slow moving asteroids with average speed of 10 km per second form craters with a diameter of about 10 m [3, 4]. The composition of the M-type slow moving asteroid as follows: nickel, iron, platinum-group metals. C-type slow moving asteroids compose of carbon and organics, water. S-type slow moving asteroids contain silicates. Reserves of minerals in craters formed by slow moving asteroids are estimated by V.V. Shevchenko in his work. Shevchenko in his article investigates slow moving asteroids enriched by S-type and M-type metal fraction close approaching to the Earth and the Moon [5]. As results of simulating the S-type asteroid impact showed that an impact crater with a diameter of 10.1 m and a depth of 2 m on the lunar surface was formed by an impacted stone asteroid 0.8 m in size, whose speed was 10 km / sec. With an asteroid mass of 803.8 kg, the asteroid substance proportion that remained after the impact is 22% of the whole impacted mass. The metal content of asteroids includes: iron - 270.89 kg, nickel - 48.23 kg, cobalt - 2.41 kg, platinum and platinoids - 0.012 kg. In case of M-type asteroid impact with total mass of 660 kg at the same crater parameters the asteroid substance will have a fully metal content: iron - 556.1 kg, nickel - 99.1, cobalt - 4.9 kg, platinum and platinoids - 0.025 kg.

Conclusions:

The mining profitability of both categories above shall be determined by the technical complexity and cost of their extraction and transportation to the place of use compared to their terrestrial analogues. Delivering hundreds tons of fuel beyond the Earth is a difficult and extremely costly task. Nevertheless, already now there are two relatively large private companies that look forward to explore and produce minerals on asteroids in the future. The first to announce its plans was Planetary Resources, headed by Eric Anderson, who was engaged in space tourism business (his company Space Adventures organized flights of all space tourists to the International Space Station). The company promised launching the first space "fuel depot" by 2020. Now the company launched two trial near-Earth satellite-telescopes that shall demonstrate the prospecting technology. The private American company Deep Space Industries supported by the Luxembourg government looks forward to start active extraction of valuable metals and water already by 2023. Today the first prototype satellite, Prospector-X, is ready to be launched. The research projects of the Moon are of great scientific and practical importance. Water ice and molecular hydrogen point up the fact that there are real resources on the Moon which can be used in future missions.

References:

- [1] Bland P.A. et al., Asteroids on the Moon: projectile survival during low velocity impact // LPSC XXXIX. 2008. 2045-1-2045-2.
- [2] Collins G.S. et al., Earth impact effects program for calculating the regional environ-349-abstract

- mental consequences of a meteoroid impact on Earth // *Meteoritics & Planetary Science*. 2005. V.40. № 6. P. 817 – 840.
- [3] Hamilton D.P. Solar System Collisions, <http://velocity.umd.edu/cgi-bin/astro/impact/>. // 2017.
- [4] Salamunićcar G. et al., Hybrid method for crater detection based on topography reconstruction from optical images and the new LU78287GT catalogue of Lunar impact craters // *Advances in Space Research*, Accepted. 2013. URL: <http://dx.doi.org/10.1016/j.asr.2013.06.024>
- [5] Shevchenko V.V. Utilization of the asteroid subject on the Moon – A more economic way to obtain cosmic resources of high value // *Space technology and technology*. 2018. № 1, P. 6-20.
- [6] Speyerer E.J. et al., Quantifying crater production and regolith Overturn on the Moon with temporal imaging // *Nature*. 2016. V.538. Issue 7624. P. 215 – 218.
- [7] Svetsov B.D., Shuvalov B.B. Water delivery to the Moon by asteroidal and cometary impacts // *Planetary and Space Science*. November 2015. V. 117. P. 444-452.

EXPERIMENTAL SIMULATING OF A MICROMETEORITE IMPACT ON THE MOON

E.M. Sorokin¹, M.V.Gerasimov², M.A. Zaitsev², V.D. Shcherbakov³,
K.M.Ryazantsev¹, I.G. Bystrov⁴, O.I. Yakovlev¹, E. N. Sluta¹

¹*Vernadsky Institute of Geochemistry and Analytical Chemistry RAS,
Moscow, Russia*

²*Institute of Space Research, RAS, Moscow, Russia*

³*Lomonosov Moscow State University, Department of Geology,
Moscow, Russia*

⁴*FGBU "VIMS", Moscow, Russia, egorgeohim@ya.ru*

Keywords:

impact, micrometeorite bombardment, evaporation differentiation, experiment, laser.

Introduction

The study of surface processes on airless bodies, in particular on the Moon, is an important task today and in the future. Most remote sensing data is obtained from the surface layer of such bodies. This loose surface layer is called regolith. It is the result of the interaction of the surface of airless bodies with outer space. One such interaction is the micrometeorite bombardment.

Investigation of the initial sample

In the article the results of the simulating of the micrometeorite bombardment on the lunar surface by millisecond laser are considered. The target in the experiment was a sample of basalt, similar in composition to the basalts of the mare regions of the Moon. This sample was studied before the experiment, with such techniques as: micro-X-ray analysis, X-ray diffraction analysis and X-ray fluorescence analysis (in %: LOI-2,12, Na₂O-2,03, MgO-6,54, Al₂O₃-14,01, SiO₂-48,71, P₂O₅-0,12, K₂O-0,26, CaO-11,54, TiO₂-1,05, MnO-0,20, Fe₂O₃-13,0).

Experimental technique

We use millisecond Nd-glass pulse laser with a laser radiation wavelength of 1.06 μm, pulse duration of 10⁻³ s, and pulse energy of ~600–700 J. The energy flux density was ~106–107 W/cm². The temperature created in the vaporized cloud was about 4000–5000 K, which corresponded to the temperature of vaporization upon hypervelocity impact processes with collision velocities of about 10–15 km/s. The target—a slice of basalt in a seal—was placed into a hermetic ~500 cm³ volume chamber with an optical window of fused silica. The chamber was purged with the model gas mixture at atmospheric pressure with a volume flow rate of 300–400 cm³/min. After the purging, the gas mixture supply was decreased to ~5 cm³ without closing it completely to avoid an ingress of the atmospheric air into the chamber. [1].

Results

After the laser "impact", the ejection products from the crater and the crater itself were analyzed by various methods. Melt and condensation beads were analyzed by scanning electron microscope. It is shown that some of the beads (about 25%) have undergone of evaporative differentiation, and correspond to the high-aluminous HASP glasses found on the Moon (Al₂O₃ > 34 wt%, SiO₂ < 32%). This can be seen on the fig.1. This graph shows ratio SiO₂/Al₂O₃ against Al₂O₃ in the glass beads. The value of 1,18 (and line with it) shows minimal ratio of SiO₂/Al₂O₃ in anorthite, so dots below this line correspond to the process of evaporative differentiation [2,3]. An important conclusion in the paper is the wide heterogeneity of the compositions of the melt glasses (fig. 2). This is the result of mixing melts in various proportions obtained by melting the original minerals (the black dots on the figure 2) of the target. This is shown by blue arrows. Genesis upon impact of such glasses is shown on partially melted grains of minerals in the crater. The depletion is readily volatile and the average chemical composition shifts to the refractory region was shown. The average composition of initial basalt sample (green dot) shifts toward

blue dot, which reflects the average composition of glass beads. The crater obtained after the laser impact was analyzed by SEM. It revealed traces (or roots) of those formations that were considered in the ejected material (fig. 3). Probably, nanophase iron was found here.

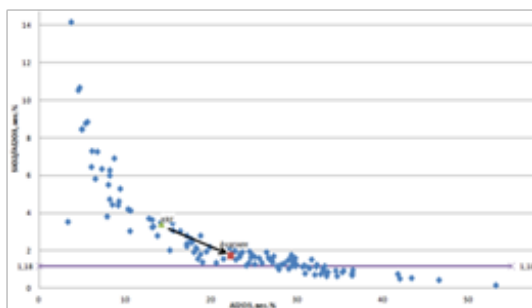


Fig. 1. Ratio $\text{SiO}_2/\text{Al}_2\text{O}_3$ against Al_2O_3 in the glass beads that have been analyzed by SEM. Beads below line at 1,18 correspond to the process of evaporative differentiation.

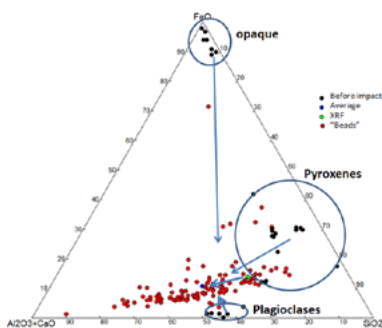


Fig. 2. Triangular diagram, in the corners of which are located oxides of different volatility. The red dots show microanalyses of glass beads. Black dots are microanalyses of the initial minerals in a basalt sample. The blue dot is the average of the analysis of glass beads. The green point is the initial chemical composition of the basalt sample, measured by the XRF method. The arrows show approximate displacements of the compositions of the initial minerals during melting and evaporation.



Fig. 3. The crater obtained by laser impact. It has a diameter of about 6 mm, and a depth of 0.6 mm. Scale bar of this figure is 200 micron.

References:

- [1] Zaitsev M.A., Gerasimov M.V., Safonova E.N., Vasilieva A.S. Peculiarities in the formation of complex organic substances in the nitrogen-methane atmosphere during Hypervelocity Impacts // *Astronomicheskii Vestnik*, 2016, Vol. 50, No. 2, p. 123-140.
- [2] Yakovlev O.I., Shornikov S.I., Ryazantsev K.M. Inversion of the flying of silica and magnesium oxides in the evaporation of hasp-glasses on the moon // *Geochemistry*, 2018, №1, p.77-81.
- [3] Yakovlev O.I., Gerasimov M.V., Dikov Yu.P. Estimation of the temperature conditions for the formation of HASP- and GASP glasses of lunar regolith // *Geochemistry*, 2011, №3, p.227-238.

COUPLED GEOPHYSICAL-GEOCHEMICAL MODELING OF THE MOON

E.V. Kronrod¹, K. Matsumoto², O.L. Kuskov¹, V.A. Kronrod¹, R. Yamada³, S. Kamata⁴

¹*Vernadsky Institute of Geochemistry and Analytical Chemistry, Moscow, Russia, e.kronrod@gmail.com;*

²*RISE Project Office, National Astronomical Observatory of Japan, Mizusawa, Oshu, Iwate, 023-0861 Japan;*

³*The University of Aizu, Research Center for Advanced Information;*

⁴*Creative Research Institution, Hokkaido University*

Keywords:

Moon, numerical modeling, inversion, internal structure, seismic, thermodynamic properties.

Introduction:

In the present work we construct the Moon models which satisfy both geophysical and geochemical data. The problem was solved by inversion of seismic and gravity data by the MCMC method (similar to [1]) combined with thermodynamic approach to calculate the phase composition and physical properties (elastic moduli and density) from chemical composition and temperature. As geochemical constraints, bulk concentrations of Fe and Al oxides were considered.

The model of the Moon:

We apply viscoelastic, spherically symmetric model of the Moon consisting of nine layers: megaregolith, core, four mantle layers, low-viscosity (LVZ) layer, liquid outer core and solid inner core. The physical properties in each zone are assumed to be constant (for the mantle they are calculated in the middle of the layers). The division of the mantle into layers was carried out in accordance with the model [2]: the boundaries between the layers are located at depths of 250, 500 and 750 km.

The concentrations of the main oxides were set equal in the four upper layers of the mantle, the magmatic ocean model was used to calculate the concentrations in the lower mantle (the concentration of oxides in the lower mantle is equal to the average concentration in the upper mantle and crust and equal to the bulk concentration in the Moon [3]. Parameters in the crust (thickness, density, shear and bulk modulus) were fixed.

Geophysical data:

For the inversion the set of geophysical data was used [1]: six geodetic - mean radius (R), mass (M), normalized moment of inertia (I_s), second-order Love number k₂, the quality of Q_m and Q_a with a period of a month and a year [4]. Data on travel times (TT) of seismic waves were taken from [6].

Geochemical models of bulk composition of the Moon:

Two types of geochemical models of the Moon were considered: 1 - bulk Al₂O₃ in the Moon is similar to that of bulk Earth's silicate part: "mean" Al₂O₃ = 4,05 ± 0,36 wt.%; 2 - concentration of Al₂O₃^{3bulk} in the Moon is higher than in silicate Earth: "mean" Al₂O₃ = 5,91 ± 0,39 wt.%. For both types of models "mean" FeO = 12,25 ± 1,33 wt.% ([3, 6] et al.).

Calculation of physical properties in the mantle:

Density and elastic moduli in the mantle are determined by thermodynamic modeling of phase relationships and physical properties in the five-component mineral CaO-FeO-MgO-Al₂O₃-SiO₂. The calculation of phase diagrams for a given composition was carried out by minimizing the Gibbs free energy using the software package and the THERMOSEISM database. The temperature profile was set linear with temperatures from 600 to 1200 °C in the middle of the mantle layers at depths of 150-1000 km. The composition of the crust was specified by the model [7].

Inversion:

A Bayesian inversion approach is an effective method to solve for a nonlinear problem such as planetary internal structure modeling ([1, 6] et al.). This study

utilizes Markov chain Monte Carlo (MCMC) algorithm to infer the parameters of the lunar internal structure. Then, the likelihood function $L(m)$ is calculated ([1]). We considered bulk chemical composition of the Moon as certain value similar to other observed data included into $L(m)$. Bulk Al_2O_3 and FeO concentrations are included into $L(m)$ as observed data. As a result, we expected to obtain probable model of the Moon which in some way optimally corresponds to whole set of constraints.

To estimate an effect of seismic data accuracy on the solution three variants of TT errors have been considered: 1) TT error from [5] – err1, 2) TT from [5] multiplied by three – err3, 3) TT from [5] multiplied by nine – err9.

Results and conclusions:

Main oxides concentrations.

The results of inversion for main oxides concentrations are represented in fig.1, only envelope of histogram bars is shown in the figure.

Though bulk concentrations of Al_2O_3 and FeO were included into $L(m)$ as observed data, in case of err1 a peak value of posterior probability is different from expected value with the difference ~ 1 wt.% (fig. 1). Furthermore, there is no normal distribution of model parameters. In case of err3 posterior distribution is normal or close to normal which conforms well with geochemical constraints. Further increasing of TT error (err9) leads to too wide range of MgO concentrations and seismic velocities (fig. 1). It can be concluded that for err3 we have calculated models of the Moon consistent with both geochemical and geochemical constraints.

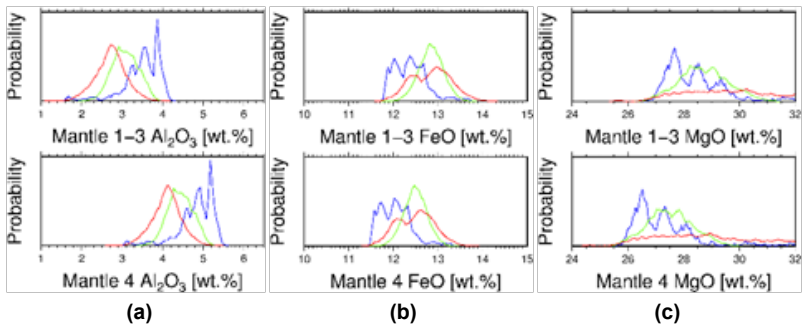


Fig.1. Posterior distribution of main oxides Al_2O_3 (a), FeO (b), MgO (c) in the mantle of the Moon for type-1 (bulk $\text{Al}_2\text{O}_3 = 4,05 \pm 0,35$ wt.% - similar to Earth's). Blue line – err1 (original TT error from [5]). Green line – err3 (TT error from [5] multiplied by 3). Red line – err9 (TT error from [5] multiplied by 9).

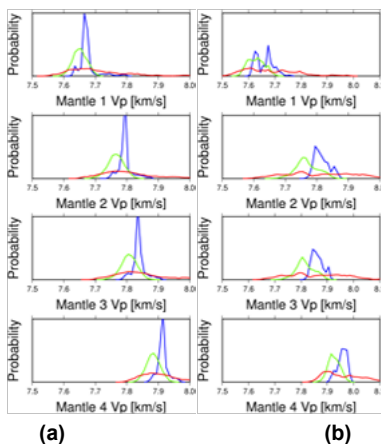


Fig.2 Posterior distribution seismic velocities Vp in the mantle of the Moon for a) type-1 (bulk $\text{Al}_2\text{O}_3 = 4,05 \pm 0,35$ wt.% - similar to Earth's), b) - type-2 ($\text{Al}_2\text{O}_3 = 5,91 \pm 0,39$ wt.% - higher than Earth's). Blue line – err1 (original TT error from [5]). Green line – err3 (TT error from [5] multiplied by 3). Red line – err9 (TT error from [5] multiplied by 9).

Seismic velocities.

The results for seismic velocities for both types of bulk composition models are shown in fig. 2. In the upper mantle (where the accuracy of TT estimation is the most precise because of large quantity of seismic events) calculated seismic velocities are in a good agreement with [2] model. However, in the lower mantle layers calculated velocities appeared to be lower than those of [2] model, and the difference increases with depth. However, velocities from our model are consistent with those from [8, table 1].

References:

- [1] Matsumoto K., Yamada R., Kikuchi F., Kamata S., Ishihara Y., Iwata T., Hanada H., Sasaki S. Internal structure of the Moon inferred from Apollo seismic data and selenodetic data from GRAIL and LLR // *Geophysical Research Letters*. 2015. V. 42, 18. P. 7351–7358. doi: 10.1002/2015GL065335
- [2] Gagnepain-Beyneix J., Lognonné P., Chenet H., Lombardi D., Spohn T. A seismic model of the lunar mantle and constraints on temperature and mineralogy // *Phys. Earth and Planet Int.* 2006. V. 159. P. 140-166.
- [3] Kronrod V.A., Kuskov O.L. Inversion of seismic and gravity data for the composition and core sizes of the Moon // *Izv. Phys. Solid Earth*. 2011. V. 47. P. 711-730.
- [4] Williams J. G. and D. H. Boggs. Tides on the Moon: Theory and determination of dissipation // *J. Geophys. Res. Planets*. 2015. V. 120. P. 689–724
- [5] Lognonné P., Gagnepain-Beyneix J., Chenet H. A new seismic model of the Moon: implications for structure, thermal evolution and formation of the Moon. *Earth and Planetary Science Letters*. 2003. V. 211. P. 27-44
- [6] Khan A., Connolly J. A. D., Maclennan J., Mosegaard K. Joint inversion of seismic and gravity data for lunar composition and thermal state // *Geophys. J. Int.* 2007. V. 168. P. 243–258.
- [7] Taylor S.R. *Planetary Science: A Lunar Perspective* // Houston. TX. LPI. 1982. P. 481.
- [8] Lognonné P. *Planetary seismology* // *Annu. Rev. Earth Planet.* 2005. V. 33. P. 571–604.

GEOMORPHOLOGICAL MAP OF THE MONS RÜMCKER PROVINCE

A.A. Dmitrovsky, E.N. Slyuta

*Institute of Geochemistry and Analytical Chemistry of the Russian Academy of Sciences, Moscow, Kosygina str., 19
andredmitrovsky@gmail.com*

Keywords:

Mons Rümker, geomorphology, Oceanus Procellarum.

Introduction:

Mons Rümker is a volcanic province, which is located in the Oceanus Procellarum (40.8°N 58.1°W). It is exceptionally attractive place because of spatial superposition of unexplored volcanic features and marine materials of wide spectrum of ages (from Lower Imbrian Series to Copernican System) in the vicinity [1]. That is why this region is supposed for being primary target for Russian heavy rover "Lunar Robot-Geologist" [2, 3]. In order to prepare for the mission, the study of morphology, history and matter of the volcanic province has been begun [4]. The dome's relative elevation is about 1 km and about 70 km in diameter [5]. It has asymmetric slopes, the eastern is gentler. The rise consists of at least ten individual volcanoes, as they are understood. Some of them have calderas at the top.

There is no detailed geomorphological map of the province created so far. To fill this gap our investigation is carried out.

Methodology:

The research is based on the LRO NAC images of the province with resolution 1-2 m/pixel. We focus on main morphological features of the province as volcanic domes, fault-like structures and lava flows and their correlation with our previous age estimations of its different parts.

Results:

Our research is still in progress. We plan to complete our map and present it by the middle of September 2018.

References:

- [1] Wilhelms D. E. USGS Prof. paper 1348, 1987
- [2] Slyuta E. N., Galimov E. M., Marov M. Ya. Fundamental space research. V. 2. Solar System. 2014, 103-128.
- [3] Slyuta E. N., 7MS3 Abst. # PS-18, 2016
- [4] Makhatadze G.V. et al., 7MS3 Abst. PS-17, 2016
- [5] Zakharova M. A. and Slyuta E.N. 7MS3 Abst. MN-15, 2016

MERCURY RELIEF: ANALYSIS AND MORPHOLOGICAL CLASSIFICATION

A.Yu. Zharkova^{1,2}, A.A. Kokhanov¹, M.M. Kolenkina¹

¹*MExLab, Moscow State University of Geodesy and Cartography, Gorokhovskiy per.4, Moscow, Russia, 105064, a_zharkova@miigaik.ru;*

²*Moscow State University Sternberg Astronomical Institute, Universiteyskiy pr.13, Moscow, Russia, 119234.*

Keywords:

Mercury, Relief features, Morphometric analysis, Morphological classification, Planetary mapping.

The study of the relief characteristics by thematic mapping helps to identify common patterns in planetary relief. Calculations of Mercury morphometric parameters were performed before according to the laser altimetry obtained by MESSENGER [1]. Now our possibilities have expanded, because we are analyzing and mapping Mercury surface by new global and local DEMs. In our work for morphometric calculations we use the newest high resolution DEMs obtained based on photogrammetric processing of MESSENGER stereo images:

- the first global Mercury DEM with the resolution 665 m/pixel [2];
- DEMs on Mercury quadrangles with resolution ~ 222 m/pixel [3].

Depending on the tasks, the statistical parameters of planetary relief are calculated in different ways. For the purposes of our study we use combination of two techniques:

- Interquartile range of the second derivative of heights. For this method we use a previously developed tool integrated into the ArcGIS software [4]. Interquartile range excellently points to smooth plains (type of surface, which typical for Mercury).
- Relative topographic position (RTP). For this method topographic position of each pixel is identified with respect to its local neighborhood [5]. Results of calculations are useful for automatic identifying rims of craters and relief depressions – concave/convex objects.

As a result, we developed the first trial version of the classification of Mercury macrolief forms and created layout of future global morphological map of Mercury. Such results can be used to process the data of the future European mission BepiColombo (2018).

Acknowledgment:

The work was supported by Russian Foundation for Basic Research (RFBR), project №18-35-00334.

References:

- [1] Kreslavsky, M.A., Head, J.W., Neumann, G.A., Zuber, M.T., Smith, D.E.: Kilometer-Scale Topographic Roughness of Mercury: Correlation with Geologic Features and Units // *Geophysical research letters*, Vol. 4, Issue 23, pp. 8245-8251, 2014.
- [2] Becker, K.J., Robinson, M.S., Becker, T.L., Weller, L.A., Edmundson, K.L. Neumann, G.A., Perry, M.E., Solomon, S.C.: First Global Digital Elevation Model of Mercury // 47th Lunar and Planetary conference, The Woodlands, Texas, March 21-25, Abstract # 1903, 2016.
- [3] Preusker, F. Oberst, J., Stark, A., Matz, K-D., Gwinner, K., Roatsch, T.: High-Resolution Topography from MESSENGER Orbital Stereo Imaging – The Southern hemisphere // *EPSC Abstracts*, Vol. 11, EPSC2017-591, 2017.
- [4] Kokhanov, A.A., Bystrov, A.Y., Kreslavsky, M.A., Matveev, E.V., Karachevtseva, I.P.: Automation of morphometric measurements for planetary surface analysis and cartography // *In Int. Arch. Photogramm. Remote Sens. Spatial Inf. Sci.*, XLI-B4, p. 431-433, 2016, doi: 10.5194/isprs-archives-XLI-B4-431-2016.
- [5] Jenness J. Topographic Position Index (TPI) v 1.2. Extension for ArcView 3x // *Jenness Enterprises*, 2006, <http://www.jennessent.com/arcview/tpi.htm>.

GEOLOGICAL MAPPING OF THE SOUTH POLE OF MOON

S.S. Krasilnikov^{1,2}, M.A. Ivanov¹

¹*Vernadsky Institute of geochemistry and analytical chemistry of RAS, Moscow, Russia, krasilnikov@mps.mpg.de;*

²*Max Planck Institute for Solar System Research, Göttingen, Germany.*

Keywords:

Moon, geology, geological map, South Pole, Luna Globe, Luna-25.

In recent time South Pole of Moon, draw attention of science society. This connected with presence of hydrogen concentration [1] and possibly in the form of ground ice [2]. Interest in South pole also explained by possibilities to explore older Moon material from pre-Nectarian (pN) and Nectarian (N) epoches [3]. South pole of Moon was selected as primary landing side for future Russian mission Luna-Glob (Luna-25). This interest needs for clarification and rescaling of classic general geological maps (eg Wilhelms et al., 1979). In our research geological map of South pole of Moon in Polar Stereographic projection with the center in -90° and radius of circle 500 km was made.

Big effect on studied region had formation of basins, especially South Pole-Aitken basin (SPA), which cross the South pole and have series of rim remnants. Secondary craters made substantial contribution in formation of terrain in South pole. Injections and secondary craters from Schrödinger crater (N) Hausen, Moretus (Eratosthenian system (E)) and Antoniadi (Imbrian system (I)) craters can be found in studied region. Flat or slightly rough surface can be found in crater or on the plain in abundance. This surfaces usually covered by secondary injections.

New geological mapping of this territory helps to understand history and formation of this region.

Acknowledgments.

This research supported by the grant of the Russian Science Foundation (project no. 17-17-01149). KSS was also supported by the Deutscher Akademischer Austauschdienst (DAAD).

References:

- [1] Sanin, A.B., Mitrofanov, I.G., Litvak, M.L., et al., Hydrogen distribution in the lunar polar regions // *Icarus*. 2017. 283. 20–30
- [2] Mitrofanov I.G., Litvak M., Sanin A., et al., Testing polar spots of water-rich permafrost on the Moon: LEND observations onboard LRO // *J. Geophys. Res.* 2012. V. 117. E00H27
- [3] Ivanov M.A., Basilevsky A.T., Bricheva S.S., et al., Fundamental Problems of Lunar Research, Technical Solutions, and Priority Lunar Regions for Research // *Solar System Research* 2017. 51(6):441-456
- [4] Wilhelms, D.E., Howard, K.A., Wilshire, H.G. Geologic map of the South Side of the Moon. US Geological Survey Map I-1192. 1979.

LUNAR ROTATION FROM HIGH-RESOLUTION LASER ALTIMETER DTMS AT THE LUNAR POLES

A. Stark¹, J. Oberst^{1,2}, S. Annibaldi¹, H. Hussmann¹

¹German Aerospace Center, Institute of Planetary Research, Rutherfordstr. 2, D-12489, Berlin, Germany, alexander.stark@dlr.de;

²Technische Universität Berlin, Institute of Geodesy and Geoinformation Science, Straße des 17. Juni 135, D-10623, Berlin, Germany

Keywords:

Moon, Rotation, Laser altimeter, DTM, Lunar poles.

Introduction:

The Moon exhibits a complex rotational state, including precessions, nutations and librations. While some early measurements were made from Earth-based telescopic observations, the current knowledge on Moon's rotation arises from decades of Lunar Laser Ranging (LLR) from Earth to retroreflectors on the lunar surface [1,2]. Indeed, the accuracy level of the orientation solution reaches up to the meter level and allows valuable insights in the deep interior of the Moon [3]. In this work we aim at providing an independent measurement of the rotational state of the Moon with the Lunar Orbiter Laser Altimeter (LOLA) data.

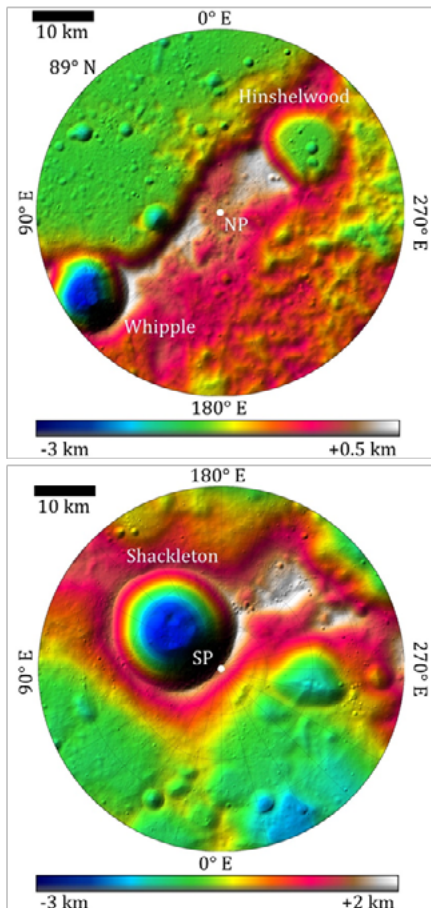


Fig. 1. Digital terrain models (DTMs) of the Lunar north (top) and south (bottom) poles. Each DTM covers an area 2889 km² (1 degree circle) and has a lateral resolution of 10 meters per grid element. The heights are referenced to a 1737.4 km sphere and are based self-registered LOLA profiles data (see text).

Method:

After more than seven years in orbit about the Moon the LOLA instrument, onboard NASA's Lunar Reconnaissance Orbiter (LRO), provided excellent coverage of the lunar topography [4]. Especially at polar regions the density of highly accurate laser altimeter measurements permits creation of digital terrain models (DTMs) with lateral resolution reaching up to 10 meters per grid element (Figure 1). In order to perform our measurements of the lunar rotation we at first construct reference DTMs by iterative self-registration. Thereby individual profiles are registered to the DTMs constructed from other profiles in the same area. Within this step we remove the offsets within the profiles caused by residual mis-modelling in LOLA pointing, LRO orbit reconstruction, and rotation state of the Moon. Finally, we compute the inertial coordinates of the nominal LOLA footprints and solve for the rotation parameters required to bring them in agreement with the reference DTMs.

Results:

Based on almost 50 million LOLA footprints from the lunar north (6441 profiles) and south (7062 profiles) pole we demonstrate the recovery of small oscillations in the orientation of the lunar rotation axis (in the order of ten arc seconds) in agreement with models obtained from LLR data [5]. With the large amount of spatially concentrated and time-distributed measurements we can precisely track the rotation of the Moon.

References:

- [1] Hofmann F. et al., JoG, in press, doi: 10.1007/s00190-018-1109-3, 2018.
- [2] Viswanathan V. et al., INPOP17a planetary ephemerides, 2017.
- [3] Williams, J. G., and D. H. Boggs (2015), JGR-Planets, 120, 689-724, doi: 10.1002/2014JE004755, 2015.
- [4] Smith D. E. et al., Icarus, 283, 70-91, doi: 10.1016/j.icarus.2016.06.006, 2017.
- [5] Williams, J. G. et al. DE421 lunar orbit, physical librations, and surface coordinates. JPL Interoffice Memorandum IOM 335-JW,DB,WF-20080314-001, 2008.

LUNAR RADIO RANGING AND THE PROSPECT OF MARTIAN RADIO RANGING

W.X. Li^{1,2,3,5}, J.S. Ping^{1,3}, Q. Meng⁴, C.Y. Chen⁴, M.Y. Wang¹, T.Y. Zhang⁴,
W.Z. Zhang^{1,6}, L. Han⁷, J.H. Zhang⁷, N. Wang^{2,3}

¹National Astronomical Observatories, CAS, China(20A Datun Road, Chaoyang District, Beijing, China) liwenxiao@xao.ac.cn;

²Xinjiang Astronomical Observatory, CAS, China;

³University of Chinese Academy of Sciences, Beijing, China;

⁴School of Information Science and Engineering, Southeast University, China;

⁵Shanghai Astronomical Observatories, CAS, China;

⁶Department of Astronomy, Beijing Normal University, China;

⁷China Xi'an Satellite Control Center Jiamusi Measurement and Control Station, China;

Keywords:

CE-3 lander, Lunar Radio Ranging, Martian Radio Ranging

Introduction:

In Dec. 2013, Chang' E 3 lander was successfully soft-landed on lunar surface of Sinus Iridum area. Radio beacon, which is carried on the lander, transmitted uplink signal for remote measurement and controlling. Basing on precise frequency and phase measurement, we achieved the Lunar Radio Ranging (LRR) and obtained high-level resolution on observation, which is about 0.18 mm/s for velocity and 0.8 mm for ranging. With this precision, we could correct the dynamical position of tracking station and lunar lander. Furthermore, the Earth Orientation Parameter could be resolved from observation independent from other techniques. Our target on Moon is the physical librations on short periods. Equivalence principle test is a long-term goal in our ranging analysis process. Expectedly, the ranging technique could be applied for Martian mission in the future. It would help us understand the dynamical procedure of Martian orbiting and spinning, and improve the ability of deep space exploration of our nation. In InSight landing mission, there is observation collaboration between China and Russia. Thus, we simulated Doppler difference between Mars with spinning and without spinning. It showed that accurate Martian spinning period would be primary result of Martian Radio Ranging.

References:

- [1] Dickey J.O., Bender P.L., Faller J.E., et al. Lunar laser ranging: a continuing legacy of the apollo program // Science. 1994. V. 265. No. 5171. P. 482-90.
- [2] Pong J.S., Meng Q., Wang M., Tang G.S., et al. Introduction about the Preliminary Radio Science Experiment in Chinese Lunar Landing Mission Chang'E-3 // IEEE. 2014. 1-4.
- [3] Petit G, Luzum B, Al E. IERS Conventions (2010) // Iers Technical Note. 2010. 36.
- [4] Folkner W.M., Asmar S.W., Dehant V, et al. The Rotation and Interior Structure Experiment (RISE) for the InSight Mission to Mars// Proceedings of the Lunar and Planetary Science Conference. The Woodlands, Texas. USA. 2012.
- [5] Yseboodt M, Dehant V, Peters M.J.. Signatures of the Martian rotation parameters in the Doppler and range observables // Planetary and Space Science. 2017. 144. 74-88

LUNAR PHYSICAL EXPLORATION SYSTEM OF CHANG'E-4 LANDING AREA

Y. Lu¹, V. V. Shevchenko²

¹National Remote Sensing Center of CHINA, MOST, luyangxiaoyi@gmail.com;

²Sternberg Astronomical Institute, Moscow, Russia

Keywords:

Chang'e-4, Queqiao data relay satellite, Lagrangian-2 point, Von Kármán crater.

Introduction:

With the successful launch of the “Queqiao” lunar data relay satellite, mankind is about to make its first soft landing on the far side of the moon and make a tour exploration. Chang'e-4 will land in the Von Kármán impact crater area of the South Pole- Aitken basin. Crater Von Kármán is a lunar impact crater that is located in the southern hemisphere on the far side of the Moon. The remainder of the outer wall is roughly circular in shape, although it is irregular and heavily worn by subsequent impacts. The lunar physical probe system will detect chemical elements in lunar soil and lunar surface materials, including water ice. The survey data will then be sent back to earth via the relay satellite.

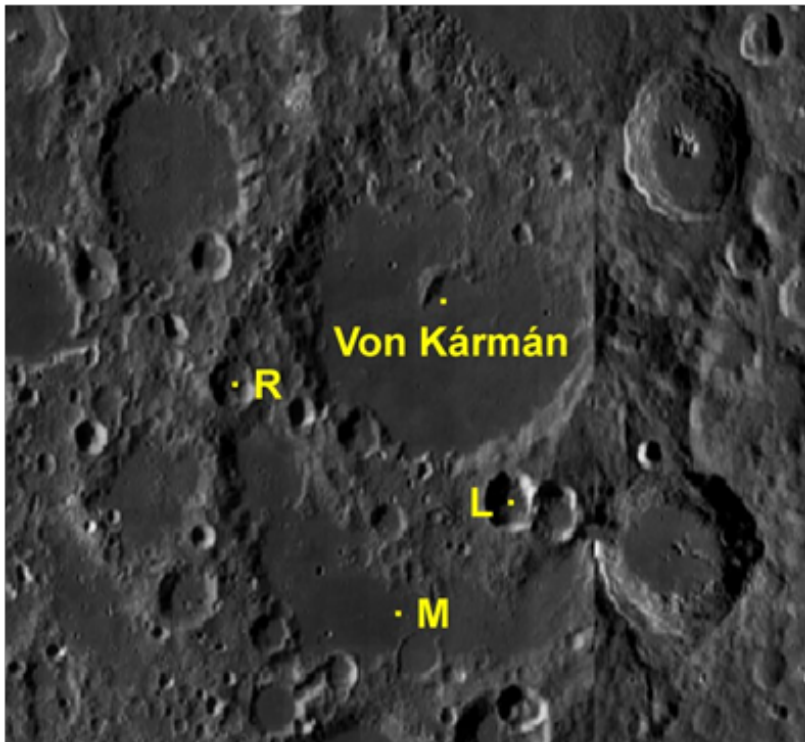


Fig.1. Crater Von Kármán

THE CHOICE OF THE LANDING SITE AND THE ROUTE OF THE LUNOKHOD FOR RESEARCH AND EXPLORATION OF VOLATILE COMPONENTS IN THE LUNAR SOIL

O.S. Tretyukhina, M.A. Sundeeva, E.N. Slyuta

Vernadsky Institute, Moscow, Kosygina street 19, 119334,
mari.al.zakharova@gmail.com;

Keywords:

WEH, route; lunokhod; lunar soil; volatile components, Moon, GIS, LRO, LOLA

Introduction:

There are three criteria of potential places of exploration of volatile components by moon Rovers:

- spatial distribution of forecast stocks of volatile components;
- the slope of the land, potential hazards to Rover/Rover, stones, steep slopes of craters;
- technical features of the lunar Rover, which determine its maximum estimated length of the route, the maximum slope of the surface on which it is able to move, the distance between the front and rear pair of wheels, the height of the clearance.

Data and area of research:

The concentration of volatile components is the most compact and high in the Central Polar Regions, and at the South Pole it is the most pronounced, which makes it the first priority for direct research by the robotic system (Fig.1, 2). For a preliminary assessment of the terrain for the construction of the optimal and most secure route, we have made two maps of the terrain for both poles. The maps are based on the data of laser altimetry of LOLA (Lunar Orbiter Laser Altimeter) module of LRO (Lunar Reconnaissance Orbiter) spacecraft. They are made in polar stereographic projection, as well as maps of distribution of volatile components. Both maps have a resolution of 30 meters and full coverage up to 75 degrees of the corresponding latitude, partial coverage reaches a parallel of 70 degrees of latitude. The scale of both maps is 1:5 000 000, the heights are painted in accordance with the classification of the relief on the steps of 500 meters. In addition, both maps contain a translucent layer with shadow relief for a more visual image of the terrain features in these areas.

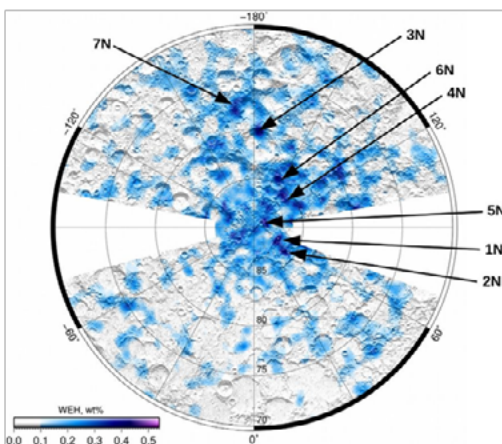


Fig. 1. A map of the distribution of the content of water equivalent hydrogen (WEH) weight% at the North pole according to the LEND instrument on LRO AMS. The arrows show the anomalies with the highest WEH content [1].

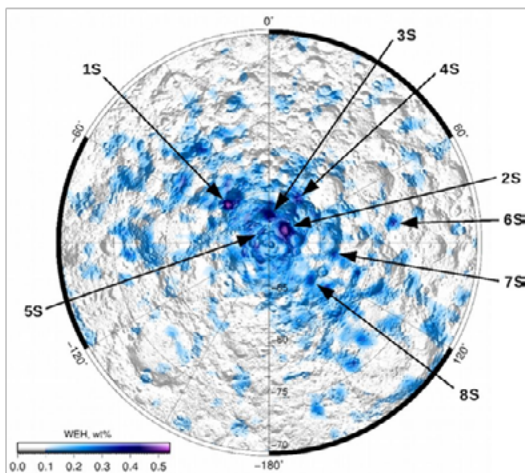


Fig. 2. A map of the distribution of the content of water equivalent hydrogen (WEH) weight% at the South pole according to the LEND instrument on LRO AMS. The arrows show the anomalies with the highest WEH content [1].

Results:

According to the results we decided that the most probable and optimal route that passes through one of the maxima of the water equivalent of hydrogen and through all categories of its distribution intensity (Fig. 3, 4). In addition, the route is built taking into account the avoidance of large craters and steep slopes and runs on a relatively flat part of the South pole. The total length of the route is 237 kilometers, while there are no technical characteristics of the future lunar Rover, this figure may change in the smaller direction, but taking into account the preservation of the route through the peak of the accumulation of volatile components.

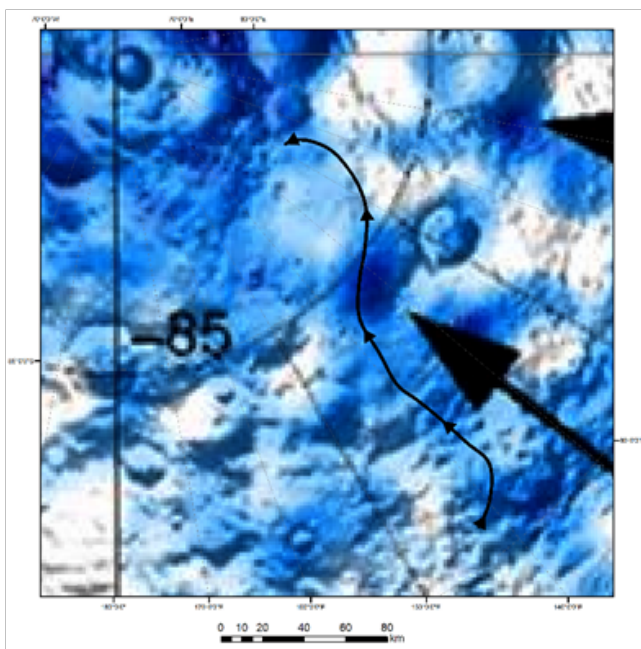


Fig. 3. The expected route of the lunar Rover on the distribution layer of volatile components.

The landing site of the module is planned to be placed accordingly in the southern part of the route closer to its beginning.

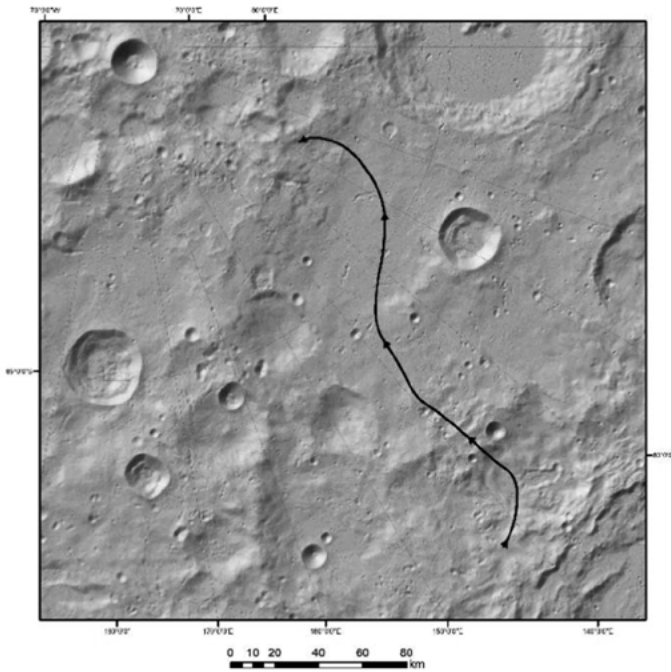


Fig. 4. The proposed route of the lunar Rover on the layer of shadow washing.

References:

- [1] Sanin A.B., Mitrofanov I.G., Litvak M.L., Bakhtin B.N., Bodnarik J., Boynton W., Chin G., Evans L., Harshman K., Fedosov F., Golovin D.V., Kozyrev A.S., Livengood T., Malakhov A.V., McClanahan T., Mokrousov M.I., Starr R.D., Sagdeev R.Z., Tret'yakov V.I., Vostrukhin A.A, Hydrogen Distribution in the Lunar Polar Regions // *Icarus*. 2017. 283. 10.1016/j.icarus.2016.06.002.

SEISMIC SHAKING ROLE IN SMALL LUNAR CRATER DEGRADATION

B.A. Ivanov

*Institute for Dynamics of Geospheres, Russian Academy of Science, Leninsky Prospect 38-1, Moscow, Russia, 119334
baivanov@idg.chph.ras.ru*

Keywords:

Crater degradation, bombardment rate, Apollo landing sites, LROC images.

Introduction:

Small lunar craters with diameters below ~ 100 m are the youngest (< 0.5 Ga) geologic formations. While a few large impact craters have been formed during this time, small lunar craters and their degradation rates in various locations allow us investigate modern lunar surface processes. Here we estimate the seismic shaking input in the small crater degradation.

Minimal model for seismic shaking efficiency:

The crater degradation due to seismic shaking is believed to be an important factor on asteroids [1, 2, 3] as well on the Moon [2]. Richardson [3] proposes that a regolith layer slowly moving down a crater slope while a seismic wave shakes the area. The idea has a problem with the correct assumption how thick is the sliding layer. Here we search for a model of a slow "creep" of the under-crater material without *a priori* assumptions for the sliding layer thickness.

We discuss the late stage of a crater degradation when the slope landslide mode mass wasting looks less probable than for steep slopes.

We assume that the surface material around a crater is in a static equilibrium where small elastic stresses around a crater depression in the lunar gravity field are locked with the dry friction forces. The characteristic elastic shear deformation, γ , is of the order of τ/G , where τ is the shear stress, and G is the shear elastic modulus. For simplicity we imagine that stressed under-crater material consists of rectangular blocks with the characteristic size x . Shear deformation results in elastic displacement $\Delta x \sim \gamma x$. The approach is quite similar to the acoustic fluidization reasoning [4]. At an enough strong seismic shaking the local friction vanishes and each block of material slightly deforms to put its γ to zero. It means a block restores its unloaded shape and moves relatively neighbor blocks to a distance of Δx . After the shaking event blocks again deforms under the gravity loading and restore their shear deformation of the order of $\gamma \approx \tau/G$. The net effect of an elementary shaking is small displacement, $\Delta x \sim \gamma x$, along block boundary. If shaking repeats over an average time period of Δt , such a behavior of a block system may be treated as viscous one. The shear strain rate is, naturally, $\dot{\epsilon} = \gamma/\Delta t$, and the evolution of elastic stresses under periodic shaking may be presented as $\tau = \text{visc} \times \dot{\epsilon}$, where "viscosity" $\text{visc} \sim G \times \Delta t$.

The shear modulus may be expressed as $G = \rho \times c_t^2$, where ρ is the granular material bulk density, and c_t is the transversal sound speed. In these terms the kinematic viscosity $\nu = \text{visc}/\rho = c_t^2 \times \Delta t$. The prominent result is that the "shaking creep" viscosity in the presented model could be estimated through the sound speed and the average time between shaking events. To make numerical estimates we assume relatively small $G \sim 100$ MPa and c_t of the order of 250 ms^{-1} , typical for blocks in a granular media, as well as for lunar regolith [5, 6]. For example, if the local shaking events are repeated every 100 years (3×10^9 s), the "shaking creep" viscosity would be of the order of $2 \times 10^{14} \text{ m}^2 \text{ s}^{-1}$. If one shaking event includes multiple critical shaking in a set of oscillations, the effective viscosity would be correspondingly smaller.

Number of seismic shaking events from nearby impacts:

With the "shaking creep viscosity estimate (see the previous section) we are able to estimate how probable is the pure seismic small lunar crater degradation. To make these estimates we use data on the life time of small craters. Following [7] we find that a crater with diameter D degrades to depth/diameter ratio of 0.06 during the time period about $T(\text{Myr}) \sim 5 \times D(\text{m})$.

Hence for craters with $1 < D(\text{m}) < 100$ m time to severally degrade is in the range from 5 to 500 Myr. This time may be compared with the viscous solution where the degradation time (a proxy for e-fold depth decay) $T \sim \nu/gD$ [8, p. 83, eq. 3.34]. Hence, for a crater of diameter D in a target with shear waves velocity c_t the almost constant T/D for $1 < D(\text{m}) < 100$ m [7] we find

$$T \sim \nu/gD = c_t^2 \times \Delta t / gD; \text{ or } N = T/\Delta t \sim c_t^2/gD \quad (1)$$

where $N = T/\Delta t$ is the number of shaking events needed for sufficient crater degradation.

For $T/D \approx \text{const}$, the number of shaking events should decrease with D as $N \sim c_t^2/gD^2$. From one side, the number of critical shaking events should dramatically decrease with the crater diameter. From the other side, the areal density of craters per unit area decreases with D as $(N/S) = A \times D^{-3}$, where A = for Neukum's chronology. If, for simplicity, we estimate the number of craters with diameters $\geq D$ to shake the crater of interest as $N/S = A \times D^{-3} \sim c_t^2/gD^2$. Hence, we can estimate the "active" area $S = \pi D_{\text{seism}}^2$ which accumulates during the time T a proper number of impacts, generated critically strong impact shaking.

Outlining once more the preliminary character of the estimate, we finalize here numerical results with the formula, expressing the ratio $f = D_{\text{seism}}/D$:

$$f \sim a \sqrt{\frac{c_t^2}{\pi g A T}} \quad (2)$$

Where a is the coefficient integrating all known uncertainties, such as a number of "shaking events" from one nearby impact. Assuming for simplicity that one impact creates one "shaking" event, we find that for a crater with $D=1$ m f is about 800, and for $D=100$ m f is about 80. It means, that to explain a crater degradation in a time period, estimated in [7], we should assume that each crater, formed closer than 400 m from a 1-m crater, or closer 4 km from a 100-m crater should result in a "critical shaking", following with a "shaking creep" episode in under-crater materials.

Discussion and conclusions:

The presented work is aimed (1) to propose a most conservative scenario for seismic shaking and the following "seismic creep" of a granular material around small craters with diameters from 1 to 100 m, and (2) to estimate how large is the "seismic" area around these craters to explain crater degradation with this "conservative seismic shaking". The following work in this project should confirm or reject the idea, that seismic shaking is able to explain observed small crater degradation rate with seismic shaking only.

With our current understanding of the seismic shaking it seems that the "seismic area" estimates given above are too large to be true. It means that other degradation mechanisms operate as proposed in [2]. From the other side, the "viscous" shaking model predicts the enhancement of seismic shaking for larger craters, there are some reasons to continue to study it. Unfortunately to this model, the larger craters penetrate more competent basement under the lunar regolith. So, the next problem is to search for a proper crater diameter where the "shaking creep" could compete other mechanisms.

Acknowledgements:

The project is supported by Program 28, Russian Academy of Science Presidium.

References:

- [1] Richardson J.E., Melosh H.J., Greenberg R.J., O'Brien D.P. The global effects of impact-induced seismic activity on fractured asteroid surface morphology // *Icarus*. 2005. V. 179. P. 325-349.
- [2] Richardson, J.E. Cratering saturation and equilibrium: A new model looks at an old problem // *Icarus*. 2009. V. 204. P. 697-715.
- [3] Richardson J.E. Three-Dimensional Modeling of Crater Degradation via the Effects of Impact Induced Seismic Shaking, with Comparison to Crater Count Data // Lunar and Planetary Science Conference, Woodland TX. USA. 2013. No. 2397.
- [4] Melosh H.J., Ivanov B.A. Impact Crater Collapse // *Annual Review of Earth and Planetary Sciences*. V. 27. PP. 385-415.
- [5] Lemrich L., Carmeliet J., Johnson P. A., Guyer R., Jia X. Dynamic induced softening in frictional granular materials investigated by discrete-element-method simulation // *Physical Review E*. 2017. V. 96. No. 6, P. 062901.

- [6] Heiken G. H., Vaniman D. T., French B. M. (Eds.) Lunar sourcebook - A user's guide to the moon // Cambridge University Press, 1991. 753p.
- [7] Ivanov, B.A. Size-Frequency Distribution of Small Lunar Craters: Widening with Degradation and Crater Lifetime // Solar System Research. 2018. V. 52. P. 1-25.
- [8] Melosh H.J. Planetary Surface Processes // Cambridge University Press. 2011. 520 p.

VARIATION OF NEAR-EARTH OBJECT POPULATION BASED ON ANALYSIS OF DIAMETERS OF LUNAR CRATERS

S. I. Ipatov¹, E. A. Feoktistova², V. V. Svetsov³

¹V.I. Vernadsky Institute of Geochemistry and Analytical Chemistry of RAS, Moscow, Russia. siipatov@hotmail.com;

²P.K. Sternberg Astronomical Institute, M.V. Lomonosov Moscow State University, Moscow, Russia

³Institute of Dynamics of Geospheres of RAS, Moscow, Russia

Keywords:

Lunar craters, diameters, impactors, near-Earth objects, the Oceanus Procellarum

Observed lunar craters:

We analyzed diameters of lunar craters in the region of the Oceanus Procellarum with age less than $T_{OS}=1.1$ Gyr. Data on the craters were taken from the database of the lunar craters of the P.K. Sternberg Astronomical Institute. The ratio r_{OS} of the area of the considered region to the full surface of the Moon is 0.176. The number N_{obs} of craters with diameter D greater than 18 or 19 km in the considered region is 49. In the above region, the number of the craters with $D \geq 15$ km is equal to 56, and the number with $D > 15$ km (the same number with $D \geq 16$ km) is 52. Results of our analysis of the number of craters of different sizes in the above region are in accordance with the earlier conclusion [1] that the number of impactors with a diameter $d > D_p$ is proportional to $D_p^{-2/3}$.

Impact velocities:

In [2] the RMS velocity of distribution of impacts of former main-belt asteroids migrated to near-Earth region with the Moon is considered to be 18.3 km/s, but velocities in their figure 10 were in the range from 7 to about 50 km/s. The mean lunar impact velocity was calculated to be 19.3 and 19.7 km/s in [3] and [4], respectively. In [5] typical velocities of planetesimals migrated from the zone of Jupiter and Saturn to the Earth and entering the Earth's sphere of action were estimated to be in the region of 21 – 24 km/s.

Diameters of impactors corresponding to diameters of lunar craters:

Werner and Ivanov [6] concluded that the final rim crater diameter, D_v (in km), for a vertical impact is $D_v = 4(D_p \cdot U^{0.58-0.91})^{0.91}$, (1)

where D_p is the diameter of the impactor, and U is the impact velocity in km/s. The formula (1) was obtained for complex craters with a diameter of more than 15 km. The size of a crater depends also on the impact angle θ approximately as $(\sin\theta)^{1/3}$ [7]. Taking into account that the impact probability density is equal to $\sin 2\theta$, for the mean (over angles) value of the diameter of the crater, the coefficient 4 in (1) should be changed for 3.3. The dependence D_v is most sensitive to U . Since $U^{0.58-0.91}$ is close to $U^{0.5}$, D_v changes by about 2 times if U varies by 4 times. In figure 11 of [2] the ratio D_v/D_p of a diameter of a crater to a diameter of an impactor varied by more than a factor of 10 at the same D_p for different possible velocities of impacts. Based on the formula (1) with the coefficient 3.3, we obtain that the average diameter D_v of the crater that is produced by impactors with a diameter $D_p=1$ km is 15.3 km, 15.7 km, and 17.7 km for the impact velocity equal to 18.3 km/s, 19.7 km/s, and 24 km/s, respectively.

The number of discovered near-Earth objects (NEOs) with diameter $d > 1$ km was 893 on July 10, 2018 (<https://cneos.jpl.nasa.gov/stats/size.html>), and the total number N_1 of such NEOs is estimated to be about 920.

Characteristic times elapsed before collisions of NEOs with the Earth and the Moon:

The ratio k_{ECO} of the number of near-Earth objects (i.e., asteroids with a perihelion distance less than 1.3 astronomical units) to the number of Earth-crossing objects (ECOs) was estimated in [8] to be about $1300/756 \approx 1.72$. The similar

ratio (6718/3906 \approx 1.72) was considered for the objects discovered before June 1, 2010 [1]. For present data from Wikipedia, this ratio is about 1.5, but this smaller (than 1.72) value can be due to that it is easier to discover small ECOs than other NEOs. ECOs include Amor and Aten objects.

Characteristic times T_E elapsed before collisions of an Apollo object and of an Aten object with the Earth were estimated in [8] to be about 164 and 15 Myr, respectively. For all ECOs T_E equaled to 67 Myr. Before 2004 the value of T_E was obtained to be 134 Myr in [9], 120 Myr for 54 Apollo objects in [10], and 105 Myr for 363 Apollo objects in [11]. The smaller than in previous papers values of T_E in [6] were due to several Atens with small inclinations discovered at the beginning of 2000th. For the increase of the inclination of the Aten object 2000 SG344 from its present value equaled 0.1° to 1°, the values of T_E in [8] were obtained to be equal to 28 Myr and 97 Myr for Atens and all ECOs, respectively. These longer times illustrate the importance of rare objects with high probabilities of collisions with the Earth. Studies of dynamics of initially Earth-crossing objects and resonant asteroids showed [8, 12] that the probability of a collision of one object with the Earth can be greater than for thousands of other objects in similar orbits. The ratio p_{EM} of probabilities of collisions of NEOs with the Earth to that with the Moon is considered to be about 22 [3].

Comparison of the number of observed lunar craters with the estimated number based on the number of NEOs:

The number of impacts of NEOs with a diameter $d > 1$ km onto the considered lunar region during time T_{OS} can be estimated to be

$$N_{est} = N_1 \cdot r_{OS} \cdot T_{OS} / (T_E \cdot p_{EM} \cdot k_{ECO}) \quad (2)$$

For $N_1 = 920$, $k_{ECO} = 1.72$, $r_{OS} = 0.176$, $T_{OS} = 1100$ Myr, $T_E = 100$ Myr, $p_{EM} = 22$, we have $920 \cdot 0.176 \cdot 1.1 / (0.1 \cdot 22 \cdot 1.72) \approx 47$. For N_{obs} equaled to 52 and 56 mentioned above, the ratio N_{obs} / N_{est} is close to 1.1^{obs} and 1.2, respectively.

According to [13], a recent catastrophic disruption of a large main-belt asteroid 160 Myr ago could increase N_1 compared to its mean value for a whole 1 Gyr interval. For such disruption, the mean value of N_1 should be smaller than the present value of N_1 , and the number N_{est} of craters should be smaller than 47, i.e. such data do not support the disruption.

As we noted above, $T_E = 67$ Myr (and $T_E \cdot k_{ECO} = 115$ Myr) was obtained in [8] for the present small inclinations of some Aten objects. Inclinations of ECOs vary with time. So some ECOs earlier could have small inclinations. In [8] 110 Atens were considered. If inclinations are randomly distributed in the range from 0 to 11°, one of them would be less than 0.1°. If inclinations are randomly distributed in the range from 0 to 22°, one of them would have inclination between 0 and 0.2°, i.e. 0.1° on average. If we consider $T_E = 67$ Myr for $T_{OS} = 1.1$ Gyr, then $N_{est} \approx 70$ and in order to have $N_{est} = N_{obs}$ for formula (2), we need to consider N_1 smaller than 52 (the number of craters with $D > 15$ km) by a factor of $70/52 \approx 1.35$, that is in accordance with the asteroid breakup 160 Myr ago considered in [13]. As it is discussed above in this paragraph, it was possible that $T_E \approx 67$ Myr for $T_{OS} = 1.1$ Gyr.

Not all craters with a large age could survive. So the actual value of N_{obs} could be greater than the present value. For greater values of $N_{est} = N_{obs}$ in formula (2) we need to consider greater values of N_1 / k_{ECO} or smaller values of T_E . In principle our estimates also allow that the mean number of NEOs during the last billion years was about the same as in the present time.

Conclusions:

We compared the distribution of diameters of lunar craters in the region of the Oceanus Procellarum with age less than 1.1 Gyr with the estimates of the number of craters made based on the number of near-Earth objects and on the characteristic times elapsed before collisions of near-Earth objects with the Moon. Our estimates allow the increase of the number of near-Earth objects after a recent catastrophic disruption of a large main-belt asteroid. However, destruction of some old craters and variation in orbital distribution of near-Earth objects with time could allow that the mean number of near-Earth objects during the last billion years could be close to the present value.

References:

- [1] Hazards due to asteroids and comets: Yesterday, today, tomorrow. / Ed. by B.M. Shustov, Rykhlova L.V. 2010. 384 p, in Russian.
- [2] Minton D.A., Richardson J.E., Fassett C.I. Re-examing the main asteroid belt as the primary source of ancient lunar craters // *Icarus*. 2015. V. 247. P. 172-190.
- [3] Leuvre M.L., Wieczorek M.A. Nonuniform cratering of the Moon and a revised crater chronology of the inner Solar System // *Icarus*. 2011. V. 214. P. 1-20.
- [4] Stuart J.S., Binzel R.P. Bias-corrected population, size distribution, and impact hazard for the near-Earth objects // *Icarus*. 2004. V. 170. P. 295-311.
- [5] Marov M.Ya., Ipatov S.I. Delivery of water and volatiles to the terrestrial planets and the Moon // *Solar System Research* (translated from *Astronomicheskii Vestnik*). 2018. V. 52, N 5, in press.
- [6] Werner S.C., Ivanov B.A. Exogenic dynamics, cratering, and surface ages // *Treatise on Geophysics* (Second Edition). 2015. V. 10. P. 327-365.
- [7] Melosh H.J. *Impact cratering: A geologic process*. Oxford Univ. Press, New York, 1989. 245 p.
- [8] Ipatov S.I. Mather J.C. Migration of Jupiter-family comets and resonant asteroids to near-Earth space // "Astrodynamics, Space Missions, and Chaos", ed. by E. Belbruno, D. Folta, and P. Gurfil, *Annals of the New York Academy of Sciences*. 2004. V. 1017. P. 46-65. <http://arXiv.org/format/astro-ph/0308448>.
- [9] Bottke W.F., Nolan M.C., Greenberg R., Kolvoord R.A. Collisional lifetimes and impact statistics of near-Earth asteroids // *Hazards due to comets and asteroids*, ed. by T. Gehrels. The University of Arizona press. Tucson & London. 1994. P. 337-357.
- [10] Dvorak R., Pilat-Lohinger E. On the dynamical evolution of the Atens and the Apollos // *Planet. Space Sci.* 1999. V. 47. P. 665-677.
- [11] Ipatov S.I. Comet hazard to the Earth // *Adv. Space Res.* 2001. V. 28. P. 1107-1116.
- [12] Ipatov S.I., Mather J.C. Migration of comets to the terrestrial planets // *Proceedings of the IAU Symposium No. 236 "Near-Earth Objects, Our Celestial Neighbors: Opportunity and Risk" (14-18 August 2006, Prague, Czech Republic)*, ed. by A. Milani, G.B. Valsecchi, D. Vokrouhlický, Cambridge Univ. Press, Cambridge. 2007. P. 55-64. <http://arXiv.org/format/astro-ph/0609721>.
- [13] Bottke W., Vokrouhlicky D., Nesvorný D. An asteroid breakup 160 Myr ago as the probable source of the K/T impactor // *Nature*. 2007. V. 449. P. 48-53.

LUNAR CRATERS FORMED BY ENCOUNTERS OF SATELLITE SYSTEMS OF NEAR-EARTH OBJECTS WITH THE MOON

E.A. Feoktistova¹, S.I. Ipatov², V.V. Svetsov³

¹*P.K. Sternberg Astronomical Institute, M.V. Lomonosov Moscow State University, Moscow, Russia;*

²*V.I. Vernadsky Institute of Geochemistry and Analytical Chemistry of RAS, Moscow, Russia*

³*Institute of Dynamics of Geospheres of RAS, Moscow, Russia*

Keywords:

Lunar craters, asteroids, impactors, near-Earth objects, triples.

Introduction:

An asteroid with a satellite (Ida) for the first time was discovered by probe Galileo in 1993. By now it is known that approximately 15% of asteroids are double or triple systems [1]. It is obvious that a number of craters located on the surface of the bodies of the solar system are formed as a result of collisions with such bodies. The number of such craters on the Moon was estimated to be about 10% of the total number of craters [1]. In this paper, we attempted to detect craters formed by the collisions of triple systems with the lunar surface in the selected region.

Sequences of three lunar craters located on the same line:

To identify the craters formed as a result of collisions of triples, we used the following assumptions: 1) craters are located close to the same spherical straight line; 2) craters have similar age, suggesting that they could be formed at the same time; 3) the distance between the craters does not exceed the characteristic values; 4) craters have certain characteristics (the ratio of a diameter to a depth).

The following areas of lunar maria on the near side of the Moon have been studied: Ocean Procellarum, Mare Imbrium, Mare Frigoris and others. The area of the studied surface is about 7320004 km² or about 19% of the surface of the Moon. For the detection of crater sequences, we used the catalog of the lunar craters of the SAI [2] containing information on nearly 15,000 craters with diameters over 10 km. Information on smaller craters for this region was obtained from the Lunar Crater catalog [3]. We investigated only craters with a low degree of degradation according to the data of [2], presumably related to the Eratosthenian and Copernican periods. Then the detected prospective sequences of craters were identified on the map of the Moon [4]. For more accurate estimate of the time and nature of the crater formation, we used data from the Geological Atlas of the Moon [5]. The morphometric parameters of the craters of the detected sequences, in particular the depth, were determined from the LOLA altimeter data [6].

In total, 247 fresh craters with diameters over 10 km and about 1500 fresh craters with diameters <10 km are located in this area. As a result, 8 possible sequences of craters, including three craters each, have been found. The coordinates and characteristics of the craters are given in Table 1. The diameters of the crater data sequences are in the range from 2 to 20 km.

Diameters of impactors corresponding to diameters of craters:

We found 8 sequences consisted of three craters in the considered region (which area is 19% of the surface of the Moon). The minimum value of the largest crater diameter in a sequence is 5.5 km. The number of craters with a diameter not less than 5.5 km in the considered area is 752. Therefore, the fraction of sequences among such craters is $8/752 \approx 0.01$. If craters of the considered sequences have been caused by collisions of NEOs having two satellites with the Moon, then this fraction means that the number of triples among NEOs could be not less than 1%. The eight considered sequences are for craters located in one line. The sequences can correspond to the case when the plane of the triple that collided with the Moon was perpendicular

Table 1. Coordinates, diameters, and depths of craters, mutual distances between craters belonging to sequences of three craters, diameters of impactors corresponding to diameters of craters, and radii of Hill spheres of impactor triples.

Number	Longitude, degree	Latitude, degree	Diameter d_{cr} of a crater, km	Depth of a crater, km	Distance D_{ist} between craters, km	Diameter d_i of an impactor, km	D_{ist}/d_{i-max}	Hill radius $R_{H3'}$ km	D_{ist}/R_{H3}
1	315.7	-4.5	19.3	2.2	45.1	1.1	41	106	0.43
	316.2	-5.9	9.1	1	65.3	0.41	59		0.62
	317	-7.9	11.4	1.2		0.54			
2	322.9	-21.6	9	1.5	56.4	0.40	120	52	1.08
	324.9	-22	10	0.9	74.6	0.46	160		1.43
	327.5	-22.3	7	1.7		0.29			
3	311.7	41.7	3	0.3	61.9	0.10	260	23	2.69
	309.2	40.9	6	0.3	122.3	0.24	500		5.41
	304.8	38.7	2	0.15		0.06			
4	351.1	-49.2	11	0.7	37.2	0.52	48	81	0.46
	350.7	-50.4	10	1.6	65.1	0.46	85		0.80
	350	-52.5	15	2.1		0.77			
5	319.3	-2.3	4.5	0.3	34.7	0.17	160	23	1.50
	319.1	-3.5	3.8	0.3	39.4	0.13	190		1.70
	318.9	-4.7	5.5	0.4		0.21			
6	30.9	-50.3	10	1.7	76.8	0.46	120	73	1.06
	32.6	-52.6	11	1.8	31.9	0.52	50		0.44
	33.5	-53.5	13	1.3		0.64			
7	304.3	-49.4	17	1	34.9	0.91	38	117	0.30
	302.8	-48.4	13	0.8	37	0.64	41		0.32
	301.2	-48.2	13	0.7		0.64			
8	334.3	-9.4	5.6	0.3	91.4	0.22	360	31	2.92
	337.3	-9.7	6.3	1.5	133.8	0.25	530		4.27
	341.8	-10.1	6	1		0.24			

to the surface of the Moon or if the three components of the triple were in one line at the time of their collision with the Moon. In many cases the plane could be oriented in another way and the components were not in one line, so a fraction of triples among NEOs could be much greater than the estimate obtained for the case when we consider only three craters located in one line or their plane perpendicular to the Moon surface. For the eighth sequence in the table the depth of the first crater is smaller by a factor 3 or 5 than the depths of two other craters with almost the same diameters. There is some probability that this sequence was not formed by the collision of a triple.

Based on the diameters d_{cr} of the craters, we estimated the mean diameters d_i of corresponding impactors for the mean velocity U of impacts on the Moon equal to 18.3 km/s [7]. We used the formula $d_{cr} = 5.1 \times d_i^{0.78} \times U^{0.44}$, where diameters are in km and velocity is in km/s. In the derivation of this formula, we used the well-known formula of Schmidt and Hausen for transient craters [8, 9], which follows from the π -theorem for non-porous rocks without friction. We took equal densities of the impactor and the target. We also took into account that the craters are relatively small and simple, and therefore the diameter of a final crater is equal to the diameter of a transient crater multiplied by 1.25 [8]. We also made averaging over the impact angles. The size of a crater depends on the impact angle θ approximately as $(\sin\theta)^{1/3}$ [9] and the impact probability density is proportional to $\sin 2\theta$. Integration of the product of these functions over the angles gives an additional factor equal to 6/7.

The ratio $D_{\text{ist}}/d_{\text{i-max}}$ of the distance D_{ist} between craters to the largest diameter $d_{\text{i-max}}$ of all three impactors in the sequence is shown in the table. This ratio is in the range from 38 to 530. The separations D_{obs} between elements of the triples that produced the discovered sequences of three craters could be greater than D_{ist} , because the equality $D_{\text{obs}}=D_{\text{ist}}$ corresponds only to that rare case when three components of the triple were at the time of the collision in one line which was parallel to the surface of the Moon.

Based on diameters of three impactors (corresponding to three craters of a considered sequence) and considering their density to be equal to 2600 kg/m³ [1] we calculated the total mass of the three impactors and the radius R_{H3} of the Hill sphere corresponding to this mass and 1 AU. The values of R_{H3} and D_{ist}/R_{H3} are presented in the table. For an object with diameter equal to 1 km and density equal to 2600 kg/m³ the ratio of the Hill radius to the physical radius is 91.5. If we suppose that D_{ist}/R_{H3} should be less than 1 (i.e., satellites moved in the Hill sphere at the moment of collision), then only for three sequences in the table $D_{\text{ist}}/R_{H3} < 1$. For two sequences (numbers 1 and 4 in the table), the sum of two values D_{ist}/R_{H3} is greater than 1, and smaller craters are located on one side from the largest crater in the sequence. For these two cases, one satellite could move outside the Hill sphere, so may be these sequences were not caused by impacts of triples. Only for one sequence (number 7 in the table) the sum of two values D_{ist}/R_{H3} is smaller than 1. In these case, components of the triple could move in their Hill sphere at the moment of collision with the Moon. For seven other sequences presented in the table, some components of the corresponding triples should move outside the Hill sphere at 1 AU. The Hill radius is proportional to the distance from the Sun, and earlier the three components could be located inside their Hill sphere when the triple was more far from the Sun. However, it is a question whether three components located in their Hill sphere at a distance of several AU from the Sun still will be close to one another when they reach the Moon. One sequence among 752 craters of a diameter greater than 5.5 km corresponds to 0.13%.

Discovered NEO triples and binaries:

Three triples have been found among more than 18,000 NEOs. These three triples have [10] the following values of diameters and separation distances (in km): (3122 Florence; 4.4, 0.2, 0.2; 4.7, 9.8), (136617, 1994 CC; 0.62, 0.113, 0.08; 1.7, 6.1), (153591, 2001 SN263; 2.6, 0.46, 1.06; 3.8, 16.6). For these three triples, the ratios of the largest component diameter to the diameters of two smaller components (equaled to 22, 22, 5.5, 7.8, 5.6, 2.4) were typically greater than the similar ratios of diameters of impactors corresponding to the same sequence presented in the table. The ratios of the separation distances D_{obs} in discovered triples to the diameters of greater components of the triples (1.1, 2.2, 2.8, 9.9, 1.5, 6.4) were smaller than the values $D_{\text{ist}}/d_{\text{i-max}}$ presented in the table. For discovered NEO binaries, the values of ratio of the distance D_{obs} between two components to the diameter of more massive component of the binary were mainly about 2 or 3, and were smaller than 4 for all binaries, except for one, for which the ratio is equal to 13.

Close components of binaries and triples could form the same crater. Typically, the diameter of a lunar crater could be greater by an order of magnitude than the diameter of an impactor. The collisions of triples, consisting of close components, with the Moon could produce craters which were not identified by us as the sequences of three craters. Our above estimates of the fraction of triples among NEOs are only for the triples with large enough separation distances (greater than 30 radii of the largest components) which have not yet been discovered. Such triples have not been discovered in space because it is easier to discover components with closer separation distance.

Conclusions:

Eight sequences consisted of three craters of close ages located in one line have been found in the area which is 19% of the surface of the Moon. The maximum crater diameter in each sequence exceeds 5.5 km. A diameter of a crater equal to 5.5 km corresponds to an impactor diameter of about 0.2 km. The fraction of triples with separation distances greater than 30 diameters of

greater components of triples could exceed 0.13% of near-Earth objects. This fraction can be much larger if we take into account that three components of a triple usually were not located in one plane, which was perpendicular to the surface of the Moon, or the three components were not in one line at the time of their collision with the Moon.

References:

- [1] Bottke W.F., Melosh H.J. Binary asteroids and the formation of doublet craters // *Icarus*. 1996. V. 124. No. 2. P. 372-391.
- [2] Rodionova J.F., et al. Morphological catalogue of the craters of the Moon. 1987.
- [3] https://astrogeology.usgs.gov/search/map/Moon/Research/Craters/GoranSalamuniccar_MoonCraters
- [4] IAU WGPSN (2015). 1:1 Million- Scale Maps of the Moon. <http://planetarynames.wr.usgs.gov/Page/Moon1to1MAtlas>.
- [5] <http://atlasofplaces.com/Geologic-Atlas-of-the-Moon-USGS>
- [6] <http://ode.rsl.wustl.edu/moon/>
- [7] Minton D.A., Richardson J.E., Fassett C.I. Re-examing the main asteroid belt as the primary source of ancient lunar craters // *Icarus*. 2015. V. 247. P. 172-190
- [8] Werner S.C., Ivanov B.A. Exogenic dynamics, cratering, and surface ages // *Treatise on Geophysics (Second Edition)*. 2015. V. 10. P. 327-365.
- [9] Melosh H.J. *Impact cratering: A geologic process*. Oxford Univ. Press, New York, 1989. 245 p.
- [10] https://en.wikipedia.org/wiki/Minor-planet_moon#List_of_minor_planets_with_moons

DOUBLET CRATERS ON THE MOON AND MERCURY

E.A. Feoktistova, S.G. Pugacheva, V.V. Shevchenko

*Sternberg State Astronomical Institute, Moscow State University,
katk@sai.msu.ru;*

Keywords:

Craters, Moon, asteroids

Introduction:

Currently are known many asteroids with satellites. According to estimates [1], about 15% of asteroids approaching the Earth are binary. The collision of such asteroids with the surface of the bodies of the solar system leads to the formation of so-called double craters. Similar craters were found on Earth, Mars and the Moon, where their share of the total number of craters is estimated as 2-4 [1,2], 2 and 10% [1], respectively. Recently, such craters were also found on asteroids. [3]. The morphological characteristics of craters formed as a result of the fall of double asteroids were investigated by [2,4]. It was shown that such craters can be located next to each other, overlapping each other or at some distance, but should not exceed a certain value. In this paper, we considered only those pairs of craters that can be classified as Peanut or Overlapping by classification from [2]. To identify such pairs of craters, images of the surface of the Moon and Mercury were analyzed. For a number of sections of the Mercury surface, the analysis was hampered by the poor quality of the available images. As a result, we identified 19 similar pairs of craters on the Moon and 15 pairs on Mercury.

References:

- [1] Bottke W.F., Melosh H.J. Binary asteroids and the formation of doublet craters // *Icarus*. 1996. V. 124. No. 2. P. 372 -391.
- [2] Miljkovic K., Collins G.S., Mannick S., Bland P.A. Morphology and population of binary asteroid impact craters // *Earth Planet Sc Lett*. 2013. V. 363. P. 121 – 132.
- [3] Wren P.F., Fevig R.A., Investigation of doublet craters on Ceres as Evidence of main belt Binary asteroid systems. LPSC 48th, abstract 2407. 2017.
- [4] Oberbeck V.R. Simultaneous impact and lunar craters. *Moon* 6. 1973. P. 83-92.

MORPHOMETRY OF LUNAR CRATERS HAVING 1-10 KM IN DIAMETER

M. Kolenkina¹, N. Kozlova¹, I. Zavyalov¹ and A. Basilevsky²

¹Moscow State University of Geodesy and Cartography (MIIGAik),
MIIGAik Extraterrestrial Laboratory (MExLab), Russia,
n_kozlova@miigaik.ru;

²Vernadsky Institute of Geochemistry and Analytical Chemistry of RAS,
Moscow, Russia.

Keywords:

Moon, craters, morphometry, crater catalogue.

The study:

The work presents first results and future plans for exploitation of Lunar crater catalogues for analysis of morphologic peculiarities of craters and comparative studies of extraterrestrial territories. The work is aimed at getting new information about morphology of the Moon via studying morphometric parameters of craters. For the study we selected craters in four lunar regions with different geology: Mare (M), Highland (H), South pole (SP), South Pole–Aitken basin (SPA).

Craters 1-10 km in diameter were manually identified on LRO WAC global mosaic (100 m/px resolution) and relative depths (dD) and maximum slopes of the crater inner slope (S) were measured based on 100-meter resolution DEMs: LDEM for SP&SPA regions and GLD100 for M&H craters. Obtained results are presented in Figures 1 and 2.

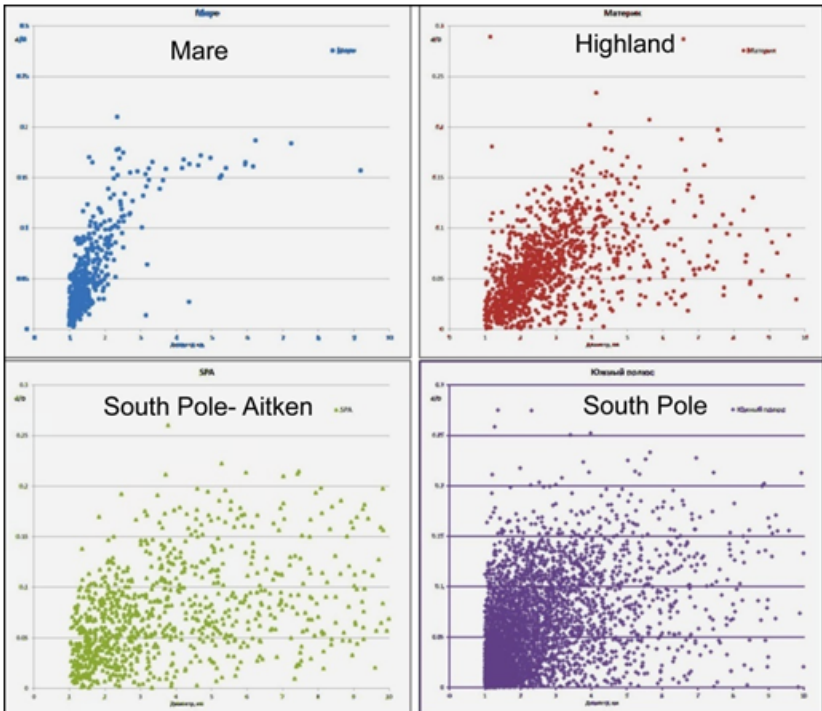


Fig. 1. Dependence of the relative depth (dD) of the craters on their diameter (D).

It is seen in Fig. 1 that among the **mare** craters in the interval $D = 1-3$ km along with D increase the percentage of craters with small relative depth decreases. For craters with $D > 3$ km, dD practically do not change (0.15-0.18). Probably it happens because there is not enough time (3.5 Ga) for mare craters to be significantly destroyed.

The **highland** crater population in its major part was formed earlier than maria's, and then rates of both crater formation and destruction were signif-

icantly higher than during the last 3.5 Ga. And we can see on the graph that relative depth for highland craters varies from 0.03 to 0.2 along all diapason of diameters.

The **South Pole** crater subpopulation shows no significant differences comparing to the highland one. In general, the South Pole area is a typical highland one and it differs from other non-polar areas only in presence of water ice (up to a few percent) in its regolith.

The dD v.s. D distribution in the **South Pole-Aitken** and South Pole subpopulations are practically the same. The known very ancient age of the South Pole-Aitken basin is essentially related to the basin itself and not to superposed crater populations.

Then we studied correlation of **maximum steepness** of crater internal slopes (S) on the crater relative depth (dD). It is expectedly positive and the strongest is for mare craters ($R^2 = 0.86$), rather moderate for highlands and South Pole-Aitken ($R^2 = 0.48$), and slightly lower for South Pole ($R^2 = 0.36$). It is seen in Figure 2 that for relatively large craters of the three considered highland areas (H, SP, and SPA) the lower dD have the S larger than one could expect S based on the mare correlation law. This is probably because in mare populations craters of 1-10 km in diameter are being destroyed by both the down-slope material movement and by infilling with ejecta of relatively small craters while in the highland areas the infilling with ejecta of relatively large craters is added.

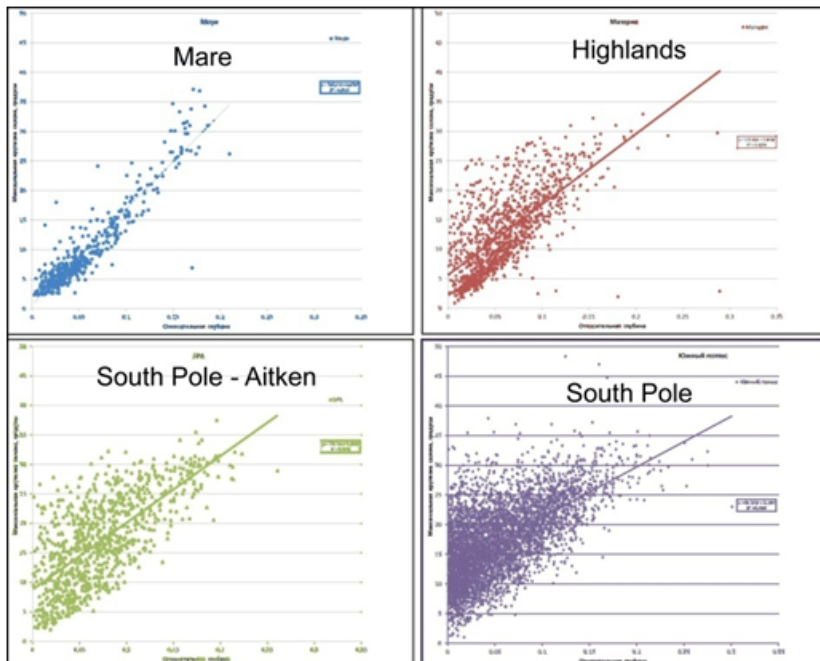


Fig. 2. Dependence of the maximum angle of internal slopes (S) of craters on their relative depth (dD).

Acknowledgements:

The work is supported by the Russian Science Foundation grant № 17-17-01149: «Reconstruction of geologic history of polar areas of the Moon using new high-accuracy data to understand sources, distribution and accumulation of volatiles (water) on the Moon».

Creation of Lunar crater catalogue (1-10 km in diameter) received founding from Russian Foundation for Basic Research (RFBR), Project No. 16-37-00323 mol_a, 2016-2017.

THE STUDY OF THE MOON'S MOVEMENTS WITH SPATIO-TEMPORAL TECHNOLOGY

N.P. Bulatova

Schmidt Institute of Physics of the Earth of Russian Academy of Sciences, Moscow. n.p.bulatova@mail.ru

Keywords:

Spatio-temporal technology; Moving Source Method; 3D model of Earth; Moon; Sun; original coordinate system.

Introduction:

The novel coordinate system including special systems has been originally developed by the author to investigate the motion of the celestial bodies in the Solar System including the Sun, the Moon and et. The corresponding technology (Bulatova, 2000) using this system was named by the Spatio-Temporal Technology (STT) [1].

Spatio-Temporal Technology

The proposed technology consists of two parts: (1) consideration of 3D Earth geometric model and (2) bases of the original «Moving - Source Method» – (MSM) developed by the author [2]. Note that the STT, and MSM algorithms can be applicable to analyze the Earth satellite movements (Bulatova, 1998, 1999, 2000, 2016).

The STT technology briefly can be described as follows.

Three coordinate systems (I, II, III) have been introduced by the author:

I - spherical for the Earth planet $-P_{\sigma}(R, \phi, \lambda)$;

II - spherical for the celestial sphere $-P_{\sigma}(S, \gamma, \alpha)$;

III - Cartesian OXYZ to combine mentioned above coordinate systems.

Note that the OZ axis is common for all coordinate systems (I, II, III). Let us stress that OZ axis is coincided with the direction vector to the North Pole of the world. The centers "O" is the same of all three (I, II, III) coordinate systems and it is coincided with the geometric center of the Geosphere O (in this 3D model of the Earth) [1-3].

The STT technology uses a new basis having two measured parameters that are angles. Common astrometric parameter is the parameter δ - visible declination. The polar zenith angle is $-\gamma : \delta + \gamma = 90^{\circ}$ is paired with hour's angle $-t$. In the line with it, STT involves two functions: $\delta(t, T)$ or $\gamma(t, T)$ where t is current time (days). The time parameter T is additionally entered indicating the date of the event. Additionally to the parameters δ, γ the following important time parameter is using – hour angle α or t (the current time of day).

The apparent declination δ (or polar angle γ) are measured as the angular distance the vector-connecting the center of the geosphere with the moving source (in the given case the Moon, the Sun). There are angular distance between direction from the axis of the Equatorial plane of the geosphere - δ (or axis OZ of the North Pole of the world - γ) and angle α or t (between direction of the axis -OX) in 3-D model of the Earth.

Note that in classical astrometry parameter δ is measuring (paired) with visible direct ascension for each monitored object. In the STT system measurements can be simultaneously made for several objects.

On Movement of the Moon

The data including measurements of the Moon and Sun relative to the Earth for the time period 1985-2003 γ . were processed using STT.

Values of the functions $\delta(t, T)$ or $\gamma(t, T)$ were obtained.

Both functions were determined for the Northern and southern hemispheres of the Earth that is important to study the influence of celestial bodies on the Earth in astronomy, geology, geophysics, climatology, etc.

Two "speed" of change of a function $\delta_{sz}(T)$, namely $(\Delta\delta(T)/\Delta T)$ and $(\Delta^2\delta(T)/(\Delta T)^2)$ to identify the "fine structure" of the changes in the apparent declination $\delta(T)$ will be analyzed in the contribution to the symposium.

Summary

Author's long experience of the STT and MSM application shows that the movement of celestial bodies can be studied as a joint simultaneous movement of several moving sources. The presented system of STT and MSM can be used by specialists who study the movements of the Moon and other celestial bodies relative to the Earth as additional valuable information about the studied subject.

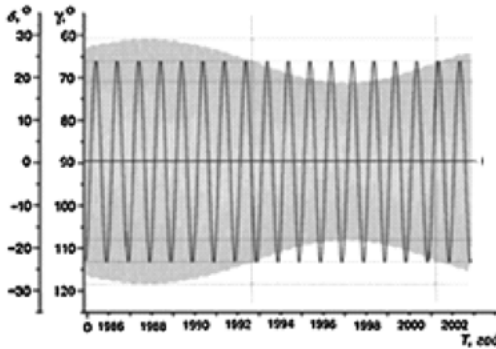


Fig. 1. The observed data change in for the period 1985-2003yy. for moving sources (S1 and S2): the visible declination is a function of $\delta(t, T)$, polar angle –function $\gamma(t, T)$. It is seen for the Sun function $f_1(T) = \delta_{s1}(T)$ is - quasi sinusoidal curve (black). Accordingly, the function $f_2(T) = \delta_{s2}(T)$ - periodic changes for the Moon (gray field). For the function $f_2(T) = \gamma_{s2}(T)$ – there is similarly. Changes $\delta_{s2}(T)$ and $\gamma_{s2}(T)$ are modulated by cyclic “lunar” frequency: $T_2 = 18,6...$ years.

References:

- [1] Bulatova N. P. Spatio-temporal technology. Part I. Basic positions. Monograph. M.: LIBROKOM, 2016. – 120 p.
- [2] Bulatova N. P. “The Method of Moving Source” and Its Application to Research of the Earth // Herald of the DGGGMS RAS, M.: UIPE, 2000. v.1, 2(12), pp.110–125. (ISBN-5-201-11905-0).
- [3] Bulatova N. P. On the Solar Neutrino Tomography of the Earth: scanning geometry // Izvestiya Physics of the Solid Earth, 1999, v.35, №2. P.150-160.
- [4] Bulatova N. P. On connection of strong earthquakes ($m \geq 7$) with relative Sun and Moon position (on the earthquake at 26.12. 2004) /. XXI Century Geophysics: 2006. Papers of the 8th V.V.Fedynski Geophysical Conference, 2006.- Tver: GERS, 2007. p.488 (P. 279-285) (ISBN-5-89176-226-9).

ANALYSIS OF OCCULTATIONS OF STARS BY THE EARTH ON THE LUNAR SKY

B.A. Epishin, M.I. Shpekin

*Kazan Federal University, Kazan, epishin.boris@yandex.ru ,
MichaelS1@yandex.ru,*

Keywords:

occultations of stars by Earth, computer program, astronomical observations on Moon, lunar sky

Observations of the Earth from the surface of the Moon are of interest from different points of view. Among the fundamental and applied problems related to the Earth, the problem of observing the Earth against the background of stars is considered. A special case of such a problem is the observation of the occultations of stars by the Earth. The report presents ephemeris calculations for observing of the occultations using the example of a one star, as well as a general analysis of the problem.

Analysis of occultations.

For the calculations, star No. 229 was chosen according to AE [1] (No. 42911 in the catalog of Hipparchus). The local circumstances of the occultations of the named star by the Earth on the Moon sky are calculated for the topocenter chosen in the Lake Spring area (selenographic longitude -85° , latitude -15°). Calculations were carried out according to the program developed by us, where the barycentric coordinates of the celestial objects of the theory of the DE 430 JPL [2] were taken as the basis of the calculations. Calculations of the selenocentric coordinates of the Earth were carried out according to the procedure of [3]. The algorithm for calculating the local circumstances of the occultations is taken from the Almanac [4].

For the Earth-based observer, the occultation of a star by the Moon is calculated more simply, unless it is more difficult to take into account the profile of the lunar limb. But for the observer from the Moon, the calculation of high-precision occultations is greatly complicated by taking into account the compression of the Earth's shape, as well as the thickness of the atmosphere. To demonstrate the account of these parameters, the ephemeris of the occultation was calculated on January 18, 2018. In calculations, the atmosphere is opaque. In Table. 1 shows the calculations for a circular Earth and taking into account the Earth's compression. Here 4.5 km is a conditionally average relief of the Earth, and 9.0 - the highest mountains on Earth. One series of occultations occurs at the descending node of the orbit, and the other - with the ascending node. Only those stars can be eclipsed (by Earth from the Moon), which are not farther from the projection of the Earth's orbit onto the celestial sphere no further than the sum of the terrestrial equatorial horizontal parallax and the visible radius of the Earth. And likewise from Earth, the stars are eclipsed by the Moon, also not farther from the lunar orbit than the sum of the lunar equatorial horizontal parallax and the apparent radius of the Moon. The apparent size of the Earth from the Moon is four times larger than the Moon from the Earth, but parallax is four times smaller. One can draw an interesting conclusion: the zone of the occultations of the stars from the ecliptic (the inclination of the orbit plus the horizontal parallax plus the apparent radius) is approximately the same for observers from the Earth and from the Moon. But one more important comment is necessary: for a given topocenter on the surface of the Moon, the number of stars occulted by the Earth per unit time will be 4 times larger than for an Earth-based observer in the case of star occultations by the Moon. A series of occultations of one star is repeated every 9.3 years, with the maximum number of occultations in the series being 11-12. For stars farther from the ecliptic, the number of their coverings is reduced, and on the boundary of the coverage zone one or two occultations will occur in the series. The maximum duration of the occultation (from the moment of disappearance to the moment of appearance) will be about 3.8 hours. In Table. 2 shows the dates of occultations (day,

month and year), moments of disappearance and appearance of the star by the Earth in hours, minutes and seconds. The position angles of the contacts of the disappearance and appearance relative to the lunar pole (P) and relative to the zenith (V). Also, which side of the Earth is light (L - Light) or dark (D - Dark) at the contacts of the disappearance and appearance, is the phase of the Earth (F) on the lunar sky at the given date of the occultation are given at the table.

Table 1. Comparison of the moments of the disappearance and appearance of the star by the Earth on a universal time ($dT = 71$ sec) with and without taking into account the compression of the Earth for different thicknesses of the atmosphere H in km.

H km	Disappearance – UTC, hms		Appearance – UTC, hms	
	Earth-circle	Earth-ellipse	Earth-circle	Earth-ellipse
0.0	0 50 35	0 50 43	3 36 15	3 35 59
4.5	0 50 29	0 50 37	3 36 21	3 36 05
9.0	0 50 23	0 50 31	3 36 27	3 36 11
60.0	0 49 15	0 49 23	3 37 35	3 37 19
120.0	0 47 55	0 48 03	3 38 54	3 38 39

Table 2. A series of star occultations by the Earth (taking into account the compression at an atmosphere thickness of 60 km) over the ephemeris time at the descending node.

Disappearance					Appearance				
D M Y	UTC	P°	V°	L	UTC	P°	V°	L	F
21De17	18 59 35	39	144	L	21 36 11	308	53	D	0.89
18Ja18	0 50 34	43	148	L	3 38 30	303	48	D	0.99
14Fe18	7 27 20	43	148	D	10 13 09	304	49	L	0.98
13Mr18	14 55 56	47	152	D	17 52 44	300	45	L	0.86
9Ap18	22 52 12	60	165	D	2 15 01	286	31	L	0.66
7Ma.18	6 44 42	77	182	D	10 24 49	270	15	L	0.44
3Jn18	14 03 21	91	196	D	17 42 54	256	1	L	0.22
30Jn18	20 35 21	98	203	D	0 09 03	248	353	L	0.07
28Jl18	2 38 46	99	204	D	6 11 18	248	353	L	0.00
24Au18	8 53 00	99	204	L	12 25 29	248	353	D	0.04
20Se18	15 52 33	105	210	L	19 17 57	242	347	D	0.17
17Oc18	23 50 20	121	226	L	2 46 04	226	331	D	0.38

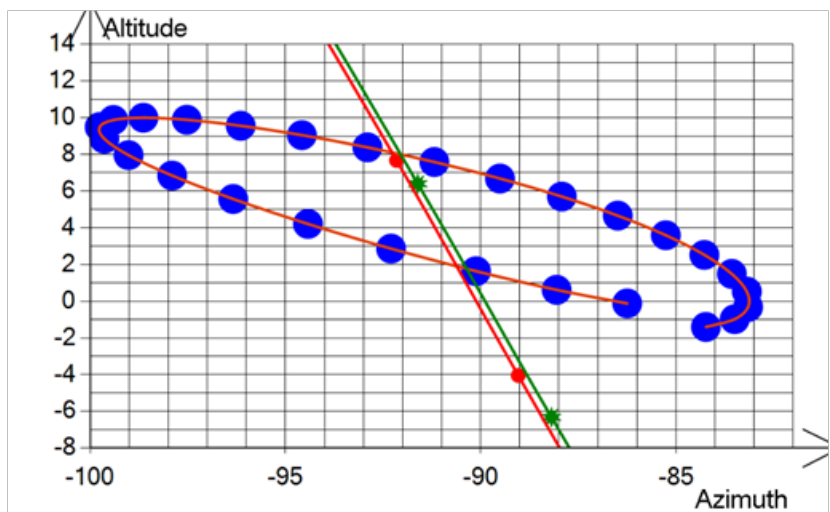


Fig.1. The graphs of the apparent motion of the center of the Earth (Blue), the Sun (Red) and the star No. 229 AE (Green) during one earth month with an interval of one day relative to the horizon from the topocentre in the Spring Lake area.

The Earth is the largest object in the lunar sky. In Fig. 1 shows the graph of the motion of the Earth, the Sun and the star relative to the local horizon in one earthly month. The Earth moves counterclockwise along an ellipse, and the Sun and the star rise upward along a straight line, crossing the horizon. In Fig. 2 shows the motion of these celestial bodies relative to the stars in the same month. For earthly month the Earth passes the entire zodiacal circle. The sun moves during this time by about 25° in longitude. The star remains motionless.

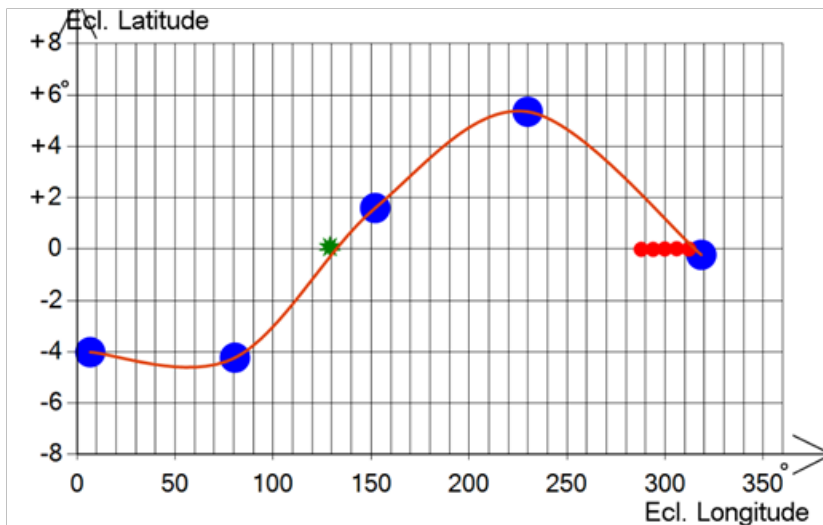


Fig.2. Graphs of the motion of the center of the Earth (Blue), the Sun (Red) and the star No. 229 AE (Green) during one earth month with an interval of 6 days in the ecliptic coordinate system.

Conclusion.

Considering the foregoing, and also taking into account the absence of an atmosphere on the Moon, one can count on a significant number of stars occultations by the Earth, accessible to the lunar observer in a relatively short period of time. Astrometrical measurements of the examined occultations in the monitoring mode can yield a rich material for determining astronomical and geodetic constants in the Earth-Moon system, for testing of terrestrial global coordinate systems, and for studies of the properties of the Earth's atmosphere. The occultations of the stars by the Earth, observed from the Moon, will also make it possible to clarify the parameters of the physical libration of the Moon.

Acknowledgement

The work is performed according to the Russian Government Program of Competitive Growth of Kazan Federal University.

References:

- [1] Astronomical Yearbook for 2011. SPb.: IAA RAS, 732 p. (in Russian).
- [2] JPL planetary and lunar ephemerides. <ftp://ssd.jpl.nasa.gov/pub/eph/planets/>
- [3] V.A.Brumberg, N.I.Glebova, M.V.Lukasheva, A.A.Malkov, E.V.Pit'eva, L.I.Rumyantseva, L.L.Sveshnikov, M.A.Fursenko. Extended explanation to "Astronomical Yearbook". – Proc. IAA RAS, Issue 10, 2004, 488 p.(in Russian).
- [4] The Astronomical almanac for the year 2012. Dept. of the Navy; Annual edition (March 15, 2011), 612 p.

MOON GALLERY ARTMOONMARS PROGRAM FOR PUBLIC ENGAGEMENT, OUTREACH, INTERNATIONAL COOPERATION, SPACE EXPLORATION THROUGH ART

A. Sitnikova¹, A. Zaklynsky¹, B.H. Foing² & ArtMoonMars Team

¹KABK The Hague, ILEWG & ESA/ESTEC Prinsessegracht 4, 2514 AN Den Haag, annesitnikova@gmail.com;

²ESA/ESTEC, ILEWG & VU Amsterdam ESTEC postbus 299 2200 AG Noordwijk, Bernard.Foing@esa.int

Keywords:

Moon, research, planetary, art, gallery, cooperation, workshop, culture, educational, platform, lander, analogue, field simulations, outreach, open call

Introduction:

1) Moon Gallery pilot platform within the framework of the Moon Village, EuroMoonMars&ILEWG. The Moon Gallery aims to serve as a focal point for inspirational ideas and visions for the Moon Village community. Art scene will play a humanistic and cultural role for the Moon Village instigating intrigue, imagination and inspiration for the global space exploration. 2) Concept: – An international collaborative art work and Moon village promotion structure. – A crowd sourced online gallery of images created by an international group of participants. – A 10 by 10 cm patch of Lunar Lander exterior paneling is one intended venue for this Gallery. (There are 100 cells available of 1 cm x 1 cm x 1 cm for art submissions) – A robust online presence, promotion structure and dissemination of information/teaching materials related to the program along with the potential of realizing an art work on the moon. 3) Field campaigns Moon Gallery test deployments have been conducted in ESTEC, Iceland, LunAres base at Pila Poland. We shall report on latest activities with application to ArtMoonMars. 4) Moon Gallery outreach campaigns/ think tank sessions have been conducted in ESA/ESTEC, Pulchri The Hague, Royal Academy of Art the Hague, ISU International Space University Delft, Iceland Art University. 5) End of November demo Moon Gallery with 25 selected artworks by international art science community will be exhibited in ESTEC and Space Expo Noordwijk 6) We participate in EuroMoonMars activities with designers & artists expanding awareness of MoonMars benefits to the society at large. This research can benefit Science, Exploration or Application programs, and International Tasks Groups (space agencies, and research partners, ILEWG, IMEWG, ISECG, SSERVI, etc...).

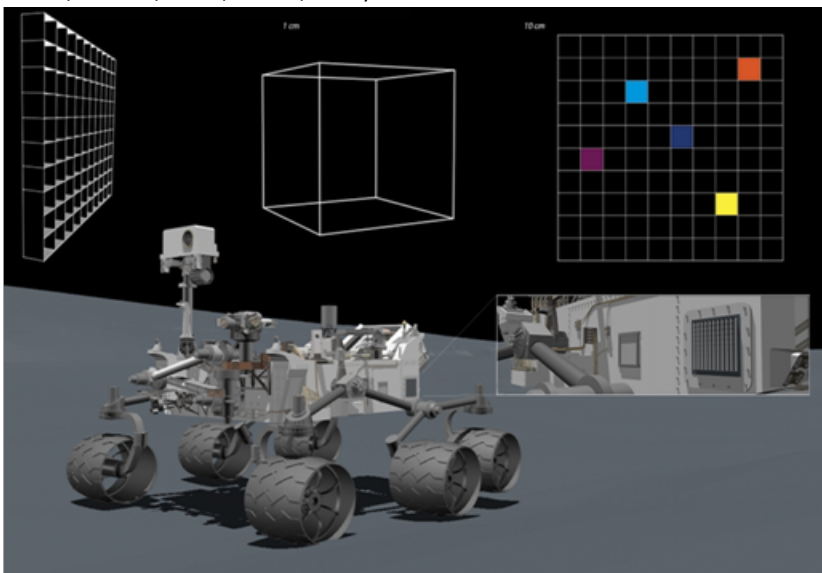


Fig.1. Moon Gallery intended venue impression

Biosolar powered holographic imaging of microscopic aerial inhabitants

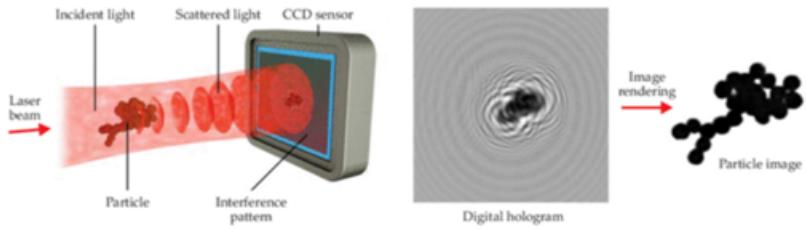


Fig.2. Art Scientist submission for Moon Gallery 1 x 1 x 1 cm cell.

References:

- [1] Zaklynsky A. et al.// ELS, 2018, p. 209;
- [2] Zaklynsky A. et al.// COSPAR, 2018;
- [3] Toroop M.// Spring Issue Pulchri, 2018, p. 11

THE HISTORY OF RESEARCHES OF THE MOON BY SPACE VEHICLES DEPICTED ON THE POSTAGE STAMPS OF THE WORLD

R. Dicati¹, Z. Rodionova²

¹USFI (Unione Stampa Filatelica Italiana) Milan, Italy,
renato.dicati@gmail.com

²Sternberg State Astronomical Institute 119992 Universitetskiy pr.13
marss8@mail.ru

Keywords:

Astrophilately, space research, astronautics, postage stamps

Astrophilately – the collection and study of postage stamps and other postal and philatelic documents and media related to astronautics and space research. Although the spatial philately was born after the launch of the first artificial satellite, Sputnik 1, the first its stamps is included in a set dedicated to Soviet Union scientists, issued in August 15, 1951, that depicts Konstantin Tsiolkovsky, the father of astronautics and the first image of a cosmic rocket. A few days after the launch of Sputnik, on October 7, 1957, two stamps were issued: the first belonging to the set dedicated to the International Geophysical Year, contains the text ‘research with rockets’ and an image in which a rocket is drawn on the background of a starry sky. The second stamp, dedicated to the birth’s centenary of Tsiolkovsky, shows the portrait of the scientist and, in the background, a rocket and the planet Saturn. On this stamp November 28, 1957, a black overprint was imprinted with the words “4 October 1957 the first Earth’s artificial satellite”. This was the first real astrophilatelic issue [1].

The first original space stamps were issued on November 5, 1957 by the Soviet Union. They represent the *Sputnik 1* satellite in orbit around the globe, with words “October 4,1957. The Soviet artificial Earth’s satellite, first in the world”. Before the end of 1957 as many as 15 stamps dedicated to Sputnik were issued by four countries (USSR, Romania, Czechoslovakia, and the German Democratic Republic). In the following years, space stamps dedicated to the most important satellites multiplied and in 1969, the year of the conquest of the Moon, at least 88 countries from all continents have already issued space stamps. Of about two thousand stamps. Approximately half of this material was devoted to astronauts and satellites of the USA and the first satellites launched from France, Italy, Canada, and UK. Since the 70s many other countries, such as Japan,, China, India and Indonesia, Israel, Sweden, Brazil, Argentina, Mexico and many others, will issue commemorative stamps of their national satellites. In 1969, the Apollo 8 issue received 900,000 First-Day cancels while others received less than half this amount.

Many of the stamps and poster documents, particularly those issued by major space countries, contain scientific information which help to build, even in details, the history of space exploration. One of the most interesting stamps that celebrates the early space missions was issued on October 12, 1959, by the Soviet Union for the mission of Luna 3 space probe that had just photographed the far side of the Moon. On a surface of about only 10 cm² there is not only the outline of the trajectory followed by the spacecraft, with relative positions of the Moon and the station during the spaceflight, but also an explanatory text of 48 words and 5 numeric values [2] (Fig. 1). On another postage stamp dedicated to the same mission a map of the Moon’s far side, with the main features and craters discovered by Luna 3, is depicted.

There are examples of postal stamps devoted to space research on Fig 1.

References:

- [1]Dicati Renato. Stamping Through Astronomy. Springer. Switzerland. 2013. 373 p.
[2]Dicati Renato. Stamping the Earth from Space. Springer. Switzerland. 2017 . 429 p.



Fig.1 Examples of postal stamps.

CUMULATIVE FORMATION OF MARES AND MASCONS ON MOON BY GALACTIC COMETS

A.A. Barenbaum¹, M. I. Shpekin²

¹Oil and Gas Research Institute RAS, Gubkin str. 3, Moscow, 119991, Russia, azary@mail.ru;

²Kazan Federal University, Kremlyovskaya 18. Kazan, Tatarstan 420008, Russia, michael1@yandex.ru

Keywords:

craters, mares and mascons, galactic comets.

Introduction:

It is known [1, 2] that the formation of large craters ($D > 10$ km), mares and mascons on the Moon, Mars and Mercury cannot be explained by falls of asteroids and comets of Solar System. This conclusion follows from the fact that the distribution along the diameters of large craters and mares on these celestial bodies (figure 1) is sharply different from the back-quadratic dependence inherent in bodies in asteroid belt. Only mariner craters with $D < 10$ km have such power-law dependence along sizes.

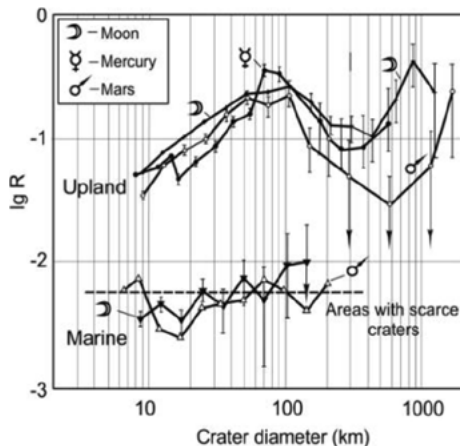


Fig. 1. Differential R-distributions of craters along diameters [3]. The upper dependences refer to “upland” craters on continental areas of the surface; the lower graphic refers to “marine” craters in sea basins

We have established [4–8] that “upland” craters, mares and mascons on the Moon, Mars and Mercury have been created not by falls of interplanetary bodies in 4–3 billion years ago, as is nowadays thought, but arose in result of ~2–3 last bombardments of Solar System by galactic comets.

Such bombardments have duration of ~2–5 million years and are cyclically repeated in 20–37 million years [9]. The last bombardment, which led to formation of these structures as well as coming of a large mass of water on Moon, occurred in the period from 0.7 million years ago. The density of cometary fallings was ~3–5 on an area of 100×100 km².

Galactic comets moved relative to Sun at a speed of ~450 km/s, they consisted mainly of water ice, had a diameter of core ~0.1÷3.5 km, a mass of $\sim 10^{12} \div 10^{17}$ g, and an energy of $\sim 10^{20} \div 10^{25}$ J. Distribution of cometary nuclei over diameters was exponential. Therefore the impact structures created by cometary bombardments also will have exponential size-distribution along diameters $N(D) = N(0)\exp(-\lambda D)$.

Actual data and their explanation:

In figure 2 [9] in semi-logarithmic coordinate system are shown cumulative distributions of densities of the “upland” craters on sizes on Moon, Mars and Mercury, constructed from the data of [10]. And in figure 3 shows similar distributions of mares on near side of Moon (black rhombuses) and on far side (red squares) respectively [2].

All distributions obey an exponential dependences indicating on of craters and mares formation by galactic comets. The size-distribution of "upland" craters is characterized by $\lambda_{cr} = 3.3 \cdot 10^{-2} \text{ km}^{-1}$. While for the mares on near side of Moon $\lambda_{ns} = 1.92 \cdot 10^{-3} \text{ km}^{-1}$ and on far side $\lambda_{fs} = 2.85 \cdot 10^{-3} \text{ km}^{-1}$.

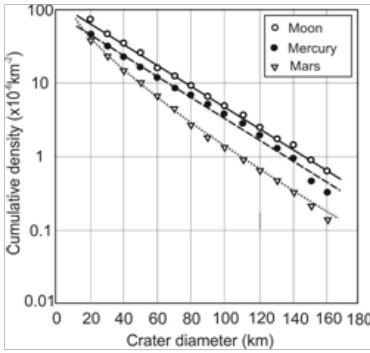


Fig. 2. Integral size-distribution of "upland" craters on Moon, Mercury and Mars [9] constructed from the data [10]

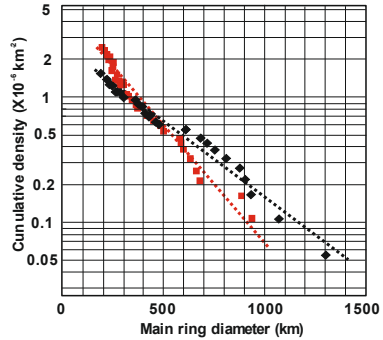


Fig. 3. Integral size-distribution of lunar mares with mascons [2] in a semi-logarithmic coordinate system

It is shown in [8] that the distinction in distribution of mares on both sides of the Moon is explained by the "cumulative" mechanism of sea basins (mares) formation. The essence of this mechanism is that with intensive cometary bombardments, crater funnels from falls of many comets are superimposed on each other. This leads to an increase in diameter of resultant crater and growth of temperature of the underlying rocks. The essence of this mechanism is that with intensive cometary bombardments, crater funnels from the falls of many comets are superimposed on each other. This leads to an increase in diameter of resultant crater and growth of temperature of the underlying rocks. At this, on the one hand, a large amount of lava is formed, which fills the crater, turning it into sea basin, and on the other, dense deep-lying (mantle) rocks undergo heating and melting, which causes their lifting, as well as the appearance over sea basins of positive Bouguer gravity anomalies.

Since the fall of galactic comets is a random process. The formation of lunar craters, mares and mascons by galactic comets can be studied on the basis of probability theory. This theory operates with values of mathematical expectations M , characterizing the average values of random variables.

Assuming that the craters formation is random process characterized by their average diameter, we define the value M as:

$$M = \frac{n_0 \int_{\alpha}^b D e^{-\lambda D} dD}{n_0 \int_{\alpha}^b e^{-\lambda D} dD} = \frac{(\alpha + \lambda^{-1}) e^{-\lambda \alpha} - (b + \lambda^{-1}) e^{-\lambda b}}{e^{-\lambda \alpha} - e^{-\lambda b}},$$

where: n_0 and λ are constants, and diameters of craters are within $\alpha \leq D \leq b$. Parameters required for the calculation, we take from data in figures 2 and 3. As a result, we obtain that for craters $M_{cr} \approx 39 \text{ km}$ and for mares on the near and far sides of Moon $M_{ns} \approx 520 \text{ km}$ and $M_{fs} \approx 350 \text{ km}$, respectively.

Assuming that mares arise as a result of accidental overlapping of craters from fall of several comets, we conclude that mares on the near side of Moon were formed on average from falls of $K = M_{ns} / M_{cr} \approx 13$ comets, and on the far side from $K = M_{fs} / M_{cr} \approx 10$ comets.

These differences we explain by the different thickness of the crust on both Moon sides. Other things being equal, a decrease in the thickness of refractory anorthosite crust leads to the formation of larger sea basins.

Note, that the "cumulative" model is also applicable to the mascons [2, 11]. As the number K increases, the thermal energy transferred to the rocks increases, as a result of which not only size of resulting crater grows, but also the volume of magmatic melts that have poured out of crater increases,

as well as the depth of occurrence under the crater of the magma chambers. Therefore, as the size of the sea basins increases, the amplitude of the Bouguer gravitational anomalies also increases (figure 4).

Conclusion:

The cumulative forming model of the sea basins and mascons on the Moon [8] as a result of accidental imposition of craters created by falls of the order of 10 galactic comets is substantiated.

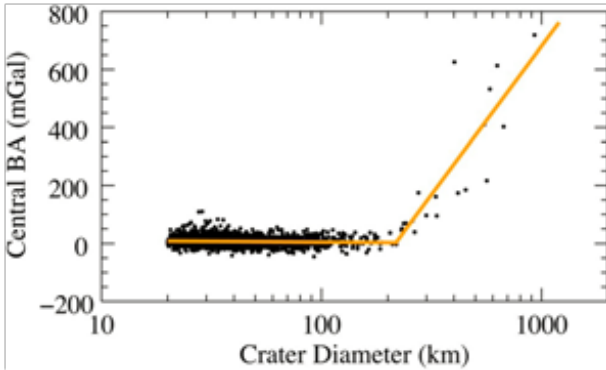


Fig. 4. Amplitude of central gravitational Bouguer anomaly over continental craters of the Moon. Orange line shows author's model [11]

References:

- [1] Woronow A. Crater saturation and equilibrium: A Monte Carlo simulation // *J. Geophys. Res.* 1977, V. 82, P. 2447–2456, doi: 10.1029/JB082i017p02447.
- [2] Neumann G.A. et al. Lunar impact basins revealed by Gravity Recovery and Interior Laboratory measurements. *Science Advances*, 1, 2015, e1500852.
- [3] Woronow A., Strom R.G., Garkis M. Interpretation of the crater chronicle: from Mercury to Ganymede and Callisto // *Satellites of Jupiter*, ed. D. Morrison, Publishing House: Mir, Moscow, 1986, V.2. P. 5–48.
- [4] Barenbaum A.A. Shpekin M.I. About age of the lunar surface // *Vestnik ONZ RAS*, V.3, NZ6011, doi: 10.2205/2011NZ000141.
- [5] Barenbaum A.A. On the mechanism of energy dissipation of galactic comets bombarding terrestrial planets // *Journal of Physics: Conf. Ser.* 2015, 653, 012073, doi: 10.1088/1742-6596/653/1/012073.
- [6] Barenbaum A.A. Shpekin M.I. To the development of the mechanism of interaction of galactic comets with the terrestrial planets // *Journal of Physics: Conf. Ser.* 2016, 774, 012096, doi:10.1088/1742-6596/774/1/012096.
- [7] Barenbaum A.A., Shpekin M.I. Problem of lunar mascons: An alternative approach // *Journal of Physics: Conf. Ser.* 2018, 946, 012079, doi:10.1088/1742-6596/946/1/012079.
- [8] Barenbaum A.A., Shpekin M.I. Origin and formation mechanism of craters, seas and mascons on the Moon // *Journal of Physics: Conf. Ser.* 2018, <http://www.ihe.d.ras.ru/elbrus18/proc/accepted/>
- [9] Barenbaum A.A. *Galactocentric Paradigm in Geology and Astronomy*. Publishing House: LIBROKOM, Moscow, 2010, 546 p.
- [10] Kazimirov D.A., Rodionova Zh.F., Sitnikov B.D., Poroshkova G.A. Planetary regularities in the craters distribution on the Mars, Moon and Mercury. Preprint GIN-GAISH, Moscow. 1981.
- [11] Soderblom J.M. et al. The fractured Moon: Production and saturation of porosity in the lunar highlands from impact cratering // *Geophys. Res. Lett.*, 2015, 42, 6939–6944, doi: 10.1002/2015GL065022.

GALAXY CYCLES IN SOLAR SYSTEM

A.A. Barenbaum

Oil and Gas Research Institute RAS, Gubkin str. 3, Moscow, 119991, Russia, Moscow, azary@mail.ru

Keywords:

Galaxy's spiral structure, galactic cycles

Introduction:

The repetition of analogous global geological events through ~ 30 , ~ 250 or more million years is a phenomenon hard established on Earth. Earlier it was considered [1] that this cyclicity is caused by processes in Earth's core. Due to the discovery of the phenomenon of jet flow of gas-dust substance from nuclear disk of spiral galaxies [2], it is now established that the cause of the cycles is bombardments of the Solar system by galactic comets. Therefore such cyclicity is a phenomenon that covers not only the Earth, but other planets and the entire Solar system.

A theoretical model has been developed that substantiates this conclusion. The model is based on calculating the orbit of Sun's motion in the Galaxy and calculating the times moments, when the Sun intersects jet streams and galactic spiral arms. At present, the model has been tested at solving a number of major problems of geology and other natural sciences [2].

The first cycle lasting 19-37 million years is due to Sun intersection of jet streams, and the second with a strict period $T = 1$ billion years is caused by Sun entry in galactic arms at a distance of the corotation radius from Galaxy center. Both cycles play an important role in the development of planets and Solar system as a whole.

Model:

Fig. 1 in the projection of Galaxy's equatorial plane shows the present position of the Sun with respect to four logarithmic arms (stained) [3] and two Archimedean jet streams (dashed lines) [4]. The calculated Keplerian orbit of the Sun motion (ellipse) in our Galaxy, which best satisfies astronomical observations and geology data [2], is also shown there.

The system of galactic arms and the nuclear disk from which jet streams expire (dotted circle in center) rotate uniformly. The rotation period of arms is $T_G = 222.23$ million years, the rotation period of nuclear disk is $T_d = 50$ million years. The Sun also revolves around Galaxy center in its orbit. Its orbital period is $T_s = 250$ million years. With the complete Sun's turn around Galaxy center the line of apses of solar orbit turns through an angle of 45° .

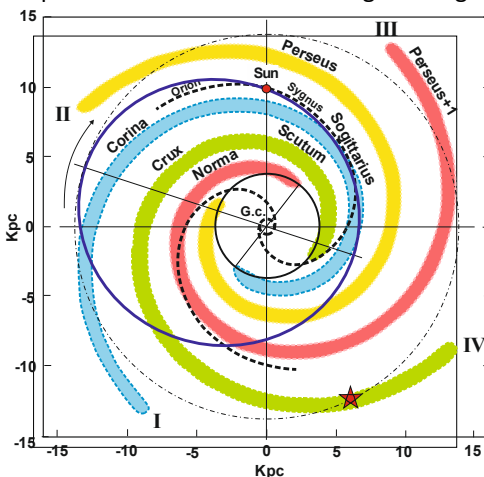


Fig. 1.

A large dotted circle denotes the corotation radius of Galaxy. The arrow

indicates the direction of Sun's movement, which coincides with rotation of galactic arms as well as of line of apses (straight line) of solar orbit. Due to different rotation speeds of nuclear disk and galactic arms, as well as the orbital Sun movement their mutual position in time varies. At that the Sun crosses spiral arms and jet streams of Galaxy for a short time. And then all planets are subjected to intense bombardments by galactic comets. In the Earth geological history these bombardments are marked as times of global natural disasters [2], which geologists consider as the boundaries of the eras, periods and epochs of the Phanerozoic geochronological scale.

The cycle lasting ~30 million years:

In Figure 2 [5] show the variation of Sun distance from Galaxy center (solid curve) and four galactic arms in time. Circles and squares on this curve correspond to the time (numerals) of Solar system's stay, respectively, in jet streams and in zones of star formation of galactic arms, when all planets are subjected to intense bombardment by galactic comets.

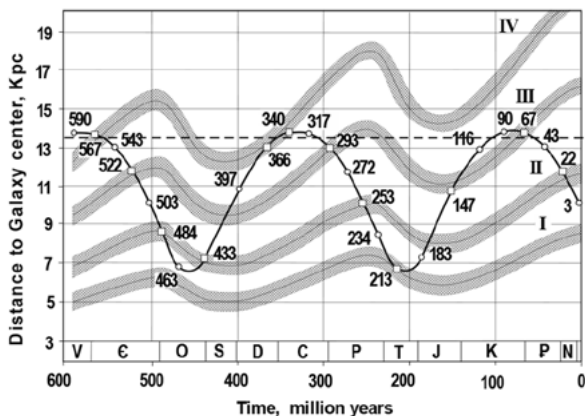


Fig. 2.

This calculation explains the nomenclature of the stratons borders of the Phanerozoic geochronological scale. Namely, borders of the "epochs" correspond to the times of the Sun's being in jet streams; borders of "periods" – in zones of star formation of galactic arms; and borders of "eras" – in the same zones at a distance of corotation radius from Galaxy center.

The last cometary bombardment took place from 5 to 0.7 million years ago, when Sun crossed the Orion-Cygnus jet flow (Fig. 1). This bombardment caused on Earth the newest uplifts of continents [6], and on Mars and Moon also led to the formation of large craters, seas and mascons [7].

The cycle with a strict period of 1 billion years:

In [8], we established that Precambrian geological mega events [9, 11] obey a general regularity (Fig. 3). Since rotation periods of Sun and galactic arms are connected by the ratio $8T_s = 9T_g$, after 8 full turnovers, Sun enters the same galactic arms as exactly 2 billion years ago.

Table 1: Communications of Precambrian mega-events with Galaxy arms

Galaxy arm	Time, billion years	Bounders of «aeons» and «eonotems» [10]
I. Corina-Sogittarius	–	
II. Perseus	1.567 3.567	Mesoproterozoic Archaean
III. Norma-Perseus+1	1.067 3.067	Neoproterozoic Mesoarchaean
IV. Crux-Scutum	0.567 2.567 4.567 6.567	Phanerozoic Proterozoic Second cycle of planet formation [2] Formation of the Solar system [2]

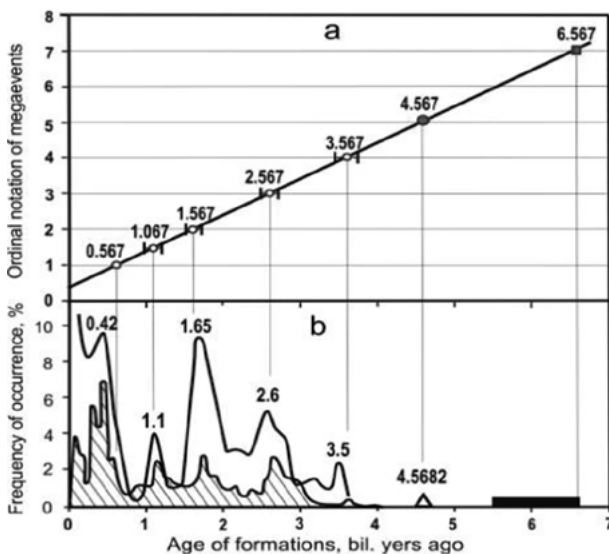


Fig. 3.

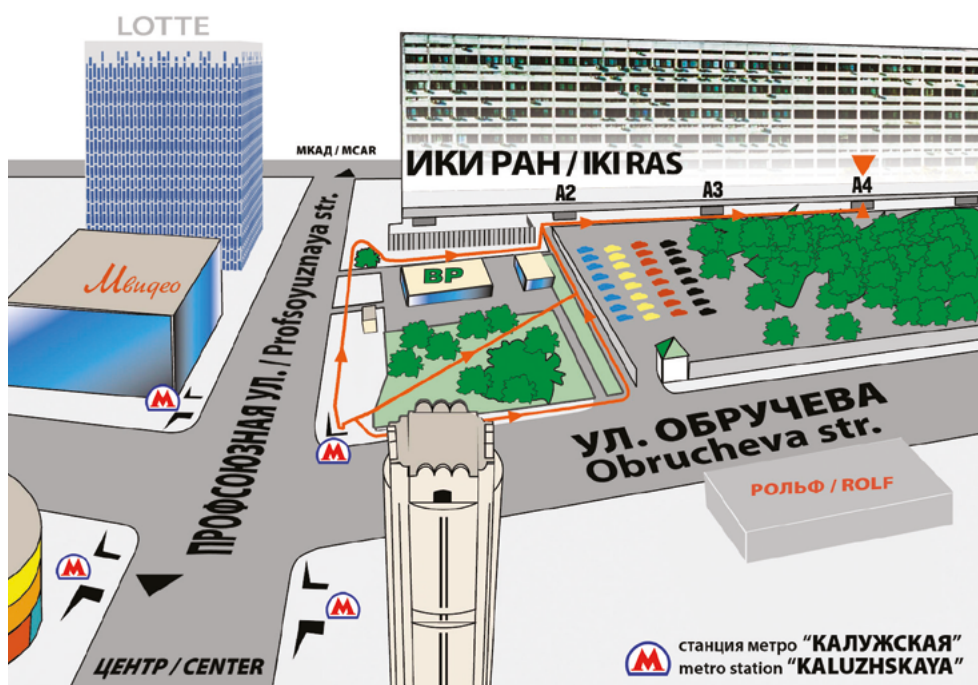
Data in Fig. 3 show that all the most important events in history of Earth and Solar System occurred in galactic arms at a distance of the corotation radius from Galaxy center. At that, both main cycles of Solar system formation [2], as well as events on Earth at borders of Phanerozoic and Proterozoic took place in the arm IV. Events of lesser significance at borders of Neoproterozoic and Mesoarchaeon are in arm III. And even less important events at borders of Archaeon and Mesoproterozoic are in arm II. Whereas analogical mega events in arm 1 apparently were absent. The place in arm IV where Solar system arose is indicated in Fig. 1 by asterisk.

Conclusion:

The author pointed to the need for a transition in comparative planetology to the representations of Galactocentric paradigm in [12]. In this article, this conclusion receives additional astronomical and geological justification.

References:

- [1] Dobretsov N.L. Mantle superplumes as the cause of the main geological periodicity and global rearrangements // *Doklady RUS.* 1997. V.457. № 6. P. 797-800.
- [2] Barenbaum A.A. Galactocentric Paradigm in Geology and Astronomy. Moscow. Publishing House: LIBROKOM. 2010. 546 p.
- [3] Valle J.P. A guided map to the spiral arms in the galactic disk of the Milky Way. <https://doi.org/10.1080/21672857.2017.1379459>
- [4] Barenbaum A.A. Galaxy, Solar system, Earth. Subordinated processes and evolution. Moscow. Publishing House: GEOS. 2002. 393 p.
- [5] Barenbaum A.A., Gladenkov Yu.B., Yasamanov N.A. Geochronological scales and astronomical time // *Stratigrafiya. Geol. korrelyatsiya.* 2002. V.10. №2. P. 3-14.
- [6] Barenbaum A.A. Shpekin M.I. To the development of the mechanism of interaction of galactic comets with the terrestrial planets // *J. Phys: Conf. Ser.* 774, 2016, 012096 doi:10.1088/1742-6596/774/1/012096
- [7] Barenbaum A.A. Shpekin M.I. Problem of lunar mascons: An alternative approach // *J. Phys.: Conf. Ser.*, 2018, 946, 012079, doi:10.1088/1742-6596/946/1/012079
- [8] Barenbaum A.A. On two approaches to the study of Cosmos in modern natural science // *J. "Actual problems of aviation and aerospace systems"*, 2017№.2(45), v.22, p.89-96,
- [9] Pushkarev Yu.D. Megacycles in the evolution of the system: Earth crust – mantle. Leningrad: Science. 1990. 217 p.
- [10] Sobotovich E.V. Isotope Cosmochemistry. Publishing House: Atomizdat, Moscow. 1974. 208 p.
- [11] Plumb K.A. New Precambrian time scale // *Episodes.* 1991. V.14. №2. P. 139-140.
- [12] Barenbaum A.A. On the modern state of comparative planetology // *The Seventh Moscow Solar System Symposium* 10-16.10.2016. 7MS3-PS-68.



ИКИ РАН

площадь академика Келдыша

Метро "Калужская", первый вагон из центра, по тоннелю — прямо, по второму поперечному тоннелю- направо, выход на площадь, далее по стрелкам на схеме

IKI RAS

You should get off at "Kalyzhskaya" metro station using the southern exit. After leaving a station lobby through glass doors you should go straight to the end of the tunnel, then take right and use the stairs to get to the surface. From this point you may follow either arrow on this map

MOSCOW METRO SCHEME



- Sokolnicheskaya
- Zamoskvoretskaya
- Arbatko-Pokrovskaya
- Filyovskaya
- Koltsevaya Circle line
- Kaluzhsko-Rizhskaya
- Tsvetnoy-Kosmoprisenenskaya
- Kakhovskaya
- Babushkinskaya
- Serpukhovsko-Timiryazevskaya
- Lyublinskoye-Dmitrovskaya
- Bobyleva Koltyevaya (big circle line)
- Kakhovskaya
- Butovskaya
- Monorail operates in tourist mode
- Moscow Central Circle
- Koshkovskaya
- Under construction
- Transfer stations
- Cross-platform transfers
- Ground transfers
- Park-and-ride
- Wheelchair-accessible stations
- ➔ DME Airports
- ➔ Aeroexpress trains to airports
- ➔ Rail terminals
- ➔ Railway stations
- ➔ Bus terminals and stations
- ➔ Bus transportation to airports
- ➔ Stadiums
- ➔ FIFA Venue Ticketing Centre
- ➔ FIFA Fan Fest
- ➔ Live counter stations
- ➔ Souvenirs

СХЕМА МОСКОВСКОГО МЕТРОПОЛИТЕНА



REGISTRATION AND INFORMATION DESK

location: IKI, entrance A-4

time:

8 october, 8:30–18:00

9 -12 october, 9.00-18.00

SCIENTIFIC SESSIONS

location: IKI conference hall, second floor

POSTER SESSIONS

location: IKI exhibition hall, ground floor

time:

8 october, 18.00-19.00

10 october, 18.00-19.00

SOCIAL PROGRAM

7 october, sunday	8 october, monday	9 october, tuesday	10 october, wednesday
16-00 TURANDOT <i>opera</i> Helikon-Opera			
18-00 STARS OF THE 21ST CENTURY KREMLIN GALA <i>ballet</i> State Kremlin Palace			
19-00 DANCE ENSEMBLES <i>concert</i> Moscow International Performing Arts Center, Svetlanov Hall	19-00 WELCOME PARTY Space Research Institute(IKI)	19-00 MOSCOW VIRTUOSI AND CHRISTIAN ZACHARIAS <i>concert</i> Moscow International Performing Arts Center, Svetlanov Hall	19-00 ORGAN AND MORE.SEQUEL <i>concert</i> Moscow International Performing Arts Center, Svetlanov Hall
19-00 L'ELISIR D'AMORE <i>opera</i> Stanislavsky and Nemirovich-Danchenko Moscow Music Theatre	19-00 MADAMA BUTTERFLY <i>opera</i> Stanislavsky and Nemirovich-Danchenko Moscow Music Theatre	19-00 JOHANN STRAUSS, THE WALTZ KING <i>concert</i> Novaya Opera Theatre Of Moscow	19-00 STATE SYMPHONY CAPELLA OF RUSSIA,VALERY POLYANSKY <i>concert</i> Tchaikovsky Concert Hall, Main Stage
	20-00 ILYA BESHEVLI, PIANO <i>concert</i> Moscow International Performing Arts Center, Svetlanov Hall		19-00 LA BOHÈME <i>opera</i> Stanislavsky And Nemirovich-Danchenko Moscow Music Theatre

for additional information please contact Mrs Tatiana Zharkova
E-mail: zharkovaiki@yandex.ru

11 october, thursday	12 october, friday	13 october, saturday
<p>17-00 CONCERT</p> <p>Space Research Institute(IKI)</p>		<p>11-00 – 22-00 THE COSMONAUTICS AND AVIATION CENTRE</p> <p>VDNH Museum’s exposition</p>
<p>18-00 RECEPTION</p> <p>Space Research Institute(IKI)</p>		
<p>19-00 P.I.TCHAIKOVSKY. SUITES AND SYMPHONIES <i>concert</i></p> <p>Tchaikovsky Concert Hall, Main Stage</p>	<p>19-00 MANON <i>ballet</i></p> <p>Stanislavsky and Nemirovich-Danchenko Moscow Music Theatre</p>	<p>19-00 JESUS CHRIST SUPERSTAR <i>rock-opera</i></p> <p>Moscow International Performing Arts Center, Theatre Hall</p>
<p>19-00 MANON <i>ballet</i></p> <p>Stanislavsky and Nemirovich-Danchenko Moscow Music Theatre</p>		<p>19-00 ROMEO AND JULIET <i>ballet</i></p> <p>State Kremlin Palace, Great Hall</p>
<p>19-00 LOHENGRIN opera</p> <p>Novaya Opera Theatre Of Moscow</p>		

INTERNET ACCESS AND WIFI

there is Internet access in and near the conference hall

точки питания вблизи ИКИ / lunch points nearest to IKI



1. ИНСТИТУТ КОСМИЧЕСКИХ ИССЛЕДОВАНИЙ РАН, столовая, 1 этаж, секция А3
SPACE RESEARCH INSTITUTE OF THE RAS, Food center, Ground Floor, Section A3
2. ТЦ "КАЛУЖСКИЙ", ул. Профсоюзная, д. 61А, зона ресторанов, 2 этаж
"KALUZHSKIY" Market Center, Profsoyuznaya Street, 61A, 2 Floor
3. Ресторан "ПроКафе" в Бизнес-центре Газпром, ул. Обручева, 23
"ProKafe" restaurant in Bussiness Center Gas Field, Obrucheveva street 23
4. Кафе "АндерСон" на ул. Обручева, д. 30/1
Café "AnderSon", Obrucheveva Street 30/1, Obrucheveva street 23

